PB83-164483

Proceedings of the Fifth Fundamental Combustion Research Contractors Workshop

Energy and Environmental Research Corp.
Irvine, CA

Prepared for

Industrial Environmental Research Lab.
Research Triangle Park, NC

Jan 83

U.S. Department of Commerce
National Technical Information Service
NTIS

PB83-164483

EPA-600/9-83-001
January 1983

PROCEEDINGS OF THE FIFTH FUNDAMENTAL COMBUSTION RESEARCH CONTRACTORS WORKSHOP

M.P. Heap, Compiler
Energy and Environmental Research Corporation
18 Mason
Irvine, California 92714

EPA Contract 68-02-2631

Symposium Chairman

W.S. Lanier
U.S. Environmental Protection Agency
Industrial Environmental Research Laboratory
Research Triangle Park, North Carolina 27711

Prepared for

U.S. Environmental Protection Agency
Office of Research and Development
Washington, DC 20460

REPRODUCED BY
NATIONAL TECHNICAL
INFORMATION SERVICE
U.S. DEPARTMENT OF COMMERCE
SPRINGFIELD, VA. 22161

TECHNICAL REPORT DATA

(Please read Instructions on the reverse before completing)

1. REPORT NO. EPA-600/9-83-001	2.	3. RECIPIENT'S ACCESSION NO. PB83-164483
4. TITLE AND SUBTITLE Proceedings of the Fifth Fundamental Combustion Research Contractors Workshop		5. REPORT DATE January 1983
		6. PERFORMING ORGANIZATION CODE
7. AUTHOR(S) M. P. Heap, Compiler		8. PERFORMING ORGANIZATION REPORT NO.
9. PERFORMING ORGANIZATION NAME AND ADDRESS Energy and Environmental Research Corporation 18 Mason Irvine, California 92714		10. PROGRAM ELEMENT NO.
		11. CONTRACT/GRANT NO. 68-02-2631
12. SPONSORING AGENCY NAME AND ADDRESS EPA, Office of Research and Development Industrial Environmental Research Laboratory Research Triangle Park, NC 27711		13. TYPE OF REPORT AND PERIOD COVERED Proceedings; 1/77-1/80
		14. SPONSORING AGENCY CODE EPA/600/13

15. SUPPLEMENTARY NOTES IERL-RTP project officer is W. Steven Lanier, Mail Drop 65, 919/541-2432.

16. ABSTRACT

These proceedings are for the Fifth EPA Fundamental Combustion Research Contractors Workshop, held January 23-25, 1980, in Newport Beach, CA. The purpose of the workshop was to exchange information between the various contractors engaged in fundamental combustion research for EPA and to coordinate their activities. In addition, the workshop provided for a review of EPA's Fundamental Combustion Research (FCR) Program by EPA's Science Advisory Board. The workshop sessions dealt with gas-phase chemistry and heterogeneous NO reduction, chemical and physical effects of thermal decomposition, bench-scale reactor studies, two-phase turbulent flames, and model development. The main thrust of EPA's FCR program is elucidating the mechanism of NO formation from fuel-bound nitrogen. Several papers addressed the gas-phase conversion of fuel nitrogen species to NO, N2, HCN, or NH3. Advanced diagnostic techniques were used to investigate the physical changes taking place during the thermal decomposition of pulverized coal particles. Bench-scale reactor data were presented on the conversion of fuel-bound nitrogen to NO in liquid- and solid-fuel flames. Studies on turbulent diffusion flames included detailed characterization of nonswirling coal flames and methods of measuring droplet size from fuel oil atomizers.

17. KEY WORDS AND DOCUMENT ANALYSIS

a. DESCRIPTORS		b. IDENTIFIERS/OPEN ENDED TERMS	c. COSATI Field/Group	
Pollution	Pyrolysis	Pollution Control	13B	
Combustion	Flames	Stationary Sources	21B	
Research	Turbulent Flow	Gas-phase Chemistry	14F	20D
Nitrogen	Mathematical Models		07B	12A
Nitrogen Oxides	Measurement			14B
Gases	Analyzing		07D	

18. DISTRIBUTION STATEMENT Release to Public	19. SECURITY CLASS *(This Report)* Unclassified	21. NO. OF PAGES 643
	20. SECURITY CLASS *(This page)* Unclassified	22. PRICE

EPA Form 2220-1 (9-73)

NOTICE

THIS DOCUMENT HAS BEEN REPRODUCED FROM THE BEST COPY FURNISHED US BY THE SPONSORING AGENCY. ALTHOUGH IT IS RECOGNIZED THAT CERTAIN PORTIONS ARE ILLEGIBLE, IT IS BEING RELEASED IN THE INTEREST OF MAKING AVAILABLE AS MUCH INFORMATION AS POSSIBLE.

NOTICE

This document has been reviewed in accordance with U.S. Environmental Protection Agency policy and approved for publication. Mention of trade names or commercial products does not constitute endorsement or recommendation for use.

BEGIN FIRST LINE OF TEXT HERE
CENTER OF PAGE
TOP OF IMAGE AREA
DROPPED HEAD; BEGIN SECTIONS HERE

ABSTRACT

These proceedings are for the Fifth EPA Fundamental Combustion Research Contractors Workshop, held January 23, 24, and 25, 1980, in Newport Beach, CA. The purpose of the workshop was to exchange information between the various contractors engaged in fundamental combustion research for EPA and to coordinate their activities. In addition, the workshop provided for a review of EPA's Fundamental Combustion Research (FCR) Program by EPA's Science Advisory Board. The five conference sessions dealt with gas-phase chemistry and heterogeneous NO reduction, chemical and physical effects of thermal decomposition, bench-scale reactor studies, two-phase turbulent flames, and model development.

The main thrust of the FCR program is elucidating the mechanism of NO formation from fuel-bound nitrogen. Several papers addressed the gas-phase conversion of fuel-bound nitrogen species to NO, N_2, HCN, or NH_3. Advanced diagnostic techniques were used to investigate the physical changes taking place during the thermal decomposition of pulverized coal particles. Bench-scale reactor data were presented on the conversion of fuel-bound nitrogen to NO in liquid- and solid-fuel flames. Studies on turbulent diffusion flames included detailed characterization of nonswirling coal flames and methods of measuring droplet size from fuel oil atomizers. Engineering analysis is a strong component of EPA's FCR program, and papers were presented on the analysis of turbulent diffusion flames.

BEGIN LAST LINE OF TEXT
3/8"
BOTTOM OF IMAGE AREA; OUTSIDE DIMENSION FOR TABLES AND ILLUSTRATIONS

PAGE NUMBER
EPA Form 2350-4 (4-80)
(PREVIOUSLY CIN. EPA FORM 287)
© U.S. GOVERNMENT PRINTING OFFICE 1981-[illegible]
TYPING GUIDE SHEET

Table of Contents

Page

"Introduction to Fifth EPA Fundamental Combustion Research Contractors Workshop," W. S. Lanier 1

Session I: Gas-Phase Chemistry and Heterogeneous NO Reduction

"Modeling of Fuel-Nitrogen Chemistry in Combustion: The Influence of Hydrocarbons," J. M. Levy 18

"Development of a Kinetic Mechanism to Describe the Fate of Fuel Nitrogen in Gaseous Systems," T. L. Corley 68

"NO_x Formation in Flat, Laminar, Opposed Jet Methane Diffusion Flames," W. A. Hahn, J. O. L. Wendt 102

"The Formation and Destruction of Nitrogenous Species During Hydrocarbon/Air Combustion," D. W. Blair 128

"Laboratory Scale Coal Studies," J. M. Beer, A. F. Sarofim, J. M. Levy, D. Altrichter, L. Timothy 146

"Mechanisms of Nitric Oxide Reduction on Solid Particles," G. G. De Soete 174

Session II: Thermal Decomposition--Chemical and Physical Effects

"Volatility of Fuel Nitrogen," R. L. Gay, A. E. Axworthy, V. H. Dayan, H. L. Recht 249

"High Temperature Pyrolysis of Oil Droplet and Coal Particle Streams," J. M. Beer, A. F. Sarofim, S. P. Hanson, A. K. Gupta . . 277

"The Characterization of Coals During Thermal Decomposition," P. R. Solomon 307

"The Physical and Chemical Effects Occurring During the Thermal Decomposition of Coal Particles and Oil Droplets," W. R. Seeker, G. S. Samuelsen, M. P. Heap 333

Session III: Bench Scale Reactor Studies

"Pollutant Formation During the Combustion of Residual Fuel Oils in a Well-Stirred Reactor," M. Murphy 358

"Pollutant Formation from Combusting Pulverized Coal Clouds," P. M. Goldberg, H. Tong, R. Kendall 359

Page

"Reactor Studies to Assess the Impact of Fuel Characteristics on Fuel NO_x Formation," M. P. Heap, D. W. Pershing, G. C. England, S. L. Chen, R. Nihart, D. P. Rees 400

"Pollutant Formation During Fixed-Bed and Suspension Coal Combustion," G. P. Starley, S. P. Purcell, S. L. Manis, D. M. Slaughter, D. W. Pershing 434

Session IV: Two Phase Turbulent Diffusion Flames

"An Experimental Approach to the Study of Heavy Oil Spray Combustion in Shear Layers," A. Vranos, B. A. Knight 461

"Spray Characterization," W. R. Seeker, G. S. Samuelsen 495

"The Application of Droplet Sizing Interferometry and Holography to the Measurement of Spray Droplet Size and Velocity," C. F. Hess, W. D. Bachalo 518

"Characterization of Long Turbulent Pulverized Coal Diffusion Flames," R. Payne 546

Session V: Model Development

"Development of a Coherent Flame Model for Turbulent Chemically Reacting Flows," F. E. Marble, J. E. Broadwell 547

"General Kinetic Analysis Codes," C. J. Kau, T. J. Tyson 610

INTRODUCTION TO FIFTH EPA FUNDAMENTAL COMBUSTION RESEARCH CONTRACTORS WORKSHOP

W. S. Lanier
U.S. EPA
Industrial Environmental Research Lab
Combustion Research Branch
Research Triangle Park, N.C.

Fifth EPA Fundamental Combustion Research Workshop
Newport Beach, California
January 23-25, 1980

INTRODUCTION

At approximately eighteen month intervals the U. S. Environmental Protection Agency sponsors a coordinating meeting which draws together principal investigators from the spectrum of projects which constitute the Fundamental Combustion Research (FCR) program. This document is a compilation of the papers presented at the fifth FCR Contractor's Coordinating Meeting in Newport Beach, California, on January 23-25, 1980. The purpose of this series of meetings is to familiarize the various principal investigators with the range of fundamental research being pursued, to assure that the principal investigators are aware of how their particular project is integrated into the overall FCR program, and, finally, to provide an open forum for candid interaction between peers.

Organizationally, the FCR program is funded through the Combustion Research Branch (CRB) of EPA's Industrial Environmental Research Laboratory in Research Triangle Park, North Carolina (IERL-RTP). The CRB charter calls for development of control technology for stationary combustion sources through modification of the basic combustion process. As such, the primary focus of CRB (and, in turn, FCR) is control of stationary source NO_x emissions.

To place the series of papers forming the body of this report in proper perspective, it is necessary to define the goals of the FCR program, the program's management structure and to provide some insight into why the particular research projects being pursued were selected for funding. To provide that pertinent background information, this introductory chapter is divided into three sections.

Section I defines the goals of FCR and briefly describes some of the limitations under which it must operate. In light of the fact that the term "fundamental research" has many connotations, this section seeks to define the type of research CRB has grouped under the general heading of FCR.

Section II of this chapter presents the contractual and managerial philosophy used in the FCR program. This section draws upon information presented in Section I since an appropriate management structure must conform to limitations imposed by program goals, time constraints, and financial resources available.

Section III of this chapter attempts to provide some of the rationale behind selecting the various research projects being pursued. This is accomplished by first defining the salient features of a pulverized coal flame (from a NO_x control perspective) and then drawing a parallel between those first order phenomena and the goals of the individual research projects.

SECTION I

DEFINITION OF FCR

For the last nine years the EPA has sponsored a series of studies (via grants and contracts) to provide deeper understanding of the chemical and physical processes controlling NO_x formation in stationary combustion sources. Though we call this grouping of studies "fundamental combustion research" (FCR), it is necessary that the intent of the program be clearly defined since the word 'fundamental' can assume many meanings.

The overall effort to develop effective NO_x control techniques is being directed by EPA's Combustion Research Branch (CRB). The CRB program is comprised of a broad spectrum of activities ranging from field testing and environmental assessment through demonstration and pilot-scale efforts to bench-scale and FCR activities. All of these activities are closely coordinated with a constant flow of information between program elements. Each of the activities plays an important role in the overall NO_x program and should be considered an integral portion rather than being evaluated in isolation. The technical driving force to the NO_x control program is a series of bench- or pilot-scale activities which systematically vary a variety of combustion parameters and attempt to identify pollution control options of maximum effectiveness. Effects of fuel type and source, varying heat removal rates, stoichiometry distributions, and fuel/air contacting processes are examples of phenomena being investigated in the bench/pilot-scale efforts. Outputs from these smaller scale studies feed into large scale pilot studies and eventually to demonstration efforts. The FCR program provides a major input to the bench-scale research by helping to explain observed phenomena and by suggesting new approaches which may prove successful. As well, the FCR program draws from the bench-scale studies in that many unexpected phenomena are identified which require a deeper understanding of combustion "fundamentals" for explanation.

With the above descriptions in hand, it should be obvious that FCR does not, in general, refer to basic research but is more accurately described as applied fundamentals. It must respond to the needs of the CRB on time scales ranging from several months to several years. Since many of the research results traditionally produced by the fundamental or academic community are not in a form which is readily usable by the hardware developers or researchers the FCR program must serve as an intermediary. That is, FCR must take existing data or information from several sources and integrate the data into a form that is usable. Researchers pursuing large pilot-scale or demonstration studies need the best answers we can provide now. One of FCR's roles is to take what we have and provide the "best guess" possible on a very short time scale. Small pilot/bench studies often uncover important trends but can afford to wait six months to two years for a fundamental explanation of the observed phenomena. Here, FCR must also use the information already available, but can augment the data with a limited number of key experimental or theoretical studies. Those studies can often be quite fundamental in nature but are selected for funding and are directed to yield a specific, needed input to a technology/hardware problem. Finally, the FCR program must anticipate the needs of the CRB by pursuing studies with expected payoffs in the 2 to 5 year timeframe. Only a small portion of the available funds can go to this type of study and no funds are available for the longer term, truly basic research.

As stated above, part of the definition of FCR within CRB derives from the financial resources available. Approximately ten percent of the CRB budget allocation has been devoted to the FCR program. That translates to a budget of roughly $750,000 to $1 million per year. At first glance that sounds like a lot of money, and it is, but it is essential to place that level of funding in perspective. One million dollars is only one fifty-thousandth of the Nation's total R&D budget. From another perspective, to measure the rate constant of a single reaction costs about $50,000 (assuming all necessary equipment is in place) and there are upwards of 150 simultaneous reactions playing an important role in a simple methane/air flame. Yet another perspective shows that one million translates into only 10 or 12 fulltime senior researchers. These illustrations are intended to show that FCR is a rather large program but that it also has very severe restraints. In selecting research topics to fund, it is not possible to pursue any and every subject which is of scientific interest, but rather it is essential that we identify those areas of first order importance to NO_x control and pursue only a select few within that group.

In the above discussion we have described how the end use of the FCR program outputs and the available resources combined to place bounds on the program. A third constraint placed on the FCR program is the fact that it must address stationary combustion sources and should have as its primary focus the control of NO_x. At first glance this would appear to be a negligible constraint since the stationary source category contains nearly the entire spectrum of combustion cycles including I.C. engines, gas turbines, utility boilers, stoker boilers, and residential furnaces. Further, it includes the entire spectrum of fuels from coal to natural gas as well as the synfuels. This constraint is thus not so much a limiting factor as much as it is a source of research prioritization. Certainly this constraint would place coal, residual oil, and synfuels as top priority items. It also helps to define the type of flames of major concern. Fully 60 percent of the stationary source NO_x emissions produced in this country come from flames with the characteristics shown in Table 1.

As indicated in Table 1, the FCR program focuses on control of NO_x and primary related pollutants generated by large, confined, atmospheric, turbulent diffusion flames produced from pulverized coal, synfuels, or residual oil which radiate to cold walls. The various research efforts being funded by FCR are selected to provide deeper insight into the spectrum of processes characterizing this flame type. Each individual research effort should be providing fundamental insight to that particular phenomena but its output should be in a form which can be integrated into a useful engineering tool.

The above discussion is intended to provide an overview of the purpose of the FCR program and to give the reader an appreciation for the constraints within which FCR must operate.

Table 1. Dominant Characteristics of Stationary Source Flames

Dominant Flame Characteristics	Significant Exceptions
• Transport is turbulent and radiative	
• Fuel/air contacting is by diffusion and particle penetration	Flame propagation in spark ignited I.C. engines; stoker boilers
• Flames are large - typically occurring in industrial/utility equipment with characteristic dimension of the energy release zone on the order of feet to tens of feet	Flames in domestic and small commercial furnaces; gas turbines; I.C. engines
• Residual oil, coal and synfuels are the principal sources of emissions due to high nitrogen content and the difficulties associated with simultaneous NO_x and particulate control	Natural gas
• The time-mean motion is in steady state	Reciprocating I.C. engines
• Pressure is atmospheric	I.C. engines; gas turbines; supercharged boilers
• Flames are confined by cold walls to which the flame radiates	Process furnaces

SECTION II

FCR MANAGEMENT APPROACH

For the first several years of the NO_x program, the FCR effort was a loosely tied group of individual research efforts. The studies were accomplished either through research contracts to industrial R&D firms or through research grants. With the recent distinction between research grants and cooperative agreements (Federal Register, Vol. 44, No. 211, October 30, 1979), it is fair to say that all of the grants previously funded would now be classified as cooperative agreements. In addition, many of the hardware oriented R&D efforts had tasks or subtasks within their scope of work which called for limited fundamental combustion research.

Four years ago IERL-RTP came under intense pressure from our Contracts Management Division to reduce the absolute number of contracts being awarded. In response to that pressure, CRB elected to consolidate its fundamental combustion research program under a single master contract. A competitive RFP was issued in FY 76 entitled Fundamental Combustion Research Applied to Pollution Control. An award was ultimately made to Energy and Environmental Research Corporation (EER) in January 1977 as EPA Contract No. 68-02-2631. The form of the contract was a 70,000 manhour level-of-effort agreement which was scheduled to run for three years. In the interim, EPA has extended the term of the contract to 40 months reflecting the fact that more than 70,000 manhours have been delivered for less than the agreed upon price ($3.3 million). Two facets of this contract distinguish it from any other effort of which I am aware. First, the scope of work calls for a large percentage of the level of effort to be expended through subcontract. EER was to expend about 30% of the effort directly while about 70% of the effort was to be subcontracted. This arrangement was in recognition of the fact that considerable expertise resided in a spectrum of organizations and institutions throughout the world and that FCR could only afford to purchase limited equipment and to train only a limited number of people. It is far more cost effective to utilize existing expertise and existing hardware. This approach also assured that a diversity of opinions would be considered.

The second distinguishing feature of FCR is that overall management is through the combined efforts of the EPA project officer and two individuals at EER. These two EER personnel are Dr. T. J. Tyson (president of EER) and Dr. M. P. Heap (vice-president). Communication between all three occurs on almost a daily basis with no major action taken without the knowledge of the other two. Each member of this management team brings a different perspective into major decisions. Dr. Heap is the principal investigator on EPA's low NO_x coal burner effort and is closely associated with a variety of bench-scale and pilot-scale studies. He is in a unique position to provide input to FCR on the fundamental needs of those major CRB efforts. Dr. Tyson provides a major expertise in numerical analysis and combustion aerodynamics. The EPA project officer provides the required perspective on EPA's goals as well as experience in coordinating a number of external research activities. Augmenting this team approach is a number of consultants who provide the needed expertise in specific areas. A major subcontract was issued to MIT to provide continual access to several of its highly qualified professors.

As regards the mechanics of the FCR program, when a particular research topic is selected for investigation a number of options are open. First, if EER has an existing expertise or if no expertise is known to exist there is the option to pursue the research at EER. This has been the dominant choice for numerical modelling activities. Other options open include sole-source, limited source, or full competitive procurement. In general, the sole-source of limited competitive route has been selected. An additional option that is available is for EPA to fund the activity directly through a contract or grant. Three such grants are now on-going (MIT, the University of Arizona, and the University of Utah). EPA also had a direct contract with TRW in the numerical modelling area. The above is meant to convey the picture that a variety of contracting options are available and many have been used.

Once a subcontract has been officially approved by EPA and is in effect, monitoring of that subcontract is the responsibility of EER. Here again, the EPA project officer plays a major role, but is legally excluded from providing direct guidance. Legally, that guidance must come through EER.

SECTION III

FCR CONTENT

With the above background on how the FCR program functions, it now seems appropriate to provide further insight into what research has been selected for study and why. Toward that goal, it is perhaps easiest to trace through some of the physical and chemical processes occurring in a flame. As schematically described in Figure 1, the typical burner consists of a fuel source at the burner centerline which issues into a flow field. Concentric with the fuel source is one or more air passages which impart swirl to the flow and combine with the fuel stream to establish a unique flow field. The swirl component to the air coupled with the divergent geometry at the burner exit generate a series of recirculation zones in the furnace volume. A toroidal recirculation zone is formed between the furnace walls and the burner exit in the section known as the base flow region. A recirculation zone is also formed at either the centerline of the burner, or is in the shape of a toroid about the centerline. The interface of these recirculation zones is characterized by high aerodynamic shear forces which contribute heavily to the mixing rate of fuel and air. The central recirculation zone also provides a source of hot combustion products and radicals to "bootstrap" the combustion process. This central recirculation zone is equivalent in many respects to a flame holder and provides the needed flame stabilization. Changes to the shape, size, and strength of this central recirculation zone alter the flame shape and have a marked impact on the fuel/air contacting process. In turn, these variables have been shown to result in major variation in the pollutant levels generated by the flame.

From a chemical standpoint it is perhaps best to consider the case of a pulverized coal-fired boiler. The various chemical and physical processes are represented in Figure 2. The coal particles, which are on the order of 100μm in diameter are ballistically inserted into the flame by primary air representing 10 to 20% of the stoichiometric air requirements. These particles are heated by the flame (predominantly by radiation) at a rate of temperature rise on the order of 10^5 K/sec. As the particle heats, it begins to devolatilize and burn. Depending upon where the particle was ballistically injected into the flow field, and the physical characteristics of the coal, it will undergo different burning processes. If the particle is in a quiescent region, it

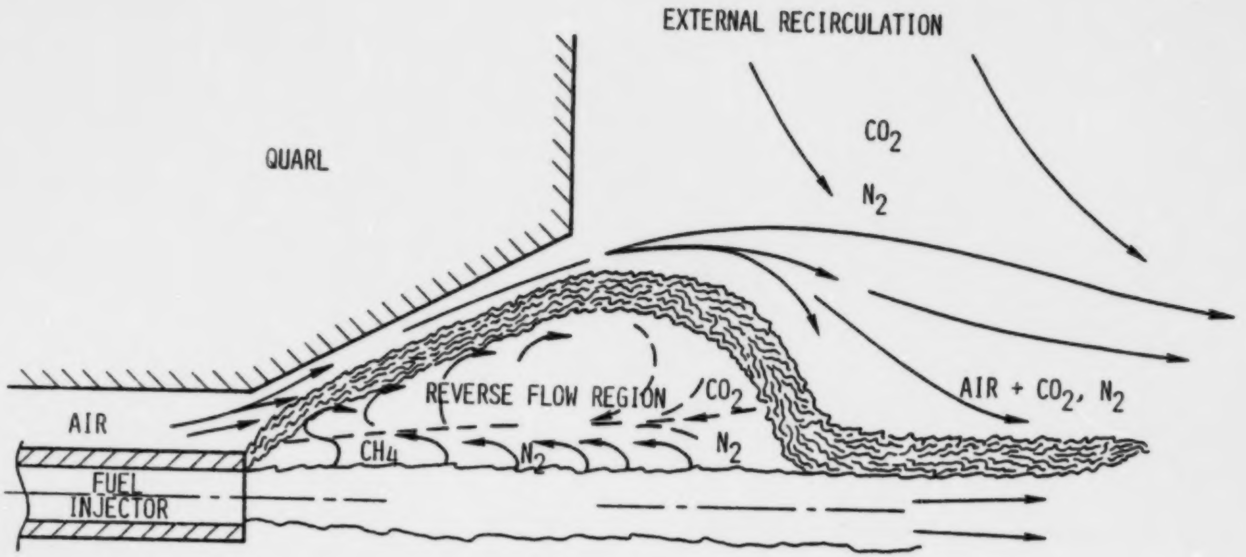

Figure 1. Diagramatic Representation of Conditions at the Base of a High Intensity Type I Flame.

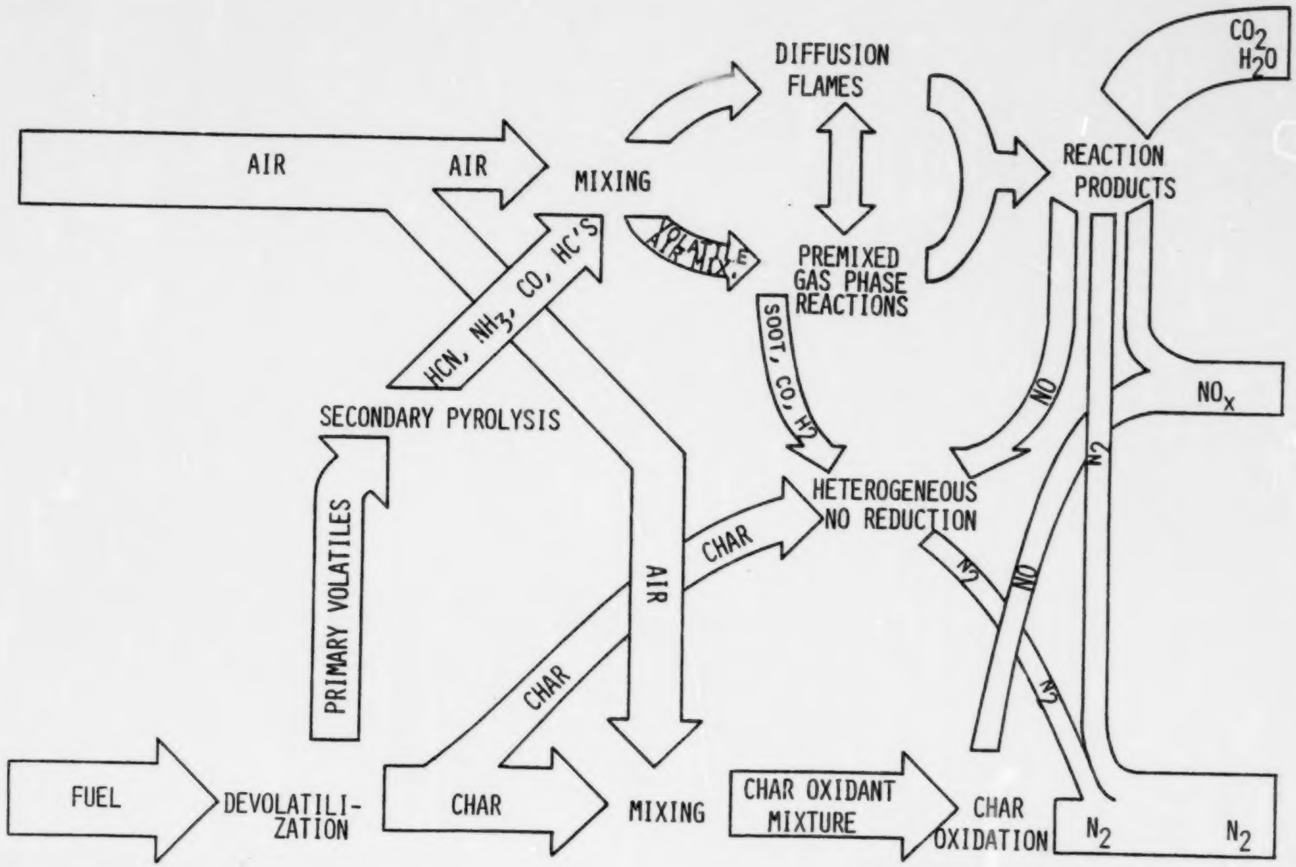

Figure 2. Physical/Chemical Processes in Combustion.

could remain within a cloud of volatiles which burn or it could issue volatiles in a jetting motion significantly separating the particle from its volatiles. If the particle experiences a strong aerodynamic shear force it would be expected that the particle would have its volatiles stripped away. Regardless of the process details, the particle will lose 50 to 70% of its weight through devolatilization in a relatively short period of time, with the remainder of the particle mass being consumed by two-phase surface reactions which proceed at a much slower rate.

The environment into which the volatiles are issued plays a major role in determining the level of pollutants emitted from the boiler. On a gross scale, if the early combustion process takes place in a fuel-rich environment there will be a tendency for the nitrogen bound within the coal matrix to go through complex (and ill-defined) chemical processes yielding N_2. If the early combustion process is fuel lean, however, that chemically bound nitrogen will tend to form NO. At this point in the discussion it is perhaps important to recall the work performed by Dr. D. W. Pershing (first in the CRB laboratories at RTP and later confirmed at the University of Arizona). That work conclusively showed that about 80% of the NO_x from a coal flame is directly related to the oxidation of fuel-bound nitrogen. The environment under which this chemistry takes place is obviously dictated by the aerodynamic flow field and where the coal has been placed in that field. Since the coal is transported by a small amount of carrier air the very early volatiles will probably experience a fuel-lean gas phase. That portion of the coal deposited in the central recirculation zone will emit its volatiles and will burn in an environment of hot products and fresh volatiles from other coal particles. This process is much akin to a stirred reactor with a residence time estimated to fall between 20 and 200 milliseconds. The stoichiometry is usually fuel rich. That portion of the coal which passes through the shear layer will experience an environment of almost pure air.

The combustion of the volatiles is certainly a gas phase process which can be either kinetically or diffusion controlled. The speciation of the volatiles will depend upon the composition of the parent coal and in turn when the volatiles were released. Previous work by Axworthy at Rocketdyne has investigated pyrolysis of a spectrum of model fuel-nitrogen compounds as well as different coals. These studies indicate that for the model compounds, pyrolyzed in an inert two-stage reactor, the nitrogen in those compounds was quantitatively converted to HCN. For real coals, Axworthy was not able to close the nitrogen balance. We know that for coal, the bound nitrogen is fairly equally distributed throughout the coal matrix and that much of the nitrogen is associated with very heavy ends. Model fuel-nitrogen compounds (such as pyridine or benzonitrile) have low boiling points and cannot be expected to represent the heavy end volatiles. It is obvious, however, that oxidation of HCN is a key area of chemical concern if FCR is to understand NO_x formation and control. Axworthy's experiments also show that under oxidative pyrolysis conditions much of the bound nitrogen can form NH_3 or amine-type compounds. Further, there is evidence to indicate that the conversion of the bound nitrogen to ammonia or hydrogen cyanide occurs on an extremely short time scale and that, to first order accuracy, we can assume the fuel-nitrogen to issue from the coal in that form. Obviously, this assumption is not completely correct, especially as regards late volatiles, but it is a good starting point for examining the gas phase combustion process for the burning of coal. The details of the gas phase burning process will also depend upon the speciation of the hydrocarbons evolved. Here again much variation is expected between different coals. Due to the large amount of data available on the kinetics of combustion for H_2, CO, and CH_4, these species have been used as the starting point for kinetic modeling activities in FCR. A variety of experiments have shown that coal volatiles contain a variety of higher hydrocarbons and those species should also be considered.

As mentioned earlier, the char which is left after devolatilization burns out via surface reactions which are slow relative to the gas phase consumption of the fuel. The possibility exists for these two-phase reactions to significantly alter the level of pollutants emitted. Work by Wendt and Pershing at the University of Arizona has shown that any residual nitrogen remaining with the char is predominantly converted to N_2 with only about 10% converted to NO. Work by Sarofim and Beer at MIT has shown that coal char can effectively reduce NO formed early in the flame to N_2. DeSoete at the Institute Francais du Petrol has also shown that ash particles and flame-formed soot can reduce NO emission levels. The extent of these two-phase reduction mechanisms is, however, dependent upon particle size and morphology as well as the composition of the gas phase reactants and their temperature.

In general, the size of the radiant section of a boiler is set by the time required to burn out the solid phase. At the exit of the radiant section sufficient heat has been removed to drop the temperature of the combustion products to about 700 or $800^{\circ}K$. At these temperatures the kinetic processes associated with NO_x formation (and most NO_x destruction processes) have slowed to the point that the mixture may be considered "frozen." Significant amounts of heat still must be removed in the convective sections but that process has little to no impact on NO_x control.

The above description is not meant to be an exhaustive review of the coal combustion process but rather to delineate several of the important features known to play a dominant role relative to NO_x control. The FCR program has a variety of research efforts underway attempting to give a better understanding (in an engineering sense) of those first order processes. The FCR contractors' coordinating meeting is organized such as to group the various studies according to the portion of the combustion process they address. The morning and early afternoon of the first day will be devoted to a series of theoretical and experimental efforts which address the chemistry of volatile combustion. The experimental studies are intended to fill critical data gaps especially as regards fuel-bound nitrogen chemistry. These experiments are being performed in well-stirred reactors, plug-flow reactors, and opposed-jet diffusion flames. No studies are being funded which utilize flat flame burners since there is already a wealth of data from such devices desperately needing thorough theoretical analysis. The theoretical efforts draw from the ongoing experiments as well as a significant body of data in the literature (including flat flames and shock tubes) and are attempting to compile a set of elementary reaction kinetics which consistently describe that data. Such a reaction set can then be used in numerical experiments to help explain observed phenomena from pilot-scale tests and to identify kinetic regimes which can be exploited for enhanced emission control. These studies can also be used in limit case studies to determine the lower bounds of NO_x control set by combustion chemistry.

The afternoon of the first day jumps to the tail end of the combustion process and will present two studies which address reduction of NO by char and/or solid particles. The morning of the second day switches back to the early stages of combustion and will address a series of four studies designed to give insight into how liquid and solid fuels decompose. These four studies are similar to the extent that they examine a common group of coals and/or heavy oils but are examining thermal decomposition under different conditions and with varying levels of detail. They range from an inert pyrolysis study which integrates primary and secondary decomposition, through inert and oxidative pyrolysis of single particles or droplets, to detailed studies of the composition and structure of both the parent coals and its volatiles. The fourth piece of work has accomplished holographic recordings of coal particles as they are injected into a methane/air flame. This latter study provides visual data on the physical processes occurring while a range of coals decompose and burn.

The afternoon of the second day addresses a group of diverse bench-scale reactor studies. The first paper of the afternoon will present work not formally part of the FCR contract but being funded directly by EPA under a cooperative agreement (or grant) with the University of Utah. This study is addressing the combustion of coal under conditions pertinent to stoker-fired operation. Two papers will deal with experimental programs to build and test stirred reactors burning residual oil and coal, respectively. As was mentioned earlier, these studies are particularly pertinent to the central recirculation zone found in a large industrial or utility boiler burner and have been sized to address the residence time associated with those recirculation zones. The fourth presentation will cover attempts by the FCR program to develop a computer model describing two-phase stirred reactors. The final paper of the second day is also not directly funded by the FCR program, but is a fundamental component of two large development efforts. This paper will describe tunnel furnace experiments burning several coals, petroleum-derived residual oils, and synfuels. These studies have provided much insight into the important processes occurring in real flames and have uncovered a number of phenomena for which the FCR program must provide explanations.

The third day of the meeting will concentrate more heavily upon combustion aerodynamics, i.e., how flow fields interact with fuel ballistics, measurement of pertinent phenomena in flames and the various activities associated with modelling two-phase, turbulent, reacting flows. The importance of combustion aerodynamics in NO_x control has been pointed out earlier in this section and is an important area of research for FCR. Due to funding constraints, this is unfortunately one area which has not received the attention it warrants. It is our intent to give significantly more emphasis to this area in future FCR activities.

There are several other areas of key interest to the FCR program which have not been addressed, primarily for financial reasons, but also because no approach was found which would yield results on a short timescale or with a high probability of success. This comment is especially true for soot formation since it is well known that the lower limits of NO_x control during the combustion of heavy oils and synfuels is set by unacceptable smoke emissions.

Having provided this background information, the stage should be properly set to proceed with the individual papers presented at the meeting.

SESSION I

GAS-PHASE CHEMISTRY AND HETEROGENEOUS NO REDUCTION

W. S. LANIER
SESSION CHAIRMAN

MODELING OF FUEL-NITROGEN CHEMISTRY IN COMBUSTION: THE INFLUENCE OF HYDROCARBONS

J. M. Levy
MIT Energy Laboratory
Cambridge, Massachusetts 02139

Fifth EPA Fundamental Combustion Research Workshop
Newport Beach, California
January 23-25, 1980

SECTION I

INTRODUCTION

Studies of the oxidation of fuel-bound nitrogen in fossil fuel combustion (1,2) suggest that abatement of NO_x emissions is best achieved through staged combustion in which the first stage is operated fuel-rich (3,4,5). Because residence times in practically sized combustors are insufficient for the attainment of chemical equilibrium, the chemical kinetics of fuel-nitrogen conversion must be considered for the design optimization of low-NO_x emission combustors. To this end, development of a predictive chemical kinetic model has received considerable attention under the EPA Fundamental Combustion Research Program.

Unfortunately, trace emissions from rich stationary source combustors are the product of several, lumped chemical/physical processes, and, even if the problems of coupling finite-rate chemistry with complex flow-fields are neglected for the moment, the necessity of computing NO_x levels to within the ppm range places rather stringent requirements on the mechanistic accuracy of whatever model is invoked.

Despite residual uncertainties in the currently available mechanistic and kinetic data base, adequate, if imperfect, modeling of fuel-nitrogen conversion in the presence of "simple" fuels can now be achieved (2,6,7). Unfortunately, however, real combustion systems, i.e. real fossil fuels, present incremental mechanistic complexities which do not decouple easily from solution of the fuel-nitrogen problem. It is to an assessment of these complexities and to the development of a methodology for dealing with them - as well as demonstration of encouraging preliminary results - that this paper is addressed.

SECTION II

THE FUEL-NITROGEN MECHANISM

A large literature has appeared recently directed towards the experimental elucidation of the mechanistic details of fuel-nitrogen conversion under flame conditions (3,8). Synthesis of these observations into a master reaction set has been the subject of other studies reported elsewhere (9,10,11). Validation and refinement of the reaction set, based upon efforts to model independent data under as broad a range of conditions as possible, is an ongoing effort (2), current details of which are the subject of another presentation at this symposium (6). This study has, however, concentrated less on systematic examination of current computational limitations under rather ideal conditions (6), but has focussed instead on development of modeling capabilities to deal with mechanistic limitations - namely, the influence of a hydrocarbon environment upon fuel-nitrogen chemistry-anticipated to present computational difficulties in applications of fuel-nitrogen modeling to real fuel environments.

To this end, equal success has been achieved in modeling the post-flame zones of several nitrogen-doped hydrocarbon flames using the "minimum subset" of fuel nitrogen reactions shown in Table 1, as with the larger master set currently in use at EER(6). It is cautioned, however, that the full range of applicability of this minimum subset is not yet established. Thus, for example, though significant contribution to the destruction of NO by reaction with NH_2 is precluded in modeling post-flame data in the range of 2000 K, recent indications (12) of the very strong inverse temperature coefficient of the effective $NO + NH_2$ rate constant suggests that that mechanistic addition may still prove appropriate at lower temperatures. The basic mechanistic flow of the reaction set used is shown, diagramatically, in Figure 1.

An example of the modeling success achievable is indicated in Figure 2, showing the data of Haynes (13) in the post-flame gases of a rich ($\phi = 1.52$), atmospheric pressure, ethylene/oxygen/nitrogen flame doped with 700 ppm of ammonia. In view of Haynes' rather flat temperature profile (22 degree variation over 9.6 msec) and the arbitrariness of any

TABLE 1. SIMPLIFIED FUEL-NITROGEN REACTION MECHANISM*

Rate constant, $k_f = AT^n \exp(-E/RT)$

	REACTION	A (cm^3/mole-sec)	n	E (cal/mole)	REFERENCE
1	$HCN + OH \rightarrow CN + H_2O$	2.00×10^{11}	0.60	5000.	b
2	$CN + H_2 \rightarrow HCN + H$	3.16×10^{12}	0	5000.	c
3	$CN + OH \rightarrow NCO + H$	5.60×10^{13}	0	0	d
4	$HCN + OH \rightarrow HNCO + H$	4.00×10^{11}	0	0	e
5	$NCO + H_2 \rightarrow HNCO + H$	3.20×10^{11}	0	0	a
6	$NCO + H \rightarrow NH + CO$	3.00×10^{14}	0	0	a
7	$HNCO + H \rightarrow NH_2 + CO$	1.00×10^{13}	0	0	a
8	$NH_3 + H \rightarrow NH_2 + H_2$	5.00×10^{11}	0.50	2000.	f
9	$NH_3 + OH \rightarrow NH_2 + H_2O$	1.39×10^{11}	0	1600.	m, n, o
10	$NH_2 + H \rightarrow NH + H_2$	3.50×10^{10}	0.79	4460.	g
11	$NH_2 + OH \rightarrow NH + H_2O$	3.00×10^{10}	0.68	1300.	f
12	$NH + H \rightarrow N + H_2$	1.00×10^{12}	0.68	1900.	f
13	$NH + OH \rightarrow N + H_2O$	5.00×10^{11}	0.50	2000.	f
14	$NO + H \rightarrow N + OH$	1.34×10^{14}	0	49200.	h
15	$N + NO \rightarrow N_2 + O$	3.10×10^{13}	0	334.	i
16	$NH + NO \rightarrow N_2O + H$	9.00×10^{9}	0.75	0.	j
17	$N_2O + H \rightarrow N_2 + OH$	7.60×10^{13}	0	15101.	k
18	$N_2O + M \rightarrow N_2 + O + M$	1.42×10^{14}	0	51280.	l
19	$NH + NH \rightarrow N + NH_2$	3.60×10^{11}	0.55	1900.	f
20	$N + NH_3 \rightarrow NH_2 + NH_2$	2.10×10^{11}	0.50	23160.	f
21	$NH + N \rightarrow N_2 + H$	6.30×10^{11}	0.50	0.	q, r
22	$NH_2 + NH_2 \rightarrow NH + NH_3$	1.70×10^{11}	0.63	3600.	f, p

REFERENCES - TABLE 1

* For a discussion of reactions 1 - 18, see Reference [a].

[a] Foster, D.E., J.B. Heywood, J.C. Keck, J.P. Longwell, A.F. Sarofim, and B.R. Taylor, "Control of NO_x Emissions from Combustion of Fuels Derived from Shale and Coal," Summary Technical Progress Report, October 23, 1978. Prepared for the Department of Energy, under Contract EX-76-A-01-2295, The Energy Labcratory, MIT.

[b] Tunder, R., S. Mayer, E. Cook, and L. Schieler, Aerospace Corp., Thermochemistry Research Dept., Aerospace Report No. TR-1001 (9210-02)-1, AD 813 485 (1967).

[c] Benson, S.W., D.M. Golden, and R. Shaw, "Estimating the Kinetics of Combustion," EPA Report EPA-600/2-75-019 (1975).

[d] Haynes, B.S., "The Formation and Behavior of Nitrogen Species in Fuel-Rich Hydrocarbon Flames," Ph.D. Thesis, The University of New South Wales (1975).

[e] Estimate, this work.

[f] Bahn, G.S., *Reaction Rate Compilation for the N-O-H System*, Gordon and Breach (1968).

[g] Mayer, S.W., L. Schieler, and H.S. Johnston, "Computations of High-Temperature Rate Constants for BiMolecular Reactions of Combustion Products," Eleventh Symposium (International) on Combustion, The Combustion Institute, Pittsurgh, Pa. (1967).

[h] Flower, W.L., R.K. Hanson, and C.H. Kruger, "Kinetics of the Reaction of Nitric Oxide with Hydrogen," *Fifteenth Symposium (International) on Combustion*, The Combustion Institute, p.823 (1974).

[i] Baulch, D.L., D.D. Drysdale, and A.C. Lloyd, "Critical Evaluation of Rate Data for Homogeneous, Gas-Phase Reactions of Interest in High Temperature Systems, Vol. 4," The University, Leeds 2, England (1969).

[j] Roose, T.R., R.K. Hanson, and C.H. Kruger, "Decomposition of NO in the Presence of NH_2," presented at the 11th Annual International Shock Tube Symposium, Seattle Washington, (1974).

[k] Baulch, D.L. *et al.*, *Evaluated Kinetic Data for High Temperature Reactions, Volume 2*, CRC Press (1973).

[l] Monat, J.P., R.K. Hanson, and C.H. Kruger, "Kinetics of Nitrous Oxide Decomposition," *Combustion Science and Technology*, *16*, 21-28 (1977).

[m] Dove, J.E. and S.N. Wing, "Shock Tube Studies of the Reactions of Hydrogen Atoms: I - The Reaction of $H+NH_3 \rightarrow H_2+NH_2$", *Can. J. Chem.*, *52*, 1171 (1974).

[n] Zellner, R. and I.W. Smith, "Rate Constants for the Reactions of OH with NH_3 and HNO_3," *Chemical Physics Letters*, *26* (1) (1974).

[o] Perry, R.A., R. Atkinson and J.N. Pitts Jr., "Rate Constants for the Reactions of $OH+H_2S \rightarrow H_2O+SH$ and $OH+NH_3 \rightarrow H_2O+NH$ Over the Temperature Range 297 - 427°K," *The Journal of Chemical Physics, 64* (8) 3237 (1976).

[p] Mayer, S.W. and L. Schieler, Aerospace Corp. Report TR-66 (8210-02)-3 (June, 1966).

[q] Engleman, V.S., "Survey and Evaluation of Kinetic Data on Reactions in Methane/Air Combustion, EPA Report, EPA-600/2-76-003 (1976).

[r] Benson, S.W., D.M. Golden, R.W. Lawrence and R. Shaw, Quarterly Progress Report No. 2, EPA Grant #R-800798 (Feb. 1973).

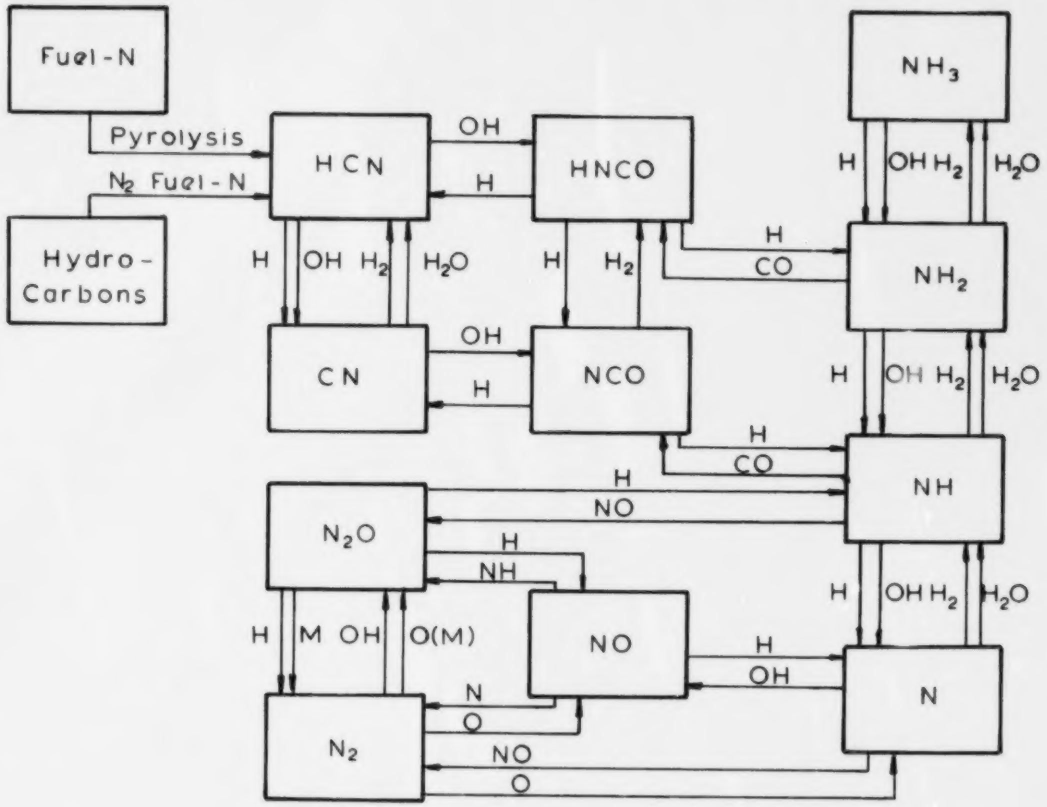

Figure 1. The basic fuel-nitrogen mechanism

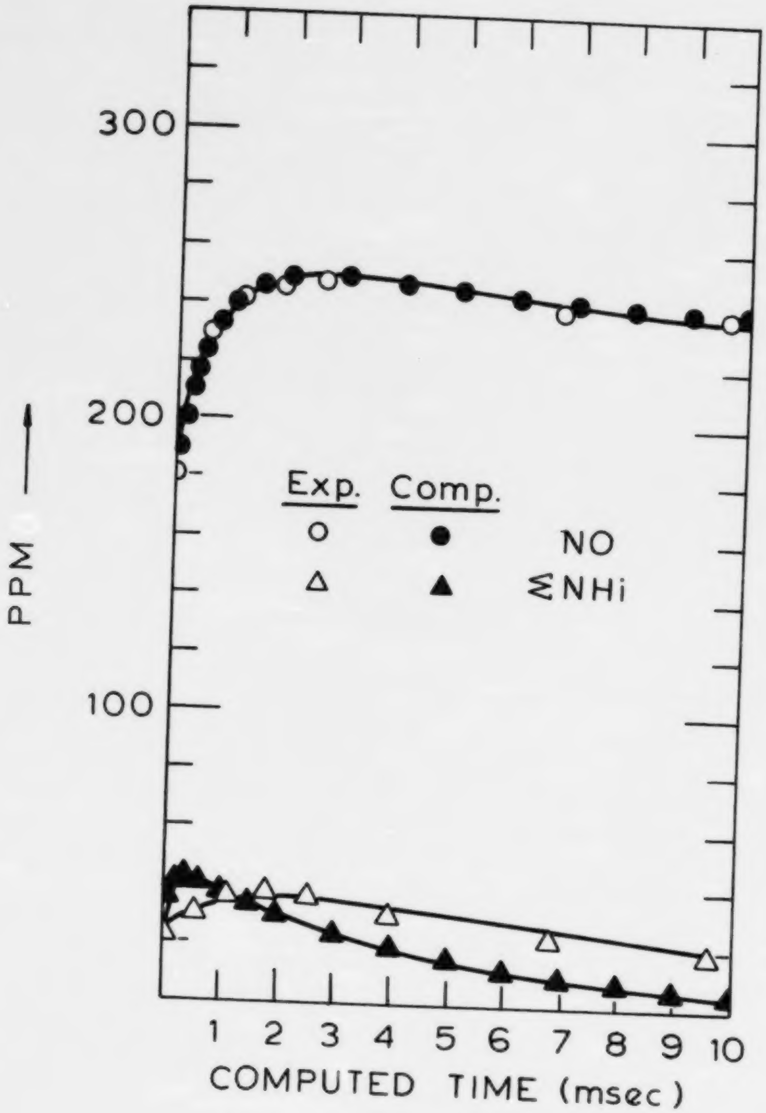

Figure 2a. Post-flame zone of a $C_2H_4/O_2/N_2$ flame doped with 700 PPM NH_3 (ϕ=1.52, T=2010 K) modeled with the Reaction set of Table 1. Data from Haynes [13].

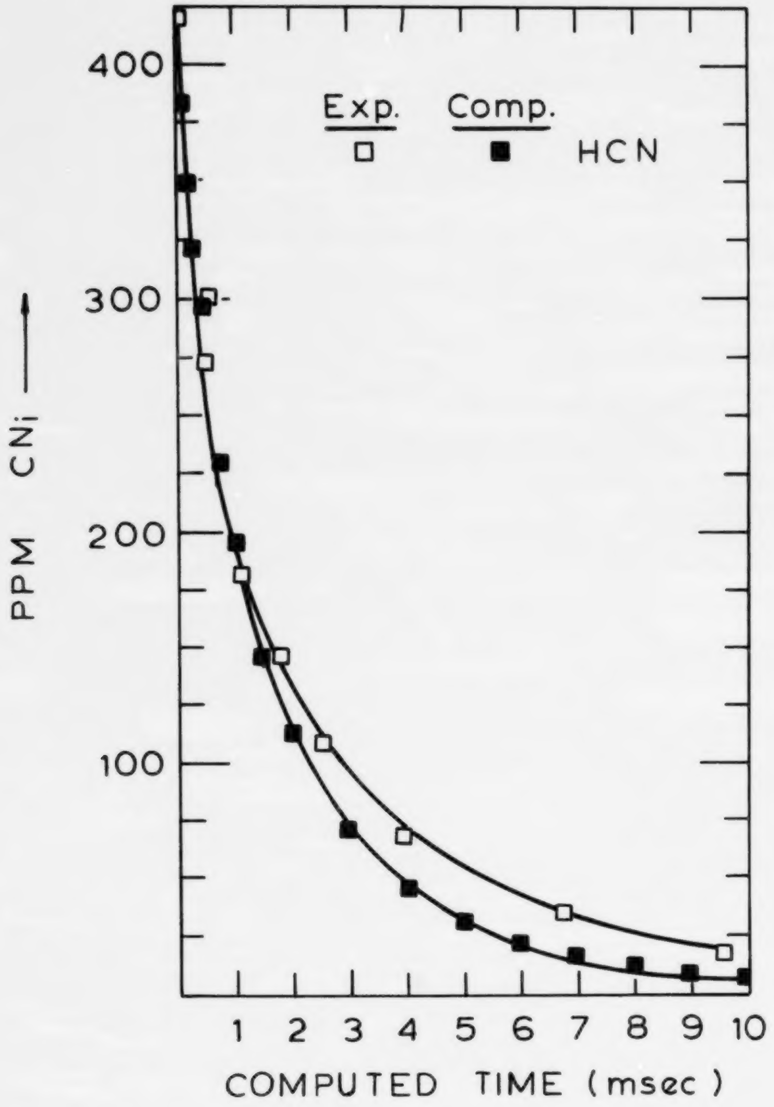

Figure 2b. Post-flame zone of a $C_2H_4/O_2/N_2$ flame doped with 700 PPM NH_3 (ϕ=1.52, T=2010 K) modeled with the Reaction set of Table 1. Data from Haynes [13].

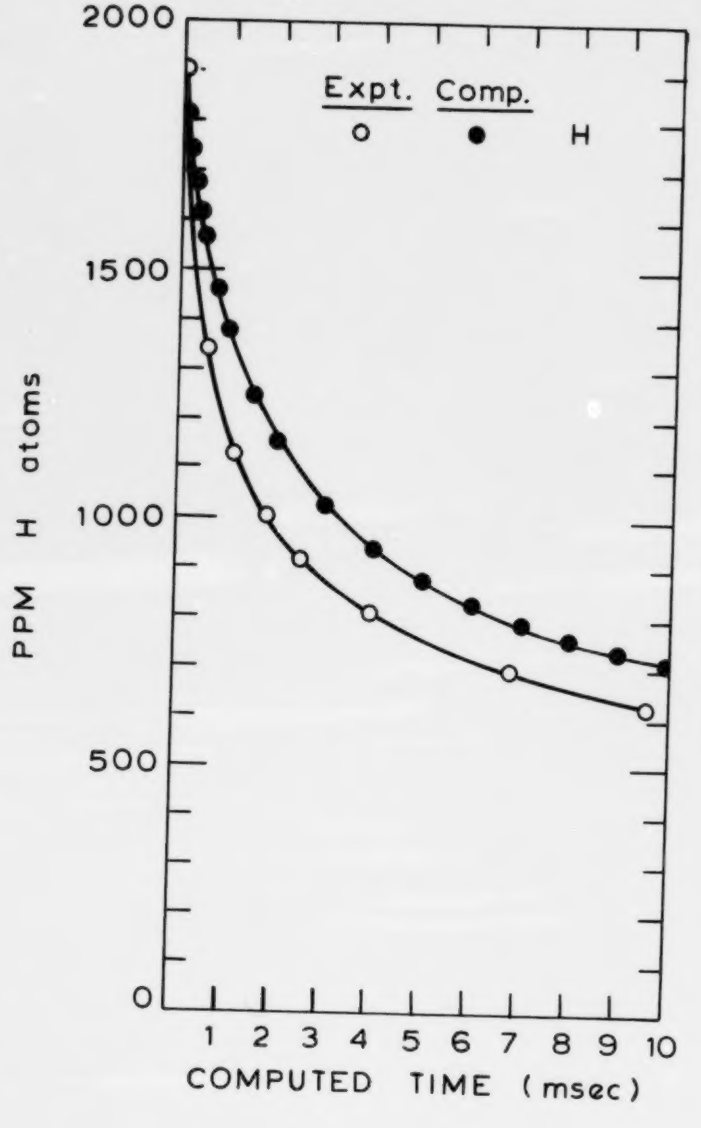

Figure 2c. Post-flame zone of a $C_2H_4/O_2/N_2$ flame doped with 700 PPM NH_3 (ϕ=1.52, T=2010 K) modeled with the Reaction set of Table 1. Data from Haynes [13].

assumed rate of heat loss, modeling was performed isothermally at an average temperature of 2010 K. Calculations were in plug-flow, initialized assuming partial equilibration of the radical pool, and were performed on an IBM 360/65 using a computer code written at MIT for the integration of the stiff rate equations. Essential to the discussion to follow is the observation that no hydrocarbon species were observed in the post-flame zone of this flame.

Contrasting with the results of Figure 2 are those shown in Figure 3 for Haynes' richer ethylene/air flame ($\phi = 1.66$) doped with 500 ppm NO. The major distinction is this flame is the "breakthrough" of hydrocarbons (roughly 0.2% of the total flow) into the post-flame zone. The results of Figure 3 were generated using the identical reaction set and initialization method as in the $\phi = 1.52$ flame, accepting the slight inaccuracy in material balances generated by ignoring the hydrocarbons. Although the fits to the concentration profiles are not really bad, better success in fitting the HCN and NO profiles have been achieved (see below) through consideration of the pertinent hydrocarbon chemistry. (Ammonia profiles remain systematically in error.) It should be clearly noted, also, that the influence of hydrocarbons upon fuel-nitrogen chemistry is potentially much greater in the highly backmixed environment of a practical combustor than may be suggested by Figure 3. This is demonstrated by a series of computations performed (using the older EER mechanism) on a methane/air system doped with 1% ammonia. In these calculations, a well-stirred reactor (WSR) section of varying residence time fed a plug-flow reactor (PFR) section, also of varying residence time, such that the total residence time remained approximately constant. Bound nitrogen concentrations are shown in Figure 4 for an adiabatic calculation at a fuel/air equivalence ratio of 1.33, and demonstrate nicely that for a fixed total reaction time, HCN exit concentrations (the major product of fuel-nitrogen/hydrocarbon interactions) are increased with increased stirred reactor residence time. This conclusion follows logically, of course, from the recognition that strong backmixing necessarily increases the possiblity for reaction between hydrocarbon and nitrogenous fragments.

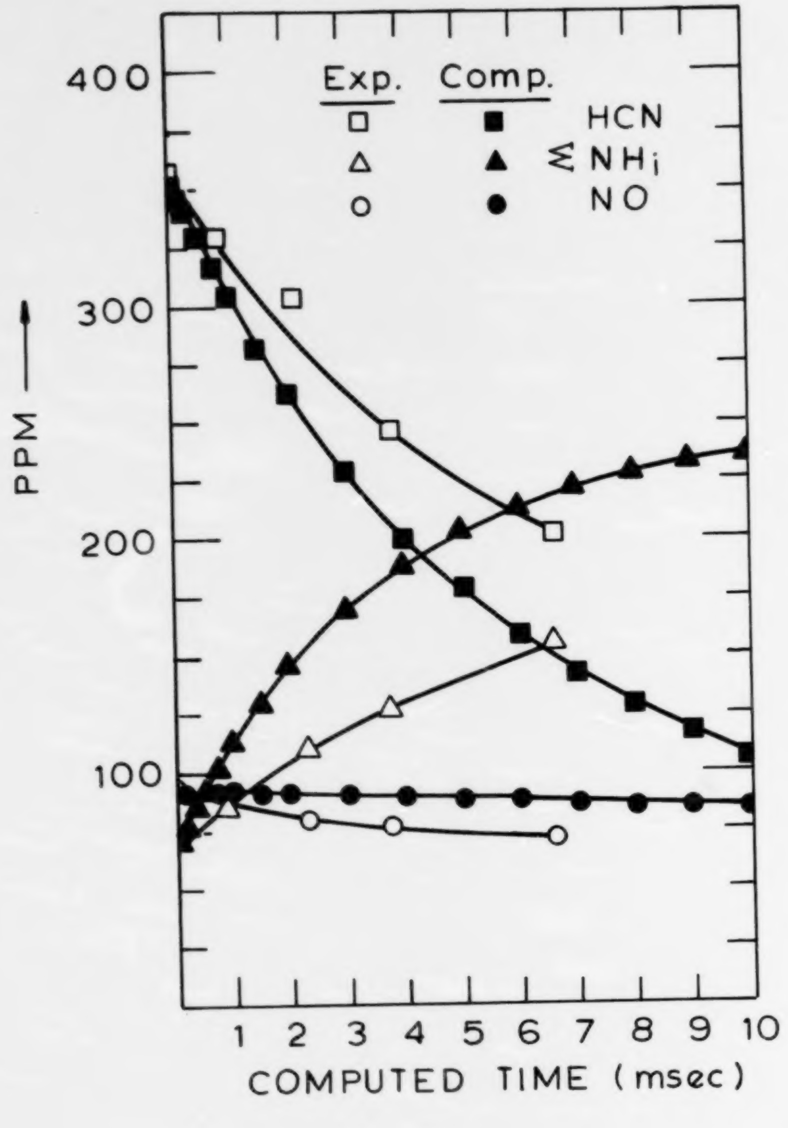

Figure 3a. Post-flame zone of a C_2H_4/air flame doped with 500 PPM NO (ϕ=1.66, T=2000 K) modeled with the hydrocarbon-free reaction set of Table 1. Data from Haynes [13].

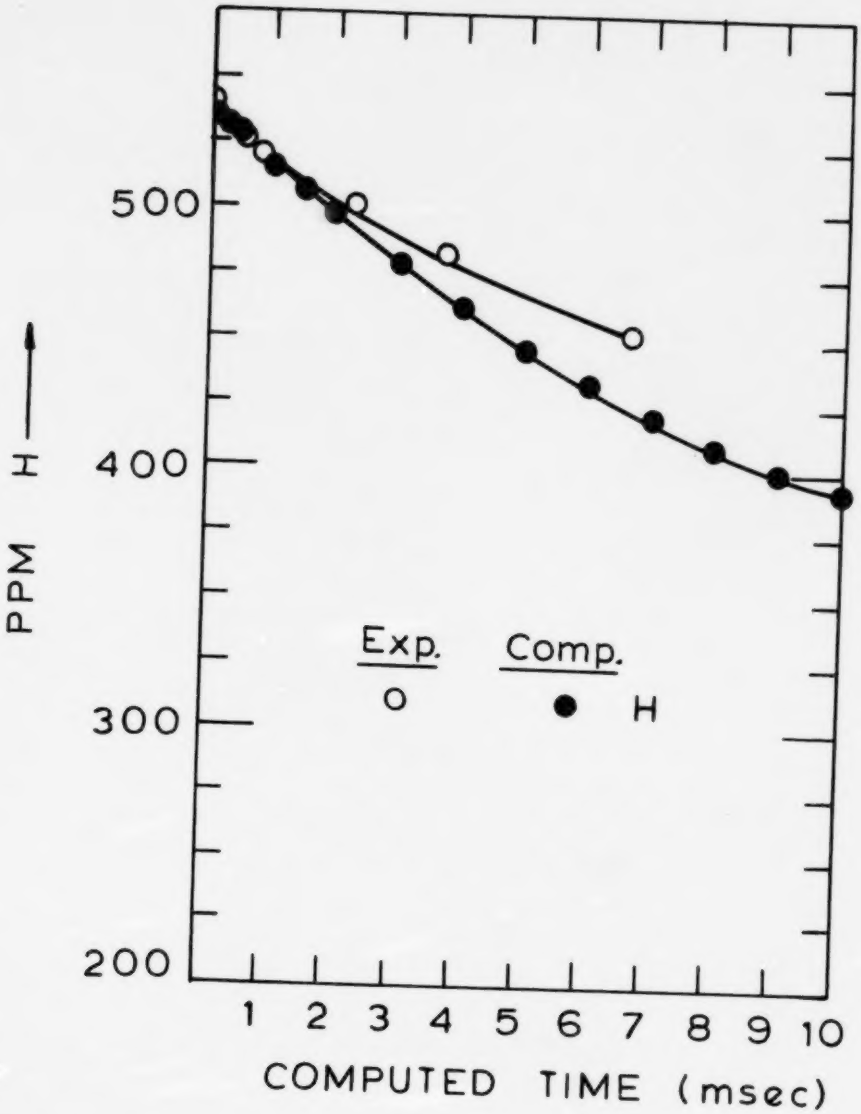

Figure 3b. Post-flame zone of a C_2H_4/air flame doped with 500 PPM NO (ϕ=1.66, T=2000 K) modeled with the hydrocarbon-free reaction set of Table 1. Data from Haynes [13].

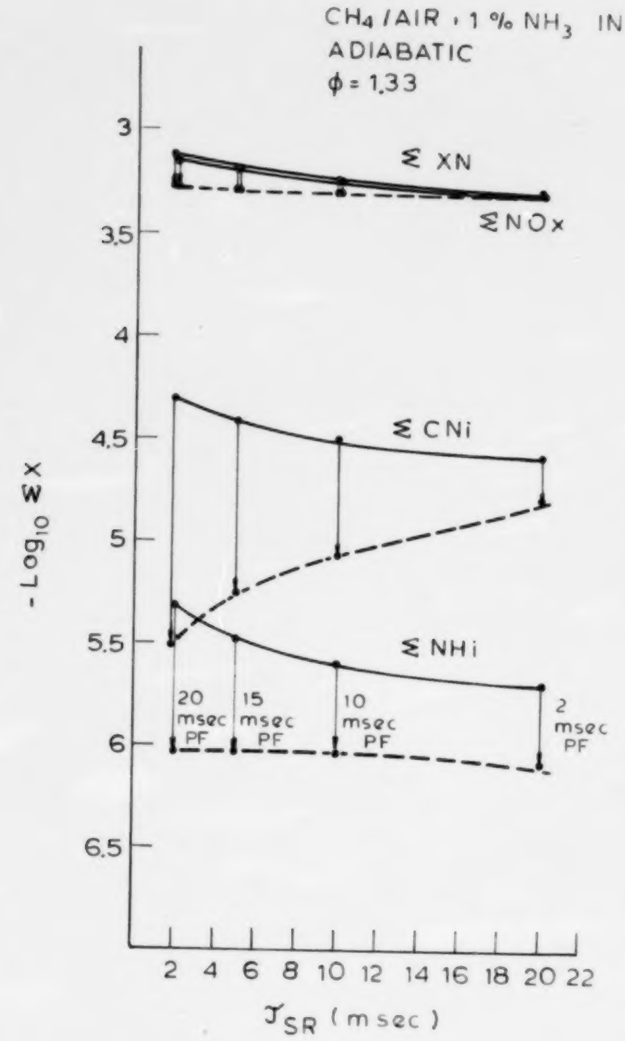

Figure 4.

Figure 4. Species mole fractions as function of residence time (T_{SR}) in an adiabatic stirred-reactor. CH_4/air flame doped with 1% NH_3, ϕ=1.33. The vertical lines denote, for comparison, the effects of varying times in plug-flow following the stirred-reactor section, the plug-flow residence times being (from left to right) 20 msec, 15 msec, 10 msec and 2 msec. The (curved) dashed lines denote species concentrations for combined stirred-reactor and plug-flow sections. Thus ΣCN_i equals 4.88 x 10^{-5} for T_{SR}=2 msec, but falls to 3.08 x 10^{-6} after an additional 20 msec in plug-flow (total reaction time = 22 msec), wheras ΣCN_i equals 2.51 x 10^{-5} for T_{SR} = 20 msec, but falls to 1.51 x 10^{-5} after an additional 2 msec in plug-flow.

SECTION III

THE HYDROCARBON PROBLEM

The results of Figure 3 serve in miniature to demonstrate that additional mechanistic complexities arise in the computation of fuel-nitrogen chemistry when hydrocarbons are present. Indeed, predictive modeling of bound-nitrogen emissions in a real-fuel, fuel-rich environment can be seen to be dependent upon the capability to model hydrocarbon decay kinetics for the following reasons:

(1) Interactions of fuel-nitrogen and hydrocarbon fragments may be quite significant, especially in recycling NO back to HCN. Omission of this class of reactions is consistent with the enhanced NO profile and diminished HCN profile calculated in Figure 3. Also,

(2) the radical pool (H,O,OH) which drives the fuel-nitrogen chemistry is determined primarily by the hydrocarbon chemistry which dominates the system at early times.

Insofar as fuel-rich operation contributes to NO_x abatement strategies, it seems necessary to model hydrocarbon burnout if ppm-level accuracy is to be demanded of a fuel-nitrogen mechanism. Unfortunately, even modeling the combustion of methane--the simplest of hydrocarbons--currently strains the state-of-the-art, and only a phenomenological knowledge of the specifics of the interactive reactions between hydrocarbons and nitrogenous species are available. In addition, the validity of generalizing conclusions applicable to design considerations of real fuel systems based upon computations using methane as a model hydrocarbon fuel is still not, a priori, clear. Indeed, methane is an atypical fuel in that

(1) its H/C ratio of 4 greatly exceeds the H/C ratios of fuels of interest (H/C might equal 1.3, for example, for a coal-derived liquid),

(2) its combustion details might simulate paraffin-type species, but many fuels of practical nature are highly aromatic in character, and

(3) even as a paraffin, methane may be atypical in that methyl recombinations may be of unusual significance in its combustion mechanism.

Two questions of significance have, therefore, been identified.

(1) To what extent can the results of NO_x modeling in the presence of methane be taken as representative of fuels of practical interest? And, in order to answer that question,

(2) how can the combustion kinetics of higher hydrocarbons, more representative of fuels of practical interest, be modeled for the purposes of predicting fuel-nitrogen conversion to NO_x?

SECTION IV

METHODOLOGY FOR DEALING WITH HIGHER HYDROCARBONS

1 Detailed Kinetics

In this method, all species of significance and all essential elementary reactions of each species are identified, resulting in an extensive set of coupled rate equations which describe the kinetic behavior of the system. This, of course, is the most correct way to characterize the system, and is the method currently employed in the EER methane mechanism. The method suffers, however, from the limitations that:

a) For higher hydrocarbons, even straight chain paraffins, neither a complete set of species nor, certainly, of reactions is known – i.e., with few exceptions, the detailed combustion mechanisms are simply not available.

b) Theoretical synthesis of combustion mechanisms for higher hydrocarbons (as performed for CH_4, for example, by the method of Engleman(14,15)) is impractical because the magnitude of the problem grows exponentially (16) with the number of carbon atoms, resulting in reaction sets impractically large for computational studies, and because, in any event, virtually none of the elementary reaction rate constants are known. Additionally,

c) Even if such an approach were viable, the time and cost necessary to screen such reaction sets down to reasonable sizes, as well as the current dearth of experimental data necessary for model validation would render the method impractical.

Detailed kinetics are therefore rejected as a viable method of modeling the combustion chemistry of fuels of practical interest.

2 The Global and Semi-Global Methods

In this method, hydrocarbon burnout is modeled by a single "global" (or overall) relation of the form

$$CnHm + (n + \frac{m}{4})\ O_2 \rightarrow nCO_2 + \frac{m}{2}H_2O$$

for which a rate expression must be empirically determined. Even as a first estimate, this method really has little basis in theory, and has been shown to be applicable only where a single major heat release step is involved, thereby excluding its applicability to hydrocarbon oxidation. In any event, the method completely overlooks elementary reaction kinetics and intermediate radical formation and is of no utility in computing NO_x levels.

Hydrocarbon oxidation can be conceived of occuring, however, in two overlapping heat release steps: a rapid oxidation of the hydrocarbon to carbon monoxide and hydrogen (or water), followed by subsequent oxidation of the CO (and H_2). It is possible, therefore, to develop a semi-global method utilizing two (or more) sequential global steps and one (or more) stable intermediate species to describe the overall combustion process. Thus, for example

$$C_nH_m + (\frac{n}{2} + \frac{m}{4})O_2 \rightarrow nCO + (m/2)H_2O$$

followed by

$$CO + 1/2\ O_2 \rightarrow CO_2$$

This method has been used with some success (17) for the relatively simple case of methane oxidation, but again, in any case, suffers from the limitation of completely neglecting intermediate, radical species essential to prediction of trace NO formation levels.

A conceptually similar, but somewhat more detailed semi-global method has been under development by Dryer (18) for application to hydrocarbon burnout. In this method, paraffin oxidation has been separable into three global steps of the form

$$\text{Alkane} \rightarrow \text{Alkene} \rightarrow CO \rightarrow CO_2$$

Although this may be regarded as a significant improvement over two-step semi-global modeling for purposes of modeling heat release, it offers little practical improvement for purposes of modeling NO levels. Additionally, empirical rate expressions characterizing each global step are currently available only for paraffins up to butane. No rates are yet available for aromatic systems.

Global and semi-global methods are therefore inappropriate for NO_x modeling.

3 The Quasi-Global Method

In this method, the simple global step

$$C_nH_m + \frac{n}{2} O_2 \rightarrow nCO + \frac{m}{2} H_2$$

is followed by an elementary reaction mechanism (which is well known) for the $H_2/CO/O_2$ system. Because the time scale for CO burnout is long compared with the global conversion of the parent hydrocarbon to CO, a certain amount of modeling success may be achieved by assuming the global step to occur at an infinite rate - especially if attention is focussed primarily upon post-flame reactions - although, following the work of Edelman and Fortune (19), a finite rate expression for the global step may also be used to enhance modeling accuracy. Utilization of detailed kinetics for the CO/H_2 oxidation admits free radical chemistry to the mechanism, thus opening the door to computations coupling the detailed kinetics of fuel-nitrogen conversion with hydrocarbon burnout.

Several serious limitations to this method, however, must be noted:

a) Although a degree of "elementary" reaction chemistry is preserved in modeling the CO/H_2 oxidation step via detailed kinetics, the actual temporal history of the free radical pool may be seriously mis-calculated. Thus, attempts to model thermal-NO_x formation (20) in a methane flame by means of the quasi-global method have proven inadequate largely due to errors in the computed oxygen atom levels.

b) The nature of the global step is such as to remove all consideration of hydrocarbons from the model. However, as suggested by Figure 4 above, "recycling" of NO to form HCN in fuel-rich systems via reactions with hydrocarbons (e.g., $CH + NO \rightarrow HCN + O$) is a limiting factor in bound nitrogen decay in the presence of hydrocarbons, and must be considered in developing staging strategies to eliminate bound nitrogen from the combustor exhaust stream. Omission of all hydrocarbons from consideration is tantamount to neglect of many of the processes which require modeling.

c) Distinction among different hydrocarbon fuels is not readily apparent in any manner other than purely stoichiometric in the quasi-global model, although differences in molar enthalpies of fuels should lead to somewhat different computed time/temperature histories. Of course, the degree to which mechanistic chemistry differences (rather than temperature differences) distinguish NO_x emission levels from the combustion of different hydrocarbons is currently unclear (no definitive experimental data are currently available), and the hope is that mechanistic differences (for example, the distribution of intermediate hydrocarbon fragments) will prove to have only a second order influence upon NO_x levels. However, construction of a computational model which *a priori* neglects such considerations does seem less desirable than one which permits them.

It is concluded, therefore, that the quasi-global method, as currently utilized, is, if not inapplicable to the modeling of NO_x emissions from higher hydrocarbons, at least undesirable as a method with adequate predictive capabilities.

4 Development of a new Quasi-Global Method - QUAGMIRE

Having exhausted, as impractical or inapplicable, all existing methods of treating hydrocarbons of which we are aware, we propose a new quasi-global method of the following, general form:

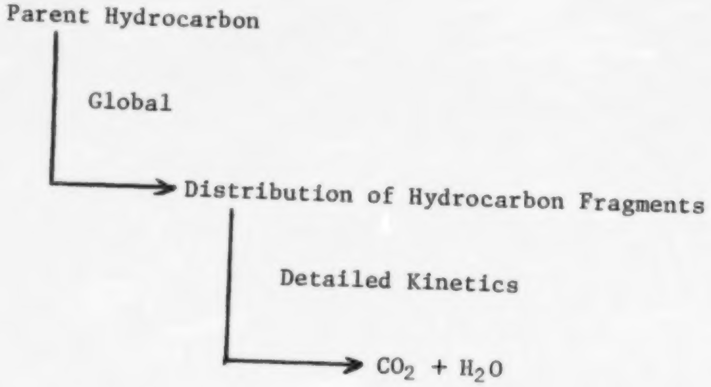

The basis underlying this hypothesized method rests upon the assumptions that the initial degradation of the parent hydrocarbon in the preflame zone via pyrolysis and oxidative pyrolysis routes is very rapid; that the initial decomposition products may be represented by a relatively small set of low molecular weight, stable and/or unstable hydrocarbon species; and, of course, that the decomposition mechanism can be justifiably represented by a global step.

The potential utility of the method lies in the following:

a) The advantages of modeling free radical chemistry by detailed kinetics are retained, but the magnitude of the elementary reaction set required is vastly reduced. Again, this reflects the exponential-like growth in reaction set magnitude with number of carbon atoms in the parent species. If only hydrocarbon fragments with relatively few carbon atoms are present following the global step, then the magnitudes of the reaction set - given by the union of the combustion reaction sets of the fragment species - will be small relative to the (hypothetical) reaction set of the parent hydrocarbon.

b) Whereas, even if the magnitude of the problem could be handled computationally, the detailed combustion mechanism of the parent hydrocarbon is generally unknown, detailed combustion mechanisms of many of the hydrocarbon fragments, which may be assumed to predominate at flame conditions, (see below) are known or are in varying stages of development.

c) Unlike the quasi-global method of Edelman and Fortune, hydrocarbons are retained in the elementary reaction scheme.

d) To the extent that an initial global step is applicable according to the method of Edelman and Fortune, the approximation should be more accurate here. This reflects a reduction in the mechanistic size of the global step, or, more significantly, a reduction in the magnitude of the reaction time or extent encompassed by the global step. That is, whereas the method of Edelman and Fortune takes a giant global step nearly to the postflame zone (where hydrocarbons have disappeared and CO has formed), it is arguable that the global step proposed here is completed in the preflame zone or early into the primary reaction zone (21) - which is where much of the essential fuel-nitrogen chemistry occurs! Thus, the global step may be regarded as faster on a time scale pertinent to fuel-nitrogen conversion. The probability of miscalculating the concentration/time history of the radical pool, for purposes of modeling NO_x emissions, is concurrently reduced.

In distinction to the quasi-global method of Edelman and Fortune, the technique proposed here may be referred to as the Quasi-Global Method applied to Initial Reaction Extents (QUAGMIRE).

5 Computational Applicability of QUAGMIRE

The potential utility of QUAGMIRE rests upon resolution of several key questions, definitive answers to which may, ultimately, only be found through experimentation. Included are:

a) Which hydrocarbon fragments must be considered?

b) What is the distribution function of hydrocarbon fragments?

c) Can infinite rate kinetics be used successfully for the global step, or must empirical determinations of global rates be made?

Clearly, the exact nature and distribution of the hydrocarbon fragments selected as decomposition products of the parent hydrocarbon will depend upon the identity of the parent fuel, the temperature, the equivalence ratio and time - or, put differently, upon the detailed kinetic reaction mechanism which is not, a priori, known. Certain generalizations, however, may be made.

The utility of QUAGMIRE really rests upon the ability to select a set of hydrocarbon fragments for which detailed combustion mechanisms are known. This pretty well limits the choice to C_1 and C_2 species, although the possibility of inclusion of selected C_3 and C_4 species, while not appealing, may not be beyond the realm of reason. This, in turn, implies the existence of a regime, at which point modeling commences, in which the reaction time is long enough for the parent hydrocarbon to have degraded to C_2 species, but simultaneously short enough to permit coupling with the fuel-nitrogen reactions.

That such a regime always exists for all fuels of interest is not, now, necessarily clear. But several strands of experimental evidence provide reason for optimism:

(1) the older literature on hydrocarbon prolysis and oxidative pyrolysis, as pointed out by Porter (22) in his old revitalization of the acetylene theory of soot formation, identifies the primary reactions occuring in homogeneous systems at temperatures of 700-1100°C as follows:

Higher olefins → lower olefins, paraffins, acetylene (23)
Higher paraffins → lower paraffins, olefins (24)
Methane → ethane, hydrogen (25)
Ethane → ethylene, hydrogen (26)
Ethylene → acetylene, hydrogen (27,28)
Aromatics → carbon, hydrogen, acetylene, methane (23)

Related observations were made by Singer and Grumer (29) who observed large, non-equilibrium concentrations of acetylene, methane and some ethylene in the burnt gases of rich propane/air flames, and by Fenimore, Jones, and Moore (30) who observed the same species to predominate in the post-flame gases of several hydrocarbon flames including benzene.

High temperature pyrolsis of benzene under inert conditions (Aromatic fuels pose the greatest potential problems in the context of this work) has been shown (31,32) to yield acetylene, diacetylene, hydrogen, and biphenyl as main, primary decomposition products, with enhancement (33) of fragmentation products over condensation products with increasing temperature. Ethylene and methane have also been identified (34) as decomposition products. Addition of trace amounts of O_2 (34) results in the production of CO and enhancement of the acetylene yield by an order of magnitude. Representative results of a shock tube oxidative pyrolysis study of benzene (34) are reproduced in Figure 5.

(2) The time scale on which the parent hydrocarbon decomposes to small fragments appears to be appropriate for implementation of QUAGMIRE. Thus, Figure 6 from a shock tube study by Orr (35) suggests a very favorable sequence of events in the combustion of n-heptane (iso-octane is similar). An even better example is provided from a study by Fenimore and Jones (36) of a very rich C_3H_8 flame,shown in Figure 7, in which the rapid degradation of the parent hydrocarbon to C_2 species, early in the flame zone, can readily be seen.

Apparently, the time scale for the degradation of aromatic species is similar, as can be seen in Figure 8 from a very recent study by Bittner (37) of a low pressure benzene/oxygen flame.

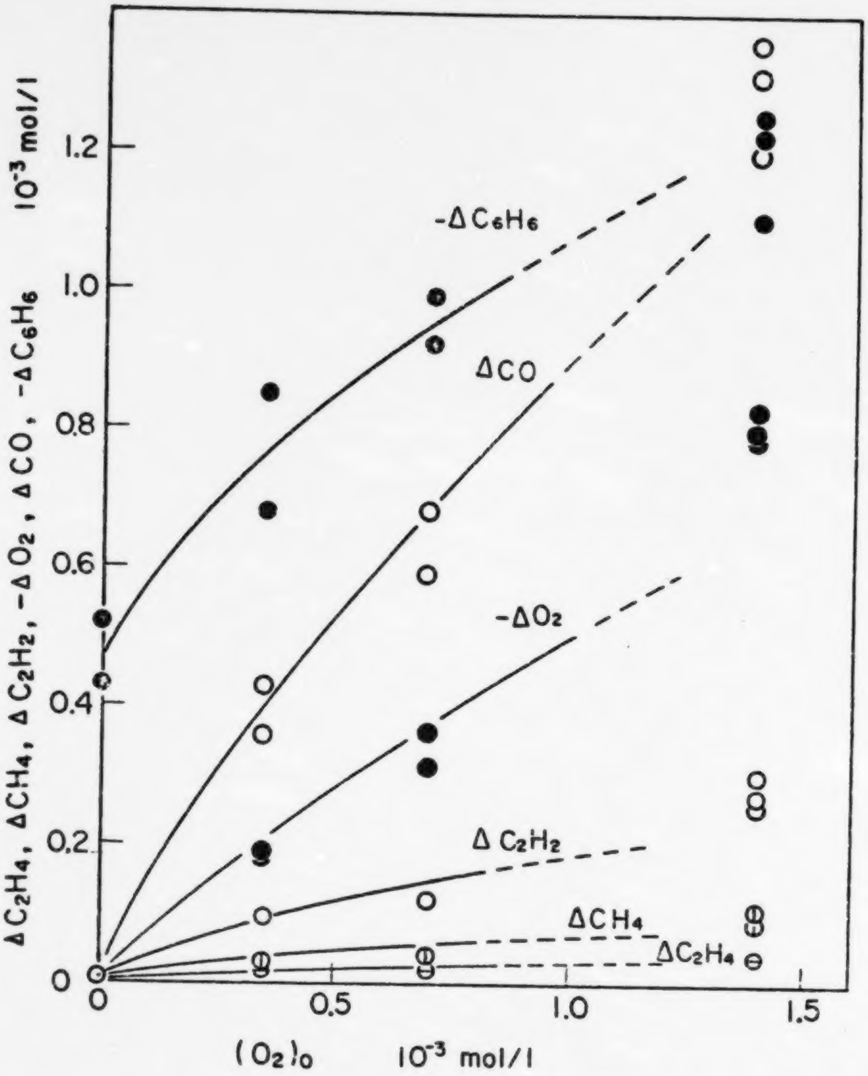

Figure 5. C_1 and C_2 oxidative pyrolysis products of Benzene. Conversions of benzene and oxygen and production of carbon monoxide and the lower hydrocarbons (acetylene, methane, and ethylene) when the initial concentration of oxygen is varied. The initial concentration of benzene is fixed at 3.5×10^{-3} mole/l; T = 1500 k. From a shock tube study by Fujii and Asaba [34].

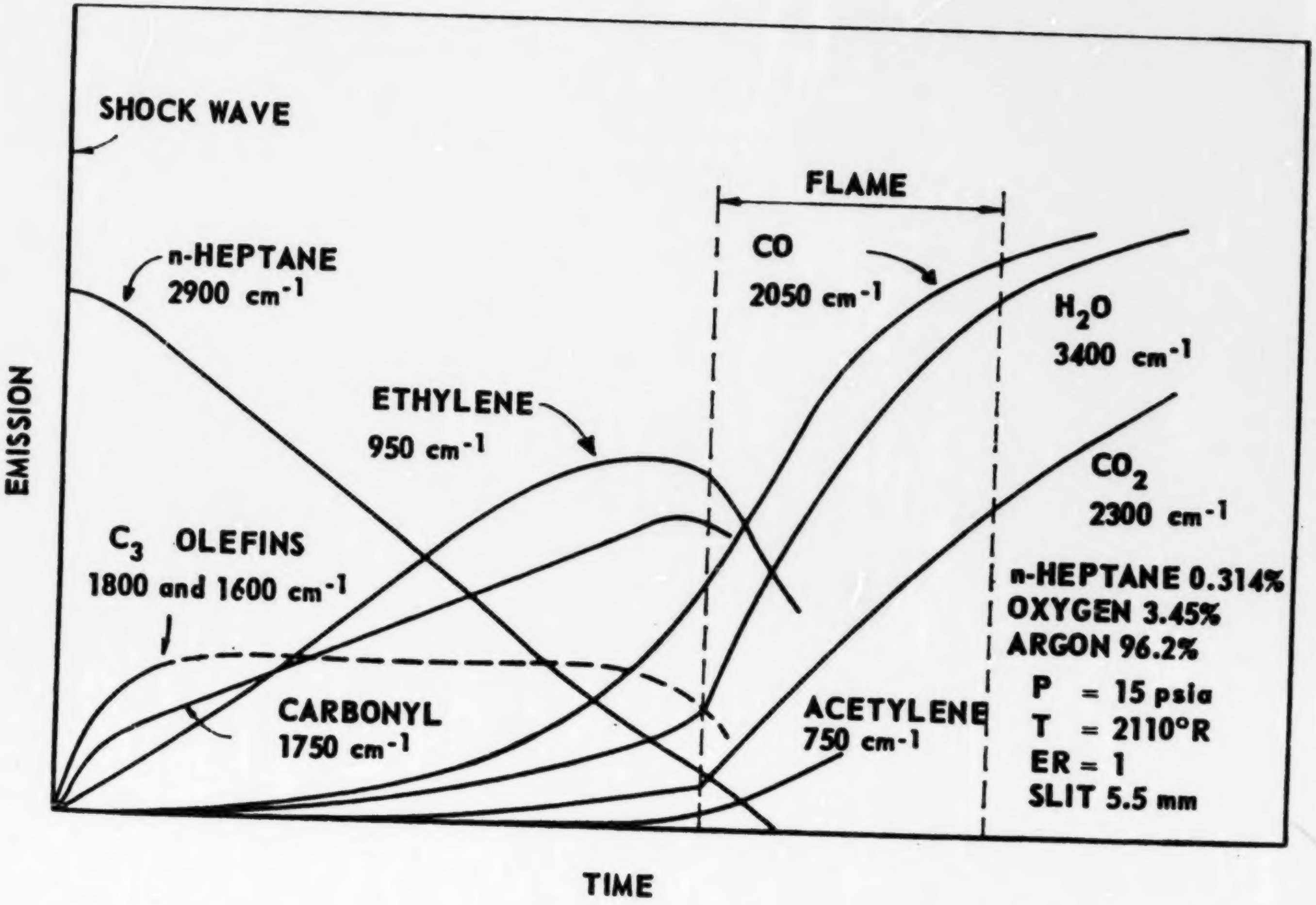

Figure 6. Lower hydrocarbon decomposition products of N-heptane. Pre-flame region. From a shock tube study by Orr [35].

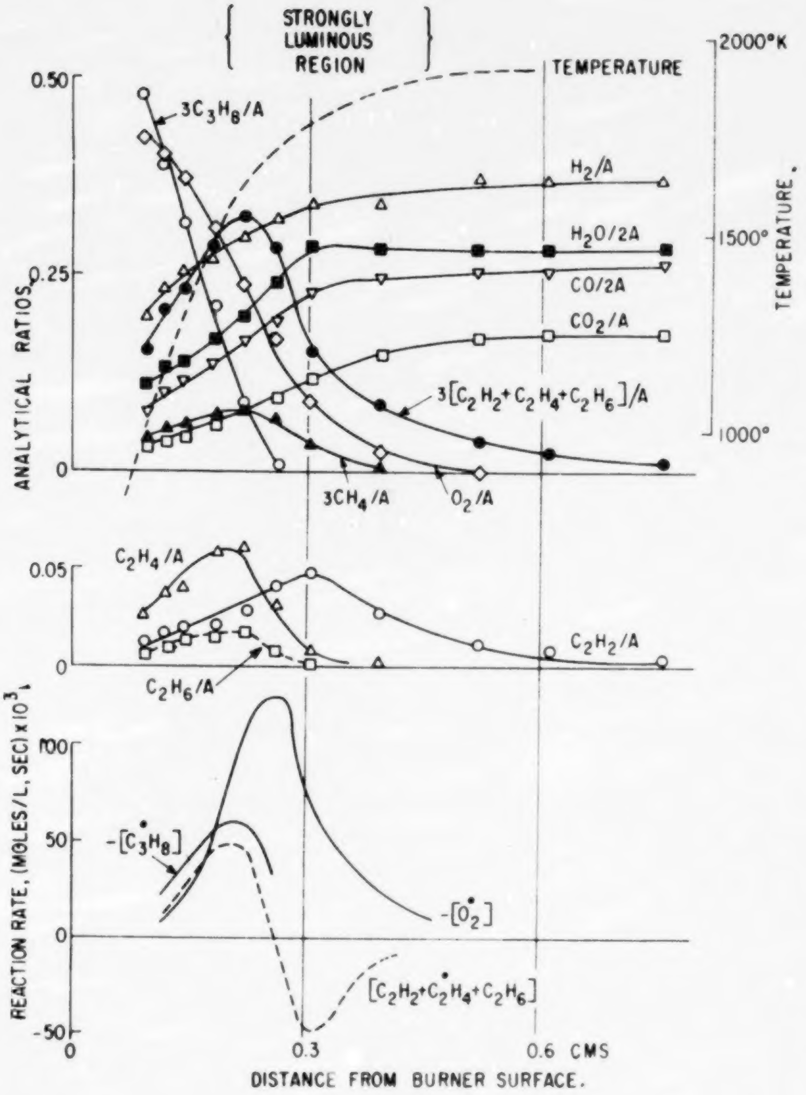

Figure 7. Rapid degradation of propane to lower hydrocarbons. From a rich flame study by Fenimore and Jones [36].

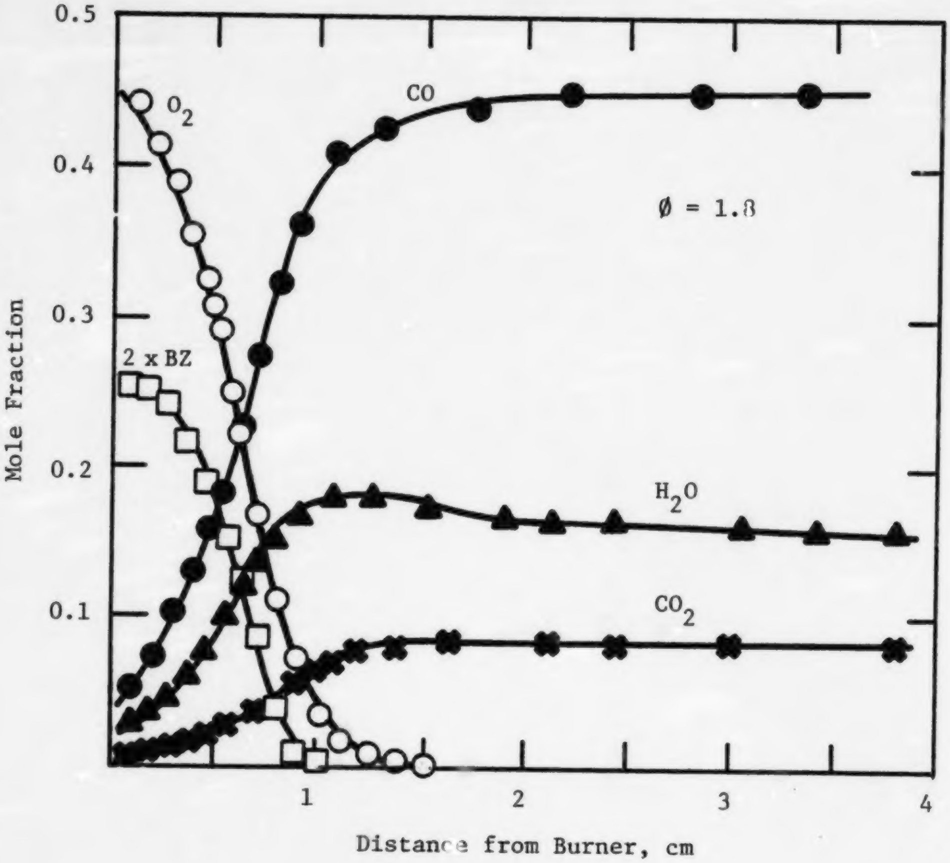

Figure 8a. Species Profiles in a Fuel-Rich (Ø = 1.8) Low-Pressure (p = 2.67, kPa = 20 torr) Benzene/Ozygen/Argon Flame. Data from Bittner (37).

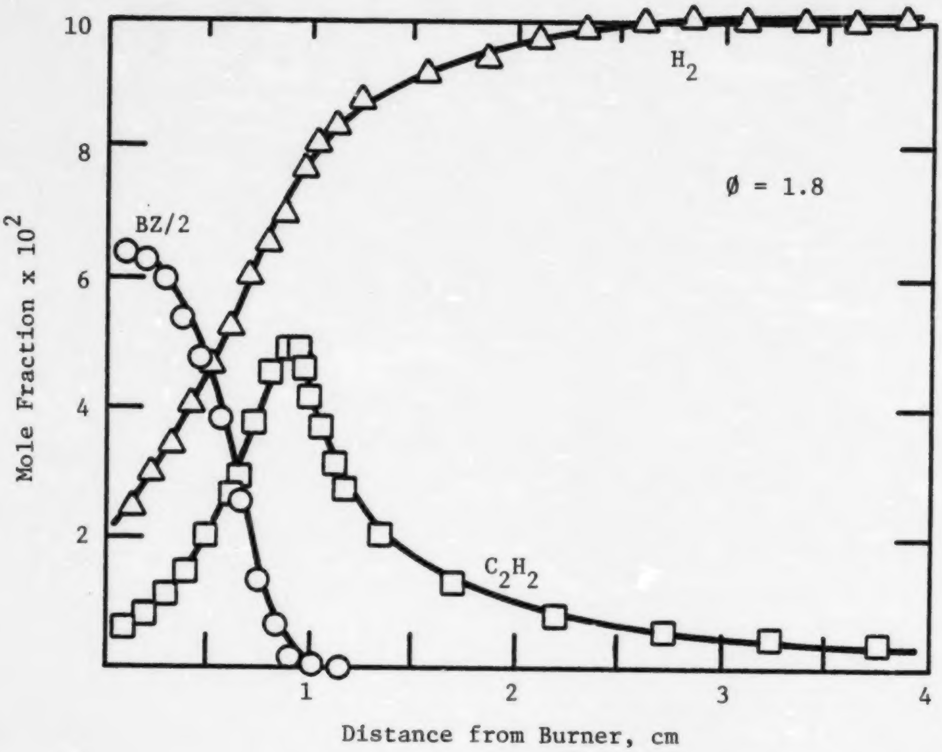

Figure 8b. Species Profiles in a Fuel-Rich ($\emptyset$ = 1.8) Low Pressure (p = 2.67, kPa = 20 torr) Benzen/Oxygen/Argon Flame. Data from Bittner (37).

It should be noted as above that although it is not true that the primary pyrolysis products of most hydrocarbons are uniformly C_1 and C_2 species, secondary and tertiary pyrolysis products are expected to be increasingly rich in these species. (22). (The major pyrolysis products of propane (38), for example, are H_2, CH_4, C_2H_4, and C_3H_6). The assumption underlying the applicability of QUAGMIRE is merely that the system eventually degrades to an adequately simple set of fragments to permit modeling by detailed kinetics, and that the time required to cascade down to this distribution is short enough to permit coupling with the fuel-nitrogen chemistry.

It appears logically appropriate, therefore, to take CH_4, C_2H_2, C_2H_4, CO, H_2, and possibly C_2H_6 and C_4H_2 as the initial set of stable hydrocarbon fragments.

The applicability of an infinite-rate global step would appear to rest on the time scale necessary for the system to decompose far enough to be described by this limited species set, or upon the willingness to expand this set to include earlier-time pyrolysis products. The alternative, of course, requires empirical determination of the global rate through experimentation.

SECTION V

THE C_2 MECHANISM

Having identified the C_1 and C_2 species as the basic building blocks of QUAGMIRE, the scope of the mechanistic hydrocarbon problem is vastly reduced, and it remains only to establish valid C_2 mechanisms in order to test the validity of QUAGMIRE. Indeed, an initial review of the literature turned up two similar C_2 mechanisms (39,40). Olson and Gardiner's (39), of course, is a mechanism developed primarily as a methane set which includes C_2 and C_4 species, and which, Gardiner reports (41), renders the closest fit of all available methane sets to a wide range of shock tube data. Jachimowski's (40) is an ethylene and acetylene set designed to fit fuel-lean shock tube results, and is, therefore, of less assistance in modeling fuel-rich data.

In an attempt to model Haynes' rich ethylene/air post-flame hydrocarbon decay data (Figure 3), Gardiner's reaction set was combined with the minimum subset fuel-nitrogen mechanism of Table 1, a small subset of CH-generating reactions borrowed from the EER/Engleman (14) methane reaction set compilation, shown in Table 2 (Gardiner's set does not include CH), and a small set of postulated hydrocarbon/fuel-nitrogen interactions, shown in Table 3, of which all but one are gleaned from the EER/Engleman compilation (14), the remaining, dominant (global) reaction of CH_3 with NO being taken from Haynes' (10,13) analysis. The resulting reaction mechanism of 101 reactions in 35 species is integrated to yield the results shown in Figure 9. Clearly, the "hump" generated in the methane profile is considerably in error. A computational study of the species flow identified the problem as Gardiner's reaction 42, $C_2H_2 + OH \rightarrow CH_3 + CO$, which accounts for most of the acetylene decay, but which feeds strongly into the CH_i set. Attempts to substitute related reactions as postulated by Breen and Glass (42), e.g. $C_2H_2 + OH \rightarrow CH + CH_2O$, improved the situation slightly, but still led to a hump, albeit smaller, in the methane profile. This encourages the conclusion that acetylene does not, mechanistically, decay through methane and that hydroxyl attack on acetylene does not yield products in the CH_i family. Interestingly, Gardiner

TABLE 2. REACTIONS INVOLVING CH TO BE APPENDED TO THE OLSON AND GARDINER MECHANISM

$$k_f = AT^N \exp\{-E/RT\}$$

	Reaction	A(cm^3/mole-sec)	N	E(Cal/mole)
1	$CH_2 + H = CH + H_2$	3.16×10^{11}	0.70	5,000
2	$CH_2 + OH = CH + H_2O$	5.00×10^{11}	0.50	6,000
3	$CH + CO_2 = CHO + CO$	1.00×10^{10}	0.50	6,000
4	$CH + OH = CHO + H$	5.00×10^{11}	0.50	10,000
5	$CH + O_2 = CHO + O$	5.00×10^{11}	0.50	6,000
6	$CH + O = CO + H$	5.00×10^{11}	0.50	0

All rates from Engleman, V.S., "Survey and Evaluation of Kinetic Data on Reactions in Methane/Air Combustion," EPA Report EPA-600/2-76-003 (1976)

TABLE 3. HYDROCARBON FRAGMENT/FUEL-NITROGEN INTERACTIONS
$k_f = AT^N \exp\{-E/RT\}$

	Reaction	$A(cm^3/mole\text{-}sec)$	N	E (Cal/mole)	Ref.
1	$CH_4 + CN = CH_3 + HCN$	3.16×10^{11}	0.70	5,000	a
2	$CH_2 + N_2 = HCN + NH$	1.00×10^{14}	0	60,000	b
3	$CH_2 + NO = CH_2O + N$	1.60×10^{12}	0	7,000	a
4	$CHO + N = CH + NO$	1.00×10^{14}	0	48,600	c
5	$CHO + N = HCN + O$	1.00×10^{14}	0	0	a
6	$CHO + N = CO + NH$	2.00×10^{11}	0.50	2,000	a
7	$HCN + N = CH + N_2$	2.50×10^{11}	0	16,000	b
8	$HCN + O = CH + NO$	1.00×10^{14}	0	72,000	b
9	$CN + NH = CH + N_2$	1.00×10^{14}	0	40,000	b
10	$CH_3 + NO = \ldots = HCN + H_2O$	2.20×10^{11}	0	0	d

References

[a] Engleman, V.S., "Survey and Evaluation of Kinetic Data on Reactions in Methane/Air Combustion," EPA Report, EPA-600/2-76-003 (1976).

[b] Benson, S.W., D.M. Golden, R.W. Lawrence, R. Shaw and R.W. Woolfolk, "Estimating the Kinetics of Combustion: Including Oxides of Nitrogen and Sulfur," EPA Report, EPA-600/2-75-019 (1975), and estimates based thereon.

[c] Estimate based upon Engleman (Reference [a]).

[d] Haynes, B.S., "Kinetics of Nitrogen Oxide Formation in Combustion," in *Progress in Astronautics and Aeronautics, Vol. 62: Alternative Hydrocarbon Fuels: Combustion and Chemical Kinetics*, (C.T. Bowman and J. Birkeland, eds.) American Institute of Aeronautics and Astronautics (1978).

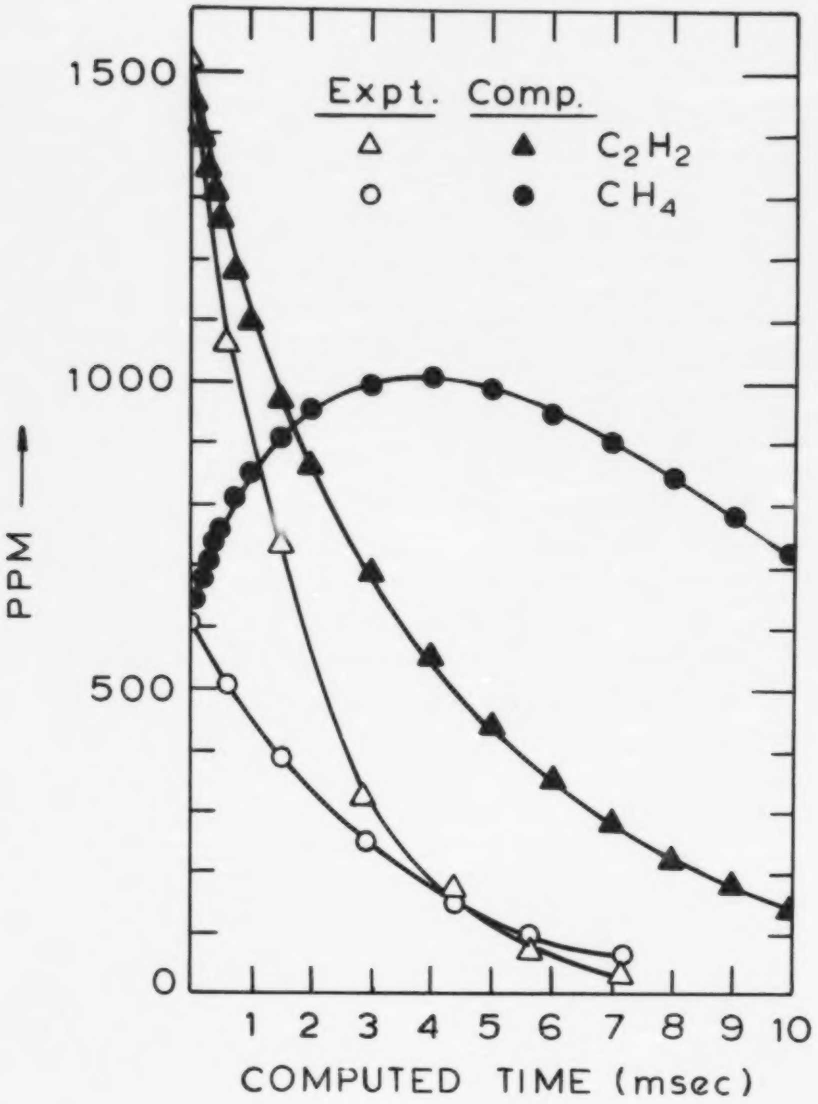

Figure 9a. Post-flame zone of a C_2H_4/air flame doped with 500 PPM NO (ϕ=1.66, T=2000 K) including hydrocarbon "breakthrough", modeled with Gardiner's reaction set [39] supplemented by the reactions of Tables 1 - 3. Data from Haynes [13].

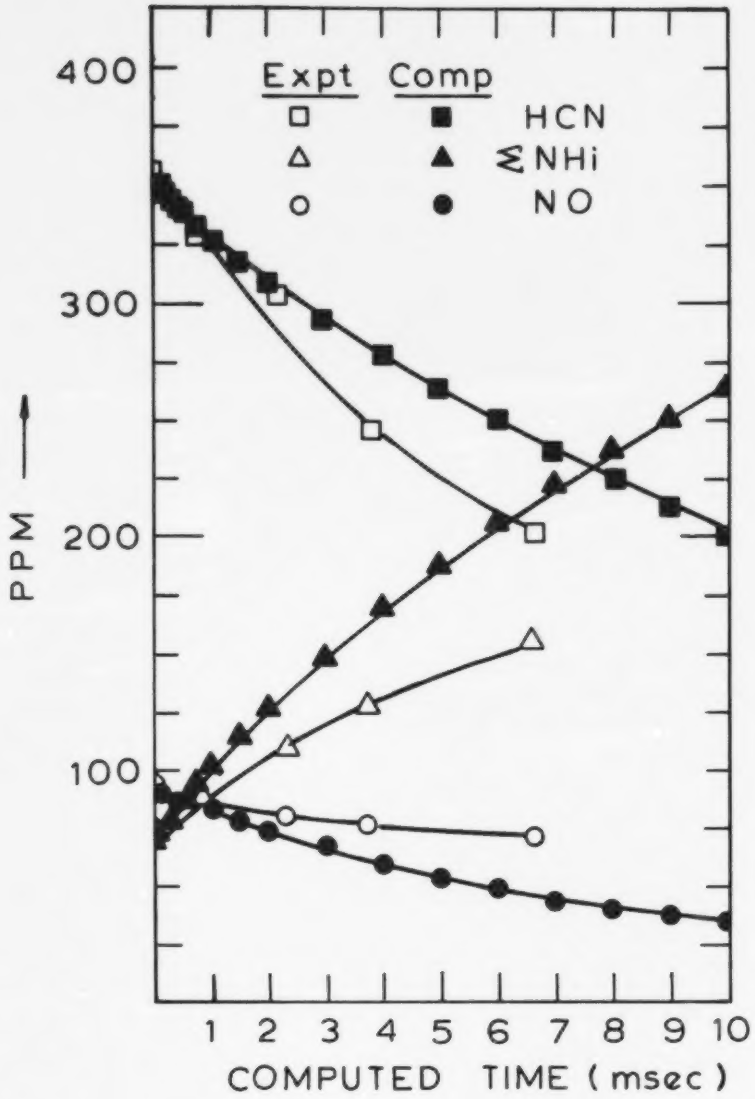

Figure 9b. Post-flame zone of a C H /air flame doped with 500 PPM NO (ϕ=1.66, T=2000 K) including hydrocarbon "breakthrough", modeled with Gardiner's reaction set [39] supplemented by the reactions of Tables 1 - 3. Data from Haynes [13].

(43) has reported that his own modeling efforts of C_2 shock tube data reveal deficiencies in this mechanism, and this may be one of them. Also of interest is the recent information (44) that the older, reported observation (45) of CH_3 as a primary product of OH attack on acetylene is now regarded as an experimental artifact. The uniqueness of access to experimental data showing the simultaneous decay of methane and acetylene has, as stated above, led firmly to the conclusion that, at least under the conditions tested here, acetylene does not decay through methane. Lean, oxygen atom rich conditions may be different.

Under fuel-rich conditons, however, there is really no question that the primary step which destroys acetylene is reaction with the hydroxyl radical. Not only is this assertion supported by past work (46), but omission of the C_2H_2/OH reaction entirely from the oomputations can be shown to virtually turn off the acetylene decay.

Insofar as the products of this reaction cannot be members of the methane family, and are, more likely, addition products (47), one is led to suggest that the primary product of OH attack upon acetylene is CH_2CO, ketene in accordance with the speculations of Vandooren and Van Tiggelen (48) and others (49). Gardiner's reaction (42), is, therefore, replaced, minimally, with the following pair of reactions:

A: $C_2H_2 + OH \rightarrow CH_2CO + H$

B: $CH_2CO + OH \rightarrow CH_2O + CHO$

where k_A is taken as 2.0×10^{12} cm^3/mole-sec in accordance with Bittner's (37) recent estimate (This is approximately a factor of two greater than Gardiner's rate at 2000K), and k_B is arbitrarily taken as 1.0×10^{13} cm^3/mole-sec, selected to assure rapid throughput of the ketene intermediate. The thermochemistry of ketene was estimated from an extension of Benson's (50) compliation. The computed results. shown in Figure 10 demonstrate the desired decay behavior as well as fuel-nitrogen profiles improved over those of Figure 3.

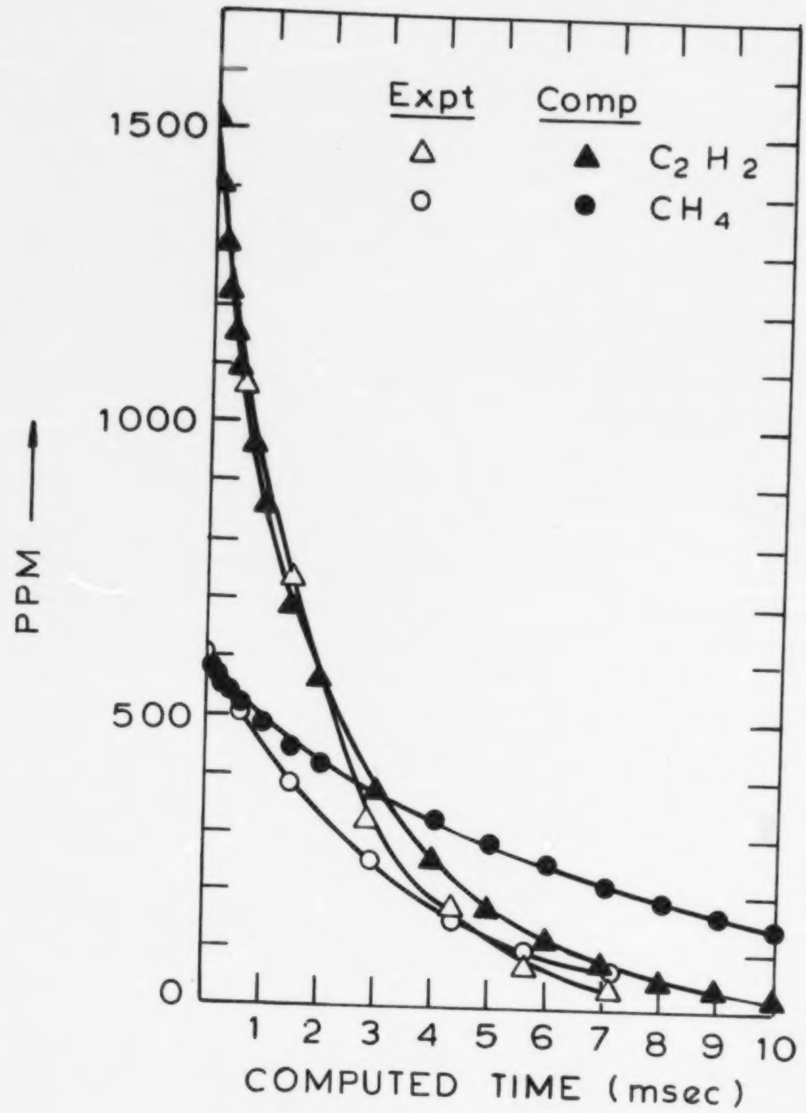

Figure 10a. Post-flame zone of a C_2H_4/air flame doped with 500 PPM NO (ϕ=1.66, T=2000 K) including hydrocarbon "breakthrough", modeled with Gardiner's reaction set [39] altered to include a ketene intermediate, supplemented by the reactions of Tables 1 - 3. Data from Haynes [13].

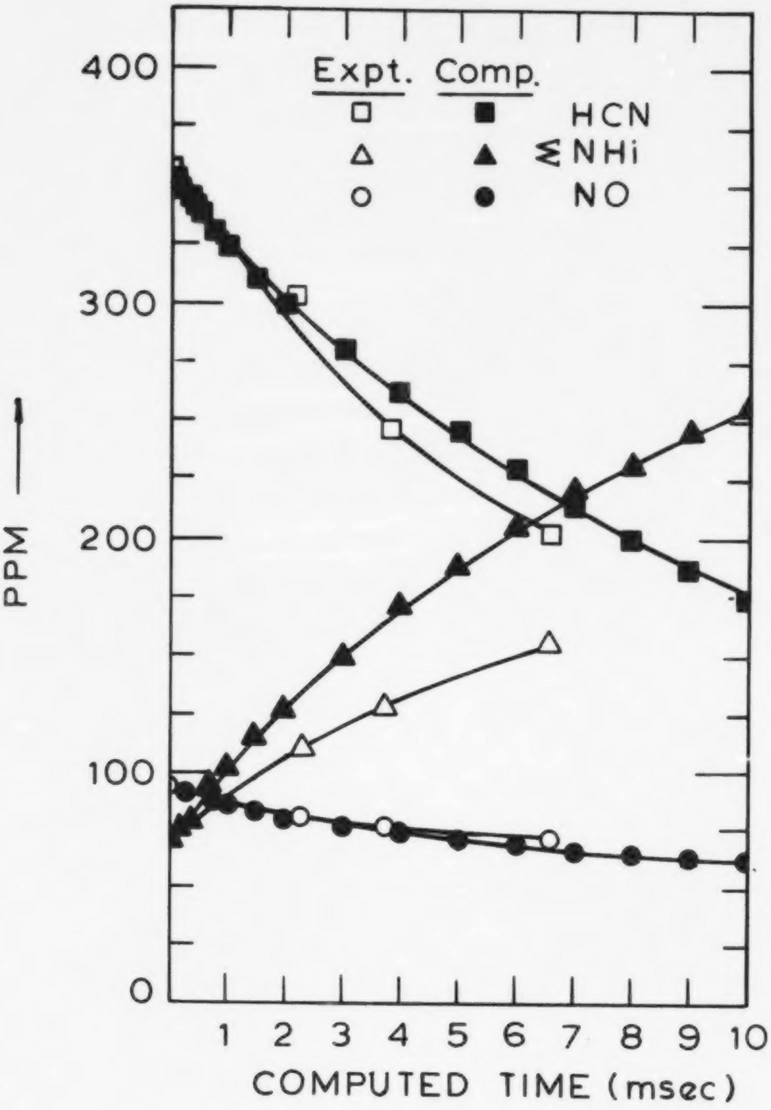

Figure 10b. Post-flame zone of a C_2H_4/air flame doped with 500 PPM NO (ϕ=1.66, T=2000 K) including hydrocarbon "breakthrough", modeled with Gardiner's reaction set [39] altered to include a ketene intermediate, supplemented by the reactions of Tables 1 - 3. Data from Haynes [13].

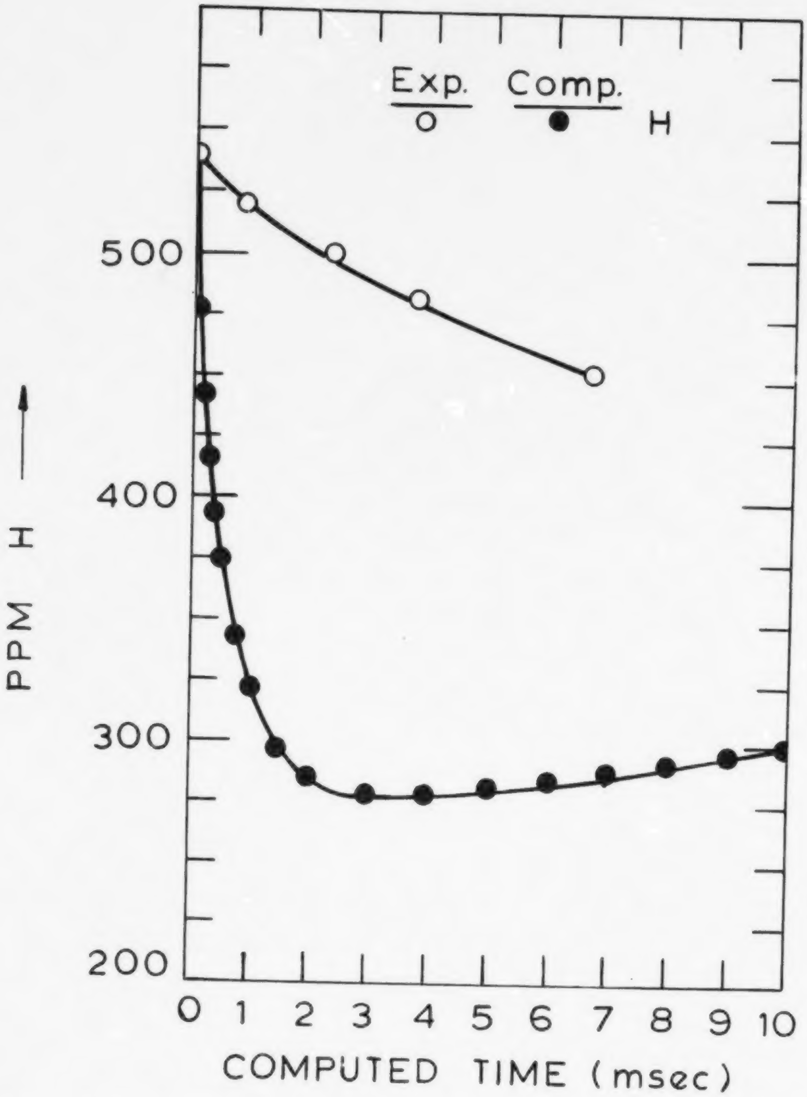

Figure 10c. Post-flame zone of a C_2H_4/air flame doped with 500 PPM NO (ϕ=1.66, T=2000 K) including hydrocarbon "breakthrough", modeled with Gardiner's reaction set [39] altered to include a ketene intermediate, supplemented by the reactions of Tables 1 - 3. Data from Haynes [13].

As a check on the hydrocarbon reaction mechanism used, similar calculations were performed on an independent set of data acquired recently in a complementary flame study at MIT (51). The decay of acetylene, methane, and ethylene, measured by gas chromatography in the post-flame gases of a rich ($\phi = 1.82$), atmospheric pressure ethylene/air flame, and the profiles computed isothermally in plug-flow are shown in Figure 11. The reaction mechanism is identical to that used in Figure 10. Because neither experimental temperature nor free-radical profiles are yet available, initialization of the calculations assumed equilibration of the H/O radial pool with the burnt gases, as supported by the observations of Fenimore and Jones (36,46,52) and Reid and Wheeler (53) that under conditions of hydrocarbon breakthrough, radical overshoot is surpressed. In view of the proximity of the flame to blowoff, the adiabatic flame temperature of 2127 K was assumed. Calculated acetylene and methane profiles fit the data closely, although the decay of ethylene (present in only minute quantities) is not simulated well.

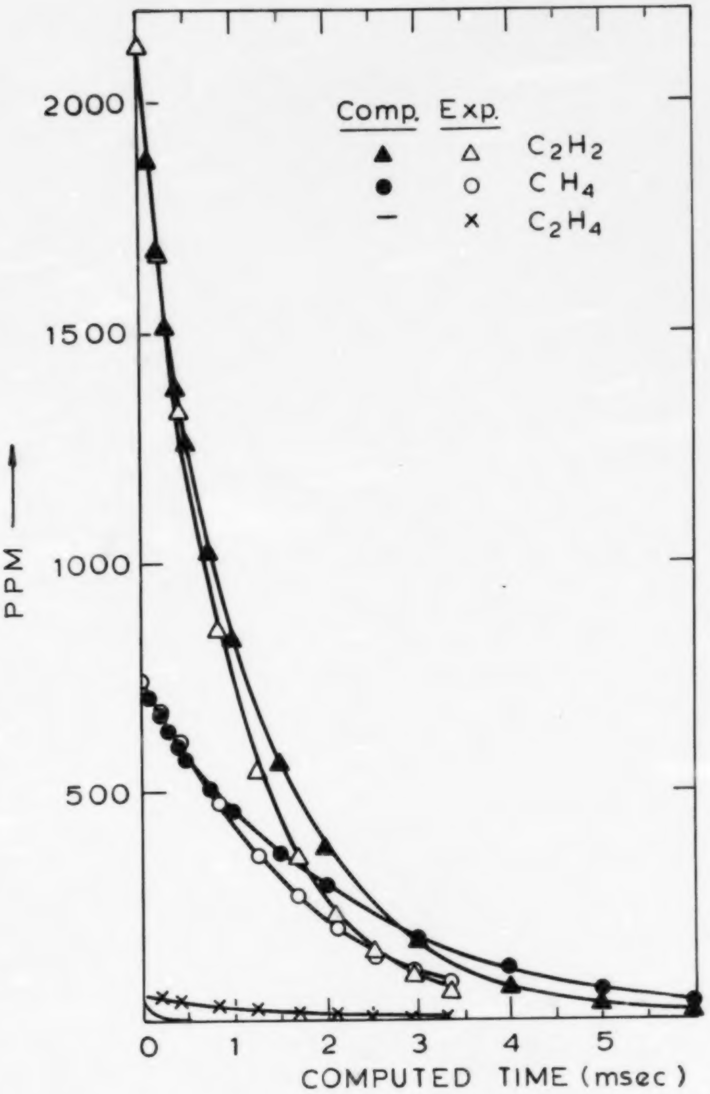

Figure 11. Hydrocarbon decay in the post-flame zone of a C_2H_4/air Flame (ϕ=1.82, T=2127 K) modeled using the ketene mechanism. Data from Taylor [51].

SECTION VI

DISCUSSION

Calculation of bound nitrogen species in a hydrocarbon combustion environment requires a reaction mechanism which can be viewed as a synthesis of three subsets: Fuel-nitrogen conversion, hydrocarbon oxidation, and hydrocarbon/nitrogen interactions.

Large, master fuel-nitrogen sets have been proposed and studied,(2,11) though the subset of Table 1 is probably equivalent for predictive modeling at high temperatures. In either case, as evidenced by Figures 2 and 10, a deficiency exists in the computation of ammonia levels. It has become clear from this as well as earlier studies,(8c,10) that an accerated mechanistic path from amines to N_2 (not reaction of NO with NH_2), possibly through N_2H_i species, is probably of importance.

The reaction set representing hydrocarbon/fuel-nitrogen interactions (Table 3) is rather speculative. As written, its influence on bound nitrogen levels is dominated by the CH_3/NO reaction, as suggested by Haynes,(10) although the global nature of this reaction, as written, should make it clear that only phenomenological significance can be attached to it. Clearly, insofar as CH_3 levels are much higher than those of the other hydrocarbon fragments considered, this reaction predominates. It is noteworthy, that interactions with higher hydrocarbons are omitted, although they too could be postulated. However, at this point it seems reasonable not to further clutter an uncertain mechanism, especially in view of the study of Hayhurst & Vince(54) in which "prompt NO" formed in hydrocarbon-doped $H_2/O_2/N_2$ flames, found to be proportional to the number of carbon atoms per molecule of hydrocarbon additive, suggested C_1 species to dominate the interactive chemistry with N_2.

Calculation of the elementary reaction kinetics of high temperature hydrocarbon combustion clearly strains the current state-of-the-art, even for the most limited set of C_1 and C_2 species, although alteration of the primary step of hydroxyl attack upon acetylene to include a ketene intermediate has been shown to greatly improve the situation. This mechanistic change, however, is phenomenological in that it merely provides a plausible mode of acetylene decay which does not feed into the methane set. Proof positive of this, or any, reaction sequence, however, rests at very least upon comparison with experimental measurements of a much fuller set of intermediate species profiles. Indeed, despite the mechanistic improvement to the acetylene set, observation of the H-atom profile of Figure 10c (Compare with Figure 3b) clearly demonstrates a deficiency inherent to the hydrocarbon reaction model - namely, too rapid a decline in the computed free radical pool. It would appear, at first glance, that, for the purposes of modeling bound-nitrogen levels, inclusion of hydrocarbon chemistry has, even with hydrocarbon/fuel-nitrogen interactions included, merely substituted one limitation for another. This, of course, is not quite true, as the calculated bound-nitrogen profiles of Figure 10 really are better than those of Figure 3. Quite clearly, also, one can see that were the computed radical pool to fall more slowly, the HCN decay profile (as well as the C_2H_2 and CH_4 decay profiles) would decline to a level still closer to the experimental value.

Evidently, then, the outstanding phenomenological question to be raised in connection with the modeling of hydrocarbon chemistry pertains to the fate of the free-radical pool. Hydrocarbon fragments, as is well known, effectively catalyze radical recombinations. The specific mechanism of this process is not clearly delineated, but may be ascribed either to hydrocarbon molecules acting as highly efficient third bodies(55) because of their capacity to store large amounts of energy in internal modes, or to interactive processes of the form(56)

$$\begin{array}{l} H + C_2H_2 \rightarrow C_2H + H_2 \\ C_2H + H + M \rightarrow C_2H_2 + M \\ \hline H + H + M \rightarrow H_2 + M \end{array}$$

or to other unknown mechanisms. In any case, free radical overshoots in hydrocarbon-rich systems are observed to be very small relative to those in hydrocarbon-free systems, the radical pool tending towards an equilibrium value(36,46,52,53)in the case of hydrocarbon breakthrough. The problem demonstrated in Figure 10c, however, is that too rapid a decline in the radical concentration is computed, which suggests, if the experimental data are to be believed, that some additional branching step is missing from the hydrocarbon mechanism employed here. Indeed, it is known that under fuel lean conditions, primary steps in the mechanism of acetylene decay include(57,58)

$$C_2H_2 + O \rightarrow [C_2H_2O] \rightarrow CH_2 + CO$$
$$CH_2 + O \rightarrow CO + H + H$$

where it has been shown that methylene generated in the former reaction is in its triplet state(59)(In agreement with spin-conservation considerations), and, more significantly for the purposes of this discussion, that the latter reaction is unambiguously chain-branching(58,60) producing dissociated hydrogen atoms. Although these particular reactions with O-atoms cannot be of great significane under the extremely fuel rich conditions of interest here (H:OH:O ~500:50:0.1), inclusion of this class of branching reaction may well prove to be the key to the disappearing radical phenomenon otherwise computed. Indeed, a crude estimate of radical versus hydrocarbon consumption from Haynes' data (Figure 10) suggests that approximately one radical is destroyed per four methane molecules consumed (The acetylene mechanism, running through the ketene intermediate, roughly conserves free-radicals) whereas the computational sequence invoked consumes roughly 0.4 to 0.6 free radicals per methane molecule. This suggests that addition of a chain branching step through which roughly one quarter of the methane would be routed might be adequate to restore the computed radical pool to the experimentally determined level.

REFERENCES

1. Levy, J.M., J.H. Pohl,A.F.Sarofim and Y.H. Song, "Combustion Research on the Fate of Fuel-Nitrogen Under Conditions of Pulverized Coal Combustion," EPA Report EPA-600/7-78-165 (August, 1978).
2. Levy, J.M., J.P. Longwell, A.F. Sarofim, T.L. Corley, M.P. Heap and T.J. Tyson, "NO_x Abatement in Fossil Fuel Combustion: Chemical Kinetic Considerations," *Proceedings of the Third Symposium on Stationary Source Combustion, Vol. IV*, EPA-600/7-79-050, p.3 (March, 1979).
3. Fenimore, C.P., "Formation of Nitric Oxide from Fuel-Nitrogen in Ethylene Flames," *Comb. and Flame 19*, 289 (1972).

4a. DeSoete, G.G., "Le Mecanisme de Formation, d'Oxyde Azotique a Partir d'Amoniac et d'Amines dans les Flammes d'Hydrocabures," *Revue de L'Institute Francais du Petrole 28*, 95 (1973).

4b. DeSoete, G.G. and A. Queraud, "Formation d'Oxyde d'Azote dans les Flammes: Formation d'Oxyde d'Azote a Partir de l'Azote du Combustible - C-Addition de NO dans les Melanges Inflammable," Report No. I.F.P. No. 21.681, Institute Francais du Petrole, Rueil Malmaison, France (1973).

5. Sarofim, A.F., G.C. Williams, M. Modell and S.M. Slater, "Conversion of Fuel-Nitrogen to Nitric Oxide in Premixed and Diffusion Flames," AIChE Symposium Series 148, Volume 7, 51, (1975).
6. Corley, T.L., this Symposium.
7. Heap, M.P., T.J. Tyson, J.E. Cichanwicz, R. Gersham, C.J. Kau, G.B. Martin and W.S. Lanier, "Environmental Aspects of low BTU Gas Combustion," Sixteenth Symposium (International) on Combustion, The Combustion Institute, p.535 (1977).
8. Recent examples include:
    a. Fenimore, C.P., "Reactions of Fuel-Nitrogen in Rich Flame Gases," *Comb. and Flame 26*, 249 (1976).
    b. Morley, C., "The Formation and Destruction of Hydrogen Cyanide from Atmospheric and Fuel-Nitrogen in Rich, Atmospheric-Pressure Flames," *Comb. and Flame 27*, 189 (1976).
    c. Haynes, B.S., "Reactions of Ammonia and Nitric Oxide in the Burnt Gases of Fuel-Rich Hydrocarbon-Air Flames," *Comb. and Flame 28*, 81 (1977).
    d. Haynes, B.S., "The Oxidation of Hydrogen Cyanide in Fuel-Rich Flames," *Comb. and Flame 28*, 113 (1977).

9. Sarofim, A.F., J.H. Pohl, and B.R. Taylor, "Strategies for Controlling Nitrogen Oxide Emissions During Combustion of Nitrogen Bearing Fuels," AIChE 69th Annual Meeting, Chicago (1976).

10. Haynes, B.S., "Kinetics of Nitrogen Oxide Formation in Combustion," in *Progress in Astronautics and Aeronautics, Volume 62* (C.T. Bowman and J. Birkeland, eds.), *Alternative Hydrocarbon Fuels: Combustion and Chemical Kinetics,* American Institute of Aeronautics and Astronautics (1978).

11. Levy, J.M., J.P. Longwell and A.F. Sarofim, "Conversion of Fuel-Nitrogen to Nitrogen Oxides in Fossil Fuel Combustion: Mechanistic Considerations," Report to Energy and Environmental Research Corp. by the MIT Energy Laboratory. EPA FCR Program (1978).

12. Hack, W., H. Schacke, M. Schröter and H.G. Wagner, "Reaction Rates of NH_2 Radicals with NO, NO_2, C_2H_2, C_2H_4 and Other Hydrocarbons," Seventeenth Symposium (International) on Combustion, The Combustion Institute, p. 505 (1979).

13. Haynes, B.S., "The Formation and Behavior of Nitrogen Species in Fuel Rich Hydrocarbon Flames," Ph.D. Thesis, University of New South Wales, Sydney, Australia (1975).

14. Engleman, V.S., "Survey and Evaluation of Kinetic Data on Reactions in Methane/Air Combustion," EPA Report, EPA-600/2-76-003 (1976).

15. Engleman, V.S., "Detailed Approach to Kinetic Mechanisms in Complex Systems," *J. Phys. Chem. 81*, 2320 (1977).

16. Cohen, R.C., "The High Temperature Oxidation and Pyrolysis of Ethane," Ph.D. Thesis, Princeton University, Department of Aerospace and Mechanical Sciences (1972).

17a. Dryer, F.L., "High Temperature Oxidation of Carbon Monoxide and Methane in a Turbulent Flow Reactor," Ph.D. Thesis, Princeton University, Department of Aerospace and Mechanical Sciences (1972).

17b. Dryer, F.L. and I. Glassman, "High Temperature Oxidation of CO and CH_4", Fourteenth Symposium (International) on Combustion, The Combustion Institute, Pittsburgh, Pa. p.987 (1973).

18. Dryer, F.L. and I. Glassman, "Combustion Chemistry of Chain Hydrocarbons," in *Progress in Astronautics and Aeronautics, Volume 62* (Bowman, C.T. and J. Birkeland eds.) *Alternative Hydrocarbon Fuels: Combustion and Chemical Kinetics*, American Institute of Aeronautics and Astronautics (1978).

19. Edelman, R.B. and O.F. Fortune, "A Quaisi-Global Chemical Kinetic Model for the Finite Rate Combustion of Hydrocarbon Fuels with Application to Turbulent Burning and Mixing in Hypersonic Engines and Nozzle," AIAA Paper No. 69-86 (1969).

20. Bowman, C.T. and A.S. Kesten, "Kinetic Modeling of Nitric Oxide Formation in Combustion Processes," presented at the Fall Meeting, Western States Section of The Combustion Institute, Paper No. 71-28, Irvine, California (October, 1971).

21. Millikan, R.C., "Non-equilibrium Soot Formation in Premixed Flames," *J. Phys. Chem. 66*, 794 (1962).

22. Porter, G., "Carbon Formation in the Combustion Wave," Fourth Symposium (International) on Combustion, The Combustion Institute, p.248 (1953).

23. Egloff, G., *Reactions of Pure Hydrocarbons*, A.C.S. Monograph (1937).

24. Stubbs, F.J. and C.N. Hinshelwood, "The Thermal Decomposition of Hydrocarbons," *Disc. Farad. Soc. 10*, 129 (1951).

25. Storch, H.H., "The Thermal Decompositon of Methane by a Carbon Filament," *J. Am. Chem. Soc. 54*, 4188 (1932).

26. Tropsch, H. and G. Egloff, "High Temperature Pyrolysis of Gaseous Paraffin Hydrocarbons," *Ind. Eng. Chem. 27*, 1063 (1935).

27. Storch, H.H., "Acetylene Formation in Thermal Decomposition of Hydrocarbons," *Ind. Eng. Chem. 26*, 56 (1934).

28. Knox, K., R.G. Norrish and G. Porter, "The Photochemical Decomposition of Keten by Means of Light of Very High Intensity," *J. Chem. Soc.* 1477 (1952).

29. Singer, J.M. and J. Grummer, "Carbon Formation in Very Rich Hydrocarbon-Air Flames: I - Studies of Chemical Content, Temperature, Ionization and Particulate Matter," Seventh Symposium (International) on Combustion, The Combustion Institute, p.559 (1959).

30. Fenimore, C.P., G.W. Jones and G.E. Moore, "Carbon Formation in Quenched Flat Flames at 1600° K, Sixth Symposium (International) on Combustion" The Combustion Institute, p.242 (1957).

31. Kinney, C.R. and R.S. Slysh, "On the Mechanism of Carbonization of Benzene, Acetylene, and Diacetylene at 1200° C", *Proceedings of the Fourth Conference on Carbon*, Pergamon Press, New York, p.301 (1960).

32. Asaba, T. and N. Fujii, "Shock-Tube Study of High-Temperature Pyrolysis of Benzene," Thirteenth Symposium (International) on Combustion, The Combustion Institute, Pittsburgh, Pa. p.155 (1971).

33. Graham, S.C., J.B. Homer and J.L.J. Rosenfeld, "The Formation and Coagulation of Soot Aerosols Generated by the Pyrolysis of Aromatic Hydrocarbons," *Proceedings of the Royal Society of London, 344,* 259 (1975).

34. Fujii, N. and T. Asaba, "Shock-Tube Study of the Reaction of Rich Mixtures of Benzene and Oxygen," Fourteenth Symposium (International) on Combustion, The Combustion Institute, Pittsburgh, Pa. p.433 (1973).

35. Orr, C.R., "Combustion of Hydrocarbons Behind a Shock Wave," Ninth Symposium (International) on Combustion, The Combustion Institute, Pittsburgh, Pa. p.1034 (1963).

36. Fenimore, C.P. and G.W. Jones, "Consumption of Oxygen Molecules in Hydrocarbon Flames Chiefly by Reaction with Hydrogen Atoms," *J. Phys. Chem. 63,* 1834 (1959).

37. Bittner, J.D., Ph.D. Thesis, MIT Department of Chemical Engineering, in preparation.

38. Volkar, A.G. and G.C. April, "Survey of Propane Pyrolysis Literature," *INd. Eng. Chem. Process Des. Dev. 16,* 429 (1977).

39. Olson, D.B. and W.C. Gardiner, Jr., "Combustion of Methane in Fuel-Rich Mixtures," *Comb. and Flame 32,* 151 (1978).

40. Jachimowski, C.J., "An Experimental and Analytical Study of Acetylene and Ethylene Oxidation behind Shock Waves," *Comb. and Flame 29,* 55 (1977).

41. Olson, D.B. and W.C. Gardiner Jr., "An Evaluation of Methane Combustion Mechanisms," *J. Phys. Chem. 81,* 2514 (1977).

42. Breen, J.E. and G.P. Glass, "The Reaction of the Hydroxyl Radical with Acetylene," *International J. Chem. Kinetics 3,* 145 (1970).

43. White, J.N. and W.C. Gardiner Jr., "An Evaluation of Methane Combustion Mechanisms: 2 - Comparison of Model Predictions with Experimental Data from Shock-initiated Combustion of C_2H_2, C_2H_4, and C_2H_6," *J. Phys. Chem. 83,* 562 (1979).

44. Warnatz, J., Institut fur Physikalische Chemie, Technische Hochschuler, Darmstadt, Germany, private communication.

45. Gehring, M., K. Hoyermann, H.G. Wagner and J. Wolfrom, "Eine Direkte Bestimmung der Primärprodukte von Radikal-Molekül-Reaktionen: $OH+C_2H_2 \rightarrow CO+CH_3$ und $OH+N_2H_4 \rightarrow NH_3+NH_2O$," *Z. Naturforsh. A25,* 675 (1970).

46. Fenimore, C.P. and G.W. Jones, "Rate of Destruction of Acetylene in Flame Gases," *J. Chem. Phys. 41*, 1887 (1964).

47. Kydd, P.H., "Hydrocarbon Products from Rich Hydrocarbon Flames," *Comb. and Flame 3*, 133 (1959).

48. Vandooren, J. and P.J. Van Tiggelen, "Reaction Mechanisms of Combustion in Low Pressure Acetylene-Oxygen Flames," Sixteenth Symposium (International) on Combustion, The Combustion Institute, p.1133 (1977).

49. Kanofsky, J.R., D. Lucas, F. Pruss and D. Gutman, "Direct Identification of the Reactive Channels in the Reactions of Oxygen Atoms and Hydroxyl Radicals with Acetylene and Methylacetylene," *J. Phys. Chem. 78*, 311 (1974).

50. Benson, S.W., *Thermochemical Kinetics*, 2nd edition, John Wiley & Sons, Inc. (1976).

51. Taylor, B.R., MIT Department of Chemical Engineering, unpublished data.

52. Fenimore, C.P. and G.W. Jones, "Determination of Hydrogen Atoms in Rich, Flat, Premixed Flames by Reaction with Heavy Water," *J. Phys. Chem. 62*, 693 (1958).

53. Reid, R. and R. Wheeler, "Hydrogen Atom Excesses in some Propane Flames," *J. Phys. Chem. 65*, 527 (1961).

54. Hayhurst, A.N. and I.M. Vince, "Production of Prompt Nitric Oxide and Decomposition of Hydrocarbons in Flames," *Nature 266*, 524 (1977).

55. Kaskan, W.E. and J.J. Reuther, "Limiting Equivalence Ratio, Dissociation and Self-Inhibition in Premixed, Quenched, Fuel-Rich Hydrocarbon/Air Flames," Sixteenth Symposium (International) on Combustion, The Combustion Institute, p.1083 (1977).

56a. Tollefson, E.L. and D.J. LeRoy, "The Reaction of Atomic Hydrogen with Acetylene," *J. Chem. Phys. 16*, 1057 (1948).

56b. Dingle, J.R. and D.J. LeRoy, "Kinetics of the Reaction of Atomic Hydrogen with Acetylene," *J. Chem. Phys. 18*, 1632 (1950).

57. Jones, I.T.N. and K.D. Bayes, "Free-Radical Formation in the $O+C_2H_2$ Reaction," Fourteenth Symposium (International) on Combustion, The Combustion Institute, p.277 (1973).

58. Eberius, K.H., K. Hoyermann, and H.G.Wagner, "Structure of Lean Acetylene-Oxygen Flames," Fourteenth Symposium (International) on Combustion, The Combustion Institute, p.147 (1973).

59. Jones, I.T.N. and K.D. Bayes, "The Kinetics and Mechanism of the Reaction of Atomic Oxygen with Acetylene," *Proc. Royal Soc. London, A335*, 547 (1973).

60. Brown, J.M. and B.A. Thrush, "E.S.R. Studies of the Reactions of Atomic Oxygen and Hydrogen with Simple Hydrocarbons," *Trans. Farad. Soc.* *63*, 630 (1967).

DEVELOPMENT OF A KINETIC MECHANISM TO DESCRIBE THE FATE OF FUEL NITROGEN IN GASEOUS SYSTEMS

T. L. Corley
Energy and Environmental Research Corporation
Irvine, California 92705

Fifth EPA Fundamental Combustion Research Workshop
Newport Beach, California
January 23-25, 1980

SECTION I

INTRODUCTION

Combustion of coal and liquid fuels involve physical and chemical transformations of the fuels, mass transfer between condensed and gaseous phases, pyrolysis and oxidation of gas phase species, fluid mechanics, and heat transfer. Production of NO during oxidation of these fuels occurs via thermal fixation of molecular oxygen and nitrogen introduced with combustion air and via oxidation of nitrogeneous compounds present in the fuel. Computer models which can adequately predict the formation of NO from combustion of coal and liquid fuels provide additional tools which can be used in conjunction with experimental programs to investigate low NO_x combustion configurations. Valid models facilitate interpretation of existing data bases and can be used to evaluate conceptual hardware and operational designs related to reduction of pollutant formation.

This paper focuses on the development of a kinetic mechanism which can adequately predict the conversion of fuel nitrogen compounds to NO in gaseous systems. The major objective is to provide a validated reaction model which can then be used as one component of more complex models describing the combustion of coal and liquid fuels.

SECTION II

IDENTIFICATION OF AREAS OF ANALYSIS

Previous work in this area used jet-stirred reactor data reported by Bartok et al. (1972) and Engleman (1973; 1976) to develop a reaction mechanism for NH_3 and NO processing in CH_4-air mixtures. It was possible to reasonably predict conversion of NH_3 to NO, as shown in Figure 1, with minor adjustments to the rate coefficients for:

$$CH + NO = HCN + O$$

$$CH + N_2 = HCN + N$$

$$NH_2 + NO = N_2 + H_2O$$

Similar agreement was obtained when NO was added to the reactants. The major limitation was that other nitrogenous species - HCN, NH_3 - were not measured. Therefore, the capabilities of the kinetic mechanism to predict interconversion of fuel nitrogen species and interactions with hydrocarbons could not be fully assessed. In addition, the experimental temperatures were above 1700K; the predictive capabilities of the model could not be verified at lower temperatures with the jet-stirred reactor data.

Applications of this reaction mechanism indicated that the predicted behavior of HCN and NO under fuel-rich conditions was inconsistent with experimental observations. Figure 2a shows the half-life of HCN for a single ideal reactor configuration as a function of temperature and stoichiometry. The time scales are much greater (10 to 1000 times higher) than the data of De Soete (1975) and Haynes (1977) would indicate for post-flame decay of HCN in rich hydrocarbon systems.

Figure 2b shows that a substantial decay of NO was predicted under fuel-rich conditions when hydrocarbons were not present. The initial composition corresponded to adiabatic combustion products of a CH_4-Ar-O_2 mixture of a stoichiometric ratio of 0.80. The half-life of NO decreased

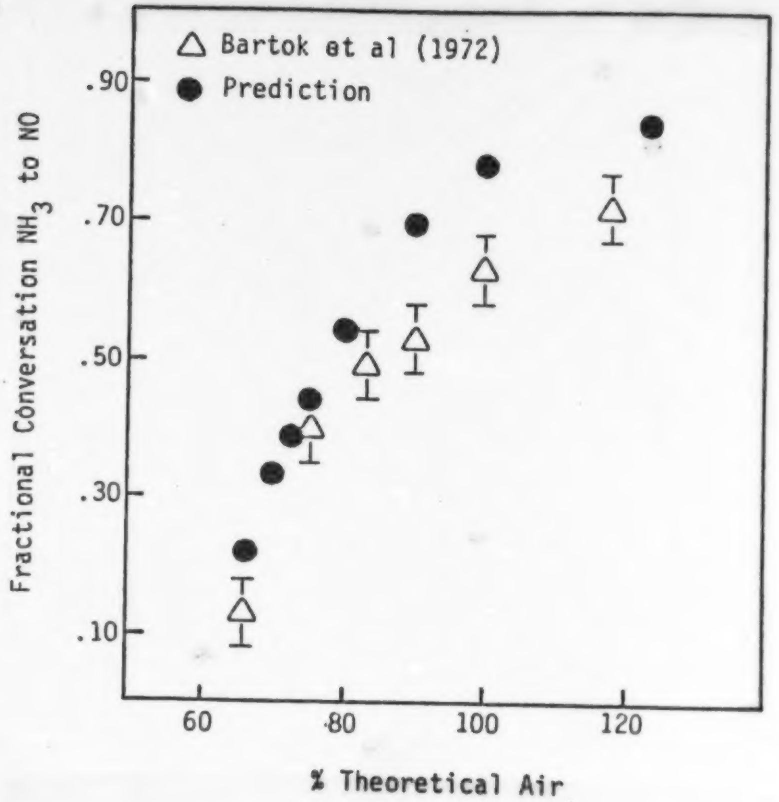

Figure 1. Conversion of NH_3 to NO in CH_4 - Air Stirred Reactor Experiments.

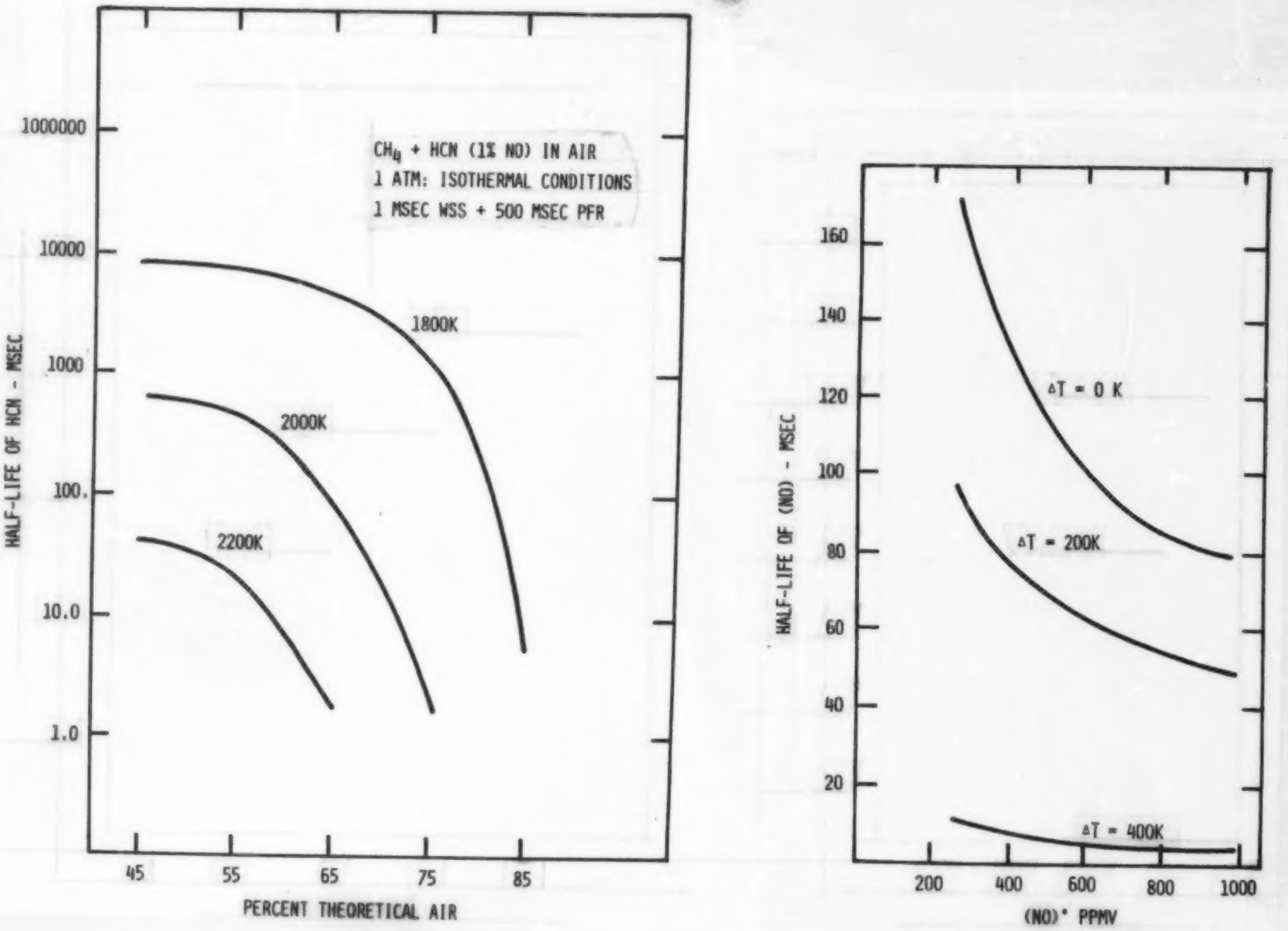

(a)

(b)

Figure 2. Predicted Behavior of Nitrogenous Compounds
a) HCN decay in Rich CH_4- air mixtures.
b) NO decay in the Absence of Hydrocarbons.

when the instantaneous temperature drop was increased. Although the results suggested that rapid thermal quenching of moderately fuel-rich combustion products could reduce NO emissions, it was not possible to quantitatively or qualitatively reproduce the behavior experimentally.

Numerical studies were also done to test the reaction mechanism against H_2, $CO-H_2O$, and CH_4 flame data. Agreement with burning velocities and species profiles for fuel-lean combustion was excellent. However, under fuel-rich conditions the reaction model predicted burning velocities for H_2, $CO-H_2O$ and CH_4 were 50 to 100 percent higher than observed. The discrepancies increased as the stoichiometry decreased.

The set of calculations outlined above, as well as other simulations and experimental data, identified several areas which required additional analysis to isolate and correct deficiencies in the reaction mechanism.

- Fuel-rich chemistry
  - H_2/O_2
  - $CO/H_2/O_2$, $CO/H_2O/O_2$
  - CH_4/O_2
- C_2-hydrocarbon chemistry
  - Relative importance in CH_4 combustion
  - Potential impact on fuel nitrogen processing
  - Extension of studies to other fuels
- NH_3 chemistry
  - Impact of updated thermochemistry: NH, NH_2
  - NO reduction mechanism
- HCN chemistry
  - Additional oxidation paths via HNCO

The next section describes the procedures adopted to accomplish these tasks.

SECTION III

METHODOLOGY FOR KINETIC MECHANISM EVALUATION

The approach used to eliminate the major inadequacies of the kinetic mechanism is summarized by the following steps:

1. Assemble elements of reaction model
    - Species included necessary and/or sufficient
    - Accepted rate coefficients used
2. Select data sets for analysis
    - Resolution of critical questions
    - Well-defined reaction conditions
3. Identify and correct deficiencies
    - Comparison with shock tube data
    - Comparison with flame data
4. Use completed sub-element of reaction mechanism as a known element of more complex systems

It was realized at the outset that availability of data would be the limiting factor for resolution of questions in certain areas. In such cases calculations would be used to identify the limitations of the reaction mechanism and the data required to extend its range of applicability.

The shock tube system was selected as a basis for comparison because of the ability to vary temperature independently of stoichiometry and time. In addition, it is a one-dimensional system in which diffusion is not important. Depending upon the observations made, predictions can be assessed against ignition delays, characteristic growth constants for species in the system, and time-resolved profiles.

Flame data was included since processing of fuel nitrogen in flame environments is of major interest. Since temperature is time- and stoichiometry-dependent in flames, comparison of predictions with such data provides a stringent test of the range of applicability of the kinetic mechanism. Evaluation of the reaction model can be based on its ability to predict burning velocities, which is an overall check on heat release, and on its ability to reproduce species profiles in flames.

Step 4 of the methodology refers to the manner in which particular sub-elements of the kinetic mechanism are incorporated into more complex elements of the reaction model. After an element of the mechanism has successfully reproduced the shock tube and flame data selected for comparison, it is assumed to be complete. It cannot be modified when used in the analysis of more complex elements of the reaction model unless it is shown that discrepancies in the new system can only be corrected by changing features of the sub-element. If this step is required, the modified sub-element must again be checked against the relevant data to determine that it is still able to predict the observations. This feedback loop ensures the internal consistency of the final kinetic mechanism.

SECTION IV

RESULTS OF SPECIFIC CALCULATIONS

The elements of the kinetic mechanism can be divided into four major subcomponents as shown in Figure 3. Each box on the figure indicates that experimental data is available which can be used to assess the particular element of the reaction model. The figure also shows that the development of the kinetic mechanism involves sequential, parallel, and simultaneous applications of the methodology.

Analysis begins with the simple fuels H_2 and CO-H_2 which are also important intermediates in hydrocarbon oxidation. After this subcomponent is completed, studies of hydrocarbon and fuel nitrogen mechanisms can be conducted in parallel. Evaluation of the hydrocarbon reaction mechanism is more complex because CH_4, C_2H_2, C_2H_4 and C_2H_6 may be formed regardless of the initial hydrocarbon. Corrections made to the reaction mechanism of a pure hydrocarbon, such as C_2H_6, must be included in analyses of the other hydrocarbon oxidation mechanisms to determine whether the modification would require changes in the CH_4, C_2H_2, and C_2H_4 chemistry. If an alternation of the CH_4, C_2H_2, or C_2H_4 oxidation chemistry was indicated, then its impact on the C_2H_6 mechanism would also have to be checked.

The following sections discuss calculations which have been completed for the simple fuels, fuel nitrogen and hydrocarbon subcomponents. Significant conclusions are highlighted and additional requirements for evaluation of the mechanisms are identified.

Simple Fuels

The hydrogen oxidation mechanism includes eight species - H_2, O_2, H_2O, H_2O_2, H, OH, HO_2, O - and 18 reactions. Figures 4a and 4b show that the reaction model can predict ignition delays for fuel-rich and stoichiometric hydrogen mixtures, if relative third body efficiencies for recombination reactions are considered. The initial growth of free radicals

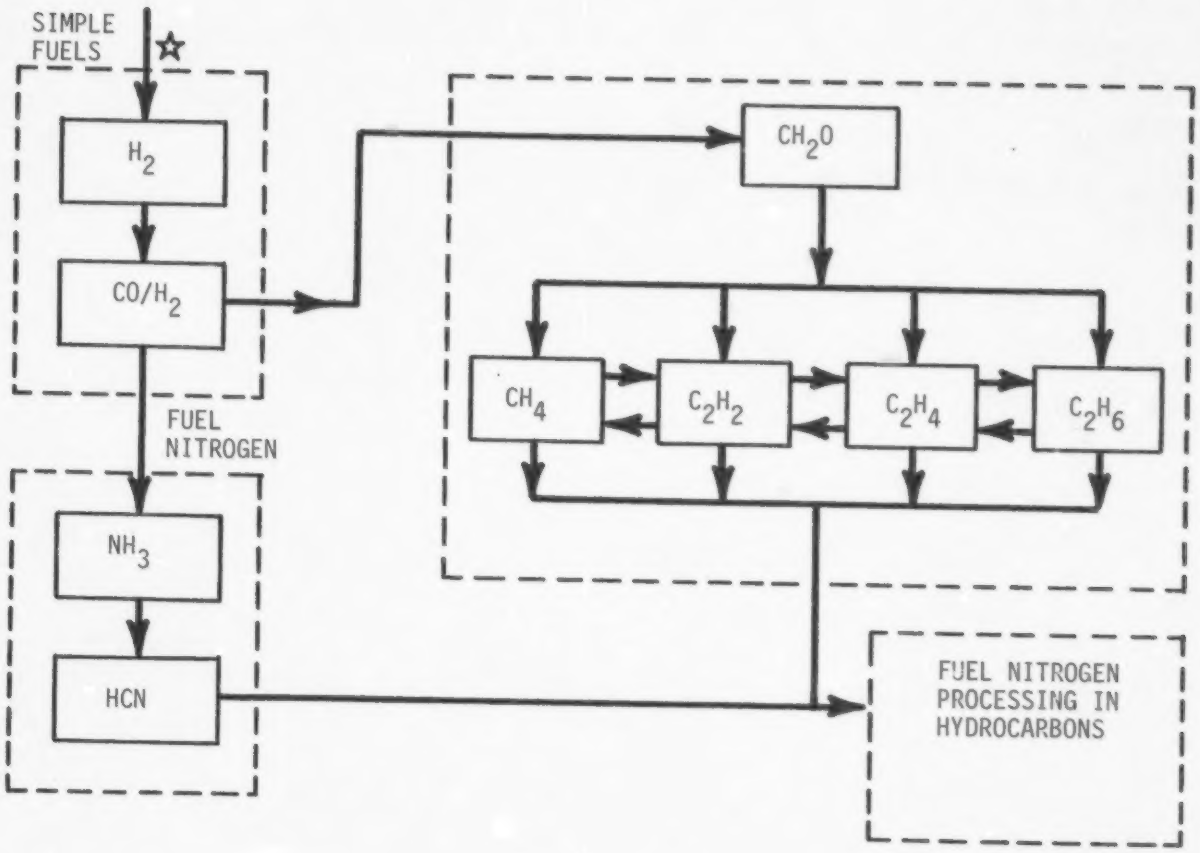

Figure 3. Overview of Kinetic Mechanism.

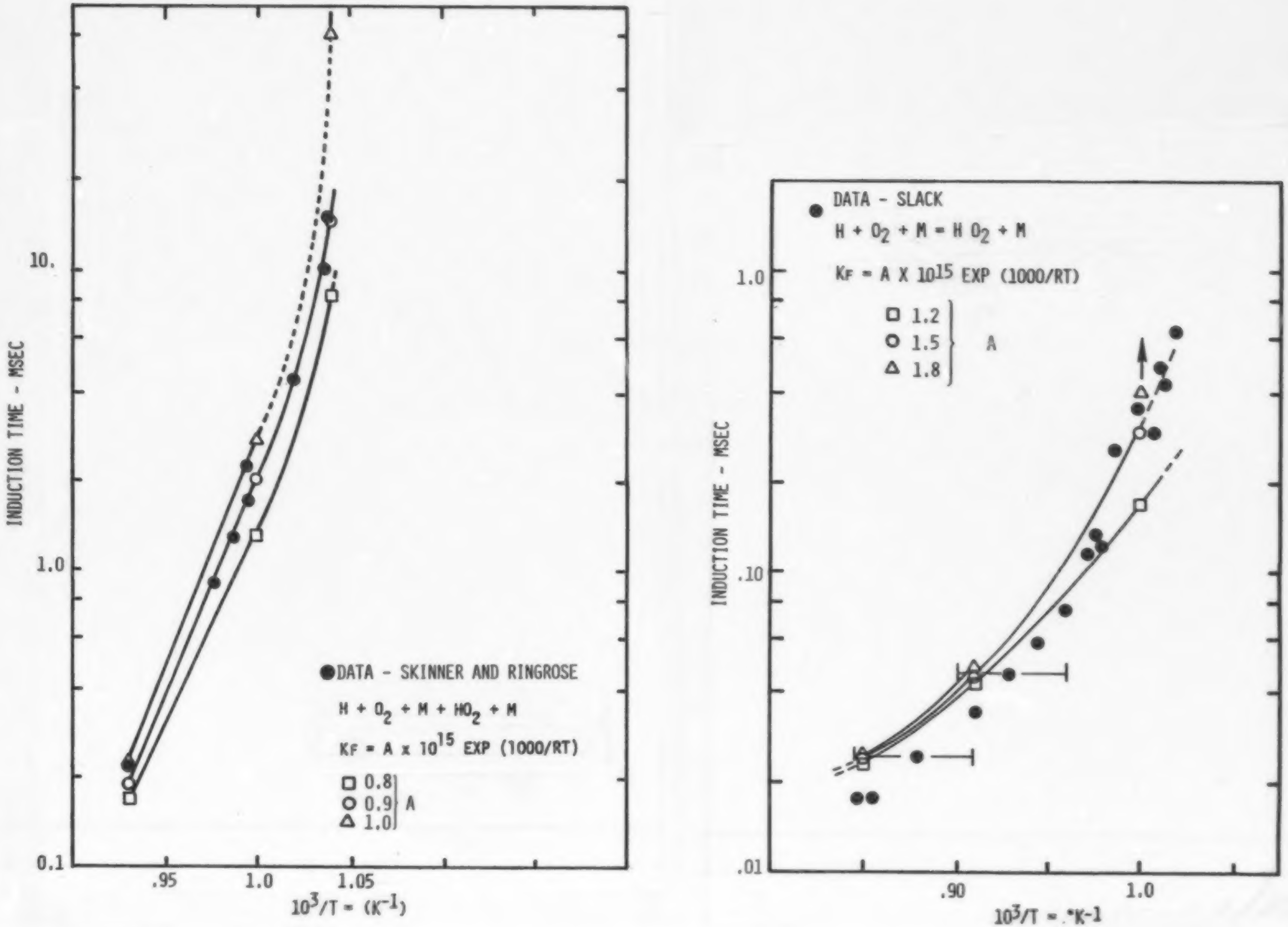

(a)

(b)

Figure 4. Ignition Delays for H_2: (a) Fuel-Rich H_2-O_2-AR = 8/2/90; P = 5 ATM; (b) Stoichiometric H_2-Air; P = 2 ATM.

is controlled by the competition of the following reactions:

$$H + O_2 + M = HO_2 + M \qquad (1)$$

$$H + O_2 = OH + O \qquad (2)$$

The relative third body efficiencies used were: $H_2O:H_2:N_2:Ar = 15:2.5:1:0.72$ (Baulch et al., 1972). All other species were assumed to have the same efficiency as N_2.

Calculations of the burning velocity of freely propagating H_2-air flames are compared with data in Figure 5. The hydrogen mechanism did not require any modifications to achieve the very satisfactory agreement indicated. Figure 6 shows the peak mole fraction of several species as a function of percent theoretical air. The predicted levels of H_2O_2 suggest that this species has an important role in determining radical concentrations below 1000K.

The CO-H_2 oxidation mechanism includes three additional species - CO, CO_2, HCO - and 10 additional reactions. The major test of the mechanism was based on comparisons with shock tube data. Brabbs, Belles and Brokaw (1971) reported that the exponential growth of free radicals (O, OH, H) was governed by the following reactions:

$$OH + H_2 = H_2O + H$$

$$H + O_2 = OH + O$$

$$O + H_2 = OH + H$$

$$H + O_2 + M = HO_2 + M$$

$$CO + OH = CO_2 + H$$

It is possible to derive an analytical expression for the growth constant, λ, by considering the set of homogeneous, linear differential equations which describe O, OH, and H-atoms in this simple reaction scheme. The exponential growth constant is the positive root of the characteristic cubic equation and is a function of the rate coefficients and initial species concentrations.

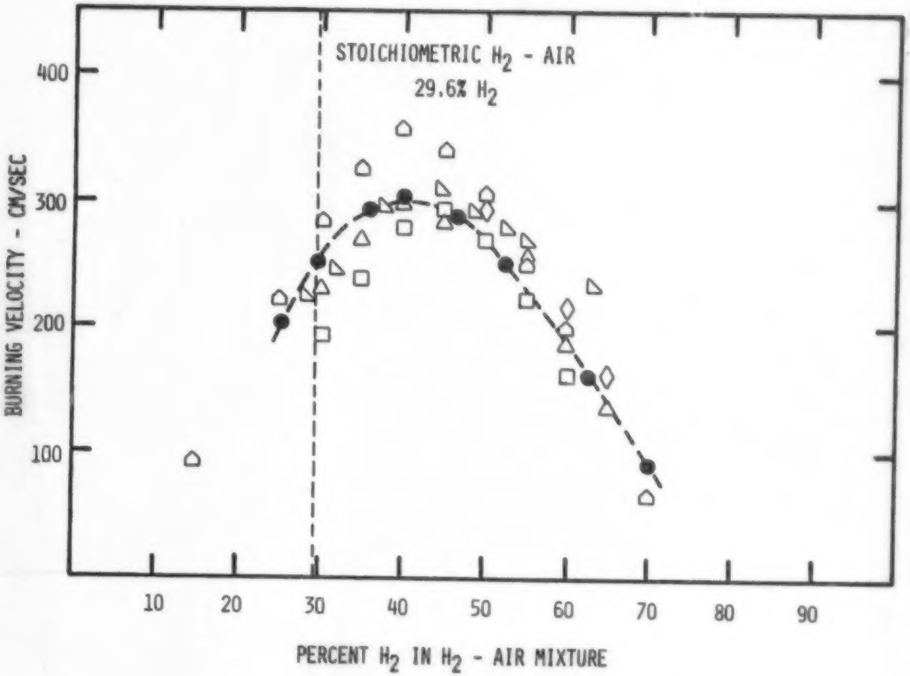

Figure 5. Burning Velocities for the H_2-Air Flame (T=298K, P=1 Atm in the unburnt gases).

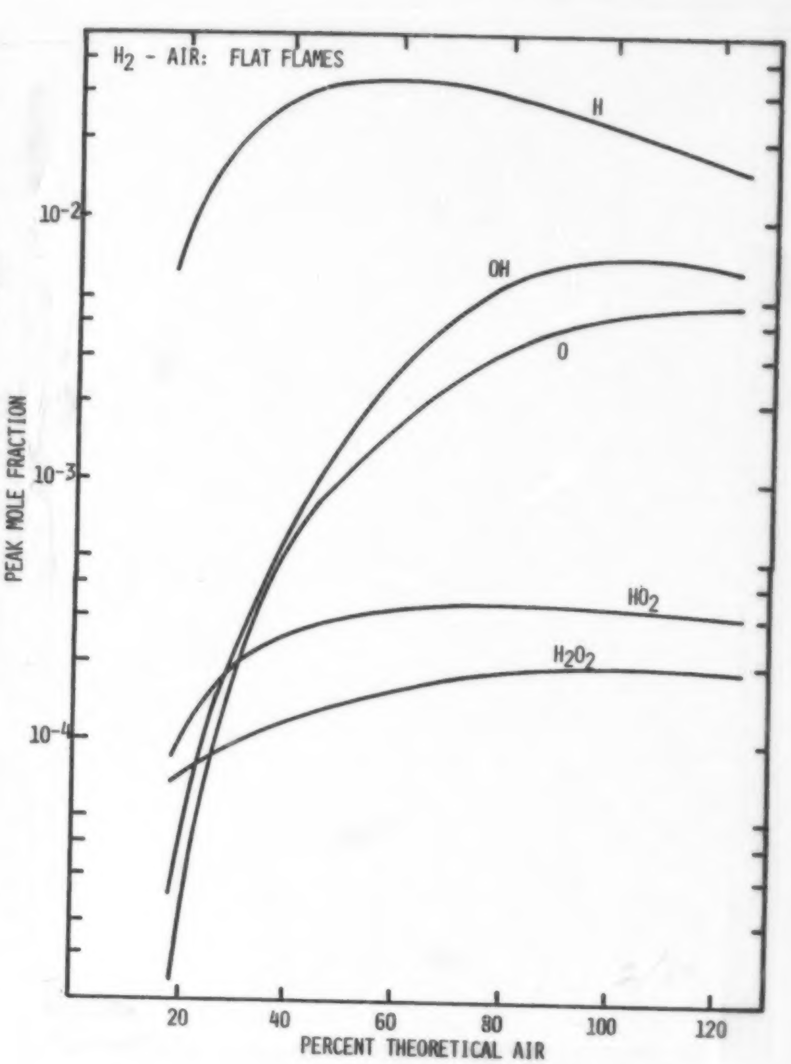

Figure 6. Variation of Maximum Specie Concentration with Stoichiometry.

Evaluation of the CO-H_2 oxidation mechanism included complete kinetic simulations of data reported by Brabbs et al. (1971). In addition, the rate coefficients used for the simplified, five-step mechanism above were used to calculate analytical growth constants. This latter approach was done to assess the impact of the simplifications by comparing with the complete dynamic simulations and to extend the number of conditions examined. The results are shown in Figure 7 and are in reasonable agreement with the data. The calculations also show that the analytical derivation of λ is essentially identical to that obtained with the complete kinetic mechanism. As a result, comparisons with other data reported by the authors for different initial compositions only used the analytical expression for λ. The additional calculations indicated that the rate coefficients used could predict growth of radicals for fuel-rich and fuel-lean CO-H_2-O_2 mixtures between 1150 and 1650K.

The CO-H_2 reaction mechanism was also compared with data reported by Dean, Steiner and Wang (1978) at temperatures above 2000K. These authors measured CO_2 concentrations versus time behind reflected shock waves. Ignition delays based on the time at which the tangent to the CO_2 profile intercepted the time axis, and times at which CO_2 reached a specific concentration (13.3×10^{-9} mole/cm^3) were reported. Results of the calculations are compared with data in Figures 8a and 8b. Although the reaction mechanism predicts ignition delays in good agreement with observations, the times at which CO_2 reaches a particular level are longer than observed. Analysis of the reaction mechanism suggested that the discrepancies in Figure 8b were due to the rate coefficient used for the dominate CO oxidation step:

$$CO + OH = CO_2 + H$$

The value used for the rate coefficient is that recommended by Baulch and Drysdale (1974). These authors indicate that the rate coefficient is accurate to 2000K, but has too low a temperature dependence at higher temperatures. However, no change in the rate coefficient is recommended without further fundamental data above 2000K which more accurately defines its temperature dependence.

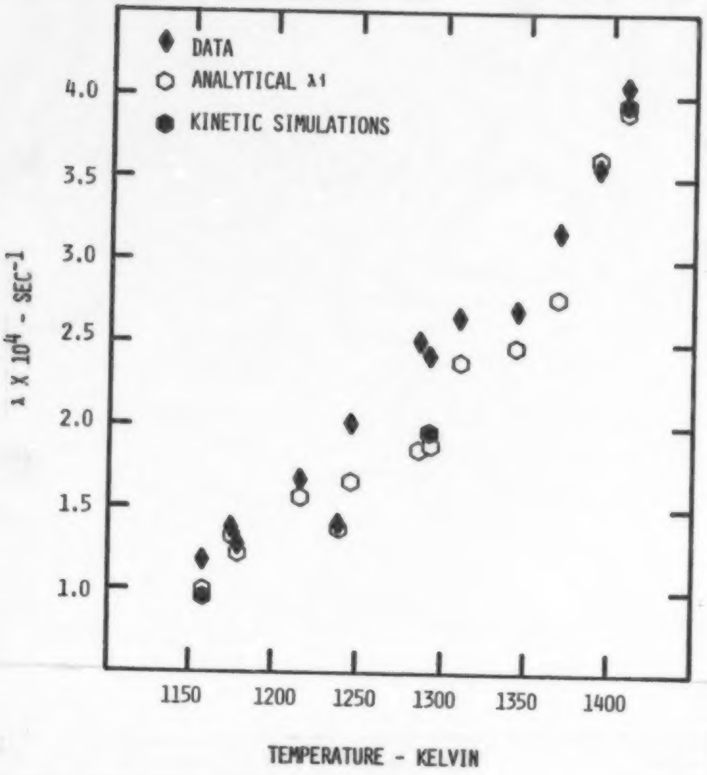

Figure 7. Exponential Growth Constant for O-Atoms In Fuel-Rich CO-H_2-O_2-AR (6/5/.5/88.5).

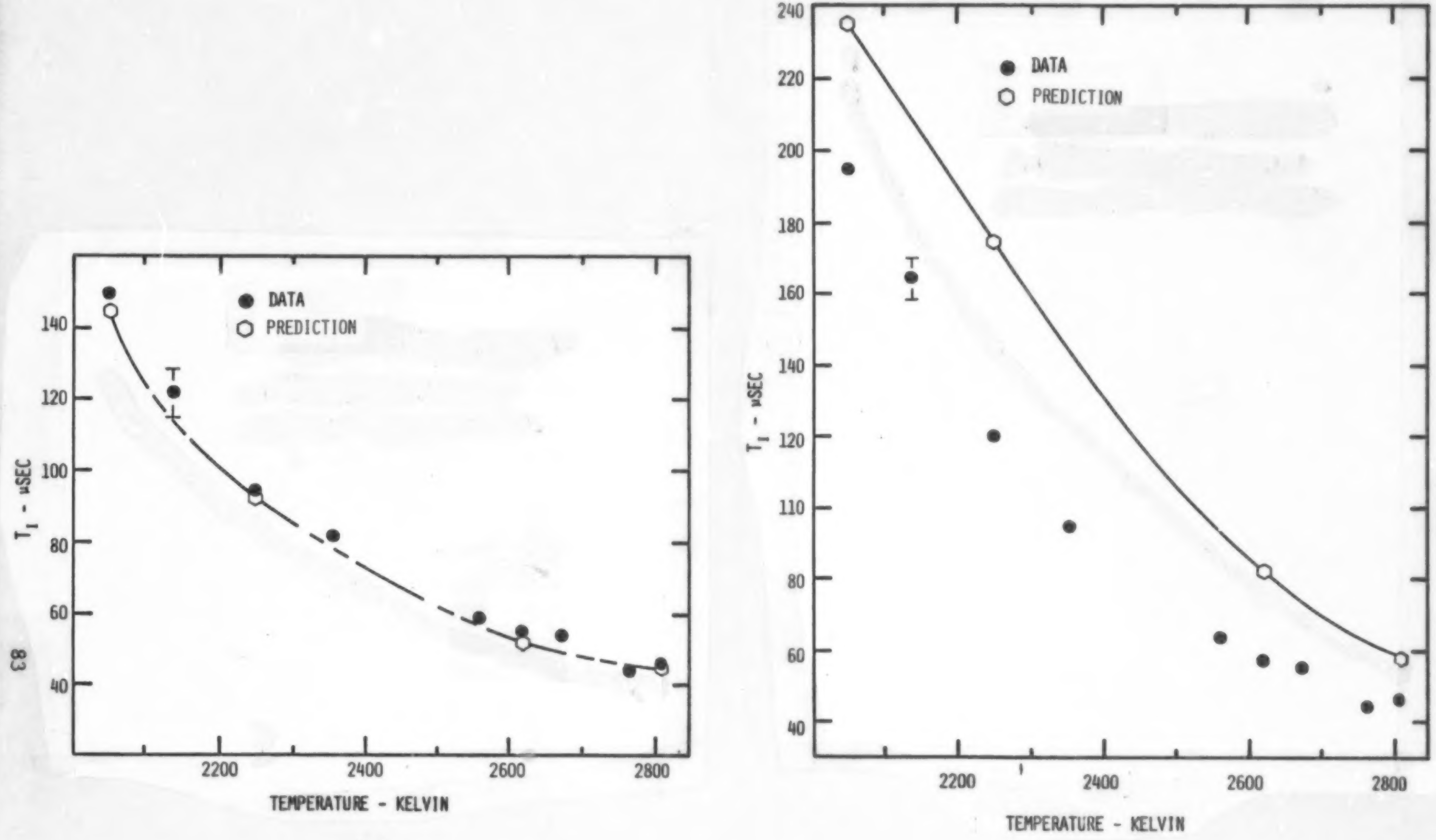

(a)

(b)

Figure 8. Characteristic Times in Fuel-Rich CO-H_2-O_2-AR Mixtures (3.28) .49/1.01/95.
(a) Ignition Delays; (b) Time for CO_2 to Reach 13.3 X 10^{-9}mole/om^3.

The CO-H_2 reaction mechanism was used to predict burning velocities for freely propagating CO-H_2O-air and CO-H_2-air flames. Examination of the data reported in the literature indicates that the burning velocity measurements are suspect because of the technique used or because H_2 or H_2O levels in the feed were unknown. The latter point is illustrated by the results shown in Figure 9a. Gunther and Janisch (1972) reported measured burning velocities for "dry" CO-air mixtures; the calculations yield values consistent with this set of data with 2500 ppm H_2O in the feed.

Although the simulations could not be quantitatively checked with experimental observations, the predicted variation of burning velocity with stoichiometry (Figure 9a) is consistent with observations. The effect of H_2 or H_2O concentration on the burning velocity of stoichiometric CO-air mixtures is shown in Figure 9b. Again, data was not available for quantitative comparison with predicted values. However, the trends are consistent with data for burning velocities of CO-O_2 mixtures to which H_2 or H_2O was added (Prince and Ponter, 1953; Wires, Watermeser, and Strellow, 1959). These data also show no significant difference in the effect of H_2 versus H_2O on burning velocity at initial concentrations less than 1 to 2%.

A significant result of these numerical studies is the relative importance of HCO chemistry. Inclusion of reactions describing the formation and destruction of this species decreases predicted burning velocities by as much as a factor of two for rich CO-H_2O-air flames (SR < 0.5), even though the maximum predicted concentration is less than 1 ppm. This is due to the chain-terminating nature of the HCO reactions:

$$H + CO + M = HCO + M$$

$$H + HCO = CO + H_2$$

$$OH + HCO = CO + H_2O$$

The formyl radical was not important in the shock tube studies.

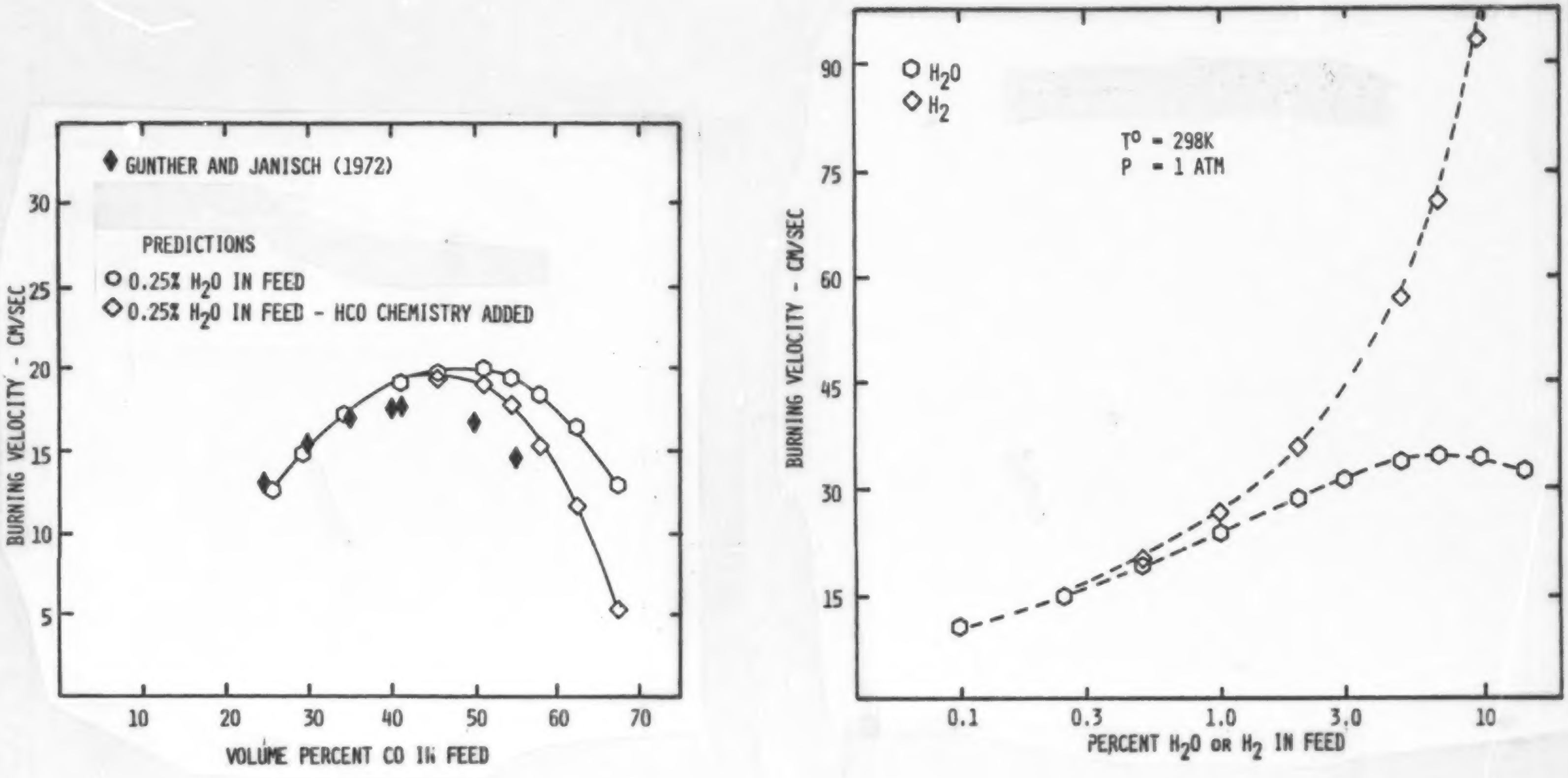

Figure 9. Burning Velocities for CO-H_2O and $CH_2$1 - Air Mixtures:

(a) Effect of Stoichiometry and HCO Chemistry

(b) Effect of H_2 or H_2O Concentrations for Stoichiometric CO-Air Mixture.

Fuel Nitrogen Chemistry

The NH_3 oxidation mechanism includes 17 species (NH_3, NO, N_2, N_2O, NO_2, NH, N, HNO plus H_2-O_2) and 69 reactions. Evaluation of this element involved comparisons with the following shock tube studies:

- NH_3 pyrolysis - Dove and Nip (1979)
- NH_3-O_2 ignition delays - Drummond (1972), Takeyama and Miyama (1967), Bull (1968)

In addition, calculations were made to determine whether the NH_3 reaction mechanism could qualitatively reproduce phenomena associated with the low temperatures reduction of NO in the presence of NH_3.

Dove and Nip (1979) measured NH_3, N_2, NH_2 and NH profiles behind reflected shock waves with a time-of-flight mass spectrometer. The sensitivity of the mass spectrometer to NH_2 and NH was assumed to be identical to the sensitivity to NH_3. Although this introduces an uncertainty with regard to the absolute levels of these species, the qualitative behavior should not be affected. The authors also used Kr as the diluent; however, comparison of the NH_3 decomposition rate coefficient derived by the authors is in good agreement with that obtained by Roose, Hanson and Kruger (1979) with Ar for the diluent.

Results of the calculations are compared with data in Figure 10. The most significant finding is that N_2 formation cannot be explained with reasonable rate coefficients for the NH_3-H_2 mechanism. Agreement for N_2 formation and the decomposition of NH_3 is improved if the following semiglobal step is included:

$$NH_2 + NH_2 \longrightarrow N_2 + 2H_2$$

with $K_f = 4 \times 10^{12} \exp(-12000/RT)$. It was found that N_2 production could be correlated by either of the following global processes:

$$NH_2 + NH_3 \longrightarrow N_2 + \text{-----}$$

$$NH_2 + NH_2 \longrightarrow N_2 + \text{-----}$$

An explanation in terms of elementary reaction steps would require inclusion of additional species in the reaction mechanism: N_2H_i. The

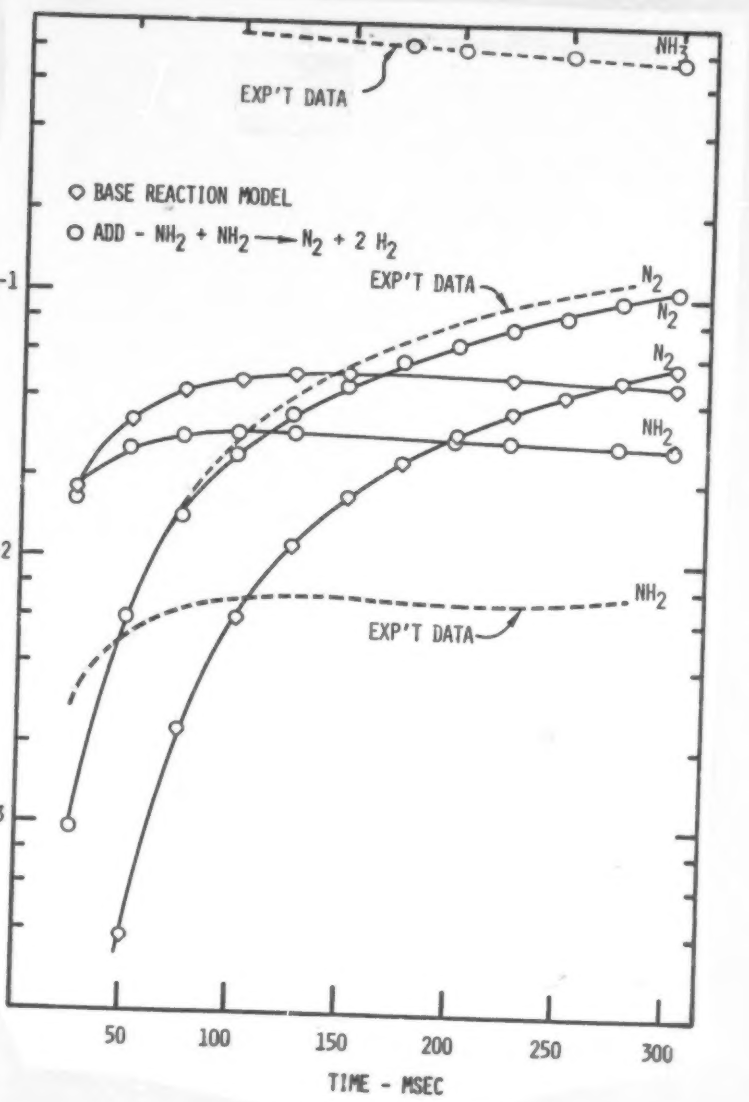

Figure 10. Profiles in NH_3-H_2 Pyrolysis: $NH_3/H_2/\text{Inert} = 6.1/518/88.1$; 2600 K; 0.36 Atm.

impact on very rich processing of NH_3 in other systems remains to be evaluated.

The predicted ignition delay correlation for a lean NH_3-O_2-Ar (2/2/96) mixture is compared with data in Figure 11. Analysis of the results indicated that the initial growth of radicals was controlled by the following reactions:

$$NH_2 + O_2 = HNO + OH$$

$$HNO + M = H + NO + M$$

$$H + O_2 = OH + O$$

The correlation of ignition delays predicted by the reaction mechanism is in excellent agreement with the data reported by Drummond (1972). However, this test is not sufficient to conclude that the reaction mechanism can describe the oxidation of NH_3.

Additional calculations examined the ability of the reaction mechanism to describe the reduction of NO due to NH_3 at low temperatures. The simulations were not compared to a particular set of experimental data. Instead, an initial stream composition was generated by quencing adiabatic equilbrium products for CH_4-air (SR = 1.12) to a specific temperature over 150 msec. Known amounts of NH_3 and NO or NH_3, NO and H_2 were then added to the mixture and allowed to react. Results are presented in Figures 12a and 12b.

To obtain the levels of NO reduction calculated in a time period consistent with experimental studies (0.25 sec) it was necessary to modify the reaction mechanism. An additional reaction between NO and the NH_2 radical which was chain-branching had to be included:

$$NH_2 + NO = N_2 + H_2O$$

$$NH_2 + NO = N_2 + H + OH$$

The branching ratio - $k_b/(k_a + k_b)$ - was 0.368. However, the predicted effect of H_2 addition suggests that the oxidation of NH_3 is still too slow. It is not clear whether the discrepancies are due to secondary reactions

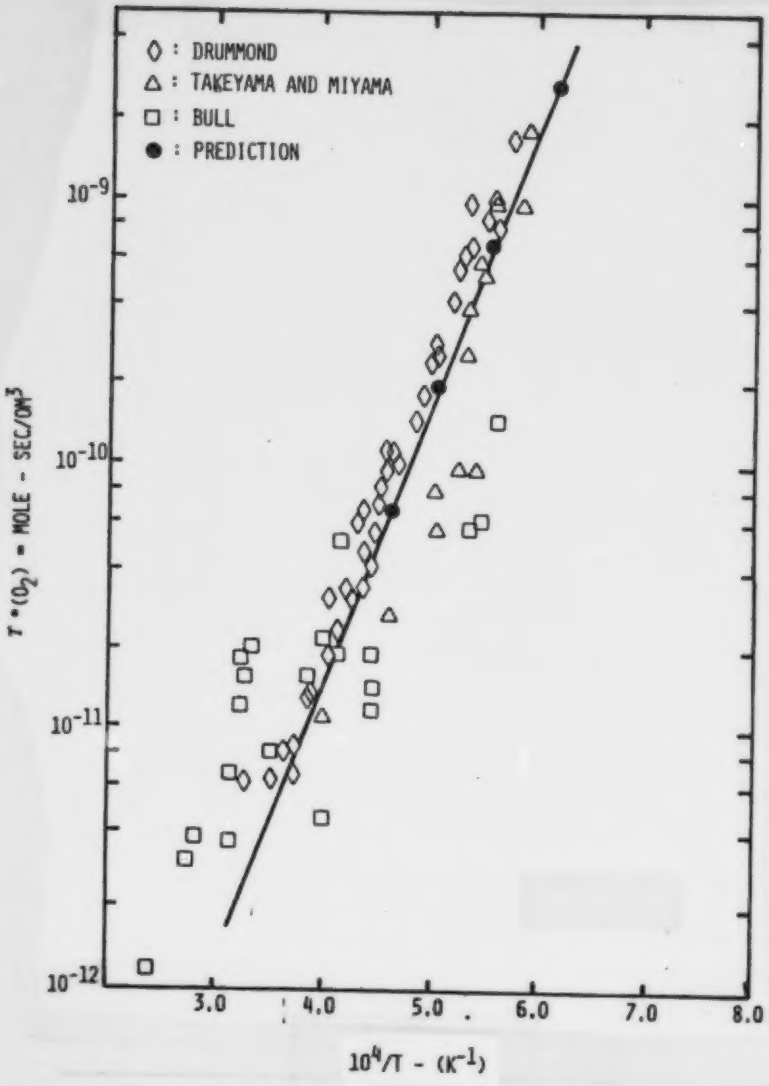

Figure 11. Correlation of Ignition Delays for NH_3-O_2-AR Mixtures.

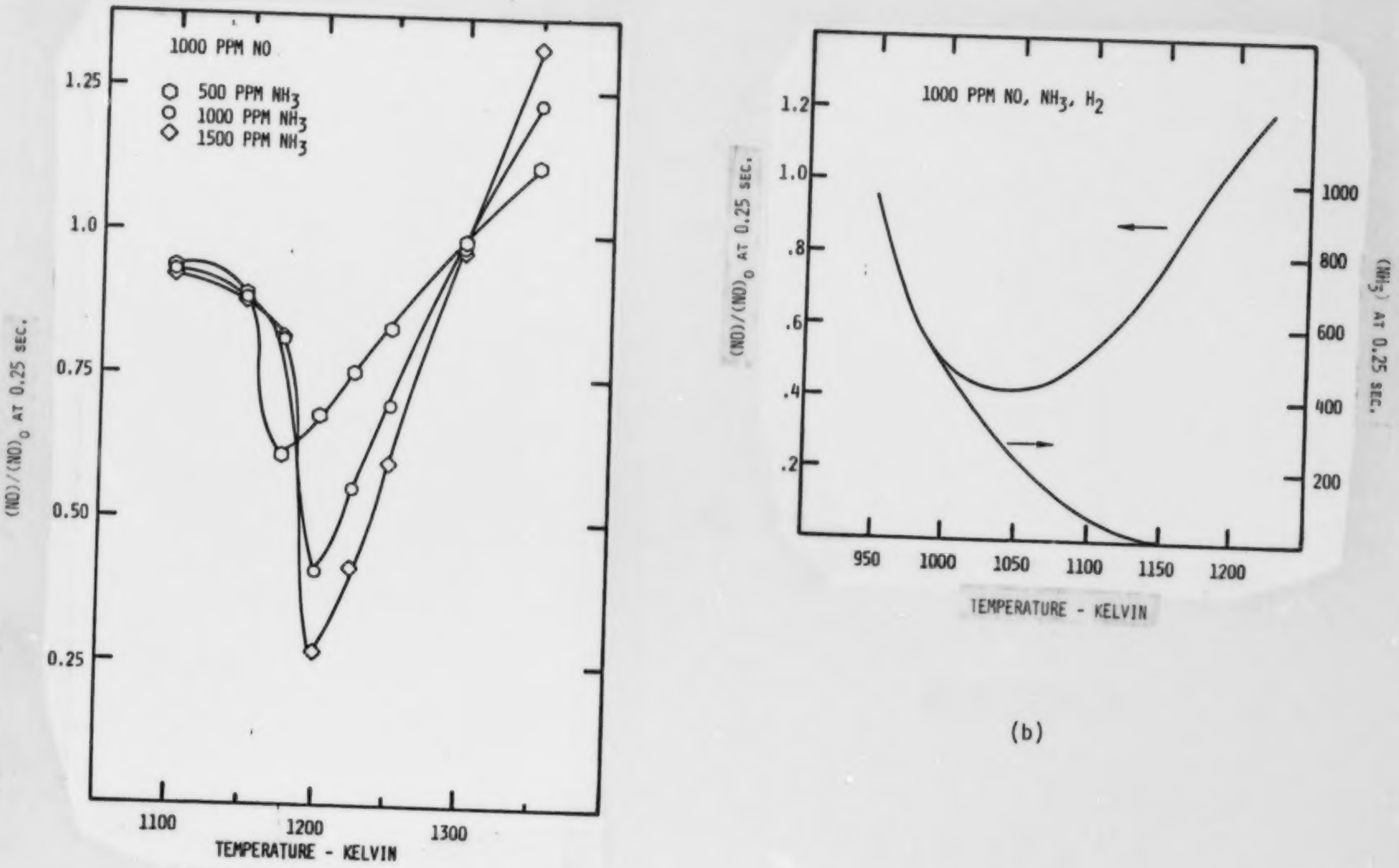

(a)

(b)

Figure 12. Homogeneous Reduction of NO by NH_3:
(a) Effect of Initial NH_3/NO Ratio
(b) Effect of Added Hydrogen

of NH_i species, missing reaction paths, additional species which have not been included in the mechanism, or incorrect rate coefficients.

The HCN oxidation mechanism includes 26 species (HCN, HNCO, CN, NCO, CH and species from $CO-H_2-NH_3-O_2$ system) and 106 reactions. An initial evaluation of the reaction model used shock tube data reported by Drummond (1970) as a basis for comparison.

Drummond measured ignition times for $HCN-N_2O-Ar$ mixtures with the ignition delay defined by the first detectable decrease of the N_2O IR emission signal. Since the sensitivity of the instruments was not given, the predicted ignition time was defined as the time at which 10 percent of the initial N_2O was consumed. The results are compared with the data in Figure 13 as an ignition delay correlation. The initial composition for the simulation was: $HCN/N_2O/Ar = 4/6/90$.

An additional set of calculations was done for this system to determine the effect of simple cyanogen (C_2N_2) mechanism on the predicted ignition times:

$$CN + CN + M = C_2N_2 + M$$

$$H + C_2N_2 = HCN + CN$$

$$O + C_2N_2 = NCO + CN$$

Figure 13 shows that these three reactions increase the consumption rate of N_2O.

The calculations done to test the HCN oxidation mechanism are not sufficient to identify any discrepancies in the reaction model. The comparison with a limited set of data suggests that HCN is oxidized too rapidly. However, other experimental data, such as the flat flame data reported by Fenimore (1979), must be used to evaluate this particular element of the kinetic mechanism.

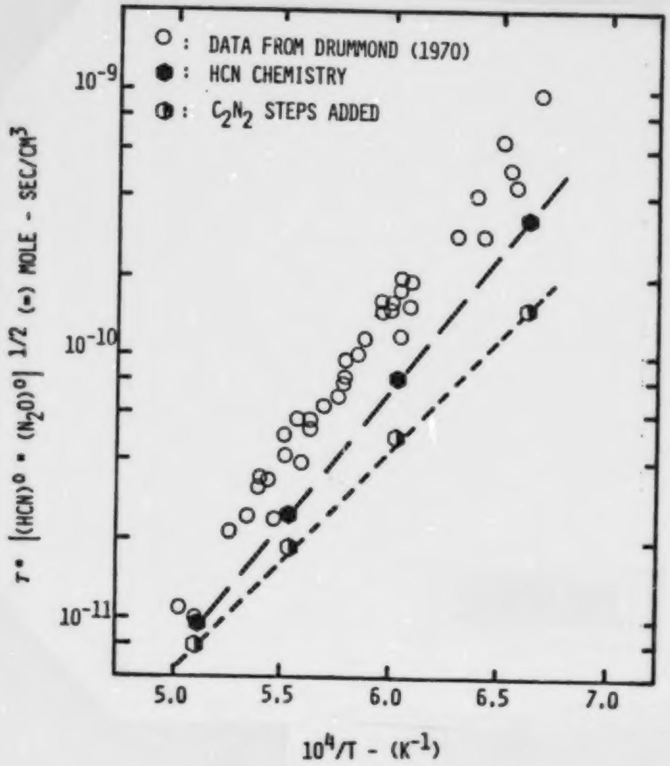

Figure 13. Ignition Correlation for HCN-N_2O-AR Mixtures.

Hydrocarbons

Formaldehyde (CH_2O) is an important intermediate in CH_4 combustion; CH_2O has also been observed during the oxidation of C_2-hydrocarbons. Validation of the CH_2O reaction mechanism without using CH_4 or C_2-hydrocarbon oxidation data reduces the complexity of the analysis. In addition, completion of this reaction mechanism allows subsequent analysis of the hydrocarbon reaction models to focus on CH_2O formation since the consumption is adequately described.

Three shock tube studies of CH_2O oxidation have been reported in the literature - Gay et al. (1965); Drummond (1971); and Dean, Johnson and Steiner (1980). The CH_2O reaction mechanism (12 species and 34 reactions) was compared to the data of Dean et al. to identify and correct discrepancies. The authors measured CO_2 profiles and report:

1. Ignition delay defined by the time at which tangent to CO_2 profile intercepts t-axis
2. Initial linear growth rate of CO_2
3. Time at which CO_2 reaches particular level

Comparisons with the first two observations are shown in Figures 14a and 14b respectively. The reaction mechanism was also able to predict the third observable.

In order to obtain agreement with this set of data it was necessary to lower the rate coefficients for the following reactions:

$$CH_2O + M = HCO + H + M \qquad K_f = 3.3 \times 10^{16} \exp(-81020/RT)$$

$$CH_2O + OH = HCO + H_2O \qquad K_v = 5 \times 10^{9}\ T \exp(-1650/RT)$$

The reaction of CH_2O with the hydroxyl radical with the rate constant listed is a factor of 5 to 10 slower than the initial rate would predict. It is also of interest that the CH_2O decomposition path and the associated rate constant suggested by Peeters and Mahnen (1973) is not consistent with this data.

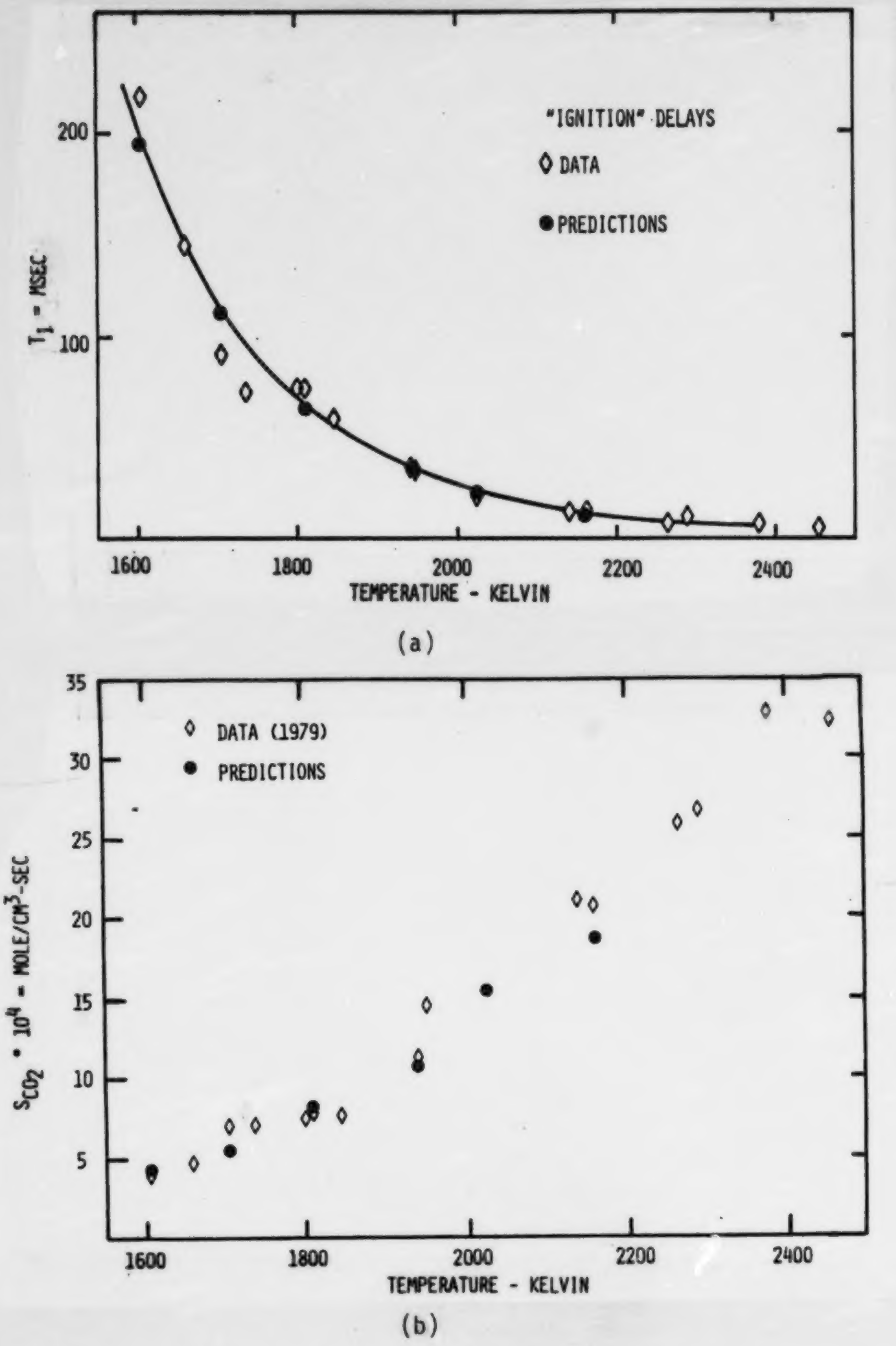

Figure 14. Oxidation of $CH_2O/O_2/CO/AR$ Mixture (.5/.92/9.15/89.43):

a) Ignition delay based on CO_2 profile;

b) Initial linear production of CO_2.

Additional calculations were done with the modified CH_2O mechanism to determine whether it could predict the data reported by Gay et al. (1965). Reasonable agreement was found when the simulations were compared with an ignition correlation replotted as $\tau(CH_2O)$. However, the scatter in the data makes more definite conclusions hazardous.

The major question which remains for the CH_2O mechanism is whether it is capable of reproducing data reported by Drummond (1971) at temperatures between 1150 and 1500K. The author reports an ignition correlation - $\tau(CH_2O)$ - which has a different temperature dependence than the data of Dean et al. and Gay et al. Additional calculations are scheduled to determine if the reaction mechanism can produce a unique correlation for CH_2O oxidation which is consistent with these three shock tube studies.

The CH_4-O_2 reaction mechanism can be divided into two components:

- C_1 - chemistry
    - 17 species: CH_4, CH_3, CH_2, CH, CH_3O + CH_2O - O_2
    - 61 reactions
- C_1 - and C_2 - chemistry
    - 23 species: CH_4, C_2H_6, C_2H_5, C_2H_4, C_2H_3, C_2H_2, C_2H
    - 101 reactions

The kinetic mechanism has been compared with shock tube data for ignition delays as a test of its capabilities. In addition, this series of calculations was used as a means to assess the relative importance of C_2-hydrocarbon chemistry in methane oxidation.

Results of the simulations are shown in Figure 15. Although there is good agreement with the data, comparison with the ignition correlation is not sufficient to determine the necessity of including C_2-hydrocarbons in the CH_4-O_2 reaction mechanism. Calculations at higher reactant concentrations, such as those used by Seery and Bowman (1970), may be of assistance.

Additional analysis of the CH_4 reaction mechanism will focus on flame data. Burning velocities and species profiles measured in flames will be

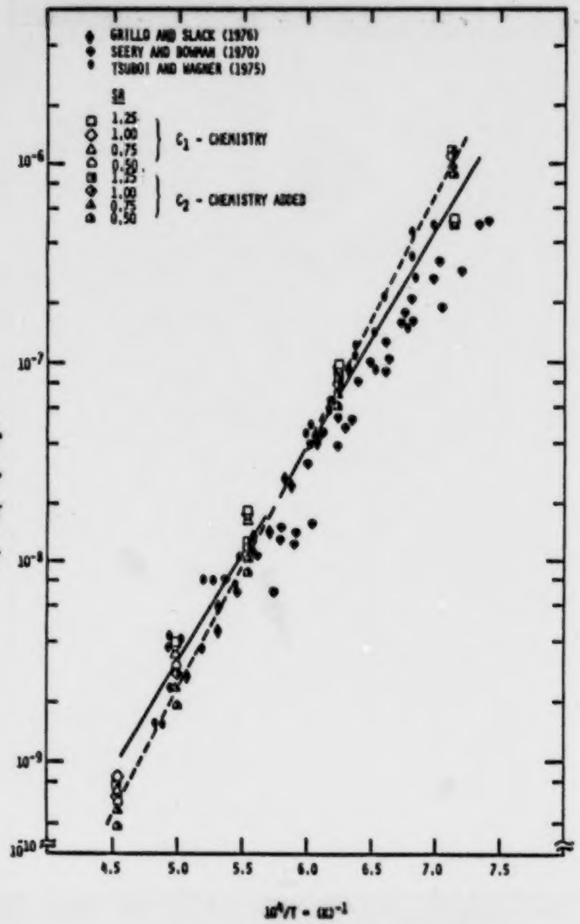

Figure 15. Correlation of Ignition Delays in CH_4-O_2-Argon.

used to complete evaluation of this element of the kinetic mechanism. Information will also be obtained as studies of C_2H_2, C_2H_4 and C_2H_6 combustion are completed.

SECTION V

SUMMARY

A methodology has been formulated which can be used to develop a kinetic mechanism to describe the processing of fuel nitrogen in gaseous systems. Application of the procedure to elements of the reaction model indicates:

- CH_2O - CO - H_2 - O_2 system is essentially complete
  - HCO is important for chain-branching in rich, wet CO flames
  - Decomposition and oxidation of CH_2O is slower than previous predictions
- NH_3 - O_2 mechanism requires additional analysis
  - Chain-branching path required: $NH_2 + NO = N_2 + H + OH$
  - Ignition delay controlled by: $NH_2 + O_2 = HNO + OH$
  - N_2H_i species may be important for rich processing of NH_3
  - Overall oxidation of NH_3 too slow with present mechanism
- HCN - O_2 reaction model must be compared with other data
- Hydrocarbon mechanisms require further study
  - Ignition delays for CH_4-O_2 predicted

The major questions remaining to be resolved will be examined by detailed comparisons with experimental data. Flame studies will be used extensively in subsequent simulations to evaluate time-resolved behavior of stable and radical species.

REFERENCES

1. Banloh, D.L., and Drysdale, D.D., Comb. Flame 23 (1974).

2. Banloh, D.L., Drysdale, D.D., Horne, D.G., and Lloyd, A.C., Evaluated Kinetic Data for High Temperature Reactions, Vol. 1, Butterworth, London (1972).

3. Bartok, W., Engleman, V.S., and Del Valle, E.G., Exxon Research and Engineering Company Report No. GRU-3GNOS-71, EPA No. APTD1168, NTIS No. PB211-480 (1972).

4. Brobbs, T.A., Belles, F.E., and Brokaw, R.S., Thirteenth Symposium (International) on Combustion (1971).

5. Bull, D.C., Comb. Flame 12 (1968).

6. Dean, A.M., Johnson, R.L., and Steiner, D.C., Comb. Flame 36 (1980).

7. Dean, A.M., Steiner, D.C., and Wang, E.E., Comb. Flame 32 (1978).

8. DeSoete, G., Institut Francais dn Petrole, Final Report No. 23306, June (1975).

9. Dove, J.E., and Nip, W.S., Can J Chem 57 (1979).

10. Drummond, L.J., Comb. Sci Tech 1 (1970).

11. Drummond, L.J., Comb. Sci Tech 3 (1971).

12. Drummond, L.J., Comb. Sci Tech 5 (1972).

13. Engleman, V.S., EPA-600/7-76-009a (1976).

14. Engleman, V.S., Bartok, W., Longwell, J.P., and Edelman, R.B., Fourteenth Symposium (International) on Combustion (1978).

15. Fenimore, C.P., Seventeenth Symposium (International) on Combustion (1979).

16. Gay, I.D., Glass, C.P., Kistiakowsky, G.B., and Niki, H., J. Chem. Phys 43 (1965).

17. Gunther, R., and Janisch, G., *Comb. Flame 19* (1972).

18. Peeters, J. and Mahnen, G., *Fourteenth Symposium (International) on Combustion* (1978).

19. Price, T.W., and Potter, J.H., *Fourth Symposium (International) on Combustion* (1953).

20. Roose, T.R., Hanson, R.K., and Kruger, C.H., Paper presented at 12th International Shook Tule Symposium, Israel, July (1979).

21. Seery, D.J., and Bowman, C.T., *Comb. Flame 14* (1970).

22. Skinner, G.B., and Ringrose, G.H., *J. Chem. Phys. 42* (1965).

23. Slack, M.W., *Comb. Flame 28* (1977).

24. Takeyama, T., and Miyama, H., *Eleventh Symposium (International) on Combustion* (1967).

25. Wires, R., Watermeier, L.A., and Strehlow, R.A., *J. Phys. Chem 63* (1959).

ACKNOWLEDGEMENTS

These studies were carried out under United States Environmental Protection Agency (EPA) Contract 68-02-2631. The author wishes to thank Dr. C.T. Bowman for many helpful discussions and his constructive comments. The author is also grateful to Dr. A.M. Dean for providing a copy of his paper in advance of publication.

NO_X FORMATION IN FLAT, LAMINAR, OPPOSED JET METHANE DIFFUSION FLAMES

W. A. Hahn and J. O. L. Wendt
Department of Chemical Engineering
University of Arizona
Tucson, Arizona 85721

Fifth EPA Fundamental Combustion Research Workshop
Newport Beach, California
January 23-25, 1980

ABSTRACT

It is shown that the detailed structure of a flat laminar opposed jet diffusion flame can be modeled, by properly coupling the momentum and energy conservation equations and by using detailed finite rate combustion kinetics.

Such a flame is one dimensional, provided that the proper velocity boundary conditions, which are a result of the model are employed. A laboratory $CH_4/N_2/O_2$ opposed jet diffusion flame was produced and gave good agreement with predictions with respect to both, one dimensionality and the temperature and species profiles within the reaction zone. However, the actual location of the reaction zone was displaced by a small distance.

The theoretical/experimental tool developed was utilized to test kinetic mechanisms of NO formation from fuel nitrogen. In this case, anhydrous ammonia was introduced first with the fuel and then with the oxidizer. The formation of NO was well predicted, using a detailed kinetic mechanism developed by others, when ammonia was introduced with the fuel, but agreement was poor when ammonia was injected in the air side. This indicates that there are some deficiencies in the ammonia pyrolysis kinetic mechanism when it is utilized in the absence of hydrocarbon fragments.

The qualitative dependence of the NO profile on flame stretching was correctly predicted by the model. This also allowed the prediction of reaction zone thickness and rate of formation of NO as functions of stretching rate and these results can be related to NO formation in strained laminar diffusion flamelets as they occur in turbulent diffusion flames.

SECTION I

INTRODUCTION

In the study of kinetic mechanisms of pollutant formation laminar diffusion flames can play a useful role. First, such flames allow the study of kinetic mechanisms, such as fuel nitrogen pyrolysis or soot formation, which are of importance in very fuel rich environments. Second, these very same fuel rich environments are important in determining the fate of fuel nitrogen in turbulent diffusion flames. One such laminar diffusion flame which has a number of additional useful attributes is the flat laminar opposed jet diffusion flame. This flame is strained in its own plane and following the lead of Williams (Ref. 1) and Broadwell and Marble (Ref. 2), it can be envisioned as a prototype model for laminar flamelets in turbulent diffusion flames. Moreover, it will be shown below that this flame is one dimensional in temperature, concentration and axial, but not radial, velocity profiles, provided the correct boundary conditions are employed for the velocities of the two incoming jets. Finally, this flame can be realized in the laboratory, and is suspended in space, thus being free of direct burner surface heat loss and catalytic effects.

In some previous work (Refs. 3-5) it was assumed that the heat released by the flame had only a negligible effect on the fluid dynamics of the flame and that the axial velocity profile remained linear with axial distance. Therefore the solution of two inviscid incompressible jets impinging on each other was used and the conservation of total mass and momentum was decoupled from the conservation equations of enthalpy and individual species. It will be shown later that a one dimensional flame can only be achieved if momentum and heat release are coupled and that the axial velocity profile is nonlinear in the vicinity of the flame; furthermore, it will be shown that the flame creates vorticity in an otherwise irrotational flow.

Other models have employed the Howarth or Dorotnitzyn transformation to convert variable density flows to constant property flows but are constrained to the use of either infinitely fast chemical kinetics or on one or two reactions with very high activation energy or a single finite rate (Refs. 4 and 6). Clearly this does not allow those theories to be used in the prediction of trace species, such as NO_x or soot, which are controlled by a complicated set of simultaneous competitive reactions.

In this work, we use a model, details of which are presented elsewhere (Ref. 7), to determine the correct velocity boundary conditions to be used in a set of well defined laboratory flat opposed jet flame experiments. The model includes the equations of continuity and momentum coupled with the equations of conservation of energy and individual species, and a detailed set of elementary finite rate chemical reactions.

The purpose of the experiments was twofold. First, agreement between theoretical predictions of the flame zone structure was checked against experimental results and the flame was checked for its one dimensionality in the neighborhood of the center axis. Second, the ability of the model to predict formation of NO and the effect of the rate of strain thereon was checked against experimental data. In both cases comparison between experiment and theory was good, indicating that the laminar opposed jet diffusion flame is a useful tool in studying the rate of formation of trace species in diffusion flames and/or a good prototype model in Williams (Ref. 1) and Marble and Broadwell's (Ref. 2) approach to turbulent diffusion flames. It should be pointed out that comparison between theory and experiment for this flame is a very severe test of any detailed kinetic mechanism, since it involves both high and low temperature regions as well as both very fuel rich and very fuel lean environments.

SECTION II

THEORY

A laminar opposed jet diffusion flame, shown schematically on Figure 1, is established between two impinging, coaxial, opposed jets; one being fuel only and the other being oxidizer only. The flame causes the stagnation plane of the flow field to be displaced, from that of the cold flow, towards the fuel lean side and the flame itself is located in the fuel lean side.

The equations representing the flame shown on Figure 1, can be transformed into the following set of ordinary differential equations (Ref. 7).

Continuity

$$\frac{d}{dx}(\rho v) + 2\varepsilon\rho\psi = 0 \qquad (1)$$

r-Momentum

$$\varepsilon^2\psi^2 + \varepsilon v \frac{d\psi}{dz} = \frac{\varepsilon^2\rho\infty}{\rho} + \frac{\varepsilon}{\rho}\frac{d}{dz}\left(\mu\frac{d\psi}{dz}\right) \qquad (2)$$

Energy

$$-2\varepsilon c\ C_p\ T\psi - C_p\frac{d}{dz}(c\ T\ v) + \frac{d}{dz}\left(k\ \frac{dT}{dz}\right) = \sum_{j=1}^{nr} r_j\Delta h_j \qquad (3)$$

Species A

$$-2\varepsilon\ c\ x_A\psi - \frac{d}{dz}(cx_Av) + \frac{d}{dz}\left(cD_A\ \frac{dx_A}{dz}\right) = -R_A \qquad (4)$$

The similarity transformation used to obtain equations (1) through (4) from the original transport equations is

$$v_r = \varepsilon r\psi(z); \quad v_z = v(z) \qquad (5)$$

$$\frac{\partial P}{\partial r} = f(r); \quad \frac{\partial P}{\partial z} = g(z) \qquad (6)$$

$$\rho = \rho(z); \quad T = T(z); \quad x_A = x_A(z) \qquad (7)$$

The similarity transform (Equation 5) is strictly valid only for flames supported by infinitely wide jets in which case no specific boundary layer like approximation is required. However, the degree to which the theory is

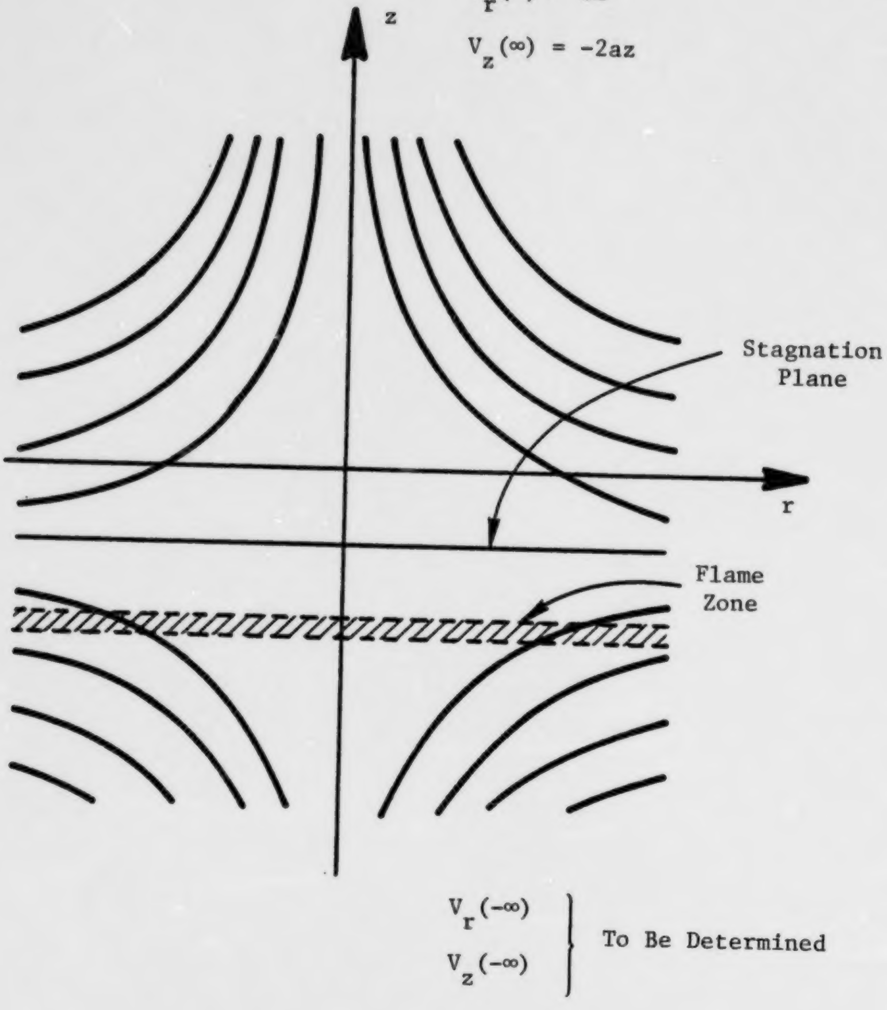

Figure 1. Schematic of the Flat Laminar Opposed Jet Diffusion Flame. The Top Jet is Fuel and the Bottom Jet is the Oxidizer.

valid for finite jets, as they can be realized in the laboratory, will be determined by experiment. It might be expected that the theory should hold in the neighborhood of the stagnation stream line, that burners should be wide compared to the burner spacing and that the burner spacing should be large compared to the reaction zone thickness, which is the region of interest.

The boundary conditions to equations (2) through (4) are the known values of ψ, T and x_A, respectively, at the position of the two burners, which are located at a distance $z = \pm \ell$ from the cold stagnation point. Equation (1) requires only one boundary condition, which is the velocity of the incoming jet at either $z = + \ell$ or $z = - \ell$; once this velocity is fixed the velocity of the other jet becomes a dependent variable and is a result of the model. From this it is clear that a truly (mathematically) flat opposed jet diffusion flame can be realized in the laboratory only after the model with some reasonably accurate representation of the heat release rate, has been solved.

Because the time constants involved in the elementary reactions describing a combustion process vary by many orders of magnitude, equations (1) through (4) are a set of stiff boundary valued differential equations. This set of equations was solved using a fully implicit iterative algorithm. The derivatives involved were expressed in finite differences and an expanding grid, which was fine near the reaction zone and coarse near the burner surfaces was employed. The resulting set of algebraic equations, represented via a block tridiagonal matrix was solved utilizing an LU decomposition, which is very efficient for this type of problem. Details on this procedure and the necessary underrelaxation technique can be found elsewhere (Ref. 8).

Transport properties of the individual species were computed using Chapman-Enskog relations with a 6-12 Lennard Jones potential. The properties of the mixture were then evaluated with mixing rules proposed by Reid, et al (Ref. 9).

The kinetic mechanism for methane oxidation with trace quantities of ammonia is shown on Table 1, with the appropriate rate coefficients. The latter were drawn from the evaluations, Levy et al (Ref. 10) and, although current, are still undergoing further development by these and other authors. The mechanism involves 26 species and 83 reactions and represents fuel pyrolysis and oxidation, ammonia pryolysis and oxidation, and NO formation and destruction, all of which are important in a diffusion flame.

Table 1 Chemical Reaction Mechanism and Rate Coefficients Utilized (After Ref 10)

```
CHEMICAL REACTION                       FORWARD RATE                                  REVERSE RATE
******** ********                       ******* ****                                  ******* ****
                                        (G-MOLE,CM,SEC)                               (G-MOLE,CM,SEC)
CH4 +M     =CH3 +H    +M     .10E+18*T**( 0.00)*EXP( -88400./(1.98*T))   .29E+12*T**( 1.00)*EXP(  18902./(1.98*T))
CHO +M     =CO  +H    +M     .25E+21*T**(-1.50)*EXP( -16800./(1.98*T))   .11E+10*T**(-0.50)*EXP(   1196./(1.98*T))
CO2 +M     =CO  +O    +M     .38E+31*T**(-4.00)*EXP(-134021./(1.98*T))   .38E+25*T**(-3.00)*EXP(  -6170./(1.98*T))
CH4 +CH2   =CH3 +CH3         .13E+13*T**( 0.70)*EXP( -20000./(1.98*T))   .23E+12*T**( 0.70)*EXP( -24215./(1.98*T))
CH4 +H     =CH3 +H2          .50E+11*T**( 1.00)*EXP( -10000./(1.98*T))   .14E+10*T**( 1.00)*EXP(  -8820./(1.98*T))
CH4 +OH    =CH3 +H2O         .30E+14*T**( 0.00)*EXP(  -5000./(1.98*T))   .41E+13*T**( 0.00)*EXP( -19231./(1.98*T))
CH4 +O     =CH3 +OH          .19E+15*T**( 0.00)*EXP( -11700./(1.98*T))   .24E+13*T**( 0.00)*EXP(  -8490./(1.98*T))
CH3 +OH    =CH2 +H2O         .20E+12*T**( 0.70)*EXP(  -2000./(1.99*T))   .15E+12*T**( 0.70)*EXP( -12016./(1.98*T))
CH3 +O     =CH2O+H           .26E+15*T**( 0.00)*EXP(  -2000./(1.98*T))   .41E+16*T**( 0.00)*EXP( -70316./(1.98*T))
CH2 +H     =CH  +H2          .32E+12*T**( 0.70)*EXP(  -5000./(1.98*T))   .19E+12*T**( 0.70)*EXP(  -7536./(1.98*T))
CH2 +OH    =CH  +H2O         .50E+12*T**( 0.50)*EXP(  -6000./(1.98*T))   .14E+13*T**( 0.50)*EXP( -23947./(1.98*T))
CH2 +OH    =CH3 +O           .50E+12*T**( 0.50)*EXP(  -6000./(1.98*T))   .74E+13*T**( 0.50)*EXP( -13426./(1.98*T))
CH2 +OH    =CH2O+H           .10E+14*T**( 0.00)*EXP(  -5000./(1.98*T))   .23E+16*T**( 0.00)*EXP( -80742./(1.98*T))
CH2 +H2    =CH3 +H           .30E+13*T**( 0.00)*EXP(  -7000./(1.98*T))   .20E+14*T**( 0.00)*EXP( -12395./(1.98*T))
CH2 +O     =CHO +H           .50E+12*T**( 0.50)*EXP(  -4000./(1.98*T))   .29E+13*T**( 0.50)*EXP( -94682./(1.98*T))
CH2 +O2    =CH2O+O           .50E+12*T**( 0.50)*EXP(  -7000./(1.98*T))   .72E+13*T**( 0.50)*EXP( -66011./(1.98*T))
CH  +CO2   =CHO +CO          .10E+11*T**( 0.50)*EXP(  -7000./(1.98*T))   .95E+09*T**( 0.50)*EXP( -72017./(1.98*T))
CH  +OH    =CHO +H           .10E+11*T**( 0.50)*EXP(  -6000./(1.98*T))   .23E+12*T**( 0.50)*EXP(-100176./(1.98*T))
CH  +O     =CO  +H           .50E+12*T**( 0.50)*EXP( -10000./(1.99*T))   .23E+14*T**( 0.50)*EXP(-175972./(1.98*T))
CH  +O2    =CHO +O           .50E+12*T**( 0.50)*EXP(      0./(1.98*T))   .69E+12*T**( 0.50)*EXP( -79446./(1.98*T))
CH2O+H     =CHO +H2          .13E+11*T**( 1.00)*EXP(  -6000./(1.98*T))   .69E+09*T**( 1.00)*EXP( -20171./(1.98*T))
CH2O+OH    =CHO +H2O         .32E+11*T**( 1.00)*EXP(  -3200./(1.98*T))   .85E+10*T**( 1.00)*EXP( -32382./(1.98*T))
CH2O+O     =CHO +OH          .20E+12*T**( 1.00)*EXP(      0./(1.98*T))   .50E+10*T**( 1.00)*EXP( -19340./(1.98*T))
CHO +HO2   =CH2O+O2          .10E+15*T**( 0.00)*EXP(  -4400./(1.98*T))   .43E+16*T**( 0.00)*EXP( -43225./(1.98*T))
CHO +O     =CO  +OH          .63E+12*T**( 1.00)*EXP(  -3000./(1.98*T))   .13E+13*T**( 1.00)*EXP( -86196./(1.98*T))
CO  +OH    =CO2 +H           .15E+08*T**( 1.30)*EXP(   -500./(1.98*T))   .36E+10*T**( 1.30)*EXP( -23394./(1.98*T))
CO  +O2    =CO2 +O           .32E+13*T**( 0.00)*EXP( -50000./(1.98*T))   .46E+14*T**( 0.00)*EXP( -57428./(1.98*T))
H2  +M     =H   +H    +M     .21E+16*T**( 0.07)*EXP(-103830./(1.98*T))   .22E+12*T**( 1.07)*EXP(   1892./(1.98*T))
OH  +O    +M  =HO2 +M        .16E+21*T**(-1.50)*EXP(      0./(1.98*T))   .10E+26*T**(-2.50)*EXP( -65257./(1.98*T))
H   +O2   +M  =HO2 +M        .30E+16*T**( 0.00)*EXP(   1000./(1.98*T))   .12E+20*T**(-1.00)*EXP( -47526./(1.98*T))
H2O +M     =OH  +H    +M     .23E+25*T**(-2.00)*EXP(-122600./(1.99*T))   .49E+20*T**(-1.00)*EXP(  -1467./(1.98*T))
H   +OH    =H2  +O           .27E+18*T**(-0.94)*EXP( -14690./(1.98*T))   .60E+18*T**(-0.94)*EXP( -16720./(1.98*T))
H   +HO2   =OH  +OH          .25E+15*T**( 0.00)*EXP(  -1900./(1.98*T))   .16E+14*T**( 0.00)*EXP( -40334./(1.98*T))
OH  +H2    =H   +H2O         .25E+14*T**( 0.00)*EXP(  -5200./(1.98*T))   .12E+15*T**( 0.00)*EXP( -20611./(1.98*T))
OH  +OH    =H2O +O           .60E+13*T**( 0.00)*EXP(  -1000./(1.98*T))   .65E+14*T**( 0.00)*EXP( -18442./(1.98*T))
OH  +O     =H   +O2          .63E+12*T**( 0.50)*EXP(      0./(1.98*T))   .10E+14*T**( 0.50)*EXP( -16731./(1.98*T))
HO2 +H     =O2  +H2          .25E+14*T**( 0.00)*EXP(   -700./(1.98*T))   .59E+14*T**( 0.00)*EXP( -57896./(1.98*T))
```

```
                                                      TABLE 1
                                                      -------
                                                      CONTINUED

CHEMICAL REACTION                              FORWARD RATE                              REVERSE RATE
-------- --------                              ------- ----                              ------- ----
                                               (G-MOLE,CM,SEC)                           (G-MOLE,CM,SEC)
HO2 +O          =OH  +O2        .50E+14*T**( 0.00)*EXP(  -1000./(1.98*T))   .53E+14*T**( 0.00)*EXP( -56165./(1.98*T))
CH4 +CN         =HCN +CH3       .32E+12*T**( 0.70)*EXP(  -5000./(1.98*T))   .39E+11*T**( 0.70)*EXP( -22913./(1.98*T))
CH3 +HNO        =CH4 +NO        .50E+12*T**( 0.50)*EXP(      0./(1.98*T))   .98E+13*T**( 0.50)*EXP( -56339./(1.98*T))
CH2 +N2         =HCN +NH        .10E+15*T**( 0.00)*EXP( -60000./(1.98*T))   .85E+14*T**( 0.00)*EXP( -29631./(1.98*T))
CH2 +NO         =CH2O+N         .16E+13*T**( 0.00)*EXP(  -7000./(1.98*T))   .11E+15*T**( 0.00)*EXP( -34131./(1.98*T))
CHO +N          =HCN +O         .10E+15*T**( 0.00)*EXP(      0./(1.98*T))   .40E+15*T**( 0.00)*EXP( -29767./(1.98*T))
HCN +OH         =CN  +H2O       .20E+12*T**( 0.60)*EXP(  -5000./(1.98*T))   .22E+12*T**( 0.60)*EXP(  -1318./(1.98*T))
HCN +H          =CH  +N2        .25E+12*T**( 0.00)*EXP( -16000./(1.98*T))   .39E+11*T**( 0.00)*EXP( -19761./(1.98*T))
HCN +O          =CH  +NO        .10E+15*T**( 0.00)*EXP( -72000./(1.98*T))   .36E+13*T**( 0.00)*EXP(   -667./(1.98*T))
CHO +N          =CH  +NO        .10E+15*T**( 0.00)*EXP( -48600./(1.98*T))   .15E+14*T**( 0.00)*EXP(  -7034./(1.98*T))
CN  +CO2        =NCO +CO        .37E+13*T**( 0.00)*EXP(      0./(1.98*T))   .55E+12*T**( 0.00)*EXP(   1988./(1.98*T))
CN  +OH         =NCO +H         .62E+14*T**( 0.00)*EXP(      0./(1.98*T))   .22E+16*T**( 0.00)*EXP( -22171./(1.98*T))
CN  +H2         =HCN +H         .62E+13*T**( 0.00)*EXP(  -5300./(1.98*T))   .28E+14*T**( 0.00)*EXP( -24393./(1.98*T))
CN  +O          =CO  +N         .63E+12*T**( 0.50)*EXP(      0./(1.98*T))   .32E+13*T**( 0.50)*EXP( -77052./(1.98*T))
NCO +H          =NH  +CO        .50E+12*T**( 0.50)*EXP(  -6970./(1.98*T))   .36E+11*T**( 0.50)*EXP( -34638./(1.98*T))
CO  +HNO        =CO2 +NH        .10E+12*T**( 0.50)*EXP(  -7000./(1.98*T))   .88E+12*T**( 0.50)*EXP(  -8963./(1.98*T))
H   +NO    +M   =HNO +M         .20E+17*T**( 0.00)*EXP(      0./(1.98*T))   .35E+20*T**(-1.00)*EXP( -50563./(1.98*T))
NO  +O     +M   =NO2 +M         .14E+22*T**(-1.82)*EXP(      0./(1.98*T))   .39E+26*T**(-2.82)*EXP( -74164./(1.98*T))
N2O +M          =N2  +O    +M   .40E+15*T**( 0.00)*EXP( -51400./(1.98*T))   .21E+09*T**( 1.00)*EXP( -10962./(1.98*T))
H   +HNO        =H2  +NO        .10E+14*T**( 0.00)*EXP(  -2500./(1.98*T))   .54E+13*T**( 0.00)*EXP( -57659./(1.98*T))
H   +N2O        =OH  +N2        .80E+14*T**( 0.00)*EXP( -15000./(1.98*T))   .18E+13*T**( 0.00)*EXP( -78253./(1.98*T))
H   +N2O        =NH  +NO        .10E+12*T**( 0.50)*EXP( -30000./(1.98*T))   .26E+09*T**( 0.50)*EXP(   8955./(1.98*T))
H   +NO2        =OH  +NO        .32E+15*T**( 0.00)*EXP(  -1500./(1.98*T))   .48E+13*T**( 0.00)*EXP( -31028./(1.98*T))
HNO +OH         =H2O +NO        .10E+13*T**( 0.00)*EXP(  -1000./(1.98*T))   .26E+13*T**( 0.00)*EXP( -71570./(1.98*T))
HNO +O          =OH  +NO        .50E+12*T**( 0.50)*EXP(      0./(1.98*T))   .12E+12*T**( 0.50)*EXP( -53128./(1.98*T))
HNO +O          =NH  +O2        .10E+12*T**( 0.50)*EXP(  -7000./(1.98*T))   .61E+11*T**( 0.50)*EXP(  -1135./(1.98*T))
OH  +N2O        =HO2 +N2        .32E+14*T**( 0.00)*EXP( -15000./(1.98*T))   .11E+14*T**( 0.00)*EXP( -39919./(1.98*T))
N   +OH         =NO  +H         .63E+12*T**( 0.50)*EXP(      0./(1.98*T))   .21E+13*T**( 0.50)*EXP( -48611./(1.98*T))
N   +NO         =N2  +O         .31E+14*T**( 0.00)*EXP(   -334./(1.98*T))   .13E+15*T**( 0.00)*EXP( -75429./(1.98*T))
N   +O2         =NO  +O         .60E+10*T**( 1.00)*EXP(  -6300./(1.98*T))   .12E+10*T**( 1.00)*EXP( -38180./(1.98*T))
NH  +H          =N   +H2        .63E+12*T**( 0.50)*EXP(  -8000./(1.98*T))   .28E+13*T**( 0.50)*EXP( -37144./(1.98*T))
NH  +OH         =H2O +N         .50E+12*T**( 0.50)*EXP(  -2000./(1.98*T))   .11E+14*T**( 0.50)*EXP( -46555./(1.98*T))
NH  +OH         =NO  +H2        .50E+12*T**( 0.50)*EXP(  -2000./(1.98*T))   .72E+13*T**( 0.50)*EXP( -79755./(1.98*T))
NH  +O          =NO  +H         .63E+12*T**( 0.50)*EXP(      0./(1.98*T))   .41E+13*T**( 0.50)*EXP( -75724./(1.98*T))
NH2 +H          =NH  +H2        .14E+12*T**( 0.67)*EXP(  -4300./(1.98*T))   .85E+11*T**( 0.67)*EXP(  -6332./(1.98*T))
NH2 +OH         =NH  +H2O       .30E+11*T**( 0.68)*EXP(  -1300./(1.98*T))   .89E+11*T**( 0.68)*EXP( -18743./(1.98*T))
NH2 +O          =NH  +OH        .92E+12*T**( 0.50)*EXP(      0./(1.98*T))   .25E+12*T**( 0.50)*EXP(     -1./(1.98*T))
```

```
                                                   TABLE 1
                                                   *******
                                                  CONTINUED
CHEMICAL REACTION
******** ********                           FORWARD RATE                                   REVERSE RATE
                                            ******* ****                                   ******* ****
                                          (G-MOLE,CM,SEC)                                (G-MOLE,CM,SEC)
NH2 +NH2     =NH3 +NH      .17E+12*T**( 0.63)*EXP(  -3600./(1.98*T))  .10E+13*T**( 0.63)*EXP(  -4634./(1.98*T))
NH3 +OH      =NH2 +H2O     .30E+11*T**( 0.68)*EXP(  -1100./(1.98*T))  .15E+11*T**( 0.68)*EXP( -17509./(1.98*T))
NH3 +H       =NH2 +H2      .19E+12*T**( 0.67)*EXP(  -3400./(1.98*T))  .19E+11*T**( 0.67)*EXP(  -4398./(1.98*T))
NH2 +NO      =N2  +H2O     .50E+13*T**( 0.00)*EXP(      0./(1.98*T))  .12E+15*T**( 0.00)*EXP(-119651./(1.98*T))
NH3 +O       =NH2 +OH      .15E+13*T**( 0.00)*EXP(  -6000./(1.98*T))  .69E+11*T**( 0.00)*EXP(  -4967./(1.98*T))
NH3 +O2      =NH2 +HO2     .50E+12*T**( 0.50)*EXP( -56000./(1.98*T))  .22E+11*T**( 0.50)*EXP(    198./(1.98*T))
NO  +HO2     =NO2 +OH      .50E+12*T**( 0.50)*EXP(  -3520./(1.98*T))  .21E+13*T**( 0.50)*EXP( -12426./(1.98*T))
```

SECTION III

EXPERIMENTAL

Combustor

A schematic of the combustor and its feed lines is shown in Figure 2. Metered amounts of fuel (CH_4, Matheson, C.P. grade), oxygen and nitrogen are mixed and fed to the two opposing burners. The flow rate of these gases is measured with critical flow orifices of size ranging from 0.076 to 0.630 mm.

Fuel nitrogen is simulated in these experiments by the addition of anhydrous ammonia to the fuel or the oxidizer stream. The flow rate of this additive was measured with a restriction and an inclined differential manometer.

The combustion chamber is a 60 x 60 x 60 cm sealed aluminum box which contains the two vertically mounted opposed burners, an uncooled quartz probe, I.D. = 0.06 cm, a platinum ignition wire, and a Pt, Pt/10% Rh thermocouple, which is mounted on the probe. The bead of this thermocouple is approximately 0.05 mm in diameter and is uncoated. The two burners are made of 6.35 cm diameter stainless steel tubes which are filled with glass beads and sealed at the ends with a stainless steel sintered disk.

Analysis

The sample was drawn with a vacuum pump at a rate of which no visual disturbance, due to sampling, could be observed in the flame (approximately 0.13 ℓ/min). This sampling rate represents a residence time of 7 msec in the tip of the probe before the sample was quenched. Calculations indicated that under these conditions, homogeneous reactions in the probe did not affect our measurements, although this does not rule out reactions on the probe wall.

The temperature of the sample lines was kept above the dew point of water. After the sample loop of a Perkin Elmer, Sigma II gas chromatograph was filled, the gas contained in it was pressurized to a standard pressure, in this case 2 atm, and then injected. Analysis with the gas chromatograph was performed for CO, CO_2, O_2, H_2 and H_2O using a 3.05 meter molecular sieve and a 1.97 meter Porapak-T column in conjunction with a hot wire and nitrogen

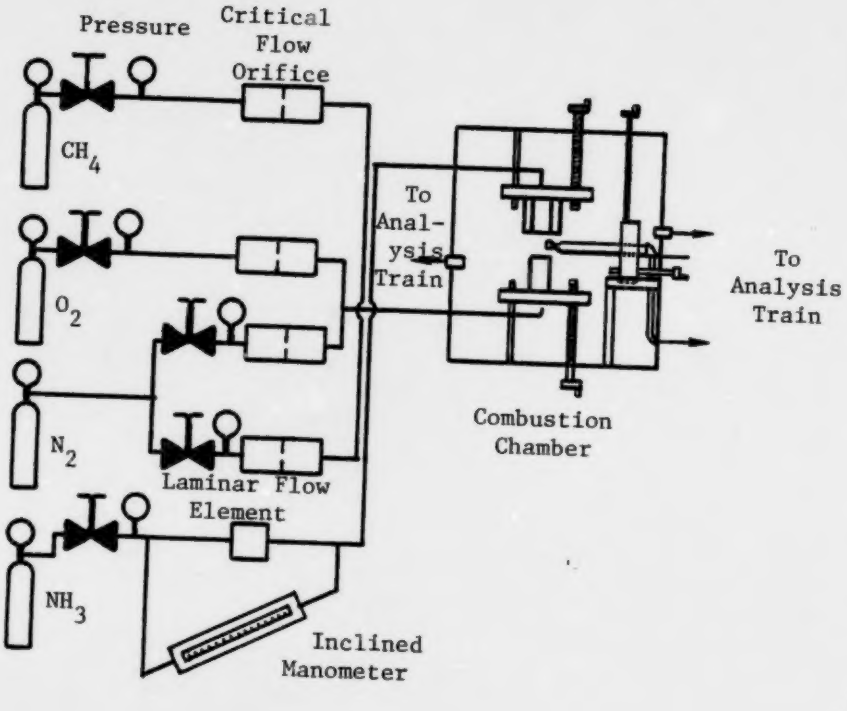

Figure 2. Schematic of the Combustor and Its Feed Lines.

phosphorous detector. In line with the gas chromatograph was a Thermo-Electron Model 10-A, self contained, Chemiluminescent NO/NO_x analyzer with stainless steel and molybdenum converters. Details of the analytical procedures can be found elsewhere (Ref. 11).

SECTION IV

RESULTS

The separation of the burners was arbitrarily chosen to be 3 cm and this distance proved to be sufficiently large compared to the thickness of the reaction zone. In the two cases which were analyzed, $\varepsilon = 3.62\ \text{sec}^{-1}$ and $\varepsilon = 1.88\ \text{sec}^{-1}$, no diffusion of products into the burners occurred. This allows the numerical algorithm to converge. The fuel stream was composed of 10% methane in nitrogen while the concentration of oxygen in the oxidizer was 52% in nitrogen.

Two experiments with the probe positioned at different radial locations, r = 0.4 cm and r = 0.9 cm (denoted as Experiment 1 and Experiment 2, respectively) were performed at a stretching rate of $\varepsilon = 3.62\ \text{sec}^{-1}$. The one dimensionality of the laminar opposed jet diffusion flame (as well as reproducibility) is confirmed by the close agreement between the data obtained in experiments 1 and 2, shown on Figures 3 through 7. At a radial position larger than 0.9 cm a discrepancy in the two measured profiles were observed, from which it can be concluded that at those radii the effect of the free surface of the jets become important and therefore the theory, which assumes infinitely wide jets, breaks down.

There was a small discrepancy between theory and experiment in that the actual location of the reaction zone appeared to be displaced by 2.5 mm from that predicted. This discrepancy may be attributable to inaccuracies in transport quantities, kinetic parameters or neglect of radiation or buoyancy in the conservation equations. However, since the focus here is on NO formation in the reaction zone, and the effect of flame stretching thereon, it is appropriate to shift all measured data points by 2.5 mm towards the fuel rich side of the flame thus allowing a proper comparison of predicted and measured flame reaction zone structure. The same shifting has been performed on all experimental data on all subsequent Figures (3 through 9). It should be noted that other than this slight displacement, there are no adjustable model parameters utilized in this comparison.

Figure 3 shows the measured and predicted profiles of the reactants and the temperature. These data show that once a correction for the location of

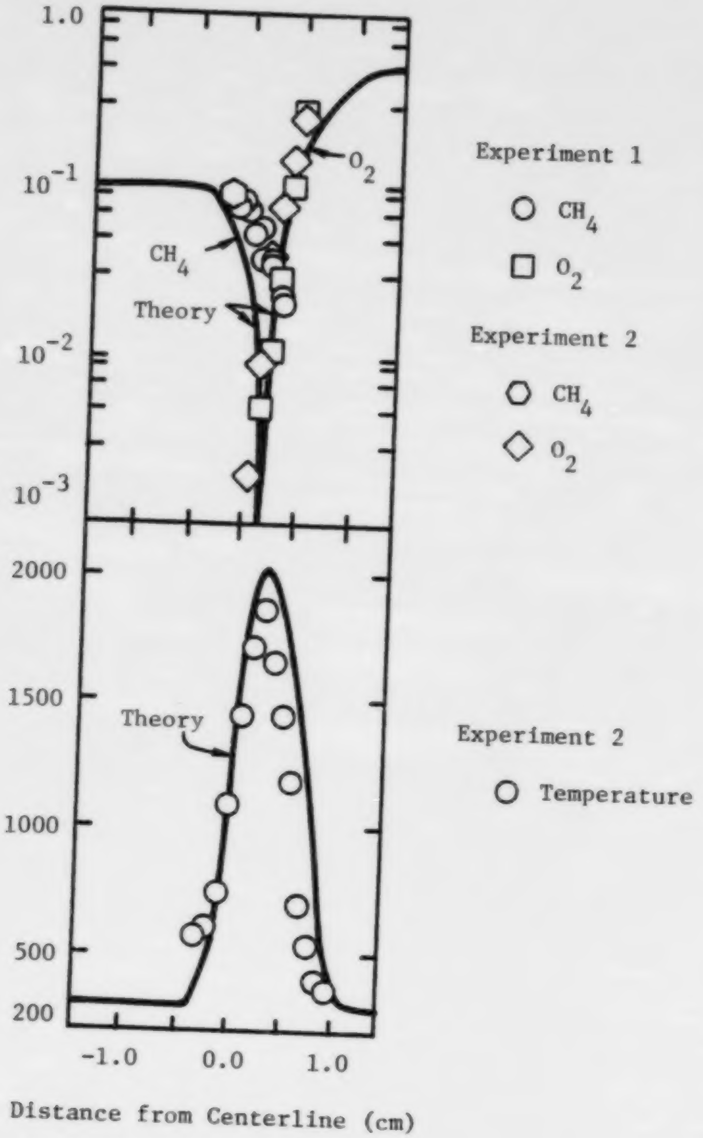

Figure 3. Axial Profiles of Reactants and Temperature; Comparison of Theory and Experiment; Data Shifted by 2.5 mm to Left (see Text). Two Independent Experiments are Reported. Experiment 1 at 4 = 0.4 cm and Experiment 2 at 4 = 0.0 cm ($\varepsilon = 3.62\ \text{sec}^{-1}$).

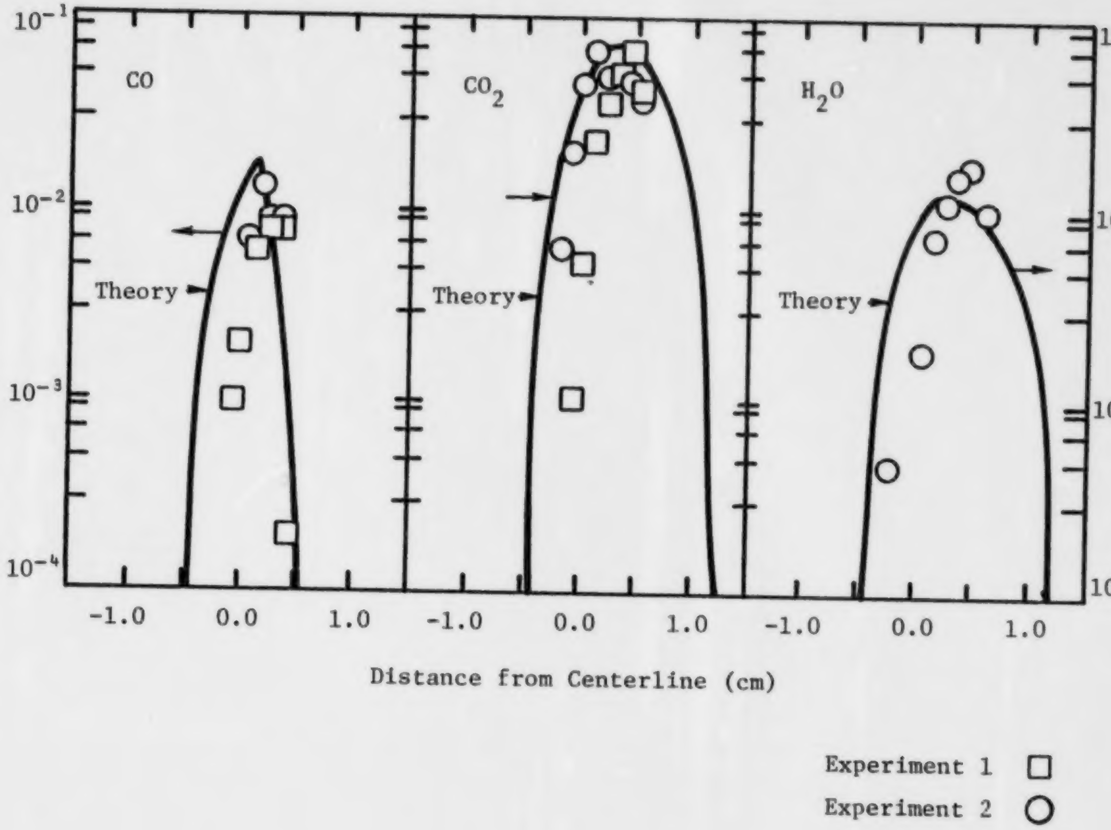

Figure 4. Axial Profiles of Major Combustion Products and Comparison of Theory and Experiment. Same Two Experiments as in Figure 3 ($\epsilon = 3.62$ sec^{-1}).

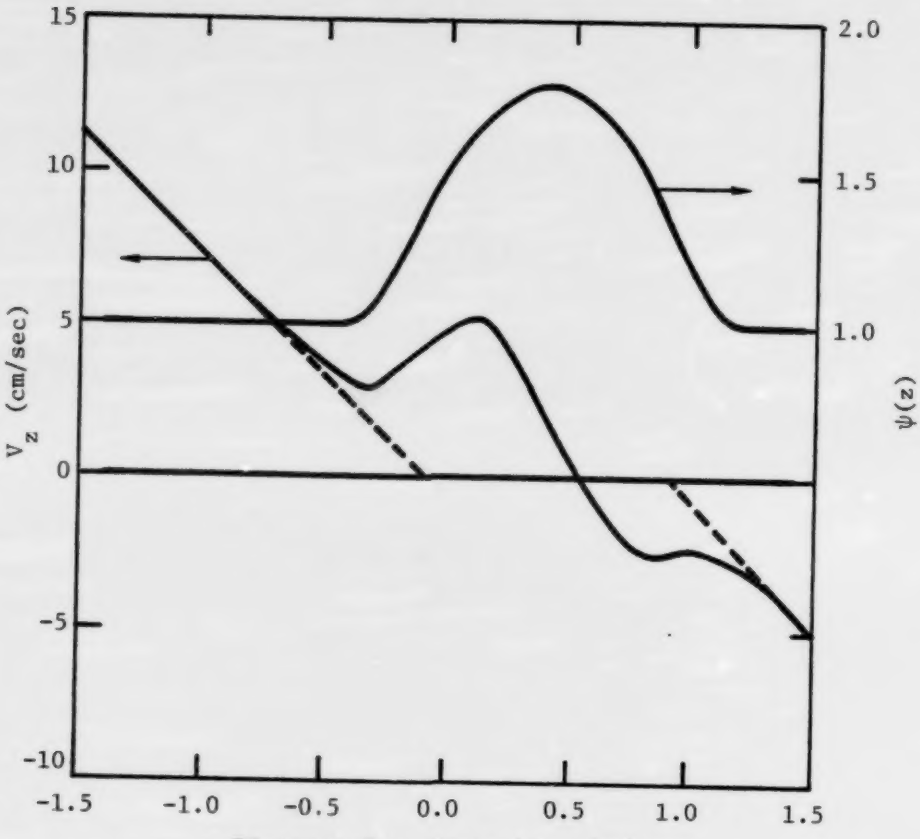

Figure 5. Axial Velocity Profile and Profile of $\psi(z)$. (ε = 3.62 sec^{-1})

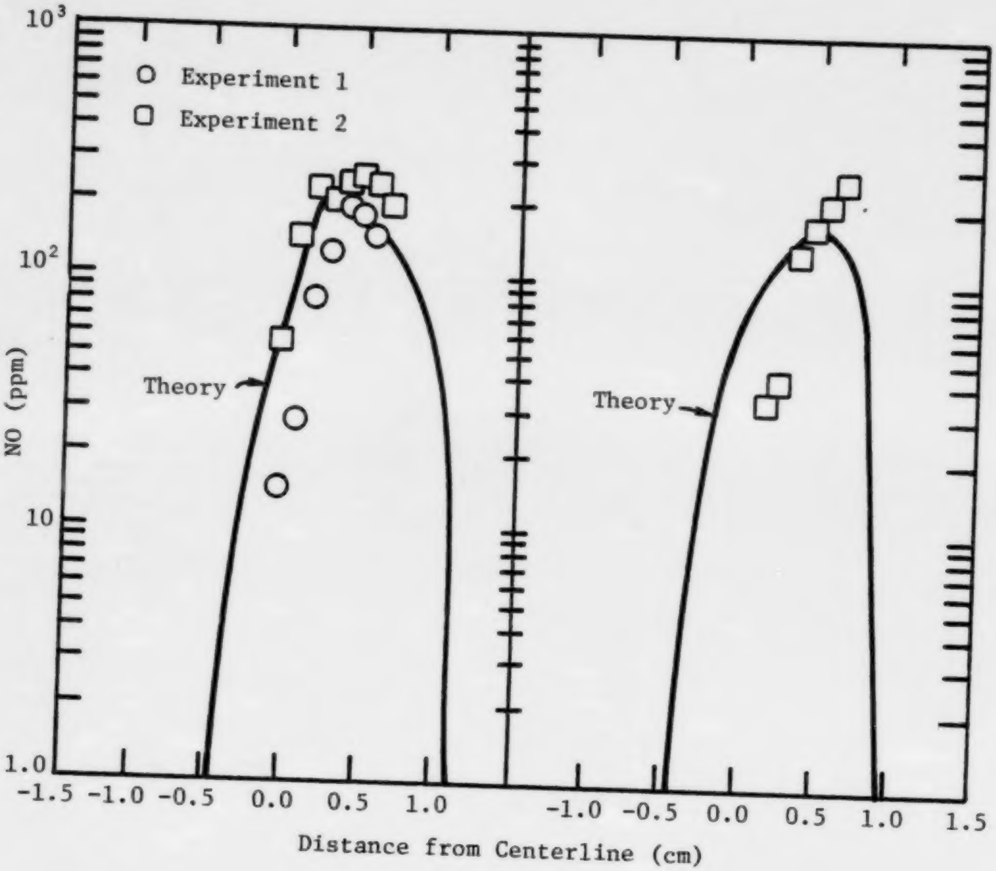

Figure 6. NO Profile When Anhydrous Ammonia is Injected Into the Flame with the Fuel (Left Figure) or with the Oxidizer (Right Figure). ($\varepsilon = 3.62 \text{ sec}^{-1}$)

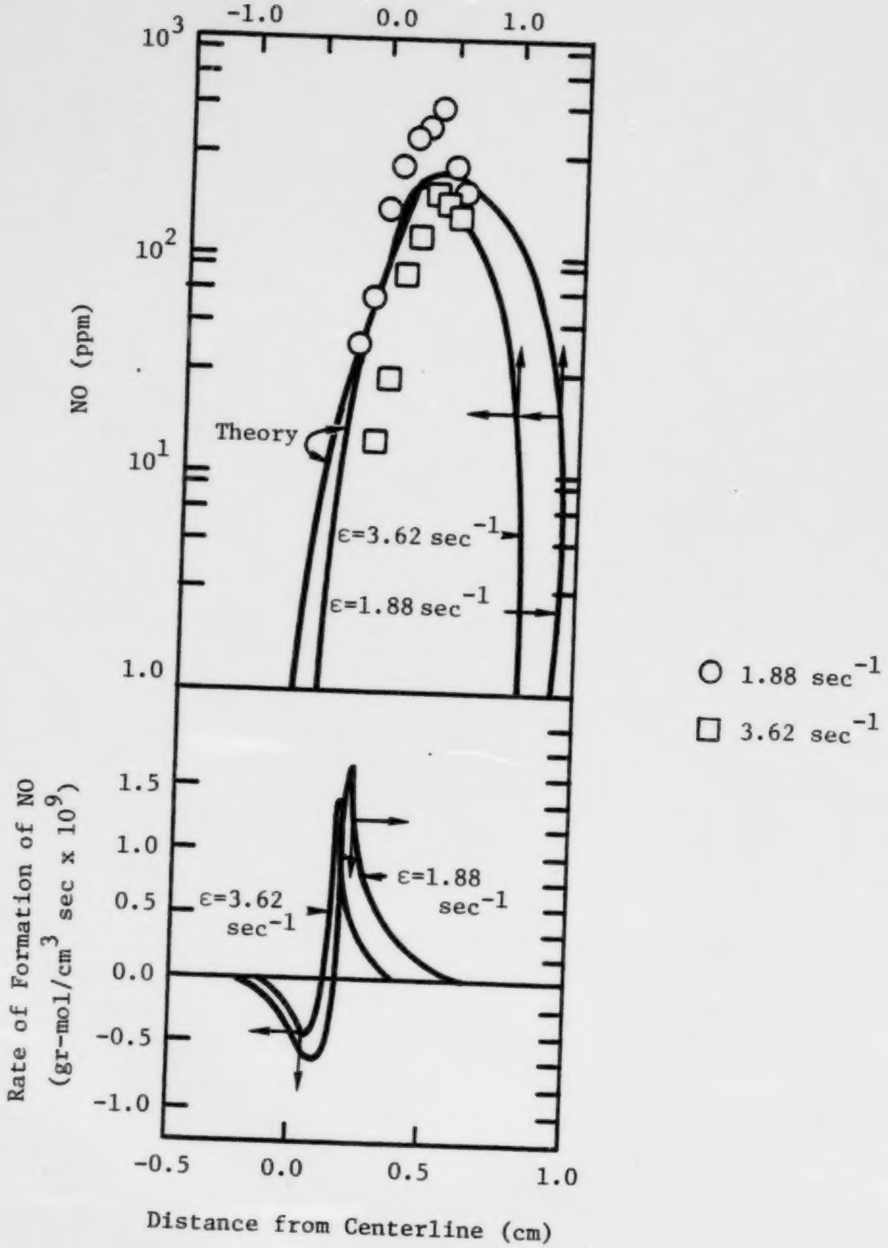

Figure 7. Effect of the Rate of Stretching on the NO Profile (Upper) and on the Rate of Formation of NO (Lower).

the flame zone is introduced, its structure which is the key parameter in the prediction of rate of formation of trace species, is very well modeled.

The predicted peak temperature of $2082^{\circ}K$ is $170^{\circ}K$ above the adiabatic flame temperature of a stoichiometric well stirred mixture of the two incoming jets, which is not surprising.

Figure 4 shows the profiles of the major reaction products, namely CO, CO_2 and H_2O. In this figure the measured profiles seem to be somewhat narrower than the theoretical predicitons, which are represented by the full lines. This may be attributed to thermal diffusion and/or heat loss of the flame to the surroundings. The agreement between experimental and theoretical peak height is very good in all three cases, which is again an indication that the model representing the flame zone structure of the laminar flat opposed jet diffusion flame has merit.

The strong influence of the heat released by the flame on its aerodynamics can be observed in Figure 5 which shows the axial volocity profile and the function ψ, which is the measure of the interaction between heat release and conservation of momentum. It can be observed that far from the flame, where the value of ψ is unity the velocity profile is linear and corresponds to that of an inviscid incompressible jet impinging on a plane perpendicular to its axis. Close to and in the flame front ψ increases reaching a maximum of 1.78 and the velocity profile becomes nonlinear. It is also of interest to note that a gradient in ψ yields local vorticity values of $w = \varepsilon ar \frac{d\psi}{dz}$, in an otherwise irrotational flow. A noteworthy fact is that both jets "perceive" different stagnation points and that the real stagnation point lies in between. Furthermore, it is of interest that the velocity of the jet at $z = + 1.5$ cm is approximately half the velocity of the other jet at $z = - 1.5$ cm, thus indicating that if equal velocities are used in both jets, the resulting flame would be two-dimensional and not flat.

The predicted and measured profiles of NO for the case when a mole fraction of 10^{-3} of anhydrous ammonia (1% of the concentration of the fuel) is injected into the fuel are shown on the left side of Figure 6. Good agreement in both peak height and width of the profiles can be observed between theoretical predictions and experimental data. When ammonia (mole fraction, 2.2×10^{-3}) is injected with the oxidant (right side of Figure 6) agreement between theory and experiment is less perfect, and measured peak values are substantially higher than those predicted. One might conclude from these experiments that ammonia pyrolysis in the presence of hydrocarbon fuel fragments is well represented by the reaction mechanism on Table 1. However, ammonia pyrolysis in the presence of mainly CO, H_2, and other products is not so well presented by this mechanism.

On Figure 7 the effect of the stretching rate on the NO profile and the net rate of formation of NO is presented. Theory predicts that the low stretching rate flame has an NO profile which is wider than the profile of the highly stretched flame and that the peak of the profile increases as the stretching rate decreases. The experimental data verify both predictions qualitatively, indicating that the effect of the stretching rate on the formation of NO in the flat, laminar opposed jet diffusion flame is well represented. Thus this flame is a useful prototype model to predict formation of trace species such as NO_x, SO_x or soot in turbulent diffusion flames since the rate of stretching is the key variable linking an ensemble of laminar flamelets, each strained in its own plane, to the mean turbulent flow field.

The profiles of the rate of formation of NO show that the reactions destroy NO in the fuel rich side of the flame are as important as the reactions forming it on the fuel lean side of the flame. Furthermore, it can be observed that when the rate of stretching is doubled, the rate of formation of NO is altered by an order of magnitude. Nevertheless, when the profiles are integrated over the z - axis, the effect is much smaller and it is estimated that the rate of formation of NO increases by a factor of two. This is consistent with the fact that increased mixing generally leads to increased conversion of fuel nitrogen, in practical turbulent diffusion flames (Ref. 12).

The predicted effect of the stretching rate on the heat release profile and the rate of formation of NO can be observed in Figure 8.

The width of the heat release profile is the true measure of the extent of the reaction zone and it can be observed that with increased stretching rate the heat release profile decreases in width while increasing in height. The increased peak height of the heat release suggests a more intense combustion in highly stretched flames. Therefore, the rate of stretching can be associated with the local combustion intensity in turbulent diffusion flames.

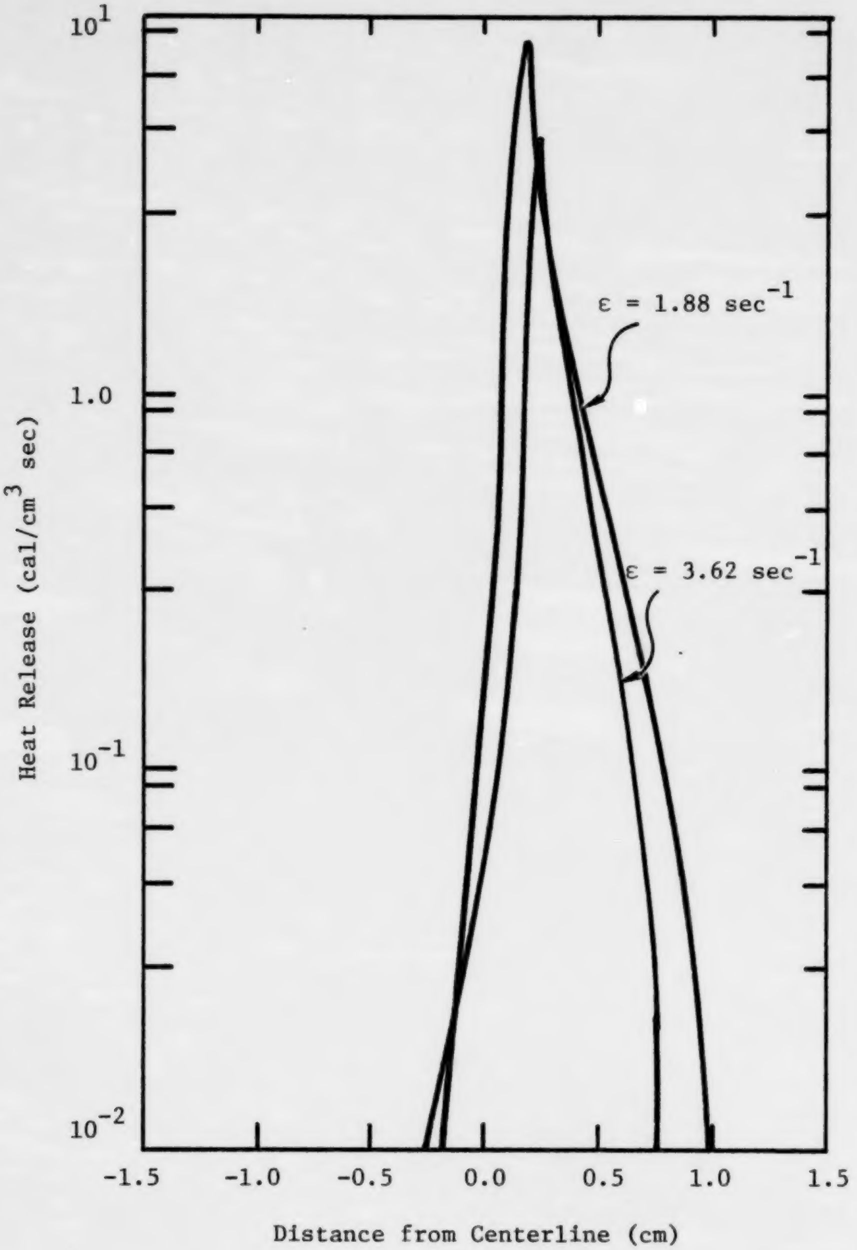

Figure 8. Effect of Stretching on Heat Release Profile.

SECTION V

CONCLUSIONS

A truly flat laminar opposed jet diffusion flame can be established in the laboratory after the appropriate model, which provides the boundary conditions for the jet velocities, has been solved. This makes this type of flame useful in studying trace species formation in fuels whose detailed chemistry and heat release rate characteristics are known a priori and where the chemistry of the trace species does not affect these quantities. Where this is not the case, an iterative procedure between theory and experiment would be required before the problem is solved. Where jets of finite width are used, the experimental evidence supplied here shows that the laminar opposed jet diffusion flame is one dimensional in temperature and concentrations, when the proper velocity ratio is used.

Use of a detailed reaction set developed by others allowed quantitative comparison between theory and experimental data for a methane-oxygen-nitrogen flat laminar opposed jet diffusion flame. The theory predicted the structure of the reaction zone well, with no additional adjustable parameters. The actual location of the reaction zone, however, was displaced slightly from that predicted, and this discrepancy may be attributable to inaccuracies in the adiabaticity assumption of the model, the transport coefficients or possibly the reaction mechanisms utilized. No attempt was made here to optimize the fit between theory and experiment.

The oxidation and pyrolysis of fuel nitrogen, as ammonia, was investigated by first injecting ammonia in the fuel and then in the air and then comparing the predicted versus measured NO profile. The good agreement between model and experiment when the ammonia was injected with the fuel indicates that there the pyrolysis reactions of ammonia in the presence of fuel hydrocarbon fragments can be described by the mechanism used. When ammonia was injected with the oxidant, the poor agreement with theory there indicates that the mechanism may not accurately describe ammonia pyrolysis in the presence of CO, CO_2, H_2O and oxidant.

This work is a very severe test of any kinetic mechanism for fuel and fuel nitrogen pyrolysis and oxidation since conditions span from the extremely fuel rich to the extremely fuel lean, and from very high to very low temperatures. In view of this, we think the degree of agreement between theory and experiment is quite encouraging.

The effect of rate of stretching on the axial NO profile is well predicted by theory. NO formation and NO destruction mechanisms are of equal importance in these type of flames, and the experimental and theoretical results presented here are in qualitative agreement with observed effects of increased turbulent intensity on NO formed in turbulent diffusion flames.

The opposed jet diffusion flame, when combined with theory and experiment, can be viewed as a novel tool for the study of mechanisms of formation of trace species, such as NO_x, SO_x or soot and also as a prototype model of local microscopic phenomena in turbulent diffusion flames.

ACKNOWLEDGEMENTS

This work was supported by the U.S. Environmental Protection Agency through Grant R803715 to the University of Arizona and through Subcontract from Contract 68-02-2631 to Energy and Environmental Research Corporation, Santa Ana, California. The authors acknowledge the help of T. L. Corley, T. J. Tyson, C. J. Kau and W. S. Lanier during the course of this project.

NOMENCLATURE

c	Molar density (gr-mol/cm^3)
C_p	Heat capacity (cal/gr-mol ^{o}K)
D_A	Pseudo binary diffusion coefficient of species A in gaseous mixture
$\underline{g}$	Body force vector
P	Pressure (atm)
r_j	Rate of reaction j (gr-mol/cm^3-sec)
R_A	Rate of formation of species A (gr-mol/cm^3-sec)
T	Temperature (^{o}K)
v	Axial velocity (cm/sec)
x_A	Mole fraction of species A
Δh_j	Heat of reaction j (cal/gr-mol)
ε	Stretching rate (sec^{-1})
ρ	Density (g/cm^3)
ψ	Similarity transformation

REFERENCES

1. Williams, F. A.: "Turbulent Mixing in Non-Reactive and Reactive Flows," Purdue University, S. N. B. Murthy, Ed., p. 189 (1974).

2. Marble, F. E., and Broadwell, J. E.: "The Coherent Flame Model for Turbulent Chemical Reactions," Proj. SQUID, 29314-6001-RU-00 (1977).

3. Spalding, D. B.: "Theory of Mixing and Chemical Reaction in the Opposed Jet Diffusion Flame," ARS Journal, 31, 763 (1961).

4. Fendell, F. E.: "Ignition and Extinction in Comb. of Initially Unmixed Reactants," J. Fluid Mech., 21, 281 (1965).

5. Jones, F. L., Becker, P. M., and Heinsohn, R. J.: "A Mathematical Model of the Opposed Jet Diffusion Flame: Effect of an Electric Field on Concentration and Temperature Profiles," Comb. & Flame, 19, 351 (1972).

6. Kent, J. H., and Williams, F. A.: "Extinction of Laminar Diffusion Flames for Liquid Fuels," Fifteenth Symp. (Int.) on Comb., p. 315, The Combustion Institute, Pittsburgh, PA (1974).

7. Hahn, W. A., Wendt, J. O. L., and Tyson, T. J.: "The Structure of the Flat Laminar Opposed Jet Diffusion Flame," AIChE J., submitted.

8. Hahn, W. A.: "Pollutant Formation in Flat Laminar Opposed Jet Diffusion Flames," Dissertation, University of Arizona, Tucson, Arizona (1979).

9. Reid, R. C., Pausnitz, J. M., and Sherwood, T. K.: "The Properties of Gases and Liquids," 3rd Ed., McGraw-Hill, N.Y. (1977).

10. Levy, J. M., Longwell, J. L., Sarofim, A. F., Corley, T. L., Heap, M., and Tyson, T. J.: "NO_x Abatement in Fossil Fuel Comb: Chem. Kinetic Considerations," Proc. of the Third Stationary Source Comb. Sym., Vol. 4, Fundamental Comb. Research and Env. Assessment, Interagency Energy/Env. Res. and Dev. Prog., Report No. EPA-600/7-79/050d, Feb (1979).

11. Wootan, E. C.: "Fate of Fuel Nitrogen in Laminar Premixed Flat Flames," M.S. Thesis, University of Arizona, Tucson, Arizona (in preparation).

12. Pershing, D. W., and Wendt, J. O. L.: "Pulverized Coal and Comb: The Influence of Flame Temperature and Coal Composition on Thermal and Fuel NO_x," Sixteenth Sym (Int.) on Comb., p. 389, The Combustion Institute, Pittsburgh, PA (1976).

THE FORMATION AND DESTRUCTION OF NITROGENOUS SPECIES DURING HYDROCARBON/AIR COMBUSTION

D. W. Blair
Exxon Research & Engineering Company
Linden, New Hampshire 07036

Fifth EPA Fundamental Combustion Research Workshop
Newport Beach, California
January 23-25, 1980

SECTION I

INTRODUCTION

This is a report on an experimental investigation of critical aspects of the formation and destruction of nitrogenous chemical species during hydrocarbon/air combustion. A primary purpose of this work was to provide reliable experimental information that can be used to provide both critical insights into computer models of NO_x formation and critical tests of those models. Thus, the results should provide both a guide and a challenge to modelers. Responding to this purpose, results have been obtained for a very wide range of experimental conditions to aid users in testing the generality of various kinetic models. To achieve this end, experiments were run in two significantly different laboratory combustors over a wide range of independent thermochemical variables (equivalence ratio, temperature, fuel species, and fuel nitrogen species).

SECTION II

EXPERIMENTAL

The first combustor used was a very strongly backmixed combustor--the jet stirred combustor (JSC). It is shown schematically in Figure 1. In this combustor premixed gaseous reactants are injected through numerous small ports in a hemispherical injector into a hemispherical ceramic reaction volume of 5.08 cm diameter. Exhaust products issue from this combustor through numerous radial exhaust ports. The average residence time within the reactor is 3 ms. The injection jets are sonic. They vigorously stir the reacting mixture to maintain highly turbulent, near homogenous conditions. These jets have a mixing time within the reactor of the order of 30 μs. Under these conditions, even "preflame" reactions occur in the presence of products from all stages of the combustion reaction mechanism. There is no physical separation of the process into preflame, intermediate, and final combustion zones. Samples of products from this reaction are withdrawn from the reactor through cooled quench-probes and analyzed for stable chemical species by standard means (Figure 2).

The second combustor was an adiabatic, laminar, quasi-plug flow combustor--the multiburner (MB). It is shown schematically in Figure 3. In this combustor a radially uniform laminar stream of premixed gaseous reactants flows upward through a porous stainless steel flat flame burner into a zirconia tube. A laminar flat flame is stabilized adjacent to the upper face of the burner, and postflame products flow upward through the cylindrical combustor tube. This tube is held at the pre-calculated adiabatic flame temperature by an electrically heated furnace which surrounds it. Because many important reactions involving nitrogenous species proceed at rates much less than those of predominant combustion reactions, nitrogen conversion occurs in the post-flame gases throughout the combustion tube. Samples of product were withdrawn through a cooled quench probe from a point 2 cm (30 ms residence time) above the burner face. These samples were analyzed by standard methods (Figure 2).

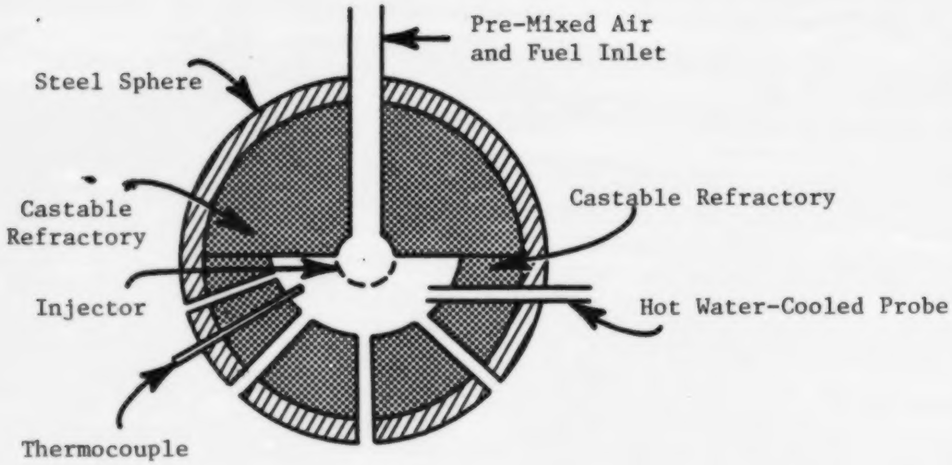

Figure 1. Schematic Diagram of the Jet Stirred Combustor.

CO_2 by Non-Dispersive IR (Lira Model 303, MB, or Beckman Model 864, JSC)

CO by Non-Dispersive IR (Lira Model 303, MB, or Beckman Model 864, JSC)

O_2 by Polarography (Beckman Model 702)

H_2 by Chromatography (Carle Model GC 8700)

UHC by FID as Methane (Beckman Model 400, MB, or Beckman Model 402, JSC)

NO by Chemiluminescence (Thermo Electron Model 10A)

HCN by Scrubbing in 0.5 M NaOH Followed by Ion-Specific Electrode Analysis

NH_3 by Scrubbing in 0.2% H_2SO_4 Followed by Ion-Specific Electrode Analysis

Figure 2. Gas Analysis.

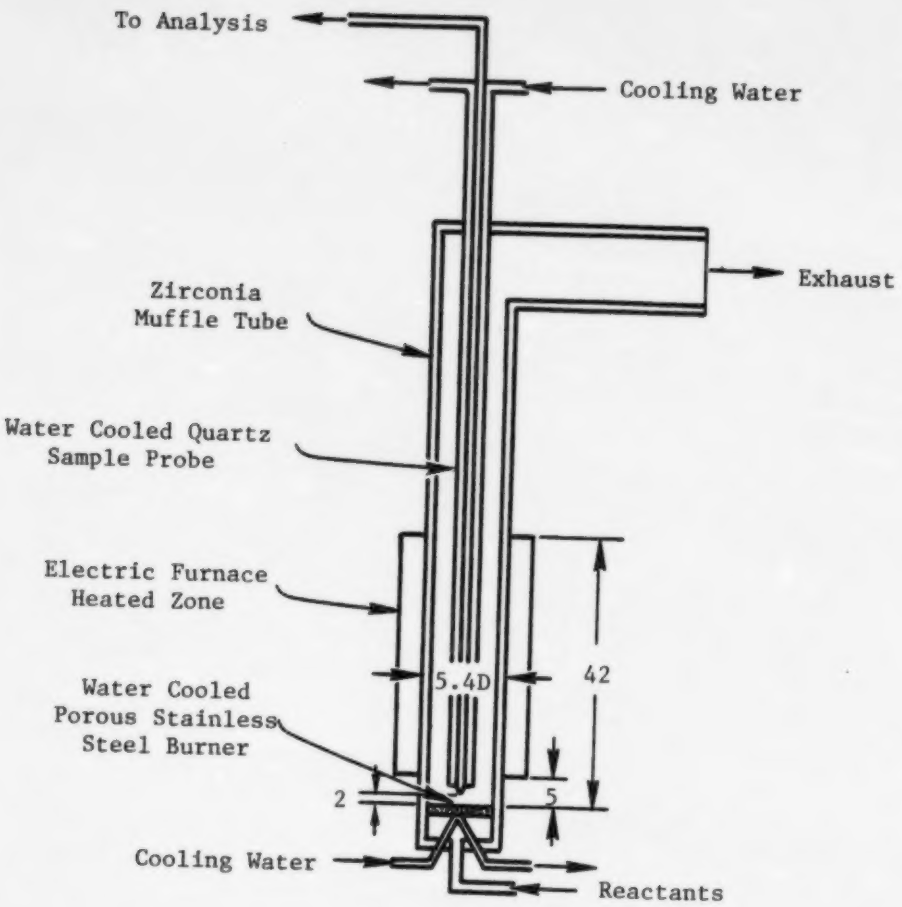
To Analysis
Cooling Water
Exhaust
Zirconia Muffle Tube
Water Cooled Quartz Sample Probe
Electric Furnace Heated Zone
Water Cooled Porous Stainless Steel Burner
5.4D
42
2
5
Cooling Water
Reactants

Figure 3. Schematic Diagram of the Multiburner.
Dimensions are in Centimeters.

SECTION III

RESULTS AND DISCUSSION

In each of the combustors, experiments were run at constant flame temperature (maintained by adjusting the N_2/O_2 ratio in the combustion "air") over a range of equivalence ratios from 0.7 to 1.8, with either CH_4, C_2H_4, or C_3H_8 as fuels, and with "fuel" nitrogen represented either by NH_3 or by a 1/1 ratio mixture of NH_3 + NO. "Fuel" nitrogen concentrations in the reactants ranged from 0 to 1000 ppm and flame temperatures of 1800, 1900, and 2000 K were investigated.

Table 1 compares results of experiments without fuel nitrogen (the resulting fixed nitrogen in the products is "thermal" nitrogen) in the two combustors with 1900 K flame temperature and CH_4 as the fuel. From this table it is observed that:

- The JSC is a more prolific producer of total fixed nitrogen (TFN) at all equivalence ratios (ϕ) than is the MB.
- For $\phi < 1.2$ the MB produces more NH_3 and HCN than does the JSC.
- For $\phi > 1.2$ the JSC produces more HCN than does the MB.
- TFN maximizes around $\phi = 1.2$ in the MB but it increases monotonically with ϕ in the JSC.
- For $\phi < 1.8$ the major product species is NO while for $\phi = 1.8$ it is HCN.

These observations raise the question whether the differences in performance of the two combustors results primarily from differences in reaction time (3 ms in the JSC vs 30 ms in the MB) or from differing chemical environment in the two combustors (backmixed vs plug flow). Because longer times should produce more thermal NO and TFN, it is concluded that combustion environment is the critical factor.

Table 2 presents the results of Table 1 as fractions of equilibrium values. It can be immediately observed that:

- Equivalence ratio 1.2 separates the regions where (lower ϕ) TFN and NO are present in less than equilibrium quantities and (higher ϕ) where they are present in greater than equilibrium quantities.

Table 1: Thermal Fixed Nitrogen from Methane Flames at 1900 K Flame Temperature

ϕ	DEVICE	FIXED NITROGEN IN COMBUSTION GAS ppm TFN	NH_3	HCN	NO
0.8	MB	18	7.2	1.8	9.2
0.8	JSC	41	1.6	1.5	38.0
1.0	MB	39	14.0	2.4	23.0
0.97	JSC	60	1.0	1.0	58.0
1.2	MB	53	4.8	17.0	31.0
1.4	MB	42	2.4	6.8	33.0
1.4	JSC	80	3.0	15.0	62.0
1.8	MB	35	2.2	27.0	5.7
1.8	JSC	133	1.4	121.0	11.0

Table 2: Ratio of Thermal Fixed Nitrogen From Methane Flames at 1900 K to Equilibrium Values

ϕ	DEVICE	TFN	NH_3	HCN	NO
0.8	MB	0.0071	2.1E5	5.3E4	0.0036
0.8	JSC	0.016	4.8E4	4.5E4	0.015
1.0	MB	0.088	2.6E4	4.0E6	0.052
0.97	JSC	0.072	1.9E3	1.7E6	0.12
1.2	MB	3.1	46.0	1.0E4	1.8
1.4	MB	5.7	7.4	7.3E2	4.7
1.4	JSC	11.0	9.2	1.6E3	8.8
1.8	MB	9.7	2.3	5.2E2	1.4
1.8	JSC	37.0	1.5	2.3E3	2.8

- NH_3 and HCN are present in greater than equilibrium quantities at all equivalence ratios but the ratio for NH_3 decreases monotonically with ϕ while that for HCN appears to maximize around $\phi = 1.0$.
- For $\phi < 1.2$ the MB is further from equilibrium than the JSC while for $\phi > 1.2$ the converse is true.

Table 3 shows the effect of flame temperature on the production of thermal TFN in methane flames in the MB. It can be understood in terms of the equilibrium ratios of Table 2.

- Below $\phi = 1.2$ (where TFN is present in subequilibrium quantities) increasing temperature *increases* TFN (drives the system *towards* equilibrium, as would be expected).
- Above $\phi = 1.2$ (where TFN is present in superequilibrium quantities) increasing temperature *decreases* TFN (drives the system *towards* equilibrium, as would be expected).

Table 4 shows the effect of fuel species on thermal TFN at 1900 K and equivalence ratio 1.4. It shows that:

- All nitrogen species and, thus, TFN show more fuel sensitivity for the MB than for the JSC.
- TFN, NH_3, and HCN decrease monotonically with carbon number in the MB but except for HCN (which increases monotonically) they appear to be highest with C_2H_4 in the JSC.
- The trends of NO with carbon number are similar in the two combustors but more is produced in the JSC.

It is reasonable to speculate that these observations reflect differing combustion environments in the two combustors. In the MB a significant period (0|1 ms|) exists for preflame reactions to occur. During this period initial fuel breakdown products are almost the only radical species present. While they influence subsequent reaction paths, they carry much of the identity of their parent fuel species with them. Later postflame reactions occur with almost no free oxygen present (for $\phi > 1$). In the JSC this preflame reaction period is very much shorter. Reaction occurs with free oxygen always present and in the presence of radicals that result predominantly from later reaction steps. These radicals carry much less of the identity of the fuel species with

Table 3: Total Thermal Fixed Nitrogen from Methane Flames in the Multiburner

	TFN, ppm			RATIO TO EQUILIBRIUM		
ϕ	1800	1900	2000 K	1800	1900	2000 K
0.8	--	18	98	--	0.0071	0.030
1.0	39	39	70	0.19	0.088	0.10
1.2	47	53	48*	15.0	3.1	1.8
1.4	64	42	43**	39.0	5.7	3.5
1.8	38	35	22	23.0	9.7	4.0

* $\phi = 1.25$

** $\phi = 1.44$

Table 4: Comparative Effect of Fuel Species on Thermal Fixed Nitrogen Produced in Flames at 1900 K and 1.4 Equivalence Ratio

DEVICE	FUEL	FIXED NITROGEN OUTPUT, ppm TFN	NH_3	HCN	NO
MB	CH_4	42	2.4	6.8	33
JSR	CH_4	80	3.0	15.0	62
MB	C_2H_4	38	2.0	2.0	34
JSR	C_2H_4	96	6.2	17.0	73
MB	C_3H_8	24	0.94	1.3	22
JSR	C_3H_8	89	3.7	26.0	59

them. Based upon these considerations one would expect backmixed systems to be more independent of fuel molecular structure than are plug flow systems.

Table 5 shows the effect of temperature on fuel nitrogen (200 ppm NH_3) conversion in CH_4 flames in the two combustors. As was the case with thermal nitrogen, TFN and NO are at subequilibrium at $\phi = 1.0$ and at superequilibrium at $\phi > 1.0$. Thus, for $\phi = 1.0$ increasing temperature increases TFN and NO (drives the system towards equilibrium) but for $\phi > 1.0$ the situation is less clear. In the JSC at $\phi > 1.0$ both TFN and NO decrease with increasing temperature (move towards Equilibrium) but this is not always true of the MB, nor does increasing temperature generally move HCN and NH_3 towards equilibrium for either burner at any ϕ. Kinetics are clearly controlling these results. The following additional observations may be drawn from this table:

- Conversion of fuel nitrogen to TFN and NO appears to be more sensitive to temperature in the MB than in the JSC and while it tends to increase with temperature in the MB it tends to decrease in the JSC.
- Conversion to NH_3 and HCN differs considerably between the MB and the JSC.

Table 6 shows the effect of fuel species and fuel nitrogen species on conversion to TFN in the multiburner at $\phi = 1.4$ and a flame temperature of 1900 K. With CH_4 as the fuel, conversion to TFN greatly increases as fuel NO is substituted for some of the fuel NH_3 but that large sensitivity disappears when C_2H_4 is the fuel. Conversion of fuel NH_3 to TFN is rather insensitive to fuel species.

Table 7 compares the effect of fuel nitrogen species on conversion to TFN in the two combustors with 1900 K CH_4 flames. The multiburner shows more sensitivity to this substitution at all ϕ than does the JSC. The substitution of NO for NH_3 as fuel nitrogen increases conversion to TFN in the MB and decreases it in the JSC. Also for $\phi = 1.4, 1.8$ this substitution causes TFN to move further from equilibrium in the MB and towards equilibrium (or leaves it unchanged) in the JSC (at $\phi = 1.0$ it causes the JSC to move away from equilibrium). While shorter residence times might be expected to increase sensitivity to fuel nitrogen species that is not the case between these two combustors. This further strengthens the hypothesis that the

Table 5: Comparative Effect of Temperature on Fuel Nitrogen (200 ppm NH_3) Conversion in Methane Flames

ϕ	DEVICE	TFN, PERCENT*		NH_3, PERCENT*		HCN, PERCENT*		NO, PERCENT*	
		1800	1900	1800	1900	1800	1900	1800	1900
1.0	MB	52 (0.49)	66 (0.32)	0.38 (3.1E3)	0.43 (-)	0.61 (1.9E7)	0.43 (-)	51 (0.49)	65 (0.32)
1.0	JSC		86 (0.19)		3.1 (-)		3.5 (-)		80 (0.18)
1.2	MB	43 (28)	175 (32)	0.52 (7.6)	69 (1.3E3)	4.9 (5.8E3)	1.1 (1.3E3)	38 (25)	105 (19)
1.2	JSC	127 (84)	100 (19)	0.64 (10)	2.1 (41)	1.5 (1.7E3)	2.9 (3.4E3)	125 (87)	95 (18)
1.4	MB	96 (112)	94 (38)	0.38 (1.8)	6.1 (37)	79 (1.6E4)	0.66 (134)	17 (26)	87 (38)
1.4	JSC	109 (128)	107 (144)	1.7 (8.1)	4.9 (29)	1.7 (743)	29 (5.8E3)	103 (162)	73 (32)

* Values in parentheses are ratios to equilibrium concentration. Where only dashes are present, the value is very large.

Table 6: The Influence of Fuel and FN Species (210 ppm FN) on Conversion in the Multiburner at 1900 K

		PERCENT AS TFN		
ϕ	FN	CH_4	C_2H_4	C_3H_8
1.4	NH_3	94	85	88
1.4	NH_3/NO	146	73	--
Ratio w/wo NO		1.6	0.86	--

Table 7: Comparative Effect of Fuel Nitrogen Species (200 ppm) on Conversion in Methane Flames at 1900 K

ϕ	DEVICE	TFN AS PERCENT OF FN* NH_3	TFN AS PERCENT OF FN* NH_3 + NO	RATIO W/WO NO
0.97	JSC	86 (0.19)	55 (0.12)	0.64
1.4	MB	94 (38)	146 (59)	1.6
1.4	JSC	107 (44)	109 (45)	1.0
1.8	MB	77 (44)	97 (55)	1.3
1.8	JSC	145 (83)	119 (68)	0.82

* Values in parentheses are ratios to equilibrium concentrations.

differences in results obtained from them stem from differences in combustion environment, not from differences in residence time.

Table 8 compares the effect of fuel species on conversion of fuel nitrogen (NH_3) in the two combustors. With all fuels, conversion in the JSC exceeds that in the MB. The MB shows a considerable fuel effect at $\phi = 1.0$ while the JSC does not. Neither combustor shows much effect of fuel species at $\phi = 1.4$.

The following conclusions are drawn from this work:

- With both equivalence ratio and flame temperature held constant, specific hydrocarbon chemistry influences both thermal nitrogen fixation and fuel nitrogen conversion.
- Fuel chemistry is more important in the multiburner than it is in the jet-stirred combustor. The contributions of combustion environment to this difference appear to exceed those of reaction time.
- While the conversion of fuel nitrogen is dependent upon fuel nitrogen species, the dependency in the MB considerably exceeds that in the JSC. This argues that differences in combustion environment between the two combustors is important.
- Because production of fixed nitrogen products differs significantly between the MB and the JSC, when choosing between these combustors as models of given practical combustors the choice should be based upon which one best approaches conditions that will exist in the given combustor.

While there is a need for considerable additional work in this area (extending range of variables, verifying results, expanding range and areas of overlap between the several independent variables) this project has terminated at ER&E Co. and further work on it is not contemplated there at this time.

Table 8: Comparative Effect of Fuel Species on the Conversion of Fuel Nitrogen (200 ppm NH_3) in Flames at 1900 K

		PERCENT AS TFN		
ϕ	DEVICE	CH_4	C_2H_4	C_3H_8
1.0	MB	66	--	14
0.97	JSC	86	101	98
Ratio JSC/MB		1.3	--	7.0
1.4	MB	94	85	88
1.4	JSC	107	107	114
Ratio JSC/MB		1.1	1.3	1.3

LABORATORY SCALE COAL STUDIES

J. M. Beer
A. F. Sarofim
J. M. Levy
D. Altrichter
and
L. Timothy
Department of Chemical Engineering
Massachusetts Institute of Technology
Cambridge, Massachusetts 02139

Fifth EPA Fundamental Combustion Research Workshop
Newport Beach, California
January 23-25, 1980

SECTION 1

INTRODUCTION

There is a possibility that in pulverized coal flames NO produced early in the combustion process is later reduced by char generated by the partial combustion of coal. Indirect evidence for the importance of NO reduction reactions in coal combustors is provided by the observation in pilot-scale combustors that the NO concentration passes through a maximum and undergoes substantial reduction in latter stages of combustion, particularly under fuel rich conditions. In order to assess the role of char in reducing NO, a three-part research program has been undertaken involving; (i) the determination of kinetics of the NO/char reaction under conditions of interest to pulverized coal combustion, (ii) the measurement of temperature-time histories and burning times of coal particles in order to provide a basis for testing models for coal combustors, (iii) the use of the kinetic information to develop a model to predict first char loading and temperature profiles, and then the reduction of NO by char under different simulated coal combustion conditions. The presentation here will provide preliminary results on the first two components of the study.

SECTION II

HIGH-TEMPERATURE STUDIES OF NO/CHAR KINETICS

Experimental Method

The kinetics of the reduction of NO on a char surface were studied in an electrically heated laminar flow furnace shown diagramatically in Figure 1. Detailed descriptions of the furnace and equipment are given elsewhere (1). Size graded, pulverized char particles are fed into the furnace in a helium stream, where they are rapidly heated to the furnace temperature by conduction from the surrounding main-gases and by radiation from the furnace walls. The main gases (NO, helium and additives such as O_2, CO or H_2O) are heated by passage through an aluminum honeycomb/flow-straightener prior to entering the furnace. Furnace temperatures of up to 1750 K can be achieved. Reaction is quenched by passage of the hot particles through a water-cooled section at the base of the furnace and collection of the char on a cold sintered bronze disk. The composition of the effluent gases are measured by a chemiluminescent analyzer (NO), non-dispersive infrared analyzer (CO, CO_2) and gas-chromatograph (O_2). Provision is also made to monitor the composition of the gases in cold-flow prior to entry to the furnace.

The experiments were performed in the laminar flow furnace as follows. Nitric oxide of a certified concentration in helium was flowed through a calibrated mass flow controller and mixed with an additional helium stream to yield the desired NO concentration (typically about 950 ppm) in cold flow. The total flow rates were determined

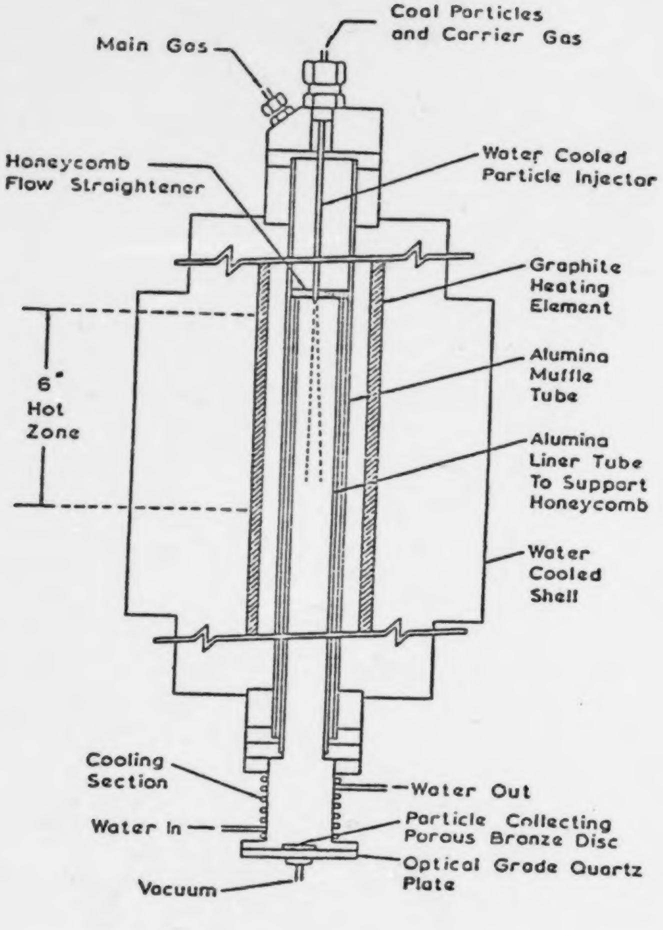

Figure 1. Furnace with Bronze Disc Collector.

from the NO dilution factor (i.e., by using NO itself as a tracer) and the known NO flow rate. Upon subsequent additions of additives, the helium flow was reduced until the initial NO concentration (measured on a chemiluminescent TECO meter) was restored. Char feeds were timed, and the weight of char fed was measured (by difference) to determine the char feed rate. The duration of each char feed was typically 90 to 210 seconds at approximately 0.1 gm/min..

During the char feed, a steady state is achieved in the furnace. Thus, from measurement of the entrance and exit NO concentrations, knowledge of the furnace volume, gas flow rate and char feed rate, it is possible to derive the effective rate constant for the reduction of NO on the char surface. The NO reduction has been found to be first-order in NO (2). For a plug-flow reactor, the following expression for the rate constant can be derived:

$$(\eta . k) = \frac{1}{7.286 \times 10^{15}} \cdot \frac{1}{A_B \cdot W/\tau} \cdot \frac{u_{in}^2}{V} \cdot T_F \cdot \int d \ln[NO]$$

where,

$\eta . k$ = effective rate constant, moles/sec. m^2

k = instrinsic rate constant

η = effectiveness factor (due to internal pore diffusion)

A_B = specific B.E.T. surface area of the char, m^2/gm

W/τ = char feed rate, gm/sec.

u_{in} = volumetric flow rate into the furnace, 1/sec. (at 298 K and 1 atm)

V = effective furnace volume, 1

T_f = furnace temperature. K

[NO] = NO concentration, ppm

The char sample fed was a Montana lignite, size-graded to 44-53μm, prepared in a crucible by heating pulverized coal to its asymptotic weight loss under an inert atmosphere at 1750 K. The elemental analysis of a char sample before and after passing through the furnace is shown below.

Table 1. Montana Lignite Char Used In NO/Char Studies Prepared By Heating In a Crucible At 1750 K

	Unreacted Char	%C	%H	%N	%S
Duplicate	C101	83.40	0.11	0.19	0.75
	C102	85.46	0.21	0.24	0.77
	Average	84.43	0.16	0.215	0.76

	Reacted Char	%C	%H	%N	%S
Duplicate	CR101	84.69	0.24	0.23	0.82
	CR102	85.39	0.12	0.23	0.78
	Average	85.04	0.18	0.23	0.80

A_B was measured on a degassed sample to be 20.3 m^2/gm, u_{in} was typically 3.4 - 3.5 ℓ/min.. V was determined by assuming a 6" isothermal hot zone. A more precise analysis would, however, require integration of furnace "slices" over the non-isothermal temperature profiles with the furnace heat zone.

A typical data plot is shown in Figure 2, in which exit NO, CO and CO_2 are plotted versus time. The depression in the NO trace occurs due to the conversion of NO in the presence of char. Conversion of the trace to its natural logarithm, and integration of the data to determine the last term in the above expression is performed on a Bascom-Turner recorder/data processing system.

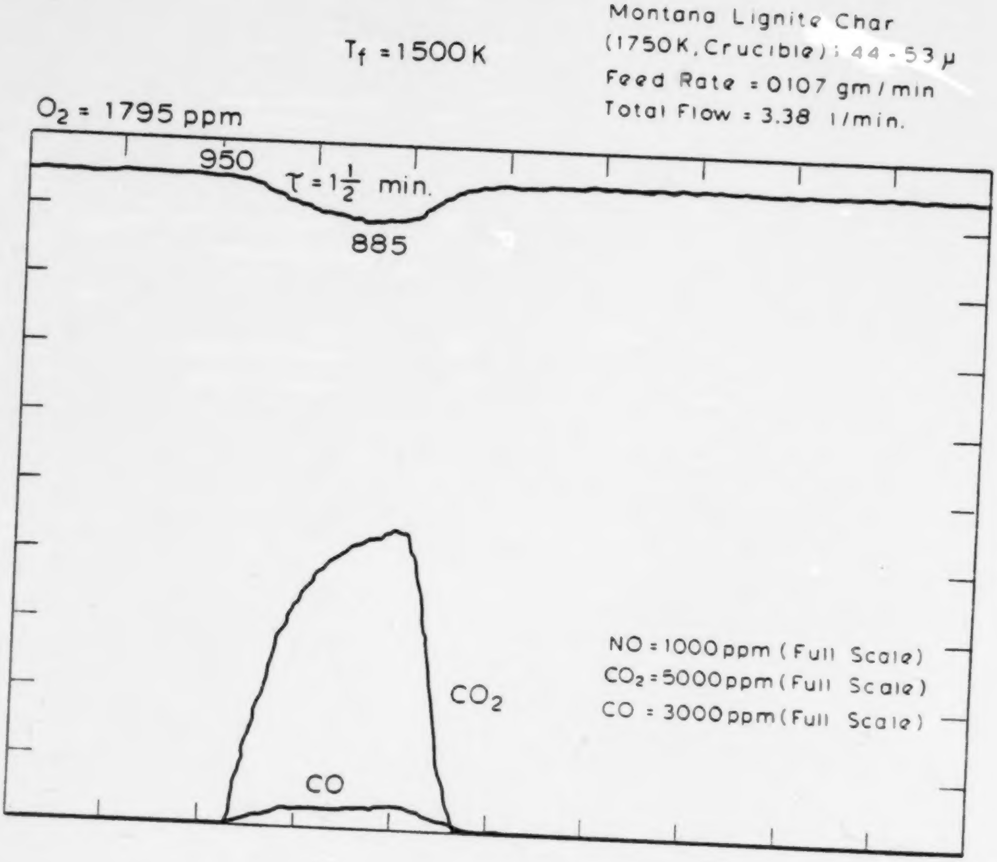

Figure 2. Representative Transient Concentrations of NO, CO and CO_2 During the Reaction of Char with an NO (950 ppm) and O_2 (1795 ppm) Mixture at 1500°K. Char is Fed for a Period of 1½ Minutes.

Experimental Results

An Arrhenius plot of the NO/char rate constant is shown in Figure 3, from which the following expression for the rate constant is derived:

$$(\eta.k) = 2.26 \times 10^{-10} \exp\left\{\frac{-35.05\text{Kcal}}{RT}\right\} \frac{\text{moles}}{\text{sec.m}^2}$$

which compares favorably with Song's (2) earlier results of $5.0 \times 10^{-11} \exp\left\{-\frac{32.7}{RT}\right\}$ obtained from a lignite char of ten times greater surface area, under different flow and feed-rate conditions.

The influence of three additives (CO, O_2, H_2O) on the NO/char reaction was also examined. Analysis of the CO data was possibly the most difficult because of a persistent transient (especially at the higher temperatures), which usually caused a downward sloping NO baseline. This effect is believed to be caused by the wall-catalyzed reaction of NO and CO, and is, apparently, dependent upon furnace conditioning. As such, no reproducible trends could be discerned and the best that could be done was to repeat the experiments until analyzable data were obtained. An example of a run acceptable for analysis is shown in Figure 4, in which the depression in the NO trace marked A & B are, respectively, due to the reaction of NO with char in the absence and presence of CO at a furnace temperature of 1600 K. It may be concluded from the similar magnitudes of depressions that the influence of CO is small. Table 2 summarizes the results of the best experiments. Enhancement of the NO/char reaction rate by 1.4% CO is seen, in all cases, to be less than 30%.

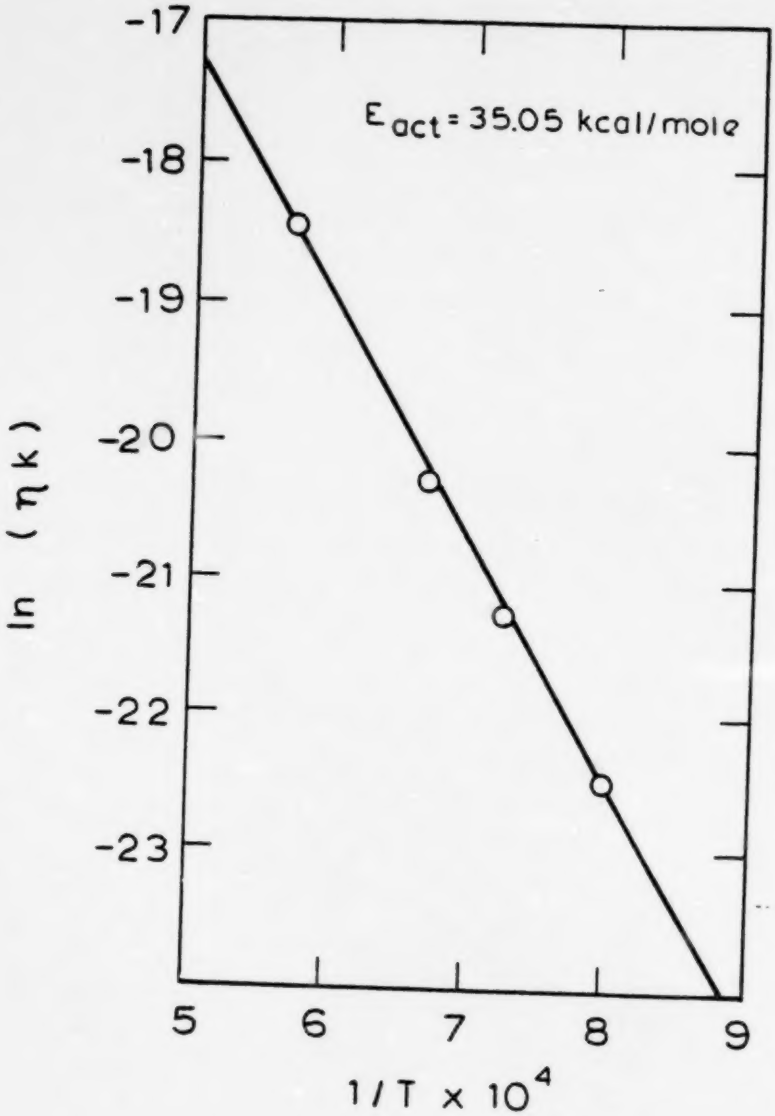

Figure 3. Plot of Product of Intrinsic Rate Constant k (in moles/m^2s) and Effectiveness Factor for the NO/Char Reaction.

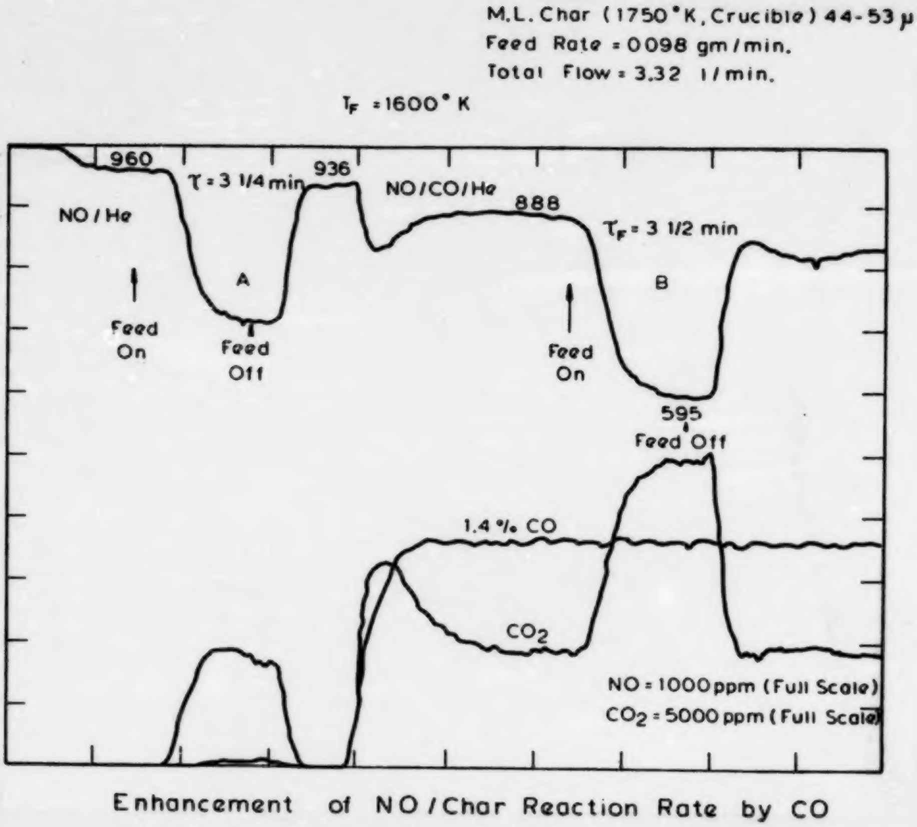

Figure 4. Effect of CO on the NO/Char Reaction. Transient Response A for Char Fed into an NO Mixture. Transient Response B for Char Fed into an NO/CO Mixture.

Table 2. Enhancement of NO/Char Reaction Rate by Added CO (1.4%)

T Furnace	k_{CO}/k	
1300 K	1.28	1.28
	1.27	
1600 K	1.28	1.14
	1.09	
	1.05	

Oxygen and water vapor, in constrast to CO, were found to have an inhibiting effect upon the rate of the NO/char reaction. The results of adding up to 6000 ppm of oxygen are shown in Figure 5. Oxygen concentrations were measured by injection into a Hewlett-Packard 5830 gas chromatograph (molecular sieve column). Because of the long transit-time through the gas sampling lines and because of the length of time required to purge the gas sampling loop, repeated injections were made into the gas chromatograph until the measured oxygen concentrations converged. Unfortunately, because the process took 15-30 minutes, oxygen exiting the furnace during the char feed could not be measured. However, analysis of the effluent CO and CO_2 data suggests that the oxygen fed was depleted, permitting the possibility of subsequent reaction, in an oxygen-free environment with NO.

The inhibitory results of analogous experiments, in which up to 13% water vapor was included in the main gas stream, are shown in Figure 6. Water was added by flowing a metered steam of helium through a thermostated bubbler connected to the furnace through heated gas-transfer lines. Flow rates were corrected accordingly. No direct measurement of water in the furnace exhaust stream was, however, available.

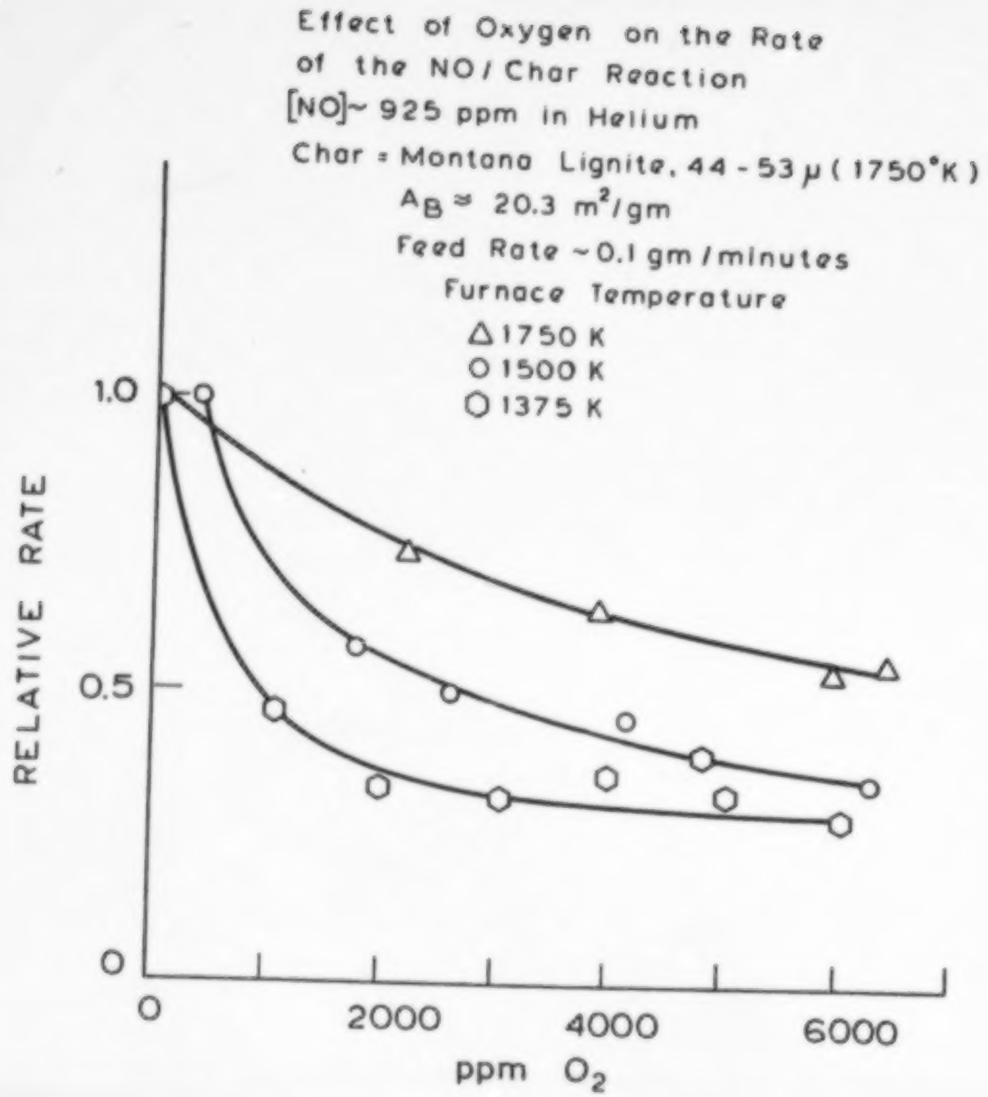

Figure 5. Inhibition of NO/CO Reaction by Oxygen. Rate of NO/Char with O_2 Present Normalized with that for the O_2-Free NO/Char Rate.

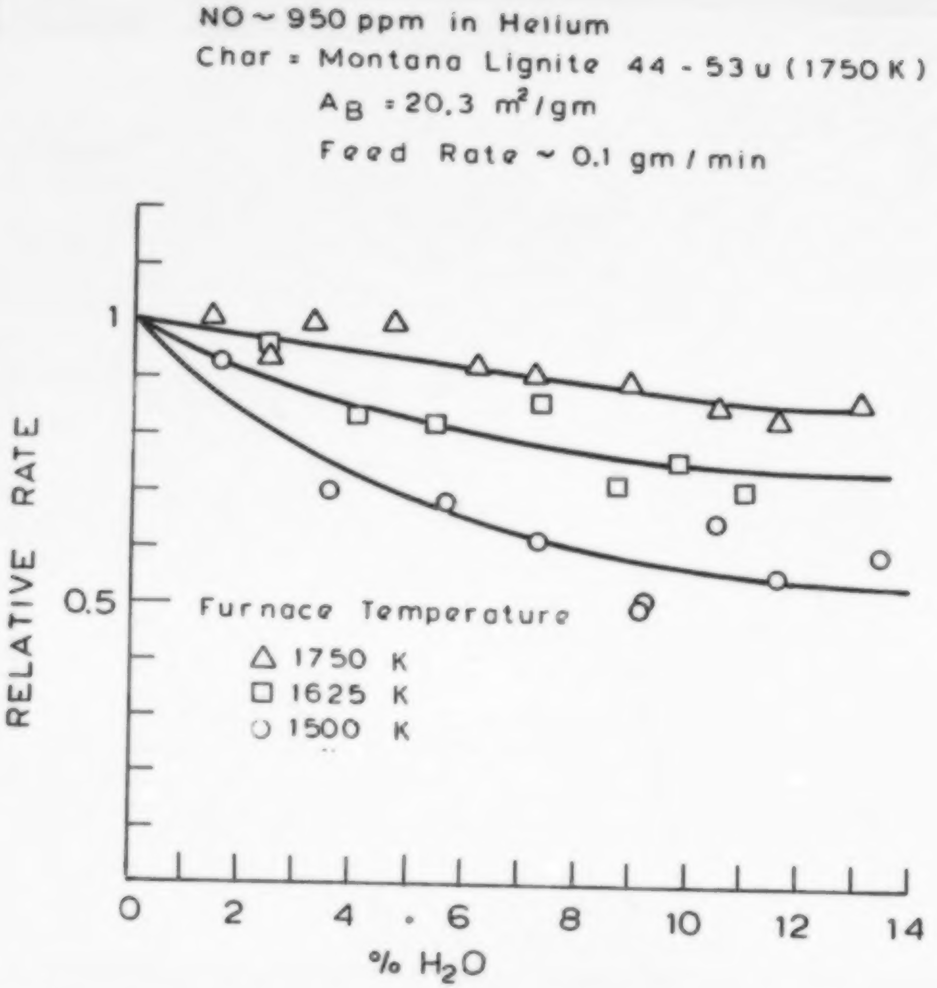

Figure 6. Effect of Water Vapor on the Rate of NO/Char Reaction.

SECTION III

MEASUREMENT OF TEMPERATURES AND BURNING TIMES OF COAL PARTICLES

Experimental Method

A two-color optical pyrometer has been developed for measuring the temperatures and burning times of individual coal particles (3). A dilute stream of coal particles was produced by feeding coal at a controlled rate by elutriation from a syringe-pump driven vial into a hyperdermic needle; the resulting coal stream was discharged as a jet into a secondary chamber. The desired additional dilution was produced by adjusting the position of the withdrawal tube in the fountain of coal particles (Figure 7). The dilute stream of coal particles is fed along the axis of a laminar furnace (Figure 8). The emission from the burning particles is focused onto an optical fiber (located at the top of the furnace which allows continuous measurement of light signal). The optical fiber splits the radiation and feeds it through two narrow band pass filters with band centers at 450 and 550 nanometers (Figure 9). The intensity of the burning particle at the two wavelengths is then measured using photomultiplier tubes (Model EMI 9824B).

The photomultipler output at a specified wave-length can be related to the temperature of a radiating surface using Wien's law:

$$S_A = C_A \varepsilon_A \lambda_A^{-5} \exp\left[\frac{-C_2}{\lambda_A T}\right] (r/R)^2$$

where: C_A is a constant that depends on the efficiencies of the optical system.

λ_A is the wave length in nanometers.

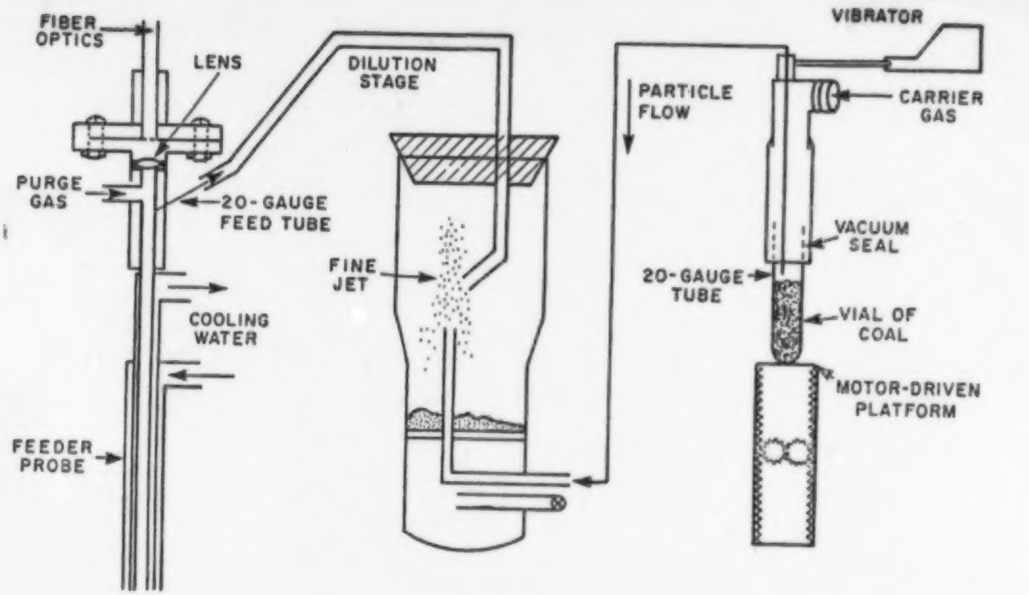

Figure 7. Two-Stage Single Particle Feed System.

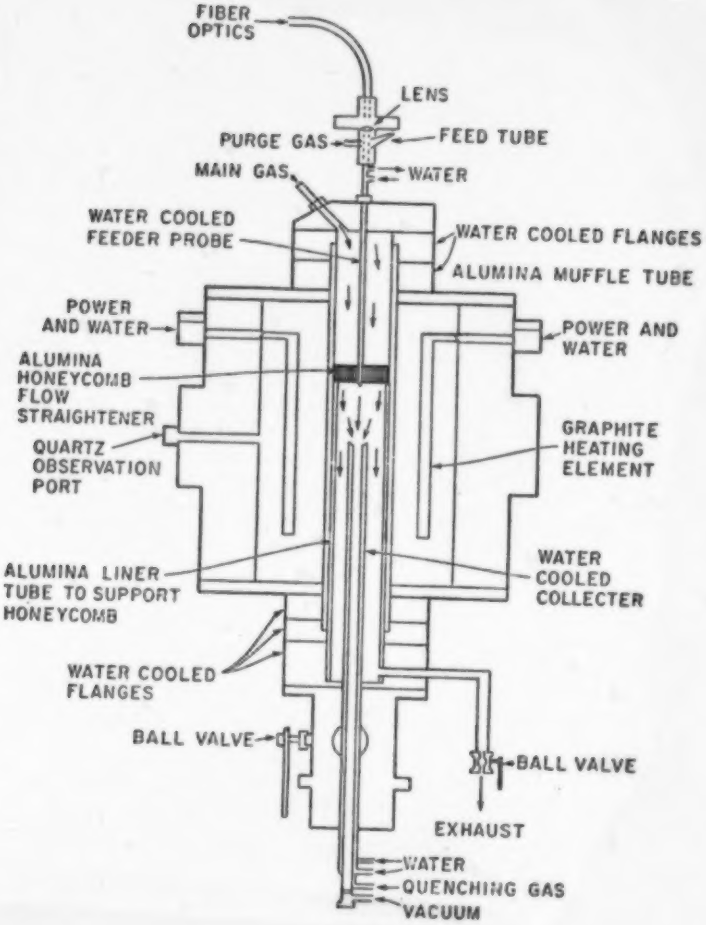

Figure 8. Laminar Flow Furnace.

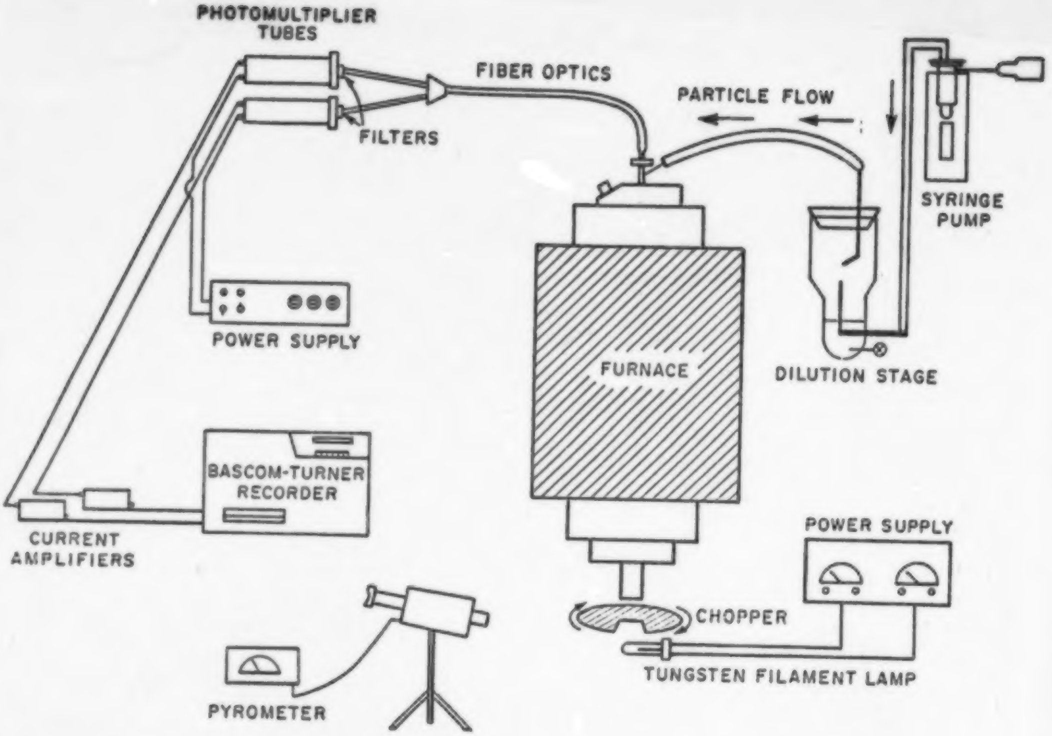

Figure 9. Operating System Schematic.

C_2 is Plank's second constant 1.44×10^7nm °K.

ε_A is the emissivity of the surface at λ_A.

T is the temperature of the radiating surface.

r is the particle radius.

R is the distance of separation of the particle and the optical receiver.

Emissivities of burning coal particles are not well known, but by assuming that the particles are gray bodies the intensities at two wave lengths can be ratioed:

$$\frac{S_A}{S_B} = \frac{C_A}{C_B} \frac{\lambda_A^{-5}}{\lambda_B^{-5}} \exp \frac{-C_2}{T} \left(\frac{1}{\lambda_A} - \frac{1}{\lambda_B} \right)$$

or

$$T = \frac{-C_2 \left(\frac{1}{\lambda_A} - \frac{1}{\lambda_B}\right)}{\left\{ \ell n \frac{S_A \; C_B \lambda_A^5}{S_B \; C_A \lambda_B^5} \right\}}$$

The signals from the photomultiplier tubes were measured with a Bascom-Turner model 8110 digital recorder that can sample simultaneously on two channels. Reference calibration signals were produced by a chopped signal from a tungsten strip lamp viewed through the furnace. The system is still under development, but some of the system's potential can be seen from the preliminary results presented in the following sections.

Representative Intensity Traces

The outputs of the photomultipliers for six lignite particles burned in 100% oxygen at 1750 K are shown in Figure 10. Each trace shows a steep rise following ignition, followed by a slower decay. The ratio

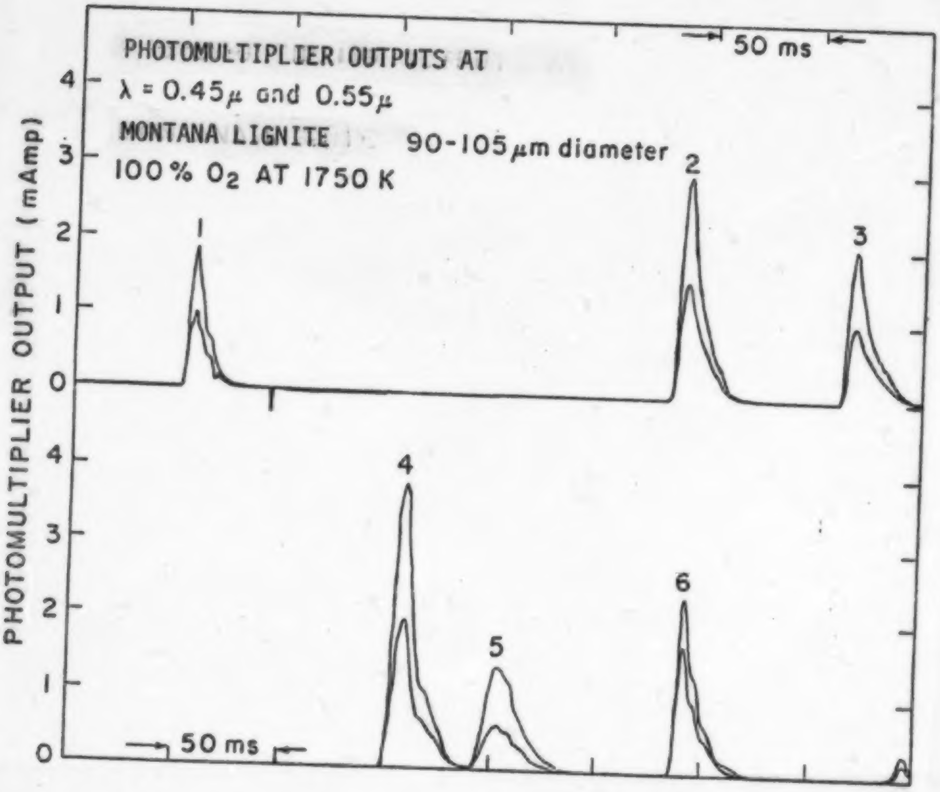

Figure 10. Outputs of the Photomultipliers for Six Lignite Particles Burned in 100% Oxygen at 1750 K.

of the two intensities provides a measure of particle temperature; examination of the signal ratios shows that particles 1 to 4 have approximately the same temperature at peak intensity, particle 5 has a higher temperature and particle 6 a lower temperature. Particle 5 shows a lower absolute intensity even though it burns hotter. This suggests that it was ignited at a larger distance R from the optical detector. The differences observed in peak temperature, burning time and ignition delay between particles are not surprising since the composition of individual coal particles varies widely; density fractionation of the 90-105 μm sized coals shows that the majority of particles (approximately 70% by weight) had a density of 1.4 to 1.5, but small amounts (approximately 3%) had densities less than 1.3 and greater than 1.85. Future trials on density-graded coals will determine the extent to which the variation in particle combustion characteristics is related to particle density (an indirect measure of ash content).

Particle Temperature

Figure 11 shows the photomultiplier outputs for the two wavelengths and the temperature inferred from them. The temperature-time relation will be used to critically test the models used to calculate the NO/char reduction. As expected, the particle temperature increases systematically with increasing oxygen partial pressure. The temperatures for the Illinois #6 bituminous coal tested were on the order of 200 K greater than for Montana lignited burned under similar conditions.

Effect of Volatile Flames

Figure 12 shows a comparison of intensity traces for an Illinois #6 bituminous coal burned in 20 and 100% oxygen at 1750 K. The intensity traces at 100% O_2 show a single peak, whereas, that at 20% O_2 shows a double peak, suggestive of a volatile and char combustion. This

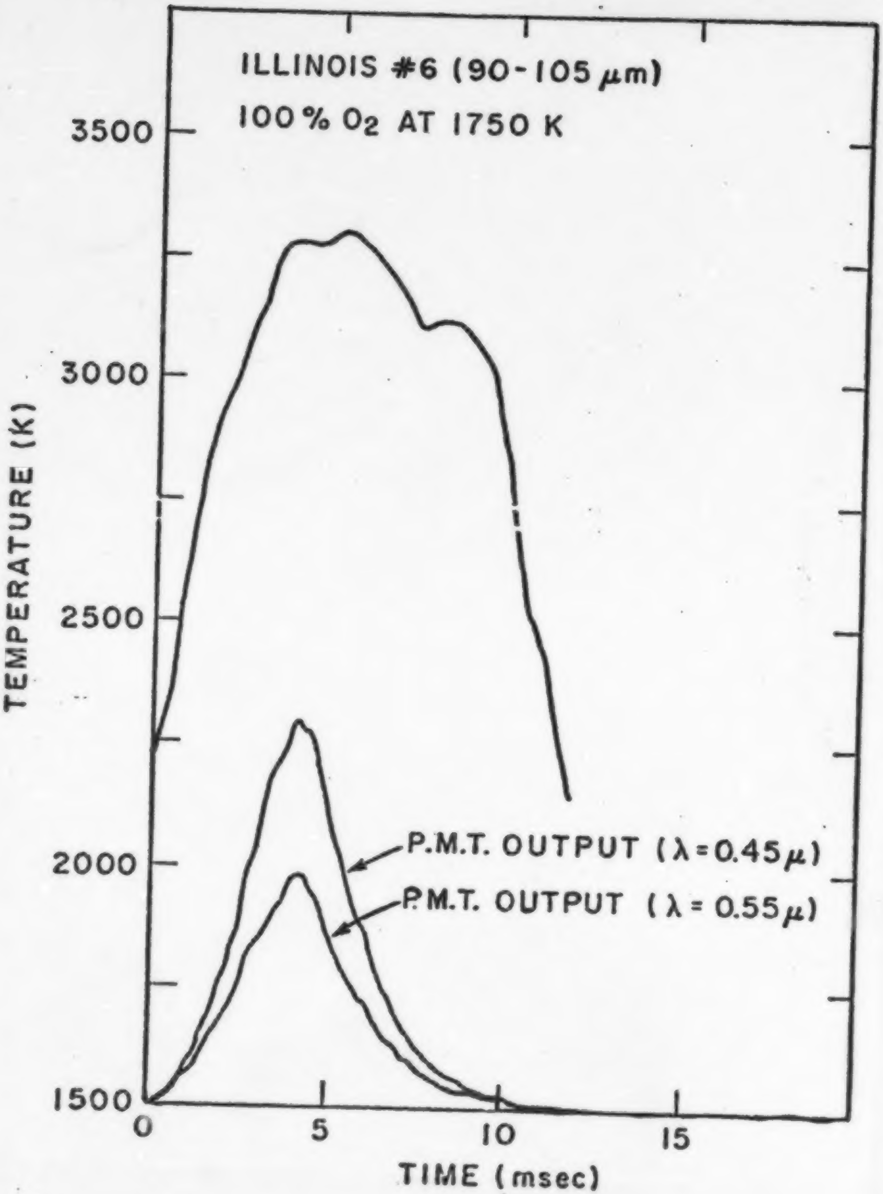

Figure 11. Photomultiplier Outputs for the Two Wave-Lengths and the Temperature Inferred From Them.

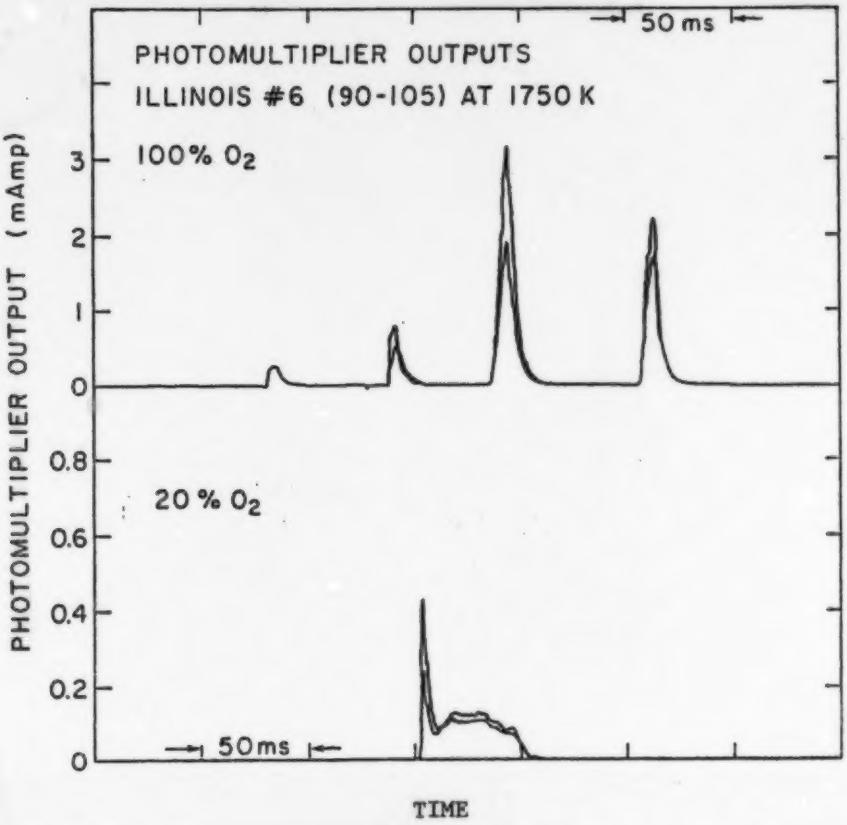

Figure 12. Comparison of Intensity Traces for an Illinois #6 Bituminous Coal.

has implications to NO_x emissions as will be discussed in greater detail in the presentation in this workshop on fuel nitrogen evolution. For some particles the peak corresponding to the volatile release was separated from that of the combustion of the char (Figure 13). Corroborating evidence for such behavior is provided by the holographic studies described elsewhere in this workshop.

Burning Times

The burning times for the Montana lignite and Illinois #6 burned in oxygen-argon mixtures at 1750 K are reported as a function of oxygen concentration in Figure 14. The error bars provide the 95% confidence limits on the burning times. The approximately two-fold difference in burning times of the lignite and bituminous coal studied will provide a critical test of the validity of the model under development.

Particle Radius

The absolute intensity, normalized by the blackbody intensity at the measured temperature, is proportional to $r^2\varepsilon/R^2$, the product of the particle area and emissivity divided by the square of the distance of separation from the detector. At high oxygen partial pressures, the burning times are short and the distance from the detector R changes imperceptibly during particle burnout. The relative particle area inferred for such a case, assuming ε to be constant, is shown in Figure 15. The decrease in particle area during the latter stages of combustion is consistent with a shrinking sphere model of combustion. The apparent increase in particle area at early times is anomalous and may be a consequence of a low emissivity volatile flame; further development is needed to resolve these areas of uncertainty.

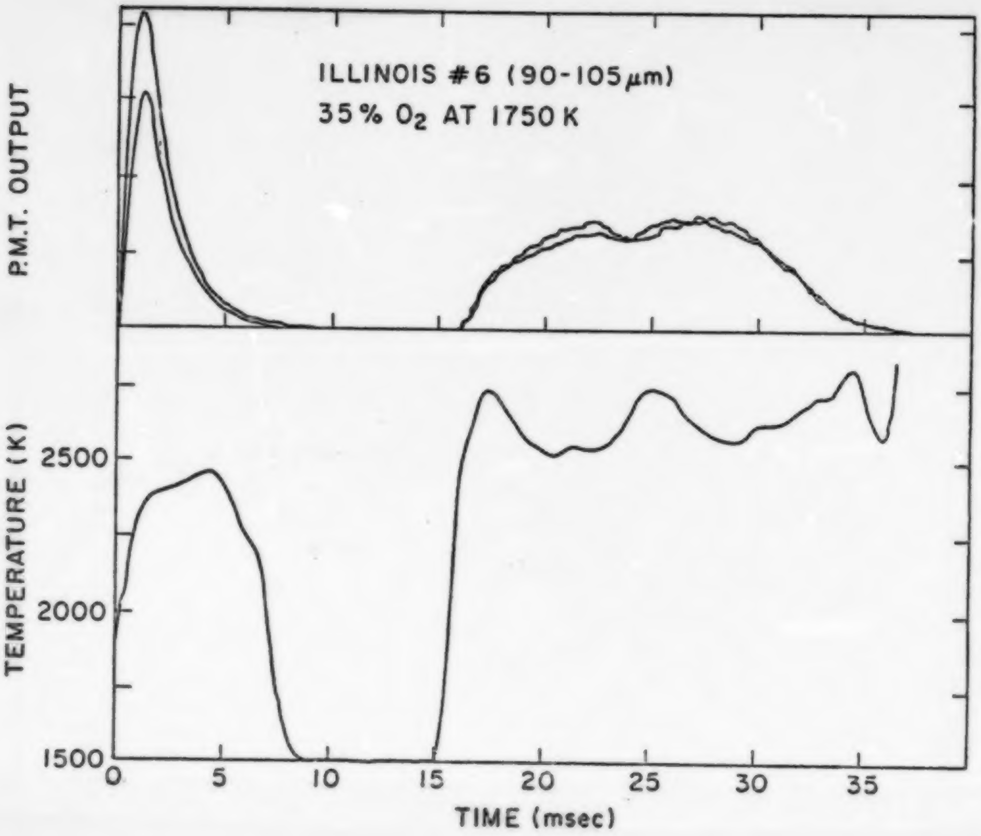

Figure 13. Temperature and Intensity as a Function of Time for an Illinois #6 Bituminous Coal.

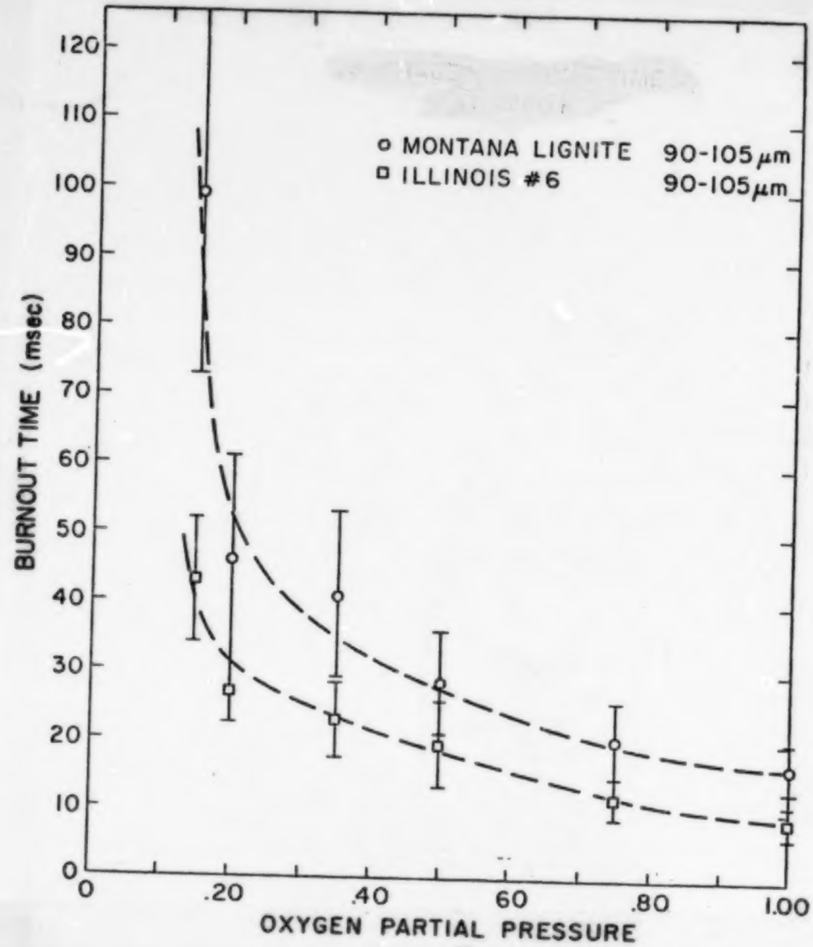

Figure 14. Average Burnout Times at 1750K.

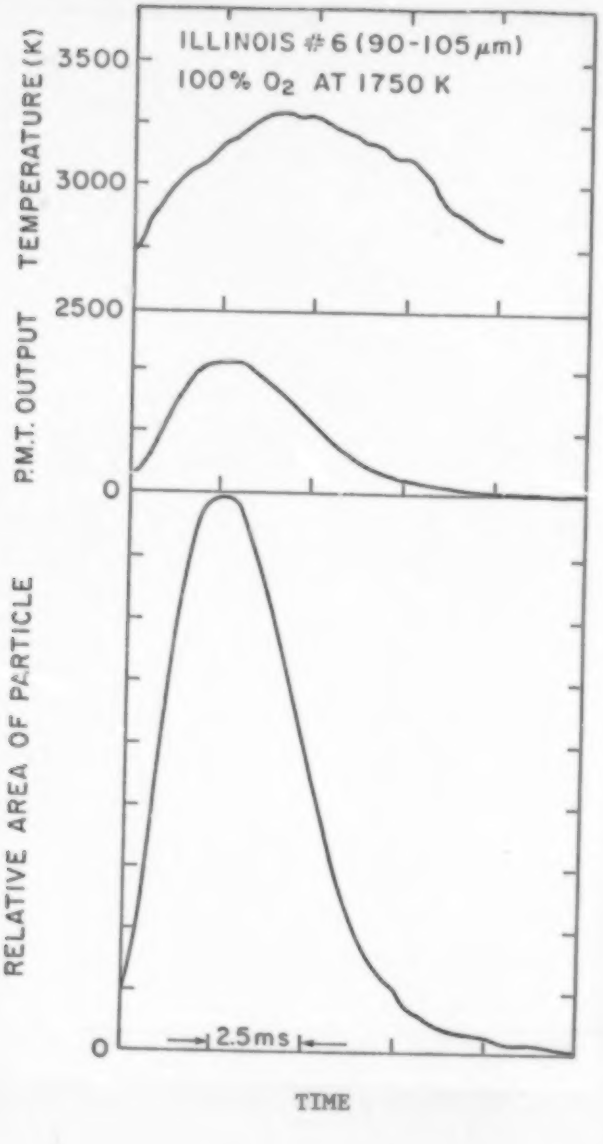
ILLINOIS #6 (90-105 μm)
100% O2 AT 1750 K
TEMPERATURE (K)
3500
3000
2500
P.M.T. OUTPUT
0
RELATIVE AREA OF PARTICLE
0
2.5ms
TIME

Figure 15.

SECTION IV

CONCLUDING COMMENTS

This paper presents preliminary data on the NO/Char reactions, and on the burning temperatures and times of coal particles for conditions encompassing the range of interest in pulverized coal flames. This information will be used to guide the development of a model which will permit the evaluation of the impact of combustion process modification on the reduction of NO by char in coal-fired combustors.

REFERENCES

1. Levy, J. M., Pohl, J. H., Sarofim, A. F. and Song, Y. H., "Combustion Research on the Fate of Fuel-Nitrogen Under Conditions of Pulverized Coal Combustion" EPA Report, EPA-600/7-78-165 (1978).

2. Mims, C. A., Dictor, R. and Sarofim, A. F., "Combustion of Pulverized Coal Under Controlled Conditions: Single Particle Time-Temperature Histories", to be submitted to Combustion Science and Technology, 1980.

3. Song, Y. H., "Fate of Fuel Nitrogen During Pulverized Coal Combustion", Sc. D. Thesis, M.I.T., Department of Chemical Engineering (1978).

MECHANISMS OF NITRIC OXIDE REDUCTION ON SOLID PARTICLES

Gérard G. de Soete
Institut Francais Du Petrole
Laboratory of Fundamental Aerothermics
Rueil-Malmaison, France

Fifth EPA Fundamental Combustion Research Workshop
Newport Beach, California
January 23-25, 1980

SECTION I

INTRODUCTION

During the last fifteen years substantial effort has been devoted to the study of catalytic reduction of nitric oxide in the external treatment of exhaust gases issuing from internal combustion engines as well as stationary combustion sources(1 to 13). However, only in the last few years has attention been explicitly focused on the role played by flame-born solid particles (e.g., soots, coal and char particles, fly ash) in the process of in situ (i.e., in the flame or in the hot combustion products) heterogeneous reduction of nitric oxides. With respect to this particular field, three main problems have to be solved:

1. Elucidate the kinetic mechanisms of this heterogeneous NO reduction under typical flame and flue gas conditions. Special attention should be paid to the nature of the reaction products of this reduction. From a pollution point of view, it is not sufficient to observe that nitric oxide has disappeared from the combustion products; generally it is required that NO has been definitely transformed into molecular nitrogen. Whenever other intermediate nitrogen-containing species are formed during NO reduction, it will be important to identify them and to carefully check the conditions of their further transformation into N_2.
2. Determine the reaction rates which control the disappearance of NO, the formation of eventual intermediate nitrogen-containing species, and finally, the transformation rates of NO and of the intermediate species into molecular nitrogen. The effect of typical combustion products (e.g., H_2, CO, O_2, H_2O...) on these reaction rates should also be examined.
3. Check the relative importance of these heterogeneous reduction paths, comparing them with homogeneous NO reducing reactions under real conditions of evolving biphasic solids/gas components in industrial flames.

The scope of the present contract work is to provide general information on the first two problems mentioned above, obtained from parametrical trials performed on packed bed reactors. The study has been restricted deliberately to a general investigation of the heterogeneous NO reducing mechanisms; no attempt has been made to elucidate the fine mechanisms of these phenomena: owing to their complexity, many years of experimental study would be required for their understanding in terms of activated surface complexes and elementary steps.

Before describing the experimental method and discussing the results, it may be useful and worthwhile to briefly describe the general features of heterogeneous NO reduction, since they will assess the choice and sequence of the experimental trials.

SECTION II

GENERAL FEATURES OF HETEROGENEOUS NO REDUCTION

The gas phase reduction of nitric oxide by gaseous reducing agents (hydrogen, carbon monoxide,...) is, even at flame temperatures, a rather slow process in the absence of hydrocarbon radicals(14). Therefore, it is mostly limited to the near flame front zone where these radicals are present in nonnegligible concentrations.

In many cases the presence of solid particles in the oxidation zone of a flame, as well as in the combustion products, gives rise to the existence of heterogeneous nitric oxide reduction on the gas/solid interface; since these heterogeneous reductions are generally faster than the gas phase reduction and their activation temperatures relatively low, one should take them into account (at least a priori) when dealing with the history of NO molecules in industrial flames, as soon as the concentration of the dispersed solid phase becomes important.

These heterogeneous NO reducing reactions may belong to two different types:

a. Either true catalytic reactions in which the solid merely catalyzes phase contact reactions, but does not participate in them as a reactant.

b. Or, reactions between solid and gas in which the solid is progressively consumed as a reactant for NO reduction. These solid-plus-gas reactions may eventually also bear a catalytic character. In this second type of heterogeneous reaction, the solid must contain some reducing functions, such as bound hydrogen or bound carbon atoms.

In both cases the reaction takes place, at least partly, at the gas/solid interface and may severely depend on the adsorption/desorption rates and equilibria of one or more of the gaseous reactants and/or products. This point is of paramount importance: the quantitative information on the different reaction rates obtained from the present study are derived under experimental conditions for which the adsorption/desorption rates are (almost) equilibrated. Owing to the rather short residence times encountered in industrial flames, these equilibria are seldom reached. Therefore, the consequences of nonequilibrium with respect to reaction rates of heterogeneous NO reduction should be carefully checked whenever one intends to model the in situ behavior of dispersed flame-born particles.

As will become clear from this study, the overall reaction paths of heterogeneous NO reduction may be divided into two groups:

a. Direct reduction reactions in which molecular nitrogen is the only direct product.

b. Indirect reduction reactions in which the reduction of NO into N_2 passes over other intermediate nitrogen-containing gaseous species, especially ammonia and hydrocyanic acid. The intermediate formation of ammonia requires the presence of a hydrogen source, whereas the intermediate formation of hydrocyanic acid requires the existence of both a hydrogen and a carbon source. Gaseous molecules (e.g., H_2, CO) as well as solid bound hydrogen and carbon atoms (-H, -C) may act as a hydrogen, respectively carbon source for the formation of NH_3 and HCN.

   It should be further emphasized that solid bound nitrogen atoms (e.g., as present in cenospherical soot and coal) may also give rise to NH_3 and HCN formation as soon as an appropriate hydrogen or carbon source is present.

From the foregoing it follows that the mechanism of heterogeneous NO reduction, even when limited to its overall reaction paths, strongly depends on (a) the chemical nature of the solid phase, and (b) the composition of the gas phase (especially the presence of reducing and oxidizing components). Therefore, in order to properly identify the different reaction paths involved and to determine their relative rates, an experimental procedure has been chosen in which a sequence of trial series are performed corresponding to different cases of progressively increasing complexity, as well as with respect to the composition of the gas phase, with respect to the chemical nature of the solid particles:

a. Increasing complexity of the solid matter: From this point of view it is convenient to distinguish between:

   1. solids having only bound nitrogen atoms in their lattic (e.g., refractory oxides like alumina, quartz, etc.). In this case, nitrogen intermediates NH_3 and HCN can only appear if a hydrogen or carbon source is supplied in the gas phase (H_2, CO, ...)
   2. particles having exclusively bound carbon atoms (-C) (e.g., graphite), which introduces a solid bound carbon source into the mechanism
   3. particles having both solid bound hydrogen and carbon atoms (-H, -C) (e.g., soot obtained by thermal cracking of pure hydrocarbons in the absence of oxygen)

      particles having solid bound (or adsorbed?) oxygen atoms (-O) besides solid bound hydrogen and carbon atoms (e.g., gas phase generated soot during the combustion of fuel-rich, pure hydrocarbon/oxygen mixtures)

   5. finally, particles having not only bound nitrogen, carbon or oxygen atoms, but also bound nitrogen (-N) and sulfur (-S) atoms, besides typical catalytic metals (vanadium, nickel) (e.g., coal and char particles; liquid phase generated cenospherical soot from heavy fuels oils).

b. Increasing complexity of the gas phase composition: The trials on each type of solid particles are arranged in such a way that the gaseous components which may play a role in the heterogeneous NO reduction are successively studied apart and in combination with each other. Since nitrogen-containing intermediates may be formed, it is convenient to distinguish between "primary" and "secondary" reactions.

1. By primary reactions we understand these reactions, the reactants of which are already present in the reactor inlet flow;

2. Secondary reactions are reactions for which at least one of the reactants was not present in the reactor inlet flow, but has been formed as a product of a primary (or other secondary) reaction.

   The determination of the overall rate of a secondary reaction regularly requires the performing of supplementary trials in which intermediate products of primary (or secondary) reactions (e.g., ammonia or hydrocynanic acid) are added into the reactor inlet flow, i.e., by converting these initially secondary reactions into primary ones.

SECTION III

DESCRIPTION OF THE EXPERIMENTAL METHOD

Apparatus

A schematical view of the experimental apparatus is given in Figure 1. The packed bed reactor (A) is made of quartz. The central bulb of it has an inner diameter of 23 mm. The packed bed of solid particles has a height ranging from 10 to 24 mm (corresponding respectively to a volume of 4.2 to 10 cm^3). The particles are supported by a sintered quartz plate located at the bottom of the reactor bulb. The reactor is placed at the inside of an electrically heated, regulated furnace (B); a shielded Alumel/Chromel thermocouple (C) is utilized for monitoring the temperature in the packed bed. This temperature could be increased to 1000°C. Different feed lines (D) are available for the mixing of the gas components; each feed line has its own flow metering system, sonical orifices of very small diameter being utilized for the measurement of the individual flow rates. The different minor components are admixed in argon as a carrier gas. Every minor component is previously mixed with the argon carrier in a high pressure cylinder on a separate mixing device prior to being fed through one of the feed lines. The total flow rate through the reactor is comprised of between 10 and 15 $Ncm^3 s^{-1}$, which, owing to the volumes of the packed bed, results in a volume/volume·second value comprised between 1 and 3.6 s^{-1}. The lower listed flow rate is a limit imposed by the analyzers. In preliminary trials it has been checked that for the given total flow rates, diffusion control is negligible. On the gas mixture manifold (E) a drying column (F) is placed in bypass, on which in some cases the gas mixture can be dried on either calcium chloride, phosphor pentoxide or water-free magnesium perchlorate. Another bypass (G) allows the analysis of the gas composition at the reactor inlet. The inlet composition will be designated by the subscript "i", $(Y)_i$ and $(X_Y)_i$ being the concentration by $(Y)_i$ (in ppm or in volume percent) and the mole fraction by it of the component Y. The pressure within the reactor is adjusted by means of a needle valve (H) and manometer (I); a constant pressure, slightly higher

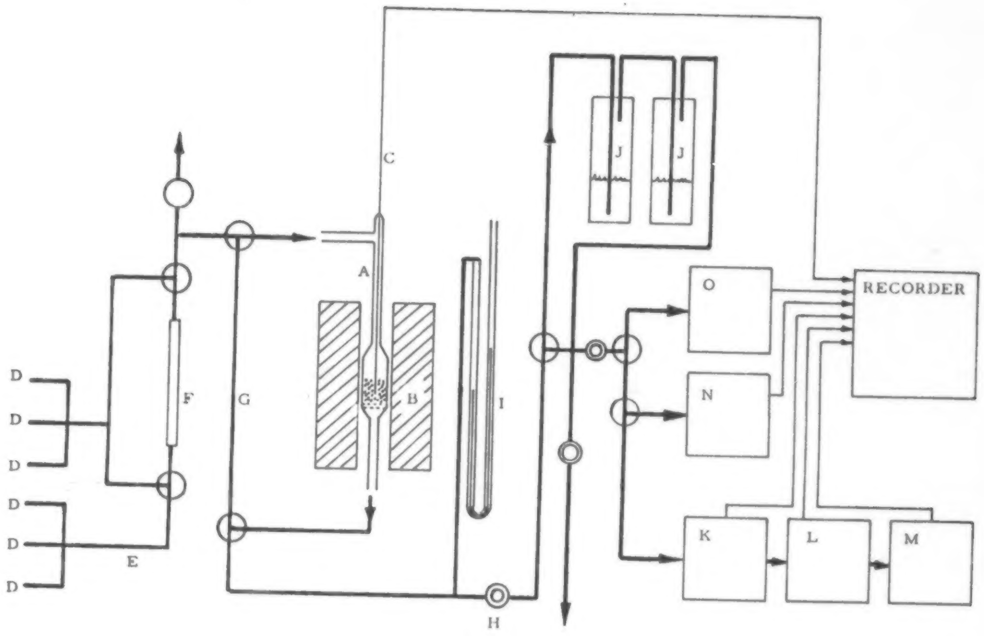

Figure 1. Schematical View of the Experimental Apparatus

than the reactor pressure drop, has been selected for all runs (30 cm Hg). The reactor outlet flow can be entered either into a scrubber unit (J) for HCN and NH_3 absorption, or into the on-line analyzers: NDIR analyzers for carbon oxide (K) and carbon dioxide (L), paramagnetic oxygen analyzer (M), chemiluminescent NO/NO_2 analyzer (N) and a chromatograph (O) intended especially for N_2 analysis. The scrubbers contain a defined amount 0.1 N aqueous KOH solution in which HCN and NH_3 are trapped as CN^- ions, respectively NH_3 gaseous solution. An electrochemical method utilizing specific CN^- and NH_3 electrodes is used for determination of hydrocyanic acid and ammonia in the reactor inlet or outlet flow. A multichannel recorder stores the information coming from the analyzers and from the thermocouple.

High purity gases have been utilized for the gas mixtures. The following four types of solid particles have been utilized systematically throughout the trials described in this paper. As may be seen from their chemical characteristics, they are representative of the different families of particles mentioned in the introduction:

1. Alumina

   Pure Al_2O_3
   Mean particle diameter: 60 to 150 microns
   Specific surface area (B.T.E. method): 150 to 170 m^2g^{-1}
   Apparent density: 1.0 $\pm$ 0.10 g cm^{-3}

2. Graphite

   Graphite carbon of 99.999 percent purity
   Impurities: Al (0.5 ppm); B (<0.01 ppm); Ca (<0.2 ppm);
   Cu (0.5 ppm); Fe (0.8 ppm); Mg (0.2 ppm);
   Si (0.4 ppm); Na (0.2 ppm); Ti (<0.1 ppm);
   V (<0.2 ppm)
   Mean particle size: 25 microns
   Specific surface area: 2 m^2g^{-1}
   Apparent density: 0.37 g cm^{-3}

3. Gas Phase Generated Soot

Obtained from fuel-rich (E.R.=2.8) $C_2H_4/O_2/Ar$ premixed flames.

As collected (early in the flame) this soot contains adsorbed polyaromatic hydrocarbons. Therefore, this soot was treated at 600/700°F under argon flow prior to being utilized in the reactor; during this thermal treatment most of the adsorbed "volatiles" are eliminated.

Characteristics after treatment:

Mean particle size: spherical particles of about 300 Å, loosely granulated to particles of 250 to 500 microns.

Specific surface area: 146 m^2g^{-1}

Apparent density: 0.032 to 0.036 g cm^{-3}

H/C (atomic ratio) = 0.29

Small quantities of absorbed or bound oxygen also present.

4. Industrial Cenospherical Soot from Heavy Fuel Oil

Origin: Thermal power plant of Porcheville (France); sampled in the cyclones

Composition (mass %): C (78.2); H (0.4); N (0.8); S (3.5); V (1.2); Ni (0.68); Na (0.6); Ca (0.33); Fe (1.2); also not specified quantities of oxygen, mostly as metal oxides

Mean particle size: 50 microns

Specific surface area: 2.5 m^2g^{-1}

Apparent density: 1.38 g cm^{-3}

Experimental Method

Measurements

For each given point of a given run a complete analysis of the species NO, NO_2, HCN, NH_3, CO, CO_2 and O_2 is made. The concentration of molecular nitrogen has been measured chromatographically only in more recent runs and under conditions where it exceeded 200 ppm. The precision of those analyses of N_2 is rather poor, but shows an acceptable agreement with concentrations calculated according to the nitrogen balance:

$$(N_2)_f = 0.5 \left[(NO)_i + (NH_3)_i + (HCN)_i - (NO)_f - (NO_2)_f - (NH_3)_f - (HCN)_f\right] \tag{1}$$

the subscripts "i" and "f" indicating the reactor inlet and the reactor outlet concentrations, respectively. NO_2 has never been found in measurable concentrations due to the fact that over the whole temperature range studied, the NO/NO_2 equilibrium is completely shifted towards NO.

Principally a new solid charge is used for each trial. In the rare cases where the charge from a foregoing trial has been utilized, it was previously treated at 1000°C under argon flow during at least one hour in order to desorb all active molecules.

For runs in which the solid charge is progressively consumed (e.g., runs with oxygen present in the gas phase, on soots), the decrease in solid mass is taken into account for the determination of the rates. The decrease ΔM of mass of the solid was calculated by the expression:

$$\Delta M = \left[(CO)_f + (CO_2)_f\right] (M_C + q\, M_H) \frac{D}{v_M} \Delta t \tag{2}$$

where M_C and M_H are the atomic mass of carbon and hydrogen, respectively; q is the atomic ratio H/C characteristic of the soot, and Δt is a time interval during which the concentrations $(CO)_f$ and $(CO_2)_f$ are remaining constant; v_M is the molar volume at standard conditions; D is the total flow rate at standard conditions.

Determination of Overall Reaction Rates

Owing to the large number of reaction rates we have to deal with, simple rate expressions have been utilized rather than expressions bearing reference to a Lanmuir or Freundlich adsorption isotherm. According to Levenspiel(15), in most cases simple rate expressions may be as suitable for practical purposes under well-defined conditions. Several times a comparison has been made between simple rate expressions obtained either by an integral or by a differential treatment of the reactor. Provided the calculations are limited to small reaction advancements, both treatments yield very comparable results. Therefore, in this paper simple rate expresions of the following general form obtained by a differential reactor treatment will be used throughout:

$$V = d(Y)/dt = \left[(X_Y)_f - (X_Y)_i\right]D/M = k_o \exp(-\theta/T)\, X_n^a\, X_m^b \qquad (3)$$

where θ is a mean activation temperature; X_n and X_m are the mole fractions of the gaseous reactants averaged over the reactor:

$$X_{n,m} = \left[(X_{n,m})_i + (X_{n,m})_f\right]/2 \qquad (4)$$

a and b are partial reaction orders with respect to species n and m; M is the instantaneous value of the solid mass. Reaction rates determined in that way have dimensions of volume·mass^{-1}·time^{-1}, and are expressed in units of $cm^3g^{-1}s^{-1}$ throughout the paper.

Identification of overall reaction paths is made from the mass balance of reactants and reaction products obtained in an experimental manner from the analysis. The heterogeneous character of these reaction paths is checked by comparison with runs performed on the empty reactor. However, it should be kept in mind that heterogeneous reactions on the hot reactor walls may also occur (see Figures 2 and 3). Owing to the relatively high concentrations of the packed solid charge, the heterogeneous reactions occurring at the reactor walls generally do not interfere with those taking place on the packed solid particles.

The determination of the rate constants (k_o, θ, a, b) of the primary reactions is performed in the classical way. In a first step the partial

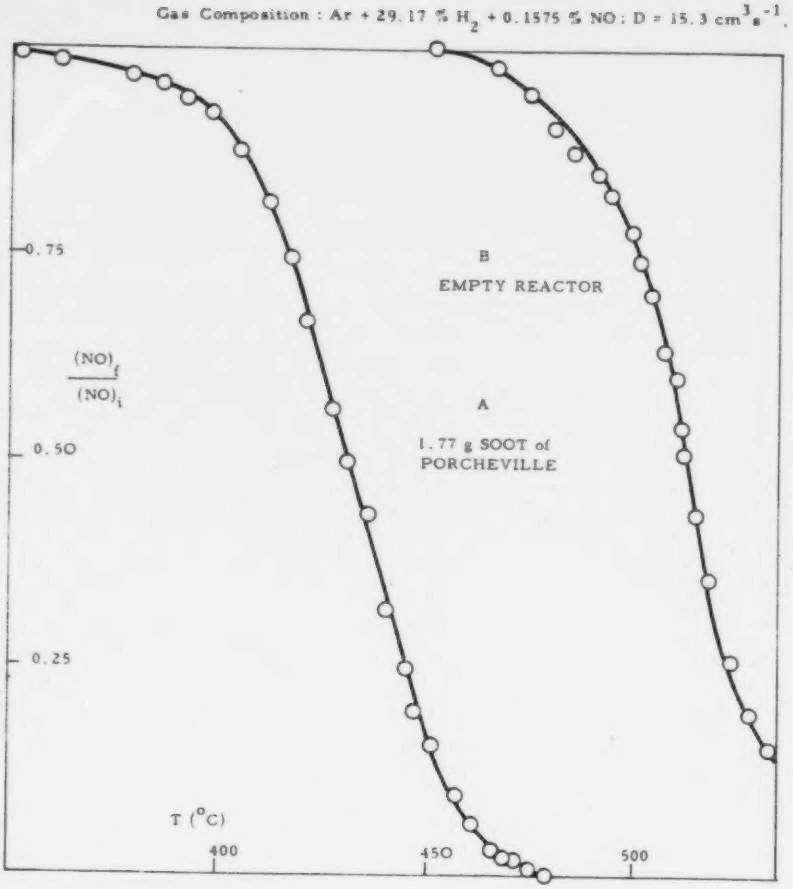

Figure 2. Effect of Empty Reactor on NO Reduction in the Presence of Hydrogen

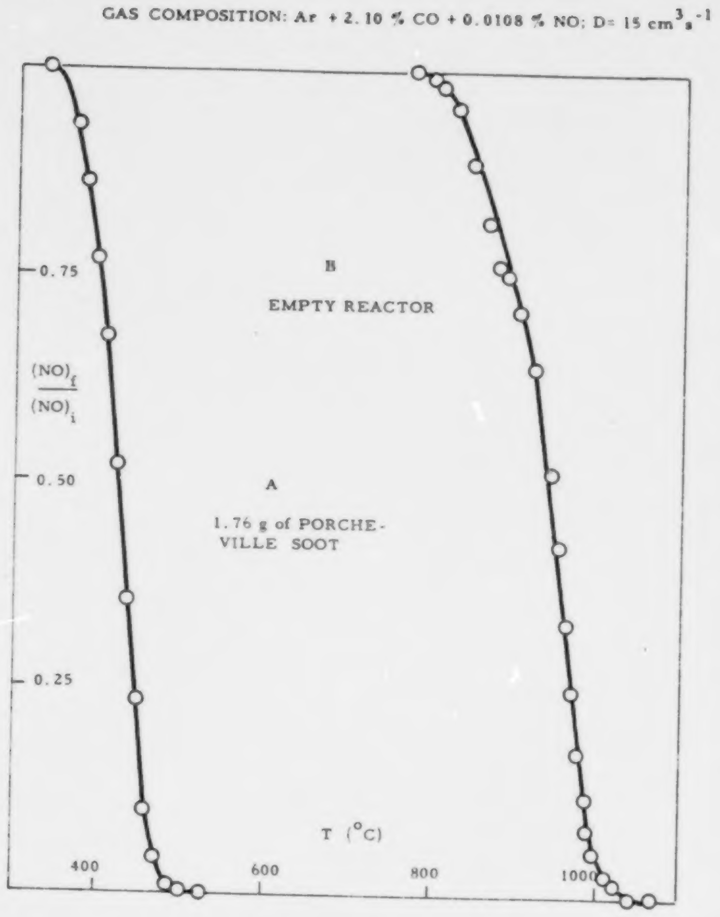

Figure 3. Effect of Empty Reactor on NO Reduction in the Presence of Carbon Monoxide

orders are determined from a series of runs in which all parameters, except the concentration of the species for which the partial order is to be determined, are kept constant. In a second step the constants k_o and θ are from runs where only the temperature is stepwise increased.

The determination of the rate constants of secondary reactions is made in the same way, under experimental conditions where these reactions actually are transformed into primary reactions, upon blending the intermediate products (ammonia, hydrocyanic acid) directly into the reactor inlet flow, as explained previously.

Three types of overall reactions may be considered:

1. Overall NO removal reactions ($\overline{V}$):

$$\overline{V} = \left[(X_{NO})_f - (X_{NO})_i\right]D/M \qquad (5)$$

   which are expressed as a function of the concentrations of effective reactants present in the reactor inlet flow.

   In all cases the symbol $\overline{V}$ will be characterized by a double subscript: a capital letter, referring to the gas composition utilized, followed by a number, referring to the family of solid particle. These subscripts refer to a given row (capital letter) and a given column (number) in Table 1, added at the end of the paper and summarizing the different gas/solid combinations studied.

   Attention is focussed once again on the fact that these overall NO removal rates, although interesting to characterize a given particle behavior in combination with a given gas phase composition, is not a good criterium from the point of view of pollution control (see Introduction).

2. Overall N_2 formation reaction ($\overline{V}_n$):

   The overall N_2 formation rate is an excellent antipollution criterium. Therefore, its knowledge is of practical interest for the characterization of a given solid particle with respect to heterogeneous NO reduction. The rate of it can be described as follows.

Table 1. Overall Heterogeneous Reactions as a Function of Gas Composition and Nature of Solid Particles

ROW	GAS COMPOSITION (one component)	SOLID-BOUND ATOMS					
		COLUMN 1: -O		COLUMN 2 : -C		COLUMN 3 : -C, -H	
		OVERALL REACTIONS	PRODUCTS	OVERALL REACTIONS	PRODUCTS	OVERALL REACTIONS	PRODUCTS
A	Thermal decomposition of solid						
B	CO	$CO + (-O) \xrightarrow{12} CO_2$					
C	H_2	$H_2 + (-O) \xrightarrow{19} H_2O$					
D	NH_3	$NH_3 \xrightarrow{13} 0.5\ N_2 + 1.5\ H_2$	H_2	$NH_3 \xrightarrow{13} 0.5\ N_2 + 1.5\ H_2$ $NH_3 + (-C) \xrightarrow{5} HCN + H_2$	H_2 HCN	$NH_3 \xrightarrow{13} 0.5\ N_2 + 1.5\ H_2$ $NH_3 + (-C) \xrightarrow{5} HCN + H_2$	H_2 HCN
E	O_2			$O_2 + (-C) \xrightarrow{24} CO,\ CO_2$	CO	$O_2 + (-C) \xrightarrow{24} CO,\ CO_2$ $O_2 + (-H) \xrightarrow{23} H_2O$	CO
F	NO			$NO + a\ (-C) \xrightarrow{1} 0.5\ N_2 + (2a - 1)\ CO + (1 - a)\ CO_2$	CO	$NO + a\ (-C) \xrightarrow{1} 0.5\ N_2 + (2a - 1)\ CO + (1 - a)\ CO_2$ $NO + a\ (-C) + b\ (-H) \xrightarrow{2} NH_3 + \frac{b-3}{2}\ H_2O + (\frac{b-5}{2} + 2a)\ CO + (\frac{5-b}{2} - a)\ CO_2$	CO NH_3
G	HCN	$HCN \xrightarrow{15} 0.5\ N_2 + 0.5\ H_2 + C$	H_2	$HCN \xrightarrow{15} 0.5\ N_2 + 0.5\ H_2 + C$	H_2	$HCN \xrightarrow{15} 0.5\ N_2 + 0.5\ H_2 + C$	H_2

Table 1 (1b) (Continued)

ROW	GAS COMPOSITION (one component)	SOLID-BOUND ATOMS			
		COLUMN 4: -C, -H, -O		COLUMN 5: -C, -H, -O, -N	
		OVERALL REACTIONS	PRODUCTS	OVERALL REACTIONS	PRODUCTS
A	Thermal decomposition of solid	$(-C) + (-O) \longrightarrow CO, CO_2$	CO	$(-C) + (-O) \rightarrow CO, CO_2$ $(-C) + (-N) + (-H) \rightarrow HCN$	CO HCN
B	CO	$CO + (-O) \xrightarrow{12} CO_2$		$CO + (-O) \xrightarrow{12} CO_2$	
C	H_2	$H_2 + (-O) \xrightarrow{19} H_2O$		$H_2 + (-O) \xrightarrow{19} H_2O$ $H_2 + (-N) \xrightarrow{21} NH_3$ $H_2 + (-N) + (-C) \xrightarrow{22} HCN$	NH_3 HCN
D	NH_3	$NH_3 \xrightarrow{13} 0.5\ N_2 + 1.5\ H_2$ $NH_3 + (-C) \xrightarrow{5} HCN + H_2$	H_2 HCN	$NH_3 \xrightarrow{13} 0.5\ N_2 + 1.5\ H_2$ $NH_3 + (-C) \xrightarrow{5} HCN + H_2$ $NH_3 + (-N) \xrightarrow{26} N_2 + 1.5\ H_2$	H_2 HCN
E	O_2	$O_2 + (-C) \xrightarrow{24} CO, CO_2$ $O_2 + (-H) \xrightarrow{23} H_2O$	CO	$O_2 + (-C) \xrightarrow{24} CO, CO_2$ $O_2 + (-H) \xrightarrow{23} H_2O$ $O_2 + (-N) \xrightarrow{25} NO$	CO NO
F	NO	$NO + a\ (-C) \xrightarrow{1} 0.5\ N_2 + (2\ a-1)\ CO + (1-a)\ CO_2$ $NO + a(-C) + b(-H) \xrightarrow{2} NH_3 + \frac{b-3}{2}\ H_2O + (\frac{b-5}{2} + 2a)\ CO + (\frac{5-b}{2} - a)\ CO_2$	CO NH_3	$NO + a(-C) \xrightarrow{1} 0.5\ N_2 + (2a-1)\ CO + (1-a)\ CO_2$ $NO + a(-C) + b(-H) \xrightarrow{2} NH_3 + \frac{b-3}{2}\ H_2O + (\frac{b-5}{2} + 2a)\ CO + (\frac{5-b}{2} - a)\ CO_2$	CO NH_3
G	HCN	$HCN \xrightarrow{15} 0.5\ N_2 + 0.5\ H_2 + C$	H_2	$HCN \xrightarrow{15} 0.5\ N_2 + 0.5\ H_2 + C$ $HCN + (-N) \xrightarrow{27} N_2 + \ldots$	H_2

Table 1 (1c) (Continued)

ROW	GAS COMPOSITION (two components)	SOLID-BOUND ATOMS					
		COLUMN 1 : -O		COLUMN 2 : -C		COLUMN 3 : -C, -H	
		OVERALL REACTIONS	PRODUCTS	OVERALL REACTIONS	PRODUCTS	OVERALL REACTIONS	PRODUCTS
H	$CO + H_2$	réaction (12)(19) of B1, C1 and: $CO + H_2 \xrightarrow{39} H_2O + C$		$CO + H_2 \xrightarrow{39} H_2O + C$		$CO + H_2 \xrightarrow{39} H_2O + C$	
I	$CO + NH_3$	reactions (12) and (13) of B1 and D1 and: $NH_3 + CO \xrightarrow{9} HCN + H_2O$	H_2 HCN	reactions (5) and (13) of D2 and: $NH_3 + CO \xrightarrow{9} HCN + H_2O$	H_2, HCN HCN	reactions (5) and (13) of D3 and: $NH_3 + CO \xrightarrow{9} HCN + H_2O$	H_2, HCN HCN
J	$CO + O_2$	reaction (12) of B1 and: $CO + 0.5\ O_2 \xrightarrow{20} CO_2$		reaction (24) of E2 and: $CO + 0.5\ O_2 \xrightarrow{20} CO_2$		reactions (24) and (23) of E3 and: $CO + 0.5\ O_2 \xrightarrow{20} CO_2$	
K	$CO + NO$	reaction (12) of B1 and: $CO + NO \xrightarrow{8} 0.5\ N_2 + CO_2$		reaction (1) of F2 and: $CO + NO \xrightarrow{8} 0.5\ N_2 + CO_2$		reactions (1) and (2) of F3 and: $CO + NO \xrightarrow{8} 0.5\ N_2 + CO_2$ $CO + NO + 3\ (-H) \xrightarrow{6} NH_3 + CO_2$	NH_3 NH_3
L	$CO + HCN$	reactions (12) and (15) of B1 and C1 (no supplementary inter-reaction between CO and HCN)	H_2	reaction (15) of G2	H_2	reaction (15) of G3	H_2

Table 1 (1d) (Continued)

ROW	GAZ COMPOSITION (two components)	SOLID-BOUND ATOMS			
		COLUMN 4: -C, -H, -O		COLUMN 5: -C, -H, -O, -N	
		OVERALL REACTIONS	PRODUCTS	OVERALL REACTIONS	PRODUCTS
H	$CO + H_2$	reactions (12) and (19) of B4 and C4 ; reactions of A4, and: $CO + H_2 \xrightarrow{39} H_2O + C$		reactions (12)(19)(21) and (22) from B5 and C5 ; reactions of A5 ; and: $CO + H_2 \xrightarrow{39} H_2O + C$	NH_3, HCN
I	$CO + NH_3$	reactions (5)(12) and (13) from B4 and D4 ; reactions of A4 and: $NH_3 + CO \xrightarrow{9} HCN + H_2O$	HCN	reactions (5)(12)(13) and (26) of B5 and D5 ; reactions of A5 and: $NH_3 + CO \xrightarrow{9} HCN + H_2O$	HCN
J	$CO + NH_3$	reactions (12)(23) and (24) of B4 and E4 ; reactions of A4, and: $CO + 0.5\ O_2 \xrightarrow{20} CO_2$		reactions (12)(23)(24) and (25) of B5 and E5 ; reactions of A5, and: $CO + 0.5\ O_2 \xrightarrow{20} CO_2$	NO, HCN
K	CO + NO	reactions (1)(2) and (12) of B4 and F4 ; reactions of A4, and: $CO + NO \xrightarrow{8} 0.5\ N_2 + CO_2$	NH_3	reactions (1)(2) and (12) of B5 and F5 ; reactions of A5, and: $CO + NO \xrightarrow{8} 0.5\ N_2 + CO_2$	NH_3 , HCN
L	CO + HCN	reactions (12) and (15) of B4 and G4 ; reactions of A4	H_2	reactions (12) and (15) of B5 and G5 ; reactions of A5	H_2

Reproduced from best available copy.

Table 1 (1e) (Continued)

ROW	GAS COMPOSITION (two components)	SOLID-BOUND ATOMS					
		COLUMN 1 : -O		COLUMN 2 : -C		COLUMN 3 : -C, -H	
		OVERALL REACTIONS	PRODUCTS	OVERALL REACTIONS	PRODUCTS	OVERALL REACTIONS	PRODUCTS
M	$H_2 + NH_3$	reactions (13) and (19) of C1 and D1		reactions (5) and (13) of D2	HCN	reactions (5) and (13) of D3	HCN
N	$H_2 + O_2$	reaction (19) of C1 and: $H_2 + 0.5\,O_2 \xrightarrow{18} H_2O$		reaction (24) of E2 and: $H_2 + 0.5\,O_2 \xrightarrow{18} H_2O$		reactions (23) and (24) of E3 and: $H_2 + 0.5\,O_2 \xrightarrow{18} H_2O$	
O	$H_2 + NO$	reaction (19) of C1 and: $NO + 2.5\,H_2 \xrightarrow{11} NH_3 + H_2O$ $NO + H_2 \xrightarrow{14} 0.5\,N_2 + H_2O$	NH_3	reaction (1) of F2 and: $NO + 2.5\,H_2 \xrightarrow{11} NH_3 + H_2O$ $NO + H_2 \xrightarrow{14} 0.5\,N_2 + H_2O$	CO NH_3	reactions (1) and (2) of F3 and: $NO + 2.5\,H_2 \xrightarrow{11} NH_3 + H_2O$ $NO + H_2 \xrightarrow{14} 0.5\,N_2 + H_2O$	CO, NH_3 NH_3
P	$H_2 + HCN$	reactions (15) and (19) of C1 and G1, and: $HCN + H_2 \xrightarrow{45} NH_3 + \ldots$	NH_3	reaction (15) of G2, and: $HCN + H_2 \xrightarrow{45} NH_3 + \ldots$	NH_3	reaction (15) of G3, and: $HCN + H_2 \xrightarrow{45} NH_3 + \ldots$	NH_3
Q	$NH_3 + O_2$	reaction (13) of D1, and: $NH_3 + 0.75\,O_2 \xrightarrow{16} 0.5\,N_2 + 1.5\,H_2O$ $NH_3 + 1.25\,O_2 \xrightarrow{17} NO + 1.5\,H_2O$	H_2 NO	reactions (5), (13) and (24) of D2 and E2, and: $NH_3 + 0.75\,O_2 \xrightarrow{16} 0.5\,N_2 + 1.5\,H_2O$ $NH_3 + 1.25\,O_2 \xrightarrow{17} NO + 1.5\,H_2O$	H_2, HCN, CO NO	reactions (5)(13)(23) and (24) of D3 and E3, and: $NH_3 + 0.75\,O_2 \xrightarrow{16} 0.5\,N_2 + 1.5\,H_2O$ $NH_3 + 1.25\,O_2 \xrightarrow{17} NO + 1.5\,H_2O$	H_2, HCN, CO NO

Table 1 (1f) (Continued)

ROW	GAZ COMPOSITION (two components)	SOLID-BOUND ATOMS			
		COLUMN 4: -C, -H, -O		COLUMN 5: -C, -H, -O, -N	
		OVERALL REACTIONS	PRODUCTS	OVERALL REACTIONS	PRODUCTS
M	$H_2 + NH_3$	reactions (5)(13) and (19) of C4 and D4 ; reactions of A4	CO, HCN	reactions (5)(13)(19)(21)(22) and (26) ; reactions of A5	CO, HCN
N	$H_2 + O_2$	reactions (19)(23) and (24) of C4 and E4 ; reactions of A4 and: $H_2 + 0.5\ O_2 \xrightarrow{18} H_2O$	CO	reactions (19)(21)(22)(23)(24) and (25) of C5 and E5 ; reactions of A5, and: $H_2 + 0.5\ O_2 \xrightarrow{18} H_2O$	CO, NH_3, HCN, NO
Ø	$H_2 + NO$	reactions (1)(2) and (19) of C4 and F4 ; reactions of A4, and: $NO + 2.5\ H_2 \xrightarrow{11} NH_3 + H_2O$ $NO + H_2 \xrightarrow{14} 0.5\ N_2 + H_2O$	CO, NH_3	reactions (1)(2)(19)(21) and (22) of C5 and F5 ; reactions of A5, and: $NO + 2.5\ H_2 \xrightarrow{11} NH_3 + H_2O$ $NO + H_2 \xrightarrow{14} 0.5\ N_2 + H_2O$	CO, HCN NH_3
P	$H_2 + HCN$	reactions (15) and (19) of C4 and G4 ; reactions of A4, and: $HCN + H_2 \xrightarrow{45} NH_3 + \ldots$	NO, CO NH_3	reactions (15)(19)(21)(22) and (27) ; reactions of A5, and: $HCN + H_2 \xrightarrow{45} NH_3 + \ldots$	CO, NH_3, NO
Q	$NH_3 + O_2$	reactions (5)(13)(23) and (24) of D4 and E4 ; reactions of A4, and: $NH_3 + 0.75\ O_2 \xrightarrow{16} 0.5\ N_2 + 1.5\ H_2O$ $NH_3 + 1.25\ O_2 \xrightarrow{17} NO + 1.5\ H_2O$	H_2, CO, HCN	reactions (5)(13)(23)(24)(25) and (26) of D5 and E5 ; reactions of A5, and: $NH_3 + 0.75\ O_2 \xrightarrow{16} 0.5\ N_2 + 1.5\ H_2O$ $NH_3 + 1.25\ O_2 \xrightarrow{17} NO + 1.5\ H_2O$	H_2, CO, NO, HCN

Table 1 (1g) (Continued)

ROW	GAS COMPOSITION	SOLID-BOUND ATOMS					
		COLUMN 1 : -O		COLUMN 2 : -C		COLUMN 3 : -C, -H	
		OVERALL REACTIONS	PRODUCTS	OVERALL REACTIONS	PRODUCTS	OVERALL REACTIONS	PRODUCTS
R	$NH_3 + NO$	reaction (13) of D1, and: $NO + n\ NH_3 \xrightarrow{4} (\frac{1+n}{2})\ N_2$ $+ H_2O + (\frac{3n-2}{2})\ H_2$	H_2	reactions (1)(5) and (13) of D2 and F2, and: $NO + n\ NH_3 \xrightarrow{4} (\frac{1+n}{2})\ N_2$ $+ H_2O + (\frac{3n-2}{2})\ H_2$	H_2, HCN, CO	reactions (1)(2)(5) and (13) of D3 and F3, and: $NO + n\ NH_3 \xrightarrow{4} (\frac{1+n}{2})\ N_2$ $+ H_2O + (\frac{3n-2}{2})\ H_2$	H_2, HCN, CO
S	NH_3 + HCN	reactions (13) and (15) of D1 and G1 and: $NH_3 + HCN \xrightarrow{10} N_2 + 2\ H_2 + C$	H_2	reactions (5)(13) and (15) of D2 and G2 and: $NH_3 + HCN \xrightarrow{10} N_2 + 2\ H_2 + C$	H_2	reactions (5)(13) and (15) of D3 and G3 and: $NH_3 + HCN \xrightarrow{10} N_2 + 2\ H_2 + C$	H_2
T	$O_2 + NO$			reactions (1) and (24) of E2 and F2	CO	reactions (1)(2)(23) and (24) of E3 and F3	
U	O_2 + HCN	reaction (15) of G1, and: $HCN + n\ O_2 \xrightarrow{38}$ N_2, NO, H_2O, CO, CO_2	H_2 NO, CO	reactions (15) and (24) of E2 and G2 and: $HCN + n\ O_2 \xrightarrow{38}$ N_2, NO, H_2O, CO, CO_2	CO, H_2 NO	reactions (15)(23) and (24) of E3 and G3 and: $HCN + n\ O_2 \xrightarrow{38}$ N_2, NO, H_2O, CO, CO_2	H_2, CO NO
V	NO + HCN	reaction (15) of G1, and: $HCN + NO \xrightarrow{40} N_2 + \ldots$	H_2	reactions (1) and (15) of F2 and G2, and: $HCN + NO \xrightarrow{40} N_2 + \ldots$	CO, H_2	reactions (1)(2) and (15) of F3 and G3, and: $HCN + NO \xrightarrow{40} N_2 + \ldots$	CO, H_2 NH_3

Table 1 (1h) (Concluded)

ROW	GAS COMPOSITION (two components)	SOLID-BOUND ATOMS			
		COLUMN 4: -C, -H, -O		COLUMN 5: -C, -H, -O, -N	
		OVERALL REACTIONS	PRODUCTS	OVERALL REACTIONS	PRODUCTS
R	$NH_3 + NO$	reactions (1)(2)(5) and (13) of D4 and F4 ; reactions of A4, and: $NO + n\ NH_3 \xrightarrow{4} (\frac{1+n}{2})\ N_2 + H_2O + (\frac{3n-2}{2})\ H_2$	CO, H_2, HCN	reactions (1)(2)(5)(13) and (26) of D5 and F5 ; reactions of A5 and: $NO + n\ NH_3 \xrightarrow{4} (\frac{1+n}{2})\ N_2 + H_2O + (\frac{3n-2}{2})\ H_2$	CO, H_2, HCN
S	$NH_3 + HCN$	reactions (5)(13) and (15) of D4 and G4 ; reactions of A4, and: $NH_3 + HCN \xrightarrow{10} N_2 + 2\ H_2 + C$	CO, H_2	reactions (5)(13)(15)(26) and (27) of D5 and G5 ; reactions of A5, and: $NH_3 + HCN \xrightarrow{10} N_2 + 2\ H_2 + C$	CO, H_2
T	$O_2 + NO$	reactions (1)(2)(23) and (24) of E4 and F4 ; reactions of A4	CO, NH_3	reactions (1)(2)(23)(24) and (25) of E5 and F5 ; reactions of A5	CO, HCN, NH_3
U	$O_2 + HCN$	reactions (15)(23) and (24) of E4 and G4 ; reactions of A4 and: $HCN + n\ O_2 \xrightarrow{38} N_2$, NO, H_2O, CO_2, CO	CO, H_2 NO	reactions (15)(23)(24)(25) and (27) of E5 and G5 ; reactions of A5, and: $HCN + n\ O_2 \xrightarrow{38} N_2$, NO, H_2O, CO, CO_2	CO, H_2, NO
V	$NO + HCN$	reactions (15)(1) and (2) of F4 and G4 ; reactions of A4, and: $HCN + NO \xrightarrow{40} N_2 + \ldots$	CO, NH_3, H_2	reactions (1)(2)(15)(27) of F5 and G5 ; reactions of A5, and: $HCN + NO \xrightarrow{40} N_2 + \ldots$	CO, NH_3, H_2

a. Either directly from the time variation of the molecular nitrogen concentration, measured experimentally or given by Eq. (1). Owing to the fact that in most cases the variation of N_2 depends actually upon a large number of intermediate reactions, the precision of the rate expression determined in that direct way is rather poor. A more suitable expression is generally obtained by the following method:

b. Or as the algebraic sum of all the reaction rates which are playing a role in the formation of molecular nitrogen (see point (3) below).

3. Specific and intermediate reactions, the sequence of which is responsible for the final transformation of NO into molecular nitrogen. Special attention is devoted to that kind of reaction paths, the rate of which is indicated by the symbol V, followed by a numerical subscript referring to the reactions identified and listed in Tables 2 and 3.

A brief look at Table 1 shows that in most cases a relatively large number of these specific reaction paths may occur, as well as parallel competitive reactions as in a series of consecutive reactions. The proper determination of their respective rate constants, therefore, appeals a special method of treatment of the experimental data. This treatment, although bearing a specific character for any given solid/gas composition combination, possesses some general features which will be explained in what follows by a typical example.

We consider the case where argon containing NO and H_2 is fed over gas phase generated soot (this is case 0.4 of Table 1, i.e., given at the intersection of row 0 and column 4). As may be seen from Table 1, we have to deal with the following set of specific reaction paths:

a. Primary reactions:

- reactions (1) and (2), characteristics of the combination NO/soot and

Table 2. List of Heterogeneous Reactions Appearing in Table 1

REACTION N°:	REMARKS
1. $NO + a\ (-C) \rightarrow 0.5\ N_2 + (2a-1)\ CO + (1-a)\ CO_2$ $(0.5 \leqslant a \leqslant 1)$	ratio $(CO)/(CO_2)$ in the reaction products dependson the temperature and on the nature of soot
2. $NO + a\ (-C) + b\ (-H) \rightarrow NH_3 + \left(\frac{b-5}{2} + 2a\right) CO + \left(\frac{5-b}{2} - a\right) CO_2 + \frac{b-3}{2} H_2O$ $(0 \leqslant a \leqslant 1\ ;\ 5 \geqslant b \geqslant 3)$	
4. $NO + nNH_3 \rightarrow \left(\frac{1+n}{2}\right) N_2 + H_2O + \left(\frac{3n-2}{2}\right) H_2$	the true stoichiometry of this reaction path seems to be situated between 4a and 4b
4a. $NO + 0.67\ NH_3 \rightarrow 0.83\ N_2 + H_2O$	
4b. $NO + NH_3 \rightarrow N_2 + H_2O + 0.5\ H_2$	
5. $NH_3 + (-C) \rightarrow HCN + H_2$	
6. $CO + NO + 3\ (-H) \rightarrow NH_3 + CO_2$	some indication seems to exist for this reaction path to be considered as distinct from reaction (2)
8. $CO + NO \rightarrow 0.5\ N_2 + CO_2$	
9. $NH_3 + CO \rightarrow HCN + H_2O$	
10. $NH_3 + HCN \rightarrow N_2 + \ldots$	(existence to be checked)
11. $NO + 2.5\ H_2 \rightarrow NH_3 + H_2O$	
12. $CO + (-O) \rightarrow CO_2$	
13. $NH_3 \rightarrow 0.5\ N_2 + 1.5\ H_2$	
14. $NO + H_2 \rightarrow 0.5\ N_2 + H_2O$	
15. $HCN \rightarrow 0.5\ N_2 + \ldots$	(not studied until now)
16. $NH_3 + 0.75\ O_2 \rightarrow 0.5\ N_2 + 1.5\ H_2O$	
17. $NH_3 + 1.25\ O_2 \rightarrow NO + 1.5\ H_2O$	
18. $H_2 + 0.5\ O_2 \rightarrow H_2O$	at temperatures beyond 500°C may become a gas phase reaction with explosive character
19. $H_2 + (-O) \rightarrow H_2O$	has not been checked, but is assumed in analogy with (12)

Table 2 (Continued)

REACTION PATH N°:	REMARKS
20. $CO + 0.5\ O_2 \rightarrow CO_2$	may become an explosive gas phase reaction
21. $0.5\ H_2 + (-N) \rightarrow NH_3$	
22. $H_2 + (-N) + (-C) \rightarrow HCN$	
23. $0.5\ O_2 + 2\ (-H) \rightarrow H_2O$	has not been checked, but assumed in analogy with (24)
24. $O_2 + (-C) \rightarrow CO,\ CO_2$	the ratio $(CO)/(CO_2)$ in the reaction products depends on temperature and nature of soot
25. $0.5\ O_2 + (-N) \rightarrow NO$	
26. $NH_3 + (-N) \rightarrow N_2 + 1.5\ H_2$	with the actual equipment, this reaction path cannot be distinguished from reaction path (13)
27. $HCN + (-N) \rightarrow N_2 + \ldots$	this reaction path cannot be distinguished from (15)
28. $NO + (-N) + (-C) \rightarrow N_2 + CO$	to check the existence of this reaction path, the N balance would be required; (28) has been disregarded
29. $CO + (-H) + (-N) \rightarrow HCN + \ldots$	has not been observed (below 1100°C)
30. $2\ CO \rightarrow CO_2 + C$	has not been observed
31. $NH_3 + (-O) \rightarrow NO + 1.5\ H_2$	has not been observed (below 1100°C)
32. $NO \rightarrow 0.5\ O_2 + 0.5\ N_2$	has not been observed (below 1100°C)
33. $2\ NO \rightarrow NO_2 + 0.5\ O_2$	has not been observed
34. $HCN + (-O) \rightarrow NO + \ldots$	has not been checked, but is not more probable than (31) in reducing medium
35. $NO + (-H) + (-C) \rightarrow HCN + \ldots$	has not been observed
36. $H_2 + HCN \rightarrow NH_3 + \ldots$	(still to be checked)
37. $NO + 0.5\ O_2 \rightarrow NO_2$	not observed at these elevated temperatures
38. $HCN + n\ O_2 \rightarrow N_2,\ NO,\ H_2O,\ CO,\ CO_2$	(still to be checked)
39. $CO + H_2 \rightarrow H_2O + C$	

Table 2 (Concluded)

REACTION PATH N°:	REMARKS
40. $HCN + NO \rightarrow N_2 + \dots$	(still to be checked)
42. $CO_2 + H_2 \rightarrow CO + H_2O$	
44. $HCN + H_2O \rightarrow NH_3 + CO$	(reverse reaction of 9 ; still to be checked)
45. $HCN + H_2 \rightarrow NH_3 + \dots$	(still to be checked)

Remark: 1) Reactants placed between brackets (e.g. (-C), (-H), (-N) etc.) are solid bound atoms

2) The numbering of the different reaction paths is the same as in the Reports (Ref. 26842, 27227 and 27622 - Internal reports IFP)

Table 3. Overall Rates of Heterogeneous NO Reduction ($cm^3\ g^{-1}\ s^{-1}$) (a.1)

GAS COMPOSITION	OVERALL REACTION	SOLID PARTICLES	
		ALUMINA (–O bound atoms)	GRAPHITE (–C bound atoms)
Ar + NO	$NO + a\ (-C) \xrightarrow{1} 0.5\ N_2 + (2a-1)\ CO + (1-a)\ CO_2$		$V_1 = -d\ (NO)/dt =$ $1.9\ 10^{11}\ \exp\ (-29000/T)\ X_{NO}$
	$NO + a\ (-C) + b\ (-H) \xrightarrow{2} NH_3 + \frac{b-3}{2}\ H_2O + (\frac{b-5}{2} + 2a)\ CO + (\frac{5-b}{2} - a)\ CO_2$		
Ar + NH_3	$NH_3 \xrightarrow{13} 0.5\ N_2 + 1.5\ H_2$	$V_{13} = -d\ (NH_3)/dt =$ $3\ 10^8\ \exp\ (-18600/T)\ X_{NH_3}$	$V_{13} = -d\ (NH_3)/dt =$ $1\ 10^8\ \exp\ (-18800/T)\ X_{NH_3}$
	$NH_3 + (-C) \xrightarrow{5} HCN + H_2$		
Ar + NO + NH_3	$NO + nNH_3 \xrightarrow{4} \frac{1+n}{2}\ N_2 + H_2O + (\frac{3n-2}{2})\ H_2$	$V_4 = -d\ (NO)/dt =$ $5.1\ 10^9\ \exp\ (-15000/T)\ X_{NO}\ X_{NH_3}$	$V_4 = -d\ (NO)/dt =$ $1.5\ 10^{10}\ \exp\ (-14600/T)\ X_{NO}\ X_{NH_3}$
Ar + NO + CO	$NO + CO \xrightarrow{8} 0.5\ N_2 + CO_2$	$V_8 = -d\ (NO)/dt =$ $6\ 10^8\ \exp\ (-15800/T)\ X_{NO}\ X_{CO}^{0.3}$	$V_8 = -d\ (NO)/dt =$ $10^5\ \exp\ (-10100/T)\ X_{NO}\ X_{CO}$

Table 3 (a.2) (Continued)

GAS COMPOSITION	OVERALL REACTION	SOLID PARTICLES	
		SOOT from C_2H_4	SOOT from HEAVY FUEL OIL (Thermal Plant of Porcheville, France)
Ar + NO	$NO + a\,(-C) \xrightarrow{1} 0.5\,N_2 + (2a-1)\,CO + (1-a)\,CO_2$	$V_1 = -d\,(NO)/dt = 1.3\ 10^{10}\ \exp\,(-22550/T)\ X_{NO}^{0.75}$	$V_1 = -d\,(NO)/dt = 9.8\ 10^{16}\ \exp\,(-33500/T)\ X_{NO}^{0.63}$
	$NO + a\,(-C) + b\,(-H) \xrightarrow{2} NH_3 + \frac{b-3}{2}\,H_2O + (\frac{b-5}{2} + 2a)\,CO + (\frac{5-b}{2} - a)\,CO_2$	$V_2 = -d\,(NO)/dt = 1.9\ 10^{6}\ \exp\,(-14300\,/T)\ X_{NO}^{0.7}$	$V_2 = -d\,(NO)/dt = 2.1\ 10^{6}\ \exp\,(-16000/T)\ X_{NO}^{0.35}$
Ar + NH_3	$NH_3 \xrightarrow{13} 0.5\,N_2 + 1.5\,H_2$	$V_{13} = -d\,(NH_3)/dt = 5.3\ 10^{8}\ \exp\,(-18600/T)\ X_{NH_3}$	$V_{13} = -d\,(NH_3)/dt = 5.3\ 10^{9}\ \exp\,(-19800/T)\ X_{NH_3}$
	$NH_3 + (-C) \xrightarrow{5} HCN + H_2$	$V_5 = -d\,(NH_3)/dt = 6\ 10^{6}\ \exp\,(-16600/T)\ X_{NH_3}$	$V_5 = -d\,(NH_3)/dt = 7.3\ 10^{7}\ \exp\,(-16600/T)\ X_{NH_3}$
Ar + NO + NH_3	$NO + nNH_3 \xrightarrow{4} \frac{1+n}{2}\,N_2 + H_2O + (3n-2)\,H_2$	$V_4 = -d\,(NO)/dt = 6\ 10^{8}\ \exp\,(-11500/T)\ X_{NO}\ X_{NH_3}$	$V_4 = -d\,(NO)/dt = 3\ 10^{10}\ \exp\,(-15300/T)\ X_{NO}\ X_{NH_3}$
Ar + NO + CO	$NO + CO \xrightarrow{8} 0.5\,N_2 + CO_2$	$V_8 = -d\,(NO)/dt = 1.7\ 10^{8}\ \exp\,(-12400/T)\ X_{NO}\ X_{CO}$	$V_8 = -d\,(NO)/dt = 2.1\ 10^{10}\ \exp\,(-14800/T)\ X_{NO}\ X_{CO}^{0.7}$

Table 3 (b.1) (Continued)

GAS COMPOSITION	OVERALL REACTION	SOLID PARTICLES	
		ALUMINA (-O bound atoms)	GRAPHITE (-C bound atoms)
$Ar + NO + CO$	$NO + CO + 3\ (-H) \xrightarrow{6} NH_3 + CO_2$		
$Ar + NH_3 + CO$	$NH_3 + CO \xrightarrow{9} HCN + H_2O$	$V_9 = -d\ (NH_3)/dt =$ $1.3\ 10^7\ \exp\ (-13800/T)\ X_{NH_3}^{0.75}\ X_{CO}$	
$Ar + NO + H_2$	$NO + H_2 \xrightarrow{14} 0.5\ N_2 + H_2O$	$V_{14} = -d\ (NO)/dt =$ $6.4\ 10^7\ \exp\ (-13500/T)\ X_{NO}\ X_{H_2}$	$V_{14} = -d\ (NO)/dt =$ $2.3\ 10^9\ \exp\ (-14000/T)\ X_{NO}\ X_{H_2}$
	$NO + 2.5\ H_2 \xrightarrow{11} NH_3 + H_2O$	$V_{11} = -d\ (NO)/dt =$ $3.5\ 10^3\ \exp\ (-8200/T)\ X_{NO}^{0.5}\ X_{H_2}$	$V_{11} = -d\ (NO)/dt =$ $7.1\ 10^6\ \exp\ (-13800/T)\ X_{NO}^{0.5}\ X_{H_2}$
$Ar + NH_3 + O_2$	$NH_3 + 0.75\ O_2 \xrightarrow{16} 0.5\ N_2 + 1.5\ H_2O$	$V_{16} = -d\ (NH_3)/dt =$ $2.2\ 10^6\ \exp\ (-13000/T)\ X_{NH_3}^{0.5}\ X_{O_2}^{0.5}$	
	$NH_3 + 1.25\ O_2 \xrightarrow{17} NO + 1.5\ H_2O$	$V_{17} = -d\ (NH_3)/dt =$ $1\ 10^5\ \exp\ (-12200/T)\ X_{NH_3}^{0.6}\ X_{O_2}^{0.3}$	

Table 3 (b.2) (Concluded)

GAS COMPOSITION	OVERALL REACTION	SOLID PARTICLES	
		SOOT from C_2H_4	SOOT from HEAVY FUEL OIL (Thermal Plant of Porcheville, France)
Ar + NO + CO	$NO + CO + 3\ (-H) \xrightarrow{6} NH_3 + CO_2$		V_6 = -d (NO)/dt = $2.7\ 10^9 \exp(-17100/T)\ X_{NO}^{0.1}\ X_{CO}$
Ar + NH_3 + CO	$NH_3 + CO \xrightarrow{9} HCN + H_2O$		
Ar + NO + H_2	$NO + H_2 \xrightarrow{14} 0.5\ N_2 + H_2O$	V_{14} = -d (NO)/dt = $6.8\ 10^8 \exp(-13260/T)\ X_{NO}\ X_{H_2}$	V_{14} = -d (NO)/dt = $1.9\ 10^7 \exp(-10800/T)\ X_{NO}^{0.8}\ X_{H_2}^{0.7}$
	$NO + 2.5\ H_2 \xrightarrow{11} NH_3 + H_2O$	V_{11} = -d (NO)/dt = $1.3\ 10^{10} \exp(-17100/T)\ X_{NO}^{0.5}\ X_{H_2}$	V_{11} = -d (NO)/dt = $2\ 10^9 \exp(-15300/T)\ X_{NO}^{0.5}\ X_{H_2}^{1.5}$
Ar + NH_3 + O_2	$NH_3 + 0.75\ O_2 \xrightarrow{16} 0.5\ N_2 + 1.5\ H_2O$	V_{16} = -d (NH_3)/dt = $9.8\ 10^6 \exp(-9900/T)\ X_{NH_3}^{0.83}\ X_{O_2}^{0.33}$	
	$NH_3 + 1.25\ O_2 \xrightarrow{17} NO + 1.5\ H_2O$	V_{17} = -d (NH_3)/dt = $2.7\ 10^2 \exp(-6050/T)\ X_{NH_3}^{0.5}\ X_{O_2}^{0.3}$	

- reactions (19), characteristic of the combination H_2/soot. However, this reaction does not change the concentration of the nitrogen-containing species and may be disregarded for the present purpose;
- reactions (11) and (14), which are specific for the combination of H_2 and NO in the presence of solid particles.

b. Secondary reactions:

Since CO and NH_3 are products of the above mentioned primary reactions, one has to also take into account the existence of the following secondary reactions:

- reaction (5) between NH_3 and (-C) (= case D.4 of Table 1);
- reaction (13) (= case D.4 of Table 1);
- reaction (8) between CO and NO (= case K.4 of Table 1);
- reaction (4) between NH_3 and NO (= case R.4 of Table 1);
- reaction (9) between NH_3 and CO (= case I.4 of Table 1);
- reaction (39) between CO and H_2 (= case H.4 of Table 1); this reaction being disregarded here since it does not affect the concentration of the nitrogen-containing species;
- since reactions (5) and (9) yield HCN as a product, we have to also take into account reactions where HCN is a reactant:
  - reaction (15) (= case G.4 of Table 1)
  - reaction (10) between HCN and NH_3 (= case S.4 of Table 1)
  - reaction (40) between HCN and NO (= case V.4 of Table 1)
  - reaction (45) between HCN and H_2 (= case P.4 of Table 1)

Actually, reactions (15), (10), (40) and (45) are second order secondary reactions (one of the reactants itself being a product of a first order secondary reaction), and therefore, in the present case they may be perfectly disregarded.

Taking into account the primary reaction paths (1, 2, 11 and 14) and the first order secondary reactions (4, 5, 8, 9 and 13), we may write the following system of differential equations, giving the time variation of the nitrogen-containing species:

$$d(NO)/dt = -V_1 - V_2 - V_4 - V_9 - V_{11} - V_{14} = \overline{V_{0.4}} \qquad (6)$$

$$d(NH_3)/dt = V_2 - nV_4 - V_5 - V_9 + V_{11} - V_{13} \qquad (7)$$

$$d(HCN)/dt = V_5 + V_9 \qquad (8)$$

$$d(N_2)/dt = 0.5V_1 + \frac{1+n}{2} V_4 + 0.5V_8 + 0.5V_{13} + 0.5V_{14} = \overline{V_n} \qquad (9)$$

The combination of the three first differential equations yields two equations allowing the separation of the two specific reaction rates V_{11} and V_{14}) characteristic for the H_2 + NO on soot case, we intend to determine:

$$-d(NO)/dt - d(NH_3)/dt - d(HCN)/dt = V_1 + (1+n)V_4 + V_8 + V_{13} + V_{14} \qquad (10)$$

$$-d(NO)/dt + d(NH_3)/dt + d(HCN)/dt = V_1 + 2V_2 + (1-n)V_4 + V_8 + 2V_{11} - V_{13} + V_{14} \qquad (11)$$

We now have to perform supplementary experiments in order to determine the reaction rates V_1, V_2, V_4, V_8 and V_{13}, under experimental conditions where those reactions are the leading primary reactions, in the following sequence for example:

a) Using an argon + ammonia flow over the same soot, V_{13} may be determined from a set of appropriate differential equations, analogous to Eqs. (6) through (11), upon neglection of the secondary reactions.

b) Using an argon + NO flow over the same soot, V_1 and V_2 may be determined from an appropriate set of differential equations

c) Using an argon + NO + NH_3 flow over the same soot, V_4 may be determined from an analogous set of differential equations, utilizing the already determined rates V_1, V_2 and V_{13}.

d) Finally, using an argon + NO + CO flow on the same soot, V_8 may be determined from an analogous set of differential equations, utilizing the already known rates V_1, V_4 and V_{13}.

Upon substitution of the thus obtained rate expressions V_1, V_4, V_8 and V_{13}, into Eq. (10), one determines the rate V_{14}. Finally, upon substitution of the thus obtained rates V_2, V_4, V_1, V_8 and V_{14} into Eq. (6), one has the possibility to calculate the rate expression V_{11}.

Actually, in particular cases the above explained general treatment allows for further simplications in that (1) it is found that most all secondary reactions may be simply disregarded for small advancements of the primary reactions, and (2) in some cases a given primary reaction starts to be competitive only at much higher temperatures than other primary reactions. For more information the reader is referred to the report given in Reference 16.

De 5-16

SECTION IV

DISCUSSION OF THE RESULTS

For practical reasons (space and time limitations) we shall limit ourselves in the present paper to a general discussion of the results; discussion concerning the identification of specific reaction paths will be omitted; this and further details may be found in the final report on that contract work(16). A survey of specific reaction rates, determined for different solid particles and gas compositions, is given in Table 3 at the end of the paper. A summary of overall NO removal reaction rates is also added in Table 4. References to these reactions will be made in the following discussion.

In a first part we shall consider the heterogeneous reduction of nitric oxide in the absence of molecular oxygen; in a second part we discuss specific effects of molecular oxygen on the heterogeneous NO reduction.

Heterogeneous NO Reduction in the Absence of Oxygen

Direct Transformation of NO into Molecular Nitrogen

In the Absence of Any Reducing Agent. Except in cases where noble metals or typical metal oxide catalysts are used (these cases are out of scope in the present work), the direct transformation of NO into molecular nitrogen in the absence of any reducing agent (either gaseous reductant such as H_2, CO, hydrocarbons, or solid bound H or C atoms), is a relatively slow process. Actually, it has been found from the present study that at temperatures below 1100°C it was impossible to measure any reduction of nitric oxide on current metal oxides like alumina and quartz.

In the Present of Reducing Agents. In the presence of reducing agents the direct transformation of NO into N_2 is seriously enhanced. The following chemical species have been shown to act as reducing agents for this direct transformation:

a. Carbon Monoxide reduces NO directly into N_2 by a gas/gas heterogeneous reacton path:

$$NO + CO \xrightarrow{8} 0.5\ N_2 + CO_2$$

Table 4. Overall NO Disappearance Rates (-d (NO)/dt, $cm^3\ g^{-1}\ s^{-1}$) as a Function of Gas Composition and Nature of Solid Particles (a)

GAS COMPOSITION	SOLID PARTICLES	
	ALUMINA	GRAPHITE
Ar + NO		$\overline{V_{F2}} = 1.9\ 10^{11}\ \exp\ (-29200/T)\ X_{NO}$
Ar + NO + CO	$\overline{V_{K1}} = 6.8\ 10^{8}\ \exp\ (-15750/T)\ X_{NO}\ X_{CO}^{0.3}$	$\overline{V_{K2}} = 10^{5}\ \exp\ (-10100/T)\ X_{NO}\ X_{CO}$
Ar + NO + H_2	$\overline{V_{\text{Ø}1}} = 8.6\ 10^{5}\ \exp\ (-11900/T)\ X_{NO}^{0.5}\ X_{H_2}$	$\overline{V_{\text{Ø}2}} = 2.5\ 10^{7}\ \exp\ (-13100/T)\ X_{NO}^{0.5}\ X_{H_2}$
Ar + NO + NH_3	$\overline{V_{R1}} = 3\ 10^{11} \exp(-18200/T)\ X_{NO} X_{NH_3}$	$\overline{V_{R2}} = 1.5\ 10^{10} \exp(-14600/T) X_{NO} X_{NH_3}$
Ar + NO + CO + O_2	$\overline{V_{JKT\ 1}} =$ $6.2\ 10^{8} \exp\ (-15600/T)\ X_{NO}\ X_{CO}^{0.3}$ $\times\ (1 + 43\ X_{O_2}^{0.35})$	
Ar + NO + H_2 + O_2	$\overline{V_{\text{NØT}\ 1}} =$ $\dfrac{8.6\ 10^{5}\ \exp\ (-11900/T)}{1 + 1.1\ 10^{8}\ \exp\ (-6000/T) X_{O_2}^{-2}}\ X_{H_2}\ X_{NO}^{0.5}$	

Table 4 (b) (Concluded)

GAS COMPOSITION	SOLID PARTICLES	
	SOOT from C_2H_4	SOOT from HEAVY FUEL OIL (Thermal Plant of Porcheville, France)
Ar + NO	$\overline{V_{F4}} = 3.4\ 10^7 \exp(-16000/T)\ X_{NO}^{0.75}$	$\overline{V_{F5}} = 6.6\ 10^8 \exp(-18600/T)\ X_{NO}^{0.5}$
Ar + NO + CO	$\overline{V_{K4}} = 3.6\ 10^8 \exp(-14700/T)\ X_{NO}\ X_{CO}^{0.45}$	$\overline{V_{K5}} = 8.4\ 10^6 \exp(-10600/T)\ X_{NO}^{0.5}\ X_{CO}$
Ar + NO + H_2	$\overline{V_{04}} = 1.7\ 10^9 \exp(-13500/T)\ X_{NO}^{0.4}\ X_{H_2}^2$	$\overline{V_{05}} = 5\ 10^8 \exp(-14300/T)\ X_{NO}^{0.5}\ X_{H_2}$
Ar + NO + NH_3	$\overline{V_{R4}} = 1.6\ 10^8 \exp(-13700/T)\ X_{NO}^{0.75}\ X_{NH_3}^{0.6}$	$\overline{V_{R5}} = 3.3\ 10^{11} \exp(-14600/T)\ X_{NO}\ X_{NH_3}$
Ar + NO + O_2	$\overline{V_{T4}} = 3.4\ 10^7 \exp(-16000/T)\ X_{NO}^{0.75}$ $\times (1 + 33\ X_{O_2}^{0.25})$	$\overline{V_{T5}} = 6.6\ 10^8 \exp(-18600/T)\ X_{NO}^{0.5}$ $\times \left[1 + 4\ 10^5 \exp(-10300/T)\ X_{O_2}\right]^{-1}$

In trials where NO + CO is fed over alumina (= case K.1, see Figure 4), reaction 8 is the only one occurring. In the case of graphite (= case K.2, see Figure 5) reaction 1 also exists (see C below), but takes place at much higher temperatures. When feeding NO + CO over soot other reactions enter into competition with reactions 8 and 1, leading to intermediate formation of ammonia (see below).

b. Molecular Hydrogen also presents a direct gas + gas heterogeneous reduction of NO into molecular nitrogen:

$$NO + H_2 \xrightarrow{14} 0.5\ N_2 + H_2O$$

However, this reaction is always accompanied by the competing reaction

$$NO + 2.5\ H_2 \xrightarrow{11} NH_3 + H_2O$$

which may be very important, as seen from Figure 6. Only a treatment, as explained earlier, together with a study of the mass balance is able to distinguish the respective rates of reactions 14 and 11.

c. Solid Bound Carbon Atoms also are able to directly reduce NO into N_2 by a gas + solid heterogeneous reaction which may be found in statu quo when feeding NO over graphite (= case F.2), at least as a primary reaction (the CO produced will add reaction 8 as a secondary reaction):

$$NO + a(-C) \xrightarrow{1} 0.5\ N_2 + (2a-1)CO + (1-a)CO_2$$

An example is given in Figure 7 for the case of graphite. Reaction 1 is always characterized by a relatively high activation temperature (see Table 3), and therefore, is almost negligibly small below 800°C.

d. An analogous direct transformation of NO into N_2 by a solid + gas reaction utilizing bound hydrogen atoms as a reducing agent probably also exists:

$$NO + 2(-H) \rightarrow 0.5\ N_2 + H_2O$$

but until now, we were not able to identify it experimentally.

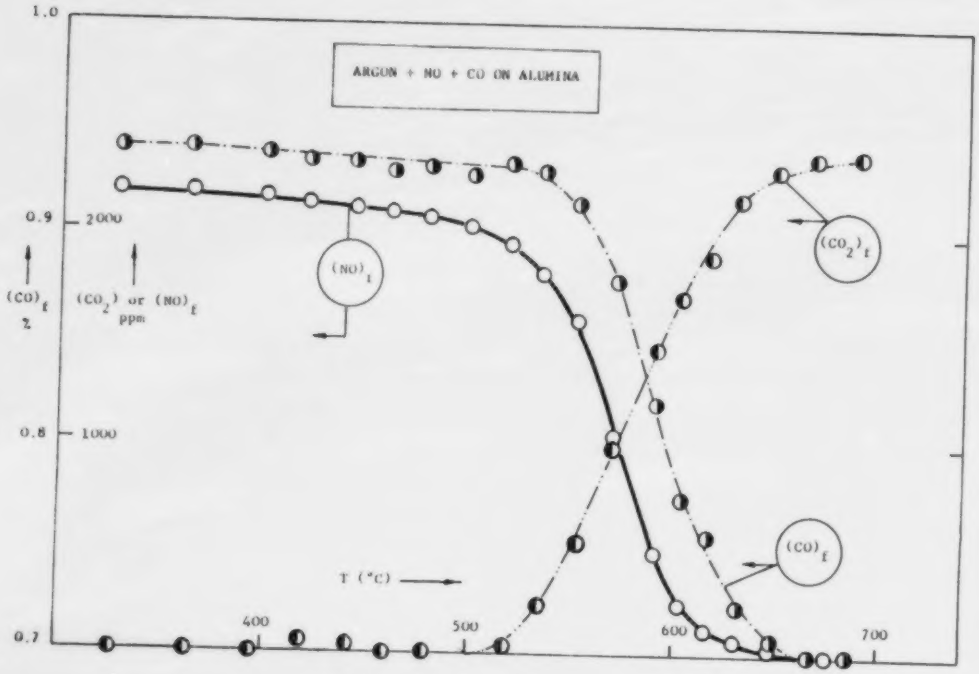

Figure 4. Argon + NO + CO on Alumina
$D = 14.4\ cm^3s^{-1}$; $(NO)_i = 2200$ ppm; $(CO)_i = 0.94\%$

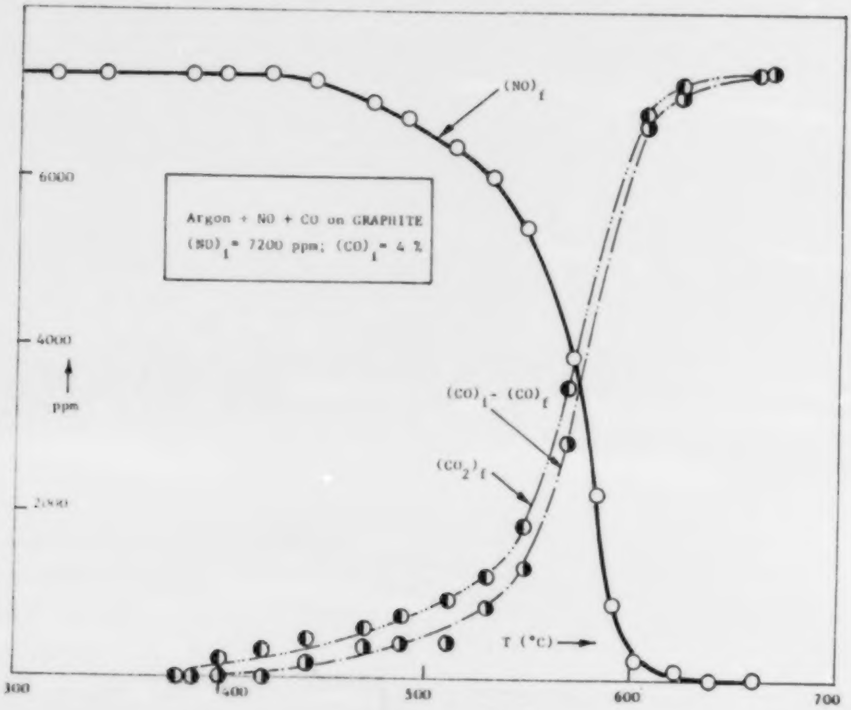

Figure 5. Argon + NO + CO on Graphite
D = 14.5 cm^3s^{-1}; $(NO)_i$ = 7200 ppm; $(CO)_i$ = 4.00%

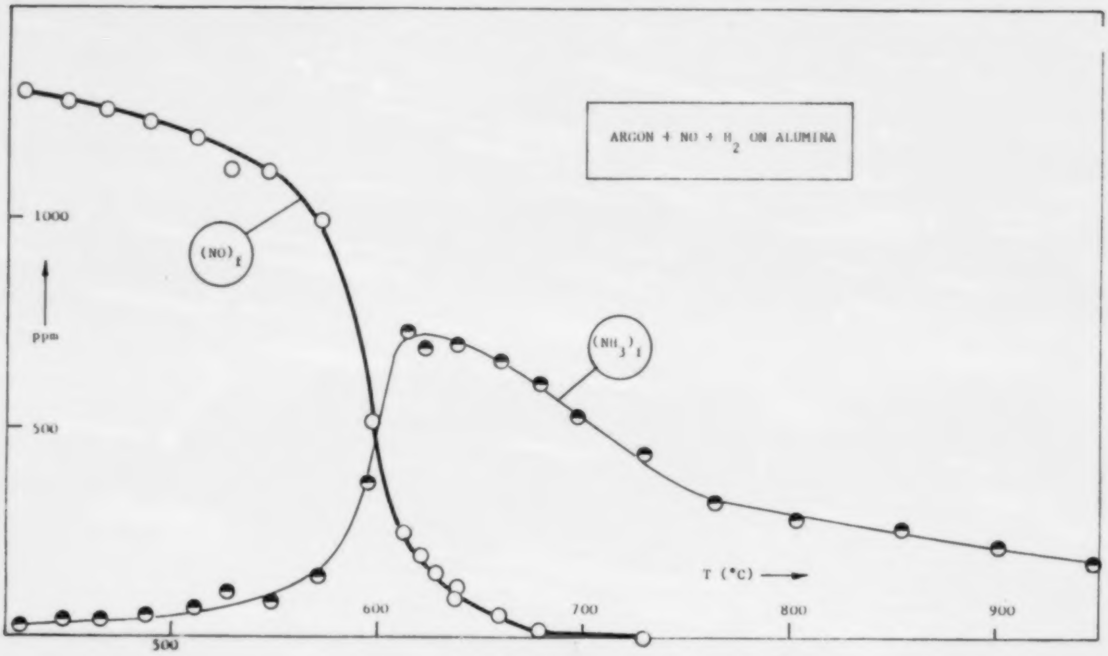

Figure 6. Argon + Hydrogen + NO on Alumina
D = 14.9 cm^3s^{-1}; $(NO)_i$ = 1330 ppm; $(H_2)_i$ = 5.52%

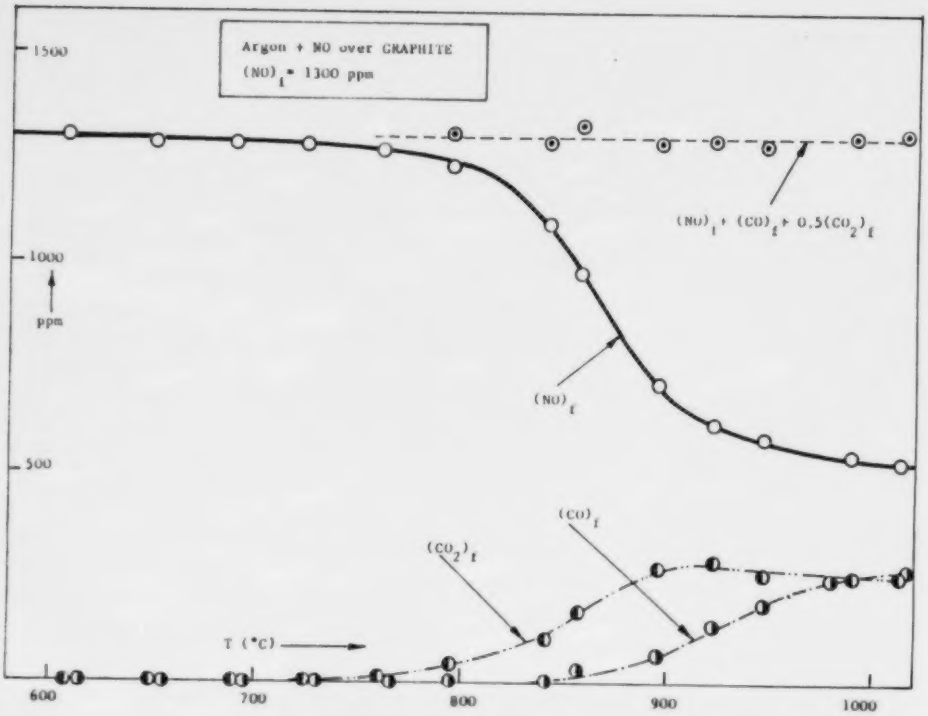

Figure 7. Argon + NO on Graphite
$D = 14.5\ cm^3 s^{-1}$; $(NO)_i = 1330$ ppm

Indirect Transformation of NO

As soon as a hydrogen source becomes available, an indirect transformation of nitric oxide into molecular nitrogen, passing over the intermediate formation of ammonia, is observed. The intermediate formation of ammonia from NO has been observed with the following hydrogen sources:

a. Solid Bound Hydrogen Atoms are able to transform NO into NH_3 by a gas + solid heterogeneous reaction:

$$NO + a(-C) + b(-H) \longrightarrow NH_3 + \left(\frac{b-5}{2} + 2a\right)CO + \left(\frac{5-b}{2} - a\right)CO_2 + \left(\frac{b-3}{2}\right) H_2O$$

as shown in Figures 8 and 9 for the two different soots utilized. In the temperature range where this reaction path is studied, the competing reaction (1) is negligible. At higher temperatures both reactions (1) and (2) are in severe competition. It is worthwhile to note that in the temperature range where reaction (2) is the only primary reaction of importance it yields mostly CO as a product in the case of ethylene soot, whereas in the case of cenospherical soot CO_2 is the only carbon oxide product.

b. Molecular Hydrogen transforms NO into NH_3 by the gas + gas heterogeneous reaction (11) already mentioned (in competition with the direct transformation of NO into N_2 by reaction 14). This is illustrated in Figure 6 (= case 0.1, NO + H_2 on alumina), Figure 10 (= case 0.2, NO + H_2 on graphite), Figure 11 (= case 0.4, NO + H_2 on ethylene soot). In all these figures it may be seen that the concentrations of ammonia released by reaction (11), using molecular hydrogen as a reductant, are much higher than in the case of reaction path (2) where bound hydrogen is the reducing agent.

c. Hydrocarbons also may constitute the hydrogen source for formation of ammonia from nitric oxide (see Figure 12), although it is not clear whether the hydrocarbon itself or its cracking products (H_2) are acting as a coreactant.

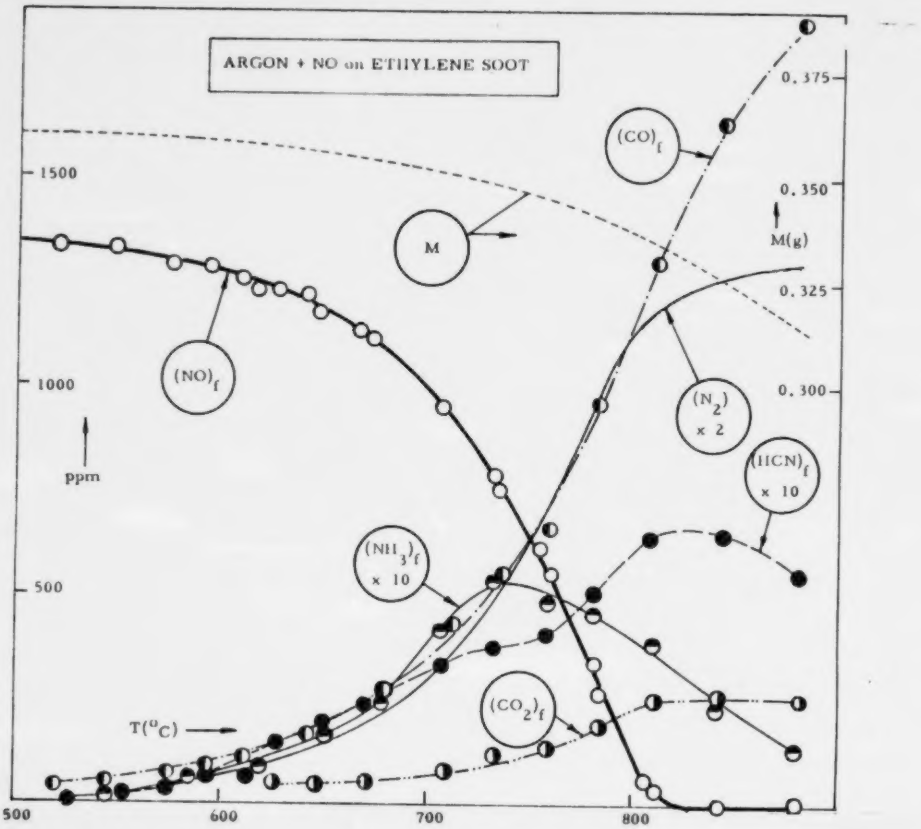

Figure 8. Argon + NO on Ethylene Soot
$D = 14.0\ cm^3s^{-1}$; $(NO)_i = 1360$ ppm

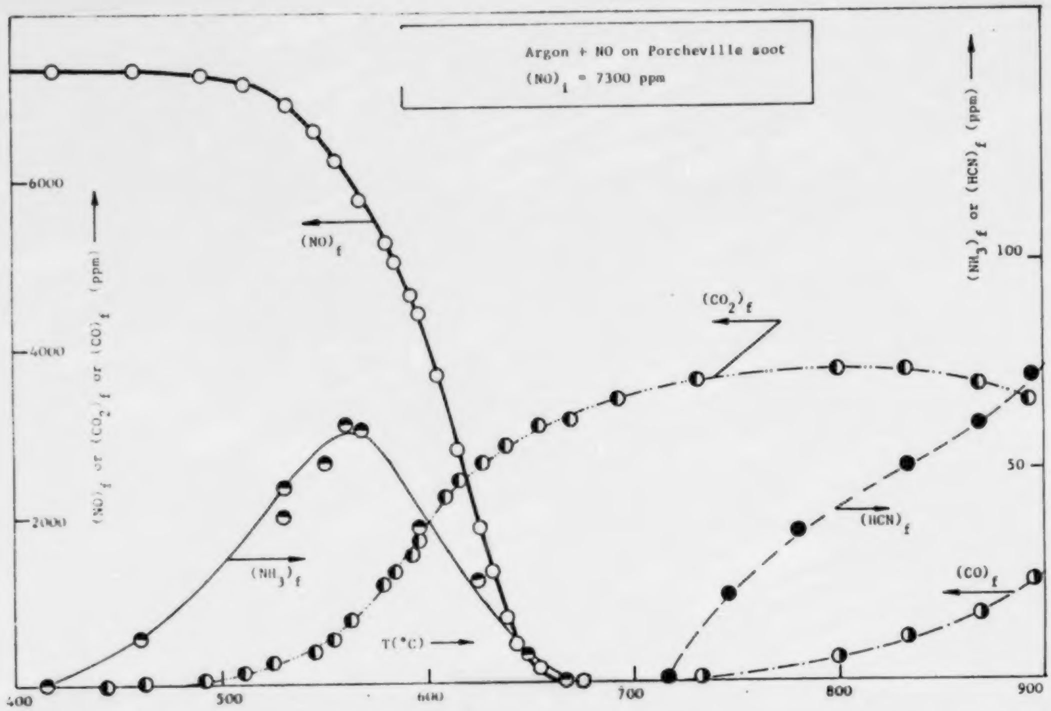

Figure 9. Argon + NO on Porcheville Soot
D = 14.5 cm^{3}s^{-1}; (NO)$_i$ = 7300 ppm

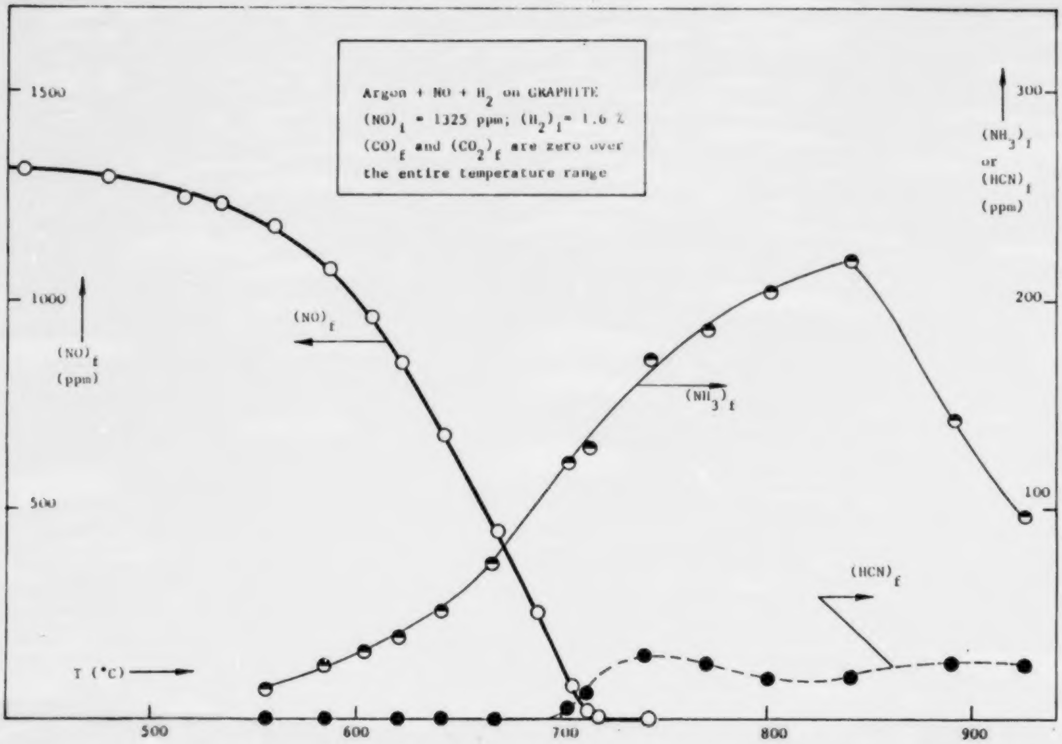

Figure 10. Argon + NO + Hydrogen on Graphite
$D = 14.5\ cm^3s^{-1}$; $(NO)_i = 1325$ ppm; $(H_2)_i = 1.60\%$

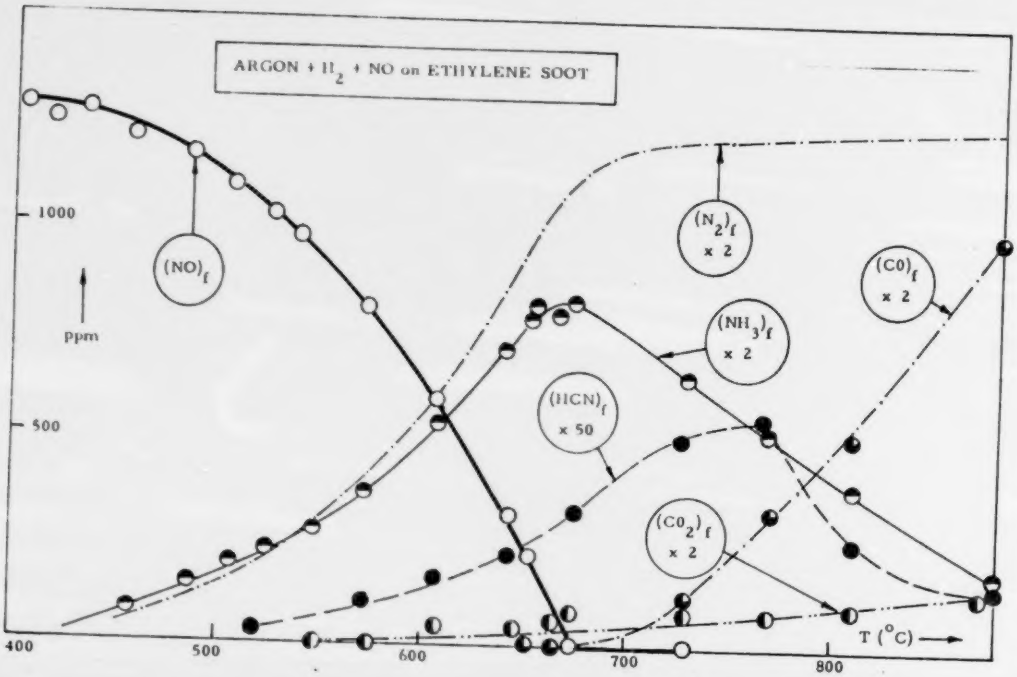

Figure 11. Argon + NO + Hydrogen on Ethylene Soot
D = 14.3 cm^3s^{-1}; $(NO)_i$ = 1280 ppm; $(H_2)_i$ = 5.52%

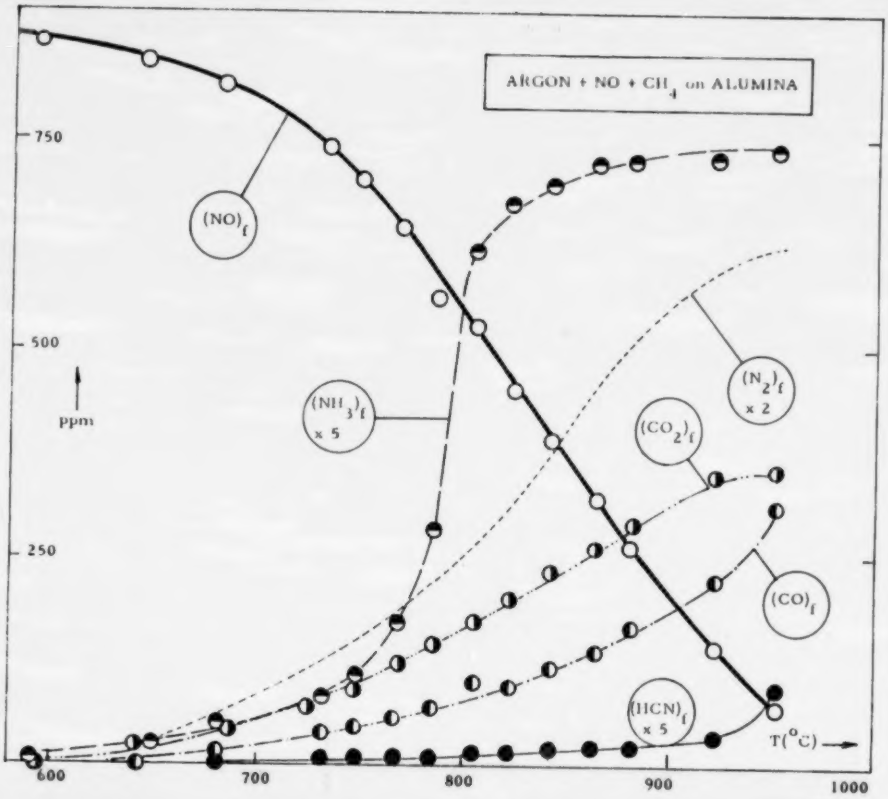

Figure 12. Argon + NO + Methane on Alumina
D = 12.6 cm^{3}s^{-1}; $(NO)_i$ = 900 ppm; $(CH_4)_i$ = 0.29%

This intermediate formation of ammonia delays the final transformation of nitric oxide into molecular nitrogen by the existence of a set of secondary reactions, the role of which is the further transformation of ammonia into N_2. This transformation of ammonia into molecular nitrogen is clearly suggested by the evolution of the experimental $(NH_3)_f/T$ curves in Figures 6, 10 and 11. A detailed study shows that this transformation of ammonia into N_2 may occur either directly or indirectly, passing over the intermediate formation of hydrocyanic acid:

a. Secondary reactions of direct transformation of ammonia into N_2.

1) Reaction of ammonia with ammonia, according to the following heterogeneous gas + gas reaction:

$$NH_3 \xrightarrow{13} 0.5\ N_2 + 1.5\ H_2$$

This secondary reaction has been identified and studied upon feeding ammonia-containing argon over the solid particles (i.e., transforming it into a primary reaction). Experimental runs are shown in Figures 13 (on alumina, = case D.1), 14 (on graphite, = case D.2), 15 (on ethylene soot, = case D.4) and 16 (on cenospherical soot, - case D.5). The CO release observed in Figure 15 is accounted for by pyrolysis of the ethylene soot, as was checked by trials in which pure argon was fed over this soot. Its existence, however, potentially switches the secondary reaction (9) into the mechanism (see below).

2) Reaction of ammonia with nitric oxide, according to the following heterogeneous gas + gas reaction:

$$NO + n\ NH_3 \xrightarrow{4} \left(\frac{1+n}{2}\right) N_2 + H_2O + \left(\frac{3n-2}{2}\right) H_2$$

(where $0.7 < n < 1$, n being close to 1 for soot)

This secondary reaction was studied as a primary reaction upon feeding $NO + NH_3$ over the solid particles. Examples

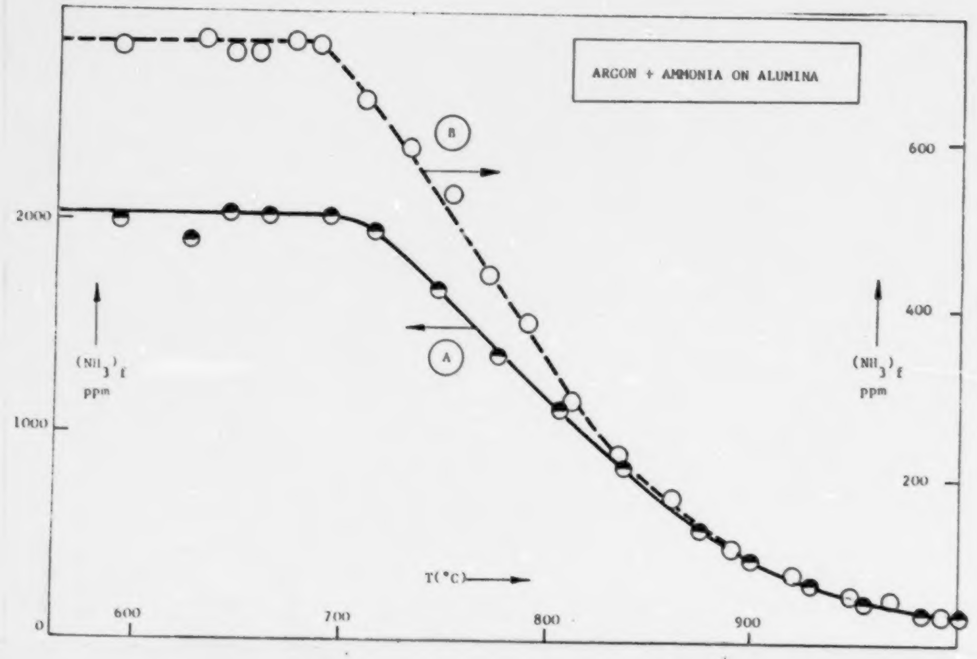

Figure 13. Argon + Ammonia on Alumina
Lower Curve (A) : D = 14.6 cm^3s^{-1}; $(NH_3)_i$ = 2030 ppm
Upper Curve (B) : D = 15.0 cm^3s^{-1}; $(NH_3)_i$ = 715 ppm

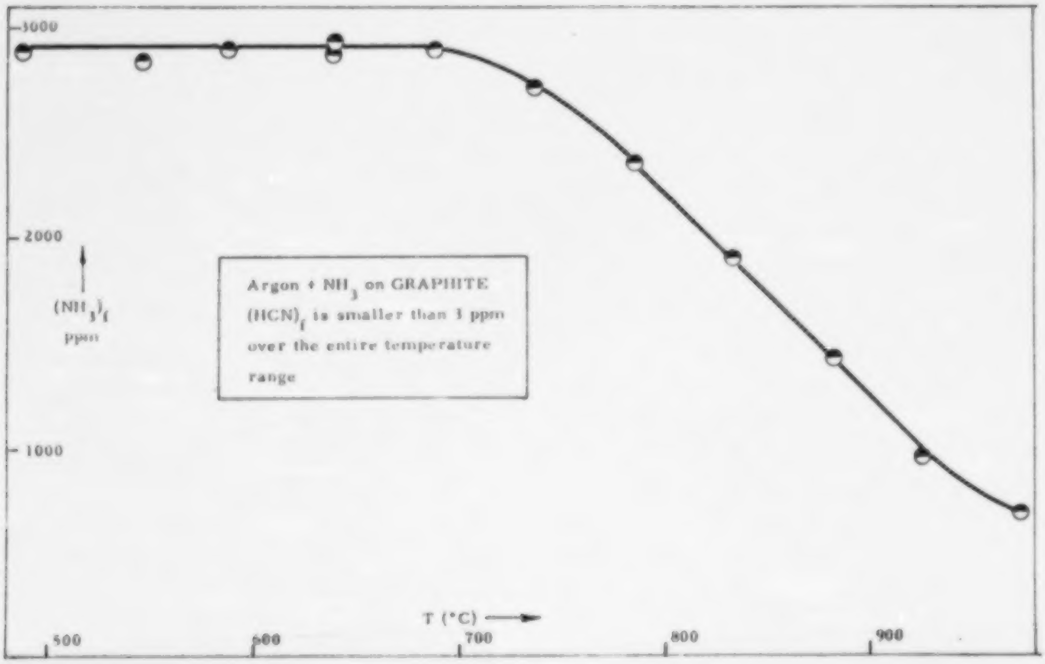

Figure 14. Argon + Ammonia on Graphite
$D = 13.3\ cm^3 s^{-1}$; $(NH_3)_i = 2900$ ppm

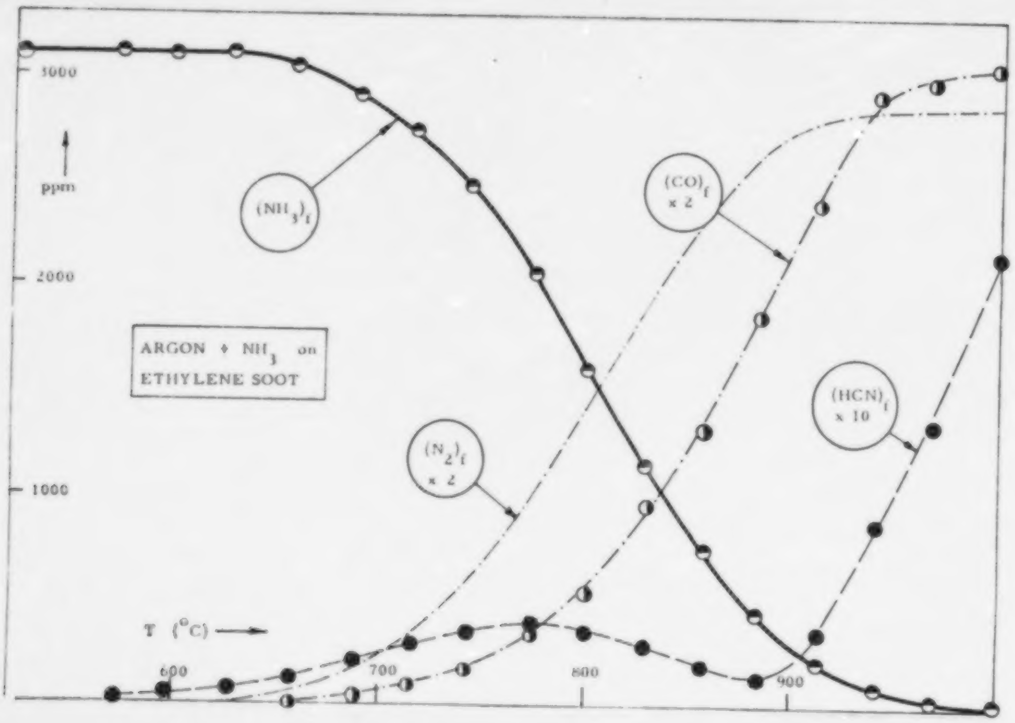

Figure 15. Argon + Ammonia on Ethylene Soot
D = 12.4 cm^{3}s^{-1}; (NH$_3$)$_i$ = 3100 ppm

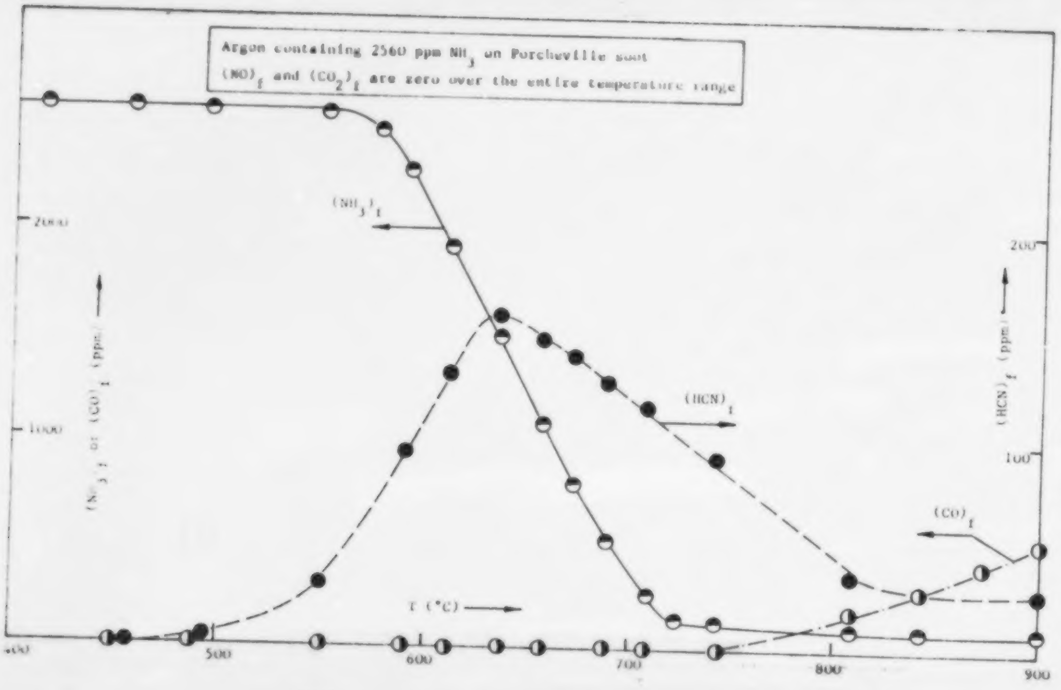

Figure 16. Argon + Ammonia on Porcheville Soot
$D = 14.5\ cm^3s^{-1}$; $(NH_3)_i = 2560$ ppm

of the experimental results are shown in Figures 17 (on alumina, - case R.1), 18 (on graphite, - case R.2), 19 (on ethylene soot, = case R.4) and 20 (on cenospherical soot, = case R.5). In these trials the primary reactions (1), (2) and (13) enter in competition with reaction (4). However, reactions (1) and (13) generally occur at temperatures beyond those where reaction (4) takes place, as is the case for alumina (in Figure 17 one may observe a good separation of reactions (4) and (13), the further decrease of ammonia at T >700°C being exclusively due to the latter).

3. On solids having bound nitrogen atoms (as is the case for cenospherical soot) a supplementary secondary reaction of direct transformation of ammonia into molecular nitrogen might occur:

$$NH_3 + (-N) \rightarrow N_2 + \dots$$

However, with the actual experimental equipment this reaction could not be identified.

b. Secondary reactions of indirect transformation of ammonia into N_2, passing over the intermediate formation of hydrocyanic acid. The formation of HCN, as an intermediate species, from ammonia is clearly suggested in Figures 15, 16, 19 and 20 (where ammonia is present in the inlet flow alone or in combination with NO), as well as in Figures 8 through 11 (where NH_3 is formed as an intermediate); the only requirement is that there be a carbon source present. Two kinds of reaction paths of HCN formation from ammonia have been idenfieid:

1) In all cases the solid + gas reaction between ammonia and solid bound carbon atoms leads to HCN formation, mostly at relatively high temperatures:

$$NH_3 + (-C) \xrightarrow{5} HCN + H_2$$

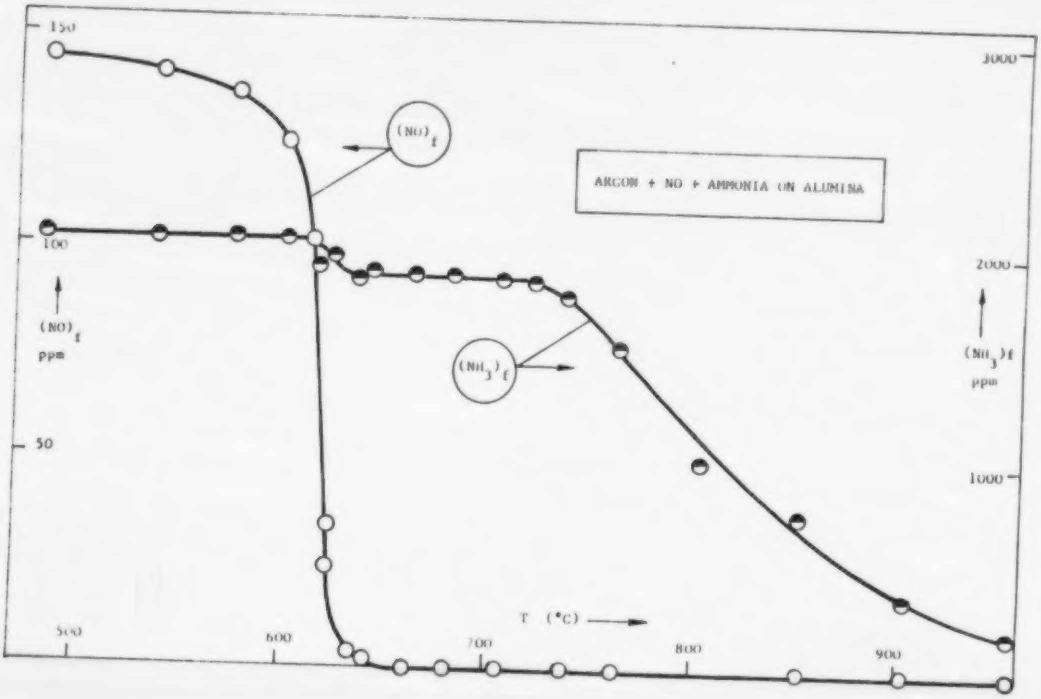

Figure 17. Argon + Ammonia + NO on Alumina
D = 14.6 cm^3s^{-1}; $(NH_3)_i$ = 2040 ppm; $(NO)_i$ = 144 ppm

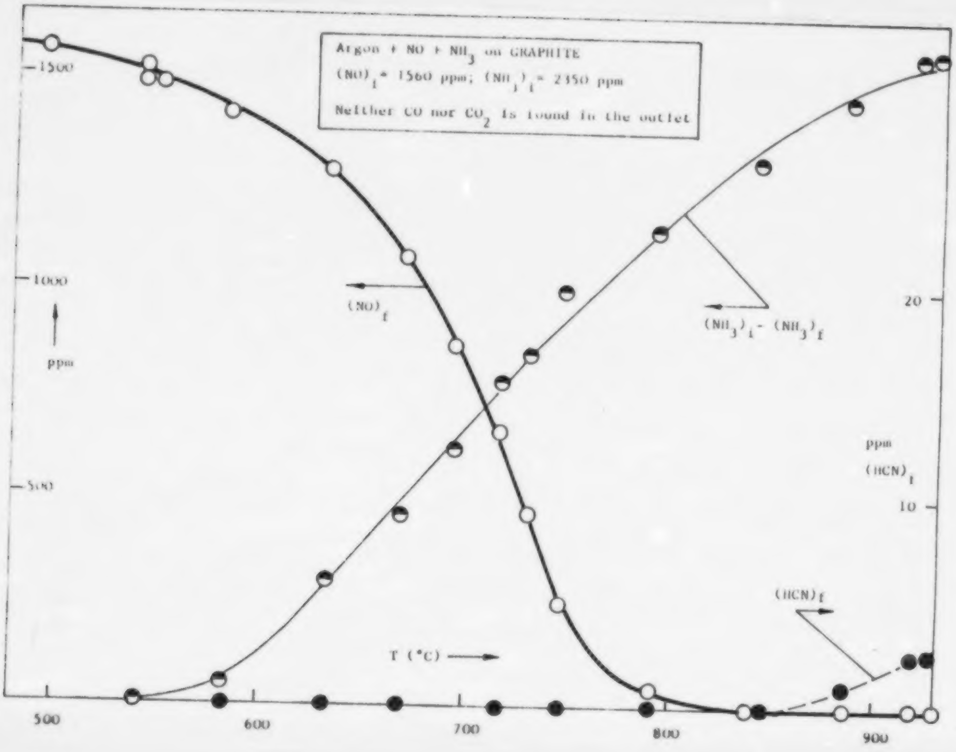

Figure 18. Argon + Ammonia + NO on Graphite
D = 14.5 cm^3s^{-1}; $(NO)_i$ = 1560 ppm; $(NH_3)_i$ = 2350 ppm

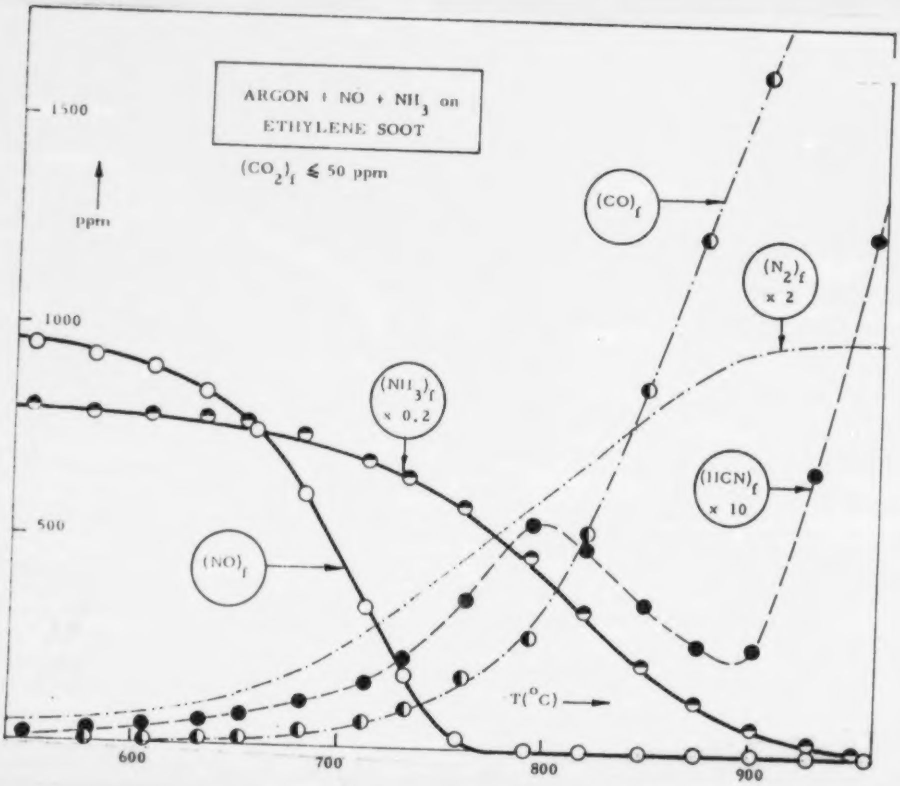

Figure 19. Argon + NO + Ammonia on Ethylene Soot
D = 12.0 $cm^3 s^{-1}$; $(NO)_i$ = 1040 ppm; $(NH_3)_i$ = 4150 ppm

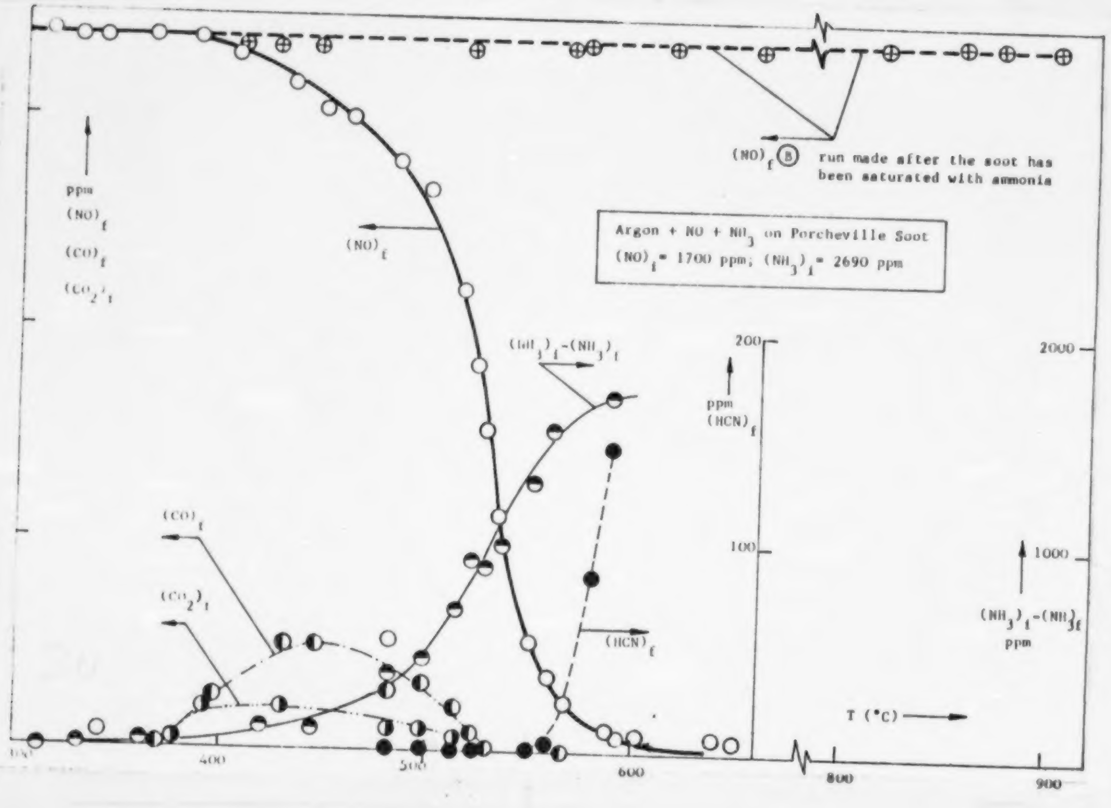

Figure 20. Argon + NO + Ammonia on Porcheville Soot
$\dot{D} = 14.5\ cm^3s^{-1}$; $(NO)_i = 1700$ ppm; $(NH_3)_i = 2690$ ppm

2) In the absence of H_2O, carbon monoxide acts as a carbon source for the formation of HCN from ammonia, by a heterogeneous gas + gas reaction:

$$NH_3 + CO \xrightarrow{9} HCN + H_2O$$

This secondary reaction has been studied as a primary one, upon feeding NH_3 + CO over alumina (= case I.1, see Figure 21), since in that case H_2O is exclusively formed by reaction (9), and therefore, never exceeds the initial ammonia concentration. When feeding the same NH_3 + CO mixture over solids containing bound H atoms (ethylene soot or cenospherical soot, = cases I.4 and I.5), it is found, upon treatment of the results, that the HCN formed in these cases (see Figures 22 and 23) is almost totally accounted for by reaction (5). When water vapor is present in sufficient quantities reaction (9) is never observed since the reverse reaction

F21

F22, 23

$$HCN + H_2O \xrightarrow{44} NH_3 + CO$$

is much faster, as has been shown by recent trials in which HCN and water vapor are fed over alumina. Up to temperatures far beyond 1000°C the equilibrium between reactions (9) and (44) is almost completely shifted towards ammonia.

The intermediate formation of hydrocyanic acid from ammonia further delays the ultimate transformation of nitric oxide into molecular nitrogen (clearly visible in Figure 21) by the existence of second order secondary reactions, which are responsible for the definite transformation of HCN into N_2. Potential reactions of this type are, for example:

$$NH_3 + HCN \xrightarrow{10} N_2 + \ldots$$

$$HCN \xrightarrow{15} 0.5\ N_2 + \ldots$$

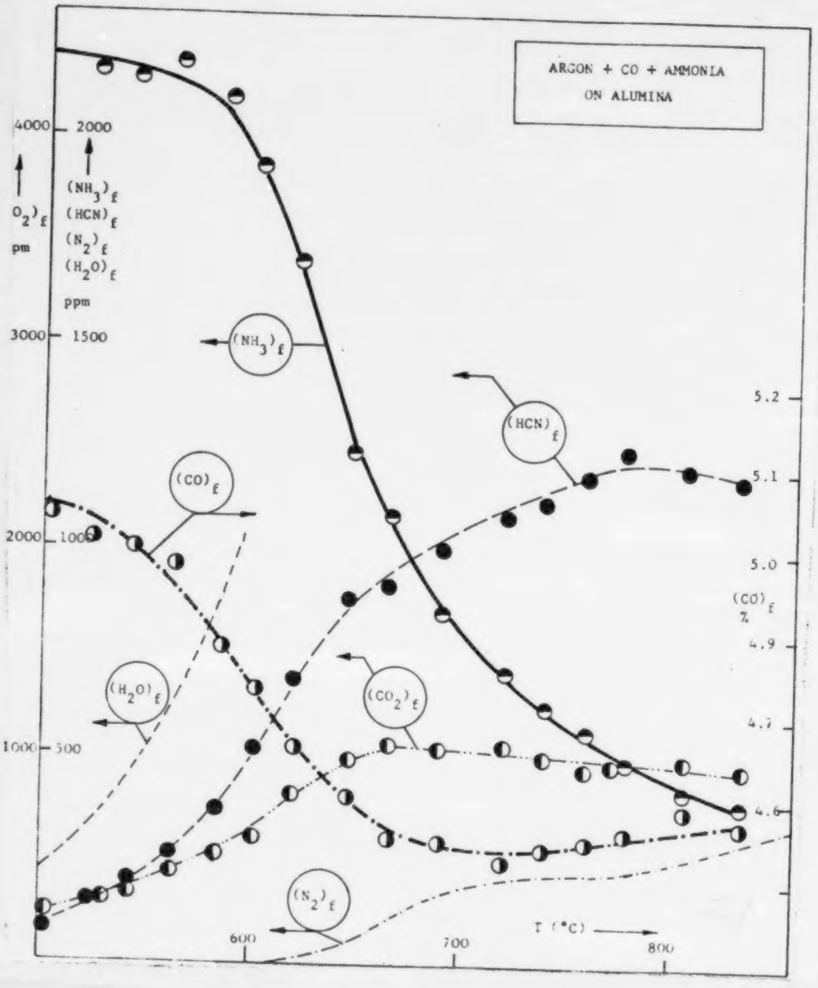

Figure 21. Argon + Ammonia + CO on Alumina
D = 14.2 cm^3s^{-1}; $(NH_3)_i$ = 2400 ppm; $(CO)_i$ = 5.09%

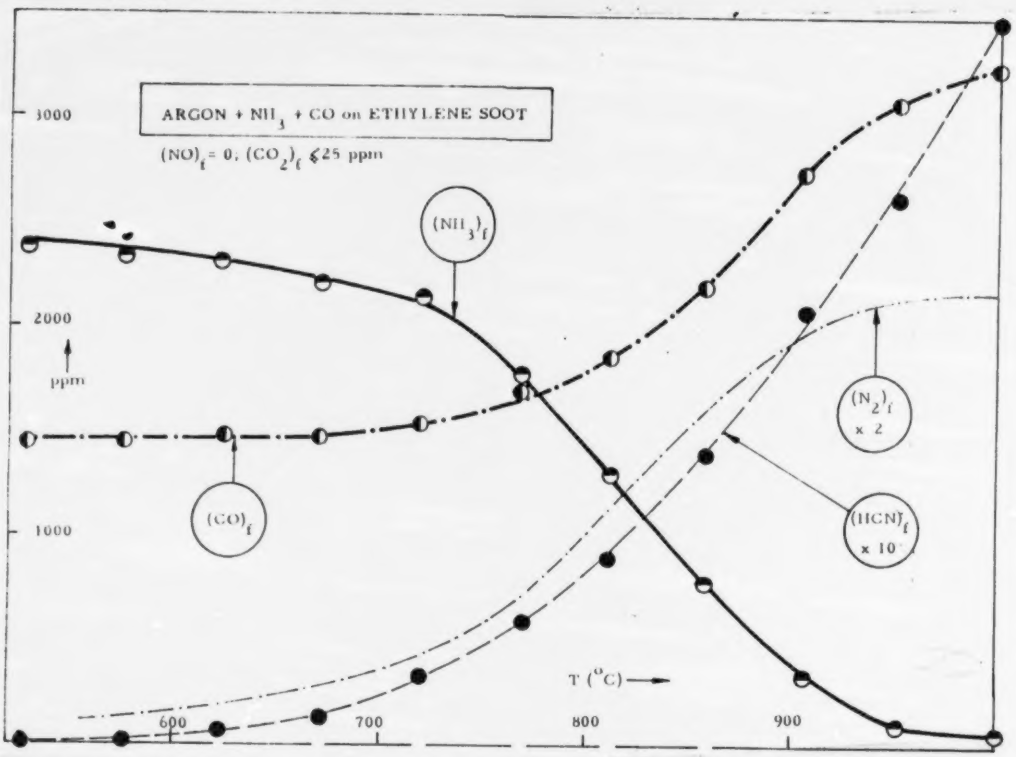

Figure 22. Argon + Ammonia + CO on Ethylene Soot
$D = 13.3\ cm^3 s^{-1}$; $(NH_3)_i = 1540$ ppm; $(CO)_i = 0.15\%$

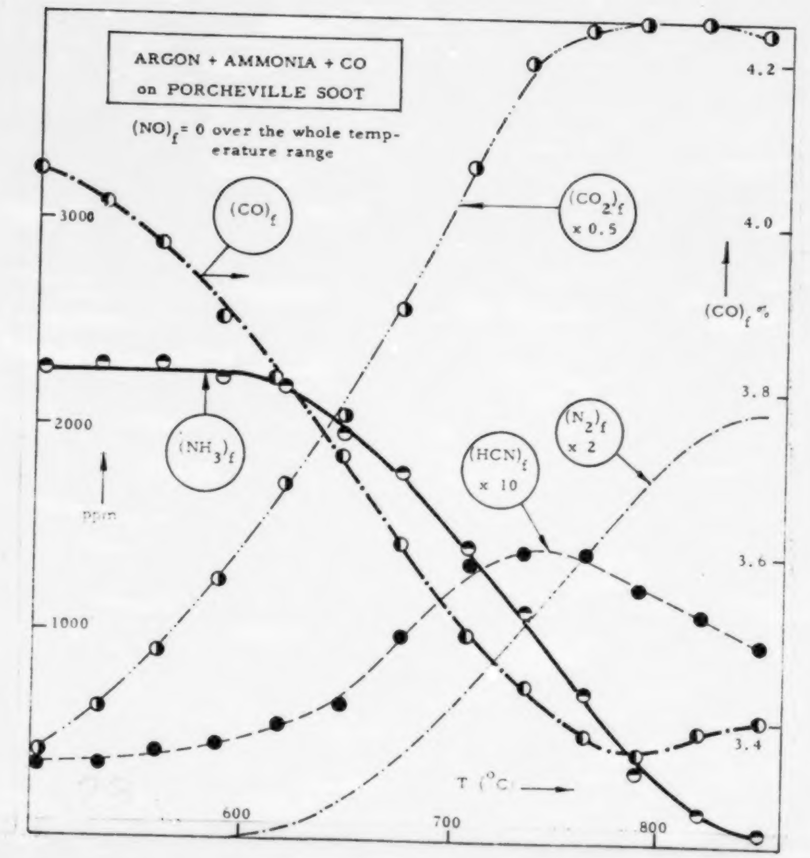

Figure 23. Argon + Ammonia + CO on Porcheville Soot
$D = 12.6\ cm^3s^{-1}$; $(NH_3)_i = 2270$ ppm; $(CO)_i = 4.15\%$

$$HCN + (-N) \xrightarrow{27} N_2 + \ldots$$

$$HCN + NO \xrightarrow{40} N_2 + \ldots$$

as well as the already mentioned reaction (44). The identification and study of these secondary reactions by trials where HCN, alone or in combination with other gases, is fed over solid particles, is actually in progress.

Qualitative indications already exist which show that reaction (10) is generally negligible, whereas reactions (15) and (40) have relatively important finite rates at higher temperatures.

Effects of Molecular Oxygen on Heterogeneous NO Reduction

In all cases where the effects of O_2 were to be elucidated by trials in which oxygen was added to the NO or other nitrogen species containing gas flows, a previous study was made on the oxidation behavior of the solid and combustible gases by performing trials in which oxygen was added in the absence of nitric oxide.

Summarizing the results obtained when molecular oxygen was added to the gas flow one finds strongly inhibiting effects, as well as nonnegligible promoting effects on the heterogeneous NO reducing mechanisms.

Inhibition of NO Reduction by Oxygen

Two typical cases of inhibition have been identified and studies: (1) in the case of heterogeneous NO reduction by molecular hydrogen, and (2) in the case of heterogeneous NO reduction without gaseous reducing agent when oxidation of soot by O_2 yields preferentially CO_2 rather than CO.

Inhibiting Effect of Oxygen on the Heterogeneous Reduction of NO by H_2.

This is illustrated in Figure 24 showing NO decrease in the presence of hydrogen as a function of temperature for increasing amounts of oxygen added. The treatment of these results shows that the effect of oxygen results in a decrease of the overall NO removal rate by multiplying it by a factor $1/[1 + 1.1\ 10^8 \exp(-6000/T)X_{O_2}^2]$(see Table 4, comparing $\overline{V_{0.1}}$ and $\overline{V_{NOT.1}}$). This inhibiting effect is not accounted for by the mere oxidation of the reducing

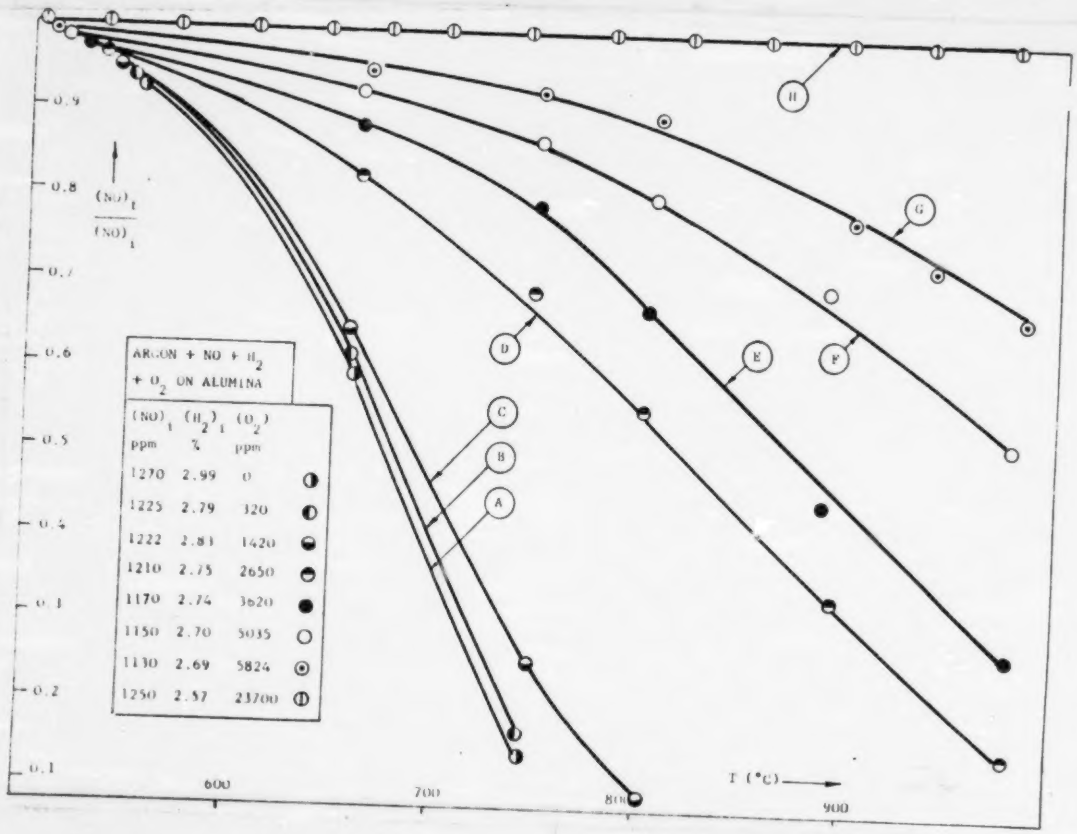

Figure 24. Argon + NO + Hydrogen + O_2 on Alumina
$D = 14.8\ cm^3s^{-1}$; effect of initial oxygen concentration on NO removal as a function of temperature

agent (H_2) nor by the increase in NO due to reaction path (17) (see below). The effect is probably due to preferential O_2 adsorption on the active sites, shielding them against NO adsorption (which is normally required for the NO reduction).

Inhibiting Effect of Oxygen on the Heterogeneous NO Reduction. In the cases where the oxidation of soot by molecular oxygen yields preferentially CO_2 rather than CO (which is the case of the cenospherical soot from heavy fuel oil combustion, used in this study, see Figure 25), the presence of oxygen decreases the overall NO removal rate, as shown, for example, in Figure 26. Again, this inhibiting effect is not accounted for by the mere oxidation of the solid, but rather by the preferential adsorption of O_2 on the active sites. The quantitative treatment of this inhibiting effect may be seen upon comparing the overall reaction rates $\overline{V_{T5}}$ and $\overline{V_{F5}}$, given in Table 4.

Promotion Effects of Oxygen on Heterogeneous NO Reduction

Three types of promoting effects have been detected:

Promoting Effect of Oxygen on the Heterogeneous NO Reduction by CO. When adding oxygen to a NO + CO mixture flowing over alumina, one observes that the overall NO removal rate is increased by a factor of $(1 + 43\ X_{O_2}^{0.35})$ (compare reaction rates $\overline{V_{JKT.1}}$ and $\overline{V_{K.1}}$ in Table 4). The treatment of the results shows that this promoting effect consists of an enhancement of reaction path (8). Actually, the reactant CO plays a self-inhibiting role on reaction (8) due to preferential CO adsorption (thus, decreasing the required NO adsorption probability). The oxidation of the adsorbed CO by molecular oxygen is, therefore, expected to enhance reaction (8) by decreasing its self-inhibition, insofar as the preferential O_2 adsorption (which is an inhibiting effect, like in the case of H_2) is not prevailing.

Promoting Effect of Oxygen on NO Reduction in the Absence of Gaseous Reducing Agents in the Inlet Flow. In the cases where the oxidation of soot by molecular oxygen yields nonnegligible quantities of CO (as in the case for ethylene soot, see Figure 27), reaction path (8) occurs in competition with other hetergoeneous NO reducing reactions (reactions 1 and 2) and results in an enhancement of the overall NO removal rate ($\overline{V_{T4}}$), as illustrated in

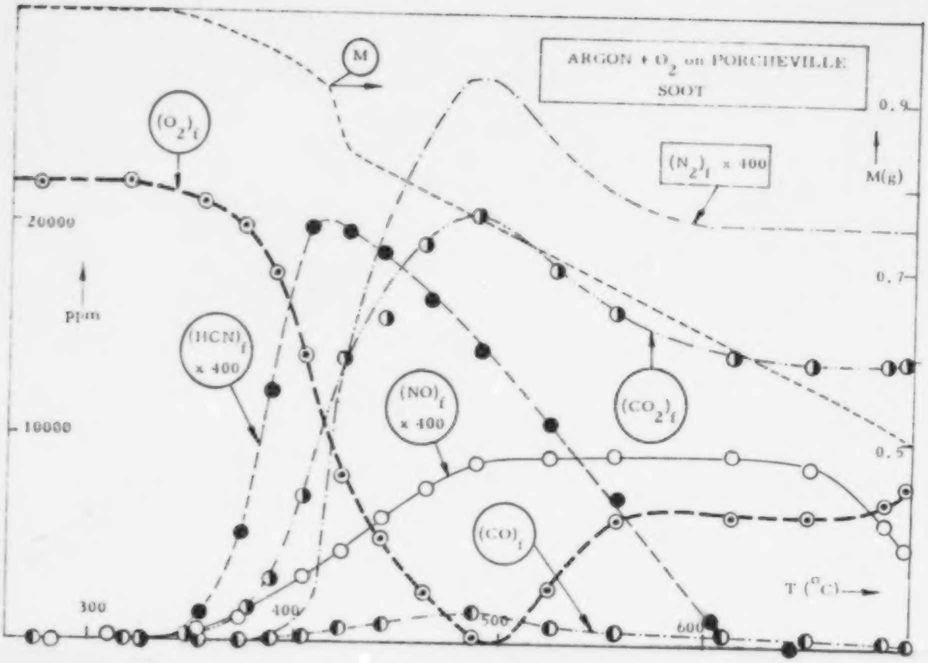

Figure 25. Argon + O_2 on Porcheville Soot
$D = 13.4\ cm^3 s^{-1}$; $(O_2)_i = 2.19\%$

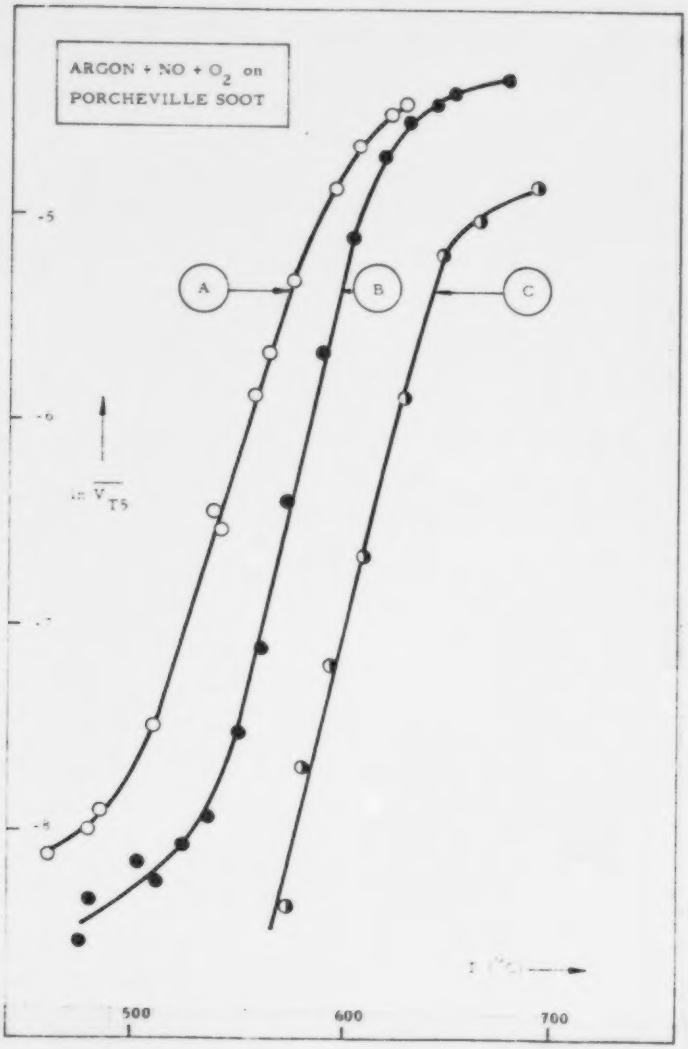

Figure 26. Argon + NO + O_2 on Porcheville Soot Variation of the overall NO removal rate $\overline{V_{T5}}$, calculated from Eq. (5), as a function of temperature for three different initial oxygen concentrations; curve A: $(O_2)_i = 0.06\%$; curve B: $(O_2)_i = 0.82\%$; curve C: $(O_2)_i = 5.04\%$; $(NO)_i = 1310$ ppm

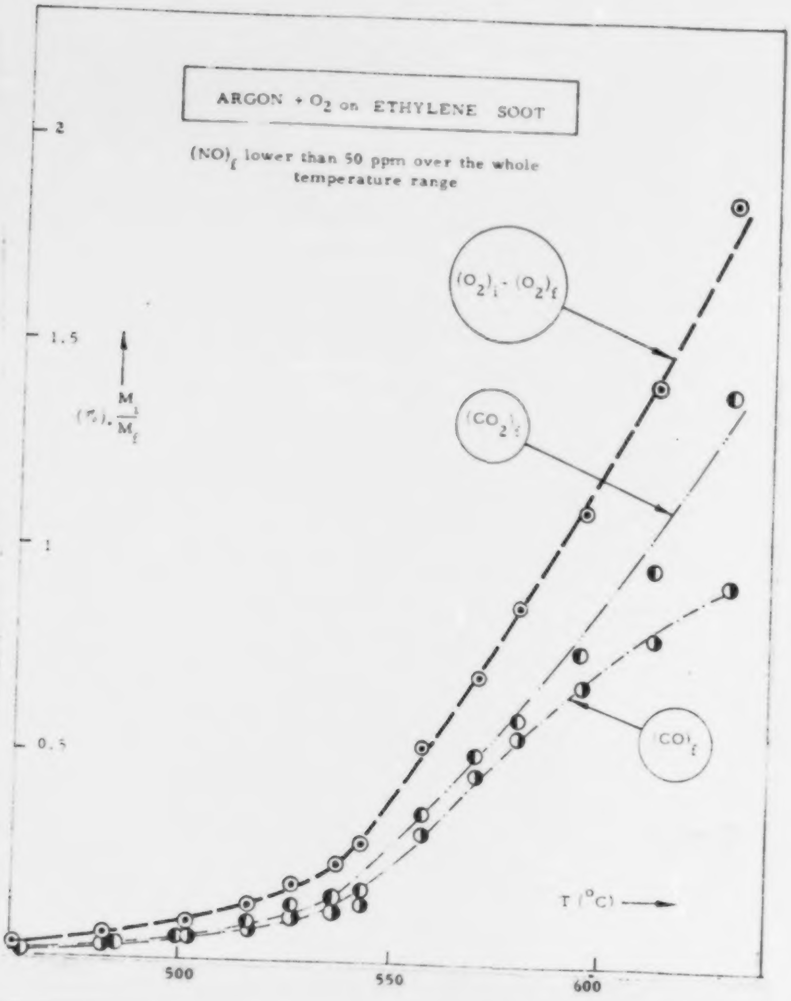

Figure 27. Argon + Oxygen on Ethylene Soot
$D = 12.3\ cm^3 s^{-1}$; $(O_2)_i = 2.12\ \%$

Figure 28 in the case of ethylene soot. A quantitative treatment shows that this overall NO removal reaction is multiplied by a factor $(1 + 33\ X_{O_2}^{0.25})$ as may be seen from the comparison of reaction rates $\overline{V_{F4}}$ and $\overline{V_{T4}}$, given in Table 4.

Promoting Effect of Oxygen on the Secondary Reactions of Transformation of Ammonia into Molecular Nitrogen. As already has been stressed (see Indirect Transformation of NO), the intermediate formation of ammonia delays the final transformation of NO into N_2; the importance of that delay depending on the number and the rate of the secondary reactions by which NH_3 is finally transformed into N_2. The promoting effect of oxygen here precisely consists of adding a supplementary secondary reaction which mainly leads to the transformation of NH_3 into N_2. Actually, upon reacting with ammonia, oxygen performs a dismutation of NH_3 into NO and N_2 according to the following overall reactions:

$$NH_3 + 0.75\ O_2 \xrightarrow{16} 0.5\ N_2 + 1.5\ H_2O$$

$$NH_3 + 1.25\ O_2 \xrightarrow{17} NO + 1.5\ H_2O$$

The identification of these stoichiometries and the study of these two overall reaction paths has been performed on feeding $NH_3 + O_2$ mixtures over the solid particles, as illustrated by Figures 29 (alumina, = case Q.1) and 30 (ethylene soot, = case Q.4).

Up to very high oxygen concentrations, this dismutation of ammonia is always in favor of N_2 formation; the ratio $(N_2)_f/(NO)_f$ always being much larger than one. Figure 31 shows the positive effect of oxygen concentration on the overall relative decrease of ammonia as a function of temperature due to the increasing importance of reaction paths (16) and (17).

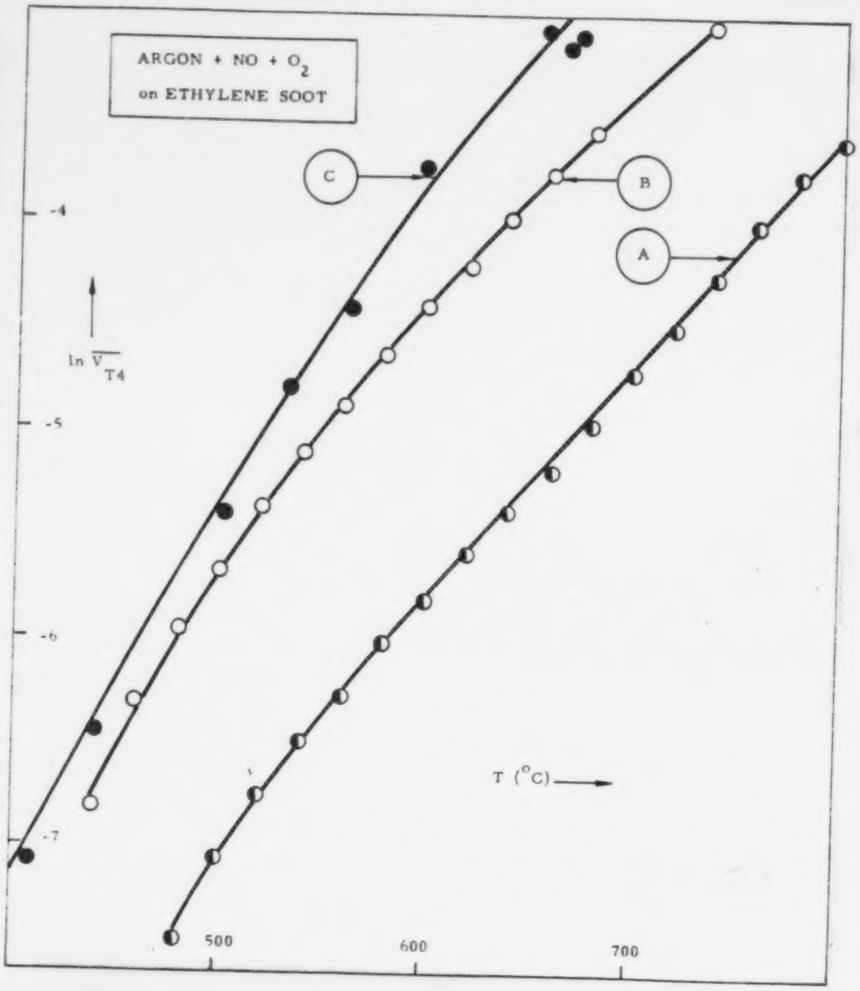

Figure 28. Argon + NO + O_2 on Ethylene Soot
$D = 12.4\ cm^3 s^{-1}$; $(NO)_i = 940$ ppm; curve A: $(O_2)_i = 0$;
curve B: $(O_2)_i = 1.56\%$, curve C: $(O_2)_i = 2.53\%$

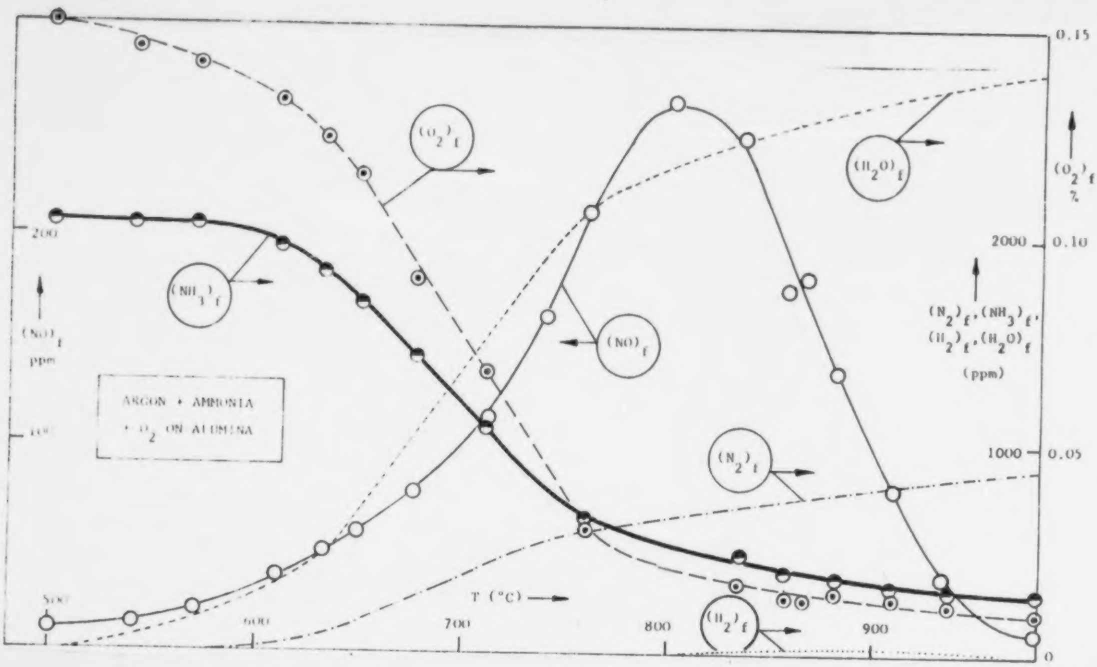

Figure 29. Argon + Ammonia + O_2 on Alumina
D = 14.6 cm^3s^{-1}; $(NH_3)_i$ = 2050 ppm; $(O_2)_i$ = 0.15%

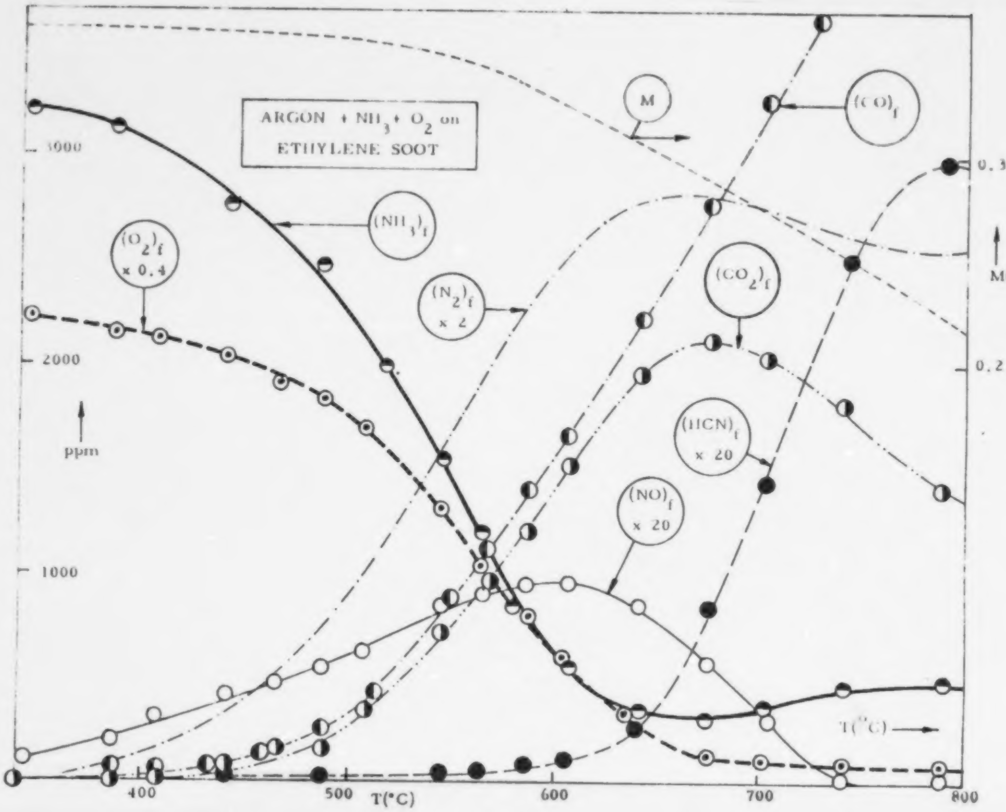

Figure 30. Argon + Ammonia + O_2 on Ethylene Soot
D = 13.4 cm^3s^{-1}; $(NH_3)_i$ = 3200 ppm; $(O_2)_i$ = 0.55%

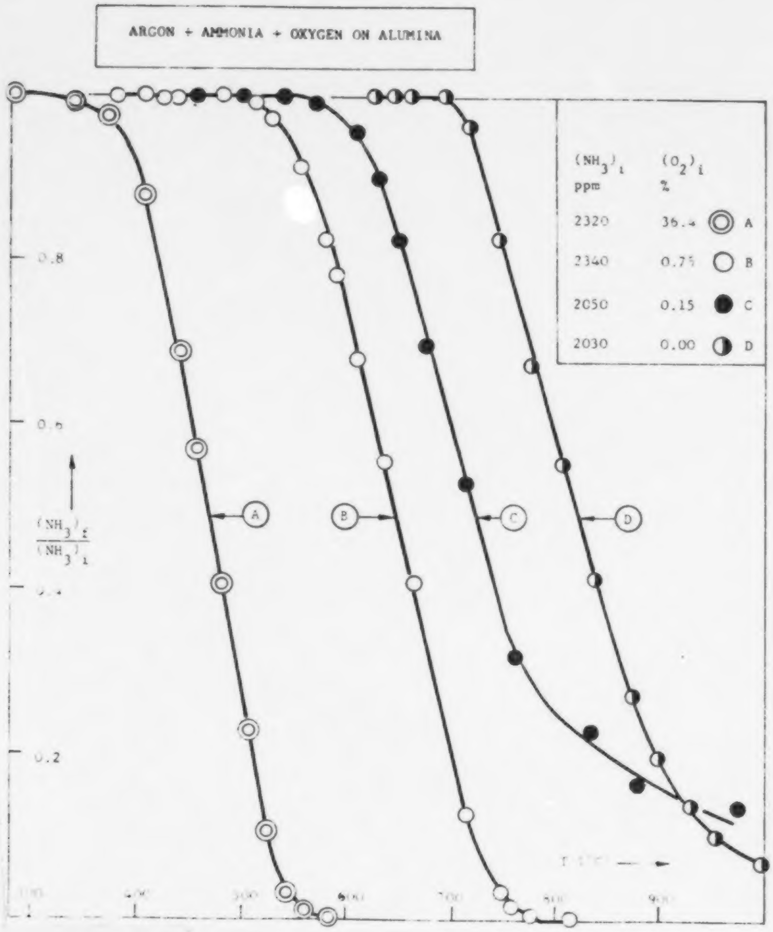

Figure 31. Argon + Ammonia + O_2 on Alumina
D = 14.3 to 15.3 cm^3s^{-1}; effect of oxygen concentration on NH_3 removal

REFERENCES

1. Shelef, M. and J. T. Kummer, Chemical Engineering Progress, Symposium Series 67 (No. 115), 1971, 74.
2. Yureva, T. M., V. V. Popovskii and G. K. Boreskov, Kinetika i Kataliz, 6, 1965, I041.
3. Winter, E. R. S., Journ, Catal., 22, 1971, 158.
4. Shelev, M. and H. S. Gandhi, Platinum Metals Rev., 18, 1974, 2.
5. Kobylinski, T. P. and B. W. Taylor, Journ, Catal., 33, 1974, 376.
6. Klimisch, R. L. and J. G. Larson, "The Catalytic Chemistry of Nitrogen Oxides" (Symposium on the Catalytic Chemistry of Nitrogen Oxides, Warren, Michigan, 1974), Plenum Press, New York, 1975.
7. Tucker, J. R., "The Reduction of Nitric Oxide on Activated Carbon at Elevated Temperatures", Ph. D. thesis, Clemson University, South Carolina, 1974.
8. Sheppard, W. M., "A Kinetic Study of the Reaction of Nitric Oxide and Activated Carbon", Ph. D. thesis, Clemson University, South Carolina, 1974.
9. Edwards, H. W., AIChE Symposium Series, No. 126, 68, 91, 1972.
10. Cerney, A. and Z. Dobovisek, Fourth International Clean Air Congress, 1977, Proceedings p. 447.
11. Bedjal, G., H. K. Orbach, and F. C. Riesenfeld, Ind. Eng. Chem. 50, 1958, 1165.
12. Puri, B. R., D. D. Singh, P. Kumar and L. R. Sharma, Chemistry and Industry, 1958, 1291.
13. Smith, R. N., J. Swinehart and D. Lesnini, Journ. of Phys, Chem. 63, 1959, 544.
14. De Soete, G. G., Internal Report I.F.P., No. 23309, June 1975.
15. Levenspiel, O., "Chemical Reaction Engineering", John Wiley and Sons, Inc., New York, 1962, Ch. 14.
16. De Soete, G. G., Internal Report I.F.P., No. 27622, December 1979.

SESSION II

THERMAL DECOMPOSITION--CHEMICAL AND PHYSICAL EFFECTS

A. F. SAROFIM
SESSION CHAIRMAN

VOLATILITY OF FUEL NITROGEN

R. L. Gay, A. E. Axworthy, V. H. Dayan and H. L. Recht
Energy Systems Group
Rockwell International
8900 De Soto Avenue
Canoga Park, California 91304

Fifth EPA Fundamental Combustion Research Workshop
Newport Beach, California
January 23-25, 1980

ABSTRACT

An experimental program has been completed for the measurement of fuel nitrogen volatility using a quartz two-stage pyrolysis reactor. Solid and liquid fossil fuels were heated in helium in the first stage of the reactor at selected temperatures up to 1100°C. The volatile nitrogen compounds released were measured by converting them to HCN in the second stage of the reactor at 1100°C. The HCN was collected in dilute sodium carbonate solution and measured colorimetrically.

Twenty fossil fuel samples consisting of petroleium-based fuel oils, synthetic oils from coal and shale, and coals were studied. All of the samples tested produced the greatest yields of volatile nitrogen compounds at a first-stage temperature of 1100°C. The maximum yields of volatile nitrogen from petroleum fuel oils were 35-48% of the nitrogen in the sample. The yield curves increased continuously from 300°C with a slight dip at 600-750°C. The maximum volatile nitrogen yields from shale oils were 70-79%, while the coal liquids yielded 50%. The nitrogen species in shale oils were very volatile at low temperatures, giving HCN yields of about 65% at a pyrolysis temperature of only 200°C.

A variety of bituminous and lignite coals were tested. In general, the coals exhibited much lower fuel nitrogen evolution than did the fuel oils. Maximum coal volatile nitrogen yields obtained at a pyrolysis temperature of 1100°C were about 15-25%. A plot of the percentage of fuel nitrogen converted to NO during combustion (measured elsewhere) vs the percentage of fuel nitrogen volatilized at 1100°C was found to give a strong linear correlation with a variety of coals. The slope of this line was 2, indicating that twice as much fuel nitrogen is converted to NO in combustion than is volatilized at 1100°C in the inert pyrolysis experiments. This correlation may provide an excellent means of predicting NO formation for any given coal simply by measuring its nitrogen volatility at 1100°C.

ACKNOWLEDGMENT

This research was supported by the U. S. Environmental Protection Agency under Subcontract No. EER-8318-4 from the Energy and Environmental Research Corporation. We wish to gratefully acknowledge the technical supervision of Dr. C. L. Nealy and technical assistance of Mr. D. O. Woolery during this program.

SECTION I

INTRODUCTION

The formation of NO_x in the combustion of fossil fuels is controlled by a number of physical and chemical processes. Sarofim, et al, (Ref. 1) have reviewed the types of chemical processes involved, and Wendt and Pershing (Ref. 2) have considered the physical mechanisms governing NO_x formation in pulverized coal flames. Different types of physical processes may be important in the combustion of solid and liquid fuels.

One of the more important "physical" factors in fuel NO_x formation is the rate at which the "volatile" fuel nitrogen is evolved from the fuel droplets or particles at various points in the combustion zone (Refs. 2-4). This evolution rate determines, in part, the conditions such as temperature and oxygen concentration under which the nitrogen reacts and is believed to strongly affect the ratio of NO to N_2 formed (Refs. 1, 2). The rate at which fuel nitrogen is evolved from coals under pyrolysis conditions has been measured as a functon of temperature in rapid-heating experiments (Ref. 5), and the total amount of volatile nitrogen evolved has been measured in both rapid-heating and long-term experiments (Refs. 3-6).

Detailed measurements have not been reported of the volatility of the bound nitrogen contained in liquid fuels. Based on distillation experiments, however, much of the nitrogen in coal-derived liquids and in shale oil is believed to be considerably more volatile than the nitrogen contained in petroleum crudes. This difference between the volatility distributions of the fuel nitrogen compounds of alternative liquid fuels and those of petroleum-based oils may have a major effect on the amount of fuel NO_x that forms under various combustion conditions.

In order to model even semiempirically the conversion of fuel nitrogen to NO and N_2 in combustion and the effects of combustion modification techniques on this conversion, it is necessary to estimate the rate of evolution of volatile nitrogen from various fuels at each point within the combustor (Refs. 1, 2). The most detailed method for obtaining data for coals that relate to this process appears to be that employed by Pohl, Sarofim, and Howard at MIT (Ref. 5). There was, however, a need for a simplified experimental procedure for investigating the volatility range distribution of the nitrogen in a variety of fuel samples. Such information has been obtained during the present program for a rather large number of fuels and fuel types. These data will permit the optimum combustion conditions for each type of fuel to be evaluated (by use of semiempirical models). Also, these preliminary nitrogen volatility data supplement the more detailed data being obtained in the MIT program for selected fuel samples and include fuel types that may not be suitable for the MIT apparatus.

Another consideration is the possibility that all of the nitrogen species evolved from fossil fuels may not be equally reactive in the formation of fuel NO_x. The evidence available at present suggests that this is not the case, but the possibility does exist. The techniques employed prior to this work to investigate nitrogen evolution from heated coal particles involved measuring the amount of nitrogen remaining in the char or residue and obtaining the total nitrogen loss by difference. The nature of the experimental procedure used in the present investigation is such that only volatile nitrogen species capable of further reaction to form NO_x in combustion are measured.

It was found in a previous EPA-sponsored program (Refs. 7, 8) performed by Rockwell that in a two-stage inert pyrolysis reactor, the reactive volatile nitrogen evolved from the fuel in the first-stage pyrolysis process is converted to HCN in the second stage when the second stage is held at about 1100°C. This two-stage reactor technique, therefore, permits the reactive nitrogen evolved at a given first-stage temperature to be measured by converting it to HCN in the second stage and measuring the HCN formed by a very sensitive colorimetric technique. In the present program, nitrogen volatility vs temperature profiles were measured in this manner for twenty fossil fuel samples including alternative fuels derived from coals and shale oils.

SECTION II

EXPERIMENTAL

Fuel Pyrolysis Apparatus

A schematic diagram of the two-stage inert pyrolysis apparatus is shown in Figure 1. The pyrolysis section of the apparatus consisted of a two-temperature-zone quartz tube heated by two muffle furnaces. The first stage was heated to the desired pyrolysis temperature, and the second stage was maintained at a temperature of 1100°C in order to convert all of the volatile nitrogen species evolved in the first-stage pyrolysis process to HCN.* The temperature at the sample position of the first stage was held constant during a given pyrolysis experiment. Typically, the first-stage temperatures studied were 300, 500, 750 and 1100°C. Insulation around the quartz tube at the ends of the furnaces was used for thermal separation between the two zones. Only the temperature near the center of each stage had to be controlled accurately, because the initial pyrolysis process and the secondary reactions of volatiles occurred at these two points.

The quartz tube used in these experiments was a 178-cm length of 2.0 mm ID x 10.0 mm OD capillary tubing. The first zone (the pyrolysis zone) was heated over a length of 32 cm. The second zone (conversion to HCN) was heated over a length of 51 cm. The ID of the quartz tubing was enlarged in the center of the second zone to form a small, 5 cm long chamber. The purpose of this chamber was to increase the residence time in the 1100°C region and thus insure conversion of the volatile nitrogen species to HCN.

The oil or coal sample, usually 1 to 3 mg, was held in a small quartz boat or tube attached to the end of a quartz rod which fitted inside the capillary tubing. The quartz rod was connected via a Teflon tube to a stainless steel rod which was used to insert the sample into the pyrolysis zone. Helium carrier gas, set at a standard flow rate of 40 cc/min, was used to carry the volatile species through the system. The front end of the tube had provision

---

*Since all of the volatile nitrogen is converted to HCN the terms "HCN yield" and "volatile nitrogen yield" are used interchangeably in this paper.

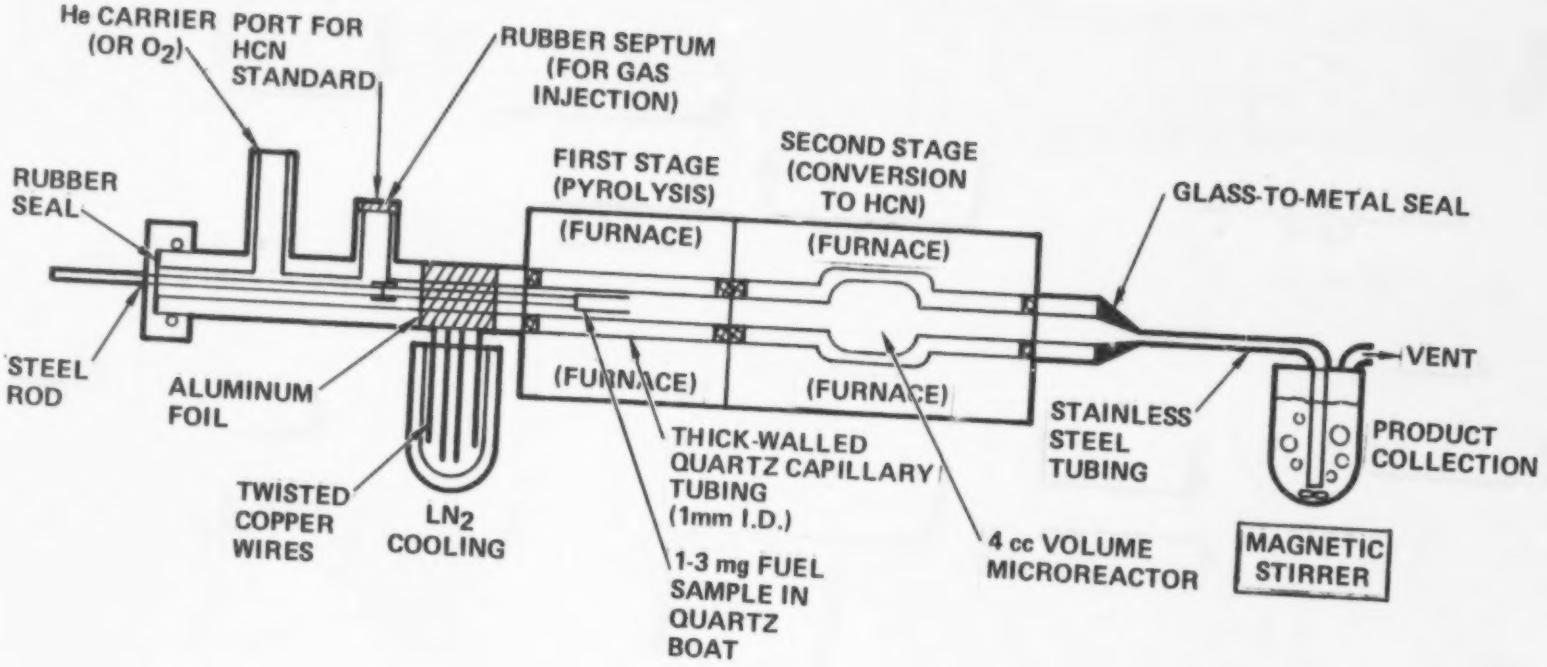

Figure 1. Inert Pyrolysis Reactor Schematic

for injection of gaseous HCN samples for standardization. A region of the tube at the entrance to the pyrolysis furnace was cooled by a metal conductor dipped in liquid nitrogen to prevent premature heating of the sample. Oxygen could also be admitted to the quartz tube to burn out deposits.

The exit of the quartz tube was connected by a glass-to-metal seal to 1.6 mm OD stainless steel tubing. For sample collection, the tubing was inserted in a small test tube containing 25 ml of dilute (5 g/ℓ) aqueous sodium carbonate solution. A small amount of cadmium carbonate powder was added to the solution to remove sulfur as CdS. The HCN was collected in the sodium carbonate solution, the solids removed by centrifugation, and the supernatant liquid analyzed for the cyanide ion according to ASTM Procedure D 2036-75 (a sensitive colorimetric analysis) (Ref. 4).

Experimental Procedure

The pyrolysis system was tested each day prior to performing pyrolysis experiments initially using an HCN-He gas mixture and later with an Ultrasystems No. 6 oil which was well characterized in terms of nitrogen volatility during this and the previous program (Refs. 7, 8). In the work with oils, it was not necessary to further condition the quartz tube before running samples. However, in order to get reproducible results with coals, it was found that a light coating of carbon (pyrolysis products) on the walls of the tube was necessary. This was produced by pyrolyzing three to four samples (1 mg each) of a Conoco low-nitrogen, lightweight No. 2 heating oil. This pretreatment was then followed by pyrolysis of the fuel samples.

The sample was placed in the quartz holder, weighed, and then inserted in the quartz reactor tube up to the liquid N_2 cooled region. It was left there for 3 to 5 min, while being purged with He, and then quickly inserted into the center of the pyrolysis zone. The pyrolysis off-gas was then collected for 3 min. The sodium carbonate collector solution was immediately centrifuged to settle solids, mainly $CdCO_3$, at the bottom of the tube. Four aliquots of the collector solution were taken for analysis. Two or more of these were analyzed as required to obtain reproducible results.

Periodically, the quartz tube was cleaned of accumulated deposits by burning out with oxygen and, if required, by then rinsing the tube with concentrated hydrofluoric acid. In the coal experiments, the tube was then preconditioned as described above.

SECTION III

TEST RESULTS AND DISCUSSION

Description of Fuels

The fuels tested in this program consisted of fuel oils, synthetic oils, and coals. The ultimate analyses of the fuel oils and synthetic oils are given in Table 1. The fuel nitrogen content of these oils varied from 0.16 wt % to 1.98 wt %. The ultimate analyses of the coals are given in Table 2. The fuel nitrogen content of the coals varied from 0.54 wt % to 1.75 wt % (as received basis). These fuels were selected because their combustion characteristics with respect to NO_x formation are being measured in other EPA-funded programs.

Procedure Verification

The procedure verification consisted of measuring the HCN yields from Ultrasystems' No. 6 fuel oil at first-stage temperatures of 250°C and 1100°C. The results obtained are shown in Curve A of Figure 2. The two-stage HCN yields obtained at 1100°C, 950°C, and 750°C (48%, 40%, and 34%, respectively) were in good agreement with those reported previously with a similar oil (Refs. 7, 8).

When the temperature was decreased below 750°C in this study, the yield surprisingly increased reaching a maximum of about 40% around 500°C. At lower temperatures, the yield decreased steadily with decreasing temperature reaching a value of 14% at 250°C.

It was not expected that an appreciable amount of the chemically-bound nitrogen in this fuel would be evolved at 250°C. This fuel oil was obtained from a Wilmington crude, and less than about 7% of the total fuel nitrogen in Wilmington crude oil is contained in the fraction that boils below 325°C (Ref. 4).

One explanation of the relatively high yield at 250°C (and the HCN yields obtained at even lower temperatures from the shale oils) would be that, because of radiative heat transfer from the second stage to the first stage, the capillary may be somewhat hotter at the boat stop position than the measured temper-

---

*Supplied to us by Ultrasystems Corporation, Irvine, California

TABLE 1

ULTIMATE ANALYSES OF FUEL OILS

Oil	Source	C, wt %	H, wt %	N, wt %	S, wt %	Ash, wt %	O, wt % (By Difference)
A	Wilmington, California[a]	85.41	11.44	0.77	1.63	0.043	0.71
B	Indonesian Malayasian	86.53	11.93	0.24	0.22	0.036	1.04
C	Gulf Coast	84.62	10.77	0.36	2.44	0.027	1.78
D	East Coast Essxex Co.	86.54	12.31	0.16	0.36	0.023	0.61
E	Middle East (Exxon)	86.78	11.95	0.18	0.67	0.012	0.41
F	Venezuelan	85.24	10.96	0.40	2.22	0.081	1.10
G	Venezuelan (Desulfurized)	85.92	12.05	0.24	0.93	0.033	0.83
H	Synthoil	-	-	1.3	0.8	-	-
I	Rocketdyne	-	-	0.62	1.05	-	-
J	Alaskan	-	-	0.51	1.63	-	-
K	Diesel Marine Fuel (Shale)	-	-	0.24	0.51	-	-
L	Crude PARAHO Shale Oil	-	-	1.98	0.67	-	-

[a] Similar to Oil A of Reference 7 and Oil H of Reference 8.

737-G.65/mec

TABLE 2

ULTIMATE ANALYSES OF COALS (AS RECEIVED BASIS)

Coal	C, wt %	H, wt %	N, wt %	S, wt %	Ash, wt %	H_2O, wt %	O, wt % (By Difference)
TRW No. 2	71.57	4.94	1.33	1.09	11.66	1.87	7.54
TRW No. 1	-	-	1.34	-	-	1.29	5.88
Utah No. 1	68.49	5.20	1.24	0.64	7.40	6.39	10.64
Scranton, ND, No. 4	42.02	2.71	0.54	0.99	7.50	34.96	11.28
Beulah, ND, No. 9	43.24	2.74	0.72	0.24	4.97	34.63	13.46
Montana Savage No. 11	41.36	2.57	0.72	0.27	4.61	36.36	14.11
Rosa, AL, No. 18	74.72	4.36	1.60	0.96	6.79	8.02	3.55
Black Creek, AL, No. 19	80.27	5.09	1.75	0.74	4.45	2.25	5.45

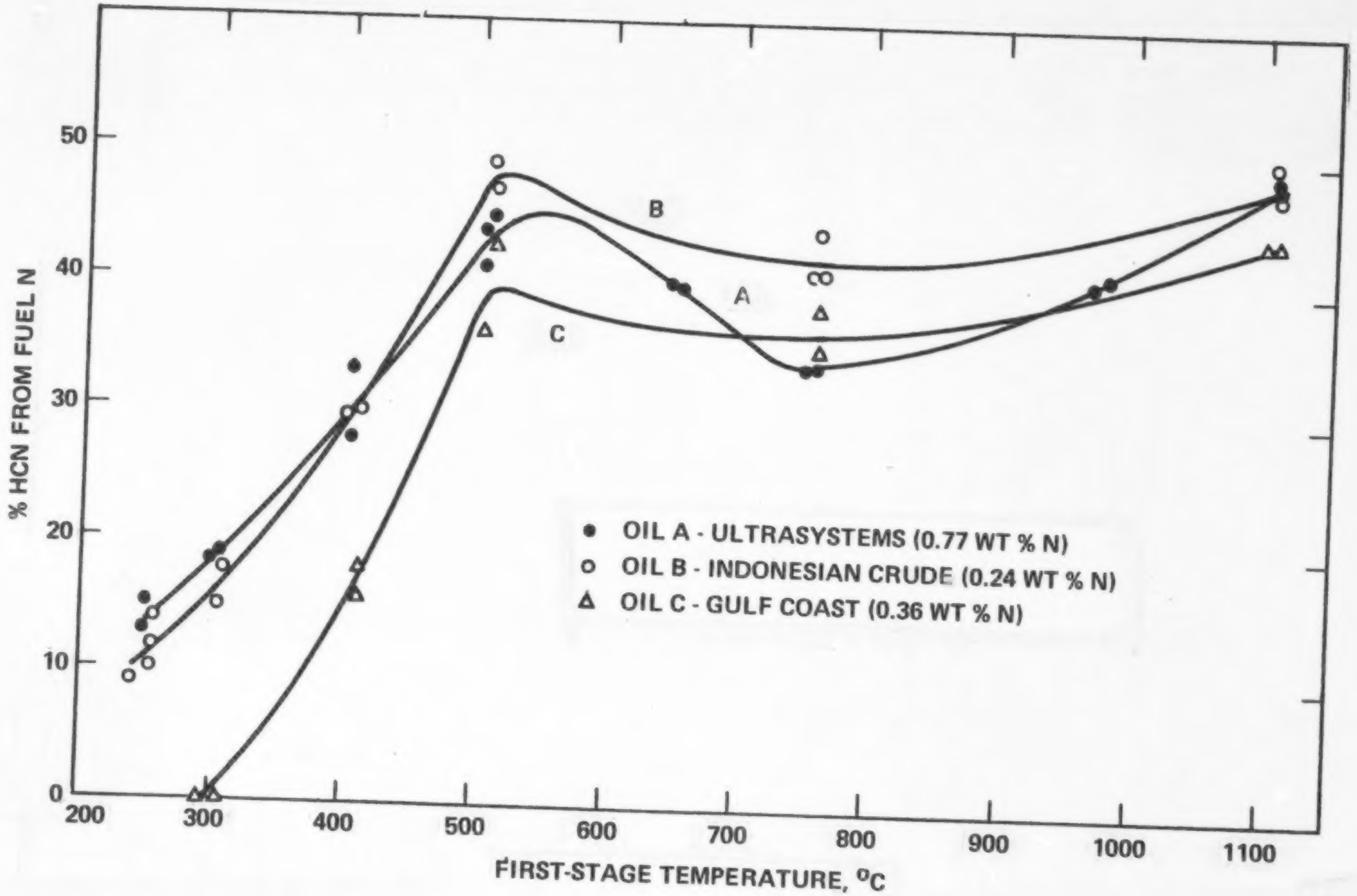

Figure 2. HCN Yield vs First-Stage Temperature for Oils A, B, and C

ature. The thermocouple tubing at this point is suspended about 3 mm from the capillary. Since the objective of this program was to compare the volatility characteristics of a number of fuels, this possible error in absolute temperature may not be important since it would be the same in all experiments and probably only occurs at very low first-stage temperatures.

Petroleum-Based Oils

Eight additional petroleum-based fuel oils were characterized with respect to fuel nitrogen volatility using the procedure described above. These oils are Oils B, C, D, E, F, G, I, and J; the analyses of these oils have been given in Table 1. The HCN yield curves obtained with these oils are presented in Figures 2 through 5.

The maximum yields of HCN (at a first-stage temperature of 1100°C) were between 44 and 48% of all of the oils except the two Venezuelan oils, F and G, and the Alaskan oil, J, which gave maximum yields of 35 to 39%. The dip in the yield curve that occurred at 750°C with Oil A (Figure 2) is indicated with some of the other oils but is less pronounced. The yields are near their maximum values at 500°C except for Oils D and E.

At lower temperatures, greater differences exist in some of the results. At 300°C, five of the oils (A, B, E, F, and G) produced HCN yields between 15 and 18%. Oil D (East Coast) and Oil I (Rocketdyne) gave slightly higher yields (22% for both oils) while Oil J (Alaskan) gave a slightly lower yield (7%). Oil C (Gulf Coast) was quite unusual in that it produced no volatile nitrogen at 300°C. Except for Oil C, the measured HCN yields ranged from 2 to 16% at 250°C and from 6 to 10% at 200°C (for those oils run at 200°C). These results indicate that, with one major exception (Oil C), the volatility characteristics of the fuel nitrogen in the petroleum-based oils are quite similar.

All of the data points in Figures 2 through 5 were from experiments in which the HCN was collected for 3 min after the oil sample was inserted into the preheated reactor. It has been demonstrated previously in higher temperature experiments that most of the HCN is formed in less than a few seconds. The 3 min collection period was chosen to allow time for any HCN that might be absorbed in the system to be evolved. One might expect that the fuel nitrogen would be evolved more slowly at the lower temperatures, and experiments were carried out to investigate this. After 3 min, the bubbler solution was removed

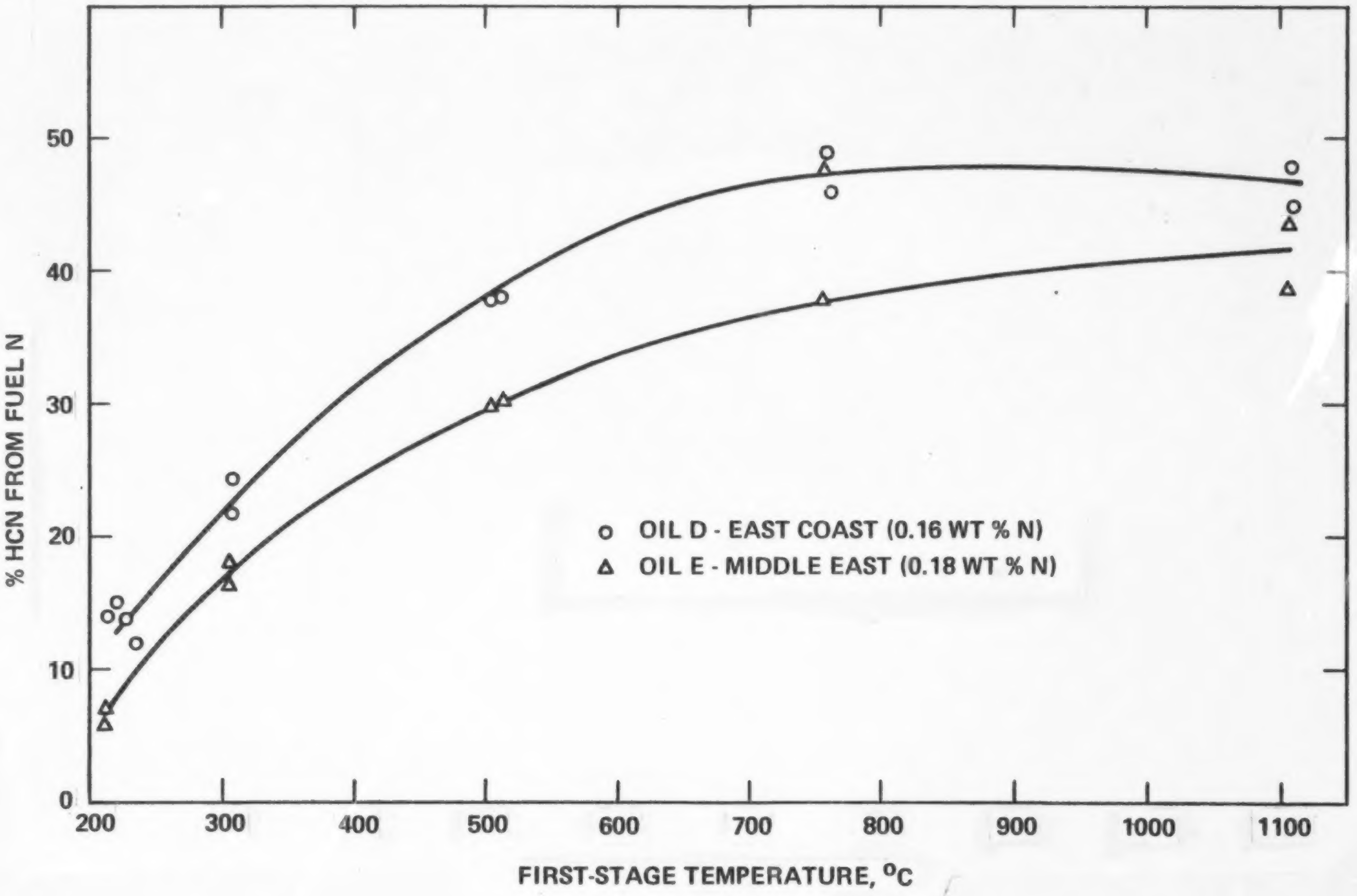

Figure 3. HCN Yield vs First-Stage Temperature for Oils D and E

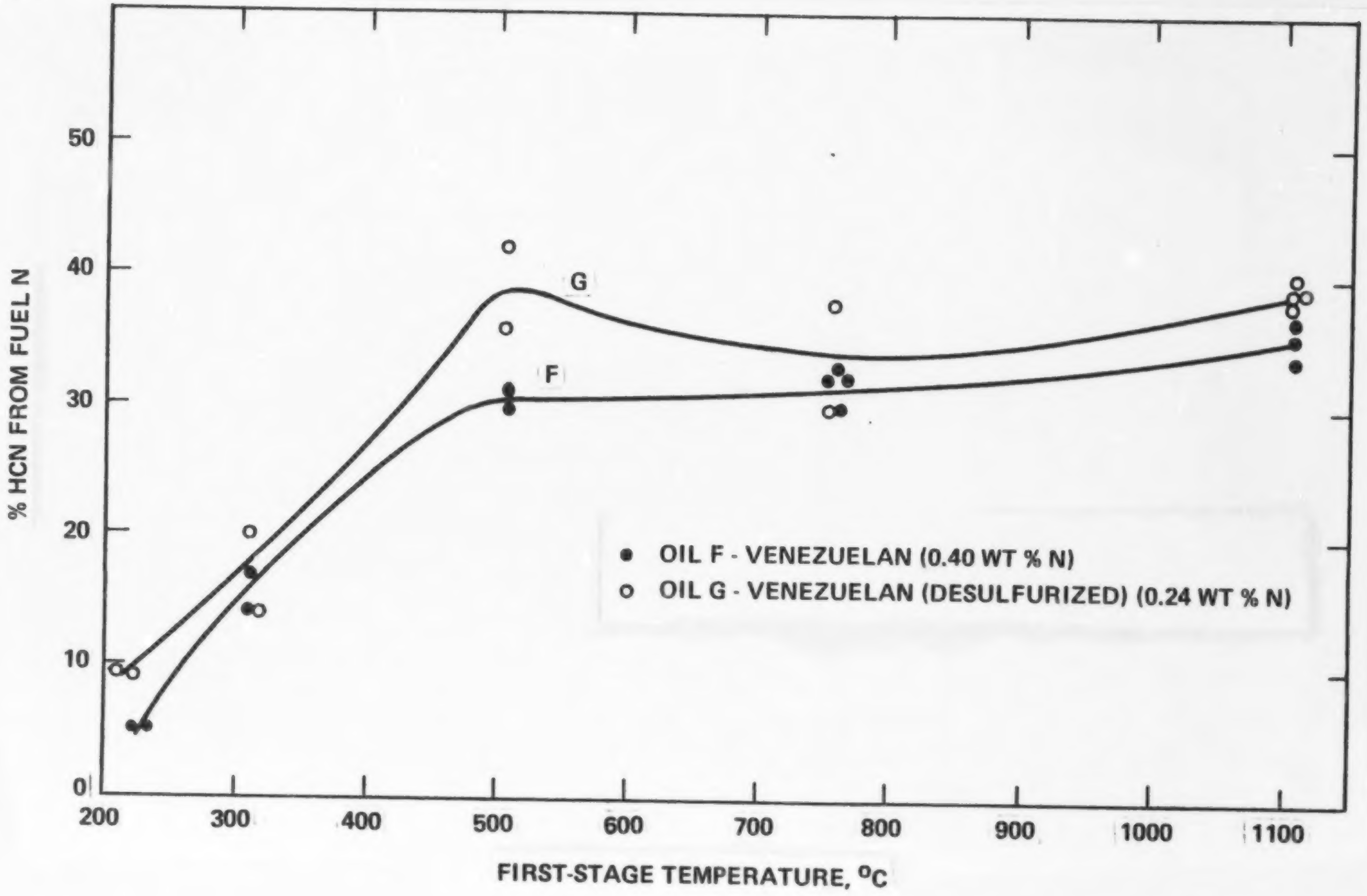

Figure 4. HCN Yields vs First-Stage Temperature for Oils F and G

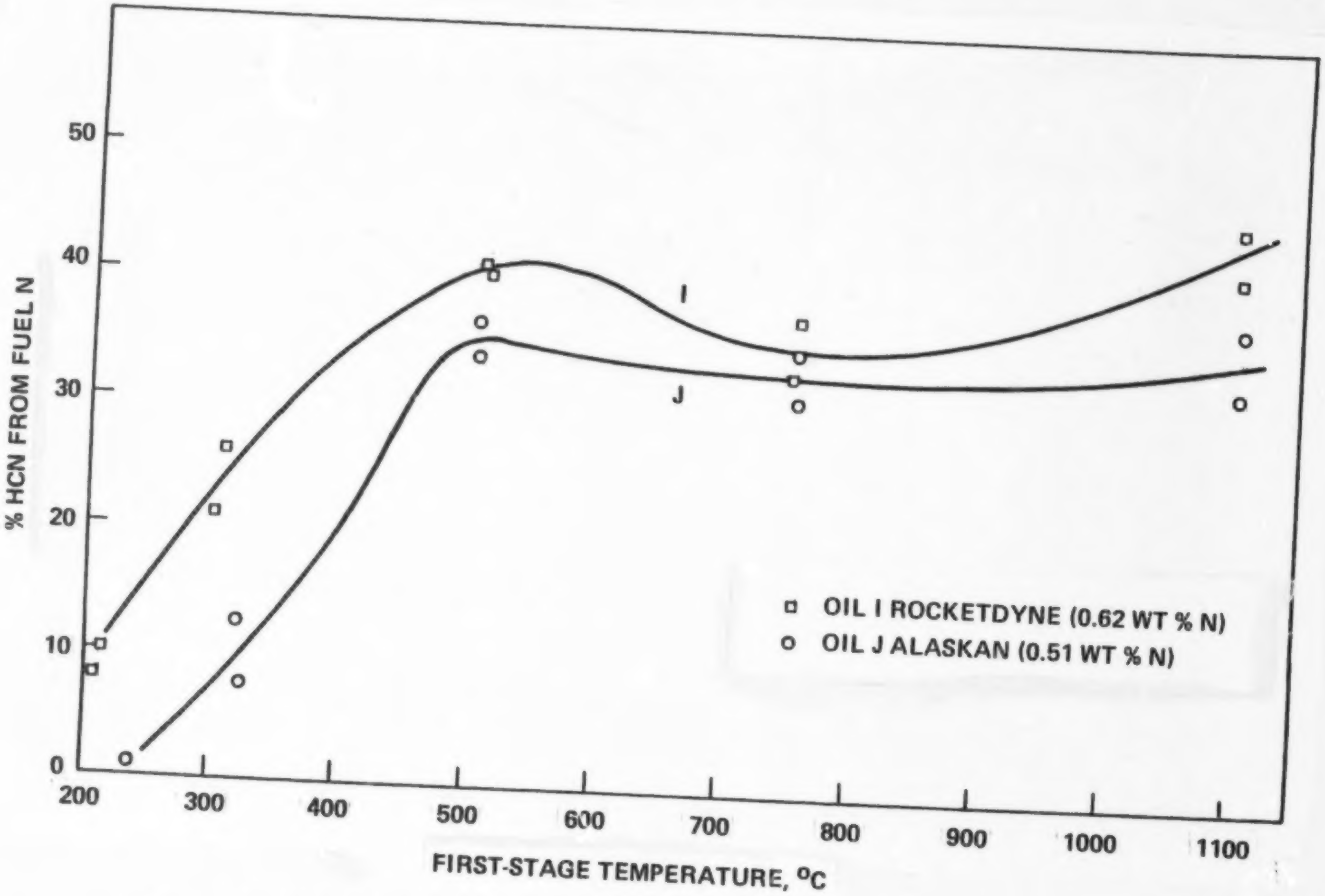

Figure 5. HCN Yield vs First-Stage Temperature for Oils I and J

and was quickly replaced with another solution that was left in place for at least 10 min.

It can be seen from Table 3 that, at 210°C, a considerable amount of HCN is formed after the first 3 min. At higher temperatures, the amount of HCN that is evolved after 3 min at a given temperature is much smaller. In the experiments with Oil A, the residuce that remained in the boat and in the first stage of the reactor was slowly heated to 750°C, and the additional HCN evolved was measured. At each of the four temperatures, the remainder of the "volatile" fuel nitrogen was evolved giving total yields similar to those obtained in 1100°C experiments.

Synthetic Fuels

The synthetic fuels tested in this program were SYNTHOIL (a liquefied coal), a shale-based diesel marine fuel, and a crude PARAHO shale oil. The HCN yields from these oils are plotted in Figure 6. The two shale oils showed much higher HCN yields than those from the coal liquefaction product. At the highest pyrolysis (first stage) temperature, 1100°C, the HCN yields of the shale oils were 70 to 79%, while the coal liquid yielded only 50%. The SYNTHOIL and shale oil results are in agreement with previous single-stage reactor results (Refs. 7,8).

In contrast to petroluem-based oils, the HCN yield did not drop off appreciably with decreasing temperature until the first-stage temperature was decreased below about 350°C for the SYNTHOIL and 200°C for the shale oils. The nitrogen species in the shale oils were very volatile, giving HCN yields of about 65% at a pyrolysis temperature of 200°C.

There are large differences in volatility between the nitrogen species in shale-based fuels and in petroleum-based fuels. This suggests that the optimum combustion modification techniques for alternative fuel combustion may be quite different than those developed for petroleum-based fuels. Combustion data on this point will be forthcoming from other investigations currently being carried out.

Coals

Eight coals were tested as part of this contract. The HCN yields for these coals are given in Table 4. These results are plotted for comparison in Figures 7 and 8.

TABLE 3
EFFECT OF REACTION TIME ON HCN YIELD

	Total HCN Yield, %		
	Oil A	Oil D	Oil G
210°C			
3 min		15	9
13 min		30[a]	13[a]
300°C			
3 min	18		
13 min	23[a]		
Inc. to 760°C (30 min)	50[b]		
400°C			
3 min	28		
13 min	33[a]		
Inc. to 750°C (20 min)	45[b]		
500°C			
3 min	41		
13 min	43[a]		
Inc. to 750°C (15 min)	47[b]		
650°C			
3 min	40		
13 min	47[a]		
Inc. to 750°C (10 min)	51[b]		

[a] Includes HCN formed during first 3 min.

[b] Includes HCN formed at lower temperature.

737-G.65/kam

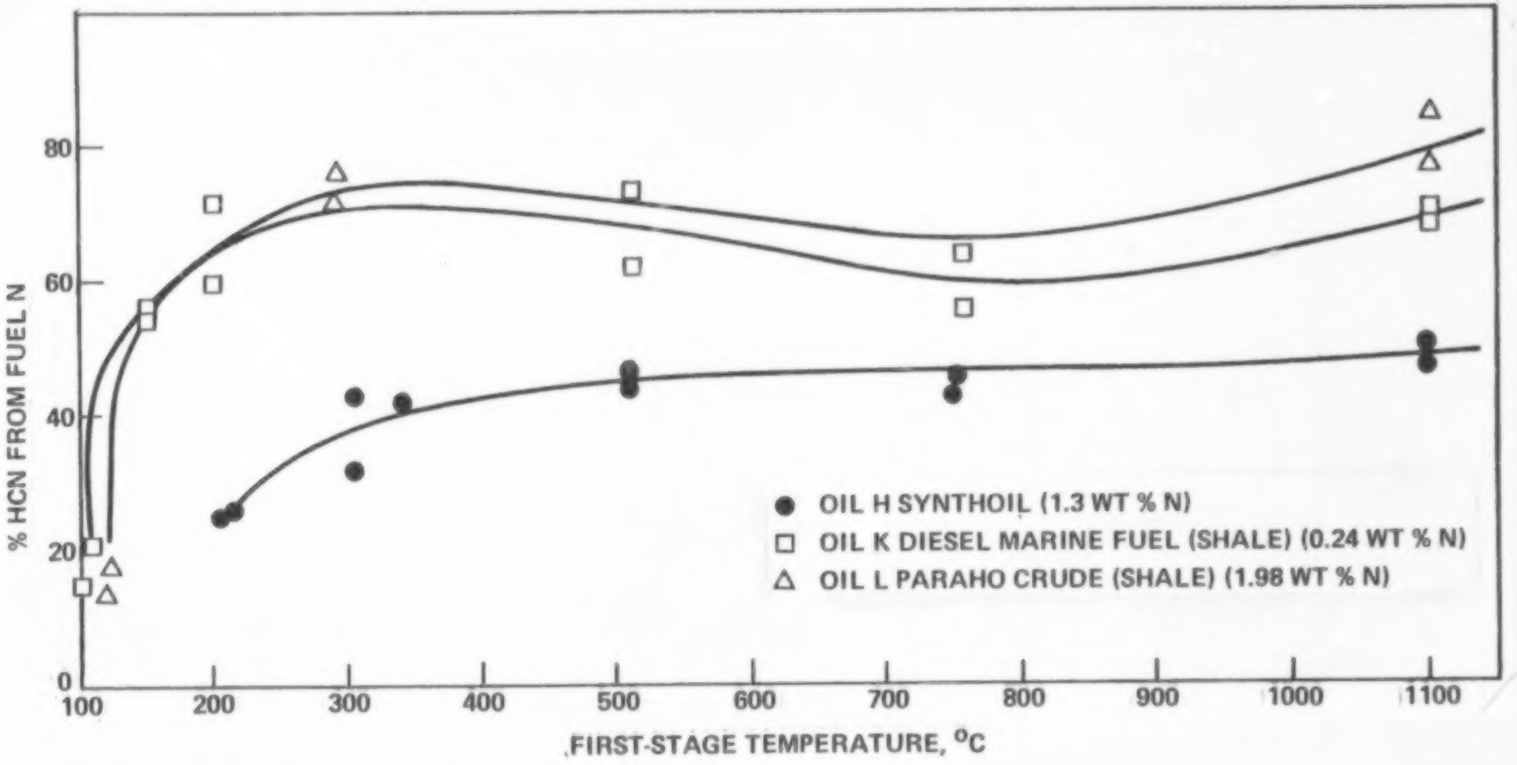

Figure 6. HCN Yield vs First-Stage Temperature for Oils H, K, and L (Synthetics)

TABLE 4
HCN YIELD (% OF FUEL N) VS FIRST-STAGE TEMPERATURE

Type of Coal	HCN Yield (%)			
	300°C	500°C	750°C	1100°C
TRW No. 2	1.1	8.3	13.4	16.4
TRW No. 1	4.3	8.3	11.6	17.2
Utah No. 1	0.4	10.5	14.6	21.4
Scranton, ND, No. 4	0.3	9.7	22.0	25.5
Beulah, ND, No. 9	4.2	8.1	10.0	11.7
Montana Savage No. 11	0.9	8.1	9.7	18.9
Rosa, AL, No. 18	0.1	8.8	14.8	16.1
Black Creek, AL, No. 19	0.1	6.7	13.5	15.8

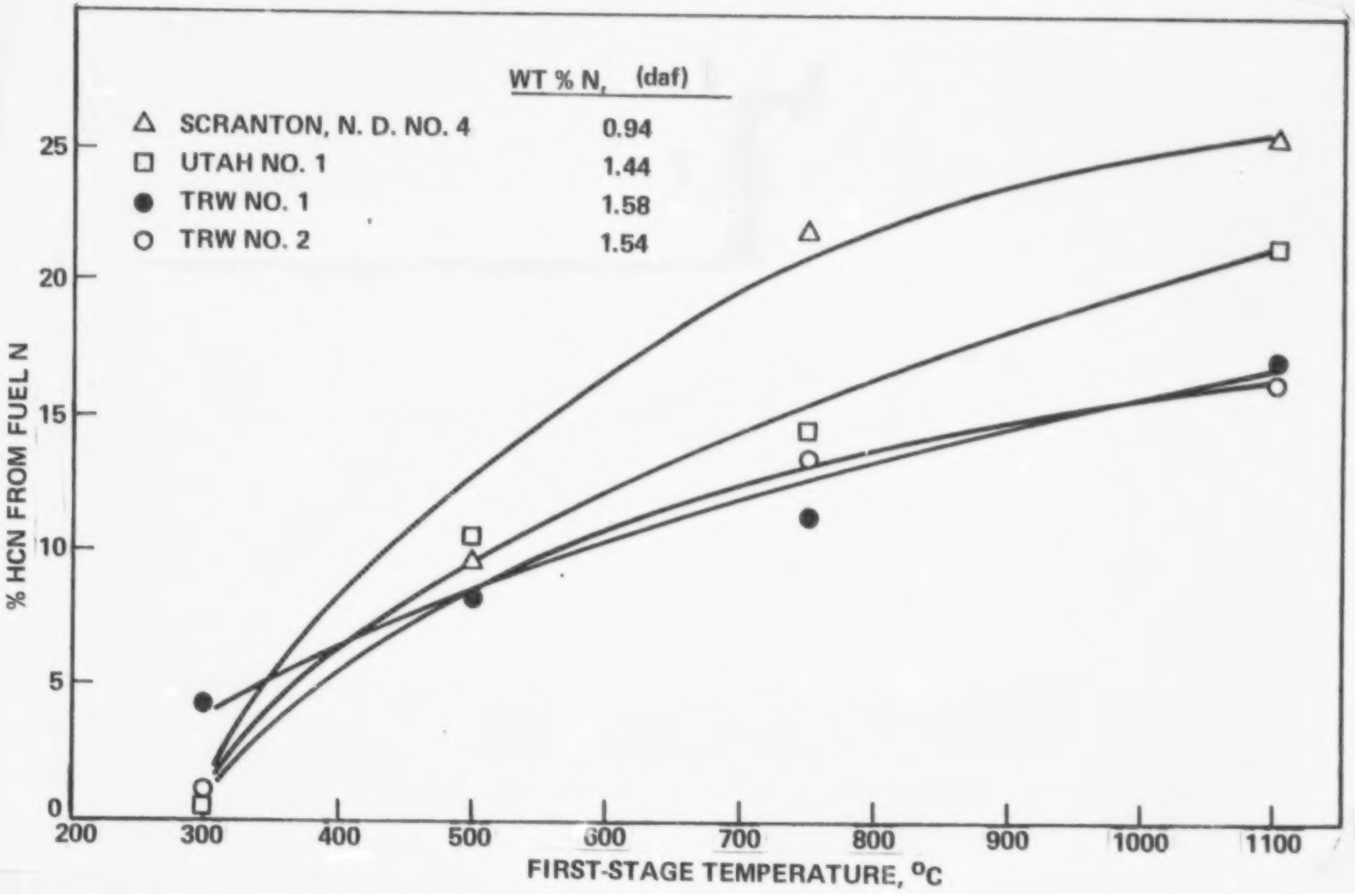

Figure 7. HCN Yield vs Firts-Stage Temperature (Second Stage at 1100°C) for Coals

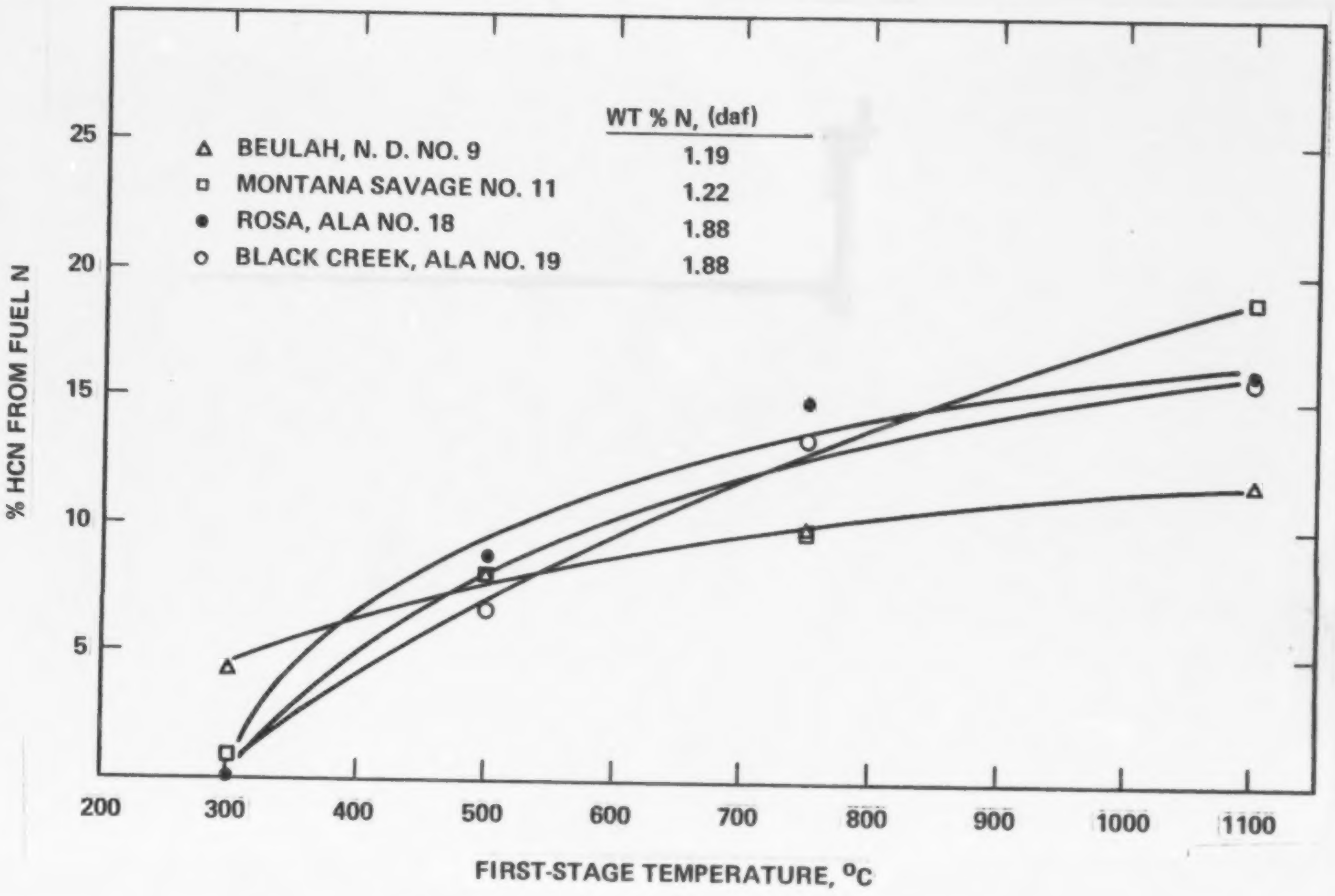

Figure 8. HCN Yield vs First-Stage Temperature (Second Stage at 1100° C) for Coals

In general, the coals exhibited lower fuel nitrogen evolution than was seen from the fuel oils. Maximum coal HCN yields (at 1100°C pyrolysis temperature) were about 15 to 25%, as compared to 35 to 50% for the fuel oils. Further analysis of the coal results is presented in the next section where the maximum HCN yields are compared to NO_x formation from fuel nitrogen during combustion.

Correlation of Test Results with NO_x Formation

It is of importance to the study of combustion processes and pollution control to compare the formation of NO_x from fuel nitrogen in combustion with the volatility of the fuel nitrogen. This is especially important for the case of coal combustion, because fuel nitrogen is the major source of NO_x emissions when burning this fuel.

A summary of the data related to fuel nitrogen volatility and NO_x formation is given in Table 5. The NO data given in Table 5 are the result of combustion of the same coals as those used in this program. These data were reported to us by D. W. Pershing (Ref. 9). His NO data were obtained from a 70,000 BTU/hr bench-scale combustor. The combustor was a premixed burner operating under excess air conditions (5% excess oxygen). The HCN data are the result of our program and are taken from Table 4.

A plot of the percentage of Fuel N converted to NO during combustion vs the wt % N in the fuel is given in Figure 9. The data do not correlate well. A similar plot for the percentage of Fuel N volatilized at 1100°C in our apparatus vs the nitrogen content of the fuel is given in Figure 10. Again the data do not correlate well.

A plot of the percentage of fuel nitrogen converted to NO during combustion vs the percentage of Fuel N volatilized at 1100°C is given in Figure 11.* There is a very strong linear correlation between the two from a variety of coals. The slope of this line is 2, indicating that twice as much NO is formed by combustion as is volatilized at 1100°C. This correlation provides an excellent means of predicting NO formation for any given coal simply by measuring the nitrogen volatility at 1100°C.

*Two values for Fuel NO were received for the Scranton No. 4 coal, one early in the program, one much later. Parentheses are used to distinguish the later value. Although one value for fuel NO appears to match the correlation very well, it is still uncertain as to which value corresponds to the coal that was tested for nitrogen volatility.

TABLE 5

SUMMARY OF DATA RELATED TO FUEL NITROGEN VOLATILITY AND NO FORMATION

Coal	% N (daf)	Moles Dry Comb. Prod. Per Gm (As Rec'd.)[a]	NO[b] (ppm)	Fuel-NO Per Gm Coal (m mole)	Fuel-N to Fuel-NO (%)	Fuel-N to HCN @ 1100°C (%)	% to NO / % to HCN
TRW No. 2	1.54	0.323	790	0.255	26.9	16.4	1.64
TRW No. 1	1.58	-	-	-	-	17.2	-
Utah No. 1	1.44	0.309	1230	0.380	42.9	21.4	2.00
Scranton, ND, No. 4	0.94	0.180	1070 (690)[c]	0.193 (0.121)	49.9 (31.2)	25.5	1.96 (1.22)
Beulah, ND, No. 9	1.19	0.182	630	0.115	22.3	11.7	1.91
Montana Savage No. 11	1.22	0.172	1020	0.175	34.1	18.9	1.80
Rosa, AL, No. 18	1.88	0.335	1100	0.368	32.3	16.1	2.01
Black Creek, AL, No. 19	1.88	0.361	1170	0.422	33.8	15.8	2.14

[a] Moles dry combustion products per gm = % C/12.01 + % N/14.01 + % S/32.06 + 3.727 (Z)
where Z = net moles O_2 = % C/12.01 + % H/4.00 + % N/28.02 + % S/32.06 - % O/32.00

[b] Personal communication from D. W. Pershing.

[c] Values in parentheses are a second set of NO values received for the Scranton, ND, No. 4 coal.

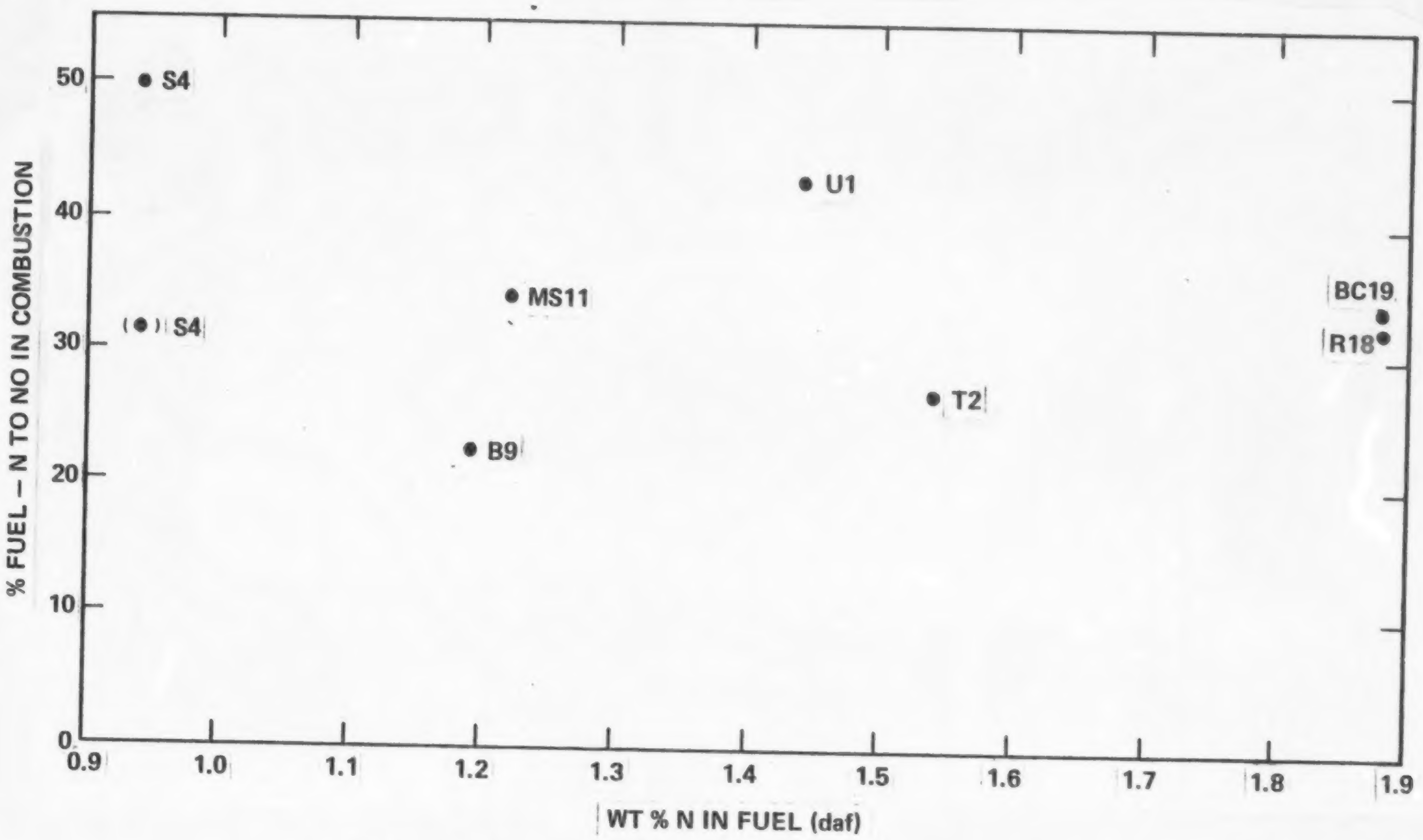

Figure 9. Percent Fuel-N to NO in Combustion vs Wt Percent N in Fuel (daf)

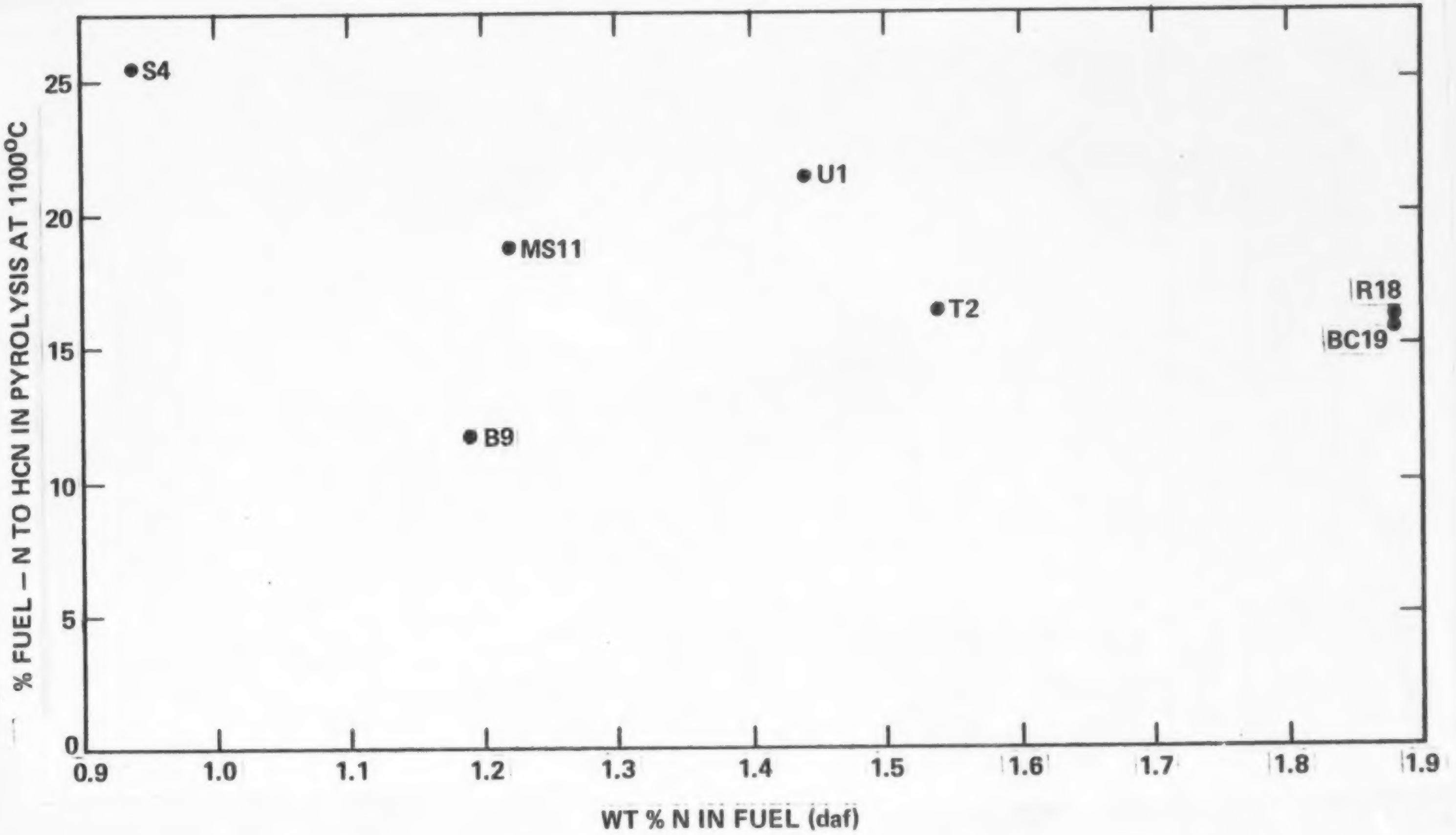

Figure 10. Percent Fuel-N to HCN in Pyrolysis at 1100°C
Wt Percent N in Fuel (daf)

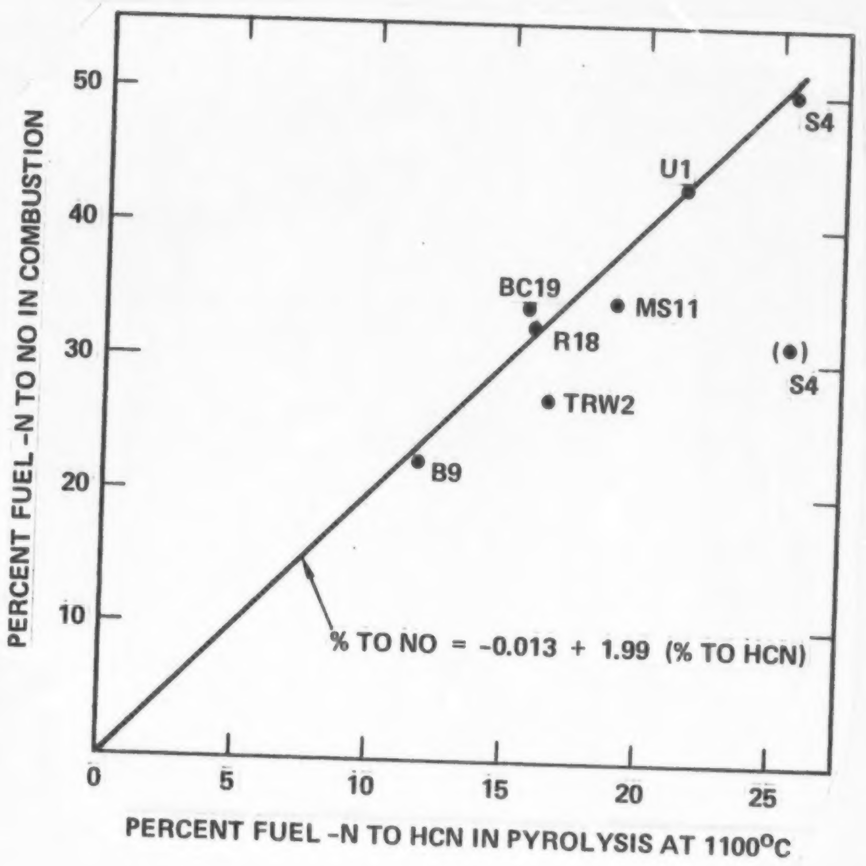

Figure 11. Percent NO in Combustion vs Percent HCN in Pyrolysis at 1100°C

REFERENCES

1. A. F. Sarofim, J. H. Pohl and B. R. Taylor, "Mechanisms and Kinetics of NO_x Formation: Recent Developments, " presented at the 69th Annual AiChe Meeting, November 1976, Paper No. 27D.

2. J. O. Wendt and D. W. Pershing, "Physical Mechanisms Governing the Oxidation of Volatile Fuel Nitrogen in Pulverized Coal Flames," Comb. Sci. & Tech. (1977)

3. A. E. Axworthy, V. H. Dayan, and G. B. Martin, "Reactions of Fuel-Nitrogen Compounds Under Conditions of Inert Pyrolysis," FUEL, Vol. 57, January 1978

4. A. E. Axworthy, et al., "Chemistry of Fuel Nitrogen Conversion to Nitrogen Oxides in Combustion, Final Report," Contract 68-02-0635, EPA-600/2-76-039, February 1976

5. J. H. Pohl and A. F. Sarofim, "Devolatilization and Oxidation of Coal Particles," presented at the 16th International Symposium on Combustion, August 1976

6. D. W. Blair, W. Bartok, J. O. L. Wendt, and D. G. Lilley, "Devolatilization and Pyrolysis of Fuel Nitrogen from Single Coal Particle Combusiton," presented at the 16th International Symposium on Combustion, August 1976

7. A. E. Axworthy and V. H. Dayan, "Chemical Reactions in the Conversion of Fuel Nitrogen to NO_x: Fuel Pyrolysis Studies," Proceedings of the Second Stationary Source Combustion Symposium,Vol. IV, Page 39, 1977, EPA-600/7-77-073d

8. A. E. Axworthy, et al., "Fuel Decomposition and Flame Reactions in Conversion of Fuel Nitrogen to NO_x, Final Report," Contract 68-02-1886 (to be issued)

9. Personal communication, D. W. Pershing, University of Utah

HIGH TEMPERATURE PYROLYSIS OF OIL DROPLET AND COAL PARTICLE STREAMS

J. M. Beer, A. F. Sarofim, S. P. Hanson and A. K. Gupta
Department of Chemical Engineering
Massachusetts Institute of Technology
Cambridge, Massachusetts 02139

Fifth EPA Fundamental Combustion Research Workshop
Newport Beach, California
January 23-25, 1980

SECTION I

INTRODUCTION

The most effective control of fuel-nitrogen conversion to NO_x in flames is staged combustion. When successfully applied staged combustion will lead to the major proportion of fuel-nitrogen being converted to N_2 in the first stage, so that there remains only a small amount of fuel-nitrogen available to form NO_x in the fuel lean stage of the combustor. Pyrolysis studies on model compounds such as pyrrole, pyridine and quinoline conducted at Rocketdyne showed that under fuel rich conditions the nitrogen in the organic compounds is converted rapidly and with high efficiency to HCN at temperatures of 1100°C and higher. It was also shown that the rates of decomposition of these model compounds were higher in the presence of oxygen, and that products of oxidative pyrolysis included N_2, N_2O, NO and NO_2 with a significant fraction of the original fuel-nitrogen converted to molecular nitrogen, N_2. The observation that N_2 is formed only in the presence of oxygen is consistent with current thought on the possible mechanism of fuel-nitrogen fragments reacting with NO.

The earlier evolved fuel-nitrogen compounds have increased residence times in the fuel-rich stage and hence an improved chance of their conversion to N_2; it is therefore of interest to understand the factors that determine the rate at which fuel-nitrogen evolves from liquid fuel droplets or coal particles during pyrolysis.

The nitrogen in fuels consists of complex, mostly heterocyclic compounds. In petroleum crudes these include pyroles, indoles, isoquinolines, acridines and porphyrins. Most of them concentrate in the heavy resin and asphaltene fractions obtained on distillation of the crude and, therefore, may be released relatively late in the combustion of residual fuel oils. Similarly, in coals the nitrogen is believed to be tied up mostly in aromatic rings and is released at a rate strongly dependent upon temperature, and time of exposure to temperature.

Some of the questions which must be answered in order to realistically model the fuel-nitrogen conversion in liquid fuel spray and pulverized coal flames are:

- How is the rate of evolution of nitrogenous compounds from a multi-component heavy fuel oil droplet affected by the dynamics of rapid heating and vaporization?
- How does the rate of volatile release and the volatile yield from a coal particle depend upon the pyrolysis temperature, particle size and the chemical composition of the environment?
- If the volatile ignites and forms a flame around the particle, how does the energy "feed-back" from the flame influence the further evolution of nitrogenous compounds from the pyrolyzing particle?

A series of high temperature flow reactor experiments were carried out with coal particle pyrolysis and combustion, and techniques were developed for heavy liquid fuel droplet pyrolysis in order to attempt to answer the above questions.

SECTION II

OIL DROPLET STUDIES

The Experimental Apparatus

For the study of fuel-nitrogen evolution from liquid fuel droplets during pyrolysis and oxidation, a laminar flow reactor (Figure 1) was designed with provision for feeding a monosize droplet array into a laminar gas stream and the capability of intercepting the droplets, after a chosen residence time, by a fast quenching sampling probe. Optical access to the pyrolyzing, burning oil droplet array through a quartz window along the full length of the uniformly heated section of the reactor enables photographic and schlieren-interferometric measurements to be made of droplet size variation, droplet velocity and the temperature distribution in the droplet boundary layer.

The objective of carrying out experiments with droplet arrays of heavy residual fuel oils, posed significant experimental problems concerning the fuel preparation and droplet generation and also the sampling. Also, the optical method for measuring temperature in the boundary layer surrounding the droplets had to be developed.

Droplet Generation and Collection

A vibrating orifice type droplet generator (Fig. 2) was chosen for the introduction of fuel droplets into the reactor. The droplet stream is injected vertically downward into the furnace through a small (50 or 100 μm) orifice mounted in a piezo-electric vibrator. The vibrator is driven by a variable frequency signal generator. The variation of oil flow rate, vibrator frequency and orifice size permits the control of droplet size and interdrop distance. A photograph taken of the liquid jet stream, immediately downstream of the orifice, is shown in Fig. 3a. A periodic instability running down the

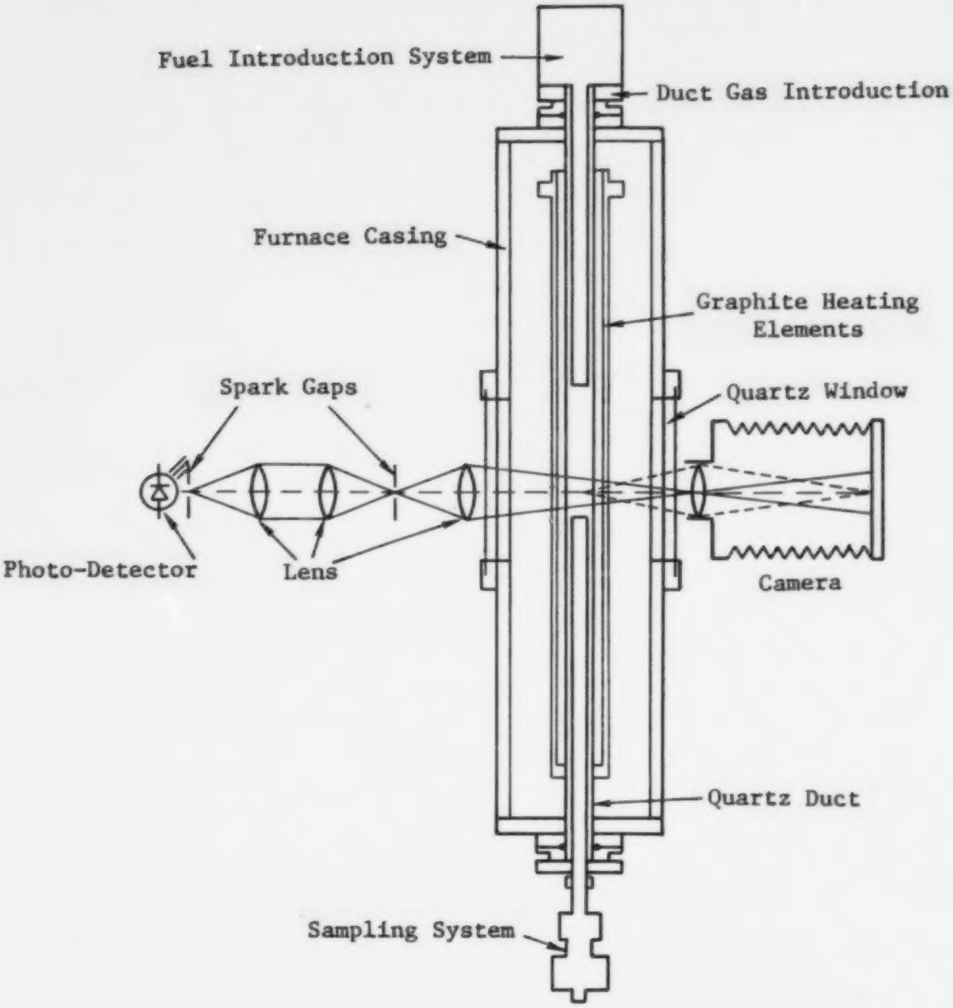

Figure 1. Laminar Flow Reactor for Liquid Fuel Studies.

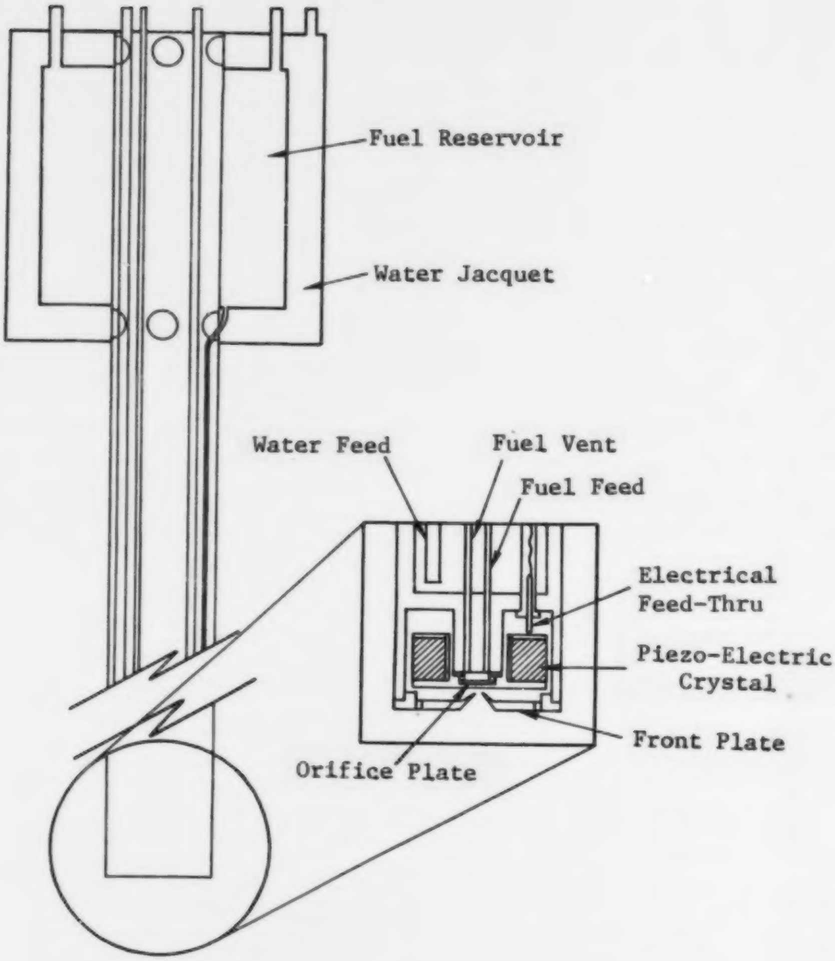

Figure 2. Fuel Introduction System.

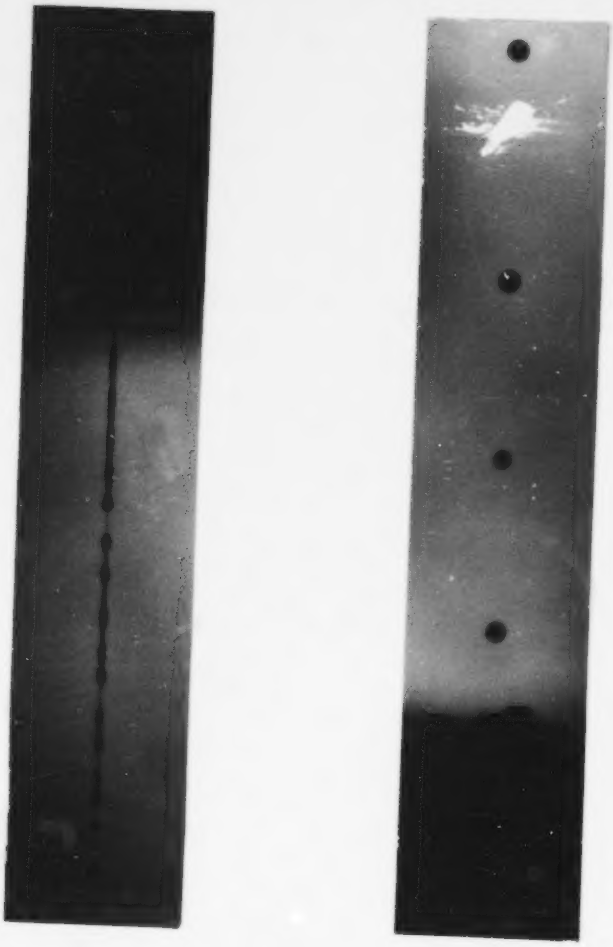

(a) (b)

Figure 3. Droplet Steam of 150 μm Raw Paraho Shale Oil at Point Origin (a) and 17 cm Downstream (b) in an Environment of Helium at 973 K.

Reproduced from best available copy.

liquid fuel jet stream in the form of a wave, is seen to result in the formation of ligaments and eventually in the generation of droplets. The stable generation of heavy fuel oil droplets requires that the viscosity be accurately maintained at a sufficiently low level, - around 20 centistokes - and the droplet stream originate as close as possible to the entrance of the working section of the reactor. The same droplet stream vaporizing in the furnace at 973°K is shown in Fig. 3b. Examination shows that the initial droplet size is 150 μm diameter and the interdrop distance is 4 diameters.

The droplets are injected into a laminar co-flowing gas stream; in our recent studies Helium was chosen to give a chemically inert environment for the vaporizing-pyrolyzing drops.

The sampling probe inserted through the base of the furnace is aligned with the drop generator by means of a small laser.

The sampling probe takes the total gas flow, the residual droplet array and the vapor. Some of the requirements of representative sampling are:

a) the sampling flow rate and probe head geometry be so chosen as to prevent stagnation or strong deceleration of the flow.

b) the sampled stream be rapidly quenched.

c) aerosol deposition on the sampling probe walls by thermophoresis and impact be prevented.

d) the liquid residue be separated from the fuel vapor.

A transpiring type of probe following the conceptual design by Mims[1], combined with a cascade impactor satisfied the above mentioned requirements

(Fig. 4). The transpiration gas (Helium) introduced along the full length of the water cooled probe serves three purposes: firstly it keeps the walls clean from deposition, secondly it quenches the reactions by dilution - both chemical and thermal - and thirdly it causes the vapor to condense in the form of a submicron fog which can then escape the cascade impactor and be trapped in a glass wool filter followed by a hydrocarbon absorbing resin (XAD-2). The liquid residue is retained on the first stage of the cascade impactor and is analyzed for its chemical composition, the condensibles collected by the filter and XAD-2 resin are extracted with methylene chloride and analyzed by gas chromatography to permit the closing of the nitrogen balance.

Determination of Temperature Profiles

In order to understand fully the pyrolysis of droplets it is necessary to have a detailed knowledge of the structure of the boundary layer enclosing a fuel droplet. For this purpose a laser schlieren interferometric system (Fig. 5) was developed to determine the spatial temperature distribution surrounding a moving vaporizing or burning fuel droplet. The technique used records on a holographic film the difference in optical path length, in the form of fringes, between two consecutive exposures of the test section. One exposure is made with the disturbance, i.e., the droplet stream, present and the other with the disturbance absent. One particular advantage of the technique is that aberrations in any optical component including the furnace windows, are eliminated by the double exposure.

Experiments using a variety of test subjects has shown the method to be versatile and sensitive. Figure 6 is a reconstructed interferogram of a burning stream of 2 mm kerosene droplets. The temperature distribution derived from this interferogram is shown in Fig. 7.

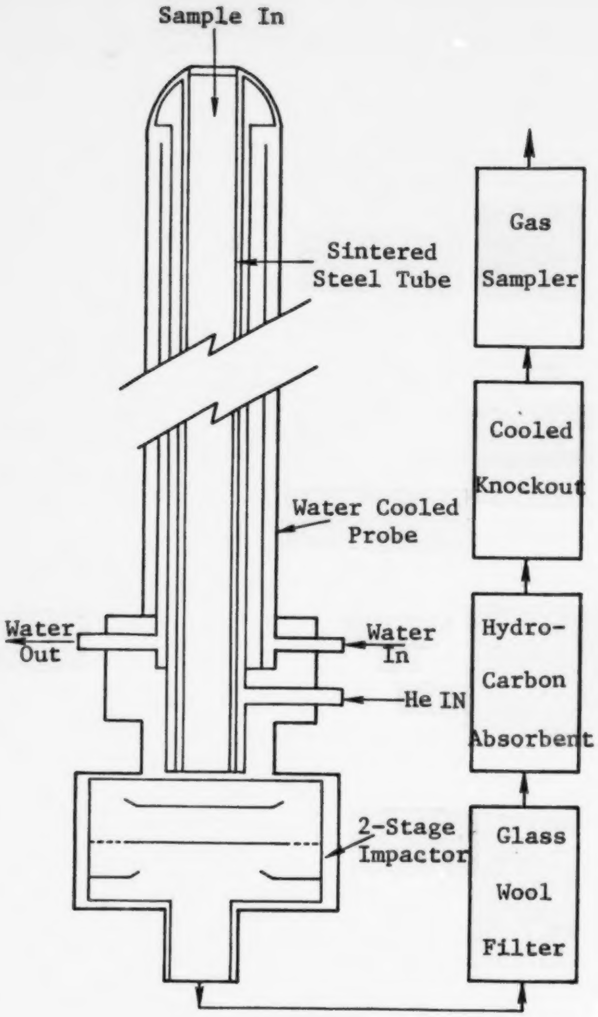

Figure 4. Transpiring Probe and Sampling Train.

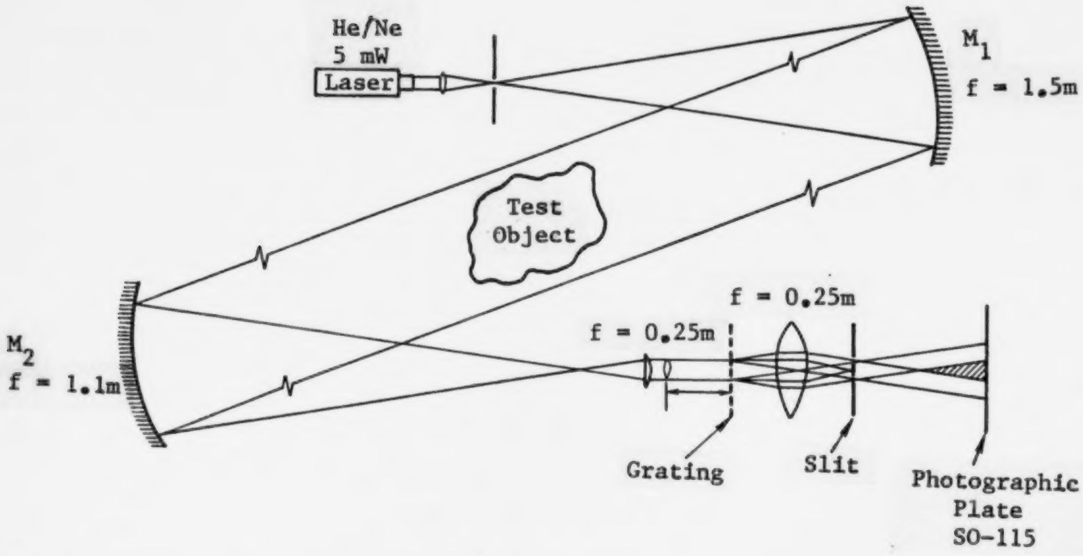

Figure 5. A Schematic Diagram of the Laser Schlieren Interferometric System.

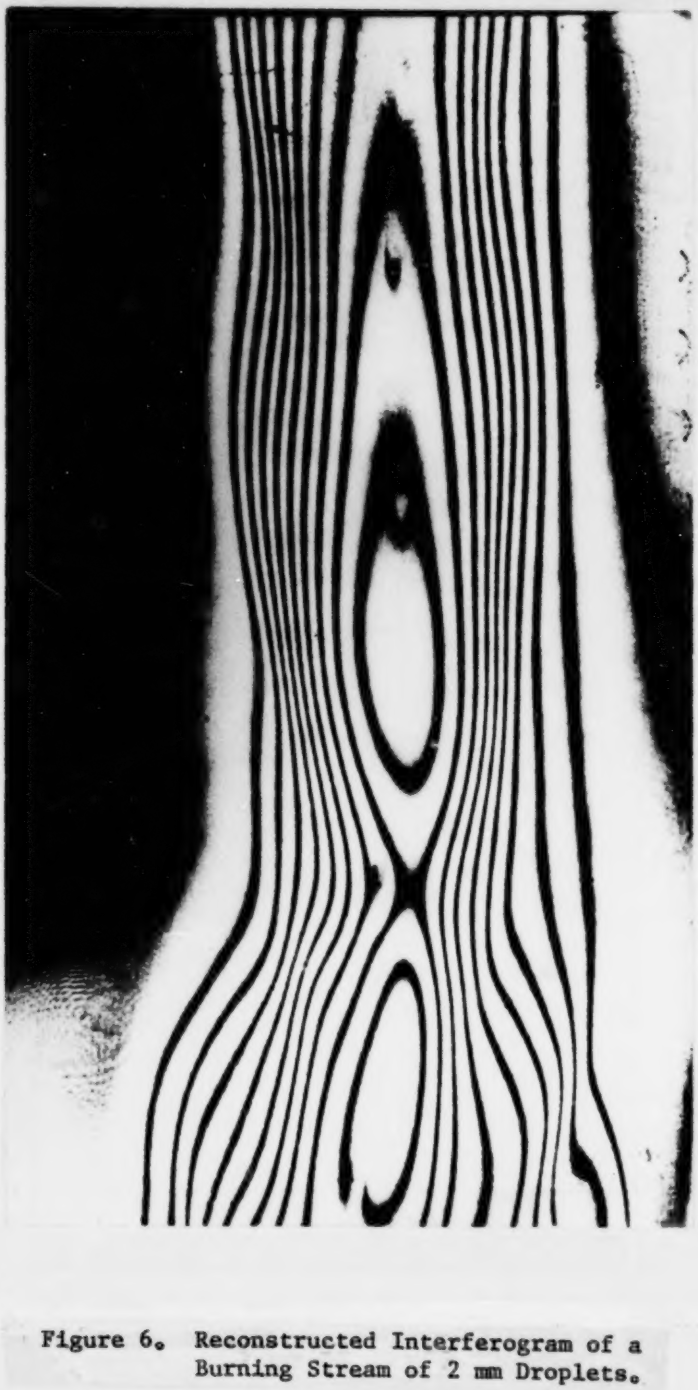

Figure 6. Reconstructed Interferogram of a Burning Stream of 2 mm Droplets.

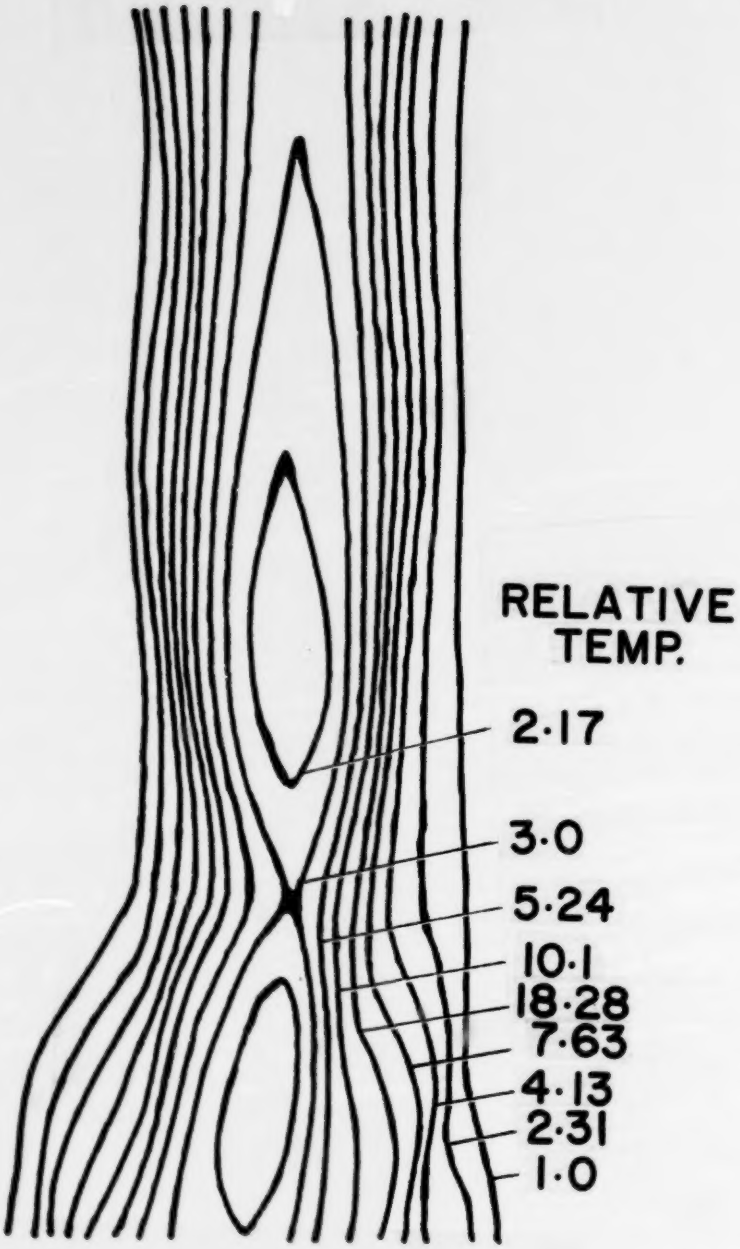

Figure 7. Relative Temperature Distribution Derived from Figure 6.

Experimental

Distillation Experiments

Results of atmospheric distillation of an Indo-Malaysian heavy residual fuel oil and a Raw Paraho Shale Oil are shown in Figs. 8 and 9. The percentage nitrogen loss can be seen to approximately equal that of the weight loss along the Shale Oil distillation curve, while it lags strongly behind the weight loss for the Indo-Malaysian fuel oil. These results show the effect of the nature of the fuel nitrogen upon its evolution under conditions close to equilibrium atmospheric distillation. When small droplets undergo rapid heating in flames, dynamic effects may cause strong departure from equilibrium conditions; the concentrations of lighter boiling fractions at the surface of a vaporizing multicomponent droplet may fall below those inside the drop due to mass transfer limitations with the effect that the surface temperature may rise and lighter boiling fractions of the oil superheat within the drop. This then will result in an increase in drop size and, in the limit, rupture of the droplet. The superheating can also cause pyrolysis cracking leaving the droplet with some residual carbon. The tendency for residual carbon formation under conditions of high heating rates and temperatures is illustrated by the distillation curve of the Indo-Malaysian Oil in Fig. 8. Data points for temperatures above 800K represent results of crucible experiments in the high temperature furnace. An interesting feature of these results is that they show almost complete loss of fuel nitrogen under (high temperature) conditions when, due to cracking and polymerization, a significant proportion of the fuel droplet mass is retained in the form of a carbonaceous residue. For a given weight loss of the fuel droplet there can be different nitrogen losses depending upon the peak temperature and rate of heating of the droplet.

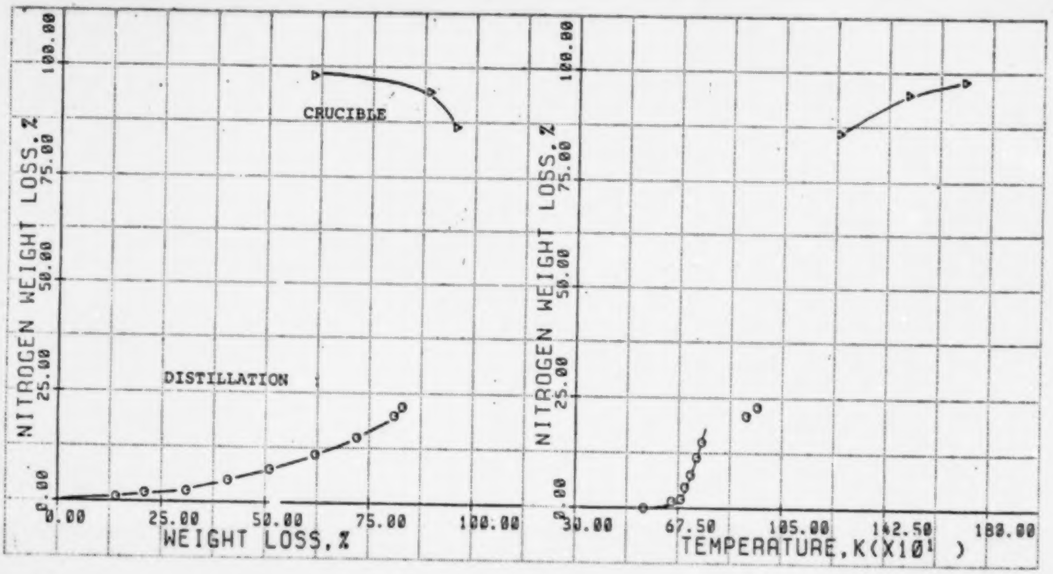

Figure 8. Fuel-Nitrogen Evolution Vs. Weight Loss and Temperature, Indo-Malaysian Residual Fuel Oil.

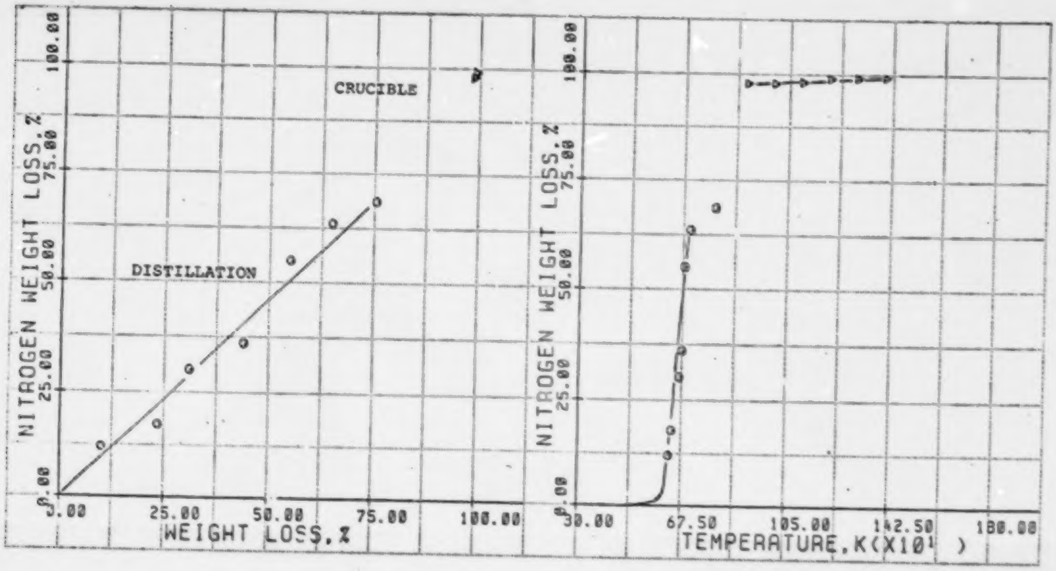

Figure 9. Fuel-Nitrogen Vs. Weight Loss and Temperature, Raw Paraho Shale Oil.

Inert Pyrolysis of Droplet Arrays of Shale Oil in the Laminar Flow Furnace

The first experiments with the laminar flow furnace were carried out with the inert pyrolysis of a Raw Paraho Shale Oil in a Helium stream at 973, 1073 and 1173K temperatures. The nominal droplet size was 150 μm. The experimental results are plotted in Fig. 10, which shows the variation of the nitrogen evolution versus the weight loss of the vaporizing droplet stream as a function of the furnace temperature. At 973K the results are very similar to those obtained from the atmospheric distillation experiments. As the temperature was raised first to 1073K and subsequently to 1173K, the evolution rate of the fuel-nitrogen lagged behind the weight loss due to the effects of rapid heating and strong departures from equilibrium distillation. These results show that even for a fuel like Shale Oil, in which the fuel nitrogen is not refractory, dynamic effects of high vaporization rates can cause retardation of fuel nitrogen evolution from the vaporizing droplet.

Photographs of the vaporizing Shale Oil Droplet stream show an increase in droplet size along the stream (Fig. 3). At this early stage of the experiments, however, a size increase due to droplet coagulation can not be ruled out and further experiments are necessary to show conclusively whether this increase in droplet size is due to the dynamic effects of multicomponent fuel vaporization.

The preliminary results show that pyrolysis of fuel droplets and the evolution rates of fuel-nitrogen compounds are strongly affected by rapid heating to high temperature conditions similar to those in practical flames.

The experimental technique developed for the study of high temperature pyrolysis and oxidation of heavy fuel oil droplet streams can yield experimental data necessary as input for the modelling of fuel-nitrogen conversion in heavy fuel oil spray flames, and is capable also of providing information

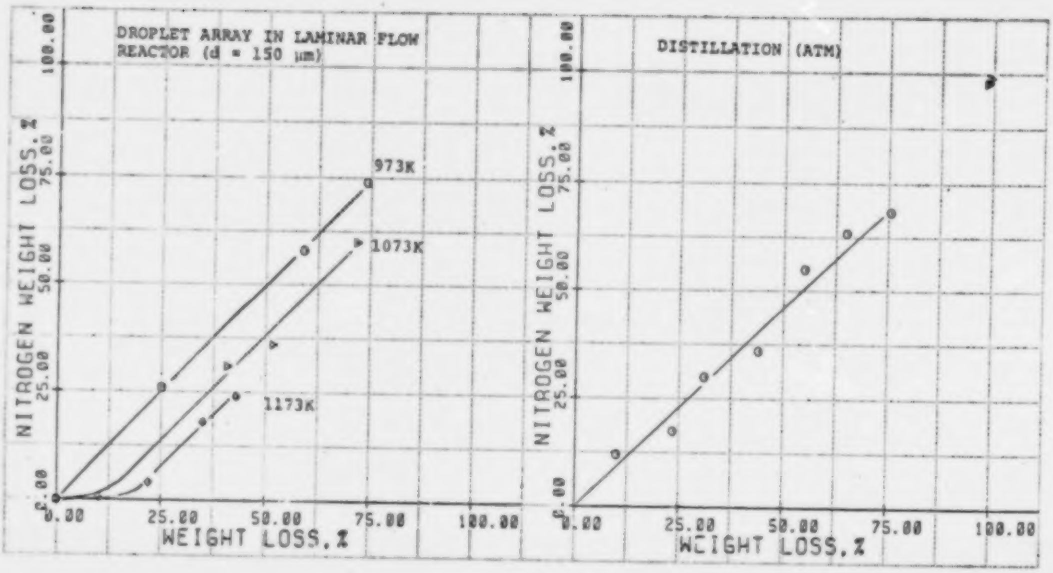

Figure 10. Fuel-Nitrogen Evolution Vs. Weight Loss, Raw Paraho Shale Oil.

on the mechanism of the processes involved in non-equilibrium multicomponent fuel droplet vaporization.

SECTION III

COAL PARTICLE STUDIES

In pyrolyzing or burning coal particles, the fuel-nitrogen is divided between the coal volatiles and the residual char. The volatile yield and composition is a function of the coal type and is strongly dependent upon the peak temperature of the particle; to a lesser extent it depends also upon the chemical environment of the pyrolyzing coal particle. Inert pyrolysis studies of pulverized coal particles were carried out by Pohl[2] under conditions closely simulating the heating rates (10^4 to 10^5 K/sec.), peak particle temperatures (1500-2100 K) and residence times (200 to 1000 μsec.) in industrial pulverized coal combustors. Time dependent measurements of nitrogen pyrolysis were correlated with a pseudo-first order rate equation giving an activation energy of 22.7 Kcal/mole.

Cheng[3] has extended these experiments with an investigation of oxidative pyrolysis of three coals; a Montana lignite, Montana sub-bituminous and a Pittsburgh bituminous at 1250 K, 1500 K and 1750 K furnace temperature, and 20% O_2 in Helium. Figures 11, 12 and 13 represent the time resolved fuel nitrogen and weight loss data from Cheng's experiments. Both Cheng and Song[4], who used the laminar flow reactor for investigating fuel nitrogen evolution from devolatized coal char under oxidizing conditions, were able to determine kinetic parameters from their studies. Cheng's rate equation for the pyrolysis of coal nitrogen gave

$$K_{pyr} = 5.24 \times 10^3 \, [\exp(-28200/RT)\mathrm{sec}^{-1}] \; .$$

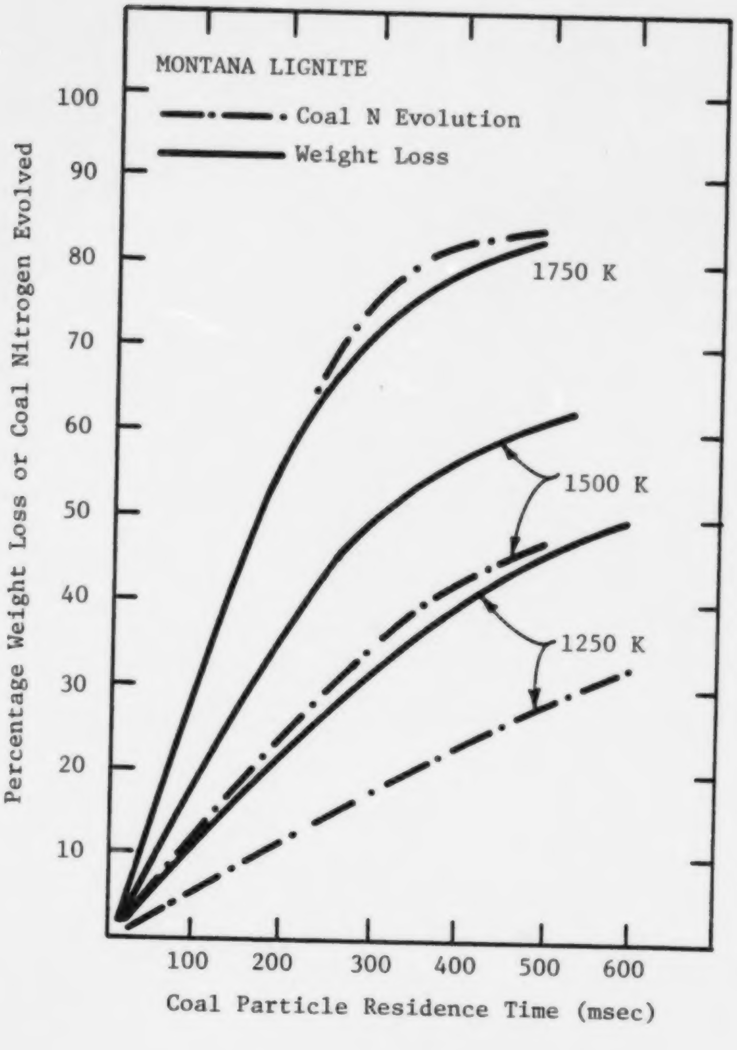

Figure 11. Time Resolved Weight Loss and Coal Nitrogen Evolution.

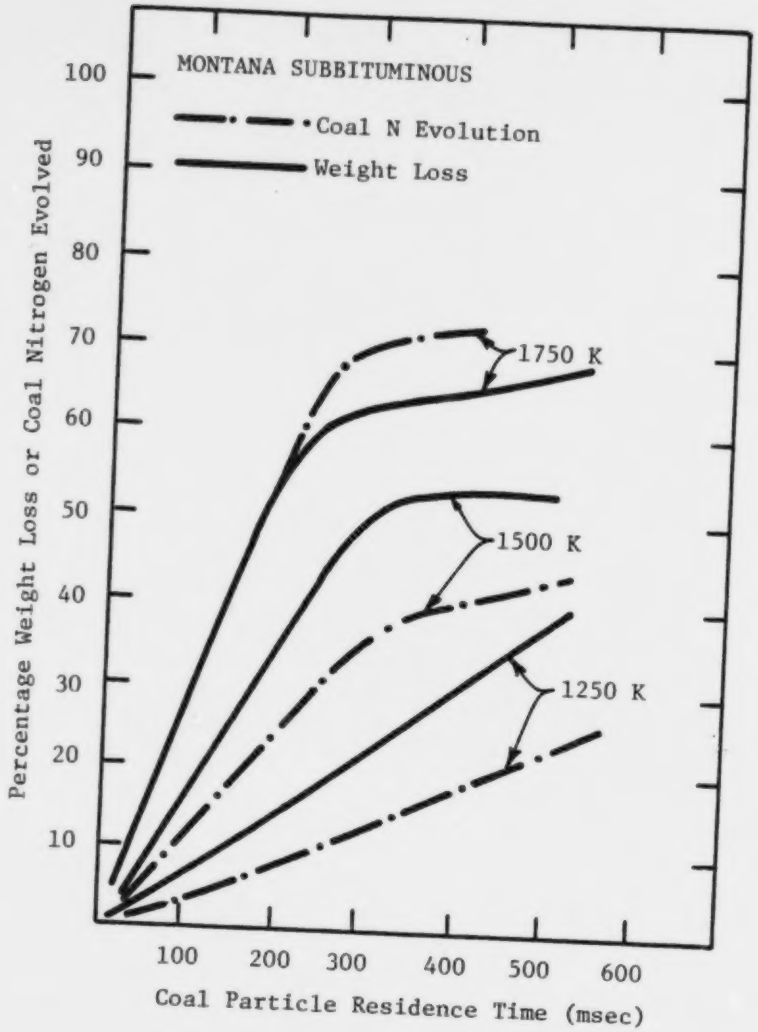

Figure 12. Time Resolved Weight Loss and Coal Nitrogen Evolution.

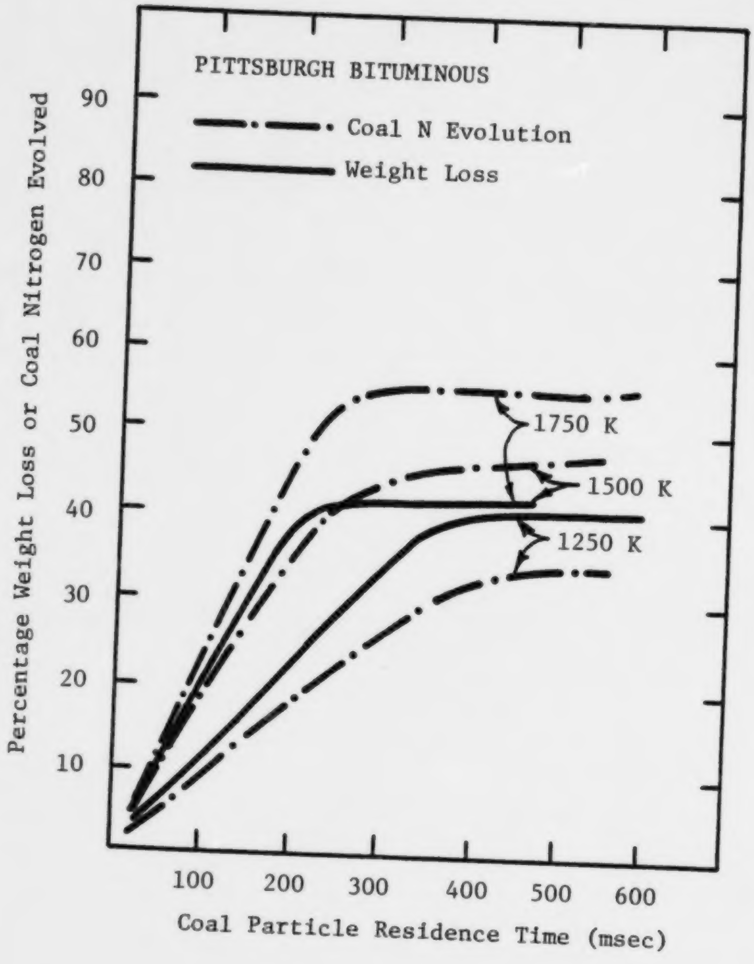

Figure 13. Time Resolved Weight Loss and Coal Nitrogen Evolution.

Figure 14 shows a comparison of rate constants determined by Cheng and Song for oxidative pyrolysis of coal and char, with Pohl's data for the initial rate of coal nitrogen devolatilization in inert atmosphere and with Solomon's[5] results from his studies at UTRC. Notwithstanding the reasonable agreement of Cheng's data with those of other workers, a difficulty of oxidative pyrolysis data interpretation remains. That is the uncertainty about the difference between the furnace and particle temperature, and "energy feed-back" from the volatile flame for the pyrolysis of the char.

Optical measurements by two color pyrometry recently gave further insight into the combustion of coal particles in oxidizing atmospheres in the laminar flow furnace, as described in the paper on NO/char reduction presented at this meeting. The particles are viewed from the top of the furnace by means of fiber optics and the time resolved signals are used for the evaluation of the particle temperature and also for the volatile and char burning times. Measurements made with a lignite and bituminous coal show the significance of the composition of the volatile matter upon the nature of the combustion process.

Figure 15 represents photomultiplier pulses for Illinois coal particles of 90 to 105 μm size at 1750 K furnace temperature, burning under conditions of varying O_2 concentration in the gas. At lower O_2 concentrations the signal starts with a spike corresponding to the volatile flame followed by the broad hump of the char burn-out. As the total burning time is reduced from about 80 milliseconds at 15% O_2 to about 15 milliseconds at 100% O_2, there is a gradual merging of the two peaks into a single peak at 100% O_2. The significance of the two peaks is that they provide evidence for an attached volatile flame, and support observations made at lower temperatures, which showed that due to lack of oxygen at the particle surface during the burning of the volatile flame

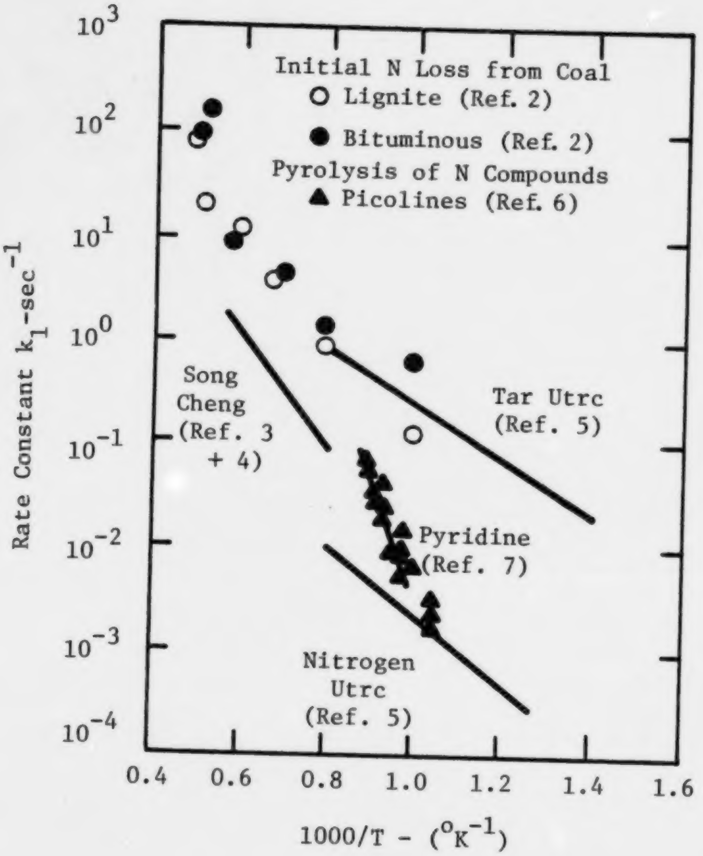

Figure 14. Rate Constants for Nitrogen Release.

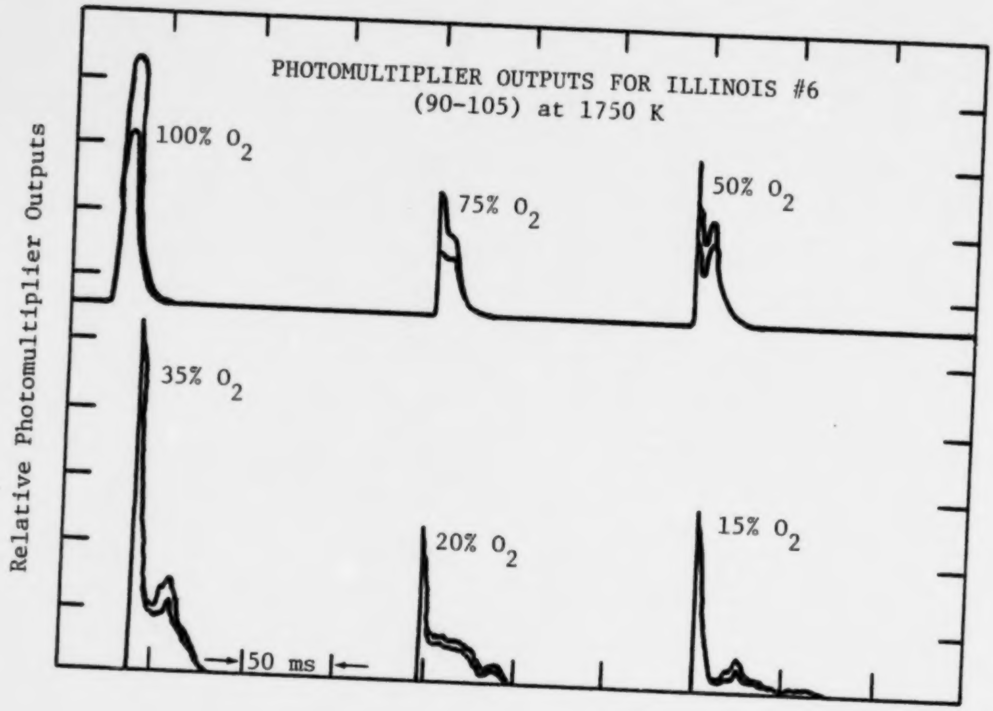

Figure 15. Optical Measurements by Two Color Pyrometry.

the particle surface temperature peaks only after the volatile flame has burned out. There is, of course, some variation about this general behavior of the particles due to the variability of particle shape and composition that occurs even with a close sieve fraction of particles from a given coal type.

Photomultiplier output traces and two color temperatures for Montana lignite and Illinois bituminous coal are shown in Figures 16 and 17. The coal type can be seen to have major influence on the mode of burning of the particle and the particle temperature. The combustion of an Illinois #6 particle of 90 to 105 μm at 1750 K furnace temperature with 20% O_2 exhibits sharp initial peaks in the signal and in the temperature, which are characteristic of bituminous coal; for a lignite these initial peaks are missing. Although the ASTM volatile content of the Montana lignite is comparable to that of the Illinois #6, the composition of the volatile is quite different. Water and CO_2 form a significant part of the lignite volatile resulting in a low calorific value gas compared to that of the bituminous coal. Due to this difference, the temperature of the lignite particle increases relatively slowly to a peak which falls considerably short of that obtained with a bituminous coal particle, even at the high O_2 concentration of 35%.

In summary, the development and application of the technique of time resolved measurement of the particle temperature presents, through the interpretation of the emission signal, insights regarding the nature of the volatile flame as to whether it is attached or detached from the particle. The nature of the data acquisition, storage and analysis of this technique permits statistical studies of coal particle time-temperature histories to be made. Such a study could make an important contribution to the resolution of the problem posed by experimental results which show different yields of NO_x from fuels of seemingly similar fuel characteristics.

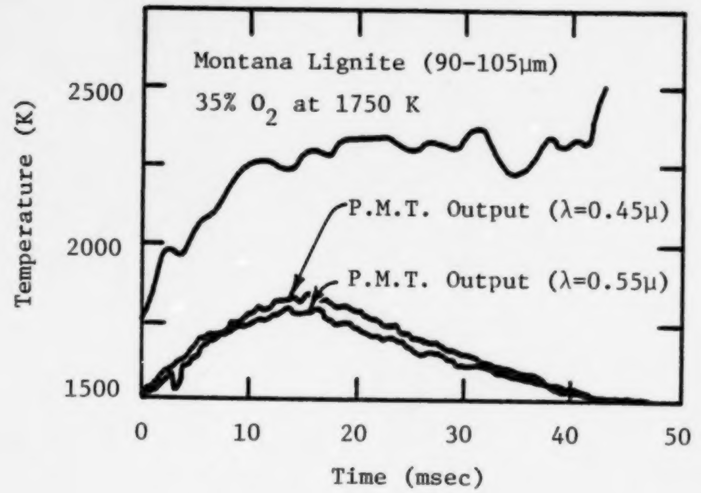

Figure 16. Temperature Measurements by Two Color Pyrometry.

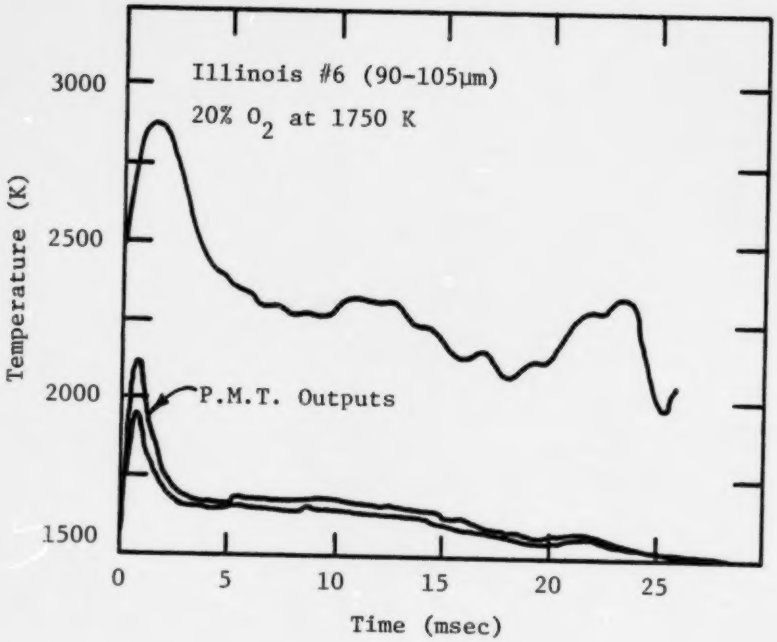

Figure 17. Temperature Measurements by Two Color Pyrometry.

REFERENCES

1. Mims et al., "Laboratory Studies of Trace Element Transformations during Coal Combustion," paper presented at the National 87th AIChE Meeting, August 19-22, 1979, Boston, Mass.

2. Pohl, J. H. and Sarofim, A. F., "Devolatilization and Oxidation of Coal Nitrogen," Sixteenth Symposium (International) on Combustion, p.491, The Combustion Institute, Pittsburgh, Pennsylvania (1977).

3. Cheng C., "Coal Nitrogen Conversion to NO_x During Simultaneous Oxidation and Pyrolysis." S. M. Thesis, M.I.T., Cambridge, Massachusetts (1978).

4. Song, Y. H., "Fate of Fuel Nitrogen During Pulverized Coal Combustion." D.Sc. Thesis, M.I.T., Cambridge, Massachusetts (1978).

5. Solomon, P. R., "The Evolution of Pollutants During the Rapid Devolatilization of Coal." Report NSF/RA-770422 NMS #PB278496/AS.

6. Hurd, C. D., and Simon, J. I., "Pyrolytic Formation of Arenes. III Pyrolysis of Pyridine, Picolines and Methyl Pyrazine," J. American Chemical Society, 84, 4509 (1962).

7. Axworthy, A. E., Dayan, V. H., Martin, G. B., "Reactions of Fuel-Nitrogen Compounds under Conditions of Inert Pyrolysis," Fuel, 57, 29 (1978).

10

THE CHARACTERIZATION OF COALS DURING THERMAL DECOMPOSITION

P. R. Solomon
United Technologies Research Center
East Hartford, Connecticut 06108

Fifth EPA Fundamental Combustion Research Workshop
Newport Beach, California
January 23-25, 1980

SECTION I

INTRODUCTION

A relation between coal organic structure and the products of thermal decomposition has been developed by measuring and modeling vacuum devolatilization of twelve bituminous coals and a lignite (Refs. 1-3). The relation allows the prediction of the time and temperature dependent evolution of the major products of pyrolysis from a knowledge of the coal's functional group distribution using a general kinetic model with rate constants independent of coal rank. The model assumes that large molecular fragments ("monomers") are released from the coal "polymer" with only minor alteration to form tar while simultaneous cracking of the chemical structure forms the light molecules of the gas. Any chemical component of the coal can, therefore, evolve as part of the tar or as an independent species. The model may be used to predict the amount of volatile fuel nitrogen evolved in pyrolysis which is essential in estimating the conversion to NO_x.

This paper reports on the application of these concepts to the study of several coals which are currently being investigated in the EPA Fundamental Combustion Research Program. Particular attention has been given to the rate and forms of nitrogen evolution.

SECTION II

EXPERIMENTAL

The apparatus is illustrated in Figure 1. It consists of a small chamber in which the coal is pyrolized connected through a glass wool filter to a large gas cell for infrared analysis. The coal is evenly distributed between the folds of a stainless steel, molybdenum or tungsten screen and a current is passed through the screen to heat the coal. Coal temperatures of 1800°C and heating rates of 2000°C/sec were achieved using the tungsten screen. Gas analysis is performed with a Nicolet (FTIR) which permits low resolution analysis at 0.2 second intervals. The low resolution analysis can determine CO, CO_2, H_2O, CH_4, COS, SO_2, CS_2, HCN, C_2H_2, C_2H_4, C_3H_6, benzene and heavy paraffins and olefins. Figure 2 shows the spectra obtained at several time intervals during a 10 second devolatilization run at about 800°C. Kinetic rate data for major species can be determined from such scans. A high resolution analysis made at the completion of a run can determine all of the above plus C_2H_6, C_3H_8, C_4H_8, NH_3 and potentially many other species which have not yet been observed. H_2 is determined by difference. Other features of the apparatus are similar to those described previously (Refs. 1-3).

The Model

The pyrolysis model has been based on the understanding of coal thermal decomposition developed by measuring and modeling vacuum pyrolysis for a large number of coals. The work is discussed in detail in Refs. 1-4. The model assumes a coal structure consisting of highly substituted aromatic ring clusters containing heteroatoms linked by relatively weak aliphatic bridges. Evidence suggests that during thermal decomposition these weak links break, releasing the clusters and attached bridge fragments which comprise the tar.

In vacuum devolatilization in a thin heated grid, the tar molecules may be removed quickly from the bed and undergo little secondary reactions. The evidence for this is the striking similarity between the tar and parent coal which has been observed in elemental analysis, FTIR spectra and NMR spectra (Refs. 1-8). The two materials are almost identical except for a higher concentration of aliphatic hydrogen (especially methyl) in the tar. This extra hydrogen is presumably abstracted from the char to stabilize the free radical

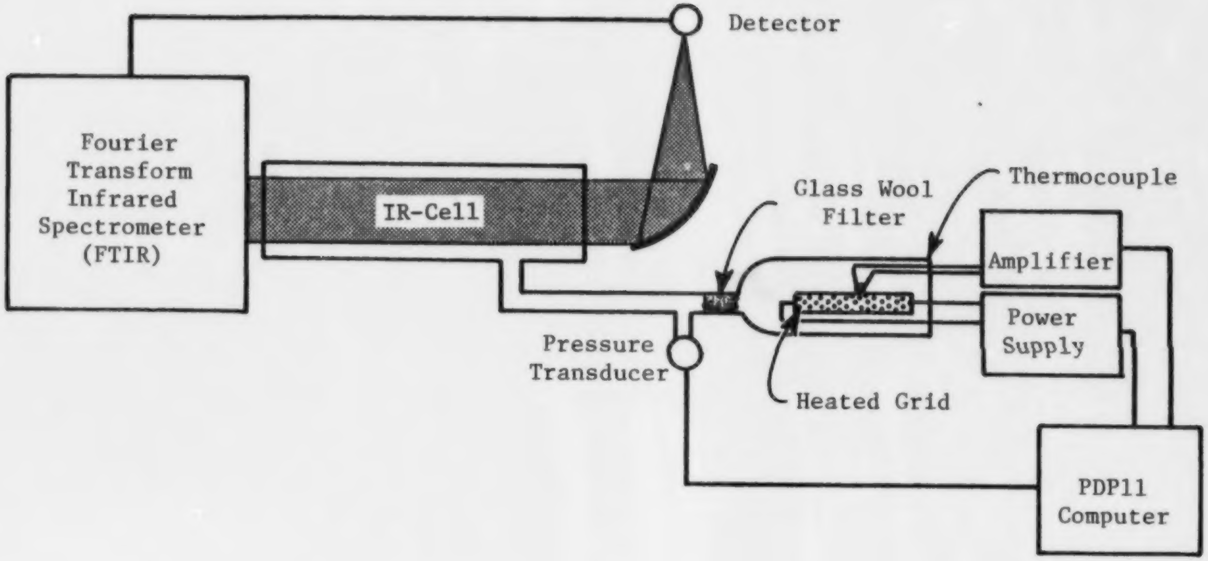

Figure 1. Pyrolysis Apparatus.

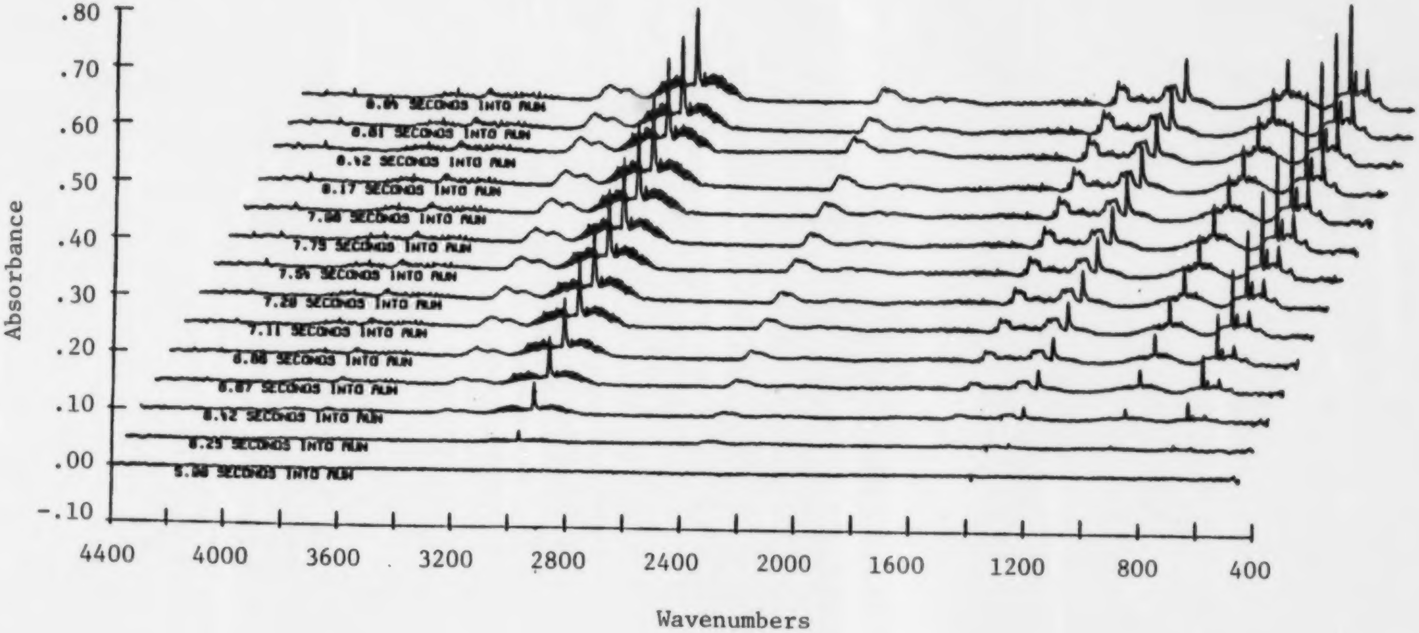
Absorbance
.80
.70
.60
.50
.40
.30
.20
.10
.00
-.10
8.84 SECONDS INTO RUN
8.61 SECONDS INTO RUN
8.42 SECONDS INTO RUN
8.17 SECONDS INTO RUN
7.98 SECONDS INTO RUN
7.75 SECONDS INTO RUN
7.54 SECONDS INTO RUN
7.28 SECONDS INTO RUN
7.11 SECONDS INTO RUN
6.88 SECONDS INTO RUN
6.87 SECONDS INTO RUN
6.42 SECONDS INTO RUN
6.25 SECONDS INTO RUN
5.98 SECONDS INTO RUN
4400
4000
3600
3200
2800
2400
2000
1600
1200
800
400
Wavenumbers

Figure 2.

sites formed when the bridges were broken. Similar arguments were given for pyrolysis of model compounds by Wolfs, van Krevelen and Waterman (Ref. 9). Since the abstracted hydrogen is most likely to come from the aliphatic portion of the coal, it is reasonable to expect the tar yield to depend on H_{al}. In Figure 3 the tar yield in vacuum pyrolysis is plotted against H_{al} for a number of coals (circles). Also plotted are the yields of heavy hydrocarbons, (i.e., oils + BTX) from hydropyrolysis (squares). Indeed, there is a strong correlation between tar yield and H_{al}.

Simultaneous with the evolution of tar molecules is the competitive cracking of bridge fragments, substituted groups and ring cluster to form the light molecular species of the gas. The quantity of each gas species depends on the functional group distribution in the original coal. At low temperatures there is very little rearrangement of the aromatic ring structure. There is decomposition of the substituted groups and aliphatic structure resulting in CO_2, H_2O, hydrocarbon gases and some CO release from the carboxyl, hydroxyl, aliphatic and weakly bound ether groups, respectively. At high temperature there is a breaking and rearrangement of the aromatic ring. In this process, H_2 is released from the aromatic hydrogen and HCN and additional CO are released from ring nitrogen and tightly bound ether linkages.

Coal Functional Group Composition

To determine the coals functional group composition quantitatively, infrared spectra were obtained on a Nicolet FTIR. The techniques of preparing KBr pellets and of correcting for scattering and mineral content was described in a previous publication (Ref. 4). Spectra for a lignite and a bituminous coal are shown in Figure 4. Quantitative determinations of the hydroxyl, aliphatic and aromatic hydrogen concentrations are made as described previously (Ref. 4).

To determine the aliphatic carbon concentration, it has been assumed that the stoichiometry of the aliphatic component is $CH_{1.8}$. The value 1.8 is an average of the aliphatic stoichiometry in coals made by several investigators. C_{ar} has been calculated using a method suggested by Brown and Ladner (Ref. 10). The method determines C_{ar} by difference

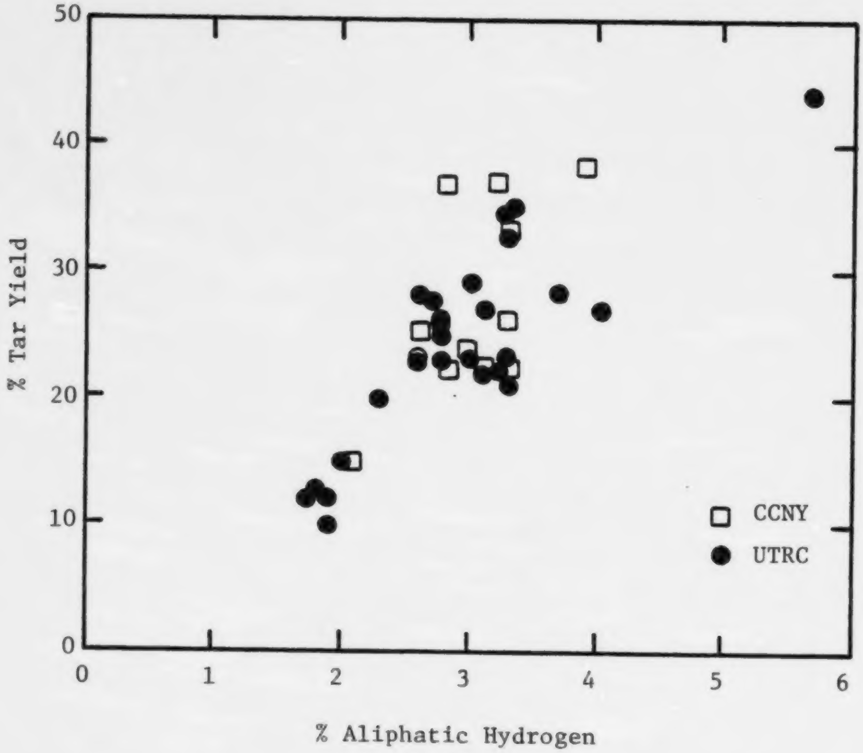

Figure 3. Variation of Tar Yield with Aliphatic Hydrogen.

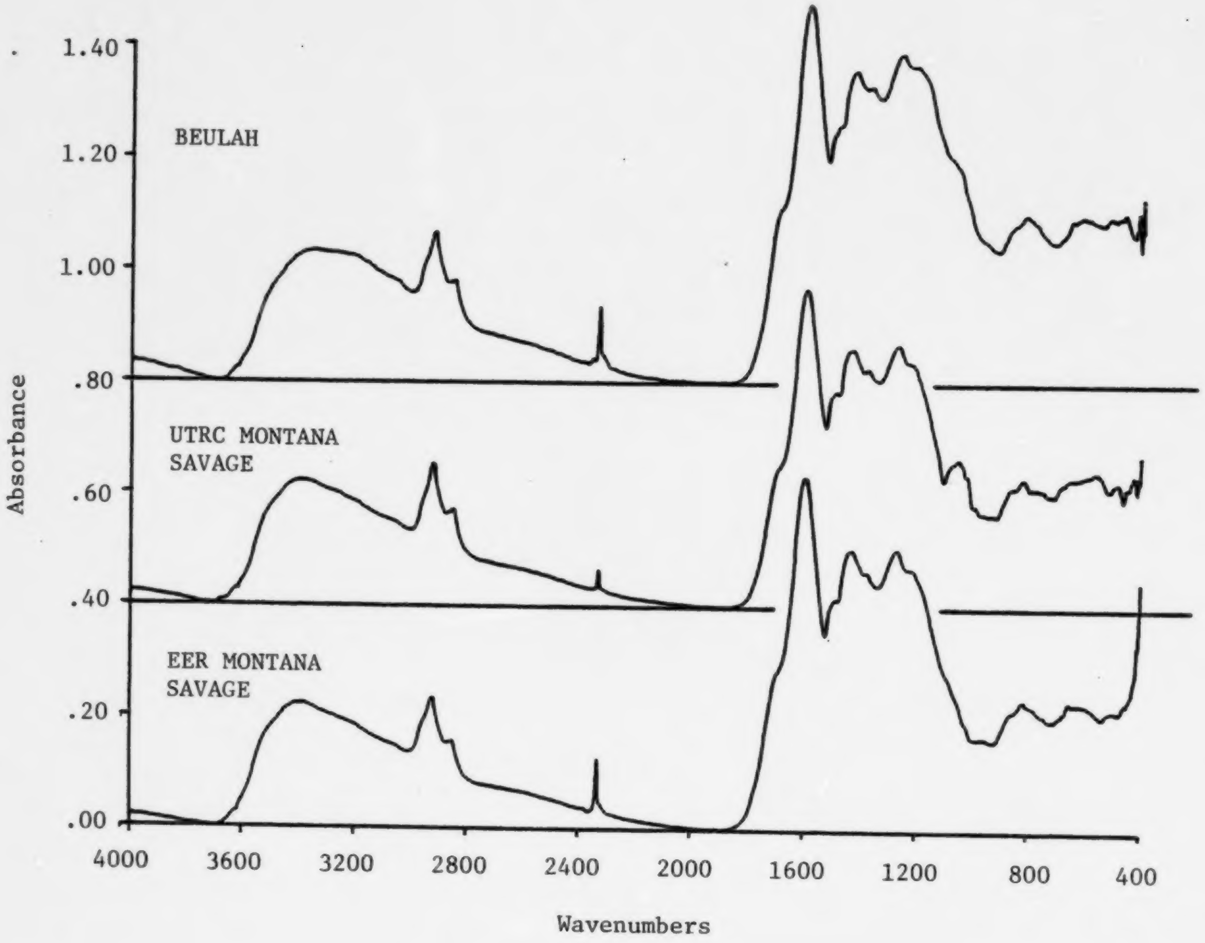

1.40
1.20
1.00
.80
.60
.40
.20
.00
Absorbance
BEULAH
UTRC MONTANA
SAVAGE
EER MONTANA
SAVAGE
4000
3600
3200
2800
2400
2000
1600
1200
800
400
Wavenumbers

Figure 4.

$$C_{ar} = C_{total} - C_{al} \tag{1}$$

$$= C_{total} - (12/x)\, H_{al} \tag{2}$$

where C_{total} is the total carbon concentration and x is a parameter which describes the stoichiometry of the aliphatic material CH_x. The accuracy of the method has recently been verified by Retcofsky et al. (Ref. 11).

SECTION III

RESULTS

Pyrolysis experiments have been performed on Beulah and North Dakota lignite, and Rosa, a bituminous coal, between 400°C and 1800°C. The data have been reduced and the results are presented in Figures 4-15, along with the model simulations for these coals. Results for a Montana lignite from the Savage mine and a Pittsburgh seam bituminous are also included for comparison. These two coals have been analyzed extensively and are discussed in Refs. 1-6. It should be emphasized that the simulation results for all four coals were performed with the same set of kinetic parameters listed in Ref. 4.

Consider first the lignites. Elemental analysis and FTIR analysis indicate that the Beulah North Dakota lignite, and the Montana Savage lignite (samples of the Savage have been supplied by EER and have been obtained directly from the Savage mine) are quite similar. The infrared spectra are presented in Figure 4. The pyrolysis data for the Beulah, when compared to the Montana Savage (UTRC) confirm the two to be almost identical and in fact both coals were fit with the identical model parameters for the functional groups (discussed in Ref. 4). One difference is that the Beulah should be fit with a slightly higher value for Y^o (ether-loose) (see Figure 8).

Infrared spectra of the Rosa and Pittsburgh seam bituminous are presented in Figure 5. Model parameters for the Rosa coal were determined from the FTIR spectrum, the elemental analysis, and the pyrolysis results as discussed in Ref. 4. The agreement between the data and the model simulation are good except for the H_2O and CO. In the model, it is assumed that roughly 1/2 of the hydroxyl oxygen is evolved as H_2O. As can be seen in Figure 9, the water evolution is much smaller than the simulation predicts. No explanation for this effect is apparent. The predicted CO level is also higher than is measured.

Figure 14 shows some interesting aspects of the evolution of nitrogen during pyrolysis. At temperatures below 1200°C, nitrogen balance is obtained by measuring the tar and char nitrogen, HCN and NH_3. At higher temperatures, there appears to be some missing material indicating some other nitrogen form evolved which is not determined. Of the gaseous species, HCN yields are

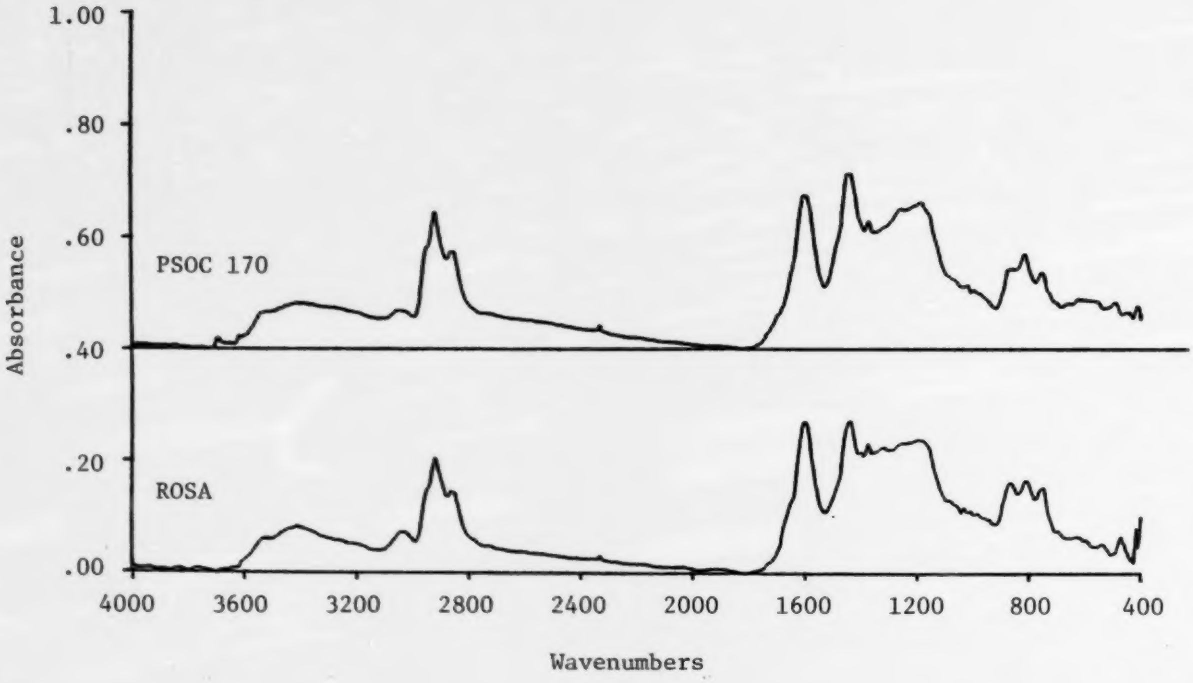
1.00
.80
.60
.40
.20
.00
Absorbance
PSOC 170
ROSA
4000
3600
3200
2800
2400
2000
1600
1200
800
400
Wavenumbers

Figure 5.

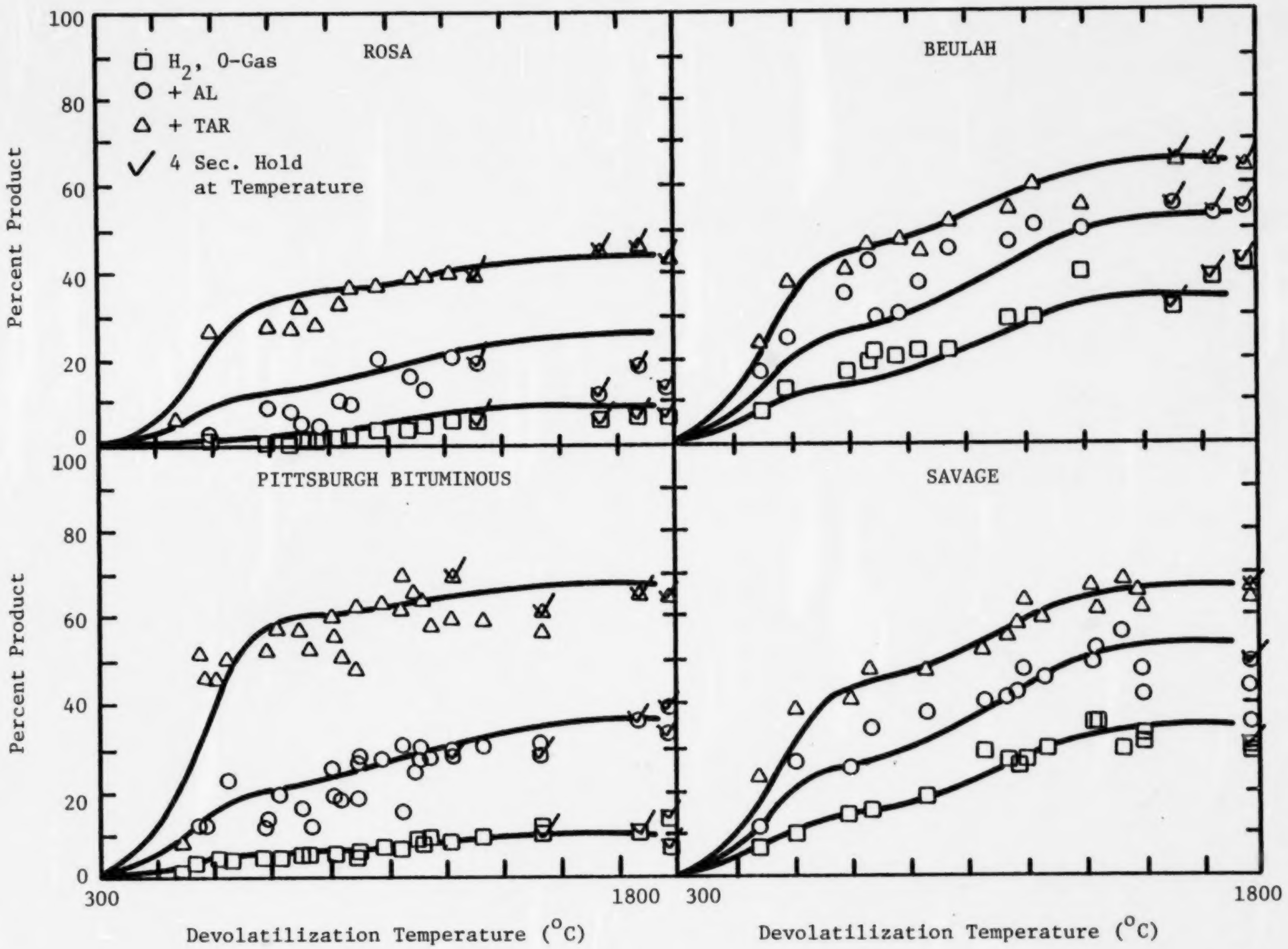
100
80
60
40
20
0
Percent Product
□ H_2, 0-Gas
○ + AL
△ + TAR
✓ 4 Sec. Hold at Temperature
ROSA
BEULAH
PITTSBURGH BITUMINOUS
SAVAGE
300
1800
Devolatilization Temperature (°C)

Figure 6.

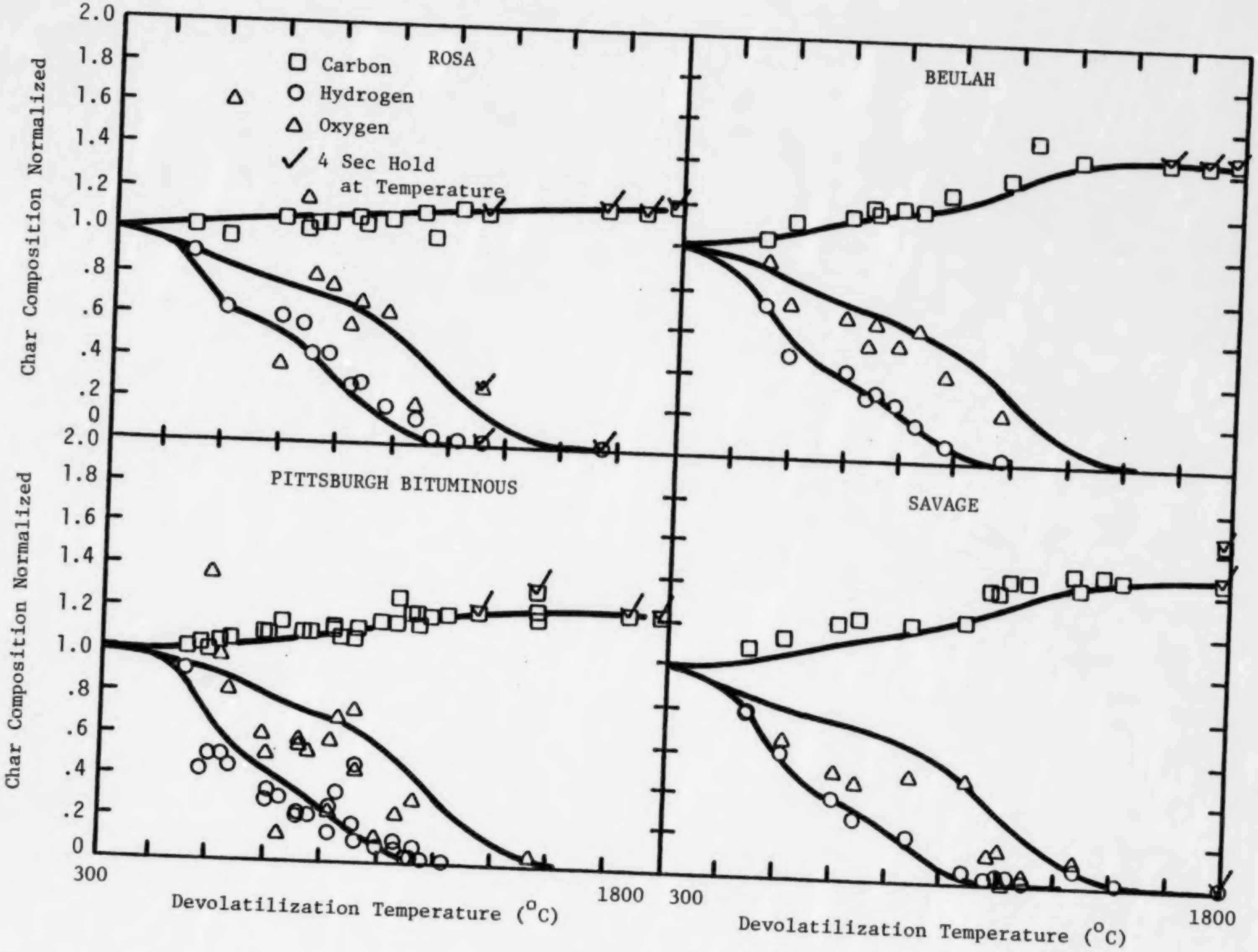
ROSA
BEULAH
PITTSBURGH BITUMINOUS
SAVAGE
□ Carbon
○ Hydrogen
△ Oxygen
✓ 4 Sec Hold at Temperature
Char Composition Normalized
2.0
1.8
1.6
1.4
1.2
1.0
.8
.6
.4
.2
0
300
1800
Devolatilization Temperature (°C)

Figure 7.

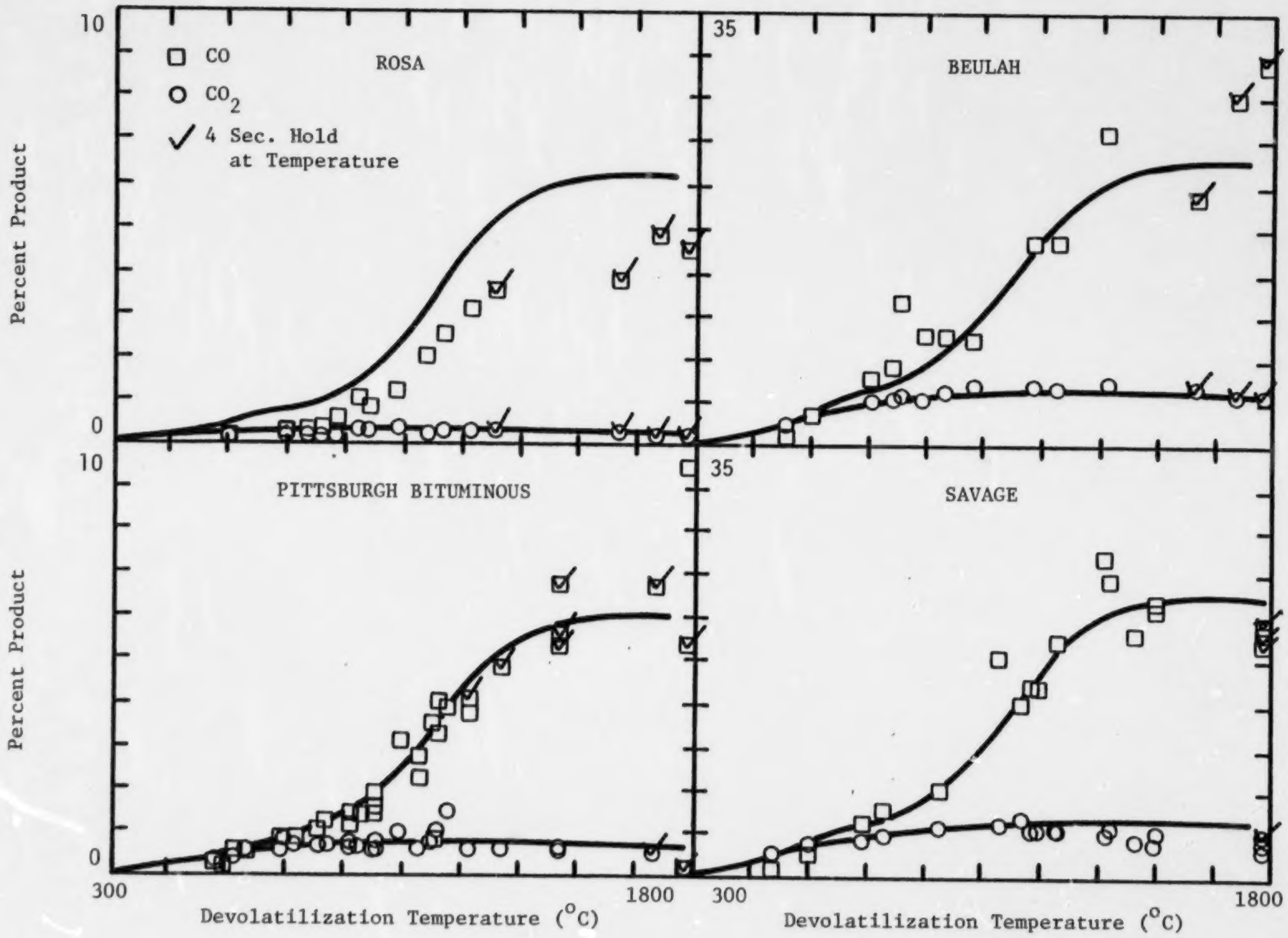
10
0
10
0
35
35
300
1800
300
1800
CO
CO2
4 Sec. Hold at Temperature
ROSA
BEULAH
PITTSBURGH BITUMINOUS
SAVAGE
Percent Product
Percent Product
Devolatilization Temperature (°C)
Devolatilization Temperature (°C)

Figure 8.

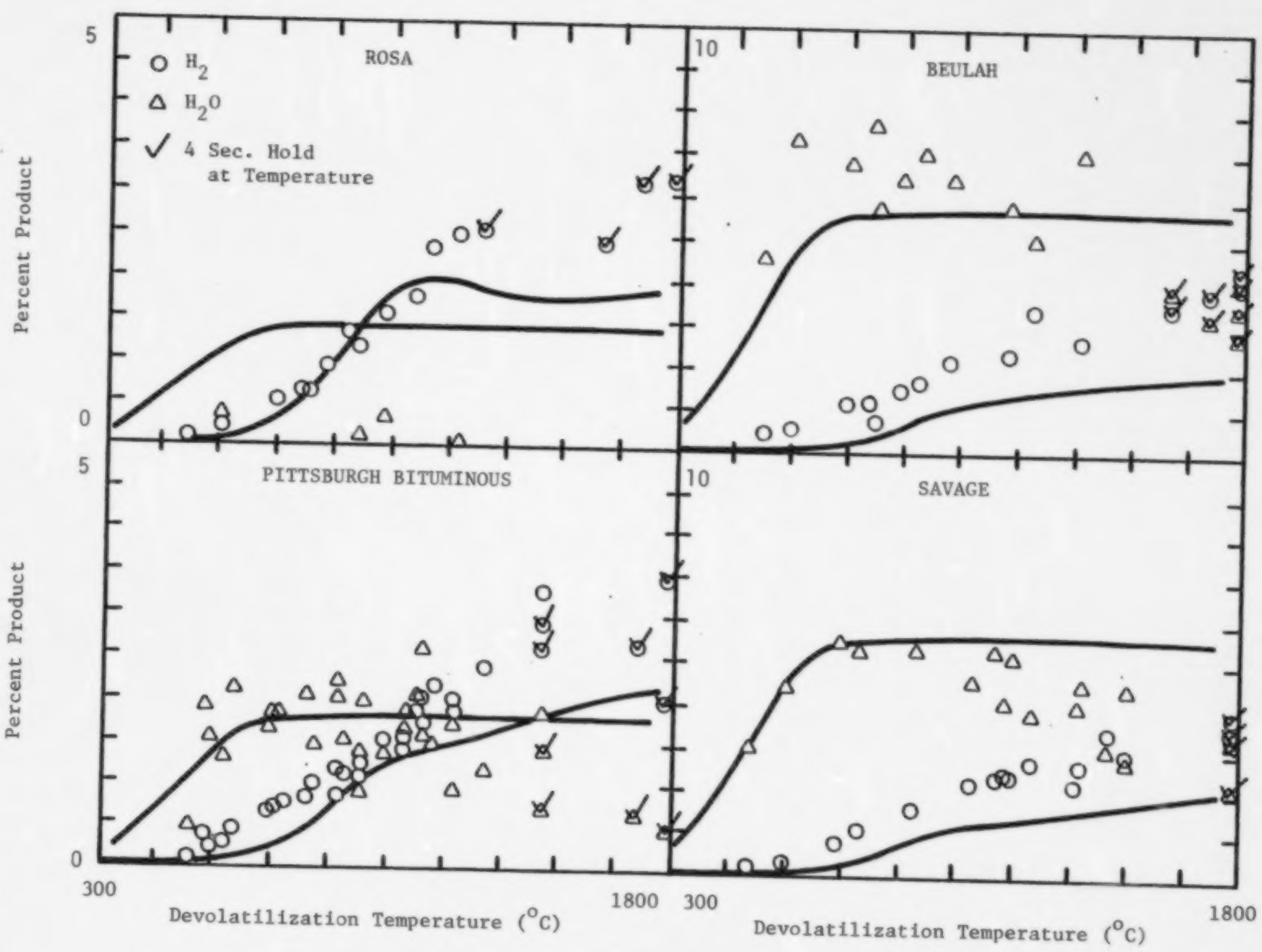
5
0
Percent Product
○ H_2
△ H_2O
✓ 4 Sec. Hold at Temperature
ROSA
10
BEULAH
5
0
Percent Product
PITTSBURGH BITUMINOUS
10
SAVAGE
300
1800
Devolatilization Temperature (°C)
300
1800
Devolatilization Temperature (°C)

Figure 9.

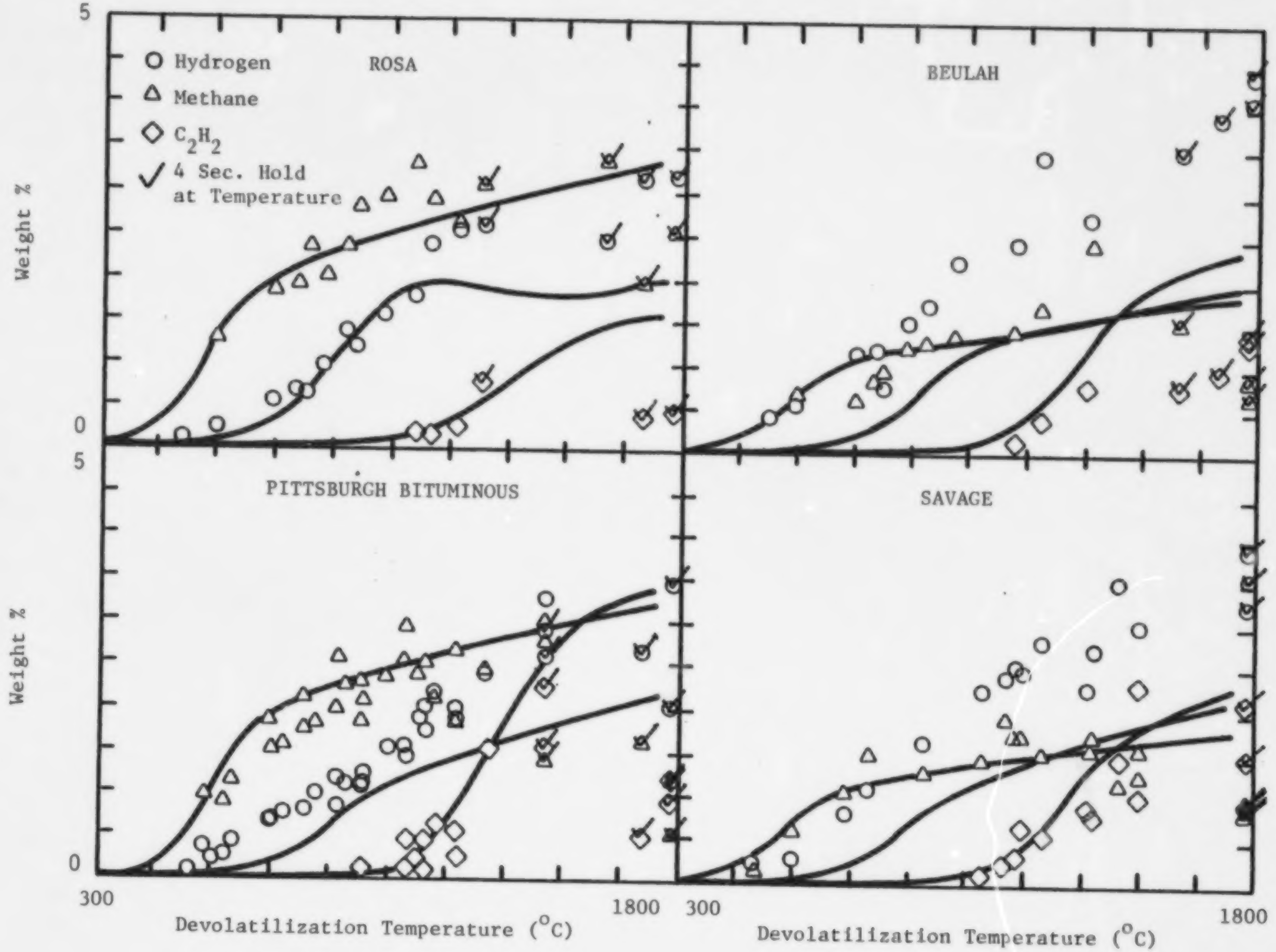
Hydrogen
Methane
C_2H_2
4 Sec. Hold at Temperature
ROSA
BEULAH
PITTSBURGH BITUMINOUS
SAVAGE
Weight %
Weight %
5
0
5
0
300
1800
300
1800
Devolatilization Temperature (°C)
Devolatilization Temperature (°C)

Figure 10.

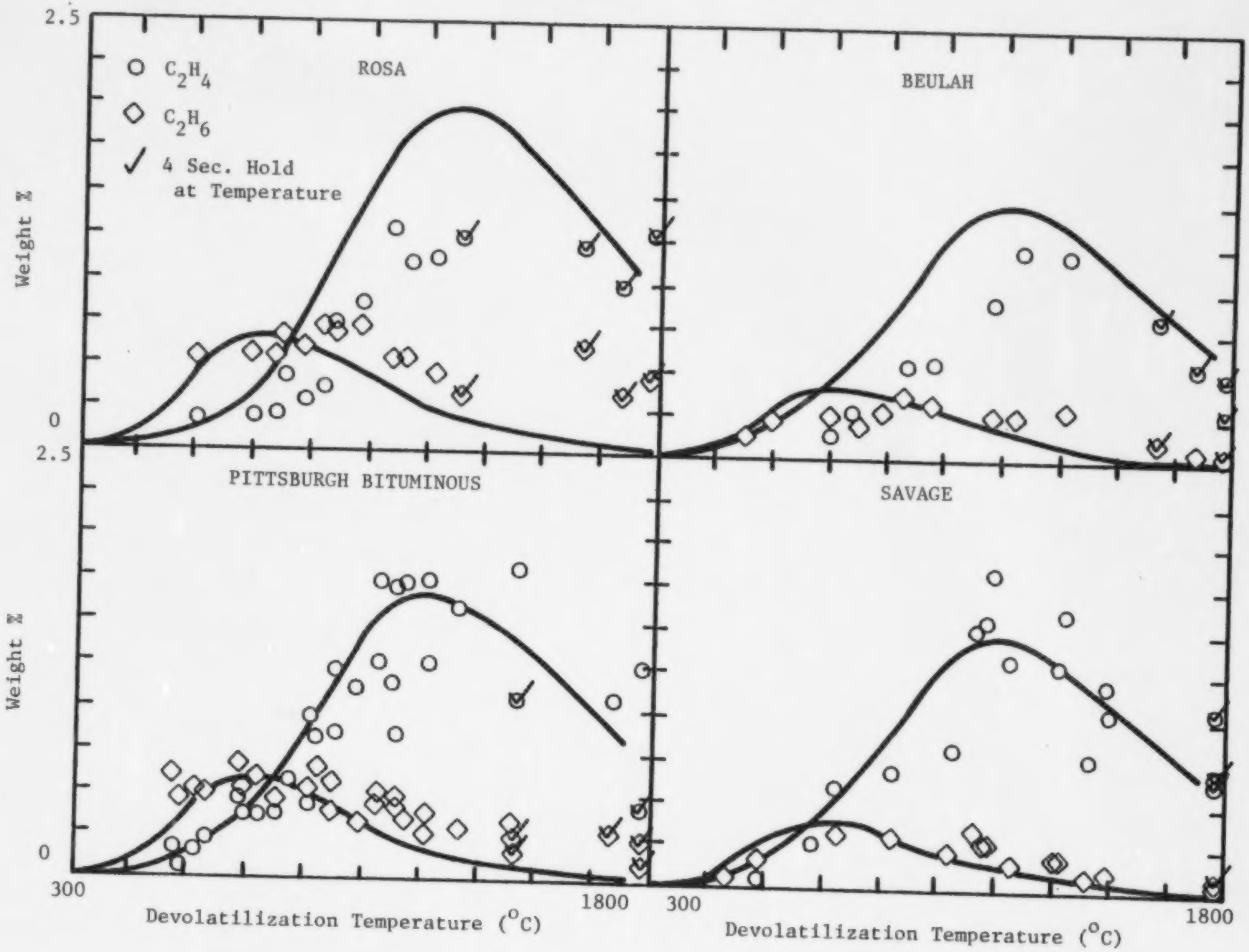
2.5
0
2.5
0
Weight %
Weight %
ROSA
BEULAH
PITTSBURGH BITUMINOUS
SAVAGE
○ C_2H_4
◇ C_2H_6
✓ 4 Sec. Hold at Temperature
300
1800
300
1800
Devolatilization Temperature (°C)
Devolatilization Temperature (°C)

Figure 11.

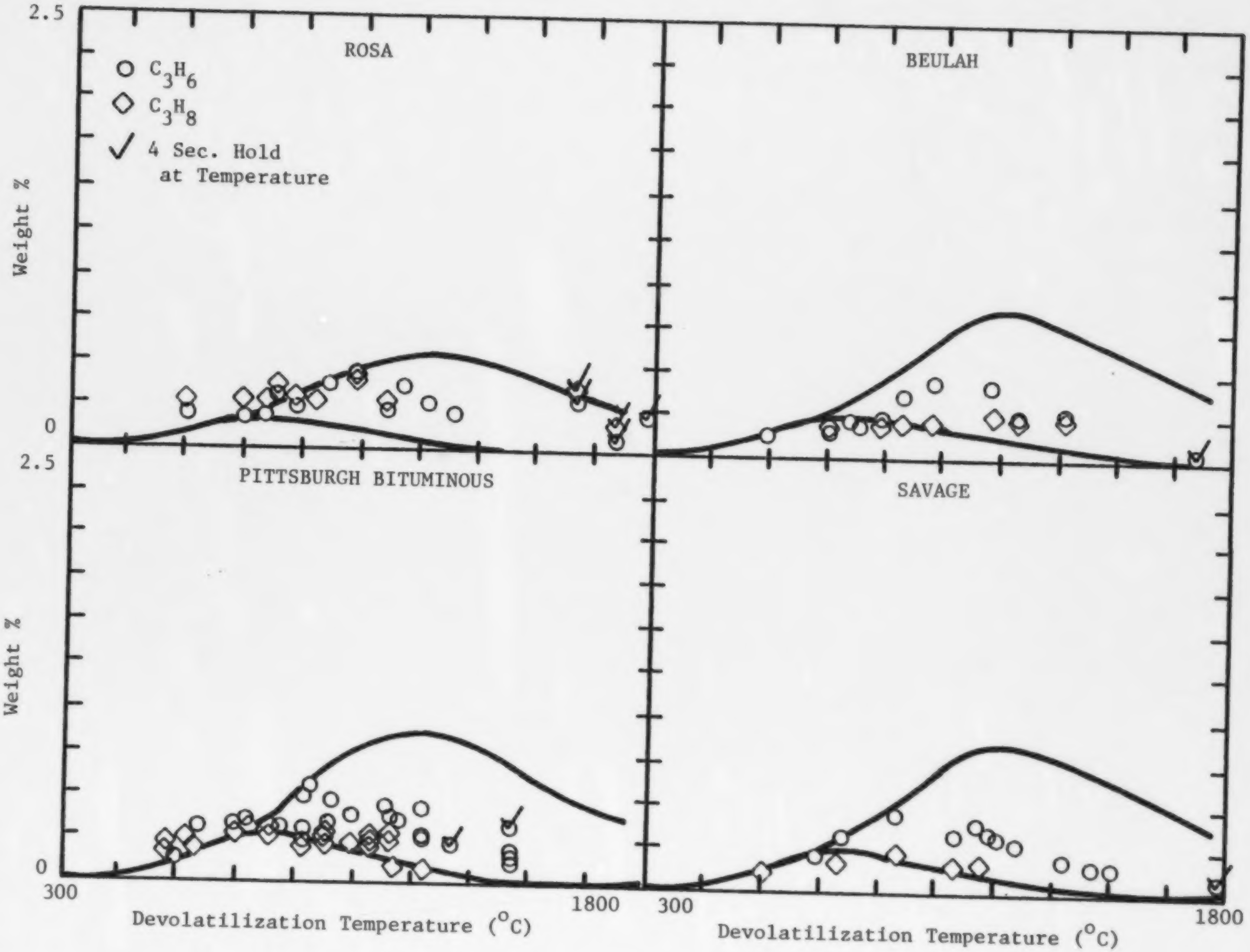
2.5
ROSA
BEULAH
○ C_3H_6
◇ C_3H_8
✓ 4 Sec. Hold at Temperature
Weight %
0
2.5
PITTSBURGH BITUMINOUS
SAVAGE
Weight %
0
300
1800
Devolatilization Temperature (°C)
300
1800
Devolatilization Temperature (°C)

Figure 12.

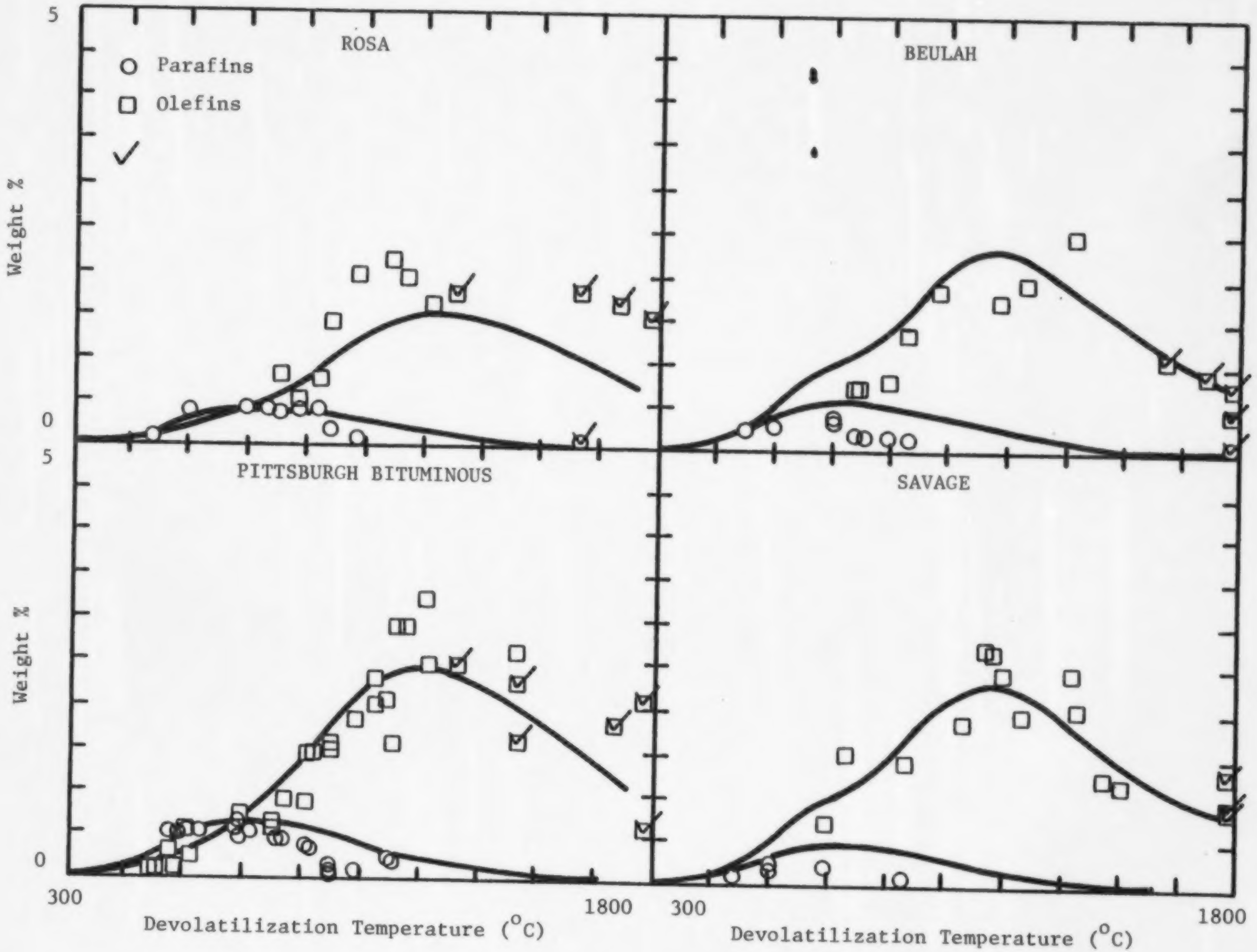
ROSA
BEULAH
PITTSBURGH BITUMINOUS
SAVAGE
○ Parafins
□ Olefins
✓
Weight %
Weight %
5
0
5
0
300
1800
300
1800
Devolatilization Temperature (°C)
Devolatilization Temperature (°C)

Figure 13.

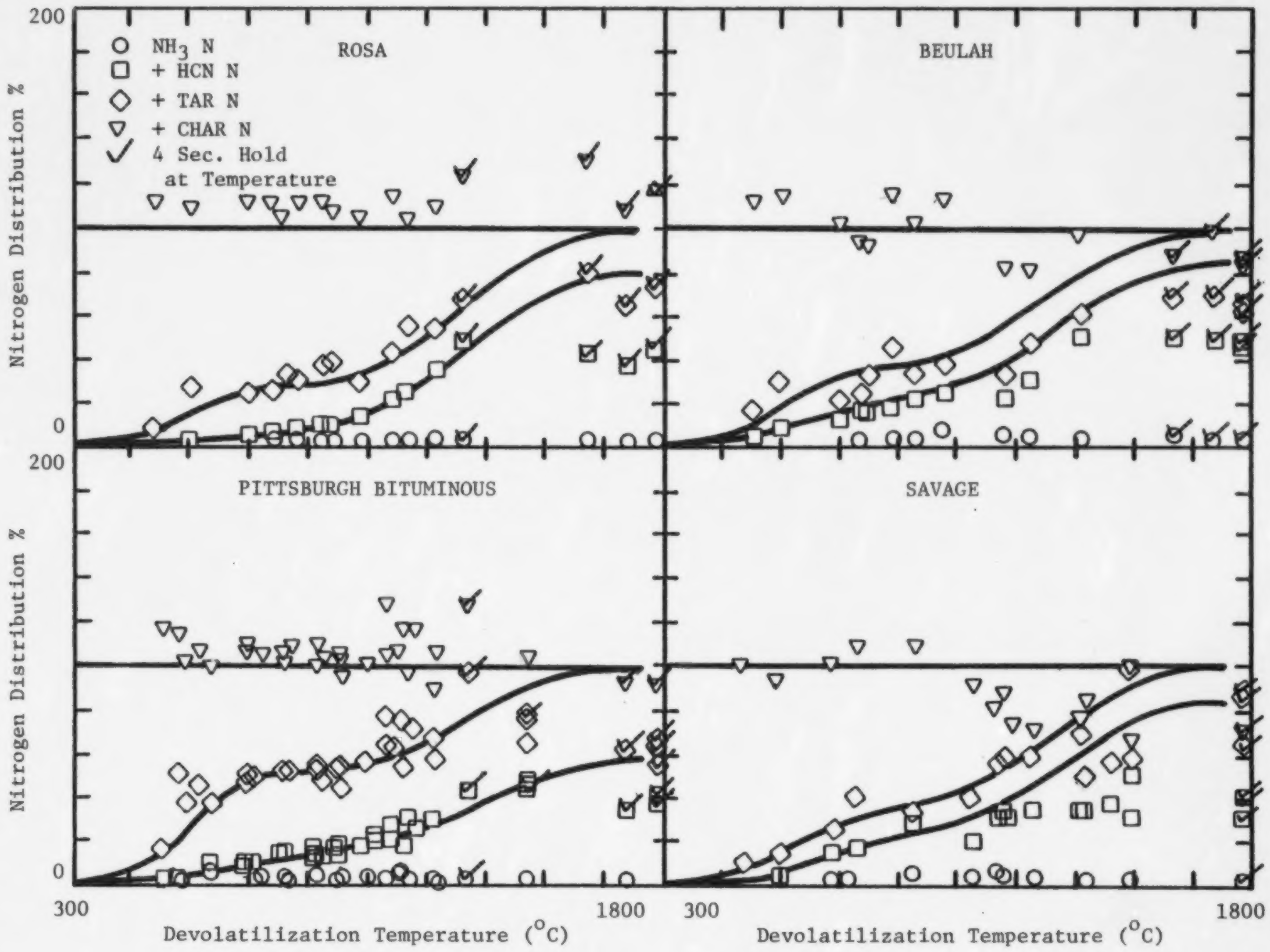
ROSA
BEULAH
PITTSBURGH BITUMINOUS
SAVAGE
○ NH_3 N
□ + HCN N
◇ + TAR N
▽ + CHAR N
✓ 4 Sec. Hold at Temperature
Nitrogen Distribution %
200
0
300
1800
Devolatilization Temperature (°C)

Figure 14.

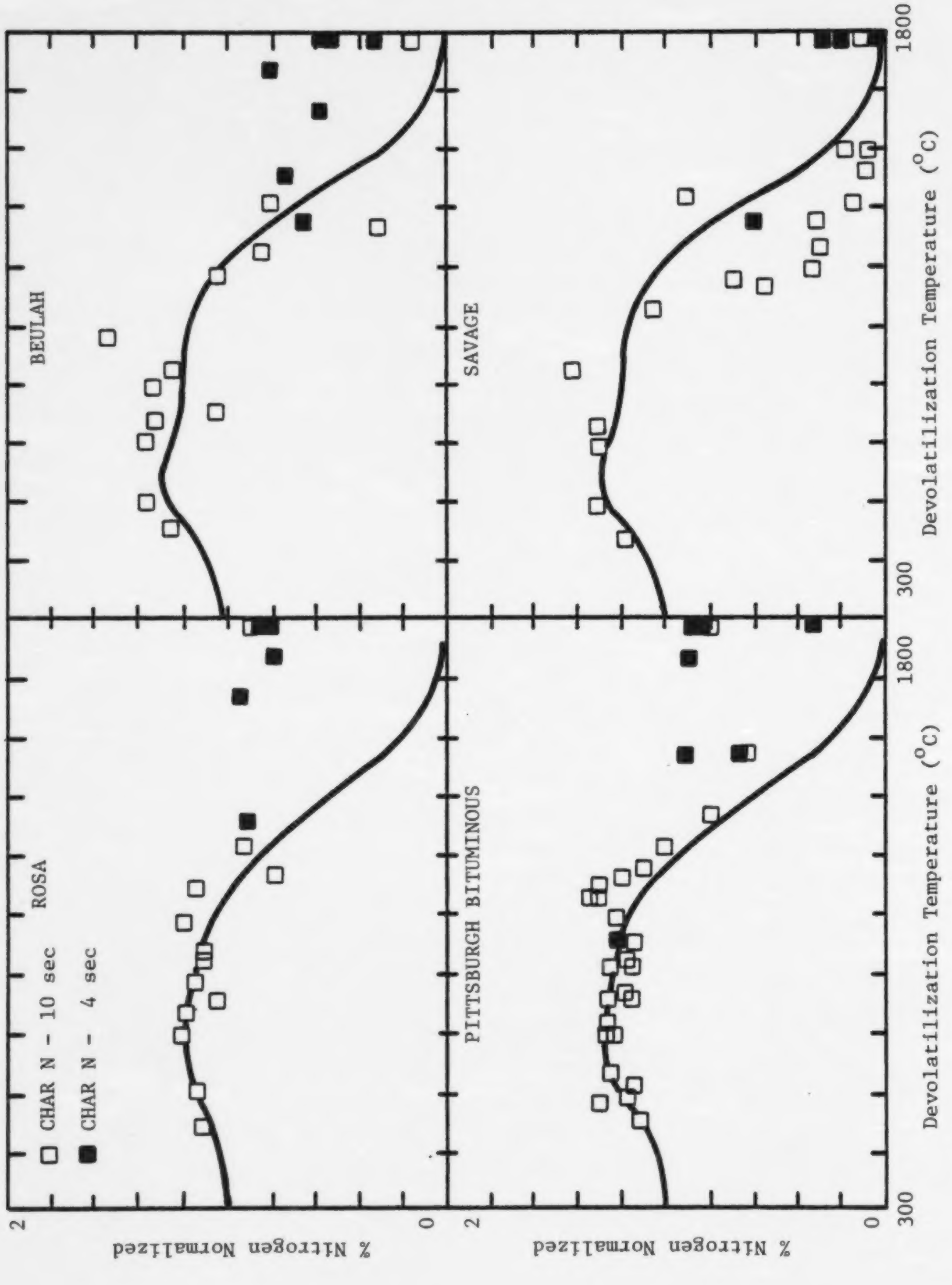

CHAR N - 10 sec
CHAR N - 4 sec
ROSA
BEULAH
PITTSBURGH BITUMINOUS
SAVAGE
% Nitrogen Normalized
% Nitrogen Normalized
2
0
2
0
300
1800
300
1800
Devolatilization Temperature (°C)
Devolatilization Temperature (°C)

Figure 15.

substantially higher than NH_3 and the ease of evolution of these two gases at low temperature appears to be rank dependent. As an example of this feature, the HCN and NH_3 yields for a variety of coals pyrolized at 850°C are plotted as a function of carbon concentration in Figures 16 and 17. The HCN yields shown in Figure 16 increase with decreasing coal rank. For the lowest rank coals almost 20 percent of the nitrogen can be released as HCN at 850°C. The HCN yield goes down drastically as the carbon concentration approaches 90 percent. The yields of nitrogen in NH_3 are about 1/10th those of HCN but show a similar trend. The evolution of these species has a strong influence on the conversion of fuel nitrogen to NO_x.

There is also a rank dependence in the retention of nitrogen in the char as indicated in Figure 15. The higher rank bituminous coals appear to retain much more nitrogen at high temperature than do the lignites. Possible explanations for this could be the higher oxygen content or the smaller aromatic cluster size in the lignite. Additional work should be pursued to understand this effect.

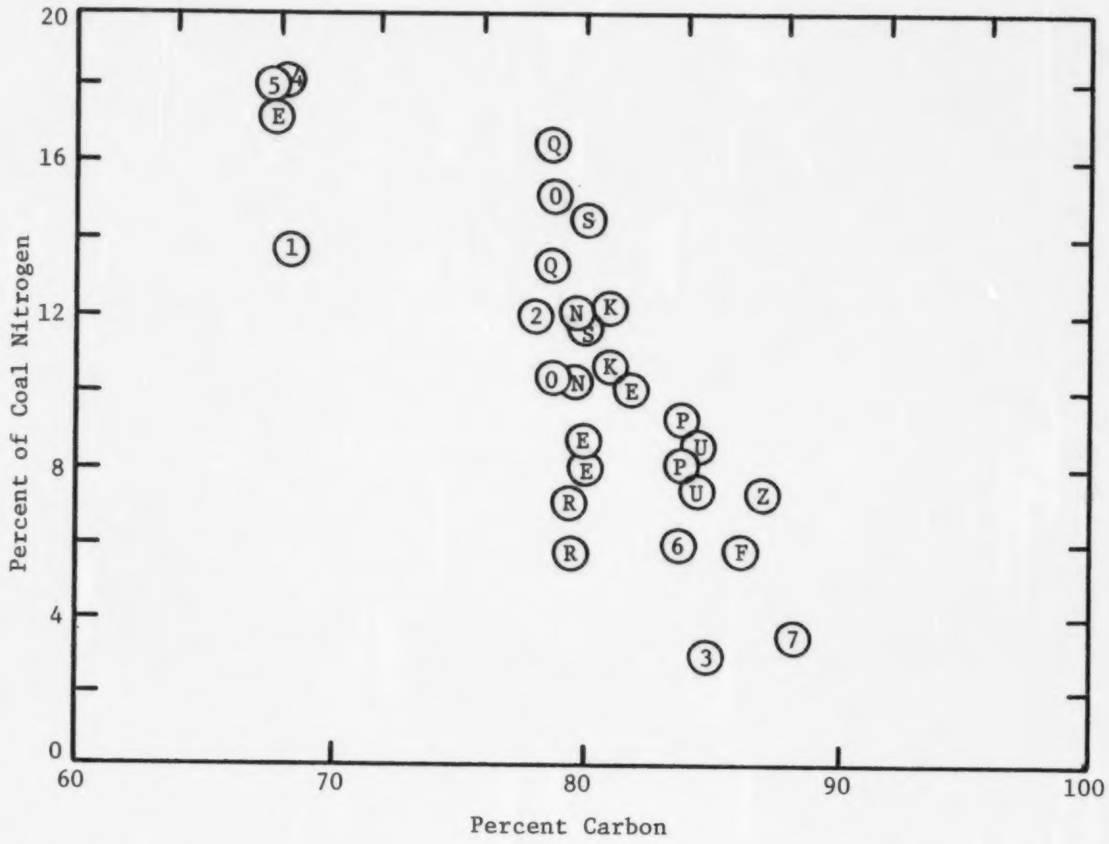

Figure 16. Percent of Coal Nitrogen in HCN.

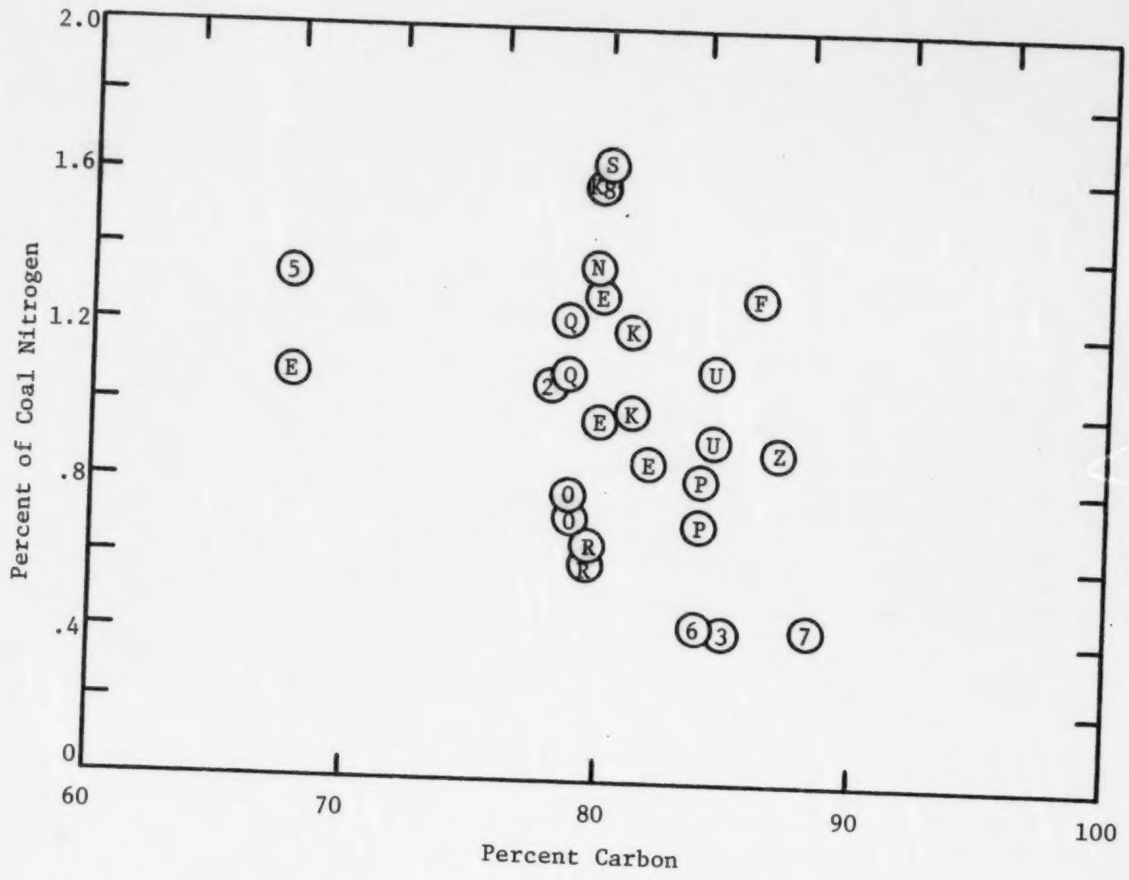

Figure 17. Percent of Coal Nitrogen in NH_3.

ACKNOWLEDGEMENTS

The author wishes to acknowledge the able technical assistance of David Santos, Gerald Wagner and Jennifer Dumala.

REFERENCES

1. Solomon, P. R.: "The Evolution of Pollutants During the Rapid Devolatilization of Coal," Report NSF-RA-770422, NTIS #PB278496/AS.
2. Solomon, P. R., and Colket, M. B.: Seventeenth Symposium (International) on Combustion, The Combustion Institute (1979), p. 137.
3. Solomon, P. R.: A.C.S. Div. of Fuel Chemistry Preprints, 24, #2, 184, (1979).
4. Solomon, P. R.: Conference on "Coal Combustion Technology and Emission Control," California Institute of Technology, Los Angeles, CA, February 5-7, 1979, (to be published) and A.C.S. Div. of Fuel Chemistry Preprints 24, #3, 154 (1979).
5. Solomon, P. R.: A.C.S. Div. of Fuel Chemistry Preprints #3, 184, (1979).
6. Solomon, P. R., and Colket, M. B.: Fuel, 57, 751 (1978).
7. Orning, A. A. and Greifer, B.: Fuel, 35, 381 (1956).
8. Brown, J. K., Dryden, I. G. C., Dunevein, D. H., Joy, W. K., and Pankhurst, K. S.: J. Inst. Fuel, 31, 259, (1958).
9. Wolfs, P. M. J., van Krevelen, D. W. and Waterman, H. I.: Fuel, 39, 25, (1960).
10. Brown, J. K., and Ladner, W. R.: Fuel, 39, 87, (1960).
11. Retcofsky, H. L., Schweighardt, F. K., and Hough, M.: Anal. Chem., 49, 585, (1977).

THE PHYSICAL AND CHEMICAL EFFECTS OCCURRING DURING THE THERMAL DECOMPOSITION OF COAL PARTICLES AND OIL DROPLETS

W. R. Seeker, G. S. Samuelsen, and M. P. Heap
Energy and Environmental Research Corporation
Irvine, California 92714

and

J. D. Trolinger and C. F. Hess
Spectron Development Laboratories, Inc.
Costa Mesa, California 92626

Fifth EPA Fundamental Combustion Research Workshop
Newport Beach, California
January 23-25, 1980

SECTION I
INTRODUCTION

The events occurring during the thermal decomposition of liquid droplets and coal particles in the initial stages of heat release in turbulent diffusion flames are of considerable significance to the designers of low pollutant emission combustors. In pulverized coal flames the partition of fuel nitrogen between the volatile and char fractions, for example, will impact the production of fuel NO. Moreover, since the fate of fuel nitrogen in the volatiles is dictated by the environment in which they react, their conversion to NO or N_2 will depend upon the degree to which they mix with the bulk flow before reacting. In liquid fuel flames the minimum achievable NO_x emissions is quite often related to the trade-off between NO_x and smoke emissions. Therefore, the factors controlling the formation of particulates under fuel-rich conditions are germane to the problem of low NO_x burner design for liquid fuels. This paper describes the initial efforts carried out on a program to assess the physical and chemical effects occurring during the thermal decomposition of both liquid droplets and pulverized coal particles. The work was funded by the FCR program at EER.

Earlier studies[1] have demonstrated that holography could be used to observe the behavior of coal particles during combustion. The approach taken in the present study was to observe particles/droplets under well-controlled conditions which simulated those encountered in real systems. This was accomplished by the construction of a reactor which allowed the particle/droplets to be injected into high temperature gases whose temperature and composition could be varied. Diagnostics were designed to allow visualization of the particle/droplets during combustion, both by holography and high-speed photography. Two-color particle pyrometry was employed to measure particle temperatures, and solid and gaseous samples were extracted to investigate the variation of composition with time.

The major goals were to explore the effects of controllable parameters on combustion phenomena and pollution formation. The specific parameters investigated included the following:

- The effect of coal type. The coals selected were those used in other CRB programs.
- The effect of particle/droplet size.
- The effect of particle number density.
- The effect of environment, i.e., either reducing or oxidizing.
- The effect of relative velocity between the particles and background gas.
- Exploratory investigation using liquid droplets.

This paper presents details of the experimental techniques and initial results for pulverized coal.

SECTION II

EXPERIMENTAL SYSTEMS

The various experimental systems employed in this investigation are presented schematically in Figure 1. The major component is a reactor which allows access for both optical and extractive diagnostics, and includes a particle or droplet feeding system and a controlled gas mixture.

Reactor

The reactor, Figure 2, was designed to satisfy two general criteria:

1. Allow the adequate control of the gaseous environment into which the particle/droplets were injected, and
2. provide ready access for extractive and optical diagnostics.

These criteria were satisfied by injecting the particles/droplets into the combustion products of a fuel/air flat flame stabilized on a three-inch square sintered bronze burner with an embedded cooling coil. The flame was down-fired within a four-inch square stainless steel chimney in order to minimize heat losses and the influence of external conditions. A small amount of nitrogen was introduced between the burner housing and the chimney wall to prevent carbon deposition. Optical access was provided by schlieren quality fused silica windows mounted on the two opposing sides of the 91 cm long chimney. For those optical diagnostics which did not require high quality viewing ports, two rectangular Vycor plates were mounted on the third side. The reactor rested on a flat plate which moved relative to a stationary optical probing height on vertical support rods over a distance greater than the separation of the highest and lowest windows. The reactor was positioned by coupling to a dovetail mechanism connected to a lead screw driven by a stepping motor which was controlled by a digital preset indexer.

Details of the flat flame burner system and the particle/droplet injection tube are presented in Figure 3. When coal particles are being investigated they were transported by air to the center tube, then diluted with the same fuel/air mixture as that used in the flat flame burner to eliminate any uncertainty in

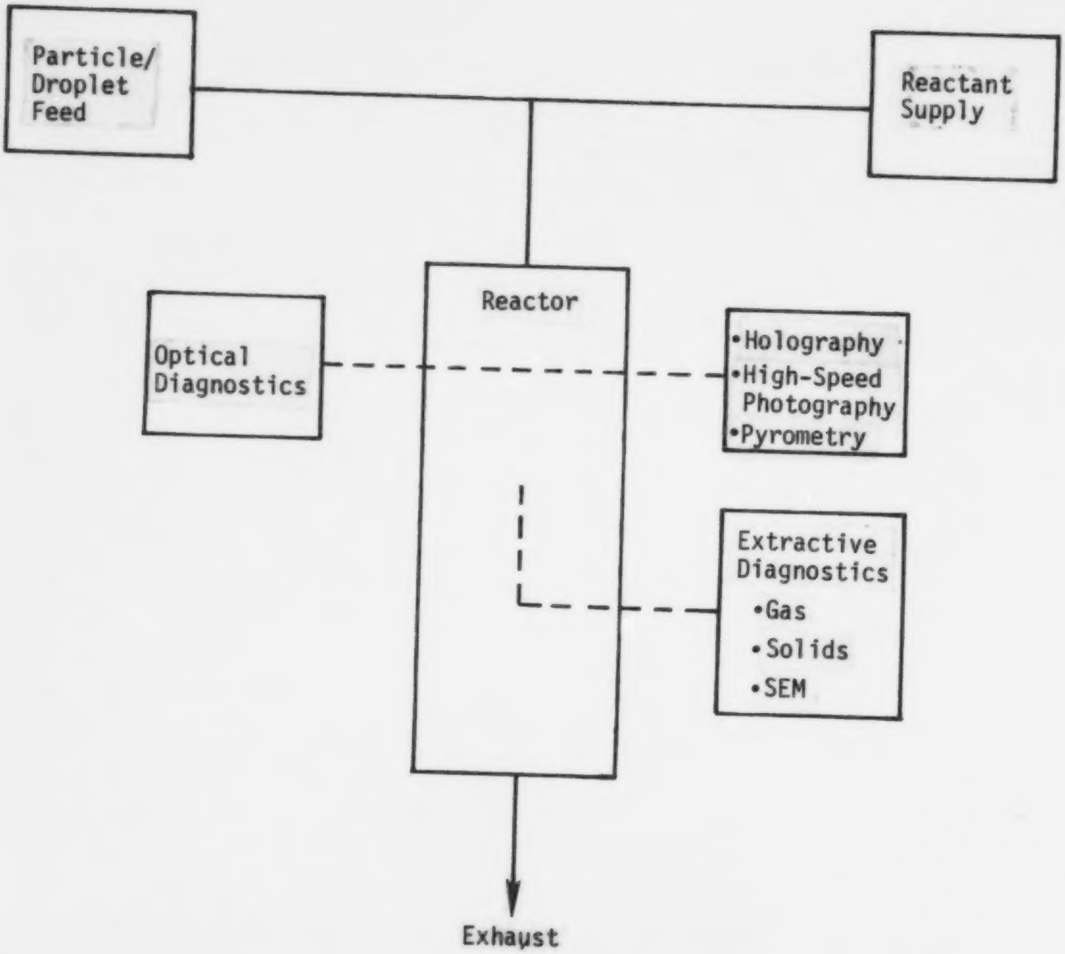

Figure 1. Experimental Systems.

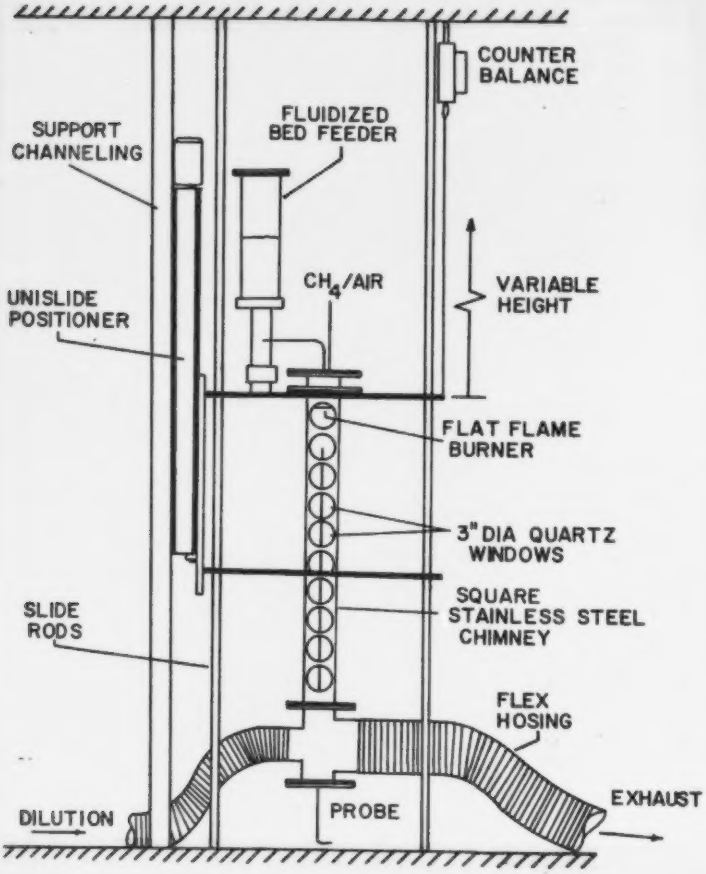

Figure 2. Reactor System.

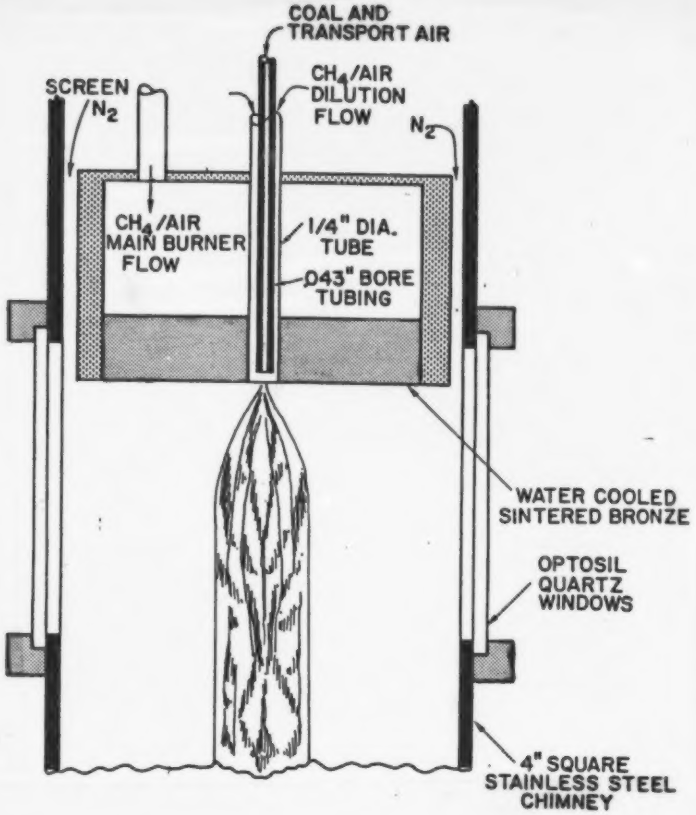

Figure 3. Particle Injection System.

Fig 3 Particle Injection System

mixing time between the carrier gas and the bulk gas. The size of this central carrier tube was selected so that there would be very little thermal shielding of the center of the coal stream. The coal particle injection velocity could be controlled by varying the distance between the end of the transport tube and the burner face. With the transport tube retracted, the coal particle injection velocity relaxes to that of the dilution flow which can be matched to the cold or hot burner velocity.

Particle/Droplet Feeder

Coal particles were fed from a fluidized bed feeder similar to the design first used by Smith^2. The feeder, shown schematically in Figure 4, is designed for feed rates of 0.5 to 5.0 gm/min. The distribution plate is made from a sintered stainless steel disk and is held in a PVC union. The fluidizing gas enters from below the disk and passes uniformly through the bed of pulverized coal. The bed was constructed of two Plexiglas sections; a 5.1 cm lower tube of 15 cm length was connected to a 10 cm diameter, 38 cm long, upper tube. The bed pressure was monitored using two magnahelic gages of different ranges. The bed exhausts from the top of the bed through a fritted glass cylinder tube which is connected to a rotometer and micrometer head regulating valve. The coal off-take tube, with a 1 mm bore, was inserted near the center of the lower section, and the coal mass flow rate was controlled by varying the bed pressure by the micrometer valve.

Reactant Supply

A schematic of the reactant supply system is presented in Figure 5, and consists of five primary legs. It has the capability of using either air or artificial nitrogen-free oxidizer with methane, carbon monoxide and hydrogen as fuels. Each primary leg was divided into two branches, one for burner flow and one for fluidized bed feeder flow. Using this branching system, the reactant control system has the capability of fluidizing and transporting the coal with a gas of the same composition as the burner flow.

Optical Diagnostics

Optical diagnostics are used for temperature measurement and in-situ visualization of the particles/droplets. It is planned to take high-speed

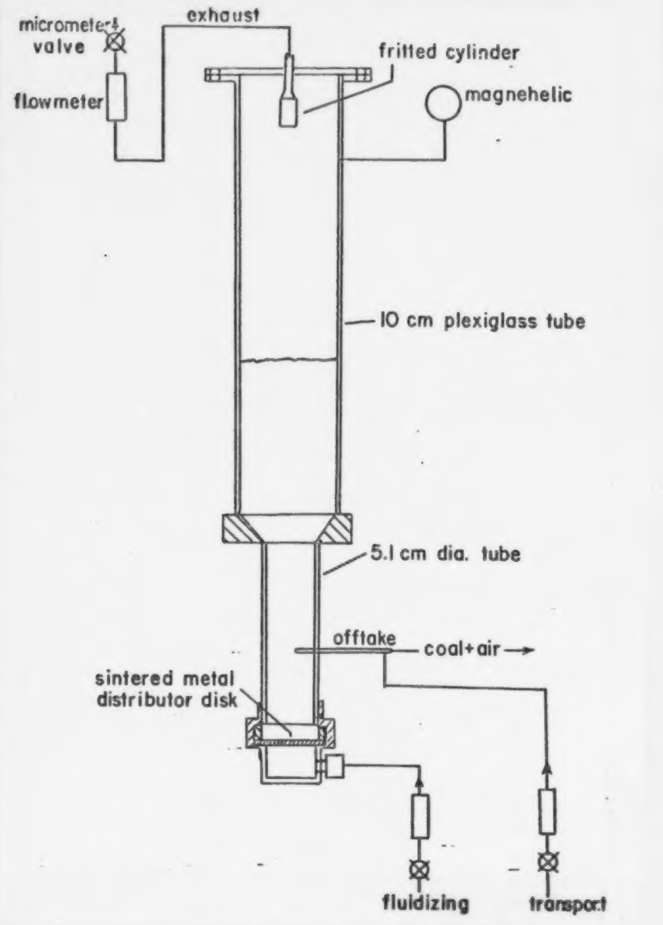

Figure 4. Fluidized Bed Feeder for Coal Flow Rates of 1.0 to 10 gm/min.

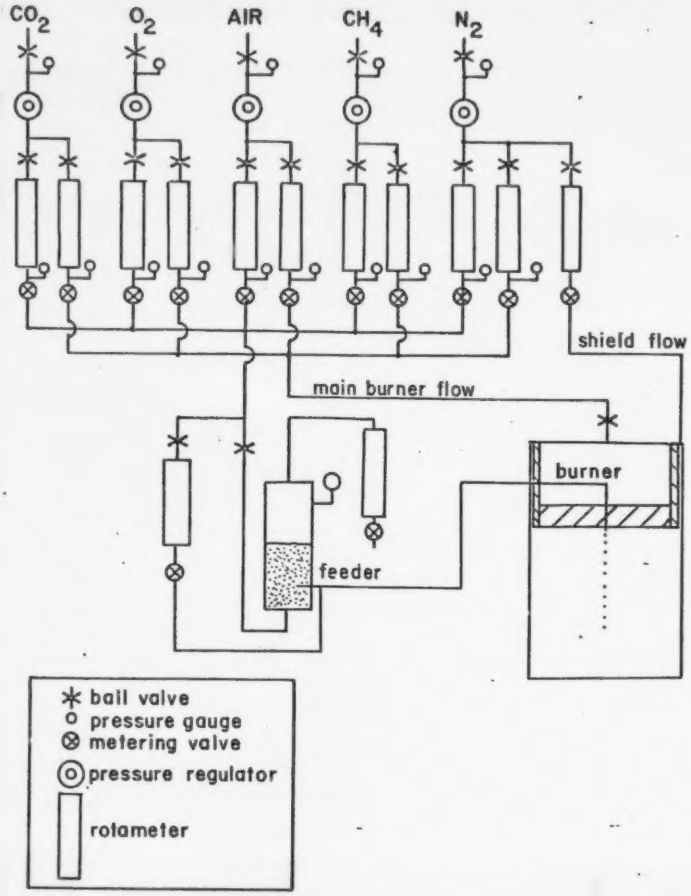

Figure 5. Reactant Supply System.

shadow movies to investigate temporal effects, although to date the only direct visualization technique employed has been holography.

Holography allows high resolution images of individual particles in a dynamic particle field to be produced. Photography or other video methods require that the particles exist in a given plane of focus, and this condition normally only exists when the particles are stationary or when the number density is extremely high. The holocamera used in the present study (Figure 6) was provided and operated by Spectron Development Laboratories under an FCR subcontract. High resolution was achieved by magnifying with high quality lenses before recording, using near image plane holography and precisely aligning the hologram during reconstruction. The Ruby laser was fired with a pulse of approximately 20 nsec, thus freezing any particle motion. The laser can also be fired in rapid succession with a time separation variable between 50 and 500 msec in order to provide dynamic information and estimates of particle velocities. A separate system was employed to reconstruct the hologram. Resolution tests demonstrated that the imaging system was capable of resolving three microns in a reconstructed hologram. The viewing depth was approximately one inch in diameter and two inches in depth.

The two-color pyrometer system based upon the technique described by Ayling and Smith[3] was used to determine particle temperatures. The technique is founded upon a ratio of emissions at two wavelengths, and therefore it is not necessary to know the emissivity of the solid body or particle cloud or the number density of particles. However, it does assume that the body whose temperature had been measured has an emissivity which is relatively independent of wavelength, and this assumption may not be valid for clouds of pulverized coal and soot particles. A schematic arrangement of the two-color particle temperature measurement system is presented in Figure 7. A water-cooled probe containing the fiber optics light guide was mounted on the side of the burner. The probe acted as a collimator for the large numerical aperature of the fiber optics, restricting the field of view. A quartz window on the opposite side of the burner acted as a background to prevent the pick-up of radiation from the warm chimney walls. Thermal emission from the particles passing through the sensing volume was received by the light guide. The fibers were bifurcated within the

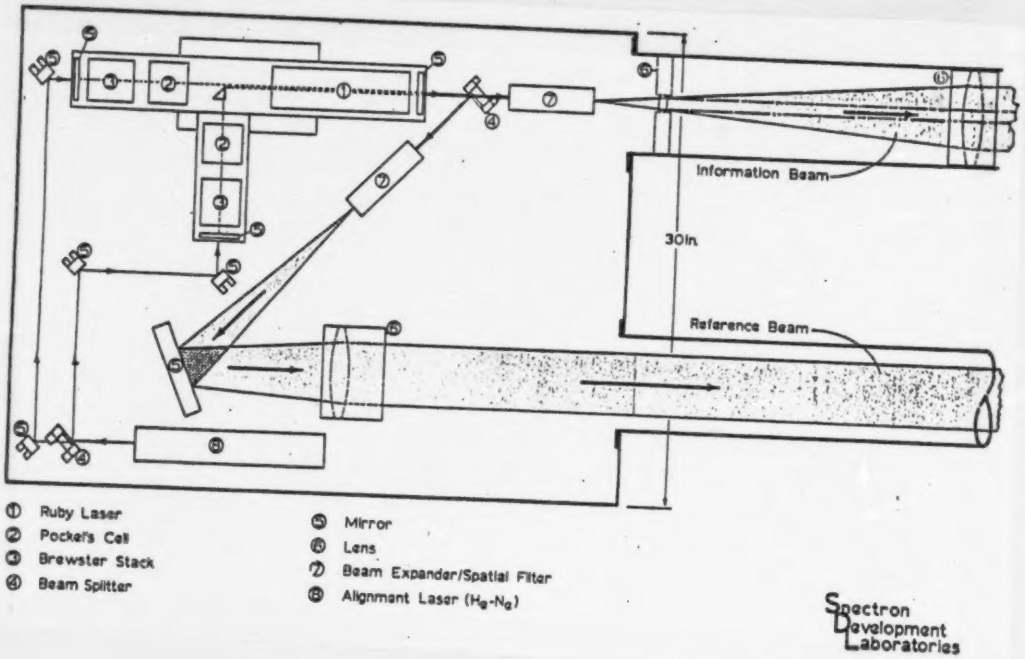

Figure 6. Holocamera Transmitter Module.

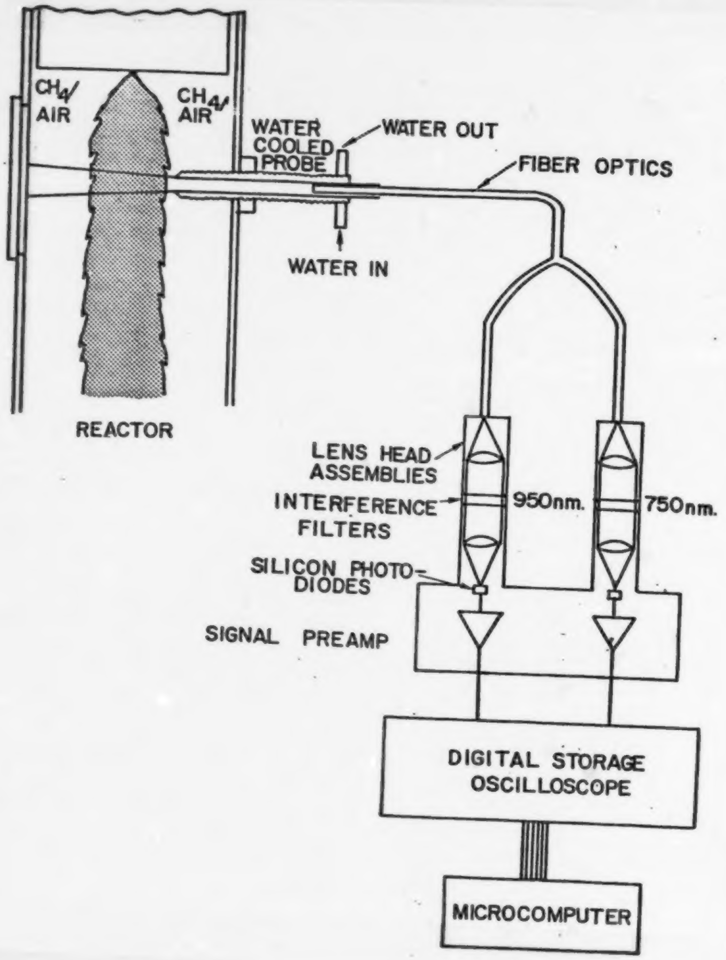

Figure 7. Two-Color Pyrometry System.

light guide, and the light signal was thus divided and directed into two lens-head assemblies which isolate the wavelength and focuses the light onto two independent silicon photodiodes. After amplification, the signals were stored in digital form. The wavelengths used in this study were 750 nm and 950 nm, respectively. These wavelengths were selected based upon considerations of signal size and spectral line noninterference. The separation between them allowed sufficient sensitivity without sacrificing accuracy.

The pyrometer was calibrated against a tungsten strip lamp, which was in turn calibrated against a disappearing filament pyrometer. The accuracy of the particle temperature measurement system was assessed by injecting inert particles and comparing their temperature with that of the combustion products. The data presented in Figure 8 indicated that the two-color optical pyrometer system gave temperatures which were in good agreement with the gas temperatures measured with sodium line reversal in the absence of particles.

Extractive Diagnostic Systems

Gas and solid samples were extracted with the double-walled water-cooled isokinetic sampling probe shown in Figure 9a. The internal tubes served as pressure taps, water inlets, quench lines, and gas sample extraction lines. Two 1/8-inch diameter lines penetrated the inner tube of the probe and could either be used to inject a stream of water or nitrogen to quench the products or to aerodynamically separate the two-phase system, allowing a portion of the gaseous products to be separated from the solid particles. Particles were also extracted from the reactor and viewed with a scanning electron microscope to provide a comparison between the *in-situ* observations made with holography and the particle morphology determined after extraction. The particles were extracted using a probe which consisted of a small stainless steel plate held on an extension rod (see Figure 9b). The cold plate was pushed into the particle stream and rapidly retracted before its temperature could change significantly. The plate was removed from the probe and coated with copper before SEM analysis.

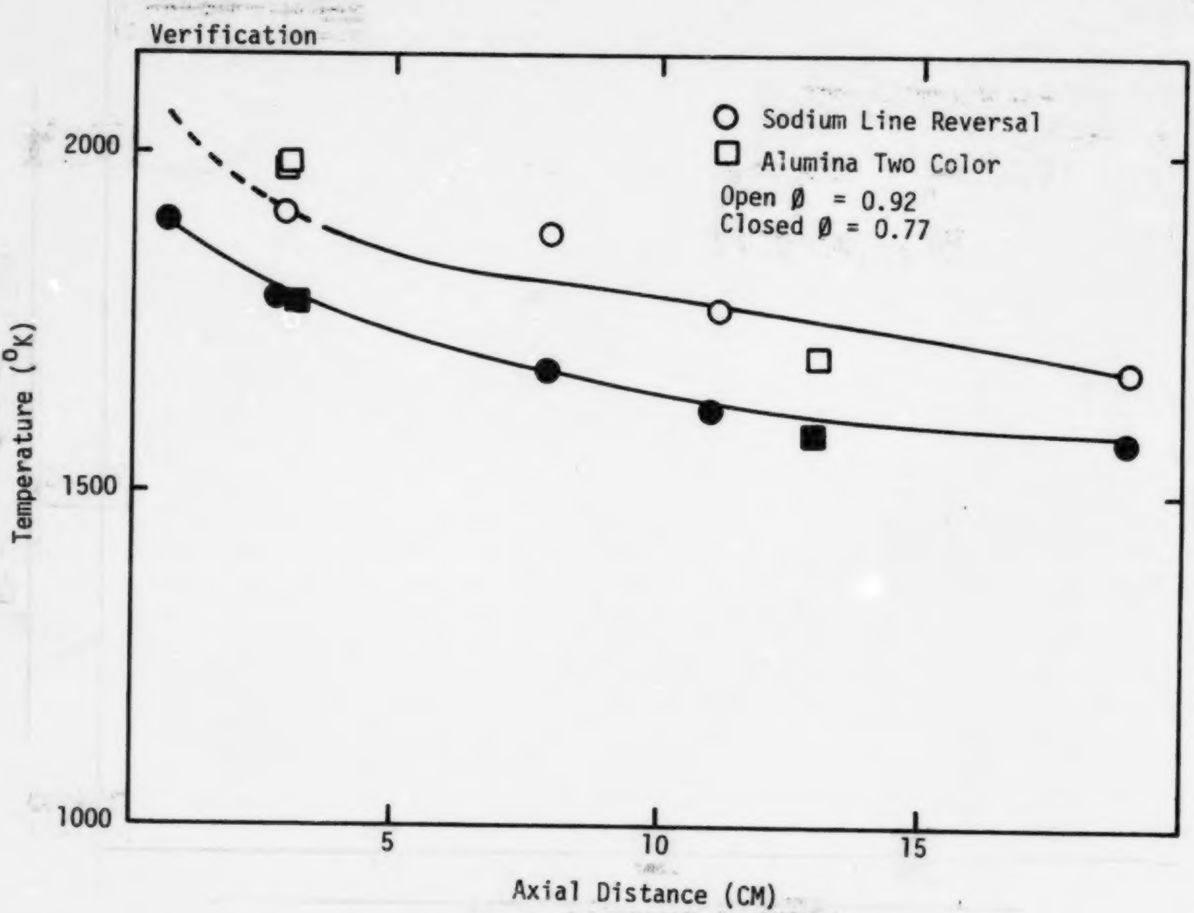

Figure 8. Comparison of Gas Temperature Measured by Sodium Line Reversal and Inert Particle Temperatures Measured by Two-Color Pyrometry.

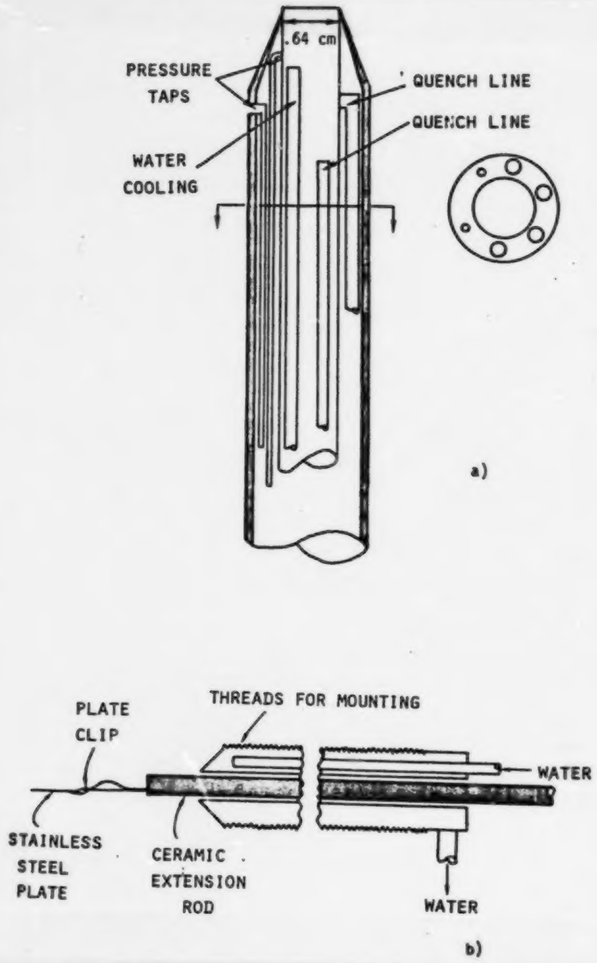

Figure 9. Extractive Probes.

SECTION III

RESULTS

Holograms have been taken for six coals and one oil; however, much of the data has yet to be interpreted. The information presented here will be limited to that obtained with a coal from Four Corners, N.M. with a 40.87 percent and a 40.5 percent volatile and fixed carbon content, respectively. This relatively high ash coal was injected into the products of a 35 percent excess air methane/air flame. The mixture ratio and velocity of the methane/air dilution flow matched those of the burner. Coal was injected through the center tube at 0.4 grams per minute, and the position of the coal transport tube was selected to match the coal particle velocity with the hot burner velocity (approximately 200 cm per second). The data presented herein were obtained with particles that had been aerodynamically classified into a narrow size cut at a diameter of 80 ± 8 microns.

The results presented in Figure 10 show the gas temperature measured by sodium line reversal in the absence of particles, the two-color particle temperature and the volatile content of the solid, all as a function of axial distance. It can be seen that the volatile content is rapidly reduced over the first 40 msec and then remains virtually constant for the next 60 msec. The particle temperature rises rapidly and within 10 msec exceeds the gas temperature. The particle temperatures peak around 30 msec, and then decay toward the gas temperature. Visual observations indicate that as the coal is injected, it initially passes through a region of almost no luminosity. The luminosity rapidly increases and peaks within 12 to 15 cm from the burner. Thereafter, the luminosity drops. The results obtained to date suggest that the phenomena occurring during the thermal decomposition of coal particles can be described by considering three major zones:

- Zone 1 - The particle heat-up region
- Zone 2 - The devolatilization region
- Zone 3 - Soot growth and char oxidation region

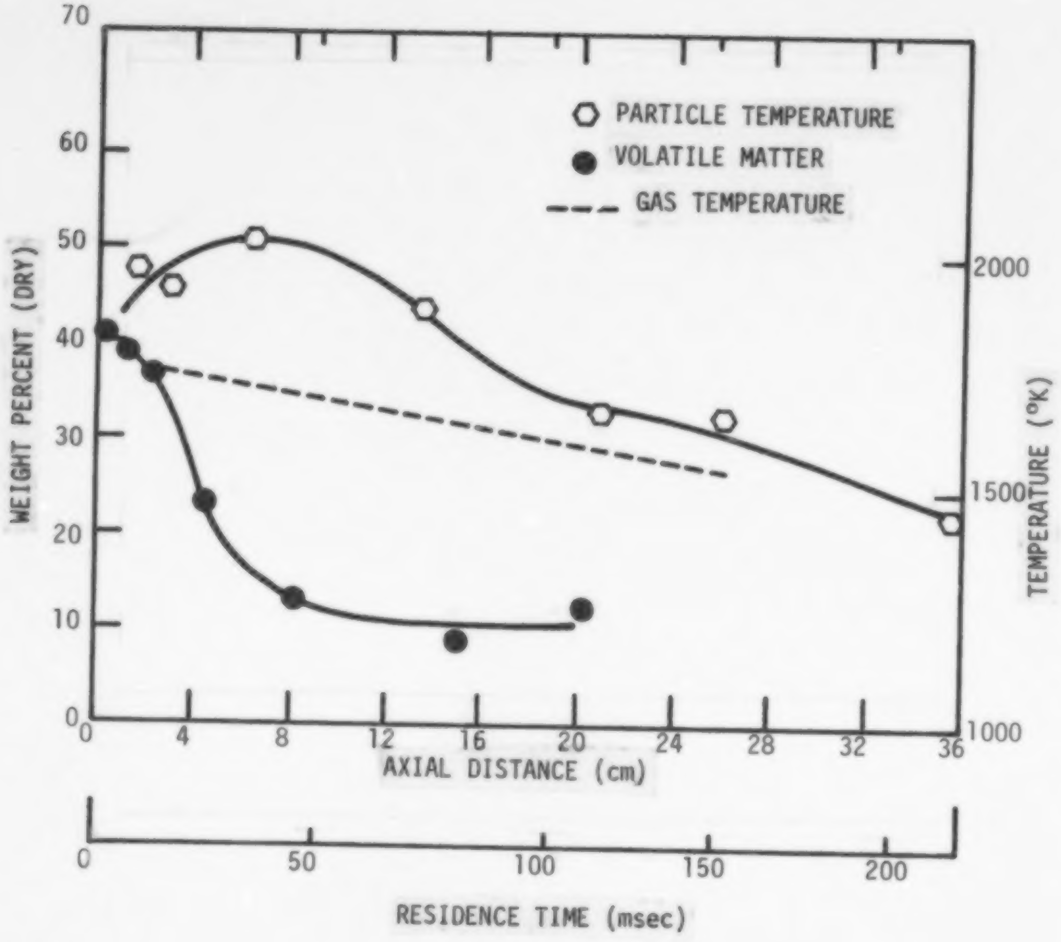

Figure 10. Axial Particle Temperatures and Volatile.

The three holograms shown in Figure 11 are representative of the general conditions observed within these zones.

Particle Heat Up

Initial particle heating is rapid, approximately 4 x 10^5 K/sec, which is typical of conditions existing within pulverized coal flames. Hologram 1 in Figure 11 indicates that the coal particles are relatively inactive in this early region, although solid samples observed with the SEM show some evidence of holes forming on the particle surface. The resolution of the solid sampling system was not sufficient to be able to extract a sample in this initial zone.

Devolatilization Region

After the very short heat-up zone, the particles begin to decompose and the volatile content is dramatically reduced in the 0 to 40 msec time period. Hologram 2 in Figure 11 is typical of the events that occur in this region. Coal particles are seen to be associated with well-defined trails which appear to be composed of very small particles. Initially these trails are relatively short; however, they increase in length with time. Their direction is entirely random, with no preferential alignment with the direction of the gas flow. It is believed that these trails of very fine particles are produced by the jetting action as the coal volatiles are ejected from the particle during the decomposition process. Many trails are observed outside the main particle field, and it is likely that particles are propelled by the jetting of these volatile fractions. Current speculation is that the trails represent high molecular weight gases which pyrolyze or burn rapidly in the region close to the parent particle, producing solids. An alternative concept suggests that because of the high pressures attained within the particle, these coal volatiles exist as a liquid and the trail is formed as these liquids are ejected from the solid particle.

Soot Growth Region

The third zone starts approximately 14 cm from the coal injection point (or approximately 70 msec) and is characterized by the growth of particles whose length is large compared to their diameter. These particles, which are not associated with the char particles, are believed to be soot formed from the bulk gas stream, and are typically 5 to 10 microns thick and several thousand microns in length. These structures continue to grow, both in length

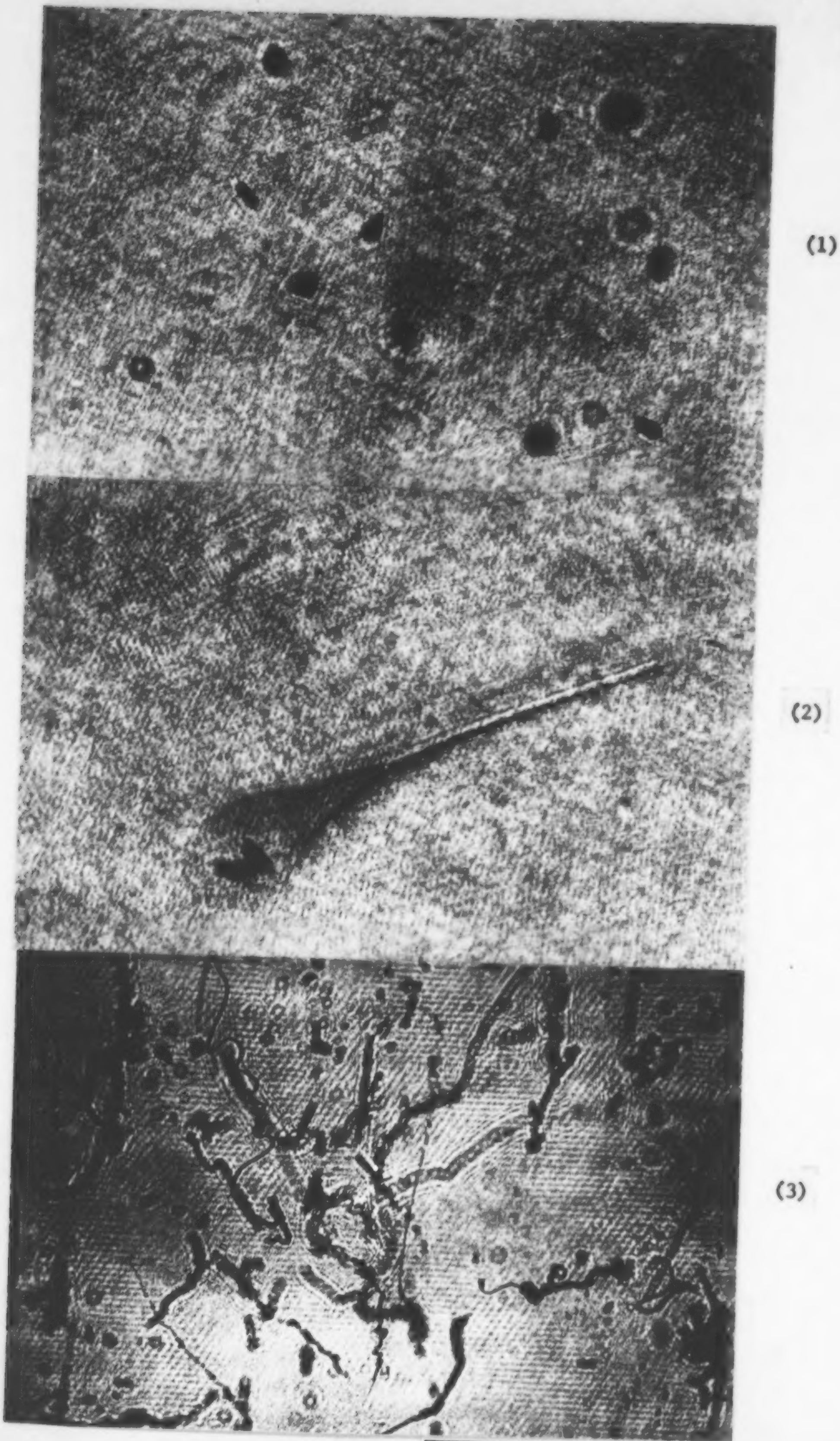

Reproduced from best available copy.

Figure 11. Typical Holograms of a Bituminous Coal at Different Axial Positions.

and width. They are now aligned with the gas flow and completely mask any remaining char (see Hologram 3, Figure 11). In this region there is no further loss of volatiles from the particulate.

Micrographs taken from this region confirm the presence of long particles whose surface structure appears to be formed from a multitude of fine particles.

SECTION IV

DISCUSSION

Data have been obtained to date on the events that occur when coal particles are injected into a high temperature gas stream. The two most significant observations appear to be the evolution of volatile compounds as jets which react close to the parent coal particle forming small particles, and the formation of soot from the bulk gas phase.

Models of NO production in pulverized coal flames which assume that the volatile fractions are mixed with the bulk gases before reaction overpredict the formation of NO in a plug flow system. The observations made during this investigation strongly suggest that the reactions occurring as the volatiles are ejected from the particle are probably significant. Bench-scale studies have shown that fuel NO formation under excess air conditions is very much higher with small particles than with large particles. Initial observations from the holograms with the New Mexico coal indicate that only large particles produce the characteristic trails shown in Figure 8. It can be assumed that with small particles the volatiles are either released uniformly over the particle surface, or the characteristic jet length is such that diffusion times are less than reaction times. This will allow the volatile fuel nitrogen fraction to mix with oxygen, thus maximizing fuel NO formation. Conversely, if the volatile fuel nitrogen fractions pyrolyze or react in the jet before mixing, then the fuel nitrogen compounds will have the opportunity to form N_2 and, therefore, large particles will not produce as much fuel NO as small particles.

One other complicating factor is the influence of particle size and coal type on particle temperature. During devolatilization particle temperatures have been observed which exceed the bulk gas temperature measured in the absence of particles. This can be attributed to the influence of local heating due to volatile gas oxidation. Coals which do not contain significant volatile content do not produce particle temperatures which exceed the background gas temperature. It is concluded that the volatiles react rapidly upon leaving the particle, giving an increase in the local temperature which results in heat feedback to the particle surface and thereby to further volatile evolution. The temperature peak will depend upon volatile evolution rate, volatile speciation and volatile evolution form. Lignites produce gases of lower heating value and their particle temperature is lower than those measured with bituminous coals under similar circumstances.

SECTION IV

CONCLUSIONS

Initial evaluations of the results obtained in this study to date on the physical phenomena which occur during the thermal decomposition of pulverized coal particles indicates that:

- Volatile coal fractions are ejected from coal particles in jets, and that for large bituminous coal particles these jets produce a trail of small particles.
- Coal composition and volatile evolution rate influences particle temperature.
- Large soot structures can be formed from the bulk gases produced when bituminous coal particles decompose.

This work will continue and further efforts will be made to verify the two-color particle temperature measurements, as well as to provide detailed information on gas composition profiles. Data, already available, have yet to be analyzed on the influence of stoichiometry, particle injection velocity, coal number density, background temperature and coal type. It is recognized that the observations described in this paper may be strongly influenced by the laminar nature of the flow and plans are underway to assess the impact of fluid mechanics on the physical effects occurring during particle/droplet decomposition.

REFERENCES

1. Samuelsen, G. S., Trolinger, J. D., Heap, M. P., and Seeker, W. R.: *Combustion Flame*, accepted for publication.

2. Hamor, R. J. and Smith, I. W.: *Fuel 50*, 394 (1971)

3. Ayling, A. B. and Smith, I. W.: *Combustion Flame 18*, 173 (1972)

SESSION III

BENCH-SCALE REACTOR STUDIES

J. P. LONGWELL
SESSION CHAIRMAN

POLLUTANT FORMATION DURING THE COMBUSTION OF RESIDUAL FUEL OILS IN A WELL-STIRRED REACTOR

M. Murphy
Battelle Columbus Laboratories
Columbus, Ohio 43201

Fifth EPA Fundamental Combustion Research Workshop
Newport Beach, California
January 23-25, 1980

No manuscript for this presentation was received at the time of the meeting. A final report on the subject subcontract is included in the FCR Program Final Report Series.

POLLUTANT FORMATION FROM COMBUSTING PULVERIZED COAL CLOUDS

Philip M. Goldberg, Henry Tong, and Robert Kendall
Acurex Corporation
Energy and Environmental Division
485 Clyde Avenue
Mountain View, California 94042

Fifth EPA Fundamental Combustion Research Workshop
Newport Beach, California
January 23-25, 1980

SECTION I

OVERVIEW

The objective of this experimental study is to provide information on the mechanisms of coal combustion and subsequent oxides of nitrogen formation under conditions similar to those found in the near-burner region of a high-intensity pulverized coal flame. A jet-stirred reactor system is utilized in this study to simulate this type of combustion environment. The stirred combustor can roughly simulate a flame region where a high degree of recirculation is present. In addition, a stirred reactor is capable of operating over a wide range of coal concentrations at high temperatures and residence times ranging between about 20 to 100 msec.

An overview of the experimental program plan by tasks is presented in Table 1. Referring to the figure, the first goal of the program was to design a well-mixed coal reactor capable of operating over a residence time range between 20 and 200 milliseconds. After completing the design and fabrication, noncombusting mixing studies were to be conducted to verify that a high level of gas phase mixing exists in the reactor. Once gas phase mixing performance was verified, subsequent experiments were to be directed at quantifying particle mixing behavior. Combustion experiments were to begin after the completion of this task.

The original experimental plan has been modified somewhat during the course of this program. Instead of one reactor, two similar reactors have been designed to cover the residence time ranges of about 20 to 50 and 50 to 100 msec, respectively, during combustion testing. The gas phase mixing efficiency of the longer time scale reactor (SRII) has been examined using a "cold" model reactor in conjunction with a He tracer method. Attempts have been made to quantify particle mixing in the SRII cold model by using a light attenuation technique. At the present time, combustion tests are being conducted using SRII. The results of the above mentioned tests are described below.

Similar testing is planned for the smaller reactor (SRI). Fabrication of the smaller reactor and its respective "cold" model has not been completed. A description of SRI is presented for completeness.

Table 1: Program Plan Outline

Task	Description
1	Design stirred reactor to be well mixed on gas over the residence time range between 20-200 msec
2	Verify (optimize) gas mixing intensity using a "cold" model of the reactor
3	Quantify coal particle mixing behavior in the stirred reactor
4	Proceed with coal combustion tests • Covering the reactor residence time range at equivalence ratios up to 4 • Performing wet sieving tests and chemical analysis on selected char samples • Using conventional gas analysis, supplemented with NH_3 and HCN measurements during selected tests

SECTION II

COMBUSTOR DESIGN

The objective of this phase of the program was to design a reactor exhibiting a high degree of gas phase mixing. The reactor was to operate on coal/air mixtures over a residence time range of 20 to 200 msec.

Since the reactor was to be mixed by its feed jets, the parameters considered to be most influential in the mixing process were:

- Jet placement
- Jet Reynolds number (Re_j)
- Ratio of jet diameter to chamber width (d/L)
- Combustion chamber shape

As mentioned above, it was originally intended to use one combustor to cover the entire operating residence time range. For a fixed reactor volume, the air turn-down would have to be approximately 10/1. Based on this requirement and its resultant effect on various operating parameters (such as jet Reynolds number), it was decided that two reactors were needed to cover the specified residence time range. Two reactors would more easily produce the desired level of mixing than one reactor operated over a very wide range of air input.

The operating parameters for the two reactors are listed in Table 2. The operating range of the large reactor, SRII, has, in part, been determined by gas phase mixing He tracer experiments to be described later. As shown in the table, the reactors are similar in terms of number of feed jets, d/L, and Reynolds numbers. Each reactor has the same relative chamber shape and jet locations as is shown in Figure 1.

The shape of the reactor as well as the number and placement of the jets were selected to eliminate stagnant regions in the reactor and provide good mixing between "old" and "new" fluid. The jet orientations were set to generate various scales of turbulence which would provide mixing on both large and small scales. The final orientations of the jets (angles with respect to the axes of the combustor) were determined by use of the gas phase mixing tracer results.

TABLE 2. REACTOR DESIGN PARAMETERS

Specifications	SRI	SRII	Units
Volume	0.06	0.27	ft^3
SR diameter	5.4	8.7	in
Number of jets	12	12	---
Jet diameter	0.13	0.22	in
SR diam/jet diam	40	40	---
Air flow	17-35	30-60	scfm
Cold residence time	0.20-0.10	0.54-0.27	sec
Jet Reynolds number	$1.7 \times 10^4 - 3.4 \times 10^4$	$1.7 \times 10^4 - 3.5 \times 10^4$	---
Jet velocity	245-490	158-316	ft/sec
SR "Reynolds number" (cold)	$3.1 \times 10^3 - 6.2 \times 10^3$	$5.5 \times 10^3 - 1.1 \times 10^4$	---

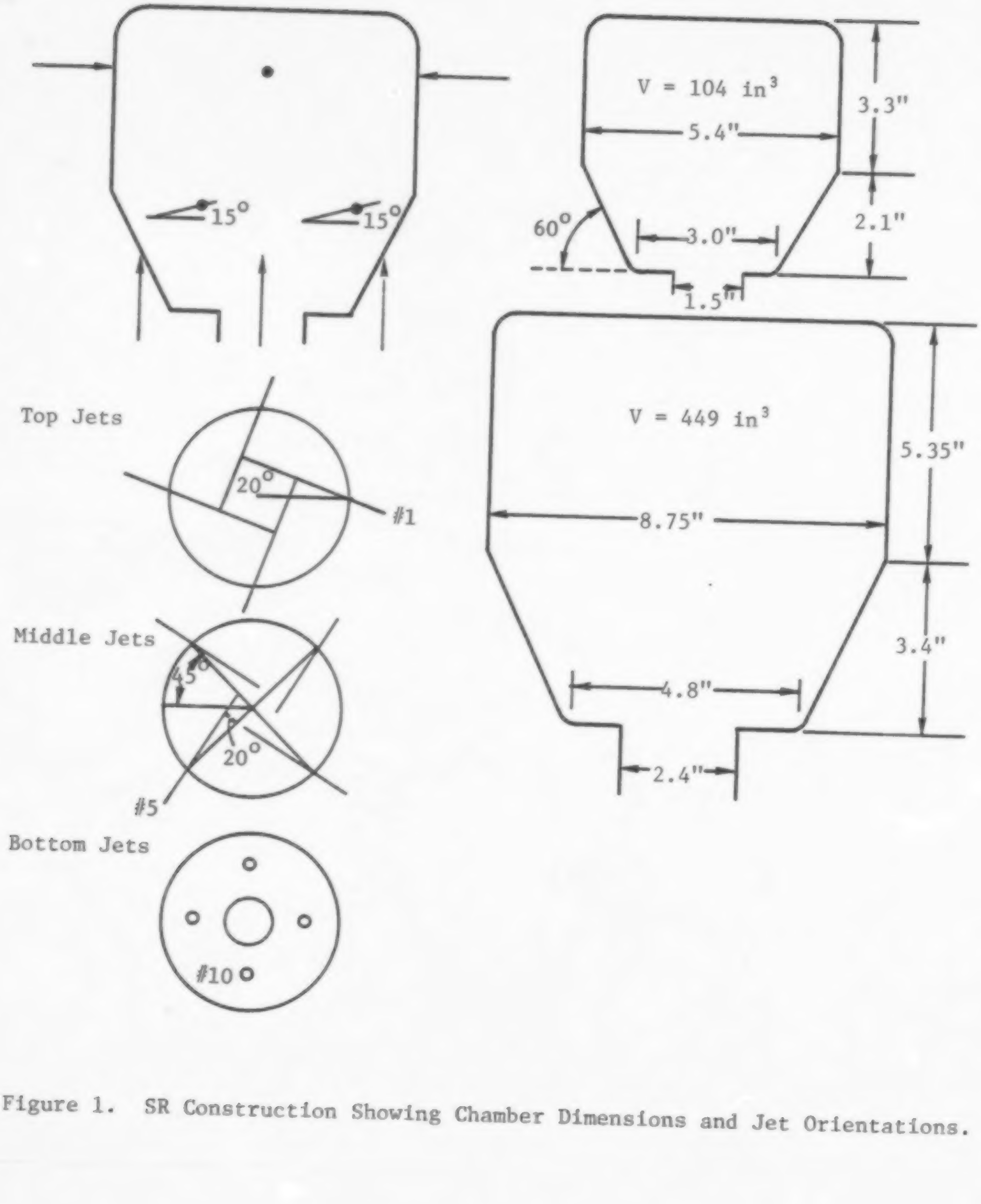

Figure 1. SR Construction Showing Chamber Dimensions and Jet Orientations.

As shown in Table 2, the cold flow jets are highly turbulent. However, some laminarization can be expected under combustion conditions due to increases in viscosity. Selection of the ratio of jet diameter to chamber width was made with the intention of achieving proper jet penetration and uniform dissipation of kinetic energy throughout the reactor volume.

Since the reactor jet gas velocities are high (Table 2), it was thought that wall impingement by the high velocity particles might produce particle fracture and significant chamber erosion. Therefore, special injectors were designed to introduce the coal particles into the reactors at lower velocities than the gas. The injector design is shown in Figure 2. The velocity values presented in Figure 3 are based on calculations assuming Stokes drag applies in the cylindrical part of the injector. A standard correlation between particle drag and Reynolds number was used to estimate particle behavior in the convergent section of the injector. Particle/particle interaction was not considered. The calculations (Figure 3) indicate that, for a 50 μm coal particle, outlet velocity is approximately one-third that of the gas.

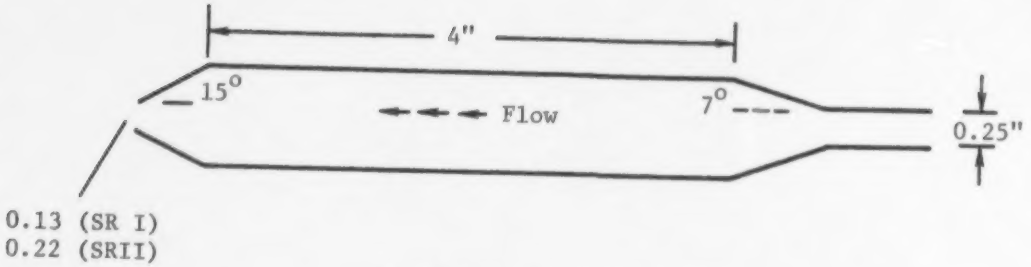

Figure 2. Injector Design.

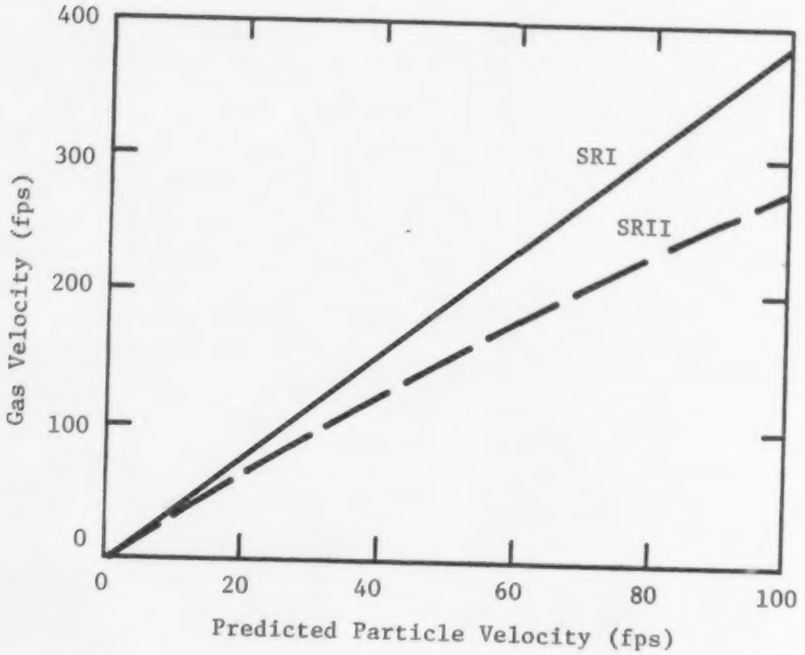

Figure 3. Predicted Injector Performance.

SECTION III

MODELING AND MIXING

After the reactors were designed, mixing studies were performed to optimize the orientation of the injectors to produce gas phase mixing and to evaluate gas and particle mixing efficiency.

Model Design

The use of a model was necessary so that injector orientations during mixing optimization tests could be adjusted with a minimum of effort. The model also allowed the easy use of He tracers for gauging gas mixing efficiency. From a large group of scaling parameters, the following were chosen as being most important to simulate cold to hot reactor mixing conditions. These parameters were:

- Jet Reynolds number (Re_j)
- Jet entrainment (M_x)
- Reactor residence time (τ)
- Geometric similarity (η)
- Power input/length^2 (β)

Jet Reynolds number and entrainment rate were considered important since mixing in the reactors was accomplished solely by the feed jets (injectors). Chamber residence time was thought to be an important scaling variable due to the dynamic nature of the mixing process. The last parameter, β, was used as a measure of potential mixing intensity. The parameter, β, is found by dividing the energy input per unit mass in the reactor by the reactor length scale squared. This parameter was used by Evangelista (Reference 1) to analytically predict the effects of imperfect mixing in a stirred reactor.

In terms of the reactor mass input, m; length, L; and jet radius, r; the above listed scaling parameters can be expressed in terms of ratio of cold to hot reactor values, denoted by subscript R, as:

- $(Re_j)_R = m_R/r_R$
- $(M_x)_R = 2.2\ m_R L_R/r_R$

- $(\tau)_R = 5\ L_R{}^3/m_R$
- $(\eta)_R = r_R/L_R$
- $(\beta)_R = m_R{}^3/5\ r_R{}^4 L_R{}^5$

In the above relations a temperature ratio of 1/5 between model and reactor has been assumed. Setting m_R, L_R, and r_R at 1, 0.6, and 1.2, respectively, the scaling parameters become:

- $(Re_j)_R = 0.8$
- $(M_x)_R = 1.0$
- $(\tau)_R = 1.1$
- $(\eta)_R = 2.0$
- $(\beta)_R = 1.2$

These results are considered to be a good compromise in modeling the hot reactor with a cold system. Based on these similarity parameter values, it was assumed the gas mixing in the model would simulate the mixing process occurring in the reactor.

Model injectors for both the gas and particle mixing studies are identical to the reactor injectors with the exception of having an exit plane radius that was larger by a factor of 12.

Gas Mixing

A standard He tracer cut-off method was used to conduct the gas mixing evaluation/optimization. The experimental set-up is shown in Figure 4. The reactor model consisted of two independently rotatable sections. Each of the jets in the top and middle level could be pivoted 20 degrees on either side and the entire injector assembly could be rotated about its major axes in 30 degree increments. The bottom jets were fixed with the positions being determined by visualization tests using smoke injection.

A hot wire anemometer having a diameter of one mil and connected to the exhaust by a short venturi section was used to monitor the He concentration in the exhaust gas. The output of the anemometer was fed into a sharp cutting

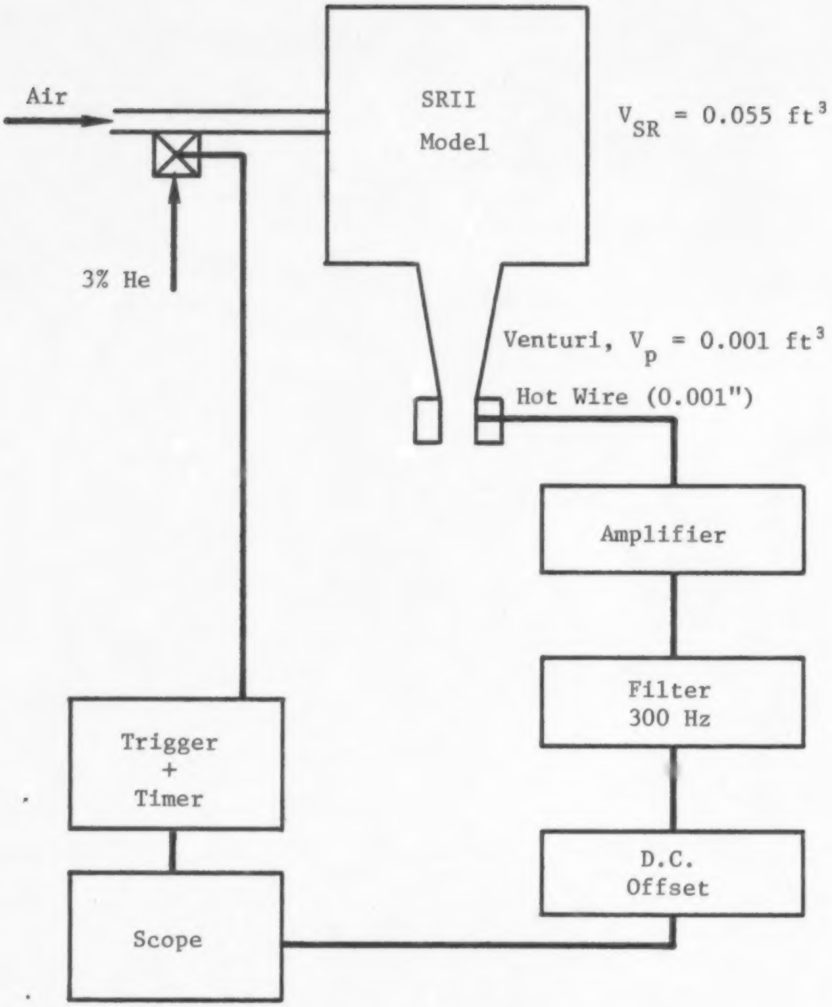

Figure 4. Setup for Helium Tracer Experiments.

filter giving a 3 db attenuation of a 300 Hz signal. After passing through the filter, the signal went to an oscilloscope for display.

During a test, the model input air flow was fixed at the desired level. Helium was brought in through one injector at a rate equal to about 3 percent of the total air flow. After a steady condition was reached, the He flow was stopped using a valve with a response time of about 2 msec. At the same time, the oscilloscope trigger was actuated recording the resultant He decay signal on the scope. The display was photographed and the same cut-off experiment was repeated several times.

An acceptable level of mixing was indicated by the following criteria:

- The cut-off response of the model to He injection through the three levels of injectors had to be similar.
- The response of the model had to be similar to a stirred reactor of proper volume based on a known air input rate.

After several tests using different jet orientations, a "best" configuration was selected. The optimal injector orientations are shown in Figure 1.

Figures 5 and 6 show the results of He tracer tests at a SR throughput of 28 and 35 scfm, respectively. The numbers under the figures indicate the jet through which the He was injected. The jet location is shown in Figure 1. Each figure represents the average of four tests. The solid lines drawn in the figures represent the average results of all tests at a given flowrate.

At a throughput of 28 scfm (Figure 5), the experimentally determined plug flow time, τ_p, was 16 msec with the stirred time, τ_{SR}, 103 msec. The theoretically expected times were 8 msec and 117 msec, respectively. At a throughput of 35 scfm, τ_p was found to be 7 msec and τ_{SR} 89 msec. The theoretically expected times for this case were 7 msec and 94 msec, respectively.

At both 28 and 35 scfm, the results of each jet falls close to the average result. However, at the lower throughput, the traces seem less straight and the experimental times differ from the expected times by about 12 percent. At 35 scfm, the traces are straight (semilog) and the experimental and expected times agree fairly well. Since it is expected that Reynolds number effects will dominate mixing, then good mixing will persist as throughput is increased above 35 scfm. Based on these results, it was decided to increase the lower

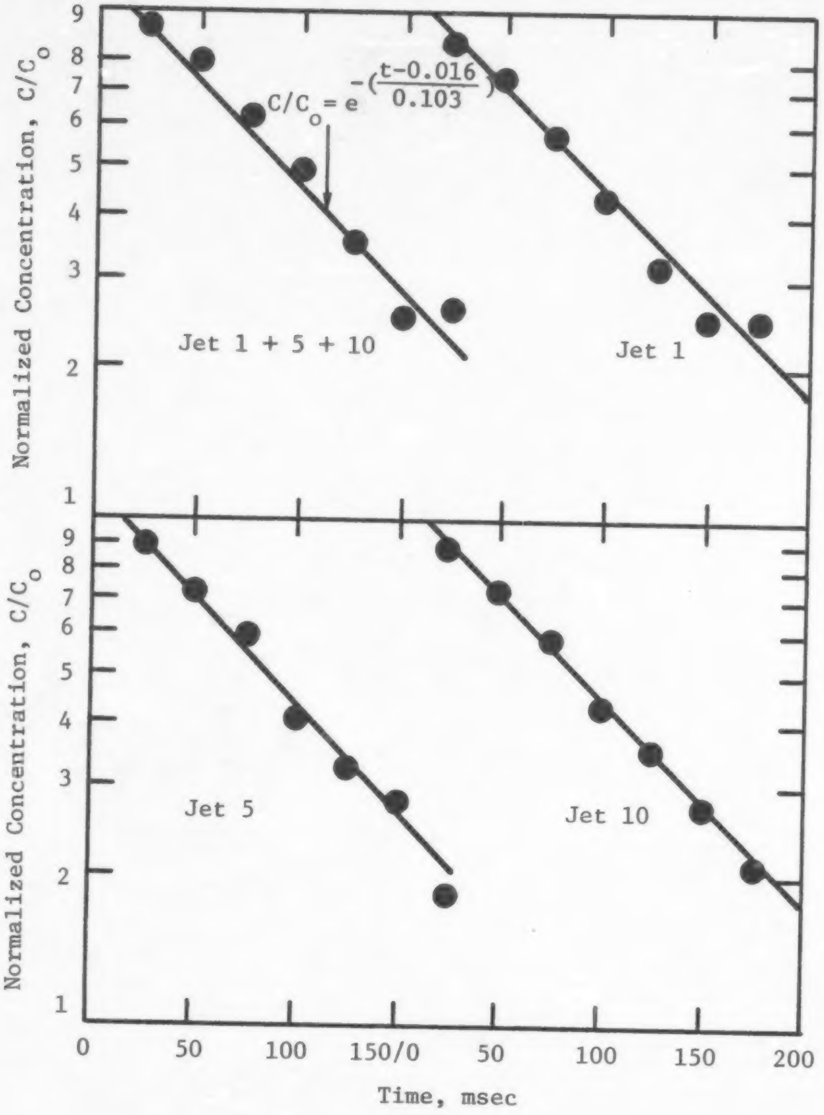

Figure 5. Results of He Tracer Tests at 28 scfm Throughput.

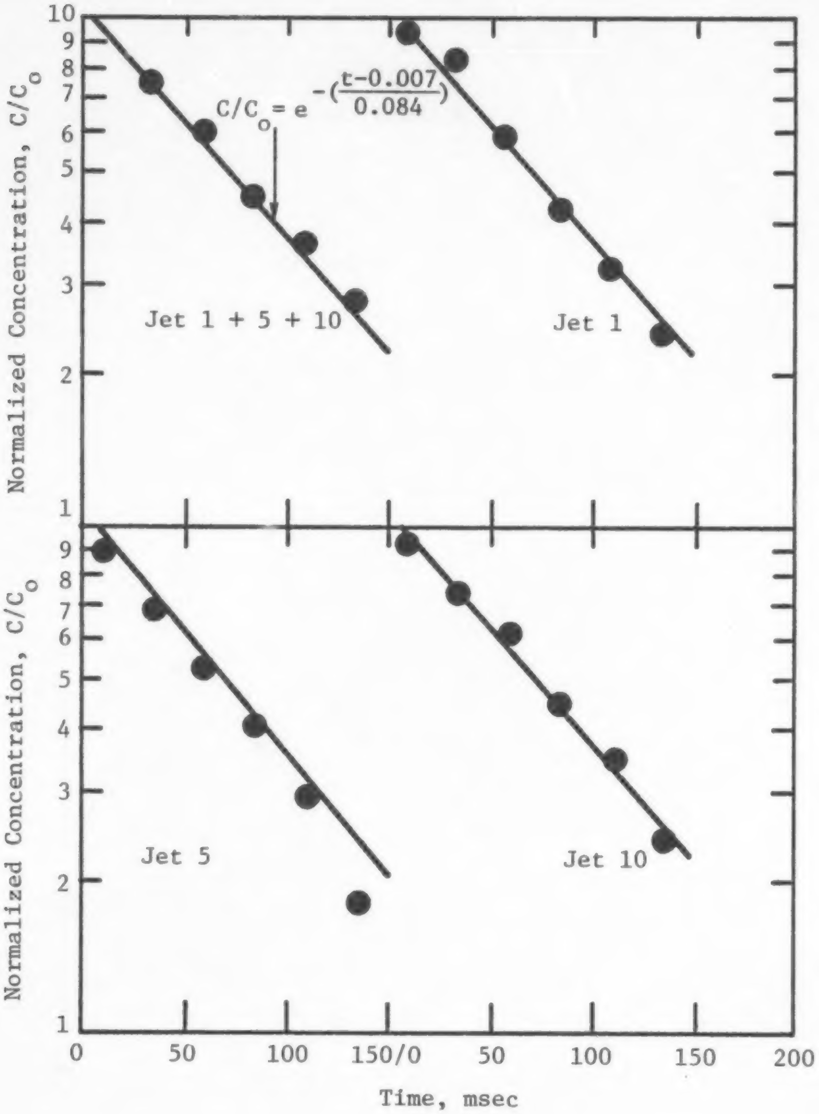

Figure 6. Results of He tracer tests at 35 scfm throughput.

limit air input to SRII for good mixing to 30 scfm. This corresponds to an upper limit hot residence time of approximately 100 msec.

Particle Mixing

For these experiments, coal was used as a 'tracer' to characterize particle mixing in the model of SRII. The particle mixing behavior was examined by both cutting off and turning on the coal flow and observing the change of coal concentration with time in the reactor exhaust. Coal was injected into the model through one injector at a time. Hence, this does not constitute a true tracer experiment. This approach was in part dictated by system limitations. Switching was done with a valve having a response time of about 10 msec. The valve exchanged a flow of air and a flow of coal and air. The particle concentration history of various streams was monitored using light attenuation.

Several tests were performed at all three injector elevations. A complete set of data for a given jet location and flow condition consisted of the following information:

1. Injector dust input concentration history.
2. SR dust output concentration history.

Given this information, attempts were made to define a mixing system that gave the correct dust concentration output history for a given input condition. A set of equal volume stirred reactors in series was chosen as the mixing system. To fit various data, it was possible to vary the number of reactors in series, the total apparent chamber volume and the mixing delay (plug flow) time.

A typical set of injector output signals is shown in Figure 7. The corresponding SR output signals are shown in Figure 8. From the figures it can be seen that the concentration decay takes much longer than the concentration rise. This is not due to the switching mechanism and is most likely an injector effect. Similar behavior at the SR exhaust is shown in Figure 8.

The solid lines in Figure 7 are the injector concentration time histories used in fitting a mixing model to the data shown in Figure 8. The solid lines in Figure 8 indicate the chosen mixing model response to the injector signal. Similarly all results were analyzed in this manner.

Table 3 presents the results of the particle mixing studies. Tests were performed at 30 scfm and 50 scfm. Equivalence ratios were varied from 0.5 to

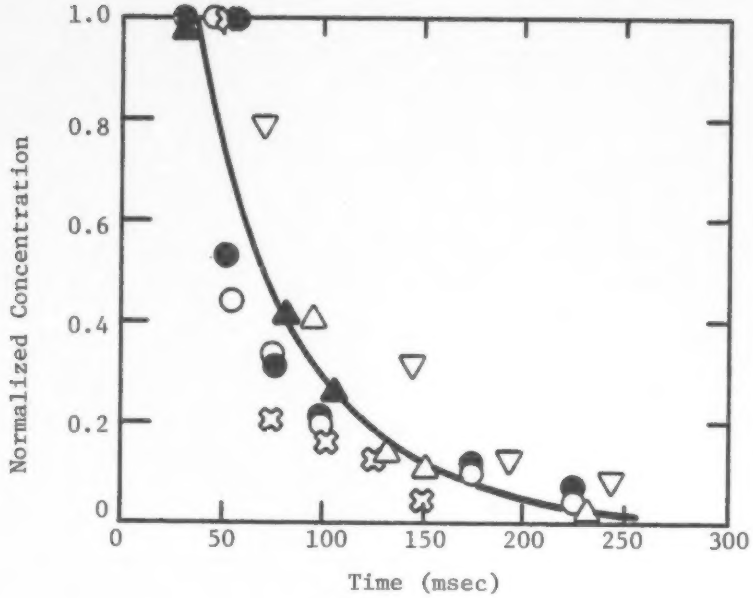

a. Coal Flow Stopped

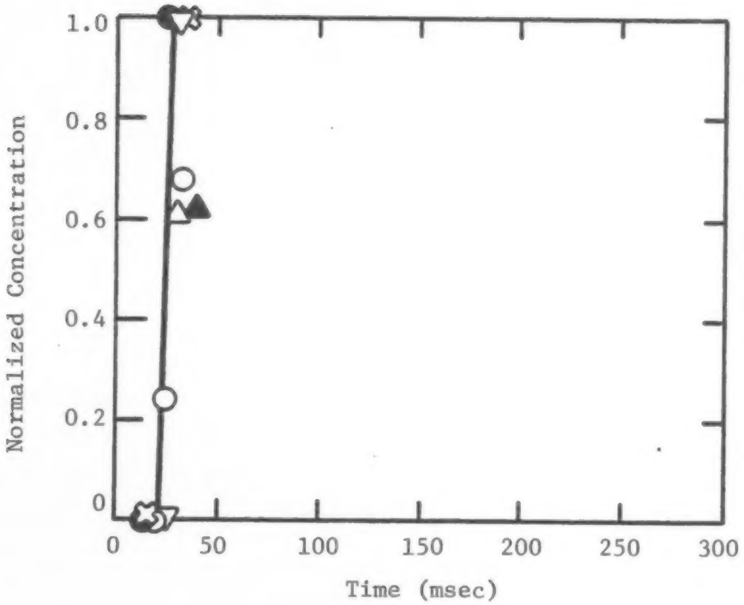

b. Coal Flow Started

Figure 7. Injector Output Signal.

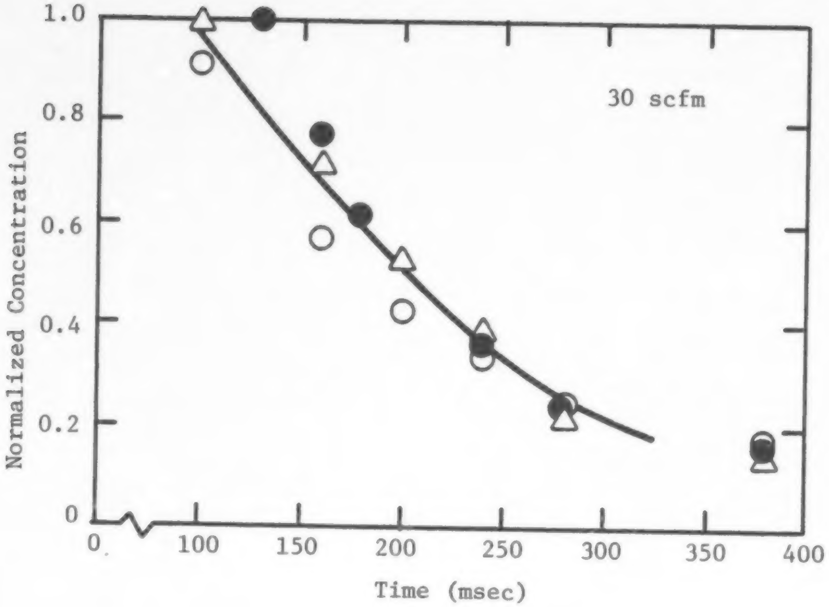

a. Coal Flow Stopped

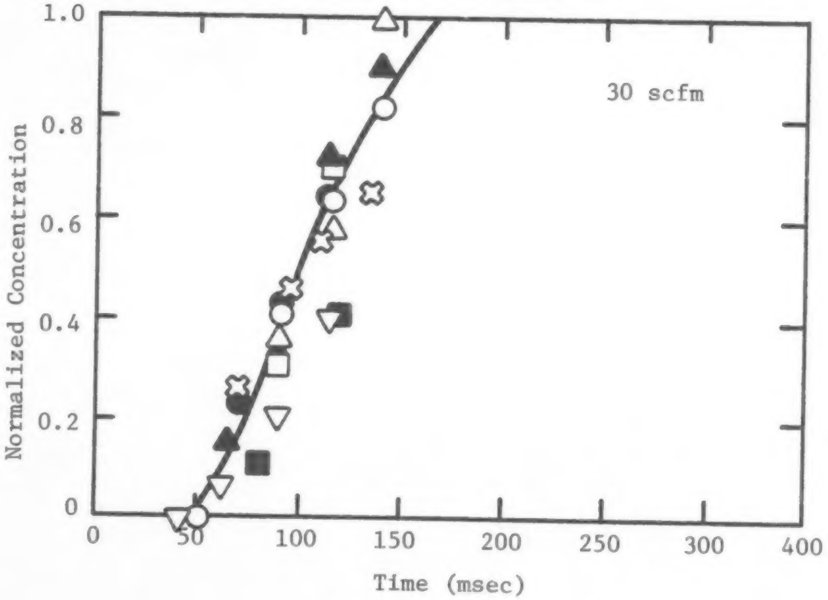

b. Coal Flow Started

Figure 8. SR Model Response.

Table 3. Dust Residence Time Modeling Results

Jet Location	Top	Middle	Bottom	Top	Middle	Bottom
Coal Flow Stopped						
Air Flow (scfm)	30	30	30	50	50	50
Number of Reactors in Series	1	1	1	1	1	2
Total Apparent Volume (ft^3)*	0.055	0.055	0.055	0.055	0.055	0.055
Mixing Delay Time (msec)	40	15	50	55	40	40
Coal Flow Started						
Air Flow (scfm)	30	30	30	50	50	50
Number of Reactors in Series	5	3	3	1	3	3
Total Apparent Volume (ft^3)*	0.040	0.055	0.055	0.095	0.055	0.062
Mixing Delay Time (msec)	0	20	20	0	15	20

*Includes stirred volume only

2.5. These values represent total concentrations and therefore injector coal concentrations were twelve times higher. At a given injector location and flow condition, dust loading did not noticeably affect mixing behavior.

The results presented in Table 3 show that there are large characteristic differences between stopping the coal flow and starting the coal flow. The reasons for this are, at present, unknown.

For a given flow condition, the fitted mixing models for the three injector elevations were combined and averaged numerically so that the SR behavior with all jets operating could be predicted. The SR global mixing models are presented in Table 4.

Although the two test methods give different results, there are similarities. A major point of similarity appears to be the existence of an apparent plug flow region inside the SR. This time ranges to about 50 msec, which can be a significant contribution to the total particle residence time in the chamber.

Figure 9 presents the projected particle residence time behavior in the SR. Aside from the fact that this particle time does not match the gas residence time, it also shows that the variation in particle residence time is much less than that of the gas.

The test method and results are still being evaluated. The results must still be considered preliminary. However, they do add concern about the assumption of particle residence time being equal to the gas residence time.

Table 4. SR Global Mixing Model

	Coal Flow Stopped		Coal Flow Started	
Air Flow (scfm)	30	50	30	50
Number of Reactors in Series	1	1	3	1
Total Apparent Volume (ft^3)	0.055	0.055	0.055	0.055
Mixing Delay Time (msec)	35	45	5	30

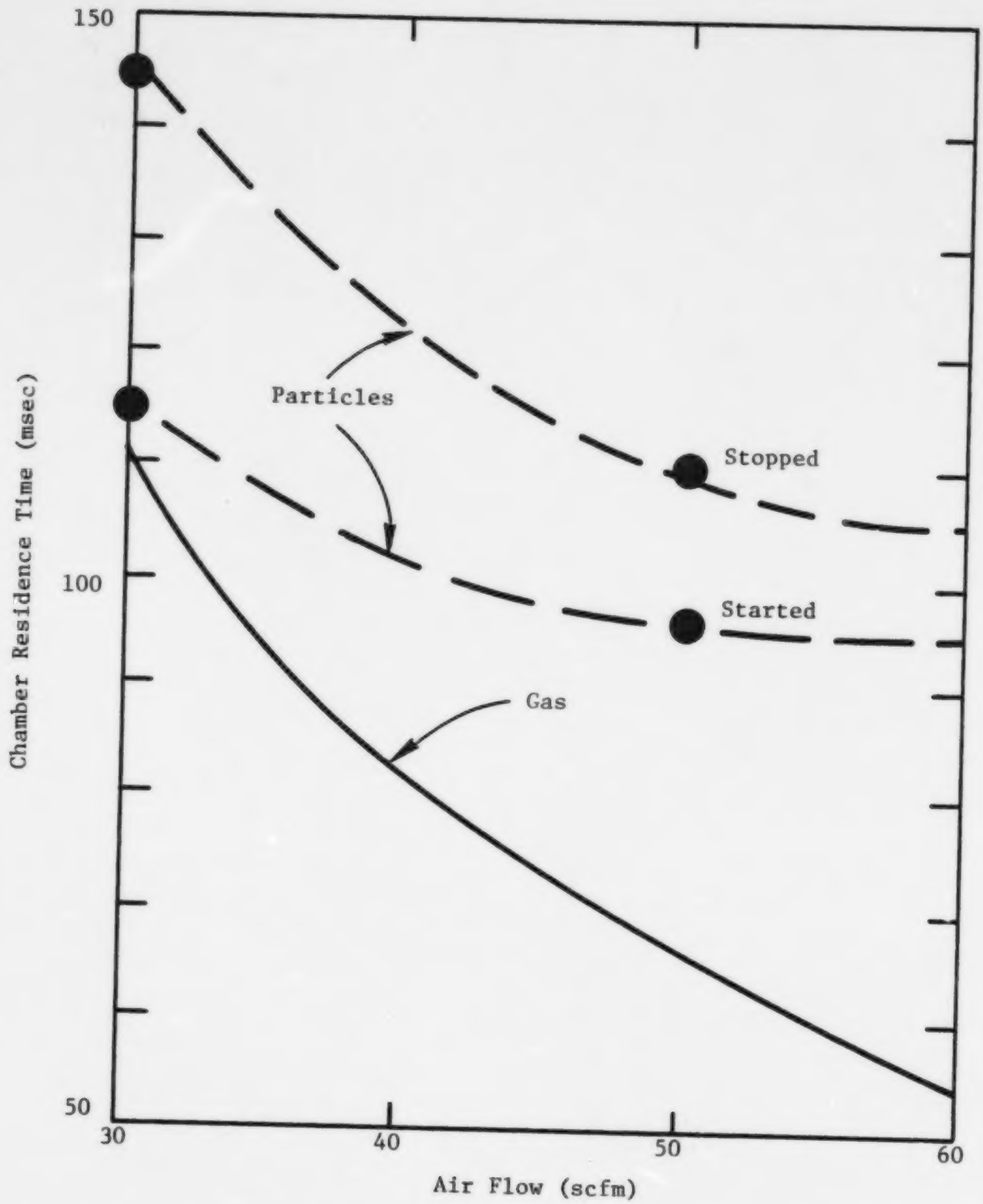

Figure 9. Residence Times Versus SRII Model Throughput.

SECTION IV

COMBUSTION TESTING

To date fourteen coal combustion tests have been conducted using SRII. Eleven of these tests have utilized coal/air mixtures. The remaining tests were performed using a mixture of coal, air, nitrogen and natural gas. These three tests were conducted primarily to gauge particle residence times. A Utah bituminous coal was used in all the testing. Coal properties are given in Table 5.

SRII Construction and Operation

A schematic of the reactor is presented in Figure 10. Jet locations are the same as those in Figure 1. The reactor has a combustion chamber volume of about 0.270 ft^3. It is fabricated in castable refractory having a wall thickness of about 3 inches. The reactor temperatures are monitored using four thermocouples. Two thermocouples are located on the outer wall of the reactor. One thermocouple monitors chamber wall temperature. The remaining thermocouple is used to monitor the chamber gas temperature. This thermocouple is located on the chamber centerline and protrudes into the combustion chamber about an inch (from the top wall).

Heatup of the reactor is accomplished using a natural gas/air mixture. The reactor is operated for over an hour on gas at a firing rate of approximately 100,000 Btu/hr. At the end of the heating period, the air flow is adjusted to the desired value, the coal flow is gradually increased and the natural gas flow is slowly decreased to zero (in tests where coal was the only fuel).

It must be mentioned that the actual time taken to reach steady state temperature conditions is much longer than the actual heating time. The time to reach steady temperatures is on the order of four hours.

A given coal/air test condition is usually held for periods ranging from fifteen to thirty minutes. However, during some low air flow and/or high coal feed rate tests, slag can accumulate and solidify in the water-cooled exhaust passage leading to premature test termination.

Table 5. Coal Properties

Moisture (%)	2.82
Carbon (%)	66.65
Hydrogen (%)	4.86
Nitrogen (%)	1.41
Sulfur (%)	0.89
Ash (%)	10.60
Oxygen (by difference) (%)	12.77
Volatiles (%)	41.8
20% Oversize (μm)	65
20% Undersize (μm)	30
Mean Size (μm)	55

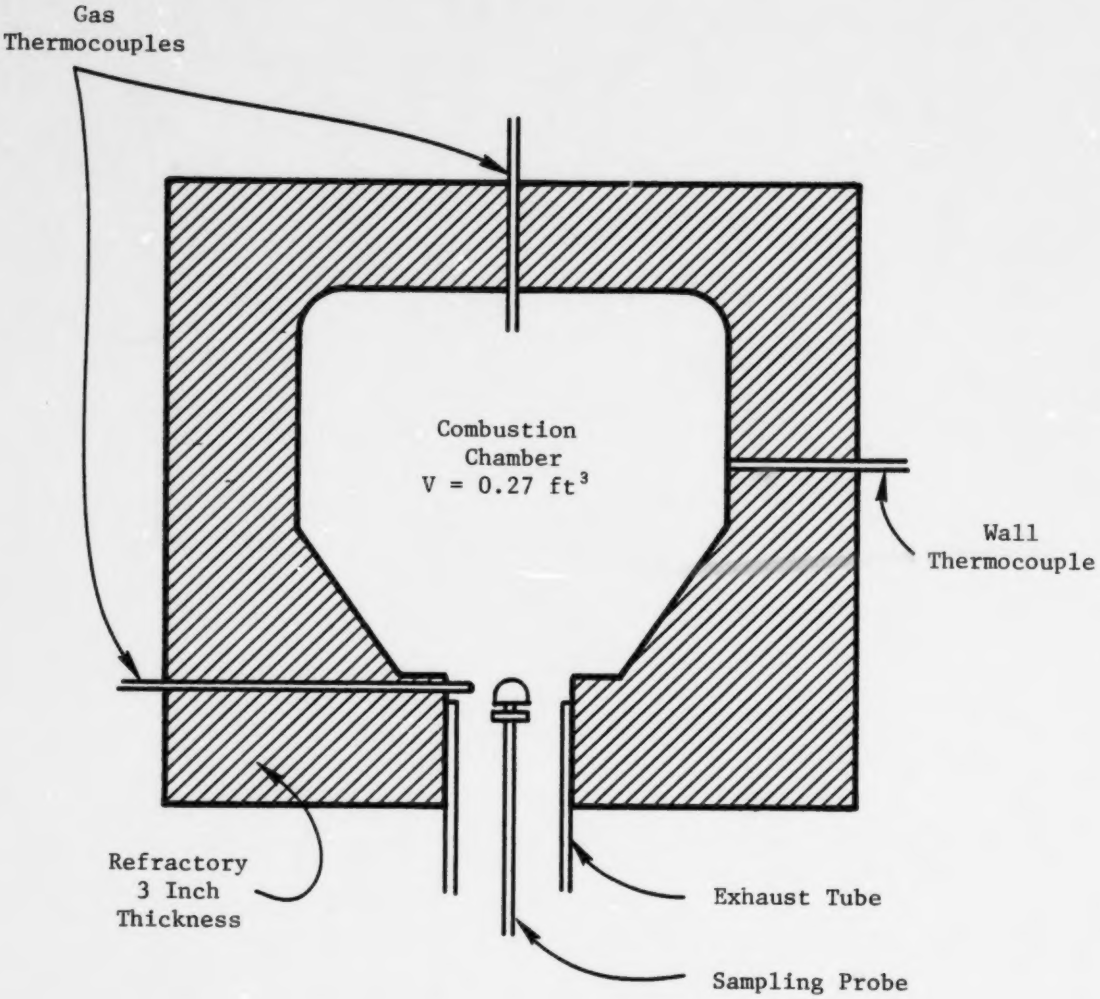

Figure 10. SRII Schematic (Without Injectors).

Sampling System

The sampling probe used to collect gas samples and indirectly collect solid samples is shown in Figure 11. The probe is constructed of water-cooled stainless steel. The tip of the probe is shaped to achieve aerodynamic separation of gas from particulate. The exhaust of the reactor passes the tip of the probe at velocities over 70 ft/sec. At these velocities, few particles can turn quickly enough to be drawn into the gas sampling openings. The water used for cooling the probe is also used for quenching the exhaust mixture. Below (but separated from) the sampling openings, water is sprayed out into the exhaust at a rate of between 10 to 15 lb/min. The water, containing the quenched char, can be collected for later examination.

Coal/Air/N_2/CH_4 Tests

Three tests were performed in SRII using coal/air/N_2/CH_4 mixtures. These tests were conducted primarily to evaluate particle residence time (with respect to calculated residence time). The CH_4/air equivalence ratio for these tests ranged from 0.8 to 1.0. It was felt that the combustion of the CH_4 and coal volatiles would provide an atmosphere sufficiently depleted of oxygen so that little char combustion would take place. The 'added' nitrogen/air ratio for the tests ranged from 0.35 to 0.5 by volume. The combined coal and CH_4 equivalence ratio was kept above 2.

The results of these tests are shown in Figure 12. As shown in the figure, temperature was held at about 2000°F with calculated residence times ranging from 52 to 96 msec. Weight loss, using ash as a tracer, N_A, was found to average 63 ± 8 percent. Volatile loss, N_{VM}, varied considerably less being 93 ± 2 percent. Beside the fact that neither N_A or N_{VM} varied significantly, it is also interesting to note that N_{VM} was higher than expected for the test temperatures and calculated times. If it is assumed that monitored temperatures are correct and that recently published devolatilization rates (Reference 2) apply, then the actual time the particles spend in the chamber must, in all cases, be over 100 msec. However, devolatilization rates obtained by Ubhayakar et al (Reference 3) predict devolatilization to be essentially complete for the temperatures and calculated residence times of this experiment.

Further evaluation of particle residence time is planned using both combustion and modeling experiments. It is expected that further devolatilization

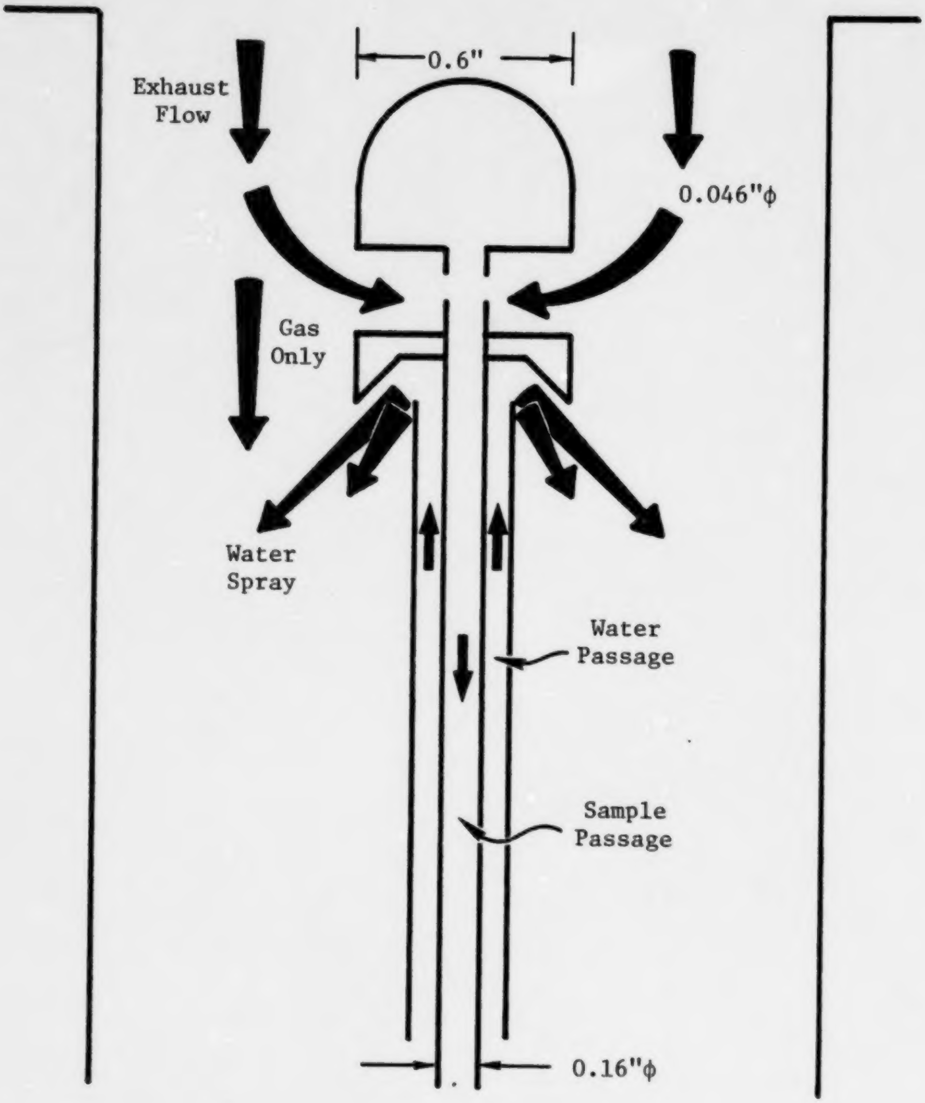

Figure 11. Sampling Probe.

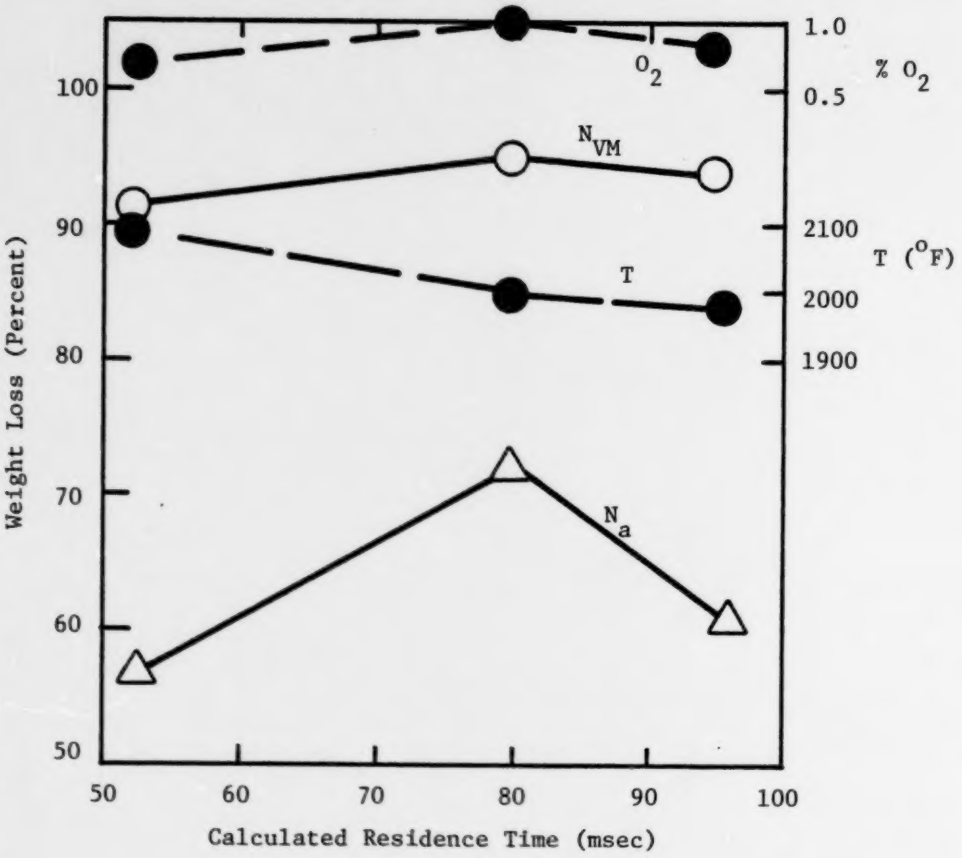

Figure 12. Results of N_2/CH_4/Air/Coal Tests.

studies in the smaller reactor, SRI, will produce much more information due to the smaller residence times and volatile yields obtainable.

Coal/Air Tests

At present, coal/air combustion tests using SRII are still in progress. The results of the eleven tests completed to date are presented in the following paragraphs.

Figure 13 shows SRII gas composition plotted against whole coal equivalence ratio, ϕ, calculated using the coal and air input rates. The trend is somewhat as expected of a conventional combustor. The CO_2 concentration peaks a bit late at ϕ approximately 1.2. The rapid fall off of CO_2 on the lean side is in part a reflection of reactor instability. In most cases, a flame could not be maintained at ϕ much less than 0.75. The concentration of O_2 and CO are as expected based on the CO_2 results. The production of CO starts at an equivalence ratio of unity (0.5 percent) and increases to about 11 percent at ϕ equaling about 2.5. Since CO_2 peaks well on the rich side, it is expected that combustion is incomplete.

An estimate of the extent of reaction based on the gas composition, N_g, has been made and the results are shown in Figure 14. N_g values lie in the region between roughly 60 to 90 percent, with a tendency to increase with decreasing ϕ. As seen in the figure, there does not seem to be any direct dependence of N_g on calculated residence time.

A plot of temperature versus equivalence ratio is presented in Figure 15. It shows temperature rising from $1950^\circ F$ at ϕ equaling 0.63 to about $2850^\circ F$ at ϕ equaling 1.2. The low temperature point represents a condition where the flame was bordering on extinction. At this condition, a ten percent reduction in the coal feed rate causes the flame to extinguish. After reaching a temperature of about $2850^\circ F$, further increases in ϕ do not produce dramatic changes in temperature. With the exception of one point, the temperature was found to remain between 2800 and $2900^\circ F$ out to an equivalence ratio of about 2.5.

It was expected that temperature would begin to drop with increasing ϕ. It is possible that the apparent insensitivity of temperature to ϕ, at values of greater than 1.2, may be due in part to the effect of SRII thermal lag. Generally tests were conducted with ϕ increasing (wall temperature increasing).

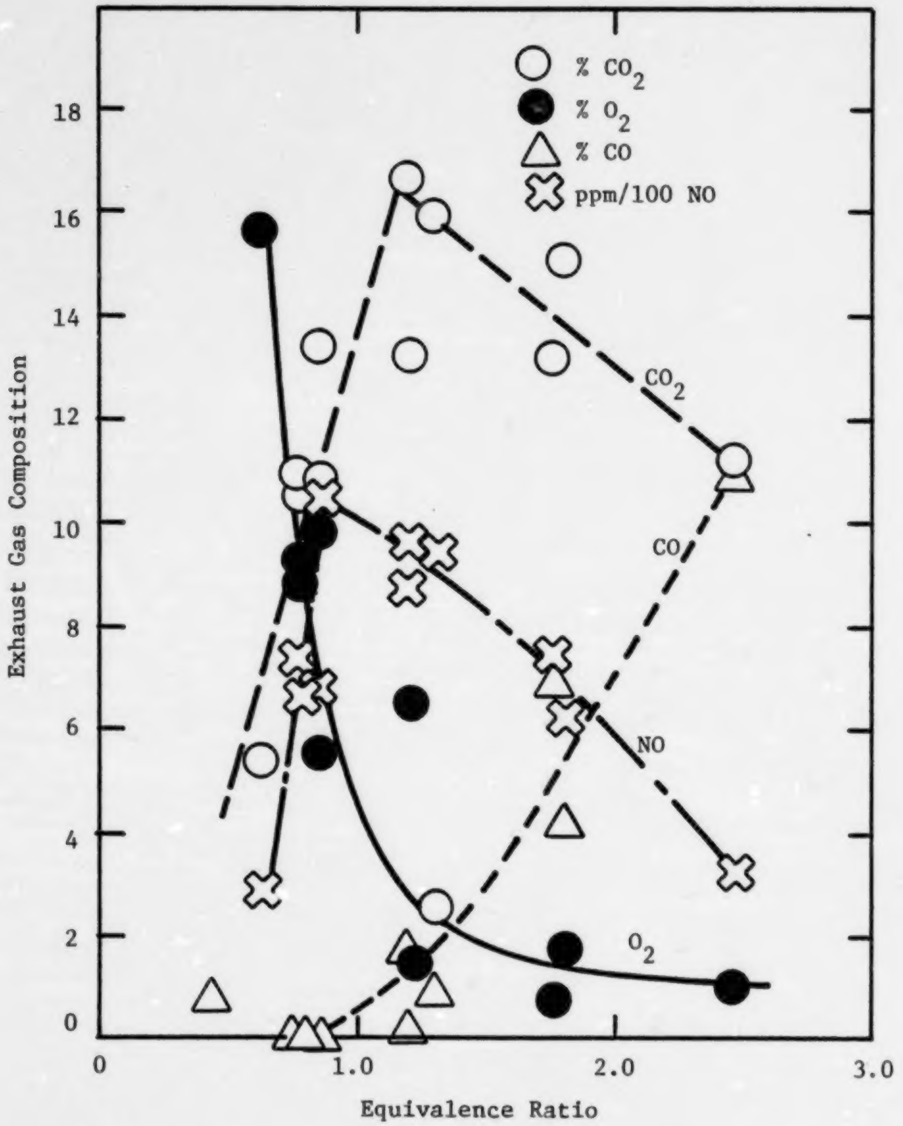

Figure 13. Gas Composition Versus Whole Coal Equivalence Ratio.

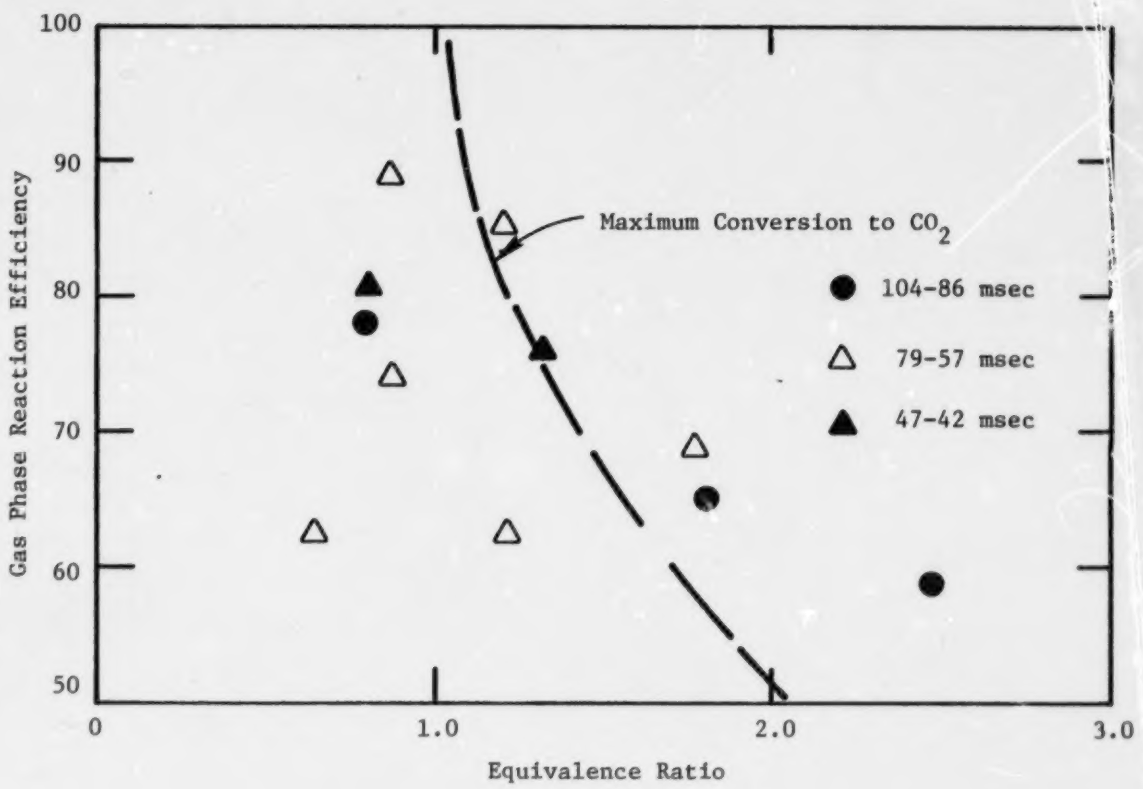

Figure 14. Reaction Efficiency Based on Exhaust Composition Versus Whole Coal Equivalence Ratio.

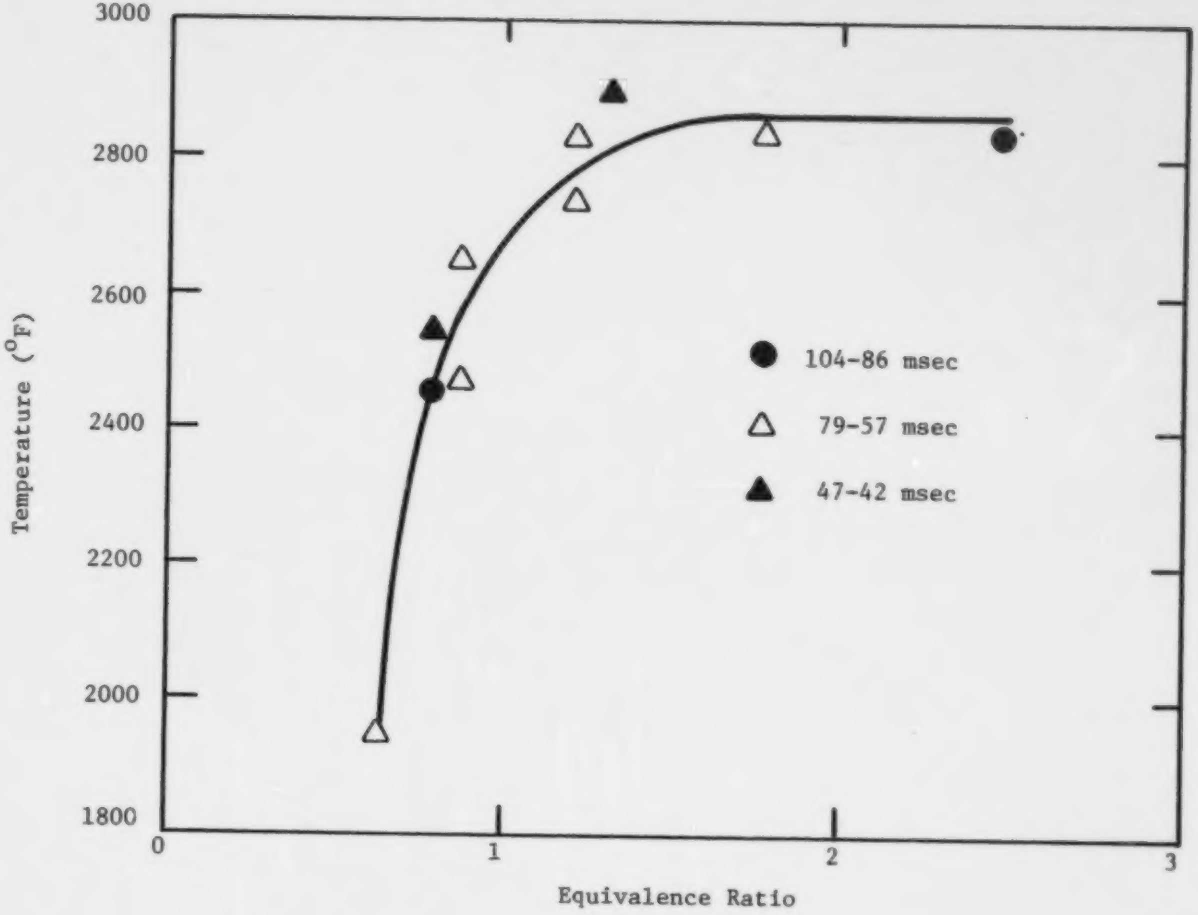

Figure 15. Temperature Versus Whole Coal Equivalence Ratio.

Referring to Figure 14, based on a relatively constant temperature at ϕ greater than 1.2, there is a definite trend for N_g to increase with decreasing equivalence ratio. There also appears to be little effect of residence time on temperature.

Four char samples have been subjected to ultimate and proximate analysis. The results are illustrated in Figure 16. In this figure, the weight loss of nitrogen and volatile matter is plotted against weight loss based on the ash content of the char, N_a. Also shown is the calculated gas phase reaction efficiency, N_g, against N_a. The extent of reaction based on ash content of the char is most likely in error due to ash vaporization at higher temperatures. This possible effor is thought to be small due to the relatively large values of N_a indicated. Several trends are of interest in Figure 16. They are:

- N_a is always greater than N_g
- No correspondence between N_a and volatiles loss is evident
- Fuel nitrogen loss roughly corresponds to N_a

Full conclusions can not be drawn from the data presented in this figure as it covers a very limited range of N_a. However there are some points to be made.

The presence of condensed combustible material in the exhaust would explain the differences between N_g and N_a. It can be expected that the lighter condensible materials are less likely to be trapped by the water spray in the exhaust passage. If they follow the gas and escape out the stack, then N_g would be expected to be less than N_a. The lack of correlation between N_a and volatile loss indicates that the coal decomposition process has been essentially completed. The results indicate that residual "char" nitrogen might be bound in the coal structure and for the temperature levels tested its removal parallels the removal of carbon.

Figure 17 and Figure 18 show the observed affect of equivalence ratio and temperature of fuel nitrogen conversion to NO, respectively. In constructing Figure 17, the maximum production of NO was determined by assuming that all of the nitrogen in the coal is converted to NO. The trend shown in Figure 17 has been observed by others (Reference 4). It shows conversion decreasing from 30 percent at an equivalence ratio of 0.8 to a conversion of less than 5 percent at an equivalence ratio of 2.5.

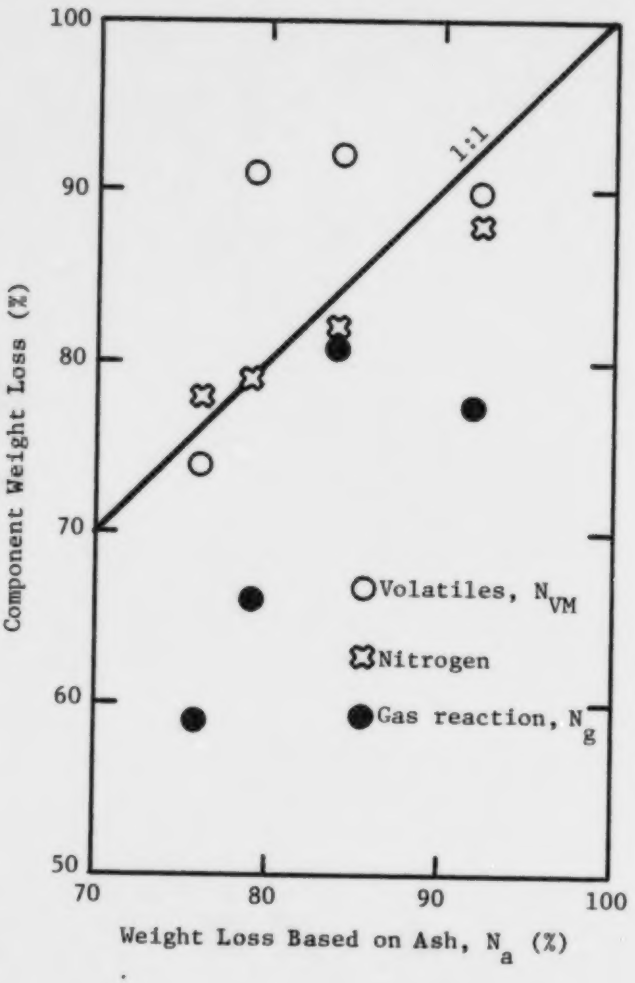

Figure 16. Component Weight Loss Versus Weight Loss Based on Ash.

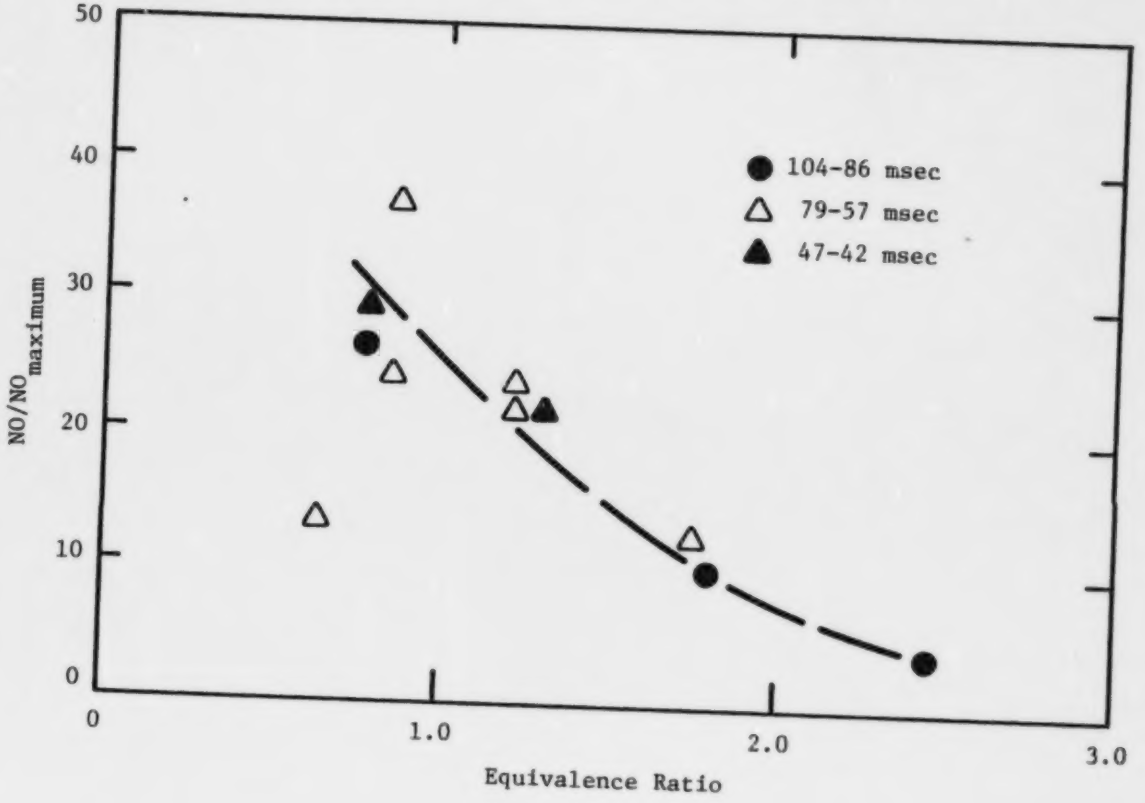

Figure 17. Fuel Nitrogen Conversion Versus Whole Coal Equivalence Ratio.

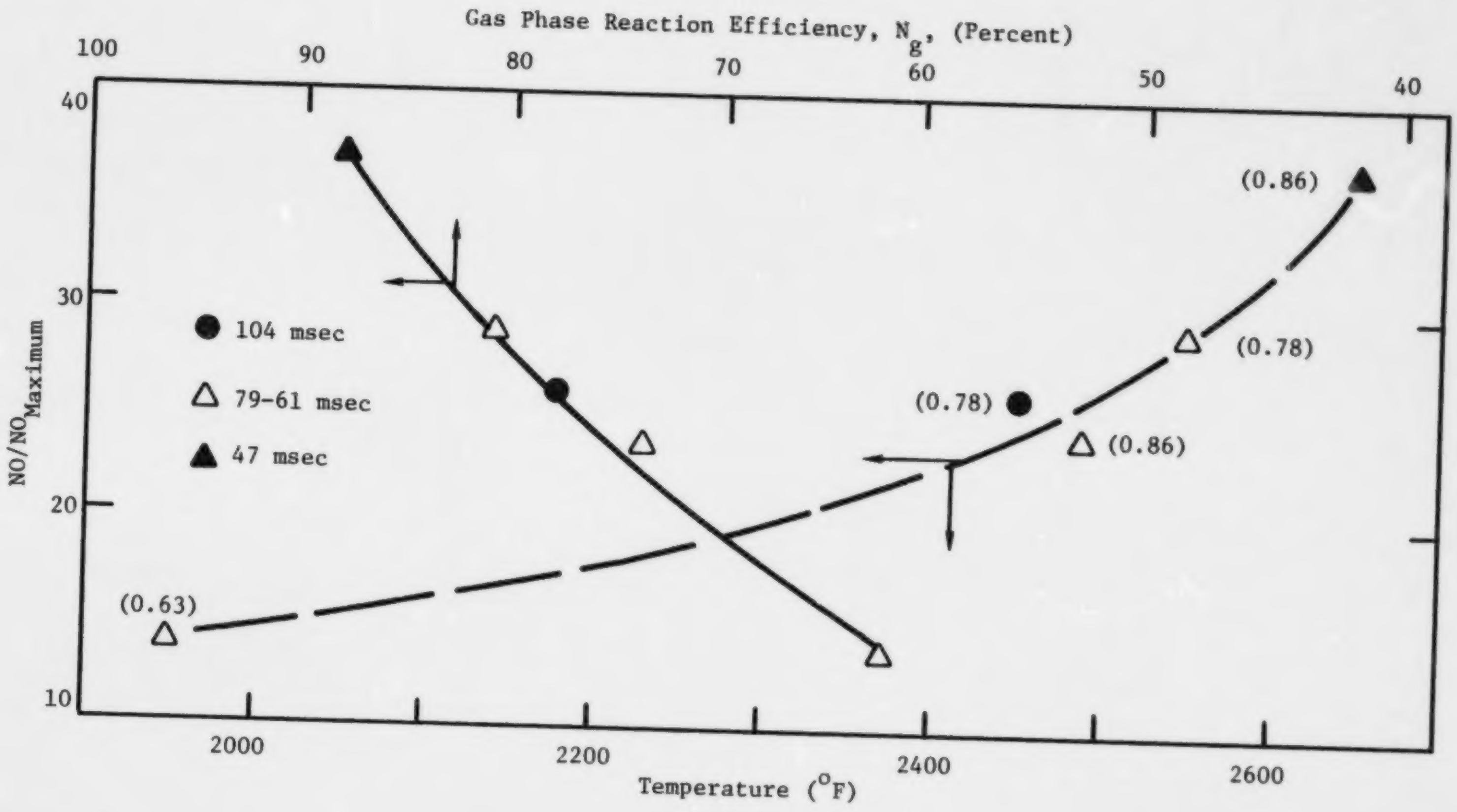

Figure 18. Fuel Nitrogen Conversion Versus Temperature and Calculated Gas Phase Reaction Efficiency. Equivalence Ratios Shown in Parenthesis.

At values of ϕ less than one the data shows some scatter. Less scatter is observed at ϕ greater than one. The increased data scatter at the lower equivalence ratios might be due to larger temperature variations (Figure 14) or changes in extent of reaction.

Figure 18 shows fuel nitrogen conversion against temperature and calculated gas phase reaction efficiency. As shown in the figure, conversion increases as temperature increases. Conversion also increases as gas reaction efficiency increases. Fuel nitrogen conversion is known to increase with temperature. If fuel nitrogen introduced into the gas phase increases with coal reaction efficiency, which is expected, then conversion of fuel nitrogen is also likely to be strongly influenced by reaction efficiency. The relative importance of temperature and reaction efficiency can not be estimated with the amount of data obtained so far.

SECTION V

DISCUSSION

Residence Time Effect

From the results presented, it appears as if residence time in the 50 to 100 msec range has little effect on either calculated reaction efficiency, volatiles loss, or NO formation. The lack of correlation of these parameters with residence time might indicate that either the calculated residence time does not correspond to the true particle residence time or that the events occurring in SRII are somewhat residence time independent over this time range.

If particle residence time is not equal to the gas residence time, then the equivalence ratio based on the coal feed would be incorrect. This does not contradict the finding shown in Figures 13, 15 and 17 indicating a somewhat expected dependence of exhaust composition, temperature, and fuel nitrogen conversion on equivalence ratio. If volatiles are the primary component involved in combustion and NO formation, then the feed equivalence ratio may be indicative of the amount of volatile 'fuel' in the combustor. This is especially true if volatile losses account for about 65 percent of the combustibles in the coal as can be inferred from Figure 12.

Fuel Nitrogen

The NO formation results presented in Figure 17 and Figure 18 show NO conversion to be correlatable both with temperature, extent of gas phase reaction, and equivalence ratio. As mentioned previously, these trends have been found by other researchers. All of the data on fuel nitrogen conversion is plotted in Figure 19 against conversion as predicted by the relation given by Wendt (Reference 6). As shown, this correlation fits the data reasonably well (although a better correlation is possible). This correlation includes a strong dependence primarily on equivalence ratio. Since equivalence ratio affects temperature, O_2 and CO concentrations, the correlation implicitly contains the effects of these variables on NO.

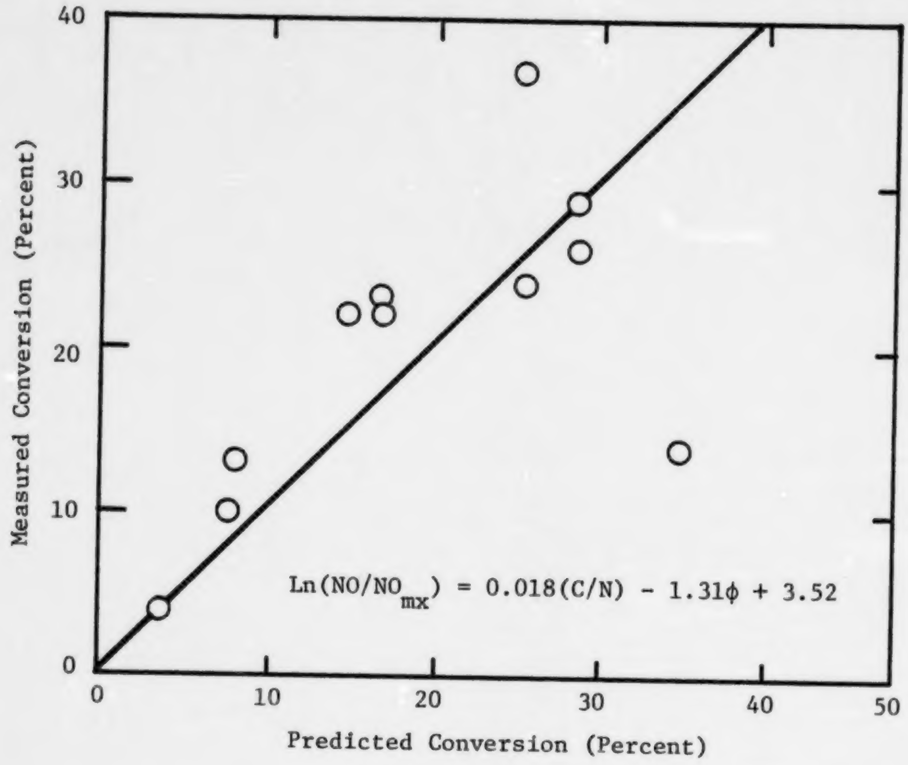

Figure 19. Measured Fuel Nitrogen Conversion Versus Predicted Conversion (Reference 6). C/N is the Original Ratio of Carbon to Nitrogen in the Coal.

SECTION VI

CONCLUSIONS

Mixing

Experiments indicate that good mixing is achieved in SRII. The particle mixing study results indicate that the particle residence time might be longer than the gas residence time. The mixing results also indicate that the particle residence time may vary significantly less than that of the gas.

Combustion

The combustion results show that devolatilization may be essentially completed in the SRII residence time range. The exhaust concentrations and temperature dependence on equivalence ratio is similar to those expected in larger time scale systems. This might lead to the conclusion that enhanced volatile yields play a major role in combustion.

It has been observed that fuel nitrogen conversion is correlatable with equivalence ratio, reaction efficiency and temperature. The trends in these correlations show similarities with other experimental work. It was also found that the nitrogen depletion of the char corresponds roughly to the weight loss exhibited by the char, although a limited range of weight loss was examined (75-95 percent).

SECTION VII

FUTURE WORK

Work in the future will include additional coal/air combustion tests using SRII. These tests will be performed mainly at fuel rich equivalence ratios up to about 4. In these additional tests, exhaust concentrations of HCN and NH_3 will be measured. Tests using coal/air/N_2/CH_4 mixtures will also be performed to evaluate extent of reaction and char nitrogen loss with constant gas residence time, and constant temperature. Also examined will be the effect of combustion on particle size.

Work using the smaller reactor, SRI, will parallel work which has been and will be conducted using SRII at residence times roughly half the values of those in SRII. Tests to be conducted include mixing experiments as well as combustion experiments.

REFERENCES

1. Evangelista, J. J., Shinnar, R. and Katz, S. The Effect of Imperfect Mixing on Stirred Combustion Reactors. Twelfth Symposium (International) on Combustion, The Combustion Institute, 1969.

2. Kobayashi, H., Howard, J. B. and Sarofim, A. F. Coal Devolatilization at High Temperatures. Sixteenth Symposium (International) on Combustion, The Combustion Institute, 1976.

3. Ubhayakar, S. K., Stickler, D. B., Von Rosenberg, Jr., C. W. and Gannon, R. E. Rapid Devolatilization of Pulverized Coal in Hot Combustion Gases. Sixteenth Symposium (International) on Combustion, The Combustion Institute, 1976.

4. Pohl, J. H. and Sarofim, A. F. Devolatilization and Oxidation of Coal Nitrogen. Sixteenth Symposium (International) on Combustion, The Combustion Institute, 1976.

5. Wendt, J. O. L., and Glass, J. W. Pollutant Control Through Staged Combustion of Pulverized Coal. United States Department of Energy Report FE-1817-6, May 1979.

REACTOR STUDIES TO ASSESS THE IMPACT OF FUEL CHARACTERISTICS ON FUEL NO_x FORMATION

M. P. Heap
D. W. Pershing
G. C. England
S. L. Chen
R. Nihart
and
D. P. Rees
Energy and Environmental Research Corporation
Irvine, California 92714

Fifth EPA Fundamental Combustion Research Workshop
Newport Beach, California
January 23-25, 1980

SECTION I

INTRODUCTION

It has been recognized for some time that the oxidation of fuel-bound nitrogen produces a significant fraction of the total nitrogen oxides (NO_x) formed during the combustion of coal and petroleum-derived liquid fuels. The data presented in Figure 1 illustrates the influence of fuel nitrogen content on the emission of NO_x from practical systems. NO_x emissions (lbs NO_x/MBtu) are shown as a function of fuel nitrogen content expressed as weight percent on a dry ash-free basis. All the information shown in Figure 1 was obtained from field tests of water walled boilers and therefore the emissions are also influenced by the boiler design and firing configuration. The production of thermal NO (formed by fixation of atmospheric nitrogen) and fuel NO (formed from fuel-bound nitrogen) is strongly dependent upon the rate of fuel/air mixing. Thus, it is not possible to establish from the information presented in Figure 1 whether fuel properties alone or in combination with the influence of firing method are responsible for the large variation of emission with fuel nitrogen content. Firing method does influence fuel nitrogen conversion because of variations in fuel air mixing. Under oxygen deficient conditions a reaction path is favored which allows the formation of molecular nitrogen. The two major methods of burning pulverized coal in utility boilers involve either circular wall burners with relatively rapid fuel/air mixing, or corner-fired fuel injectors with a much lower fuel/air mixing rate. In general, NO_x emissions from corner-fired boilers are lower than those from uncontrolled wall-fired units. NO_x control strategies for fuels containing nitrogen minimize fuel NO formation by staging the combustion process. The data presented in Figure 1 suggests that for liquid fuels NO_x emissions increase with increasing fuel nitrogen content. However, for solid fuels, emissions are not entirely dependent upon fuel nitrogen content.

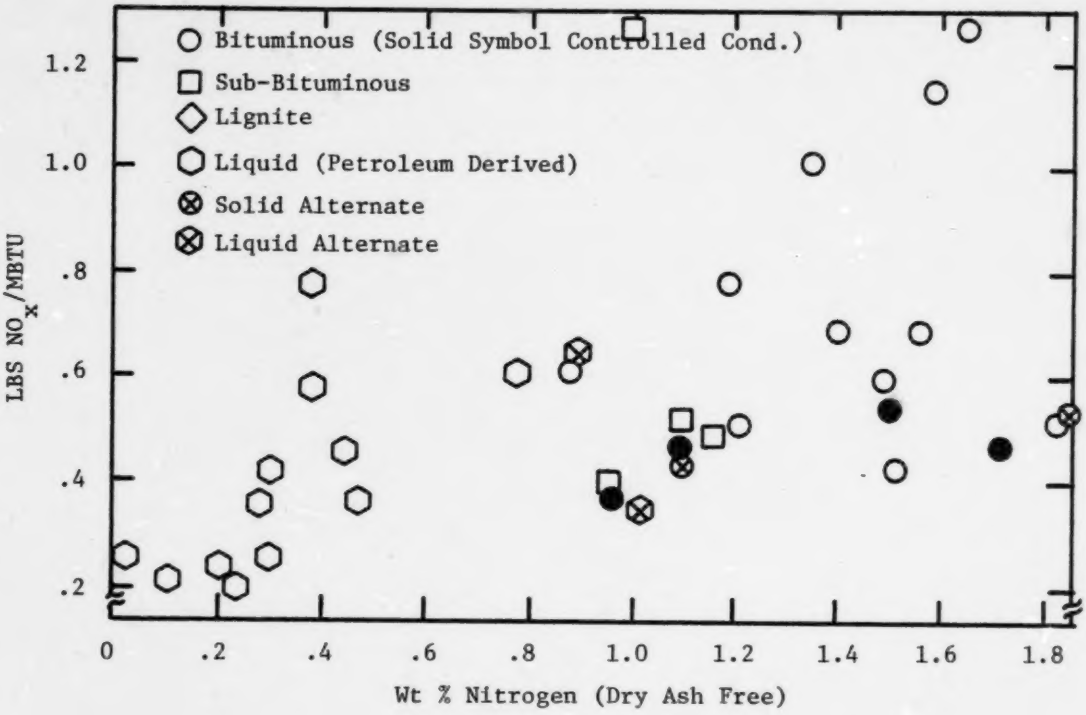

Figure 1. The Influence of Fuel Nitrogen Content on NO_x Emissions from Practical Systems.

This paper describes the results obtained to date in two ongoing investigations to assess the impact of fuel properties on pollutant formation. The effort to date has concentrated upon providing information to answer the following questions:

- What are the fuel characteristics that dominate fuel NO formation? Are they entirely chemical in nature? What is the impact of physical properties such as particle/droplet size or thermal environment on fuel NO formation?
- To what extent does fuel/air contacting interact with fuel characteristics in the formation of fuel NO?
- Is it possible to assess the emission characteristics of fuels in practical systems without prior field tests? This is particularly important in the evaluation of the impact of increased use of alternate fuels on air quality because of their high fuel-bound nitrogen content.

The approach taken in both of these investigations was experimental, wherein both solid and liquid fuels were burned in the absence of molecular nitrogen. The oxidant consisted of a mixture of oxygen, argon and carbon dioxide (21 percent by volume O_2). The carbon dioxide was added in order to maintain the same adiabatic flame temperature for both the artificial oxidant and air. NO formed during combustion with this artificial N_2-free oxidant is called fuel NO. Two other techniques have been used to assess the contribution of thermal NO to the emission of nitrogen-containing fuels. One of these involves the addition of cold recirculating combustion products to the combustion air to eliminate thermal NO formation. Some investigators burn non-nitrogen-containing fuel and consider the thermal NO produced to be the same as that which would have been produced with a nitrogen-containing fuel. All three methods are open to criticism. The addition of flue gas recirculation does not eliminate all thermal NO, and it is known that under certain fuel/air mixing conditions total NO_x emissions may increase with the addition of recirculated flue gases. Thermal NO formation may also be dependent upon fuel characteristics and the assumption that the fuel nitrogen conversion can be assessed from a subtraction of NO produced with a non-nitrogen fuel may only be useful for doped distillate oils. The artificial oxidant technique used in these investigations has two potential drawbacks:

- Reactions involving nitrogen species may be affected because of the lack of the large number of nitrogen molecules present when air is used as the oxidant;
- The use of CO_2 to balance flame temperatures may affect local radical concentrations which are involved in the formation of N_2 from nitrogen species under fuel-rich conditions.

Since a major objective of these investigations was the comparison of the fate of fuel nitrogen in solid and liquid fuels, the use of artificial nitrogen-free oxidant mixtures provides the most appropriate method of determining fuel NO formation.

The investigations described in this paper were not funded as part of the FCR program. However, they are part of burner development programs which require fundamental information to allow the maximum use to be made of the information obtained. After describing the experimental equipment and the characteristics of the fuels investigated, the results will be discussed under two separate headings. The first major topic involves fuel screening studies. In these studies, the fuels were burned under identical conditions to establish the impact of fuel characteristics on NO production under both excess air and staged combustion conditions. The second topic to be discussed involves the use of bench-scale reactors to determine optimum conditions for NO_x control. These investigations have only recently been initiated, and the results presented in this paper must be considered as preliminary and as such, probably do not represent optimum configurations for NO control via combustion modification.

SECTION II

EXPERIMENTAL SYSTEMS

The experimental systems used in both investigations involving liquid and solid fuels are most conveniently described by dividing them into four subsystems as follows:

1. Reactors
2. Fuel Delivery
3. Air/Artificial Oxidant Delivery
4. Measurement Procedures

Reactors

The design of the liquid and solid fuel reactors has been described in detail elsewhere.[1] They consist of refractory downfired tunnel furnaces with ready access for both flame observation and the addition of staged air through sidewall ports. The reactor wall temperatures were monitored continuously and when not in use the reactors were fired with propane and maintained at thermal equilibrium. The fuel characterization studies were carried out in simple furnaces 80 and 60 mm inner diameter for the liquid and solid reactors respectively. The liquid fuel fired reactor was rebuild with the same diameter as the solid fuel reactor and additional modules were constructed for both fuels to investigate optimum control configurations.

A schematic of the modified reactor is shown in Figure 2. The modified reactors were then capable of operating with three independent zones as follows:

1. An initial fuel-rich zone that could be isolated from a down-stream section with a radiation choke.
2. A fuel-rich zone with or without heat extraction using removable cooling coils.
3. A second staged air injection system which allowed for a choke prior to injection of the second stage air to facilitate stabilization of a diffusion flame. The staging air could be added normal to or along the combustor axis to vary the mixing rate between primary products and second stage air.

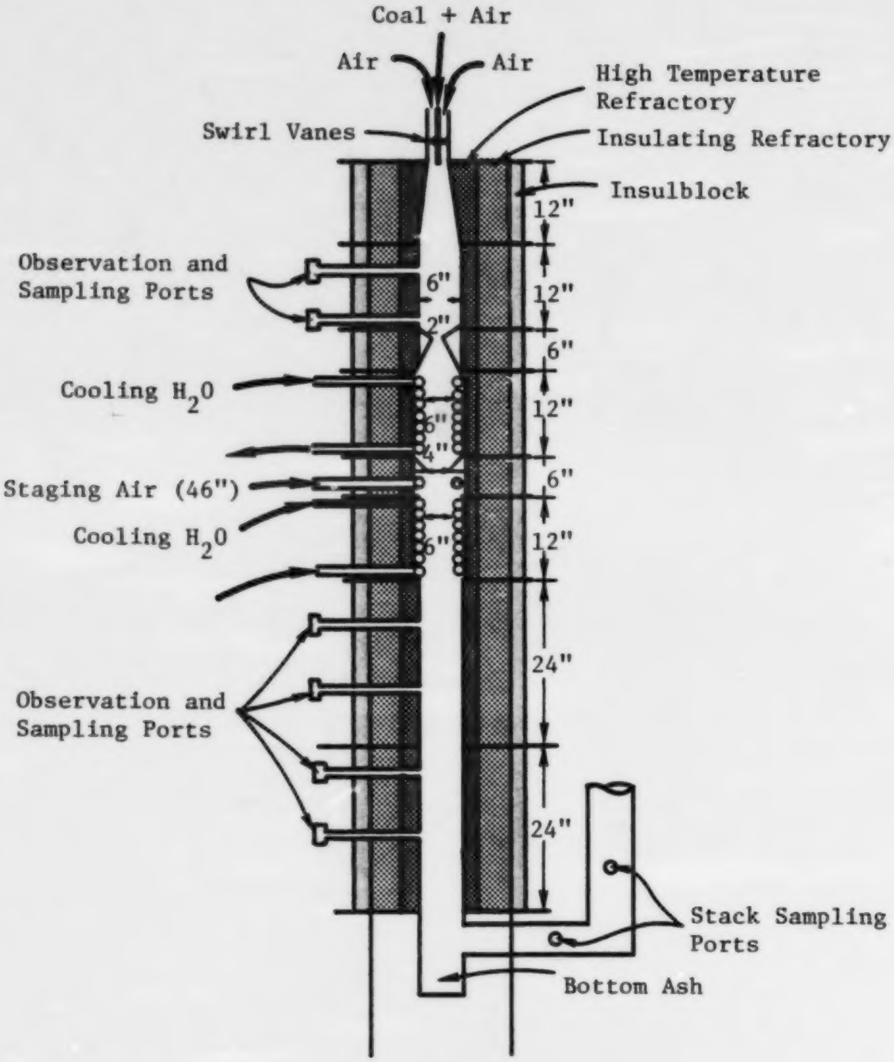

Figure 2. Schematic of Bench-Scle Furnace for Experiments on Effects of Solid and Liquid Fuels.

4. A burnout zone with the possibility of heat extraction, using removable cooling coils.

Fuel Delivery

The burners used for both solid and liquid fuels are shown in Figure 3. All the liquid fuel investigations were carried out with a double concentric burner using axial airflow, and the major portion of the data was collected using an ultrasonic oil atomizer (capacity 0.55 cc/sec). It provided adequate atomization of the heavy fuel oils at relatively low oil flow rates. The tip of the fuel nozzle was positioned at the beginning of the burner divergent, and in general, the visible flame front was displaced approximately one nozzle diameter from the nozzle tip. The liquid fuels were preheated electrically in a small supply tank, drawn through a six micron filter into a variable speed Zenith metering pump. The pump outlet pressure was maintained constant and the oil flow rate was varied by direct mechanical adjustment of the pump speed. The viscosity of the fuel oil was maintained constant at the nozzle by the temperature control provided by a cartridge heater fitted within the fuel gun.

Pulverized coal was supplied pneumatically from a hopper-fed screw feeder to one of two burners which allowed the coal to be burned entirely premixed or as a diffusion flame. Premixing was achieved by direct impingement of the coal jets with the main combustion air supply in a premixing chamber which was separated from the combustion zone by a series of water-cooled tubes to prevent flashback (see Figure 3). The coal/air mixture burned in a plug flow mode with the ignition zone situated in the refractory divergent. The coal-plus-transport-air could also be supplied to a variable swirl burner and injected either axially or radially, thus allowing experiments to be conducted with radically different fuel/air mixing rates. Variable swirl was achieved by dividing the total oxidant flow into two; one stream which flowed axially around the fuel injector and the other through fixed swirl vanes which gave a tangential velocity component to the mixed flow.

Air/Artificial Oxidant Delivery

Combustion air and artificial oxidant mixtures were supplied from a high pressure source and metered by 600 mm length rotameters, and preheated by

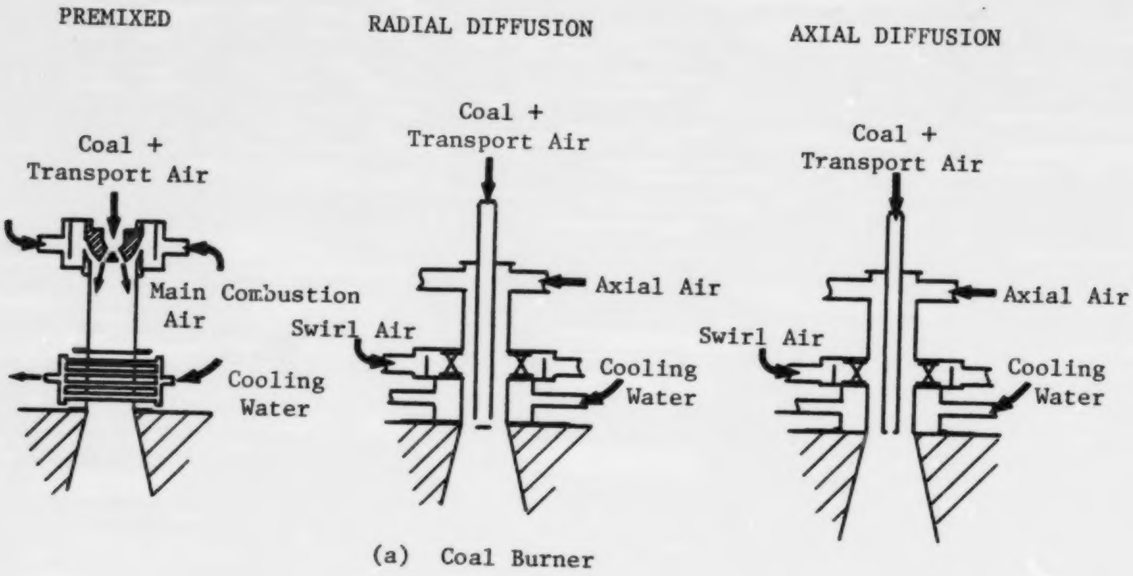

Figure 3. Different Burners Used on the Bench-Scale Furnaces.

electric circulation heaters. Throughout the experiments involving artificial oxidants, the oxygen concentration of the mixture was monitored continuously.

Measurement Procedures

Two types of measurements are discussed in this paper. All exhaust measurements were made under excess air conditions using a similar sampling and analysis system for both reactors. It allowed for continuous monitoring of NO, NO_x, CO, CO_2 and O_2. Combustion products were withdrawn from the appropriate exhaust duct through a water-cooled stainless steel probe. Sample conditioning prior to the instrumentation consisted of an ice bath water condensor, quartz wool filters and a stainless steel Teflon sampling pump. All sample lines were Teflon and stainless steel.

In-flame sampling was also carried out to measure NO, NO_2, HCN and NH_3 concentrations. NO and NO_x were monitored by a chemiluminescent analyzer and concentrations of NH_3 and HCN were determined using ion specification electrodes taking appropriate precautions to minimize sulfide interference with HCN measurements. A water quench probe was used to withdraw the samples from both the liquid and solid reactors. It was found that repeatability of both HCN and ammonia measurements was acceptable in the solid fuel reactor. The repeatability with liquid fuels was less satisfactory and the data given in this paper represents an average.

SECTION III

FUEL CHARACTERISTICS AND THE FATE OF FUEL BOUND NITROGEN

The range of fuels investigated in both programs is shown in Figure 4 which compares the nitrogen content on a dry ash free basis and is shown as a function of lbs nitrogen/MBtu. One anthracite has been tested because it represents a low volatile nitrogen containing fuel. Two other unusual fuels tested to date are an Australian lignite and a low temperature gasification char. Bituminous coals have the highest nitrogen content of the solid fuels tested and the nitrogen content decreases with decreasing rank. The nitrogen content of alternative liquid fuels depends upon the feedstock and the processing. A wide range of both coal and shale derived fuels, which exceed the total range of nitrogen contents for conventional fuels, have been tested. Typical fuel NO results are shown in Figure 5. The solid fuels were burned in the premixed mode, which provides a good comparison with the liquid fuel experiments. Under normal operating conditions, the ultrasonic nozzle produces relatively small droplets and the resulting flame conditions can be considered to be well mixed. Under these overall excess oxygen conditions, fuel NO formation is not very strongly dependent upon excess oxygen.

Figure 6 presents a composite plot comparing fuel NO formation at 5% overall excess oxygen for all the fuels studied. The data is presented as mass of nitrogen emitted as NO_2 as a function of the mass of nitrogen in the fuel normalized by the fuel heating value. It can be seen that fuel nitrogen conversion to fuel NO is higher with liquid fuels than with solid fuels. NO emissions from liquid fuels increase with increasing fuel nitrogen content and total fuel nitrogen content appears to be the dominant factor controlling fuel nitrogen emissions from nitrogen containing liquids. In a separate series of experiments fuel NO emissions from petroleum derived residual fuels were compared with those from a doped distillate oil. Under excess air conditions emissions were almost independent of the dopant and the presence of sulfur. It can also be seen in Figure 6 that alternate liquid fuels behave similarly to petroleum derived liquids. Fuel nitrogen conversions greater than 50% are higher than would be expected for practical equipment firing liquid fuels.

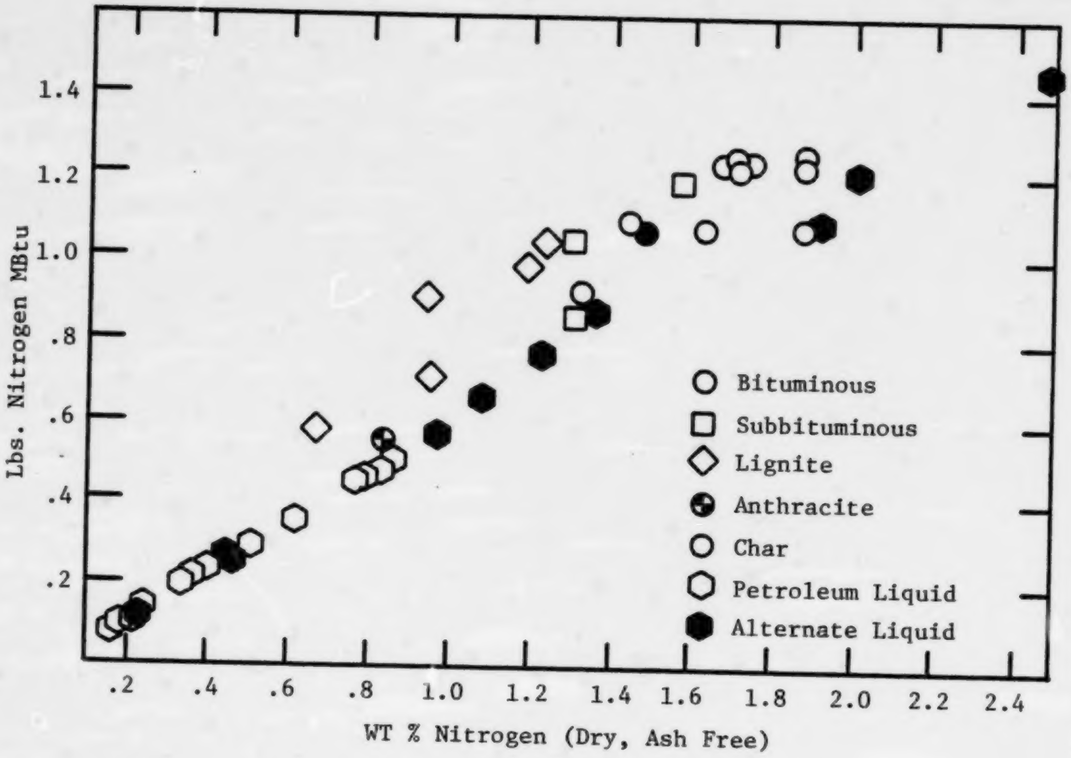

Figure 4. Characteristics of Fuels Tested.

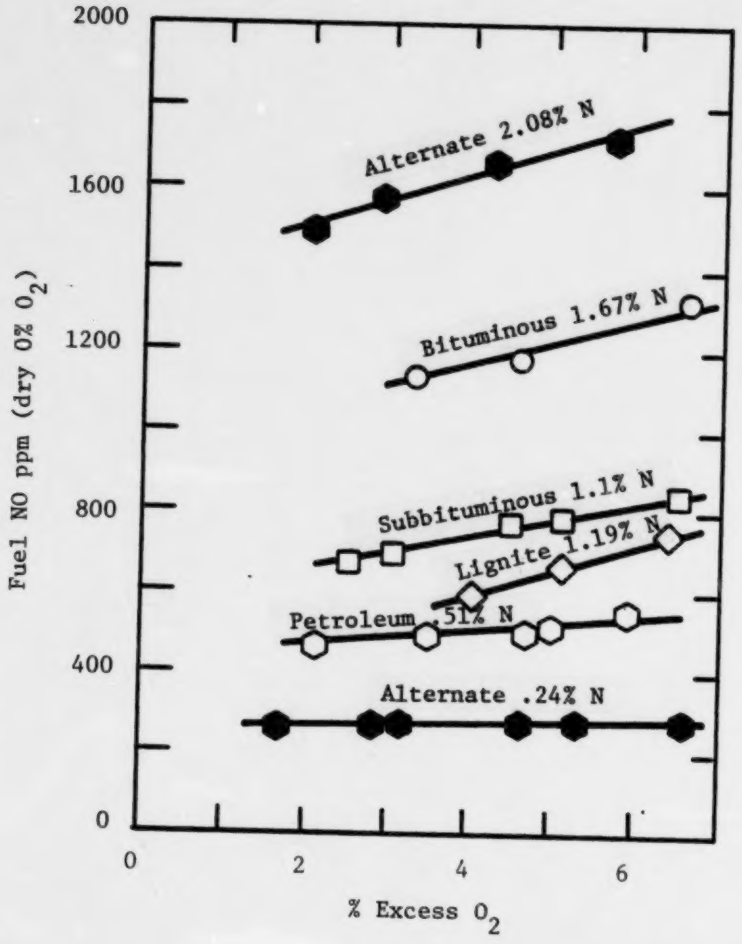

Figure 5. Fuel NO Formation as a Function of Excess Oxygen.

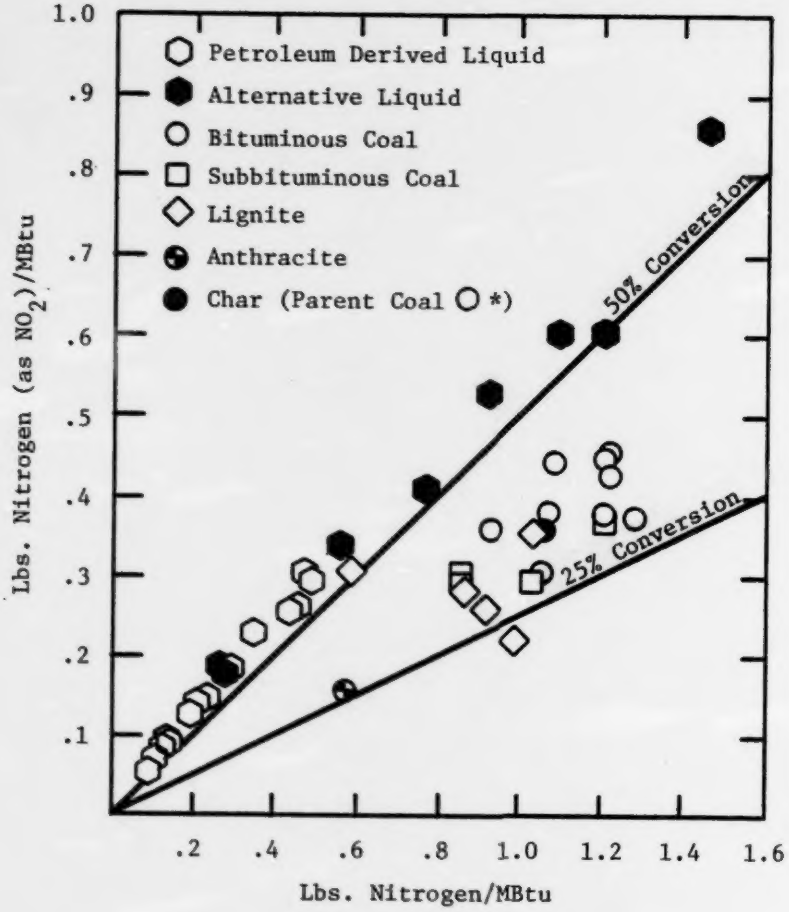

Figure 6. Fuel NO_x Emissions from Liquid Fuels Correlate with Total Nitrogen Content. Other Properties are Important with Coal.

Fuel NO emissions from premixed coal flames are also shown in Figure 6. Fuel nitrogen conversions are lower and much less dependent upon total nitrogen content. Fuel NO emissions are grouped lignite < subbituminous < bituminous although there is considerable overlap between the various ranks. The Australian lignite appears to be different from the other lignites tested. It gave a fuel nitrogen conversion of 50%. Fuel NO emissions from the gasification char were only 20% lower than the parent bituminous coal. Fuel NO emissions from the one anthracite tested were low as expected.

The fate of fuel nitrogen during combustion can be considered in the following steps:

- the solid or liquid fuel undergoes thermal decomposition transforming the fuel bound nitrogen. The nitrogen will be partitioned between gaseous and solid components. With coal, some of the nitrogen will remain in the char after volatile evolution which will give gaseous nitrogen as a primary or secondary product. High molecular weight tars may undergo secondary pyrolysis producing a nitrogen containing solid. For liquid fuels most of the nitrogen will become gaseous.
- gaseous nitrogen species will be converted either to NO or N_2 depending upon oxygen availability.
- solid nitrogen (in the form of char or soot) can also produce NO although it is generally believed that the conversion efficiency of char nitrogen to NO is low.

Assuming that char nitrogen conversion is small and independent of coal type, then fuel NO formation under excess air conditions will be maximized when oxygen availability is highest and the fraction of fuel nitrogen transformed into a gaseous species is highest. The above hypothesis suggests two NO_x control strategies. If char nitrogen conversion to NO is very small then one control strategy would involve subjecting the coal to a time/temperature history which minimized the evolution of gaseous nitrogen species. Alternatively, all the nitrogen can be converted to gaseous species and the conditions optimized to promote N_2 production. It can be argued effectively that those conditions which maximize fuel NO production under excess air conditions will be effective under the latter control strategy because volatile nitrogen evolution is maximized.

Under excess air conditions fuel NO formation would be expected to be highest when oxygen availability and volatile evolution were highest. For a given overall excess air, oxygen availability will depend upon fuel air contacting. Figure 7 shows fuel NO emissions for four coal types for the flame types in which the degree of mixing varies significantly. The highest degree of mixing will occur in the premixed flame and the axial diffusion flame will retard mixing of the fuel and air. The radial swirling diffusion flame was produced with a multiholed divergent fuel injector and the swirling combustion air produced a significant degree of backmixing and the flame was shorter than the axial diffusion flame. The results presented in Figure 7 are not the only data since the majority of coals have been tested in all three mixing modes. However, the data shown are indicative of the trends which allow the following conclusions to be drawn:

- in general, fuel NO emissions decrease as fuel air mixing rates decrease: premixed > radial swirling > axial diffusion;
- within any rank, certain coals show various degrees of fuel NO reduction as the degree of mixing varies;
- bituminous coals always show an effect of the formation of fuel air mixing on fuel NO formation.

If fuel NO requires oxygen and gaseous fuel nitrogen species, then conditions which promote the evolution of volatiles should enhance fuel NO formation under excess air conditions. Volatile evolution is temperature dependent, thus increasing particle temperatures should increase fuel NO formation. In these bench scale experiments, flame temperature could be varied by changing the amount of carbon dioxide mixed with argon and oxygen. Figure 8 shows the influence of thermal environment on fuel NO formation from solid and liquid fuels. The theoretical flame temperature is a measure of the final bulk temperature and although actual temperatures will not be as high or show the same range, it is indicative of the particle/droplet environment.

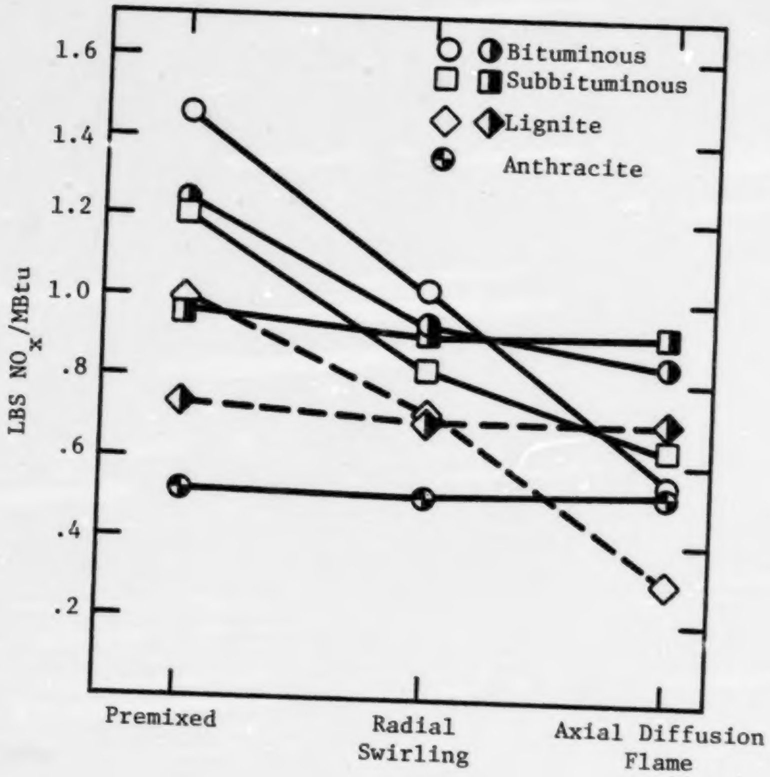

Figure 7. Impact of Fuel Air Contacting on Fuel NO Formation.

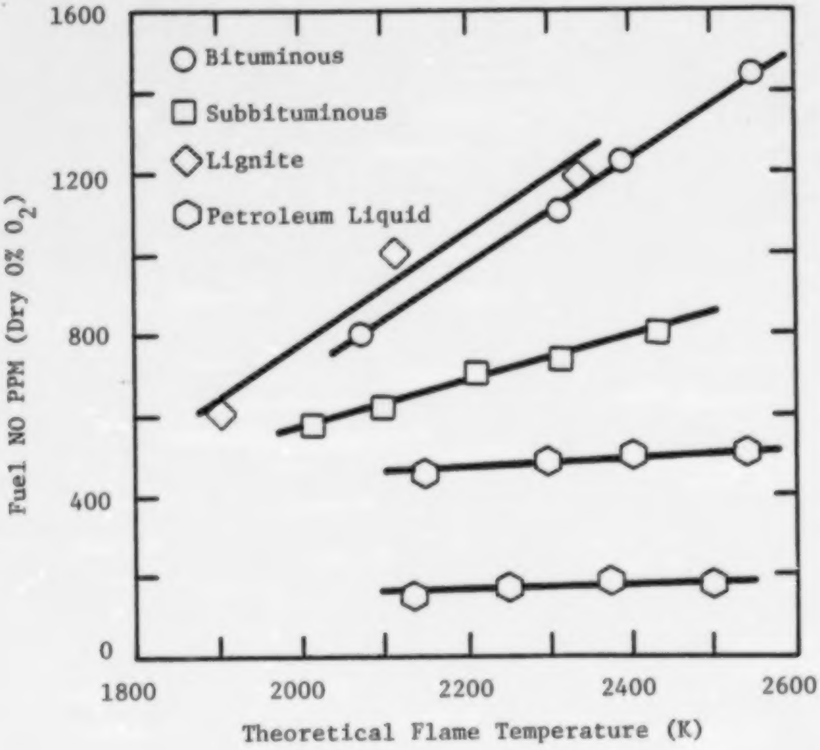

Figure 8. The Effect of Thermal Environment on Fuel NO Formation.

It can be seen that fuel NO formation from premixed coal flames increases with increasing temperature. However, temperature has a minimal effect with petroleum derived liquid fuels presumably because almost all the nitrogen is evolved at lower temperatures and the increase in temperature cannot increase the volatile nitrogen fraction. With axial diffusion coal flames, the effect of temperature is not observed. This may be because even though the volatile nitrogen fraction is increased fuel NO formation is limited because of the lack of oxygen. This limit does not apply in the premixed case.

In addition to the physical effects discussed above, fuel properties can also affect fuel NO formation because of their impact on volatile nitrogen evolution either directly or because of the volatile combustion around the particle. The heating value of these volatiles will determine the particle temperature, and the higher the temperature the greater the volatile evolution rate. Habelt et al. (2) have claimed that fuel NO formation in corner-fired boilers can be correlated by the oxygen-to-nitrogen ratio of the fuel. They believe that the coal oxygen affects fuel NO formation because it is immediately available and associated with the volatile fuel nitrogen fragments and can, therefore, readily form fuel NO. Attempts to correlate the data obtained in these studies in this way have proved largely unsuccessful. Figure 9 shows a correlation of fuel NO for the axial diffusion flame which most closely resembles the mixing conditions in a corner-fired boiler.

Some of the fuels used in these bench-scale studies have also been used in other FCR investigations concerned with the products of thermal decomposition. Workers at Rocketdyne (3) have measured the fraction of fuel nitrogen converted to HCN under inert pyrolysis conditions. Figure 10 compares the amount of fuel nitrogen converted to NO for the various mixing conditions as a function of fuel nitrogen converted to HCN under inert pyrolysis at 1100°C. For the fuels studied there is a reasonable correlation between convertible fuel nitrogen and fuel NO formation.

If oxygen is not available when the volatile nitrogen fragments are evolved from the coal, then the formation of molecular nitrogen is favored. This is the basis upon which all staged combustion control techniques operate for nitrogen-containing fuels. Figure 11 presents results from simple staging experiments involving operation of both the reactors under fuel-rich conditions

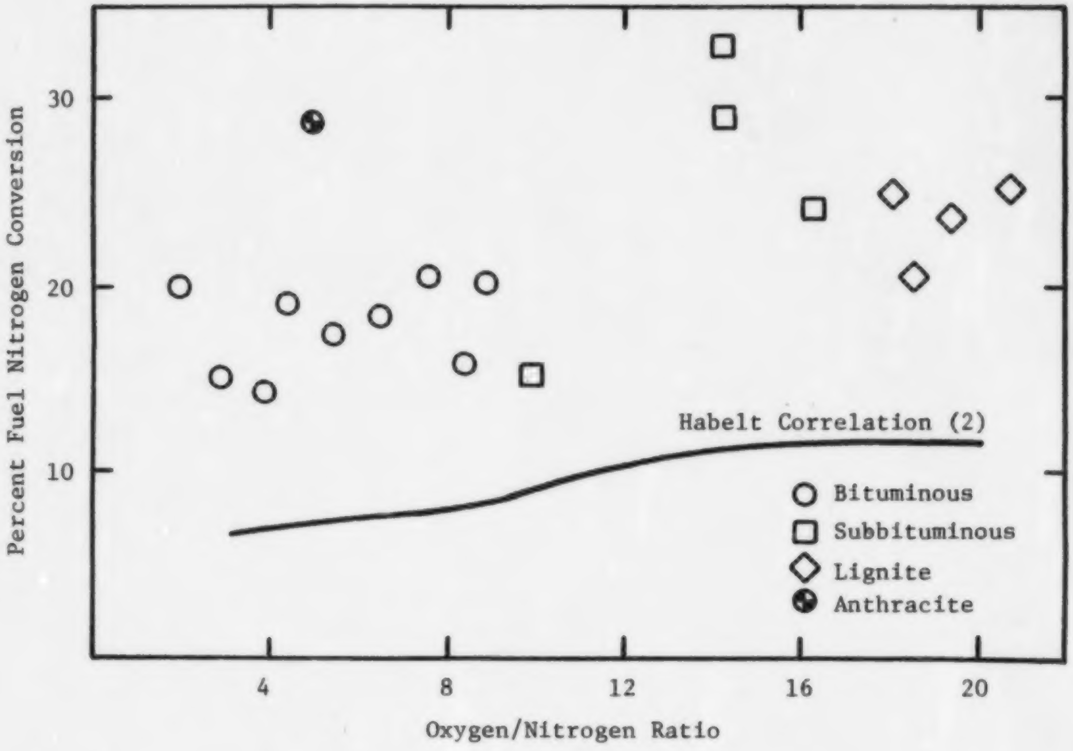

Figure 9. Effect of Fuel Oxygen/Nitrogen Ratio on Fuel Nitrogen Conversion in Axial Diffusion Flames.

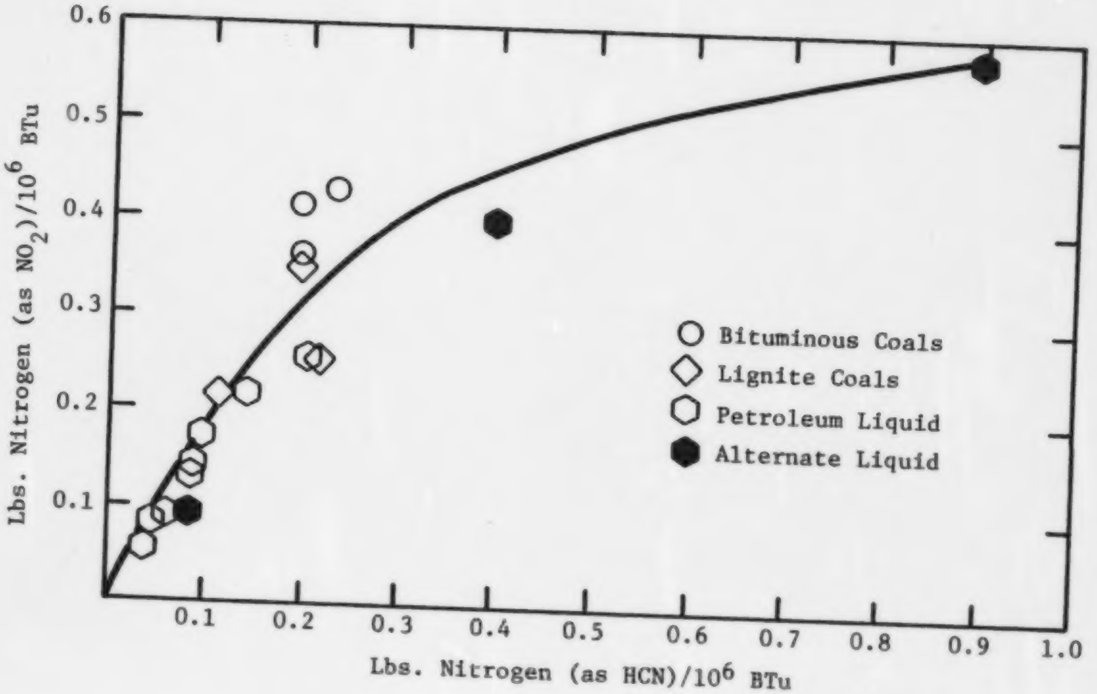

Figure 10. Relationship of Fuel NO Formed During Combustion to HCN Produced During Pyrolysis.

(a) Liquid Fuels

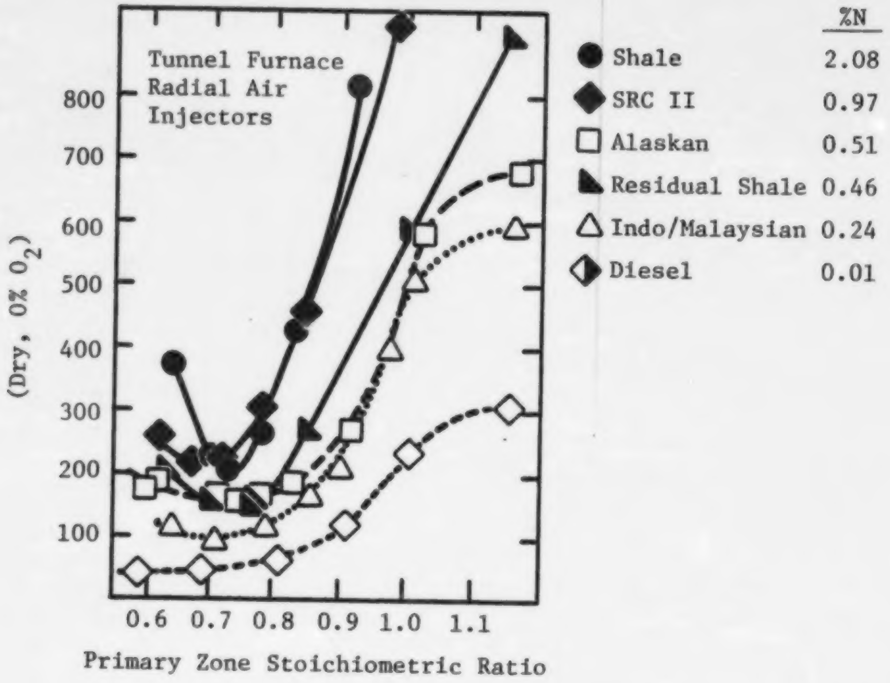

(b) Solid Fuels

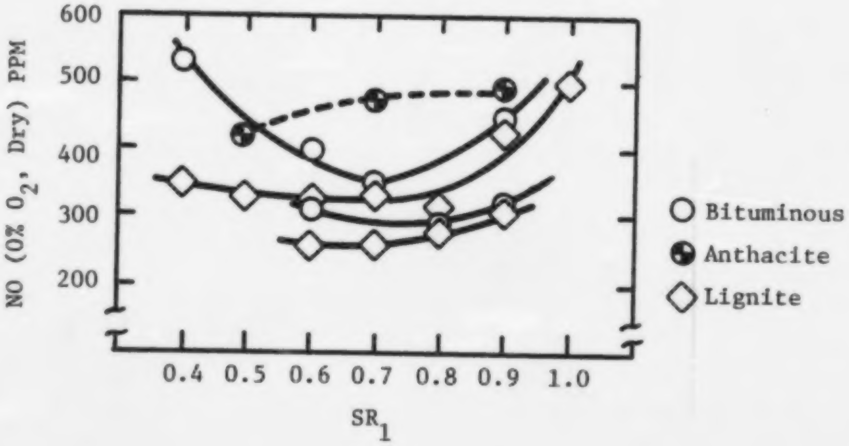

Figure 11. Effects of Staging for Solid and Liquid Fuels.

for a time of about 1 sec. and then injecting air downstream. The overall excess air is maintained constant, and the results are presented for several solid and liquid fuels. It can be seen that as the primary stoichiometry decreases, the exhaust NO_x first decreases, reaches a minimum, and then for nitrogen-containing liquid fuels increases (11a). This minimum is much more pronounced with nitrogen-containing liquid fuels than with the solid fuels, and for a non-nitrogen fuel no minimum in exhaust NO was observed. The characteristics for anthracite also differ from those for the two bituminous and two lignites shown in Figure 11b.

Figure 12 compares minimum NO emissions for the various fuels tested under simple staging conditions using a premixed primary for solid fuels or a rapidly mixed liquid fuel primary zone. It can be seen that for liquid fuels minimum emissions increase initially as the fuel nitrogen content increases. However, above 0.4 lbs of nitrogen per MBtu, emissions appear to be independent of nitrogen content for three of the alternate liquids. The one alternate liquid which appears to be different is a high boiling point shale residual. The minimum emissions from coal are almost independent of total fuel nitrogen content, and show very little trend with rank. These results are in general agreement with the trends which suggest that optimum staging conditions require maximum residence time for gaseous nitrogeneous specie in the rich zone.

Figure 13 uses the data generated in the Rocketdyne (3) experiment for coals and oils, and correlates the exhaust NO expressed as a percentage of fuel nitrogen conversion with the percentage of fuel nitrogen converted to HCN under inert pyrolysis conditions. It can be seen that the emissions from both liquid and solid fuels are consistent when plotted in this way. It is hoped that future FCR experiments will provide further insight into the impact of fuel characteristics on fuel nitrogen conversion from solid and liquid fuels, and although it is recognized that the correlation shown in Figure 13 is empirical, it indicates that fuel characterization could lead to an assessment of the impact of fuel characteristics on emissions in practical systems.

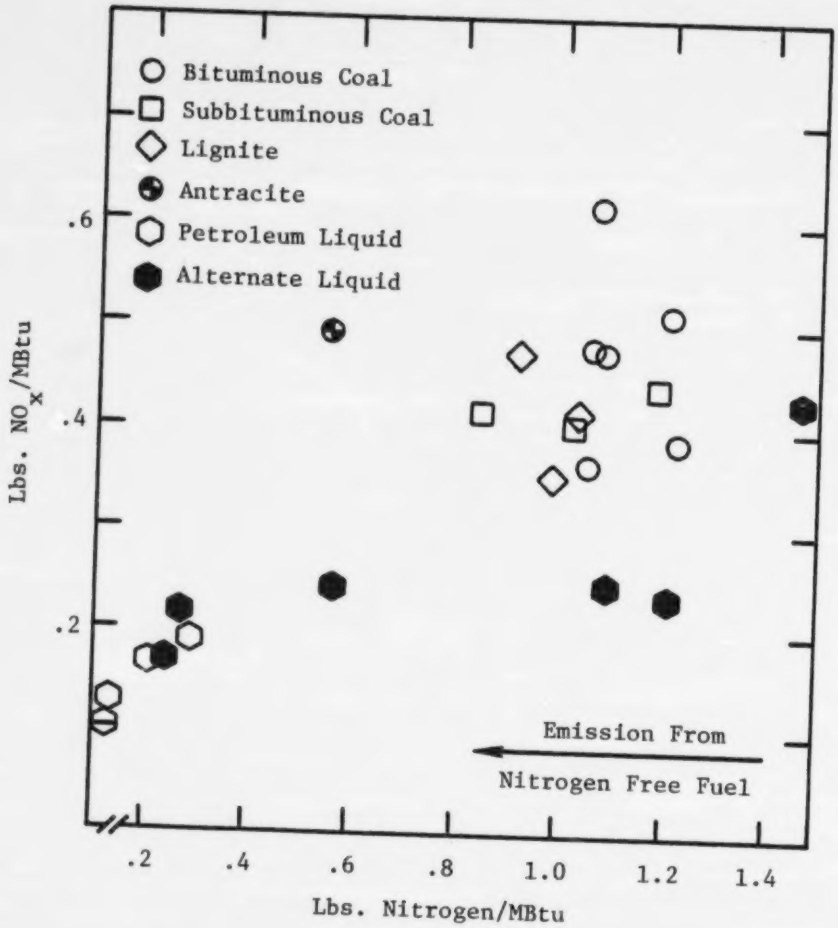

Figure 12. Minimum NO_x Emissions Staged

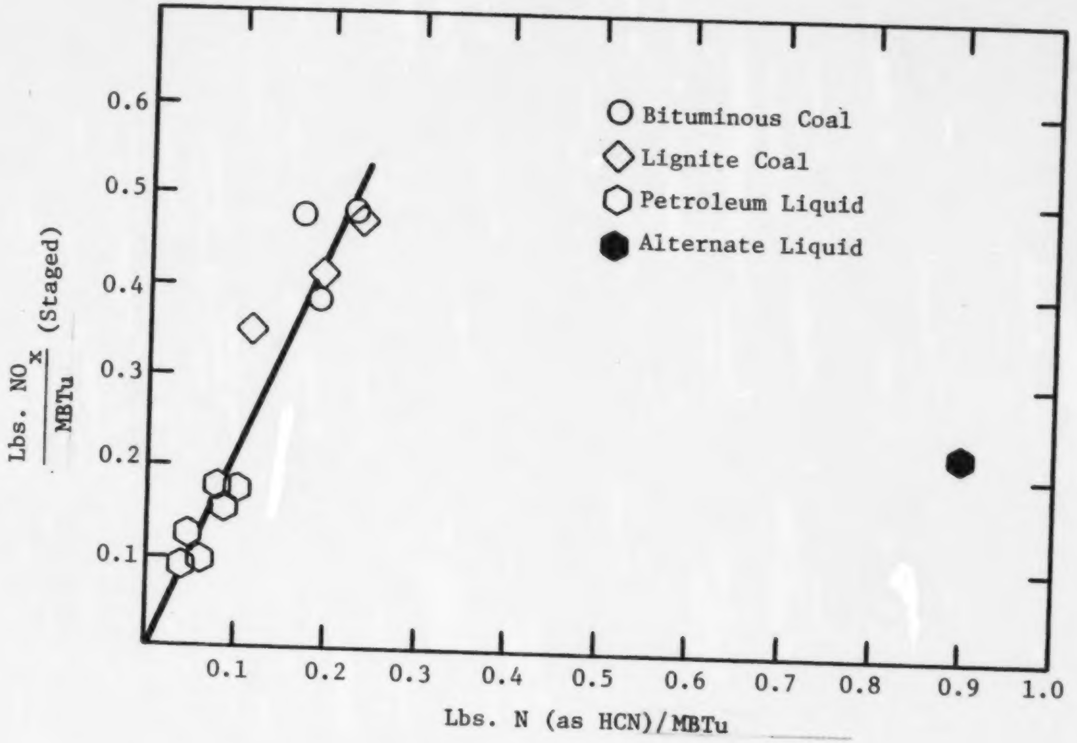

Figure 13. The Relationship Between Minimum NO Emissions Staged and HCN Produced by Pyrolysis.

4.0 OPTIMIZATION OF STAGING CONDITIONS

The previous section presented data showing the impact of fuel properties on the formation of NO_x under staged combustion conditions. Staged combustion involves operating a combustor with a primary heat release zone which is overall fuel-rich, even though the fuel may be supplied separately from the air and the initial contacting may occur fuel-lean. After some appropriate time the remainder of the combustion air is supplied to the combustor in such a way as to ensure complete combustion. Thus, it is possible to think of a staged combustor consisting of: (1) a fuel preparation zone; (2) a fuel-rich holdup zone; (3) a second stage air addition zone; and (4) the burnout zone. When the characteristics of these four zones are optimized this will represent the limit of NO_x control via combustion modification for this system. Currently, effort has progressed towards the definition of the optimum residence time, temperature and stoichiometry of the fuel-rich holdup zone for both solid and liquid fuels. The major parameters of interest in this initial study were primary zone stoichiometry and heat extraction rate.

Figures 14 and 15 present the results of detailed in-flame measurements for a shale oil and a lignite, respectively. All gas phase concentration measurements are shown on an as-measured (dry) basis, except the exhaust NO concentrations which have been reduced to 0 percent O_2 (SR = 1.0). For both liquids and solid fuels, decreasing the first stage stoichiometric ratio reduced the NO concentration leaving the first stage. However, below a stoichiometric ratio of approximately 0.8 the concentration of other oxidizable nitrogen species (e.g., HCN and NH_3) increased. For the solid fuel the particle temperatures (measured at 0.53 meters using two-color pyrometry) also decrease with decreasing stoichiometry, and a significant amount of both nitrogen and carbon remain in the solid phase and are carried into the second stage flame. Thus, for both solid and liquid fuels there exists a minimum total fixed nitrogen concentration (TFN = NO + HCN + NH_3) exiting the first stage, and this contributes to the minimum in exhaust concentrations because of the competition between decreased first staged NO and increased oxidizable gas and solid phase nitrogen species with variations in primary zone stoichiometry.

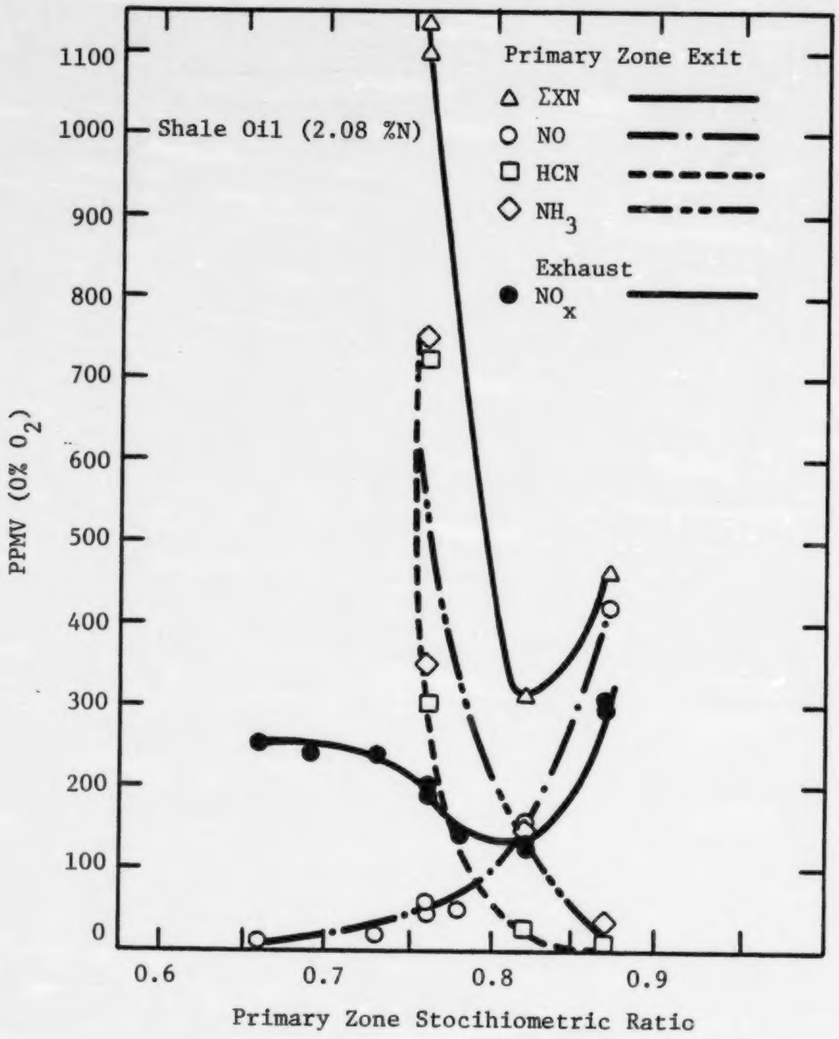

Figure 14. In-Flame Concentration of Nitrogen Species Using a Shale Oil.

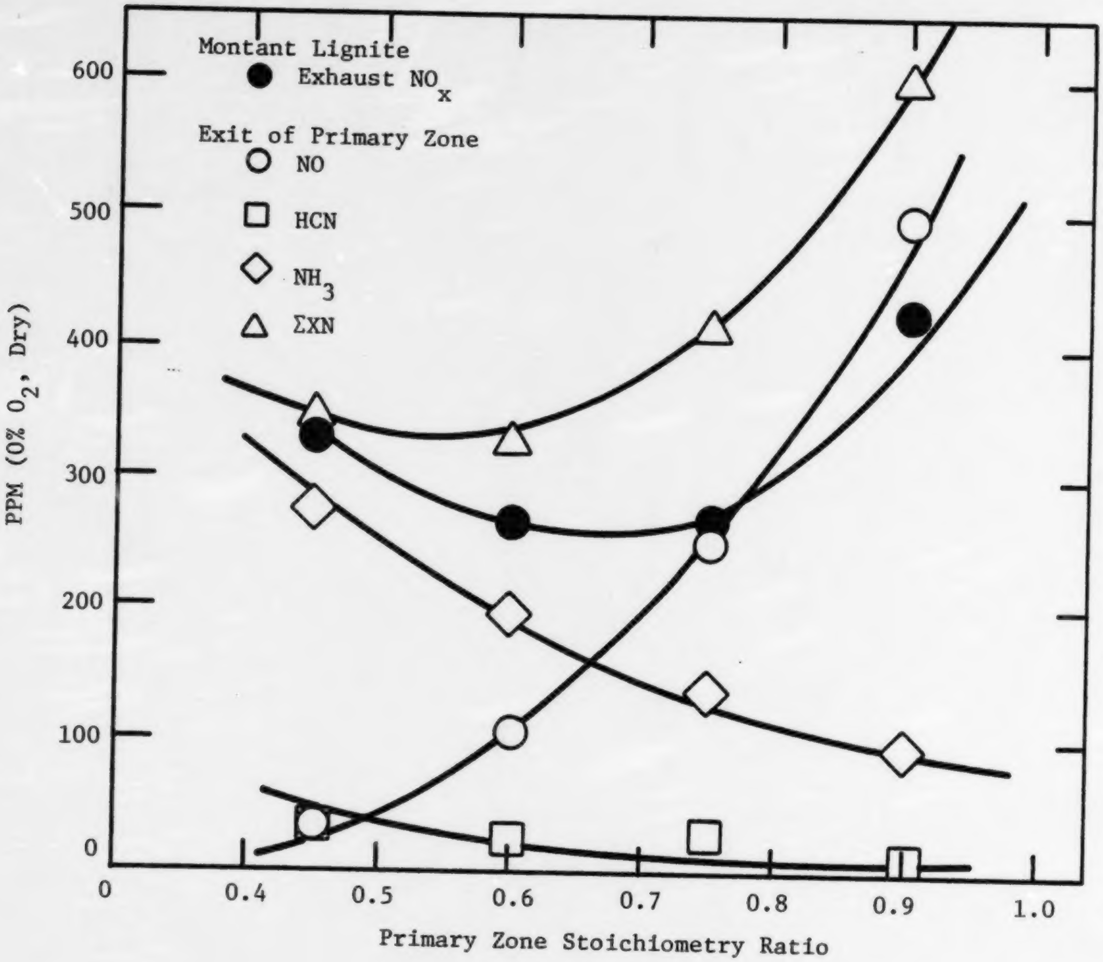

Figure 15. In-Flame Concentration of Nitrogen Species Using a Montant Lignite.

Results obtained to date show that with liquid fuels HCN is the favored fuel nitrogen species on the rich side of minimum TFN. This even applies when the initial fuel nitrogen compound is ammonia (tests have been carried out with methane-plus-ammonia gas diffusion flames). For coals the coal type has a significant impact upon the form of the gaseous nitrogen species. For example, with anthracite all of the TFN exists as NO even for primary zone stoichiometries of $SR_1 = 0.5$. For bituminous and lignite coals the major nitrogen species under conditions richer than the minimum is ammonia. HCN becomes more significant for the bituminous coals, and only in the case of one of the coals tested to date does HCN contribute the major fraction of the gaseous nitrogen species at stoichiometric ratios of 0.5 to 0.6.

The minimum total fuel nitrogen concentrations shown in Figure 14 are in excess of equilibrium levels, and Sarofim and co-workers have suggested that increasing the temperature of the primary zone would prove beneficial. The results presented in Figures 16 and 17 demonstrate the impact of first 16 stage heat loss on the fate of fuel nitrogen for solid and liquid fuels. 17 The hot conditions refer to the furnace without primary zone cooling and with the radiation choke. Figure 16 shows exhaust NO_x and primary zone gas temperature as a function of stoichiometric ratio for the two conditions when burning a liquid fuel. Minimum NO_x emissions were reduced for the hot case and the optimum stoichiometry was shifted toward more fuel-rich conditions. Detailed flame measurements indicated that heat extraction in the first stage impacted the rate of decay of TFN. Under cold conditions, both NO and HCN essentially freeze, whereas without heat extraction initial rate of decay for all three species is much faster, leading to low TFN concentrations at the exit of the fuel-rich first stage.

Figure 17 shows a similar comparison for a Utah bituminous coal operating at a first stage stoichiometry of 0.8 with the radial diffusion burner. As noted previously, HCN concentrations exceed the NH_3 concentration and the NO decays with axial distance. Figure 17 also shows data for a case in which the first stage was heavily cooled by inserting a water-cooled coil which reduced the gas temperatures by approximately 350K, apparently freezing the NO concentration. However, the HCN and NH_3 concentrations continue to decay with

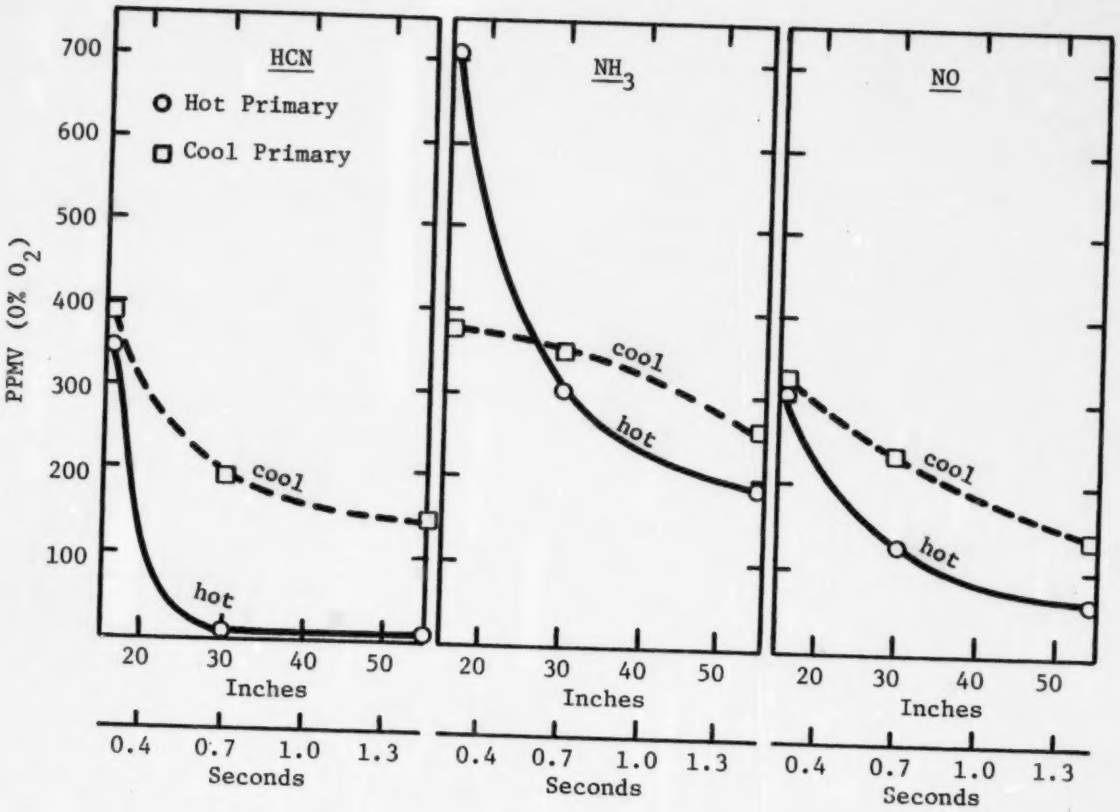

Figure 16. Effect of First-Stage Cooling Upon Nitrogen Species for a Liquid Fuel.

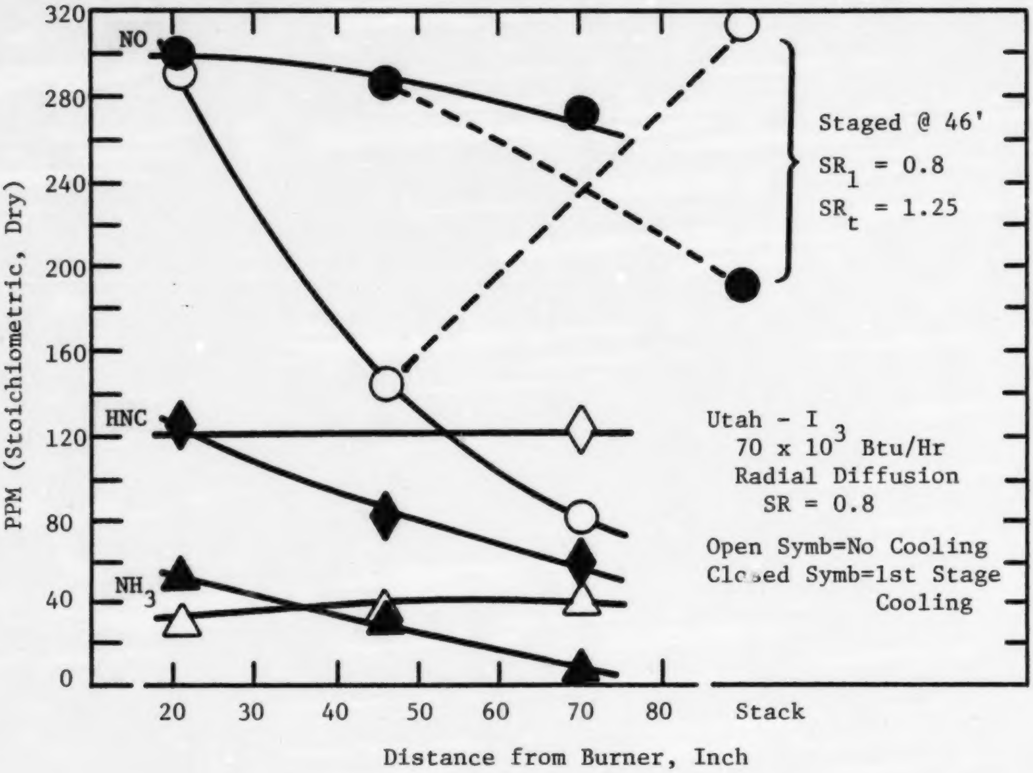

Figure 17. Effect of First-Stage Cooling Upon Nitrogen Species for a Bituminous Coal.

time. Overall reduction of the first stage temperature increased the TFN concentration at a distance of 46 inches from the injection point substantially because of the decrease rate of NO reduction. However, when second stage air was added at 46 inches the exhaust emissions were lower with the first stage temperature which gave the higher TFN concentration.

The results of these initial investigations on the optimization of the primary zone suggest that with liquid fuels the primary zone should be operated at as high a temperature as possible, realizing that as the temperature is increased the optimum stoichiometry will move towards more fuel rich values. If the temperature was increased to a too high value then the total fuel nitrogen concentration would begin to increase. However, in these experiments it is not believed that the temperature reached these levels. On the other hand, with coal it appears that cooling the primary zone results in lower NO emissions. This can be attributed to a change in the partition of nitrogen in the solid phase and the fact that char nitrogen conversion is minimal, or to the impact of fuel nitrogen speciation on second stage conversion. Further work is being directed towards answering these questions.

SECTION V

CONCLUSIONS

Liquid Fuels

Data have been presented showing the impact of fuel properties on NO_x formation from liquid fuels under both excess air and staged conditions. These data indicate:

- The formation of fuel NO from petroleum and alternative liquid fuels is mainly dependent upon their total fuel nitrogen content.
- NO_x control techniques for high nitrogen fuels which rely upon the generation of a high temperature primary fuel-rich zone appear to give the maximum opportunity for NO_x reduction.

Solid Fuels

Twenty-six coals have been tested under fuel-lean conditions, and it appears that although fuel nitrogen content is an important property, it is not the only fuel characteristic dictating fuel NO formation. It appears that the volatility of the fuel nitrogen has an important impact upon fuel NO formation, particularly under well-mixed conditions. Under fuel-rich conditions the coal composition impacts the gas phase nitrogen species distribution. With bituminous coals ammonia appears to be a substantially less fraction of the total TFN than with subbituminous and lignite coals. Of the nine coals tested in detail, only one - a Utah bituminous - formed substantial amounts of HCN under well-mixed rich conditions.

Contrary to liquid fuels, increasing the temperature of a fuel rich primary zone does not appear to reduce the stack emissions from a coal fired staged combustor.

REFERENCES

1. Heap, M. P. and Tyson, T. J., "Heterogeneous Processes Involved in the Control of Nitrogen Oxide Formation in Fossil Fuel Flames," Proceedings of the Third Stationary Source Combustion Symposium, San Francisco, California, Volume IV, p. 45 (1979).

2. Habelt, W. W., "The Influence of the Coal Oxygen to Coal Nitrogen Ratio on NO_x Formation," 70th Annual AICHE Meeting, New York, New York, (1977).

3. Gay, R. L., Axworthy, A. E., Dayan, V. H. and Recht, H. L., "Volatility of Fuel Nitrogen," this report, (1980).

POLLUTANT FORMATION DURING FIXED-BED AND SUSPENSION COAL COMBUSTION

G. P. Starley
S. P. Purcell
S. L. Manis
D. M. Slaughter
D. W. Pershing
Department of Chemical Engineering
University of Utah
Salt Lake City, Utah 84112

Fifth EPA Fundamental Combustion Research Workshop
Newport Beach, California
January 23-25, 1980

SECTION I

INTRODUCTION

In recent years, fuel oil and natural gas have become increasingly expensive and difficult to obtain. This has resulted in new emphasis on coal combustion research, particularly related to pulverized coal burning. However, many current industrial and commercial coal units are stoker-fired and these systems represent a major source of combustion technology which has been largely overlooked.

At present, stoker-fired boilers are significant in terms of both coal consumption and environmental impact. In 1974, almost 20 percent of the coal consumed in the United States was burned in stoker systems. Stoker-fired, water-tube boilers are the single largest source of particulate emissions and the fourth largest source of SO_x emissions (Mason and Waterland, 1977), because often neither is controlled. They account for 13 percent of the NO_x emissions from all coal systems and their environmental impact may be even more significant than indicated by the mass emissions, because stoker systems are often located in congested metropolitan areas. Further, the energy and environmental importance of stoker firing seems certain to grow with the increase in industrial coal utilization that is projected. It is important, therefore, that further knowledge be obtained on the formation and control of nitrogen and sulfur oxides under conditions typical of stoker firing.

Recent large-scale pilot and field tests have at least partially demonstrated the potential of combustion modifications for NO_x control in stoker-fired boilers. Giammar, et al (1979) have conducted tests on a 25,000 pph steam spreader-stoker with a water-cooled vibrating grate and found that decreased overall excess air resulted in lower NO_x emissions (at a constant load). Gabrielson and Langsjoen (1979) have tested several, large-scale industrial stokers and reported little effect of overfire percentage on NO_x emissions and an apparent increase in NO_x with increasing load. However, the fundamental mechanisms controlling these effects are not well defined.

The overall objective of this program is to study the formation of nitrogen and sulfur oxides under carefully controlled experimental conditions typical of stoker-fired boilers. In particular, this program is considering the following major research areas:

1. The evolution and oxidation of fuel nitrogen and sulfur.
2. The retention of sulfur oxides by ash and/or solid-chemical sorbents in both suspension- and fixed-bed burning.
3. The effectiveness of distributed air addition for NO_x control in stoker-fired coal systems.

In addition, the study will attempt to quantify the combustion process in a stoker environment and consider possible detrimental effects of control technology on boiler operation.

SECTION II

APPROACH

Figure 1 is a schematic of a Detroit RotoGrate stoker with a rotary spreader and a traveling grate. Conceptually the combustion process can be divided into two major parts:

- suspension burning and
- fixed-bed burning.

As the particles pass through the overthrow zone, they are heated, partially devolatilized, and may even completely burn depending on their size. Since the relative importance of these suspension-phase phenomena is completely unknown, the approach in this study has been to divide the process into the separate pieces for individual study before attempting research on the coupled system. In particular, the program consists of three major tasks:

Task 1. An experimental investigation of suspension burning of bituminous coal.

Task 2. An experimental investigation of fixed-bed burning of bituminous coal.

Task 3. An experimental optimization of combustion modification technology using a model stoker system.

Although the primary thrust of the study is experimental, each of the furnace studies is supported by analytical modeling.

The following two sections of this paper describe the hardware and results associated with the suspension and fixed-bed studies, respectively. In addition, a model spreader stoker system will ultimately be fabricated, characterized, and used for studying the integrated processes.

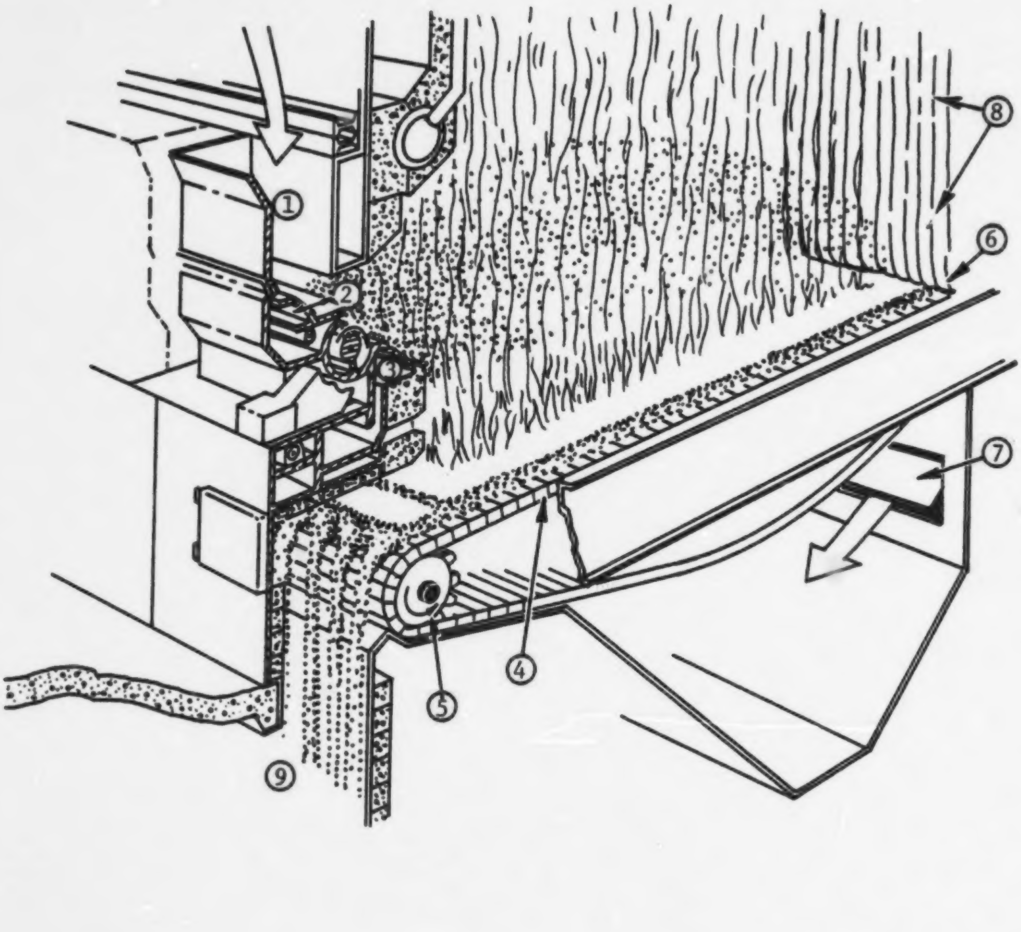

Figure 1. Schematic of a Detroit Spreader Stoker

SECTION III

SUSPENSION BURNING

Suspension Furnace

The purpose of this task is to investigate the formation of pollutant emissions during the suspension-burning phase of the combustion process. Figure 2 illustrates the furnace system which was fabricated for these studies. It utilizes three types of interchangeable furnace sections. In each case, the inner combustion chamber is six inches in diameter and the outer steel shell is 28 inches square. A cylindrical inner chamber was chosen (in preference to a square one) because it is more amenable to analytical modeling. A square outside surface was selected because it reduced the cost of fabrication and provided a more suitable base for mounting probes, thermocouples, etc.

The walls of the main furnace sections consist of an outer steel shell, five inches of $1900^{\circ}F$ insulating block, four inches of $2500^{\circ}F$ insulating refractory, and two inches of $3400^{\circ}F$ high-temperature castable refractory. Each of the mid-sections contain five, two-inch diameter ports for second-stage air injection and/or insertion of species and temperature probes.

The side walls have provision for auxiliary heating (or cooling) by firing natural gas or passing cooling air through outer channels. These channels are two inches in width and cover 50 percent of the circumference. This will allow partial independent control of the radiant heat transfer to the particles and more complete control of wall temperature. The auxiliary firing sections are completely interchangeable, so any portion of the furnace can be heated (or cooled).

A high-intensity gas burner is attached to the horizontal extension at the furnace bottom. This burner produces hot combustion gases which flow vertically upward and simulate the combustion products leaving the stoker bed. Large, stoker-size particles are fed into the furnace at the top via an auger/vibrating tray system. The partially burned particles are collected at the bottom of the furnace in a water-spray trap.

The combustion air is supplied by a 100 SCFM, 100 psi rotary vane compressor. Primary, secondary, and tertiary air are metered with 600 mm high accuracy Brooks rotameters. The second-stage air is metered with a large, 10-inch

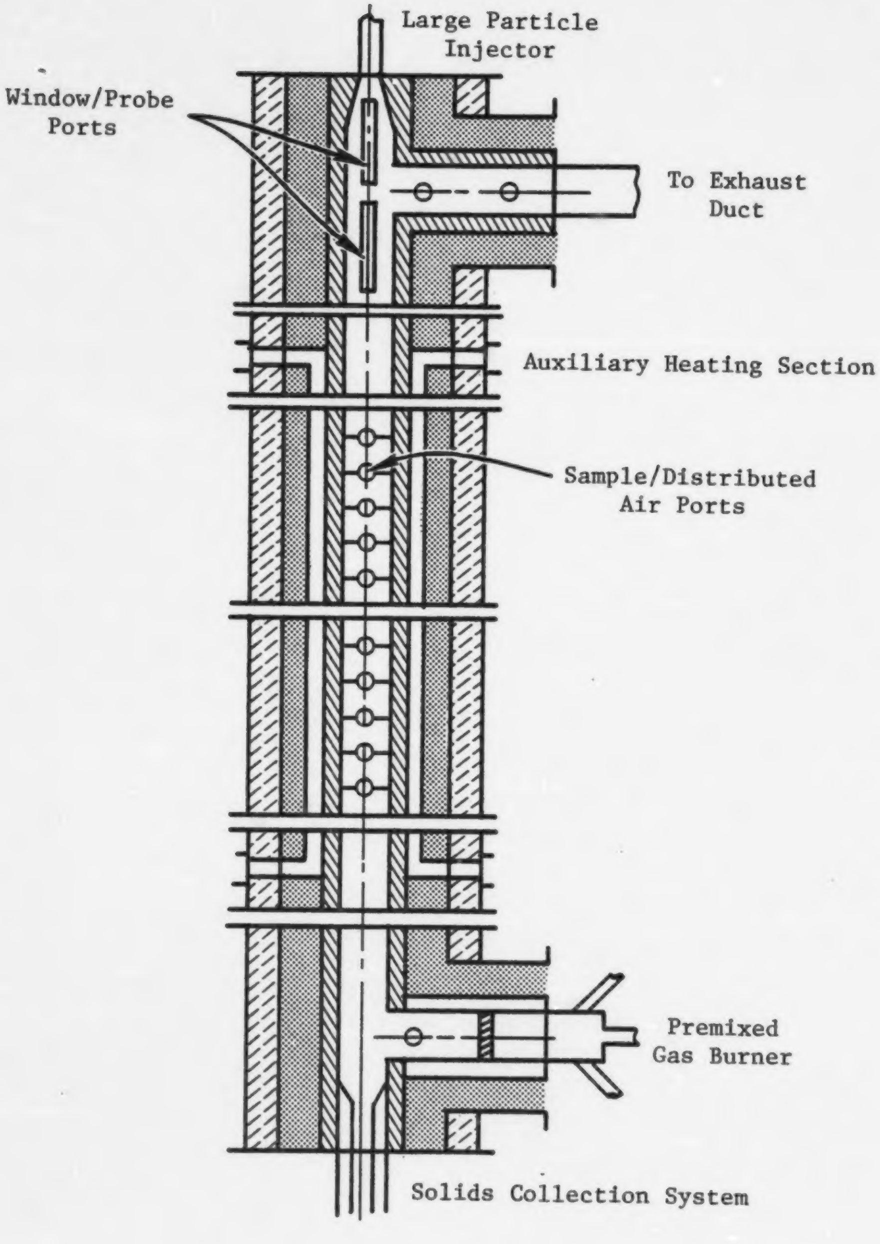

Figure 2. Suspension Furnace.

Dwyer rotameter. All other air and gas flows are metered with 10-inch Dwyer rotameters. The flow system also includes an artificial oxidant supply, so that the combustion air can be completely replaced with an atmosphere composed of argon, carbon dioxide, and oxygen in varying proportions. In each case, the pure gases are supplied from high-pressure cylinders and metered with rotameters.

Exhaust gas samples are continuously withdrawn through a water-cooled stainless steel probe positioned in the flue. NO and NO_x are measured with a chemiluminescent analyzer while CO, CO_2, and O_2 are determined by NDIR's and paramagnetic analyzers. Coal and char composition are determined with a Perkin-Elmer 240 B Elemental Analyzer.

Preliminary Results

The suspension-phase studies have just started, so only limited, preliminary data are available. In general, the results are both direct and indirect. During the actual experiment, real-time data on the nature and extent of combustion are obtained indirectly by measurement of the composition of the flue gases leaving the furnace. Subsequent to the actual experiments, the coal and partially burned particles are analyzed to directly establish the carbon, hydrogen and nitrogen loss. In these direct-coal analyses, additional work is performed to classify the coal into different size ranges so as to determine particle size effects.

Table 1 shows the ultimate and proximate analyses of the coal being used in this program. The coal is fed at a rate of 12 lbs/hr, and it is sized in accordance with industrial stoker practice (maximum particle size approximately one inch). The gas burner is fired at 150,000 Btu/hr.

The results of the indirect real-time measurements for a typical run are shown in Table 2. Also included in the table are data on the temperature of the wall at three locations. Note that although coal is being fed to the furnace at 12 lbm/hr, only about one lbm/hr actually burns.

The direct coal analysis results are shown in Figures 3 and 4. Figure 3 details the weight percent nitrogen in burned and unburned coal as a function of average particle size. The data on the unburned coal indicate that the nitrogen in the raw coal is uniformly distributed between the large and small particles. (It should, however, be noted that this is a low ash (9.6%) Utah

Table 1. Chemcial Analysis - Utah B Coal

PROXIMATE ANALYSIS

Weight %	As Received	Dry Basis
Moisture	6.22	--
Ash	9.59	10.23
Volatile Matter	37.84	40.35
Fixed Carbon	46.35	49.42
Total	100.00	100.00
Calorific Value (Btu/lb)		
Proximate Value	11,658	12,432
Mineral Matter Free	--	14,004

ULTIMATE ANALYSIS

Weight %	As Received	Dry Basis
Moisture	6.22	--
Carbon	66.44	70.85
Hydrogen	4.86	5.19
Nitrogen	1.42	1.51
Sulfur	0.88	0.94
Ash	9.59	10.23
Oxygen (difference)	10.59	11.28
Total	100.00	100.00

Table 2. Suspension Furnace Results - Indirect Measurements

Test: UB - 12/15/79-1

Fuel: Utah Bituminous

Fuel Feed Rate: 12 lbm/hr

Fuel Size: Standard Stoker Distribution

Component	Gas Flame Only	Gas Flame + Coal
CO_2	8.6%	10.3%
CO	< 0.01%	< 0.01%
NO	24 ppm	94 ppm
O_2	6.4%	4.3%

Calculated Burning Rate: 1 lbm/hr

Wall Temperature:

Bottom (13.5 inches from quench)	$1820^{o}F$
Middle (48 inches from quench)	$1652^{o}F$
Top (62 inches from quench)	$1475^{o}F$

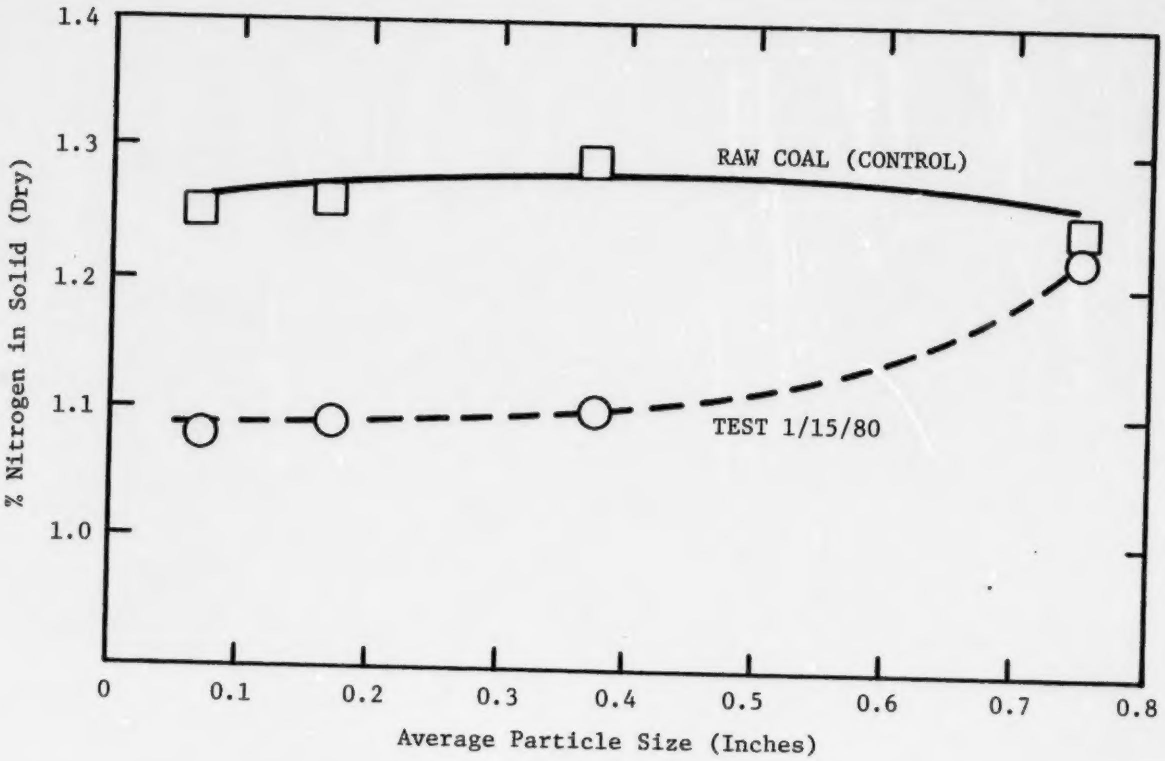

Figure 3. Nitrogen Loss - Suspension Experiments.

coal). The data from the combustion test (circles) suggest that the nitrogen content of the coal is being reduced, particularly at the smaller particle sizes.

Figure 4 presents the ratio (weight) of nitrogen to carbon (N/C) in burned and unburned coal as a function of average particle size. Because the N/C ratio is uniformly lower in the burned coal, it would appear that nitrogen is being preferentially evolved during combustion. Additionally, the data hint that there is an effect of particle size on the preferential nitrogen evolution.

By combining the direct and indirect measurements, it is possible to compute the fraction of the evolved nitrogen which is converted to NO (assuming no additional thermal NO_x).

The calculation is performed as follows: Based on the direct analysis data, the nitrogen in the coal was reduced from 1.28 percent to 1.16 percent during combustion (based on a weighted average of particle-size distribution and the ultimate analysis data). This means that nine percent of the nitrogen in the coal was evolved and the increase in the NO concentration in the gas phase corresponds to a 19 percent conversion of evolved N to NO.

Before any conclusions can be drawn regarding the role of the overthrow phase, additional particle heating rates and free-stream stoichiometries must be considered. However, the data obtained to date do not strengthen the hypothesis that the overthrow phase is of dominate importance in NO_x formation.

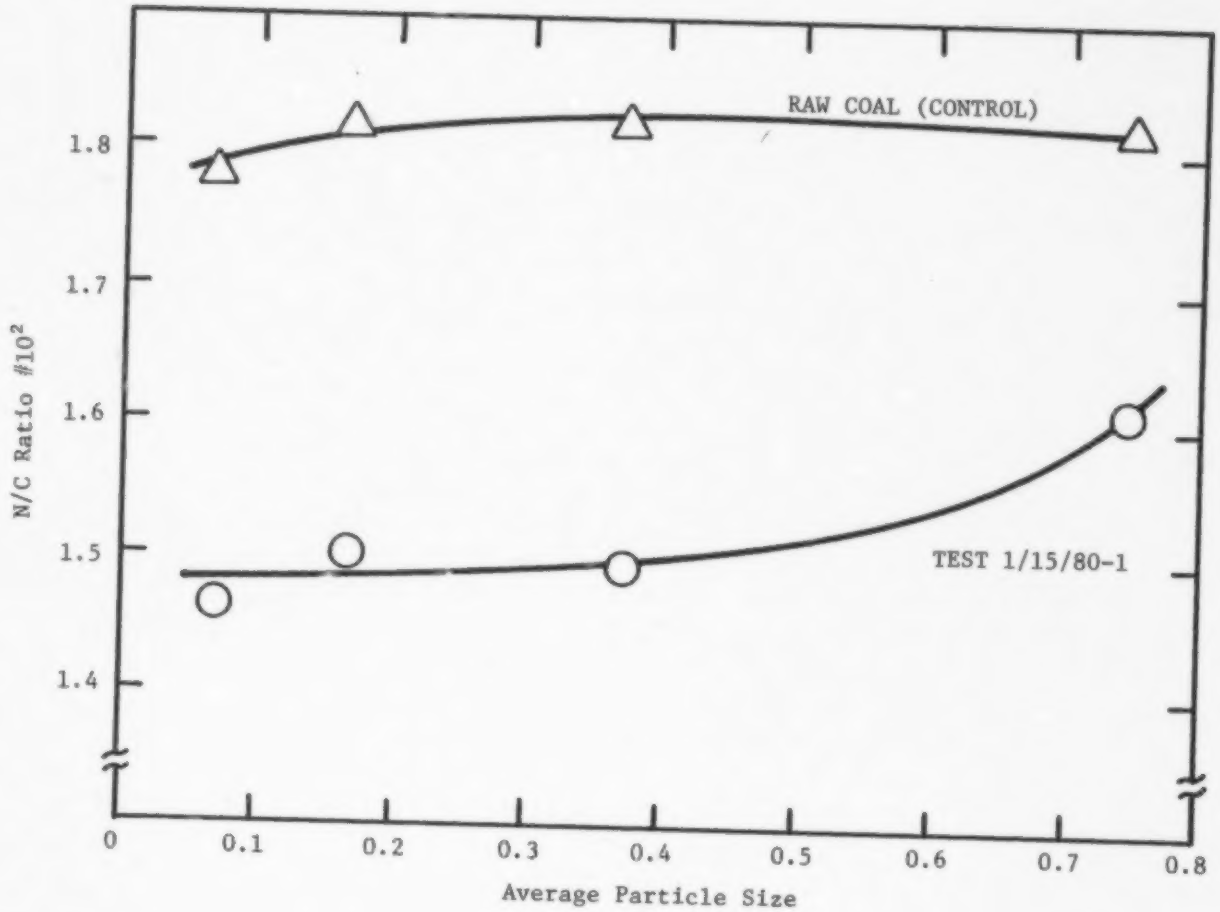

Figure 4. Nitrogen/Carbon Rates

SECTION IV

FIXED-BED COMBUSTION

Furnace Design

The fixed-bed furnace was designed to provide a Lagrangian simulation of the time/temperature/environmental history seen by small sections of the stoker bed in a large, mass-burning chain-grate or vibrating-grate stoker. In this way, the horizontal, planer dimensions were reduced dramatically compared to the full-size unit; however, the vertical dimension was scaled 1:1. Figure 5 shows a side view of the fixed-bed furnace which was designed to have a maximum superficial firing rate of approximately 600,000 Btu/hr-ft^2. The furnace itself is 27 inches by 23 inches by eight feet outside, and the inner combustion chamber is 11 inches by 15 inches.

The furnace is composed of four, separate, flanged sections. Section A, the upper most section, contains the six-inch circular flue, and a three-inch, expanding quartz window to provide a view of the combustion chamber from above. Sections B and C are the central furnace pieces and contain overfire-air slots, large observation ports and probe ports. All three of the upper furnace sections have composite walls consisting of one-eight-inch, carbon steel, four inches of block insulation, and two inches of high temperature refractory.

The lower furnace section, labeled D, contains the experimental coal bed. The bed proper is 10 inches wide and six inches deep with the total surface area of 0.42 ft^2. Immediately adjacent and surrounding the bed is a one-inch high-temperature refractory wall which is used to confine the coal. Just outside the wall there are porous, stainless steel, methane burners with an equivalent surface area (0.42 ft^2). These gas burners are used to provide uniform heating of the combustion chamber when coal is not being burned. The coal bed and gas burners are mounted in a "drawer-like" assembly which rolls out of Section D to permit easy loading of the coal particles.

The combustion air is distributed between the underfire-air plenum and two levels of overfire-air ports. In this study, the air was metered with 600 mm rotameters, but was not preheated.

Exhaust concentration measurements were made in the flue above Section A with a water-cooled, stainless steel probe. The instrumentation described in

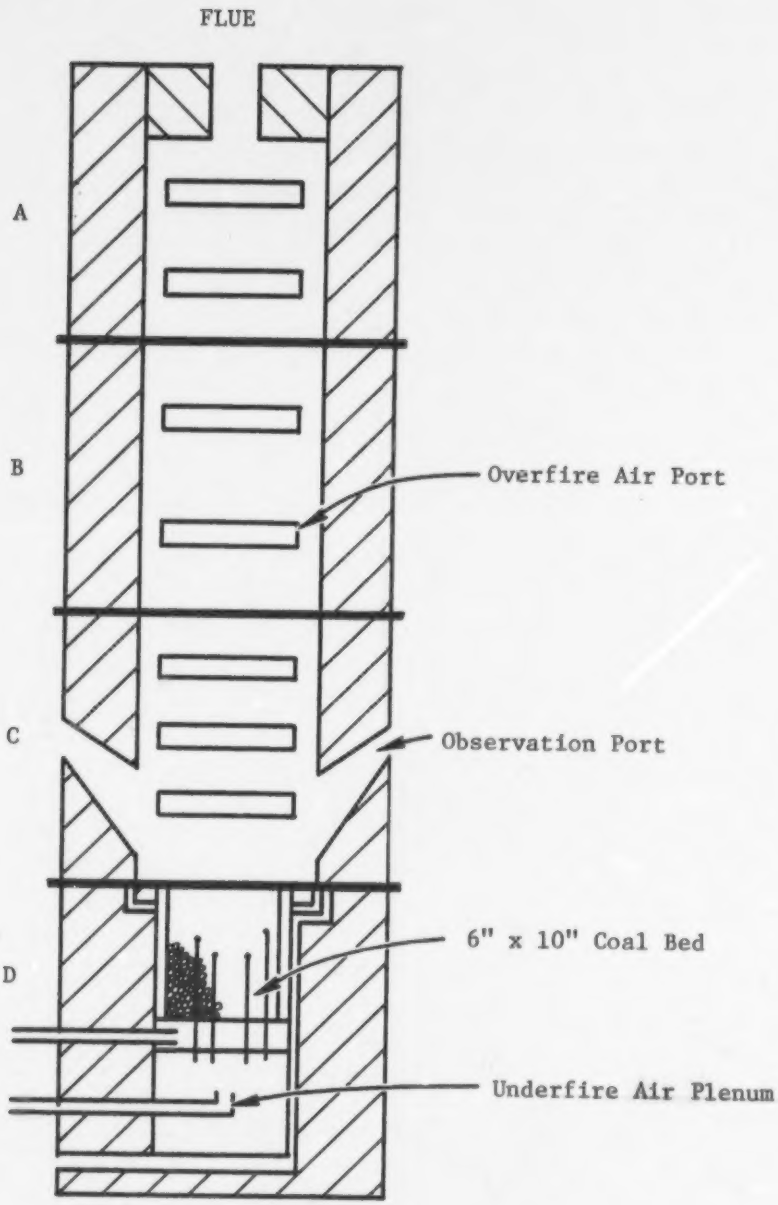

Figure 5. Side View of the Fixed-Bed Furnace.

the previous section was also used for the fixed-bed experiments.

Typical Experimental Results

Figure 6 shows typical experimental results obtained for coal-burning rates as a function of run time. The run was conducted with the Utah coal (Table 1), sized at one-half inch through one inch. The data are presented in terms of superficial burning rate; the rate of heat release per unit area of bed surface. The superficial burning rate was computed from exhaust oxygen concentrations and air-supply, flow rates. The data show that as the run proceeded the burning rate increased, reached a maximum, and then decreased. It is believed that the burning rate increase is attributable to an increase in bed temperature. Limited temperature measurements indicated that the coal bed burned in excess of 2400°F. The average coal-burning rate over the control interval (six minutes to 19 minutes in this case) was 460,000 $Btu/hr\text{-}ft^2$ as compared with industrial, chain-grate stokers observed to operate in a range from 400,000 to 500,000 $Btu/hr\text{-}ft^2$.

In order to separate parametric effects, it was necessary to keep both total and bed-region stoichiometries constant during a coal run, even though the burning rate changed significantly. This required precise control of the air supply, which was achieved by continuously monitoring the carbon dioxide concentrations in the exhaust gases.

Figure 7 gives the overall and bed-region stoichiometries as a function of run time. The stoichiometric ratios were computed from effluent gas oxygen concentrations and air-supply-flow rates at one-minute intervals. Both the overall and bed-region stoichiometries were controlled to within approximately ± 0.1 of their respective average stoichiometries for the run, except in the early stages of the experiment. A control interval was defined for each run on the basis of these narrowly bounded, average stoichiometries. Average values for NO emissions and burning rates were computed for this interval only.

Figure 8 shows the effluent-gas concentration of NO, converted to 0% exhaust O_2 as a function of run time. The exhaust gas concentration of NO increased rapidly in the initial stages of the run, passed through a maximum and then decayed toward the termination of the run. Comparison of Figures 6 and 8 indicates that NO formation peaks prior to achieving the maximum combustion rate. This "early" NO generation is typical of all the coal runs.

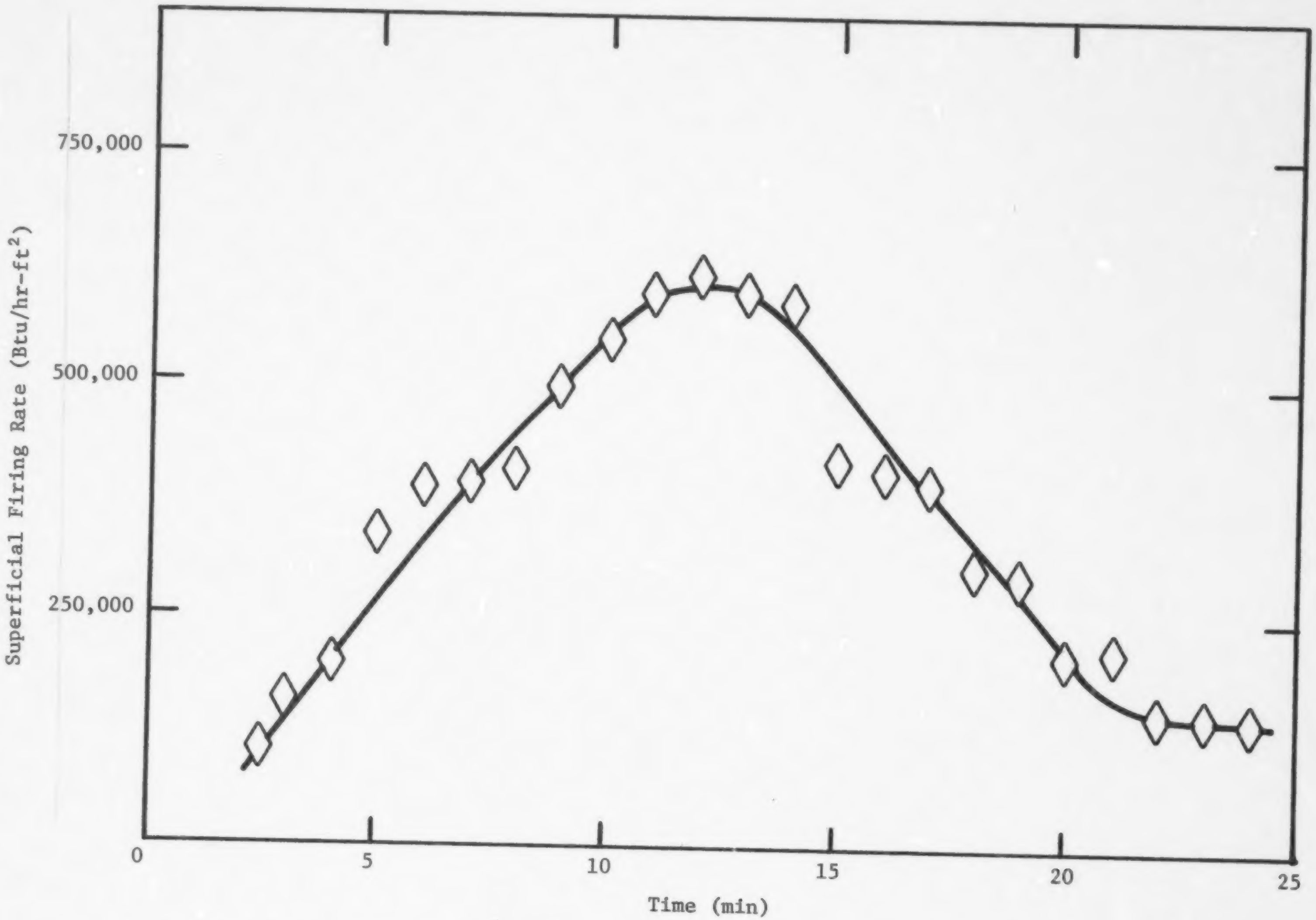

Figure 6. Typical Experimental Results Obtained for Coal-Burning Rates as a Function of Run Time.

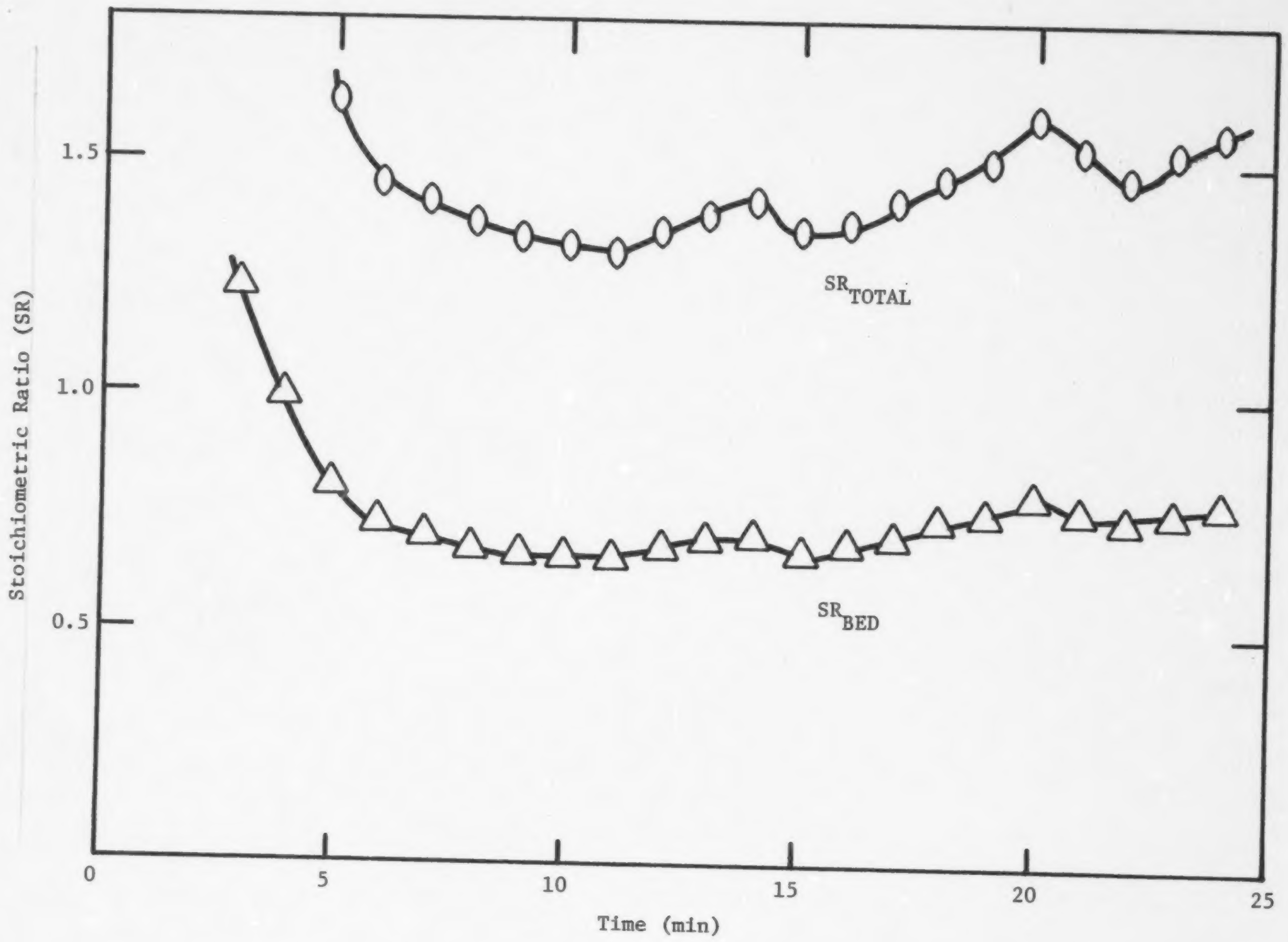

Figure 7. Overall and Bed-Region Stoichiometries as a Function of Run Time.

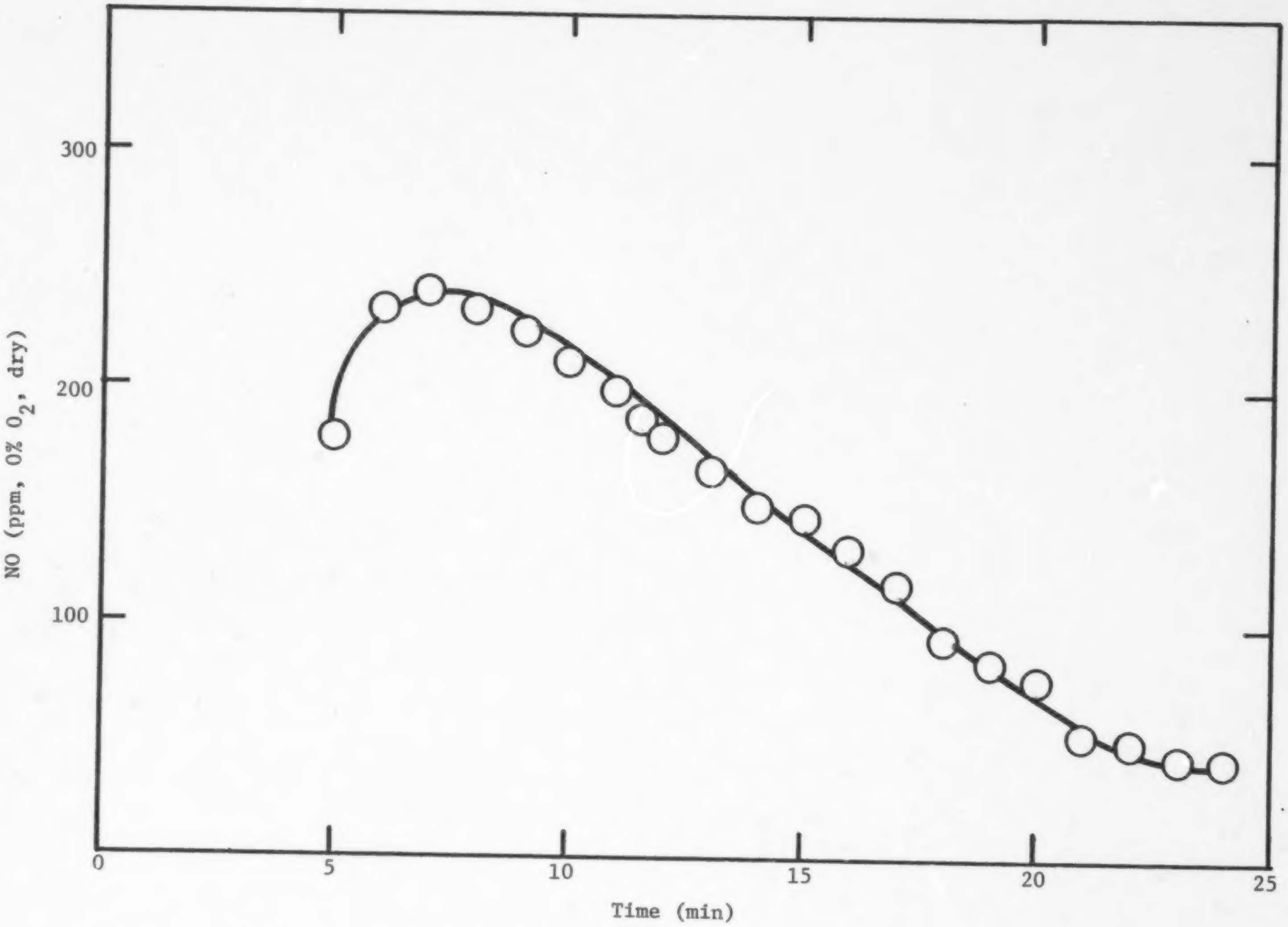

Figure 8. Effluent-Gas Concentration of NO Converted to 0% Exhaust O_2 as a Function of Run Time.

Influence of Bed Stoichiometry

Figure 9 shows NO emission results (plotted as lbs $NO_2/10^6$ Btu) for three different bed stoichiometries. In each test, the overall stoichiometry was held constant at 1.35 ± 0.03, and the firing rate was approximately 500,000 Btu/hr-ft^2. The overfire air was added in two volumetrically equivalent portions through opposing jets at 15½ inches and 44 inches above the coal bed. Neither the overfire nor the underfire air was preheated in these experiments.

As the combustion was staged, with the total air supply held constant, the NO emissions decreased substantially. Based on these limited data the dependence of NO_x on primary zone stoichiometry appears to be approximately linear, and this is in marked contrast to pulverized-coal combustion. No problems with clinkering or incomplete combustion were encountered; CO emissions were always than 0.03 percent.

Burning Rate

Figure 10 shows the integral superficial firing rates for two cases with nearly identical stoichiometric distributions ($S.R._B = 0.83 \pm 0.02$, $S.R._T = 1.37 \pm 0.05$) yet widely different burning rates. The lower burning rate experiment was conducted by significantly cooling the walls of the bed prior to charging the reactor with coal. For each experiment, the data are presented for the combustion of 4.5 pounds of coal (hence, in Figure 10, the high burning rate case ends first at 16 minutes). An average burning rate of 546,000 Btu/hr-ft^2 was achieved for the "hot" run, while a corresponding burning rate of only 398,000 Btu/hr-ft^2 was attained for the "cold" run.

Figure 11 shows NO emissions for both the "hot" and "cold" experiments. The rate of NO formation was substantially greater for the "hot" case, in spite of the fact that in both experiments the bed was fired without excess air. The disparity in rates of NO formation cannot be attributed simply to a difference in the amount of coal consumption since the data were normalized to the same basis (lbm $NO_2/10^6$ Btu) independent of coal-feed rate. The integrated emissions factor over the control interval for the high temperature run was 0.273 lbm $NO_2/10^6$ Btu as compared with the respective average emission factor for the low temperature experiment of 0.180 lbm $NO_2/10^6$ Btu. The marked difference in NO emissions between high and low load firing was observed during oxidant-rich combustion as well, indicating a strong dependence of NO formation upon

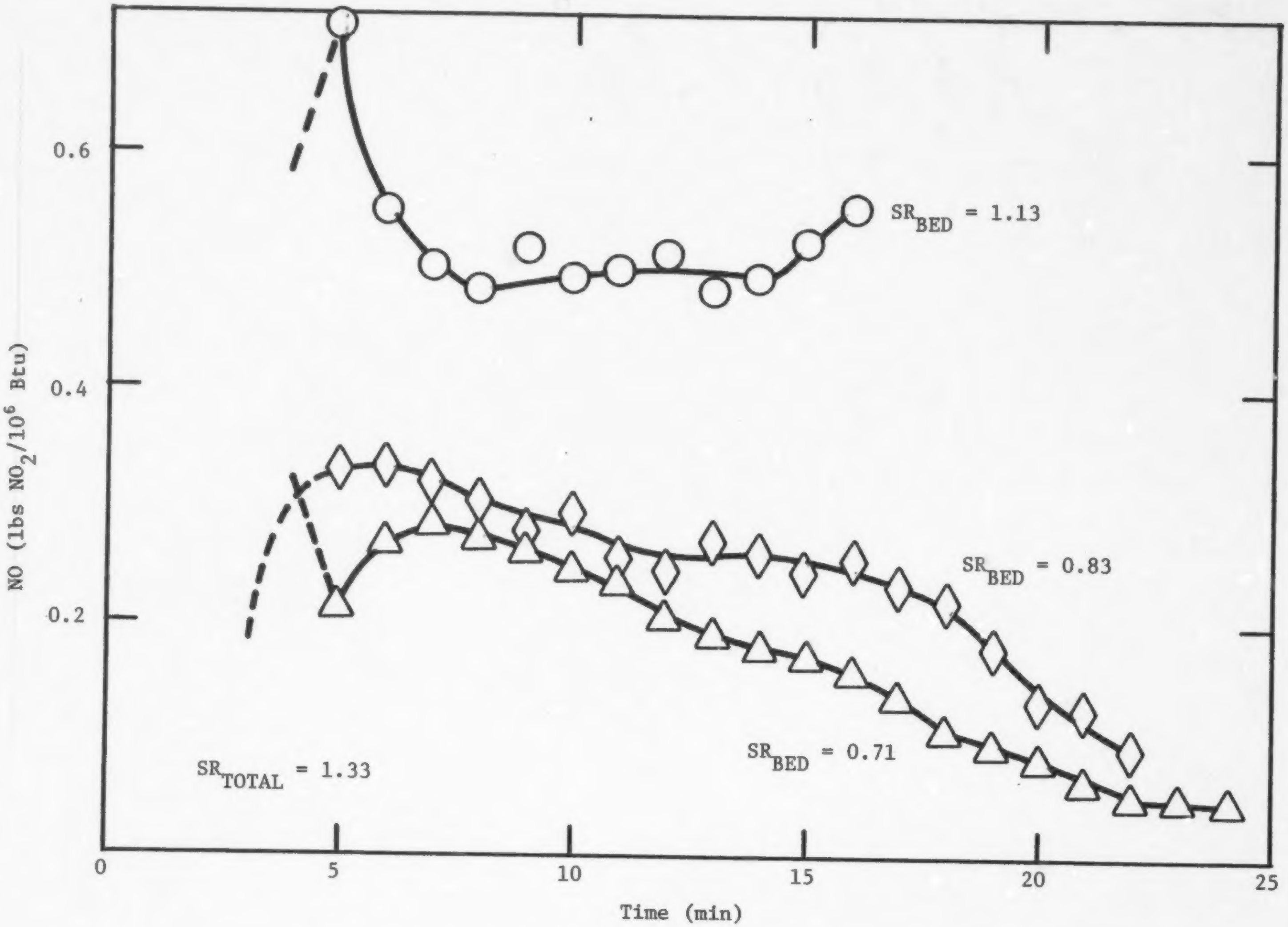

Figure 9. NO Emission Results for Three Different Bed Stoichiometries.

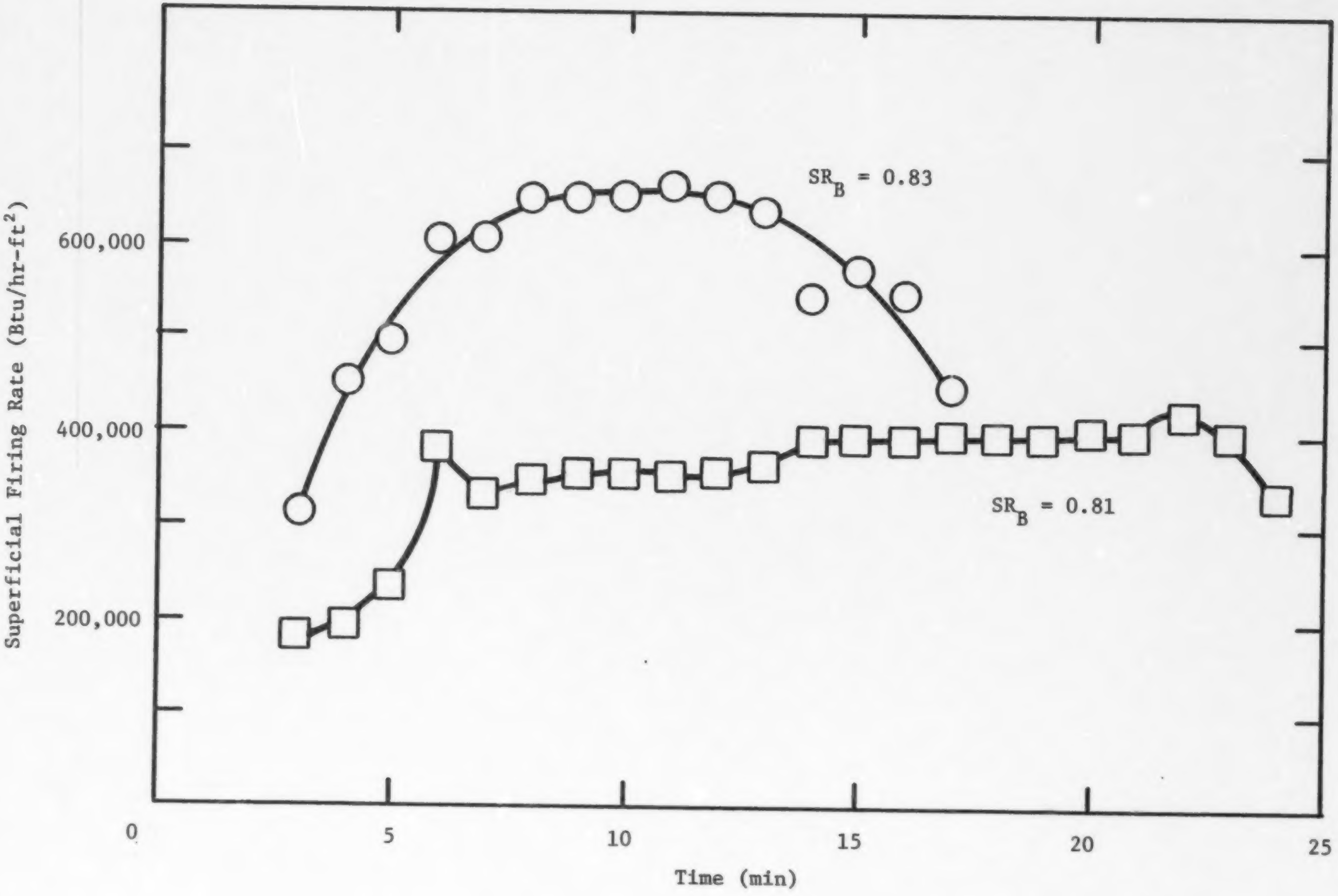

Figure 10. Firing Rate Results.

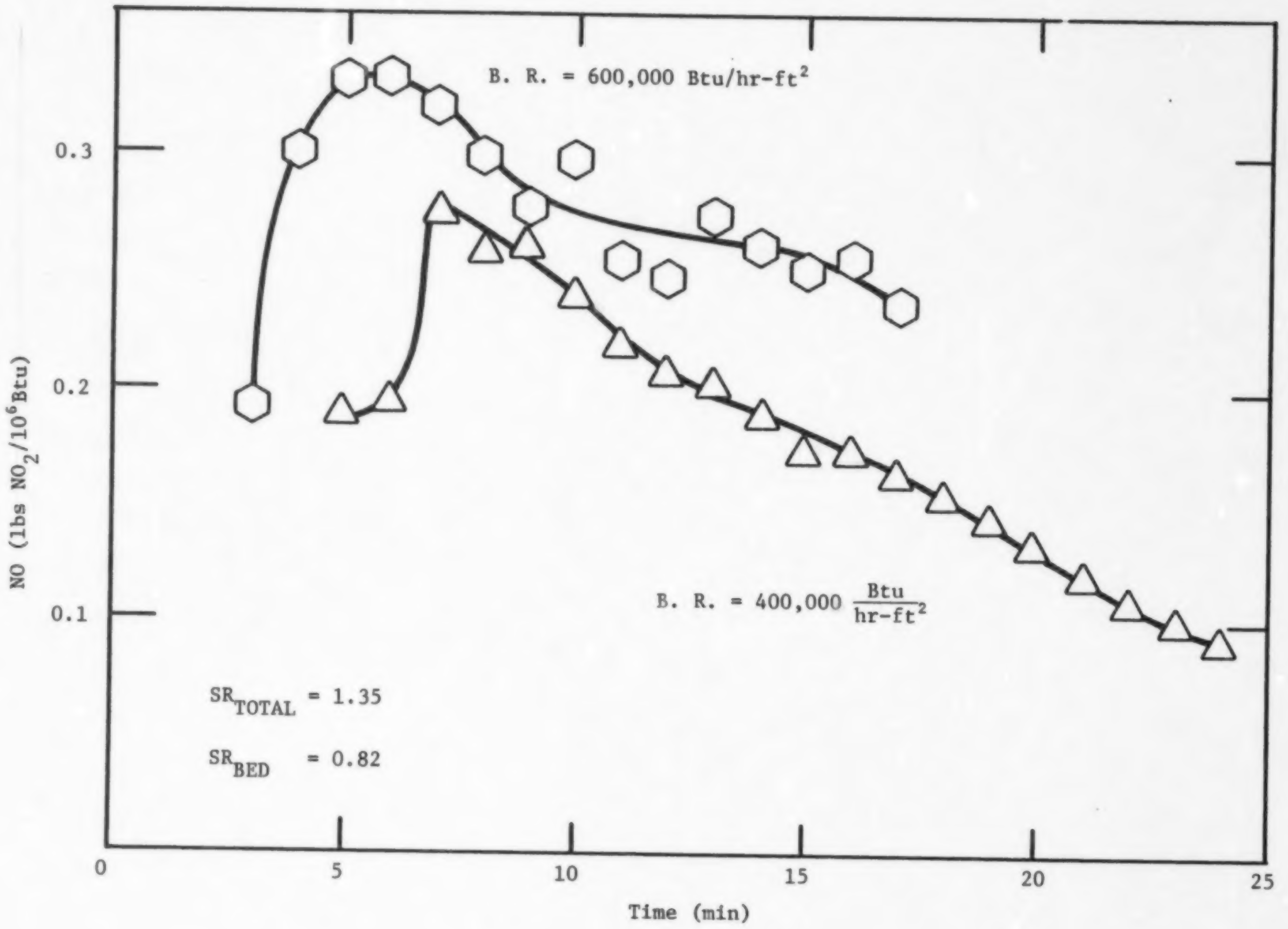

Figure 11. Influence of Burning Rate on NO Emissions.

bed heat-release rates.

The dependence of NO emissions upon bed heat-release rates suggests that as the burning rate increases, local bed temperatures increase. This may result in higher volatile nitrogen yields and, hence, higher NO_x emissions.

SECTION V

PRELIMINARY CONCLUSIONS

The results obtained with the suspension furnace do not support the hypothesis that a large fraction of the NO_x is formed in the overthrow phase; however, many additional heating rates must be studied before any firm conclusions can be reached.

The following tentative conclusions have been reached regarding the formation of nitrogen oxides in a fixed-bed combustion system:

1. NO formation is not uniform throughout the burning time of the bed. The formation maximizes early in the process, prior to the peak combustion rate and then gradually decreases.
2. Staged air addition is a potentially effective means of NO control. Exhaust concentrations decrease approximately linearly with decreasing bed stoichiometry.
3. Increasing the bed heat-release rate increases the NO_x emissions with staged-air conditions.

REFERENCES

Gabrielson, J. E. and P. L. Langsjoen, "Field Tests of Industrial Stoker-Fired Boilers for Emission Control," Proceedings of the Third Stationary Source Combustion Symposium, EPA-600/7-79-050, NTIS, Springfield, Virginia, 1979.

Giammar, R. D., et al, "Evaluation of Emissions and Control Technology for Industrial Stoker Boilers," Proceedings of the Third Stationary Source Combustion Symposium, EPA-600/7-79-050, NTIS, Springfield, Virginia, 1979.

Mason, H. B. and L. R. Waterland, "Environmental Assessment of Stationary Source NO_x Combustion Modification Technologies," Proceedings of the Second Stationary Source Combustion Symposium, EPA-600/7-77-073a, NTIS, Springfield, Virginia, 1977.

ACKNOWLEDGEMENTS

This research was supported by the United States Environmental Protection Agency under Grant No. R-805899. The considerable help and advice of G. Blair Martin, EPA Project Officer, is sincerely appreciated. In addition, input from the engineering staff at Delco-Remy Division, General Motors; Dr. David Junge, Oregon State University; Robert Giammar, Battelle; the engineering staff at Detroit Stoker; and Dr. M. P. Heap, Energy and Environmental Research, is gratefully acknowledged. Thanks are also due to the Vibra Screw Corporation for providing the very accurate solids-metering system used in this work. Last, but certainly not least, the authors gratefully acknowledge Mrs. Colleen Anderson for her help in managing the project, and preparing the required manuscripts, and Robert Brodbeck and Blake Beckstrom for their assistance in building the equipment and gathering the data.

SESSION IV

TWO-PHASE TURBULENT DIFFUSION FLAMES

W. S. LANIER
SESSION CHAIRMAN

AN EXPERIMENTAL APPROACH TO THE STUDY OF HEAVY OIL SPRAY COMBUSTION IN SHEAR LAYERS

A. Vranos and B. A. Knight
United Technologies Research Center
East Hartford, Connecticut 06108

Fifth EPA Fundamental Combustion Research Workshop
Newport Beach, California
January 23-25, 1980

ABSTRACT

This paper summarizes the work done under Contract EER-8318-7, a twelve month study of heavy oil spray combustion in shear layers. The program consisted of two phases: (1) design and fabrication of an apparatus, and (2) preliminary combustion experiments. A unique shear layer mixing and combustion apparatus was developed which stimulates high shear, diffusive combustion with heavy oil droplet injection as found in the near-field combustion zone of boilers and furnaces. The apparatus provides: (1) two dimensional mixing and combustion of uniform streams of air and rich combustion products fed from opposite sides of a splitter plate, (2) uniform injection of a monodisperse heavy oil spray into the shear layer by means of a linear array of fuel injectors located beneath the combustor wall, (3) control of droplet path, residence time, and extent of vaporization, (4) control of hot and cold stream inlet properties and (5) three dimensional probing of the flow field.

The design phase of the program consisted of two tasks; aerodynamic and thermodynamic design, and mechanical design. A wind tunnel, hot gas generator, combustion chamber, droplet injection system, and phase-sensitive sampling probe were designed in the first task. The design of the apparatus was influenced most strongly by the diverse requirements of the fuel injection system. The injector was designed so that the angle of droplet penetration into the shear layer could be varied over a wide range. Droplet trajectories were computed for vaporizing No. 6 oil droplets injected from the floor of the combustor into a hot, rich environment provided by a hot gas generator. Hot gas generator dimensions and injector locations were selected to accommodate the required droplet trajectories, provide complete vaporization if desired, and provide sufficient hot soak time for substantial conversion of volatile fuel nitrogen compounds to molecular nitrogen. The desire of a low turbulence wind tunnel, combustion chamber, and phase sensitive probe completed this task.

The experimental phase of the program consisted of (1) verification of uniform properties of the hot and cold streams at the splitter plate trailing edge, (2) demonstration of high injection velocities and uniform droplet size and penetration with No. 2, 5 and 6 oils in vibrating multicapillary injectors, (3) determination of stable flow regimes as a function of primary and secondary

stream velocities, (4) flame stability and flashback studies, (5) high speed cinematography of the shear layer with injection of No. 2 and No. 6 fuel oil, and (6) preliminary flame probing.

SECTION I

INTRODUCTION

The control of NO_x and particulates from the combustion of heavy, nitrogen-containing oils is, in practice, a very difficult problem. The most promising strategy for NO_x control proposes rich combustion with high conversion of fuel nitrogen to molecular nitrogen followed by second stage combustion of unburned fuel. This strategy engenders a high risk of producing particulates, however. Although some general statements can be made as to necessary conditions for limiting NO_x and soot in homogeneous systems with simple fuels, these guidelines are not very useful in heterogeneous and/or inhomogeneous systems as found in practice. In order to develop a predictive capability, and in particular, to tie this capability to a rich burn strategy, careful experiments are first required which will provide information on the effect of key variables such as temperature, equivalence ratio, mixing rate, and droplet dynamics on the rate of combustion and the production of NO_x and particulates.

The purpose of this study was to develop an apparatus and conduct experiments with No. 6 oil, or similar fuels, which simulates high-shear, diffusive combustion with oil droplet injection as found in the near field combustion zone of boilers and furnaces. The apparatus attempts to isolate as much as possible the effects of key variables. The shear layer in the vicinity of the fuel injector is of particular interest, and the apparatus simulates the shear layer near the injector by providing a mixing layer between a cold, fast-moving stream and a hot, slow-moving stream into which droplets may be injected. Variable angle droplet injection is provided so that two important modes of droplet distribution can be studied: (1) droplet distribution dominated by ballistics, or (2) droplet distribution dominated by turbulence. The effect of prevaporization and extended hot soak time on the formation of NO_x and particulates may also be studied by varying injection parameters.

SECTION II

APPARATUS - DESIGN AND DESCRIPTION

The apparatus is designed to allow control over droplet ballistics, mixing rate, and conditioning of vaporized fuel prior to combustion. Droplet trajectories were the most important factor influencing the geometry and overall scale of the apparatus. The maximum droplet velocity attainable with No. 6 oil in a vibrating capillary injector producing a monodisperse spray was an important consideration, since this determined maximum droplet penetration into a hot, moving stream. The dimensions of this stream were to be as large as possible for the purpose of minimizing temperature gradients in the stream, maximizing the working length of the combustor and for providing sufficient residence time for vaporization. Minimum hot gas flows were set by the requirements of minimum heat loss and flashback. Experiments early in this design phase established maximum attainable droplet velocities.

COMBUSTOR

A schematic of the combustor is shown in Figure 1. The combustor consists of four main sections: (1) wind tunnel, (2) hot gas generator, (3) fuel injection system, and (4) combustion chamber. Since the requirements imposed by the fuel injection system influenced the design most strongly, this section is discussed first.

Droplet Trajectories

One of the most important considerations in the apparatus design was the ability to conduct limit case experiments centered about the mode of transport of droplets or vaporized fuel into the shear layer. Three important cases were considered: (a) ballistic transport of droplets in the shear layer and (c) introduction of vaporized fuel into the shear layer. A concomitant factor was allowance for sufficient vapor phase residence time in fuel-rich combustion products so that substantial conversion of fuel nitrogen to molecular nitrogen could occur. The droplets are to be injected into the hot, moving stream in a manner simulating the penetration of a combustion zone in the near field of a practical combustor. Thus, in a two dimensional simulation, injection is made from injectors in the hot stream or from injectors located beneath the hot wall. The latter approach was considered the most practical. The computation

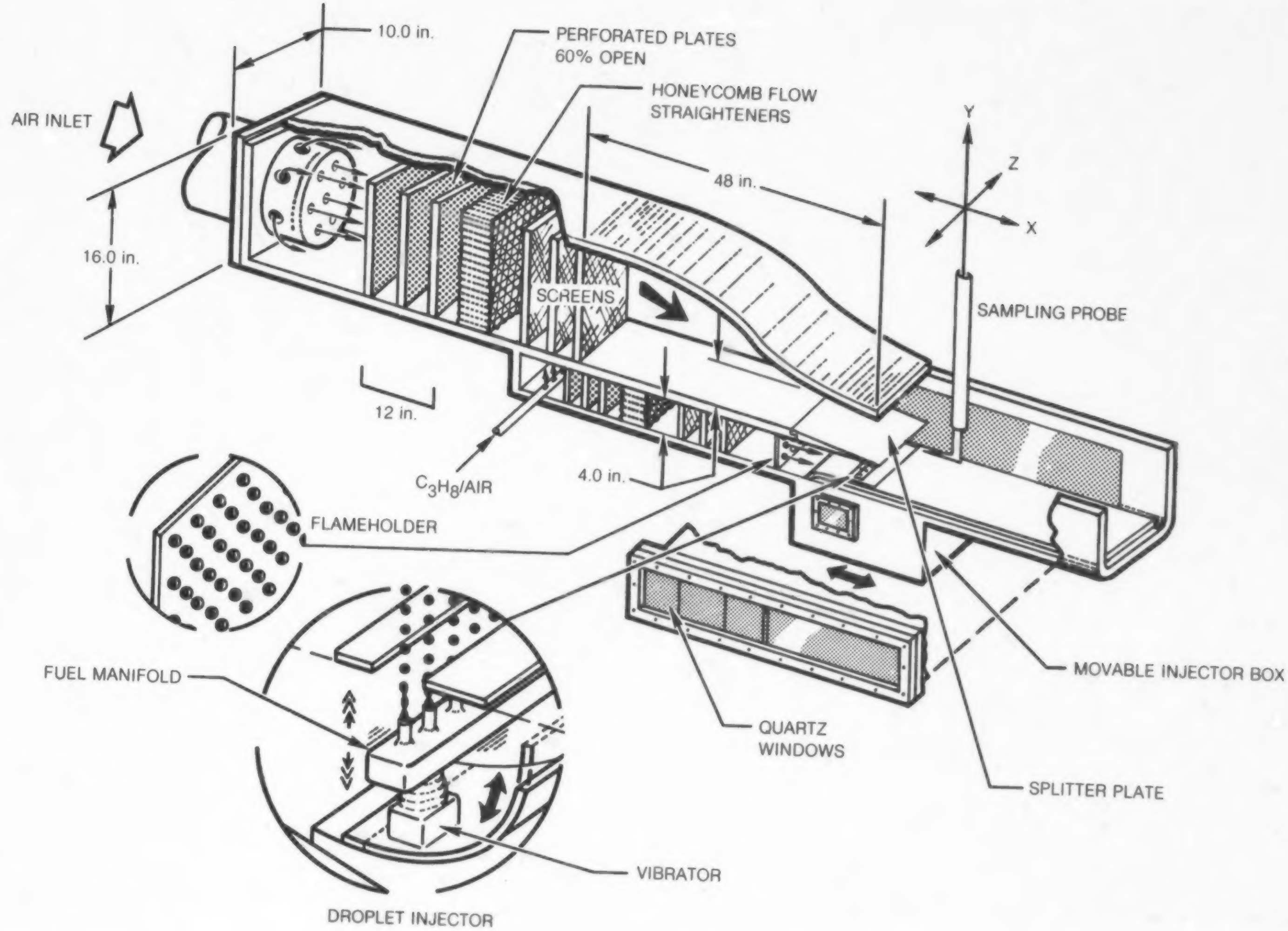

Figure 1. Heavy Oil Spray Combustor.

of droplet trajectories strongly influenced the selection of channel height, splitter plate length and droplet injection location. Calculation of droplet trajectories indicated a variable injection location was required.

A computer code was developed for computing trajectories of vaporizing droplets. The code includes the effects of convective heat transfer and droplet heat-up rates. Droplet dynamics were examined for the three cases under consideration: (a) ballistic penetration of the shear layer, (b) diffusional penetration of the shear layer, and (c) prevaporization. The time history of droplet diameter and position was calculated for various initial droplet diameters as a function of gas velocity, droplet injection velocity, injection angle, and initial droplet temperature. The effect of combustor geometry upon the droplet trajectories was also investigated. The accompanying figures illustrate some of the more interesting results of these calculations. The vaporization constant for these calculations was 0.01 cm^2/sec (Ref. 1).

In order to demonstrate case (c) above, it was determined that the only way to prevaporize in a relatively short length was to inject the droplet upstream into the hot gas flow. Upstream injection enhances the vaporization because the relative velocity between droplet and fluid is increased. Computed droplet trajectories for relatively low injection velocity and for two droplet sizes are shown in Figure 2a. It is seen that a 300 micron droplet penetrates farther upstream, but at the first shear layer entry point (corresponding to the large droplet), both droplets have vaporized to the same extent. The smaller droplet vaporizes to a greater extent by the time the second entry point is reached, however excessive length is required. Therefore, case (c) is better served by large droplet diameter, and the hot gas channel height must be large enough to accommodate the droplet trajectory.

For the droplet to enter the layer partially vaporized at a shallow angle, as in case (b), the minimum entry angle occurs when the gas velocity is maximum. This also means that an injection location different from case (c) must be used. Injecting at a location further upstream at a given gas and droplet velocity results in droplet entry at a shallower angle, but the droplet is more highly vaporized. Injecting too far downstream results in too steep an angle of penetration. The angle of entry and percent vaporized are strongly dependent upon droplet injection point. The gas velocity also effects the angle of droplet entry into the shear layer as shown in Figure 2b. It is seen that for

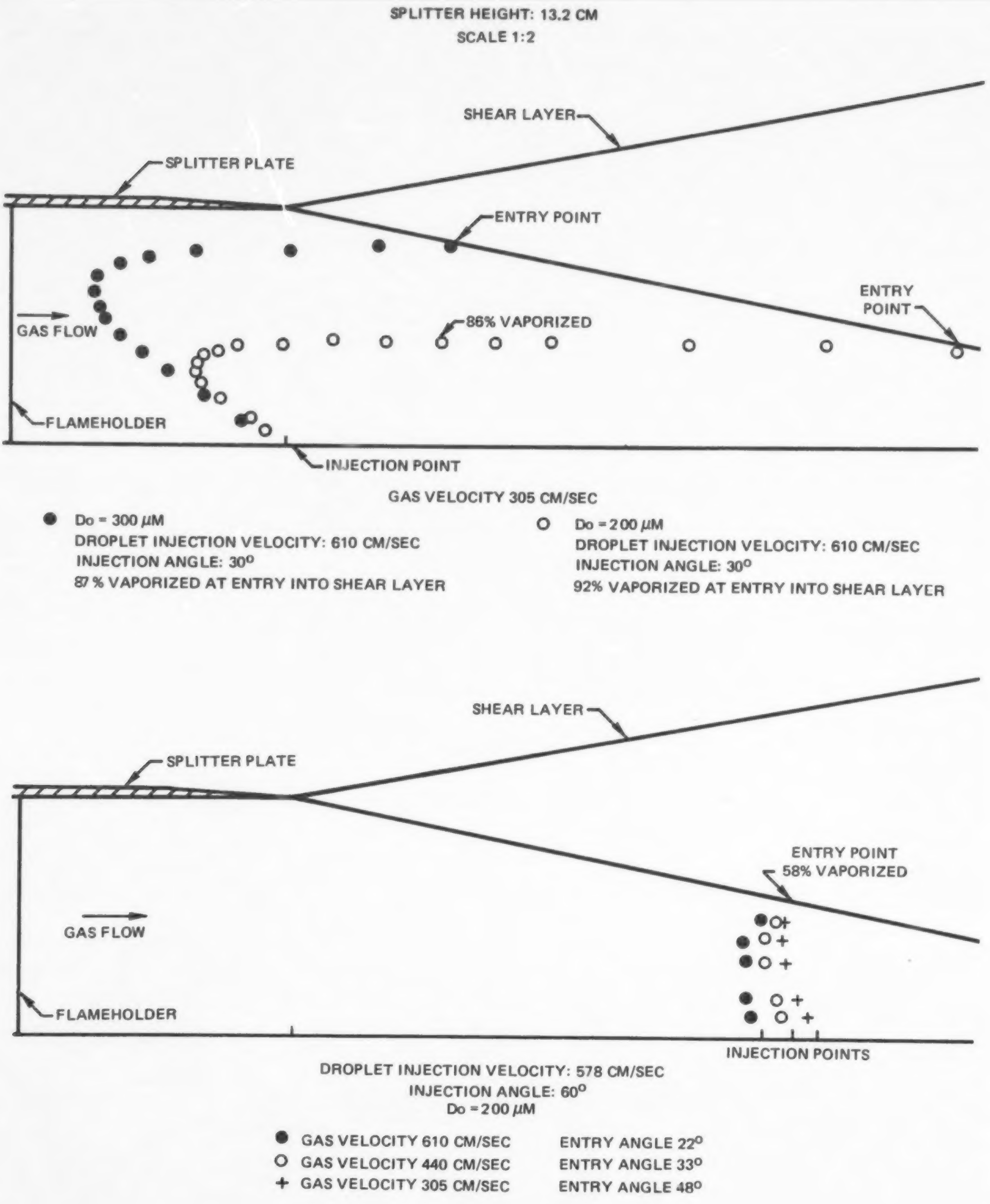

Figure 2. Droplet Trajectories.

a relatively fixed injection location, entry point, and extent of vaporization, the angle of entry is controlled by gas velocity.

The effects of droplet injection velocity and angle are shown in Figure 2c. This figure illustrates an interesting point. Because the location of the shear layer is fixed by the height of the splitter plate, there is only one choice of droplet injection parameters which will result in a partially vaporized droplet entering the shear layer at a shallow angle. Altering the angle or velocity will increase one parameter (angle at entry) but decreases the other (percent vaporized at entry). Possible combinations are shown in Figure 2c.

The optimum configuration for all three cases is shown in Figure 2d. Two injection locations and two gas velocities allow all three cases to be studied. Continuous variation of injector location is provided between the two extremes shown in Figure 2d. The flameholder height for the conditions of Figure 2d is 13.2 cm. Since the maximum upstream droplet penetration location coincides with the splitter plate trailing edge location, the flameholder may be as close to this location as desired consistent with the condition that flameholder wake effects are minimized. A length of about one inch is required for this purpose. However, it may be desirable to study the effects of high vapor fuel feed rate by injecting droplets larger than 200 micron. For this case, the distance between the flameholder and splitter plate trailing edge will be approximately six inches (see Figure 2a) in order to provide sufficient length for vaporization of larger droplets. Also, estimates of characteristic times for stabilization of vapor phase fuel nitrogen chemistry indicate that with the long splitter plate, ample time is provided before the fuel vapor enters the shear layer (~80 msec).

Fuel Injection System

The primary fuel injection system is a two-dimensional linear array of capillaries with variable angle injection. Prior experience with electromagnetic vibrators in the production of mono-disperse single droplet streams was applied to the development of a multiple capillary injector. Figure 3 shows the configuration of the fuel manifolds. The twelve capillaries, spaced 0.25 inch apart, are 0.004 inch I.D., 0.009 inch O.D. stainless steel tubes. Each tube is carefully cut to length and polished to ensure uniformity. The tubes are individually brazed into the main manifold using an electron-beam welder. The inlet to the capillary extends to the centerline of the main manifold tube.

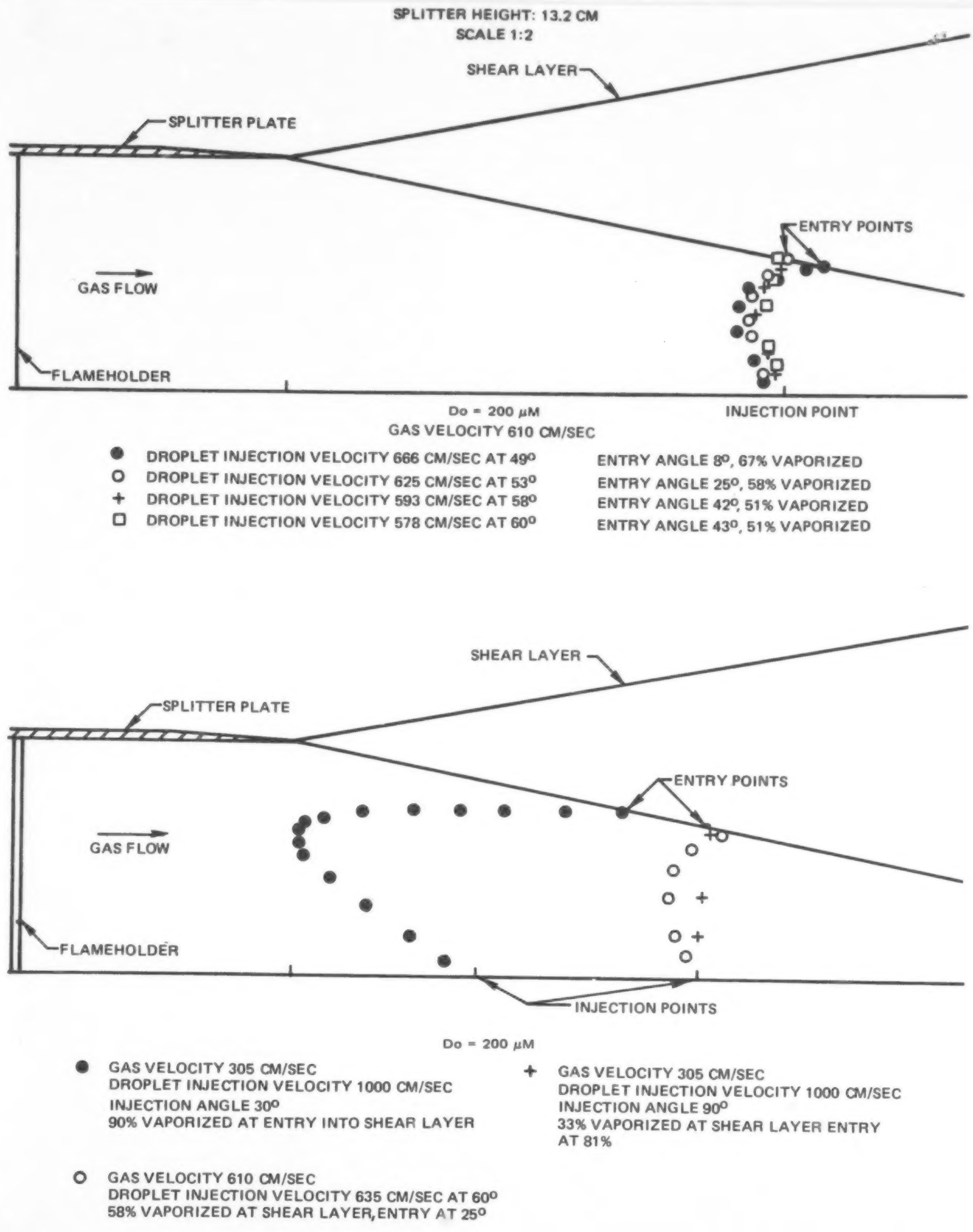
SPLITTER HEIGHT: 13.2 CM
SCALE 1:2
SHEAR LAYER
SPLITTER PLATE
ENTRY POINTS
GAS FLOW
FLAMEHOLDER
Do = 200 μM
GAS VELOCITY 610 CM/SEC
INJECTION POINT
● DROPLET INJECTION VELOCITY 666 CM/SEC AT 49° ENTRY ANGLE 8°, 67% VAPORIZED
○ DROPLET INJECTION VELOCITY 625 CM/SEC AT 53° ENTRY ANGLE 25°, 58% VAPORIZED
+ DROPLET INJECTION VELOCITY 593 CM/SEC AT 58° ENTRY ANGLE 42°, 51% VAPORIZED
☐ DROPLET INJECTION VELOCITY 578 CM/SEC AT 60° ENTRY ANGLE 43°, 51% VAPORIZED
SHEAR LAYER
SPLITTER PLATE
ENTRY POINTS
GAS FLOW
FLAMEHOLDER
INJECTION POINTS
Do = 200 μM
● GAS VELOCITY 305 CM/SEC DROPLET INJECTION VELOCITY 1000 CM/SEC INJECTION ANGLE 30° 90% VAPORIZED AT ENTRY INTO SHEAR LAYER
+ GAS VELOCITY 305 CM/SEC DROPLET INJECTION VELOCITY 1000 CM/SEC INJECTION ANGLE 90° 33% VAPORIZED AT SHEAR LAYER ENTRY AT 81%
○ GAS VELOCITY 610 CM/SEC DROPLET INJECTION VELOCITY 635 CM/SEC AT 60° 58% VAPORIZED AT SHEAR LAYER, ENTRY AT 25°

Figure 2. Droplet Trajectories (continued).

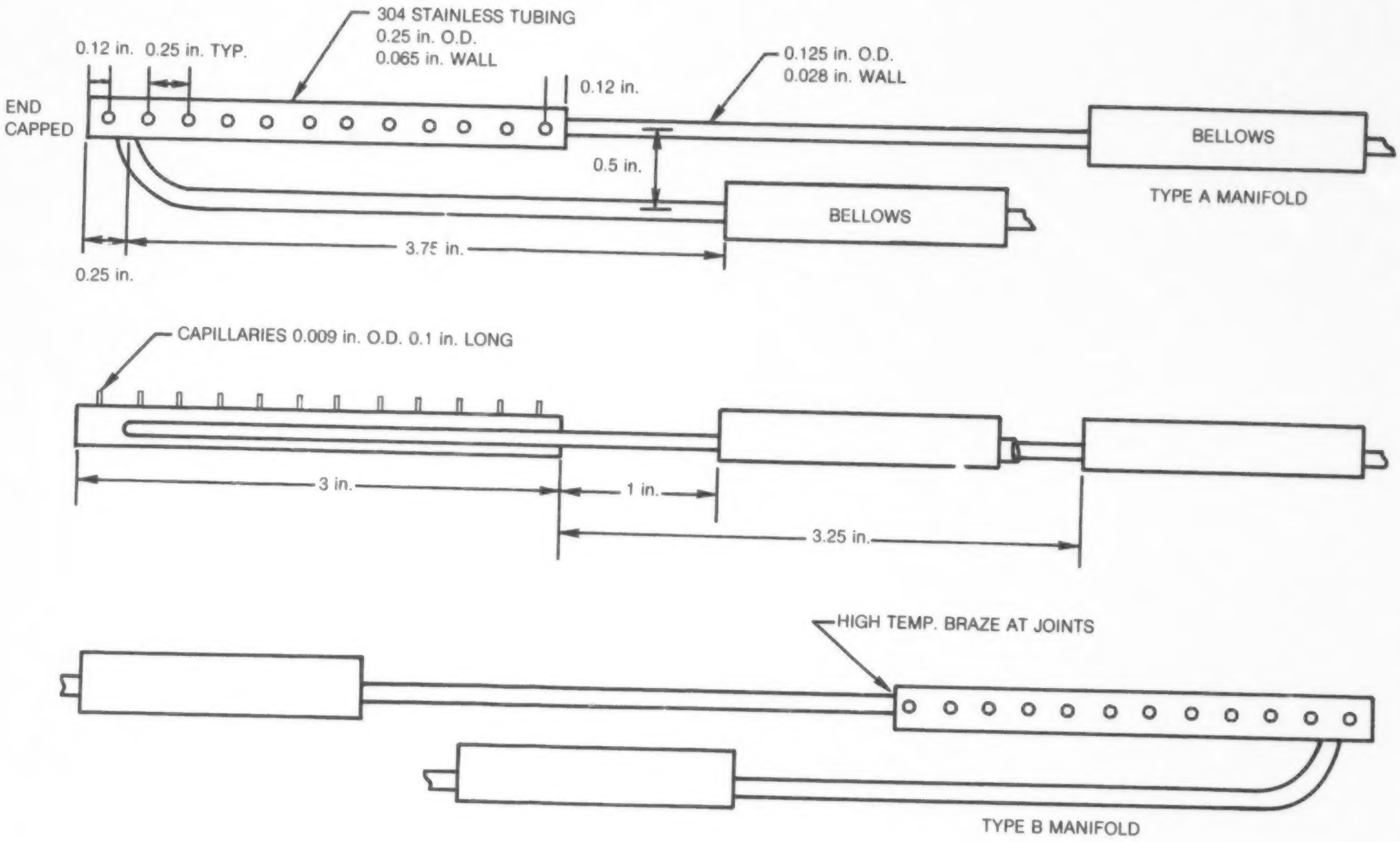

Figure 3. Multiple Capillary Fuel Manifolds.

This reduced the possibility of forcing foreign particles into the capillaries during brazing. The manifolds are driven from below by small U-shaped shafts connected to the vibrators. Teflon sleeve bearings are used to retain the shafts in the mounting plate. Each manifold has a fuel inlet and exhaust bypass line which is isolated from the support clamp with stainless steel bellows, thereby reducing the damping effect of the fuel lines on the vibrations of the manifolds. Electric resistance heaters are used to preheat the manifolds to desired operations temperature.

The 24 capillary manifold system is mounted on a support rack, seen in Figure 4. The vibrators and manifolds can be translated back and forth up to one inch by a manual traverse system which allows for fine positioning of the injectors. The entire support rack is mounted inside an injector box in such a manner that the rack can be rotated so that the capillaries form an angle of 30 to 90 degrees relative to the floor of the combustor. The rack is literally hung like a swing, and the angle of the capillaries relative to horizontal can be continuously adjusted between the above limits by the turning of a fine threaded rod (Figure 5).

The injector box is mounted beneath the floor of the combustor. A 1" x 6" slot in the combustor floor is located above the capillaries such that the droplet streams can be injected through the slot into the combustor. Because two injector locations are required the entire injector box can be moved 6 inches. Inserts in the combustor floor are used to accommodate the translation of the injector box in the X-direction. The slot in the combustor floor is also effectively moved through the use of inserts.

Individual capillaries are aimed by forcing trichloroethylene through the manifold and observing the stream trajectory through the slot. The entire line of droplet streams can be adjusted to pass through the slot by adjusting the slide upon which the support rack is mounted. The angle of injection is varied with the treaded rod which pushes a cam-follower. This in turn swings the support rack through an arc. The inlet fuel lines to the support rack are flexible so that the angle of injection can be varied without altering the fuel system or placing strain on the fuel lines. The injector box is a self-contained unit which houses the heaters for temperature regulation, the fuel manifold system, and collects any oil spill from start-up or capillary misalignment.

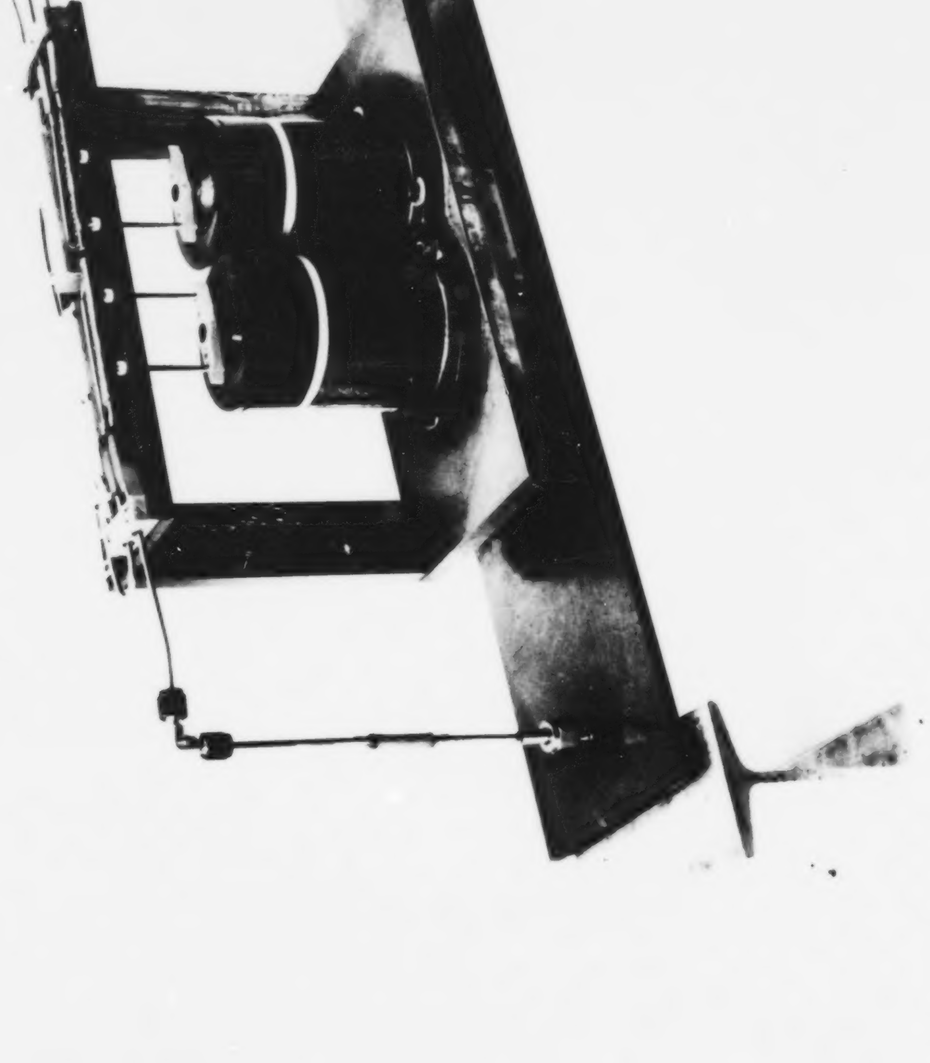

Figure 4. Fuel Injectors on Support Rack.

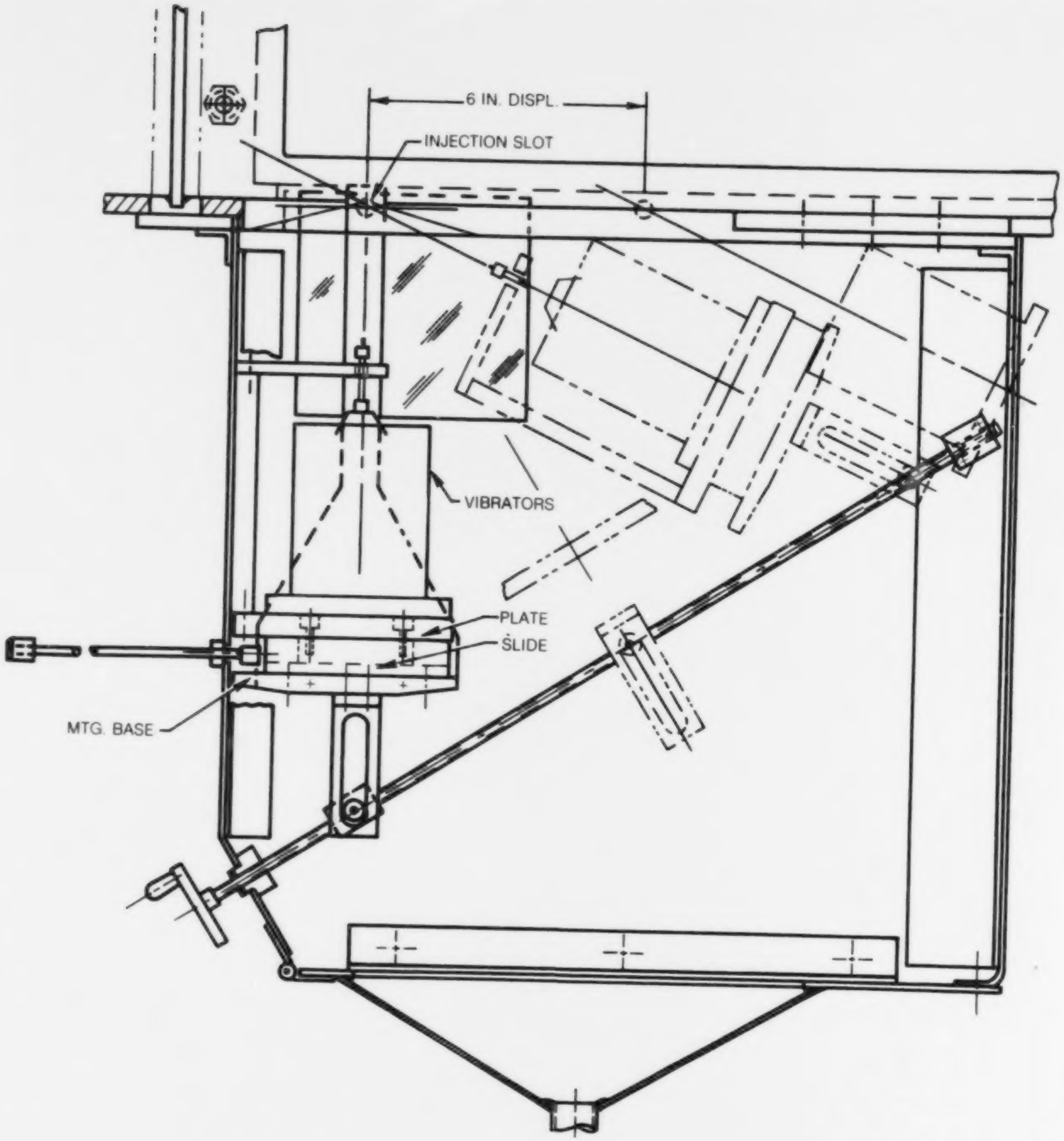

Figure 5. Oil Droplet Injector Enclosure.

The vibrators are driven by a stereo audio amplifier fed from a signal generator. An oscilloscope monitors the frequency and amplitude of the driving signal, and a stroboscope is triggered by the signal generator. A window in the injector box allows viewing of the droplet streams, and the strobe is used to "freeze" the droplet motion to allow tuning of the oscillator to the optimum frequency.

Wind Tunnel

The wind tunnel consists of a 4:1 area ratio rectangular nozzle 10 inches wide and 16 inches high at the throat. The nozzle contour consists of two cubic arcs designed to provide uniform exit flow without separation according to the method of Morel (Ref. 2). The absence of separation was verified analytically by computing the boundary layer history under the imposed potential flow field. The estimated turbulence level at the throat is 0.1% and the estimated boundary layer displacement thickness is 0.049 inch. All calculations are based on a design point throat velocity of 100 ft/sec. The nozzle is preceded by a calming section consisting of perforated plates, honeycomb cells and screens. Screens (60 mesh) and perforated plates were 50% open to prevent jet coalescence. A 60 mesh screen was placed six cell diameters downstream of the honeycomb to suppress turbulence generation by the honeycomb (Ref. 3).

Hot Gas Generator

The hot gas generator consists of the upstream mixing and calming plenum, the flameholder, and the volume bounding the hot gas upstream of the splitter plate trailing edge. Fuel (propane) is injected towards the rear of the plenum through an upstream-facing manifold and is mixed uniformly with air upon passing through the perforated plate and screens. Because of the very low flow through the plenum and the possibility of flow separation, no nozzle is provided at the plenum exhaust.

The initial flameholder consisted of equi-spaced parallel rods of 0.062 inches diameter with 50% open area and was designed to provide a stable flame at $\emptyset = 1.5$ and an approach velocity of 3 ft/sec (Ref. 4). The spacing between rods was less than the quenching diameter at $\emptyset = 1$ (Ref. 5). Flameholder solidity was 50% to prevent jet coalescence. Assuming laminar wakes, a maximum dimension of .062 inches, and a stream velocity of 20 ft/sec, the distance before the wakes begin to merge is approximately 0.5 inches. The minimum splitter plate length, 2 inches, was selected to provide uniform flow at the splitter plate trailing edge and is also the distance of closest approach of droplets to the flameholder without wake effects. A longer splitter plate is provided to increase the soak period of vaporized feed. Maximum splitter plate length is six inches.

Combustion Chamber

The three sided steel combustion chamber is 10 inches wide, 8 inches high, and 30 inches long. The top of the combustor is open in order to provide a more realistic simulation of the pressure field in a boiler or furnace flame. The open top also facilitates flame sampling. Each combustor side wall is fitted with 3.6 inch x 6 inch fused quartz windows, thus allowing optical access along one half the combustor length. The remainder of the side wall is a carbon steel water-cooled, filler piece. The positions of the windows and filler piece are interchangeable so that the entire combustion chamber can be probed optically. The bottom wall of the combustor is a water-cooled insert which is bolted to the combustor frame. This insert has a one inch radius inlet thus providing a small area contraction just downstream of the flameholder plate.

FUEL SYSTEM

The fuel system is shown schematically in Figure 6. Filtered and heated No. 6 oil is provided to the capillaries at a controlled pressure. Fuel flow rate and routing are remotely controlled. A central, remote, control panel is used to regulate pressure, read flow rates, and operate solenoid valves. The No. 6 oil is pre-filtered through a 60 micron filter and stored in a 55 gallon storage drum. This storage drum is used to preheat the fuel to 100^{o}F so that it can be easily pump-transferred to a five gallon fuel tank which serves as the fuel reservoir during testing. A high pressure gear pump is used for transferring the fuel. A steady supply pressure is applied to the accumulator. The upstream fuel supply pressure is independently regulated. The fuel is driven out of the accumulator, where it is kept at 100^{o}F, through a positive-displacement flow meter and into a steam heater where it is heated from 100^{o}F to 250^{o}F. After heating, the fuel is filtered again through a 60-micron filter before entering the fuel pressure regulator.

The fuel enters the injection box through an electrically heated, flexible section which allows for slight movement of the injector box. The fuel leaves

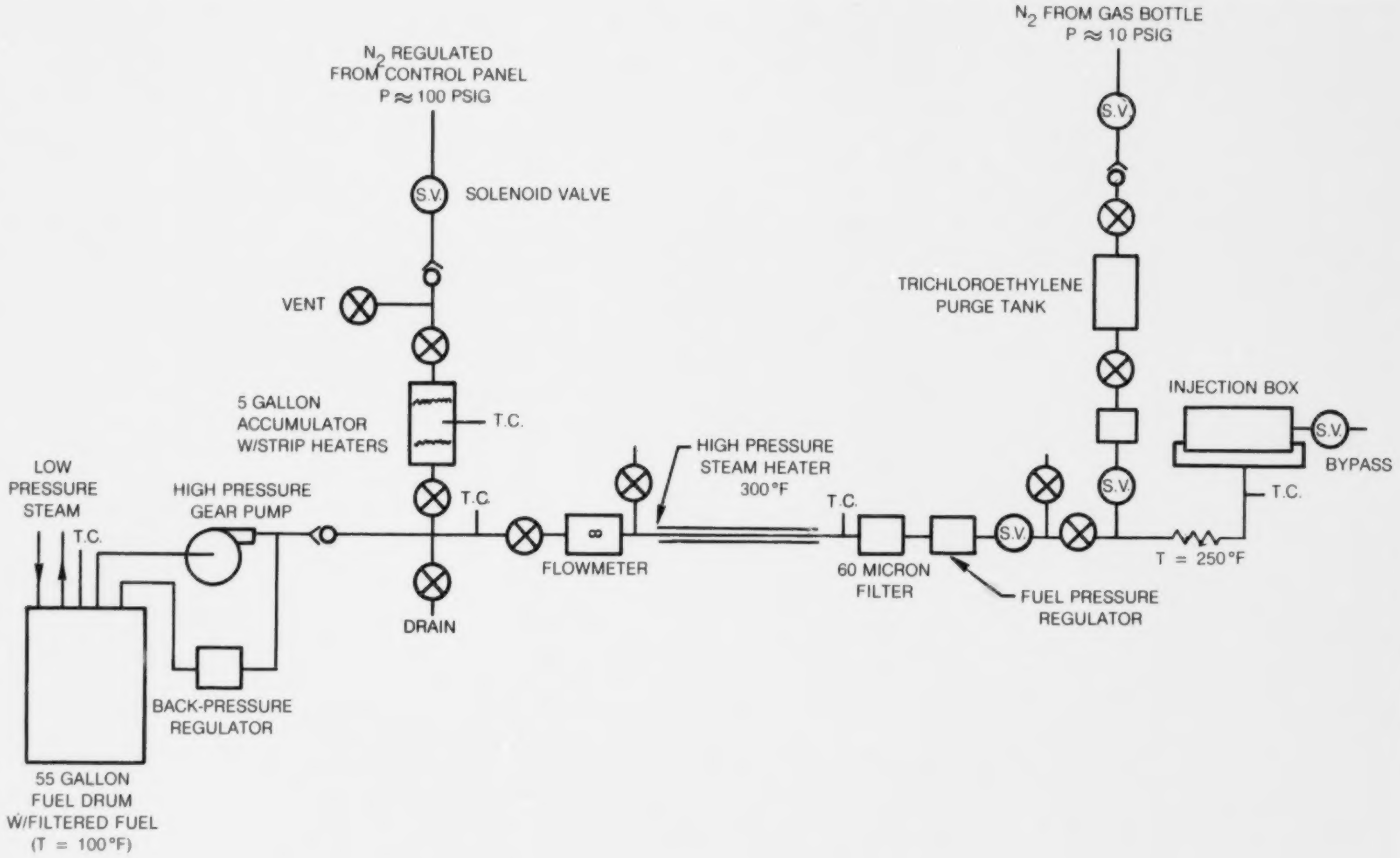

Figure 6. Heavy Oil Combustor Fuel System.

the system through the exhaust bypass or is injected directly through the capillaries. After completion of a test, the fuel is purged from the capillaries in order to prevent deposit buildup. A trichloroethylene flushing system is used for this purpose. The solvent is admitted to the fuel lines downstream of the fuel filter, then passed through the fuel lines, manifold and bypass line. Once the lines are clean, the bypass is closed and the solvent is forced through the capillaries. Use of the solvent makes aiming of the capillaries and checking of trajectories particularly easy. Prior to each test the capillaries are checked for flow without spraying oil into the combustor. During startup and prior to injection through the capillaries, the fuel flows through the system and out the exhaust bypass line until all the solvent is flushed from the system.

The temperature control is particularly important in handling the No. 6 oil. Temperature is monitored in seven locations in the fuel system to control fuel delivery temperatures and to reduce the risk of overheating.

SAMPLING PROBE

A probe was designed and constructed which can be used to obtain gas samples in regions where solid particles or liquid droplets coexist with gaseous combustion products. The well known principle of inertial separation is used to separate gases and particulates. The main stream, comprised of gas and entrained particles enters the probe and is accelerated to high velocity in a nozzle. The sample gas stream is drawn off a right-angle to the direction of flow of the main stream at the throat of the nozzle, and most of the particles and main stream are vented while the sample stream is directed to the gas analyzers. A schematic representation of the probe is shown in Figure 7.

The operating characteristics of various probe designs were determined analytically. The particle trajectory program was used to calculate the paths of droplets as a function of main gas stream velocities, sample line velocities and inlet/throat area ratios. A potential flow velocity solution was imposed on the droplets, and a rough calculation grid devised. The "cut-off" diameter for a particular probe configuration was defined as follows. All particles in a streamline 1/4 of the throat height above the sample line inlet would not be drawn into the sample line tube if their diameter was greater than the "cutoff" diameter. Some particles below the cutoff diameter would be swallowed depend-

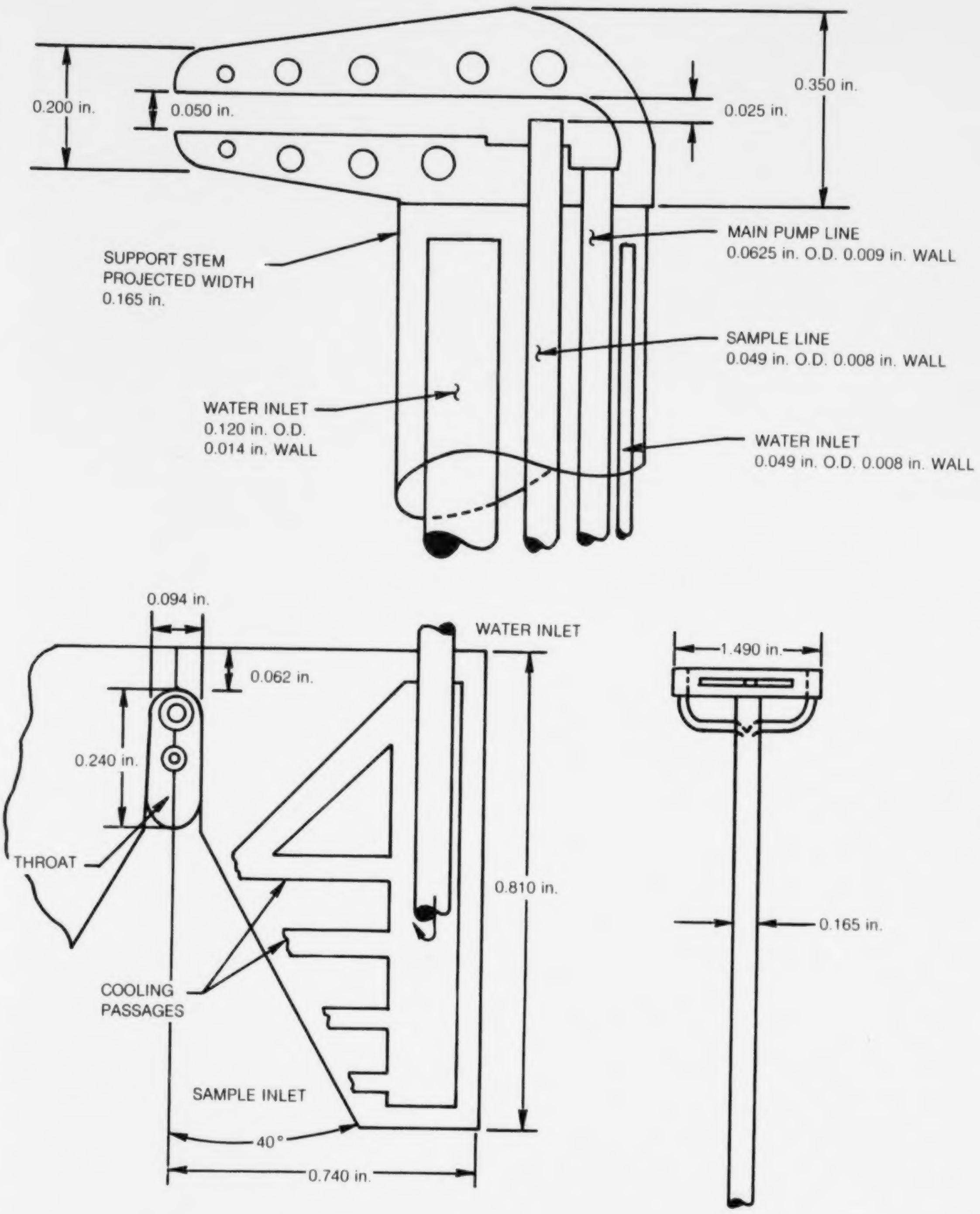

Figure 7. Phase Sensitive Probe.

ing on their size and position. All particles entering the probe below this streamline would be drawn into the sample line tube if their diameter was less than or equal to the cutoff diameter. Calculations were then performed for a given probe configuration to determine the effect of sampling velocity and main gas velocity on cutoff point. It was determined that to have a cutoff diameter of 10 microns it would be necessary to accelerate the main gas stream to 268 m/sec while maintaining a sample line inlet velocity of 64 m/sec. The sample line inlet velocity is determined by the flow requirements of the instrumentation (32 cc/sec) and the sample tube diameter. Because the probe is to be used in gas streams where the velocity would be about 30 m/sec, a large reduction in area was needed in order to maintain a probe inlet velocity nearly equal to that of the free stream while attaining a throat velocity of 268 m/sec. This contraction was effected in one dimension only in order to keep the probe profile small. At the same time, this inlet shape provides a span-wise average gas sample, i.e., the probe inlet width is greater than the separation between fuel injection source. The probe is cooled with high pressure water heated to 290^{o}F. A step at the sample line inlet allows buildup of liquid at the leading edge of the tube to be drained off into the main pump line. The sampling rate, and hence the velocities in the two streams, are regulated downstream by the use of valves.

SAMPLING SYSTEM

Detailed profiles of composition (total hydrocarbons, NO_x, CO, CO_2, N_2, H_2) are obtained with the gas sampling system shown schematically in Figure 8. An integral part of the system, not shown here, is the probe positioning device which enables the probe to be moved in increments of as small as 0.000125", with positive readout capability in two axes. This precise probe positioning is accomplished using a variable speed stepping-motor and controller in the Y axis which provides the high accuracy mentioned above, and a constant speed drive with potentiometric readout on the Z axis. The probe can be manually traversed in the X direction where repetitive high accuracy positioning is not required.

The main gas stream from the probe passes through a condenser, two filters of 60 and 10 micron rating, and a cold trap before passing through a throttling valve into the main pump. The pumping rate, and hence the sampling velocity at

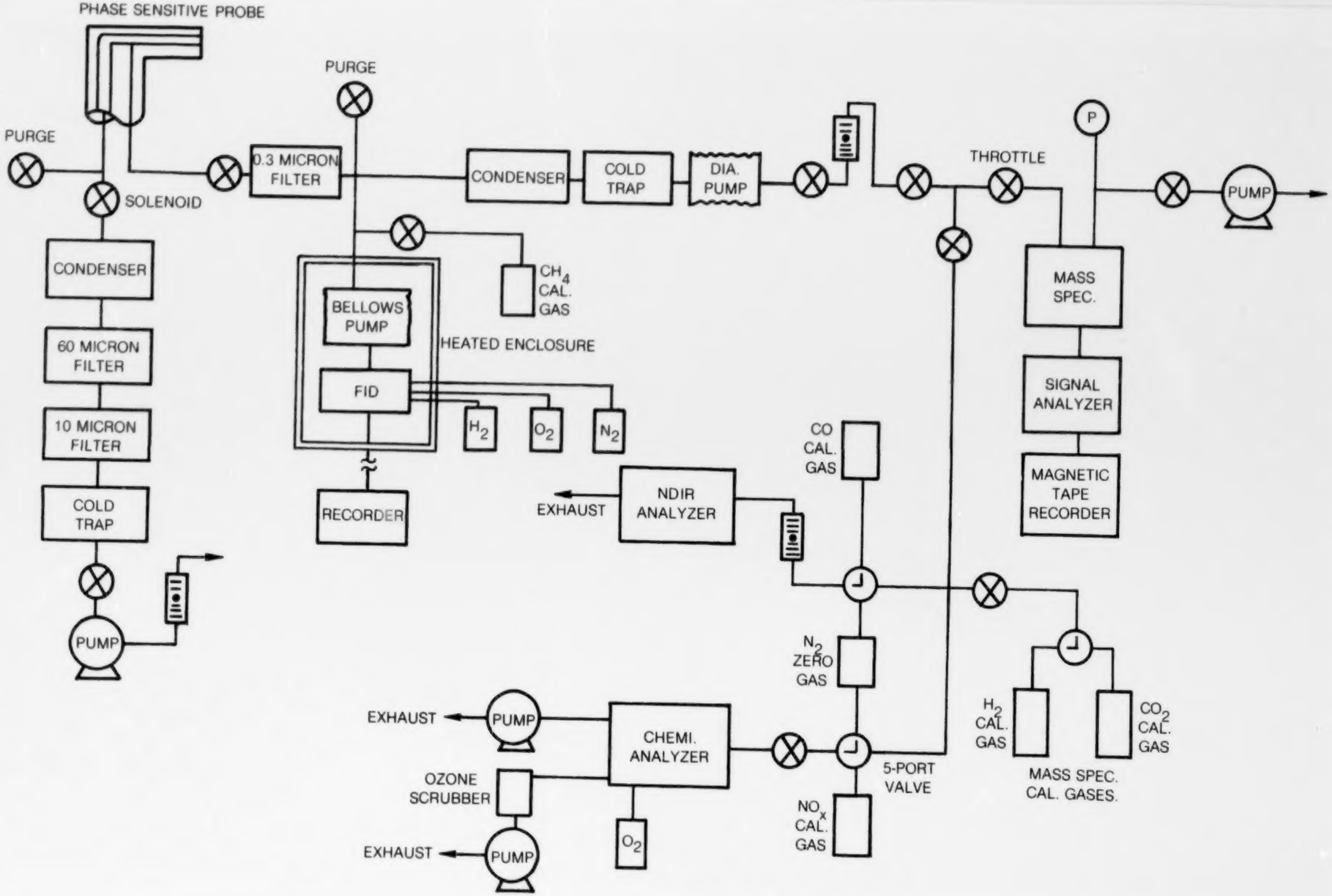

Figure 8. Heavy Oil Combustor Gas Sampling System.

the probe inlet, are controlled by the throttling valve, with total flow being measured with a rotameter at the pump exhaust.

The sample line to the hydrocarbon analyzer is teflon coated aluminum tubing, and is maintaining at 150°C. The hydrocarbon analyzer was designed and built at UTRC, and consists primarily of a heated bellows pump, flame ionization detector, and temperature regulated oven. The instrument is located alongside the combustor in order to maintain sample lines as short as possible. Oxygen is used in the flame to ensure complete combustion of the sample gases. The electrometer and recorder are located within the control room. The gas sample is also directed through a condenser, a cold trap, and two total filters, before entering the analyzers. A diaphragm pump is used which has a teflon coated head. Sample lines and instruments downstream of the pump exhaust are at slightly positive pressure, thereby eliminating the possibilities of air leakage into the sample. Sampling rate is metered. Three analyzers are used in this leg of the sampling system. A UTRC designed time-of-flight (TOF) mass spectrometer is used to determine O_2, CO_2, N_2, and H_2 concentrations. The mass spectrometer output is fed to a Northern NS-575 digital signal analyzer. A Northern NS-408F magnetic tape control interface, and a Wang MOD-7 7-track magnetic tape recorder are used to record the data. A computer program is used to convert the data to mole fractions. Mixtures of 2.76% CO, 1% H_2, or 10.3% CO_2 in nitrogen were used periodically to calibrate the mass spectrometer. Carbon monoxide (CO) concentration was determined with a Beckman model 864 Infrared Analyzer. A mixture of 2.76% CO in N_2 was used to calibrate the unit, and unit was zeroed and calibrated repetitively during the course of a run. NO/NO_x concentrations were determined using a Thermo Electron model 10AR Chemiluminescent Analyzer. A calibration gas of 395 ppm NO in N_2 was used to calibrate the unit and perform periodic checks during sampling. The entire sampling system was leak-checked prior to each test by using the mass spectrometer to detect the presence of O_2 after inserting the probe into a stream of N_2. The highly sensitive method of on-line leak checking ensured that accurate gas samples were obtained.

SECTION III

TEST RESULTS

Testing to date has consisted of fuel injection studies, cold flow mapping and turbulence measurements, recirculation studies, and preliminary flame probing both with and without oil injection.

Fuel Injector Development

Experiments have been conducted with No. 2, 5 and 6 oil in single and multiple capillary injectors in order to measure maximum attainable droplet velocities, insure a multicapillary capability, and to investigate possible capillary clogging with heated heavy oils.

The calculations indicate that velocities up to about 30 fps are required with 200 μm drops to achieve desired trajectories and fueling rates. Using an existing UTRC apparatus, a droplet velocity of 35 fps was demonstrated with #2 oil for drops about 240 μm in diameter. This system consisted of an electromagnetic vibrator driving a stainless steel tube with a small capillary soldered in one end. The capillary was 0.006" in I.D. and about 0.1" long. Fuel pressure was about 50-70 psia and the vibrator was driven at a frequency in the range of f = 10-20 kHz. Polaroid photographs were taken of the droplet stream using a pulsed light source. Uniform drops were observed to be formed and droplet size, d, and spacing, f_{λ_d}, were measured from the photographs. Droplet velocity was then calculated using the relation

$$v = f_{\lambda_d}$$

A typical set of data are given in Table I. Stable uniform droplets were observed over a frequency range of about f = 12-18 kHz. These parameters are consistent with prior observations in the field and show that the desired maximum velocity condition can be achieved conveniently with a drive frequency in the upper part of the audio band. Sufficient leeway exists among the parameters p, f, d, and f_{λ_d} in order to vary v and d_o over the desired range.

Following the tests with the single capillary injector, a three capillary model of the final fuel injector, having the same manifold size and mounting arrangement, was used to verify that monodisperse droplets could be produced in this system. Tests were conducted with No. 2 and No. 5 oil in the multiple

Table I. No. 2 Oil Injection Test Results--Single Capillary

I. Conditions

Capillary I.D. - d_c	0.0006" (0.15mm)
Fuel Supply Pressure - p	45 psig
Vibrator Frequency - f	15 kHz

II. Measurements

Droplet Spacing - λ_d	0.71 mm
Droplet Diameter - d_o	0.24 mm
Liquid Jet Diameter - d_j (vibrator off)	0.13 mm

III. Results

Droplet Velocity $v = f\lambda_d$	1068 cm/sec
Spacing to Jet Size Ratio - $_j/d_j$	5.5
Droplet Size to Jet Size Ratio d_o/d_j	1.9

(calculated value = d_o/d_j = $3\sqrt{\frac{1.5\lambda_d}{d_j}}$ = 2.0) capillary injector to demonstrate monodisperse droplet formation from capillaries at the middle and extreme ends of the injector. The fuel manifold was 3 inches long and contained three capillaries of 0.006 inches I.D. and 0.1 inches length. Initially, tests were performed with No. 2 oil at room temperature. Three parallel streams of 300 micron diameter droplets with velocity of 775 cm/sec were produced with a fuel pressure of 20 psig and a vibrator frequency of 15.5 kHz. The monodisperse streams were well behaved at a distance 9 cm from the injector tips at this low velocity. Following the No. 2 oil demonstration, the injector was operated using No. 5 oil heated to approximately 260°F. Multiple streams of 340 micron diameter droplets were produced at a velocity of 525 cm/sec, a frequency of 5.6 kHz and a fuel pressure of 30 psig. Velocities of 1050 cm/sec were obtained with 280 micron diameter droplets at a fuel pressure of 60 psig and a frequency of 10.5 kHz. The droplet streams at the high velocity were well aligned 25 cm from the injector tip.

Further tests were performed on the bench-scale capillary injector with a sample of Indonesian/Malaysian No. 6 oil. Satisfactory droplet injection was demonstrated with the oil heated to 280°F. The following relationship between injection velocity (V), vibrator frequency (f), and jet diameter (d_j) was found,

$$\frac{V}{fd_j} = 6.20$$

This value of V/fd_j is in accord with previous experience with other liquids.

A further significant development was a demonstration of several shut-down cycles without clogging. Monodisperse droplets were produced in all capillaries with only occasional plugging of a capillary. In all cases, this plugging was eliminated by flushing trichlorethylene through the manifold. The manifold flushing system proved invaluable in facilitating restarting after a cold shutdown; hot restarts did not require any flushing.

Cold Flow Velocity Profiles

Cold flow velocity profiles were determined at several axial locations from total and static pressure measurements. Lateral and vertical profiles at the nozzle exit are shown in Figure 9. Figure 9A shows lateral profile two inches below the top of the air nozzle at the nozzle exit, and 16 inches down-

Table II. No. 6 Oil Injection Test Results--Multiple Capillary

I. Conditions

Capillary I.D. - d_c	0.006" (0.15 mm)
Fuel Supply Pressure	45 psig
Vibrator Frequency	5.58 kHz

II. Measurements

Droplet Spacing - d	0.81 mm
Droplet Diameter - d_o	0.32 mm

III. Results

Droplet Velocity - $v = f\lambda_d$	450 cm/sec
Droplet Size to Jet Size Ratio d_o/d_j	2.13

(calculated value = d_o/d_j = $\sqrt[3]{\frac{1.5\lambda_d}{d_j}}$ = 1.89

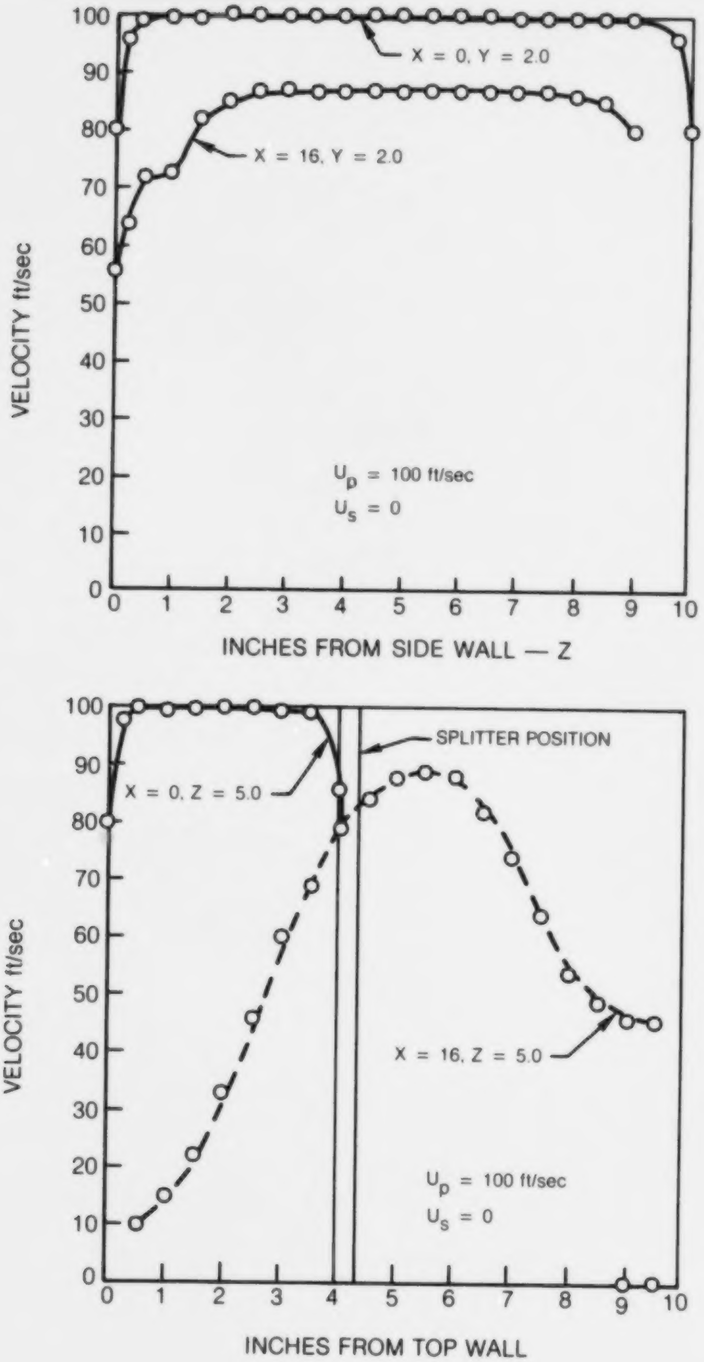

Figure 9. Velocity Profiles.

stream of the nozzle exit. Figure 9B shows vertical profiles at the nozzle mid-plane. It is seen that nozzle exit profiles are very flat. Boundary layer thicknesses are close to computed values. Figure 9B also illustrates the strong inward deflection of the primary air jet for a secondary velocity of zero. At a primary jet velocity of 100 ft/sec, static pressure at the nozzle exit was 0.5 torr below atmospheric due to the strong pumping action of the primary jet. Later on, during combustion testing, it was found that this led to air leaks, primarily through the injection slot. Turbulence levels were measured with a hot film anemometer at various radial and axial locations. The minimum turbulence level at the nozzle exit occurred at the center of the nozzle and increased toward the nozzle walls. Turbulence intensity varied from 1.3 to 2.7%. These levels are considerably higher than predicted. Spectral analysis of the velocity fluctuations indicated no predominant frequencies which might be attributed to flow oscillations or large scale instabilities. The broad spectrum of fluctuations is, therefore, attributed to green or grid noise. Further tests are planned in order to find the cause of high turbulence levels.

Recirculation Studies

It was found during the cold flow mapping studies that, under certain conditions, recirculation occurred within the duct. Consequently, several combinations of primary and secondary stream velocities were studied to define stable flow regimes. The mixing of hot and cold streams was simulated by mixing two cold streams at the same ratio of dynamic pressures as would exist under combustion conditions. For a hot stream velocity of 20 ft/sec the corresponding cold stream velocity is 7.5 ft/sec. Small tufts of yarn were taped to the combustor, splitter plate, and nozzle walls in order to visualize separation and secondary flows. Recirculation occurred at various locations along the duct depending upon velocity level and velocity ratio. Recirculation could be prevented by sloping either the upper or lower combustor walls (plexiglass inserts were used for this purpose) or retarding the rate of mixing by thickening the primary stream boundary layer. Boundary layer fences were used for this purpose. No recirculation was observed with a straight, open duct at a primary velocity of 100 ft/sec and a secondary velocity of 15 ft/sec. This high secondary flow is not desirable, however. At a secondary flow velocity of 7.5 ft/sec, a primary velocity of 50 ft/sec is permissible. The results were influenced by the type of flameholder, the smoothness of the walls and the nature of the boundary layer on the splitter plate. Best results were obtained with no flameholder in place. The high blockage, perforated plate flameholder cause secondary flows in some instances. A maximum primary velocity of 50 ft/sec was attained with a flameholder in place when a smooth contoured insert was used as the combustor bottom wall. This high velocity was not previously attainable with a flameholder in place. It appears that even higher primary velocities are attainable with combustion. The flow did not appear to recirculate at a primary velocity of 75 ft/sec when the hot gas generator was turned on. As a result of these tests, a water-cooled contoured insert was fabricated for combustion testing. This insert has a one inch radius inlet which provides a slight area contraction just downstream of the flameholder plate. Some of the test results are shown in the following table.

V_1/V_2	FLAMEHOLDER	WALL SLOPE	COMMENT
50/7.5	None	0	No separation with smooth wall insert.
50/7.5	None	Slight	No separation without insert.
50/7.5	10% Open Perforated Plate	Steep	No separation but strong cross flows on lower wall.
50/7.5	10% Open Perforated Plate	0	No separation with contoured insert.

Flame Stability Tests

The first flameholder tested had 50% open area and consisted of parallel, equi-spaced, 0.062 inch rods aligned with the floor of the combustor. The flameholder was designed to be stable to $\phi = 1.5$ with an approach velocity of 3 ft/sec. The separation between rods was less than the quenching distance of $\phi = 1$. Unfortunately, flashback occurred even at the highest approach velocity of interest, 3 ft/sec. The flame did not penetrate or damage the 200 mesh screen upstream of the flameholder, however. It was thought that flashback might have occurred from slight deviations in the rod spacing. Therefore, a slotted flameholder 50% open, consisting of uniform alternating 1/16" slots and ribs was fabricated from 1/8" steel sheet stock. The slotted flameholder also allowed flashback. At this point, it was decided that some turbulence and flow non-uniformity might be tolerated and several perforated plate flameholders were studied. Rich blowout limits generally increased with flameholders of higher solidity; rich blowout equivalence ratio varied from 1.12 to 2.1. Occasional flashback occurred with lower solidity flameholders. Several of the high blockage flameholders produced non-uniform flames of uneven luminosity. The first perforated plate flameholder tested was 30% open, with 0.050 holes. This flameholder allowed flashback at 2 ft/sec but functioned satisfactorily at higher velocity. A second perforated plate flameholder, 10% open, with 0.062 inch holes was stable at $\emptyset$ = 1.32 and did not allow flashback at 2 ft/sec. However, the flame appeared to be non-uniform. The most satisfactory performance was obtained with a commercially available filter screen manufactured by Michigan Dynamics. This flameholder consisted of 10% open perforated plate with 0.062 inch diameter holes. Two layers of fine screen were bonded to the back of the perforated plate. No flashback was encountered at an approach velocity of 1.5 ft/sec, even at stoichiometric conditions. The appearance of the flame was uniform at all conditions. Most importantly, very rich operation was possible; blowout occurred at $\emptyset$ = 1.85 at an approach velocity of 2.5 ft/sec. Subsequent gas sampling verified the uniform composition of the flame downstream of this flameholder.

Flame Probing

Initial flame probing experiments were conducted without oil injection in order to measure flame spreading rates (rich, hot gas stream), verify carbon balances and verify uniformity of the composition profiles at the hot gas generator exhaust. Since the pressure in the combustor was known to be slightly below ambient pressure, these experiments also provided information on air leaks.

Composition profiles were measured at four axial locations (X = 0, 5 1/8, 11 1/8, and 21 1/8 in.). In addition some data were obtained just downstream of the injection slot trailing edge (X = 4 in.) in order to estimate the air inspiration rate through the slot. Oxygen profiles are shown in Figure 10. The data show that the flame width is not very sensitive to axial position; apparently, turbulent spreading of the streams is offset by the inward deflection of the streamlines. The oxygen profiles exhibit a minimum. This is attributed to air leaking through the injection slot. The data at X = 0 show that there is a small leak even before the injection slot. Taking this into

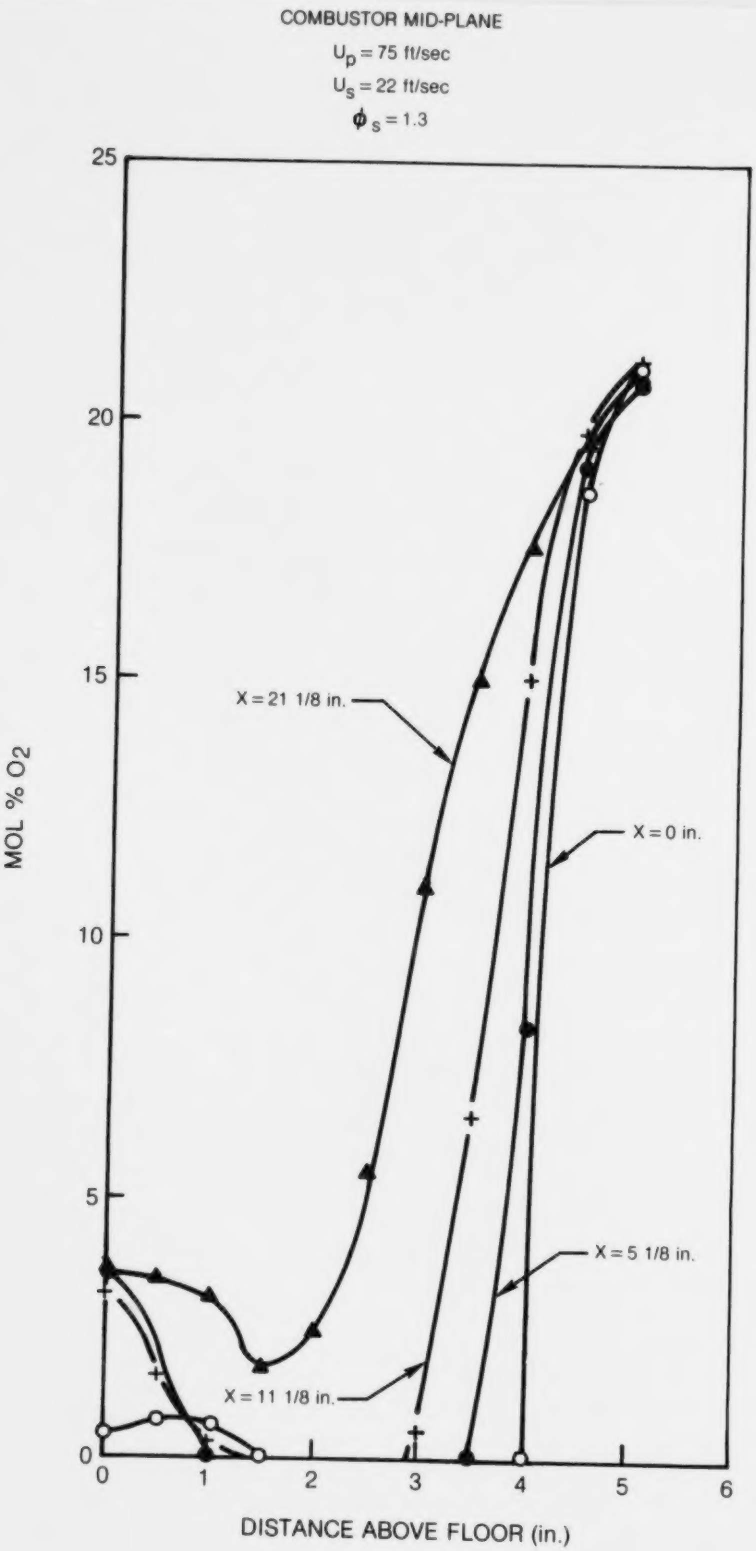

Figure 10. Oxygen Profiles.

account, it appears that the primary air stream has nearly penetrated to the combustor floor at the furthest downstream position. Thus, it is likely the edge of the mixing layer will impinge upon the combustor floor near X = 30, as intended.

Excellent carbon balances were obtained at $\phi = 0.8$ and 1.0. Metered and measured values were within 2 percent based on hot gas generator exhaust measurements. Measured CO readings were too low at $\phi = 1.3$ to give a satisfactory balance. Therefore, these data are not shown. The other composition data indicate that the hot gas generator exhaust composition is uniform. The oxygen profiles (Figure 10) are believed to be correct.

Several attempts were made to sample the flame with No. 6 oil injection. However, testing was hampered by capillary clogging. It is believed that clogging is a result of temperature-induced deposit buildup in the fuel system. Although the capillaries could be flushed clean by use of solvent, clogging recurred in subsequent tests. Subsequent inspection of the fuel system indicated heavy deposit formation in the bellows. The bellows have been replaced by high temperature flexible tubing. Also, further tests will be conducted with dilated No. 6 oil (20% No. 2 oil) so that lower fuel operating temperatures are possible.

Flame Photography

Short time exposure photographs and high speed cinematography have been used to examine the shear layer and droplet combustion. Both No. 2 and No. 6 oil sprays were photographed. High speed cinematography indicates the presence of large periodic distrubances in the shear layer, but the turbulence is three-dimensional. With oil injection, clearly observable droplet vapor trails were observed which move at the relative velocity of the droplets and gas stream. Droplet trajectories with No. 2 oil appear to be uniform, thus giving the flame a unique two dimensional structure.

SECTION IV

CONCLUSIONS

A unique combustion apparatus has been developed for the study of heavy oil spray combustion in shear layers. Linear arrays of mono-sized droplets may be injected with uniform trajectories into a two dimensional shear layer. High droplet velocities necessary for ballistic penetration of the shear layer and for droplet prevaporization have been demonstrated with several fuel oils. The problem of capillary clogging with No. 6 oil is expected to be solved by diluting the oil and reducing fuel temperature.

REFERENCES

1. Kobayasi, K., "An Experimental Study in the Combustion of a Fuel Droplet," Fifth Symposium "International" on Combustion, Reinhold, N.Y. (1955) pp. 141-148.

2. Morel, T., "Design of Two-Dimensional Wind Tunnel Contractions", J. Fluids Eng., June 1977, pp. 371-378.

3. Loehrke, R. I., and Nagib, H. M., "Experiments on Management of Free-Stream Turbulence," Agard Report No. 598, September 1972.

4. Ball, I.C., Rummel, D.H., Semerjian, H.G. and Vranos, A., "Bluff Body Stabilization of Premixed and Prevaporized Flames," Eastern States Section Combustion Institute Meeting, November 29-30 and December 1, 1978, Miami Beach, FLA.

5. Lewis, B. and von Elbe, G., "Combustion, Flames and Explosion of Gases," Second Edition, Academic Press, N.Y., NY (1961), p. 256.

SPRAY CHARACTERIZATION

W. R. Seeker and G. S. Samuelsen
Energy and Environmental Research Corporation
Irvine, California 92714

Fifth EPA Fundamental Combustion Research Workshop
Newport Beach, California
January 23-25, 1980

SECTION I

INTRODUCTION

Experimental studies have demonstrated that pollutant emissions from fuel oil furnaces are influenced by the nozzle selected for atomization. Note, for example, the results from a recent CRB study presented in Figures 1 and 2.

The data in Figure 1 were obtained from a firetube boiler simulator operating with a variety of nozzle types under three swirl conditions. The emission of NO_x is shown to depend on not only nozzle type, but on swirl condition as well. Notable is the reversal of NO_x emission performance of the Monarch and Delavan nozzles between the swirl numbers of 0.2 and 0.8.

The data of Figure 2 were obtained from a tunnel furnace that was operated (a) in the absence of swirl, and (b) with a nitrogen deficient oxidizer as well as air to isolate the fuel NO_x produced. For this case, the operating condition of a single nozzle was shown to substantially influence the NO_x emission. Thermal NO_x, for example, decreased dramatically at higher atomizing pressures.

These data point to the need for characterizing those properties of sprays that dictate the NO_x produced. Characterizations of this type require the measurement of local droplet size, local droplet velocities, and local gas velocities. To provide such information, a FCR study was established with the following overall and immediate objectives:

- Overall

  (1) To relate nozzle performance to NO_x emission in the absence of burner aerodynamics.

  (2) To relate nozzle performance to NO_x emission in the presence of burner aerodynamics.

- Immediate

  To assess applicability of the following nonintrusive diagnostics for the measurement of nozzle performance

a) Firetube Combustor

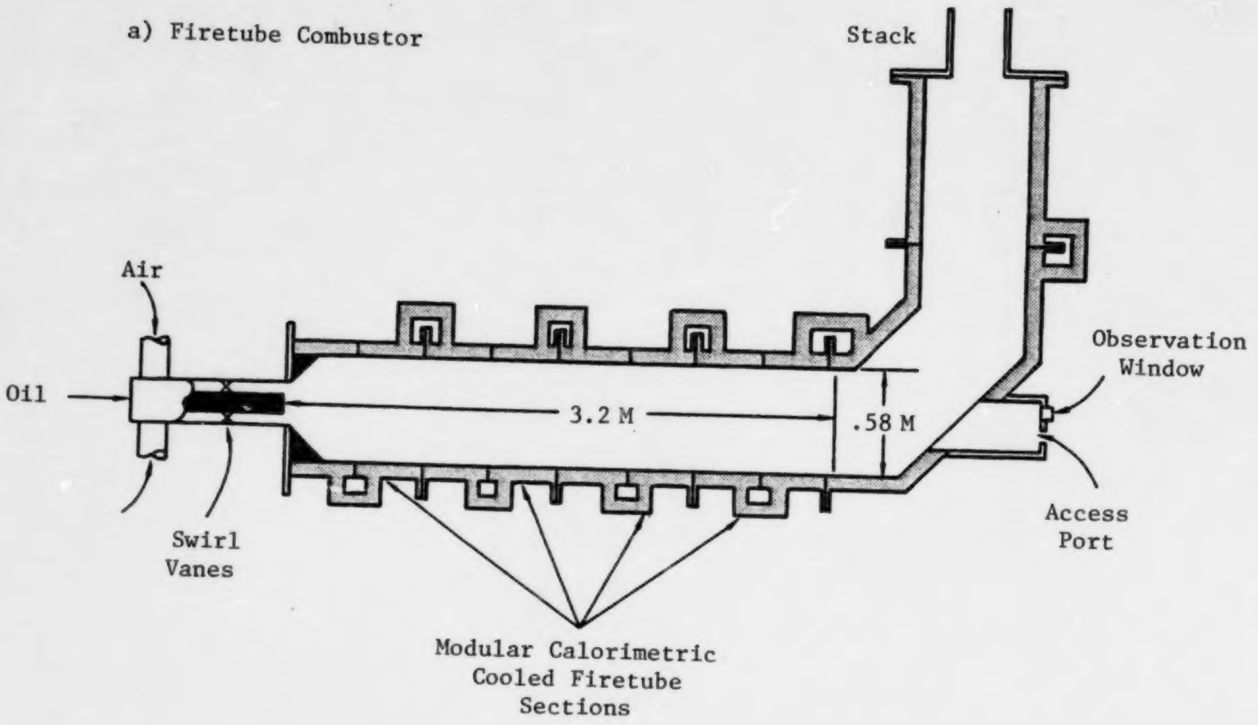

b) NO_x Emissions

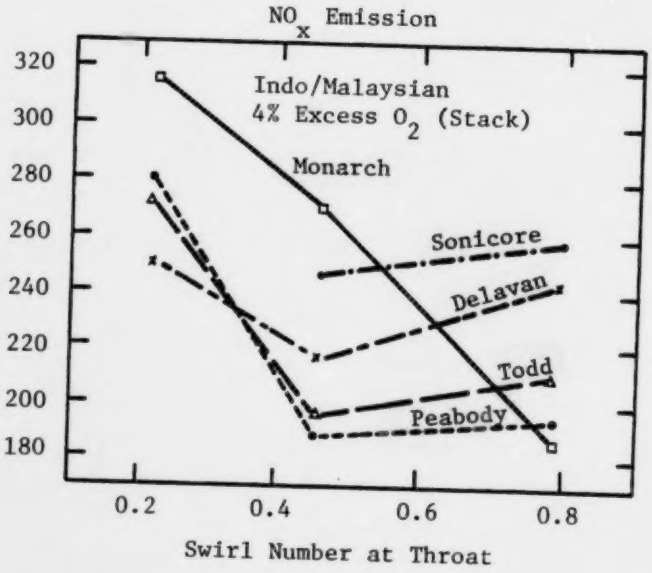

Figure 1. NO_x Emissions from a Firetube Combustor.[1]

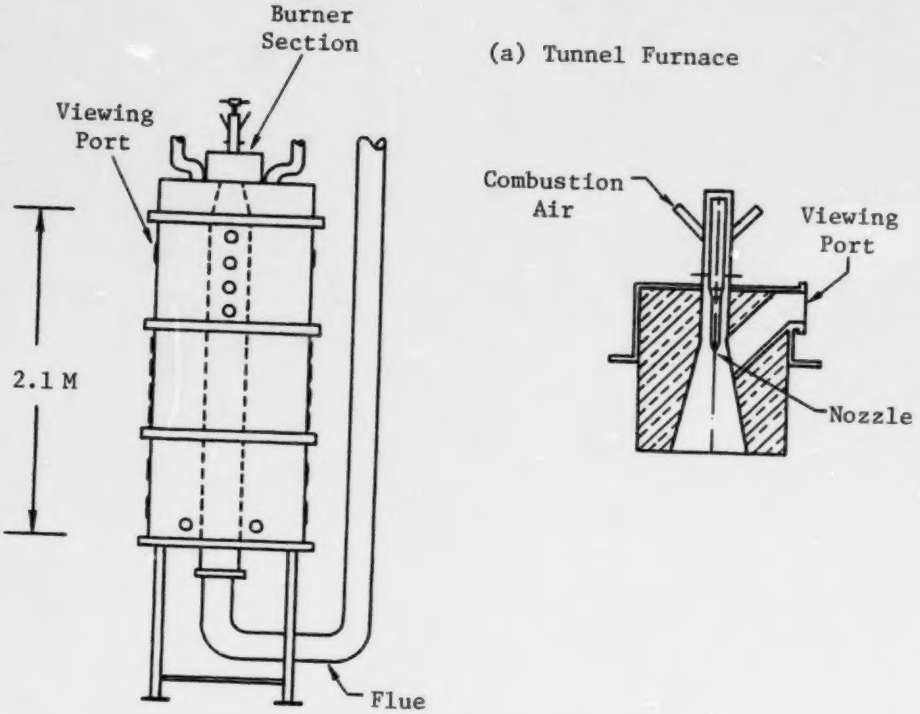

(a) Tunnel Furnace

(b) NO_x Emissions

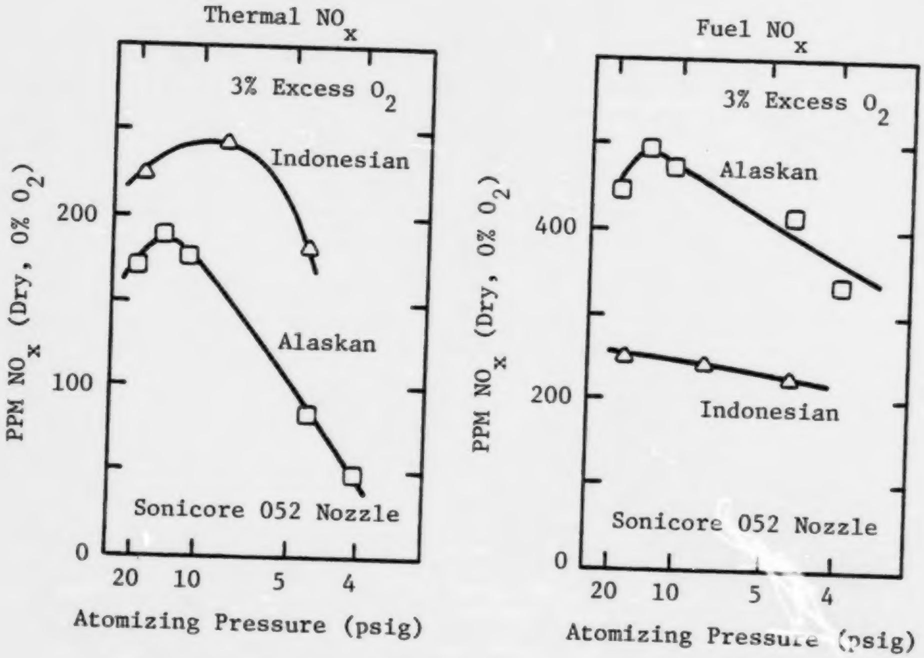

Figure 2. NO_x Emissions from a Tunnel Furnace.[2]

- laser diffraction
- laser visibility
- laser holography

This paper reports on progress made and the tasks remaining toward satisfying the immediate objective.

SECTION II

BACKGROUND

The results presented in Figures 1 and 2 prompted the conduct of a preliminary CRB study to assess the performance of the nozzles employed. The preliminary study was conducted in an existing cold flow chamber by the International Flame Research Foundation (IFRF) under subcontract to EER.

A schematic of the IFRF experiment is presented in Figure 3. A commercial laser diffraction particle sizing instrument (Malvern) was fixed in position, and axial traverses were conducted by moving the nozzle assembly up and down.

The laser diffraction technique, shown in schematic in Figure 3, was developed at the University of Sheffield[4]. A 2 mw laser beam is expanded and collimated to a 6.0 mm diameter beam for projection through the spray. Light from the beam is diffracted by droplets, the angle of diffraction depending on the particle size. (As the particle size decreases, the angle of diffracted light increases.)

The diffracted light is collected by a Fourier transform lens and focused on a 30 ring detector. The distribution of light across the 30 rings is read by a minicomputer and fit to a Rosin-Rammler distribution. The sweep time of the detector is approximately 13 ms. Usually 100 to 200 readings are required to obtain a representative, averaged reading.

The technique provides a size distribution for the droplets within the scattering volume. The technique does not measure individual drop sizes at a point, nor does the technique provide velocity information. This notwithstanding, it has the advantage of (1) providing droplet size information within minutes, and (2) being relatively simple in both the hardware and software.

An example of data provided by the laser diffraction technique is presented in Figure 4. Droplet size distributions at one axial location are presented in Figure 4a for the Sonicore nozzle employed in the tunnel furnace studies (Figure 2). The parameter in the plot is atomizing pressure. The data suggest that both the mean droplet size and size distribution are strongly dependent on atomizing pressure.

(a) Cold Chamber Experiment

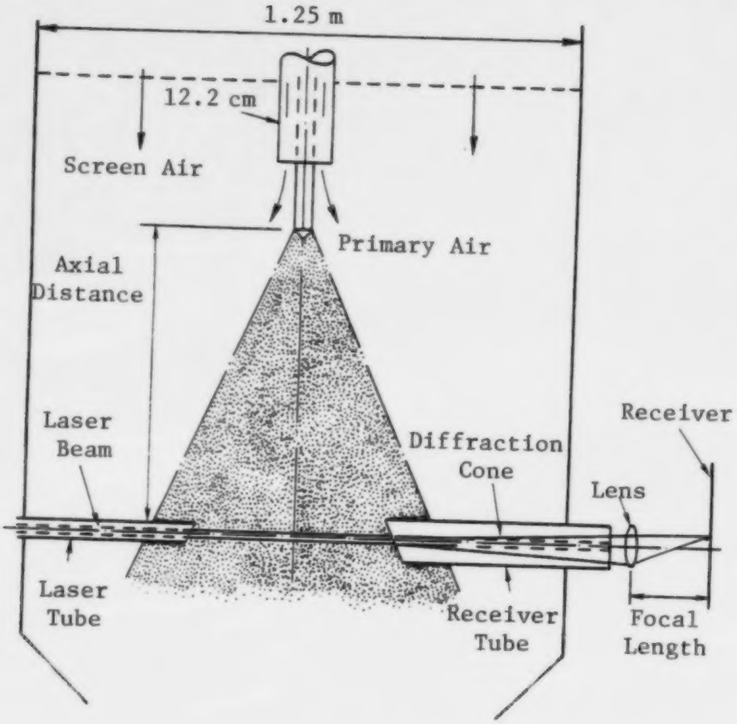

(b) Laser Diffraction Diagnostic

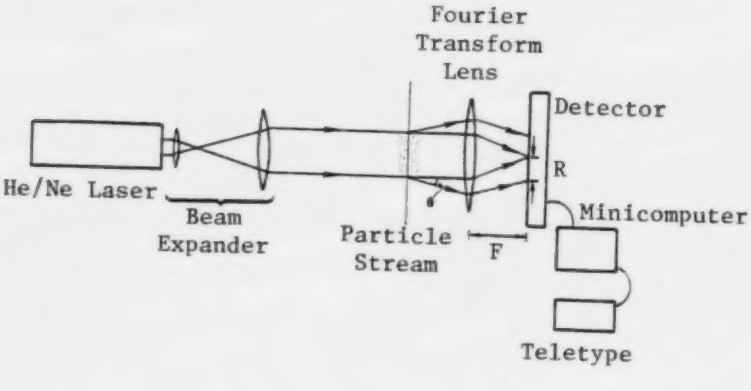

Figure 3. IFRF Spray Performance Study.[3]

(a) Droplet Size Distribution[6]

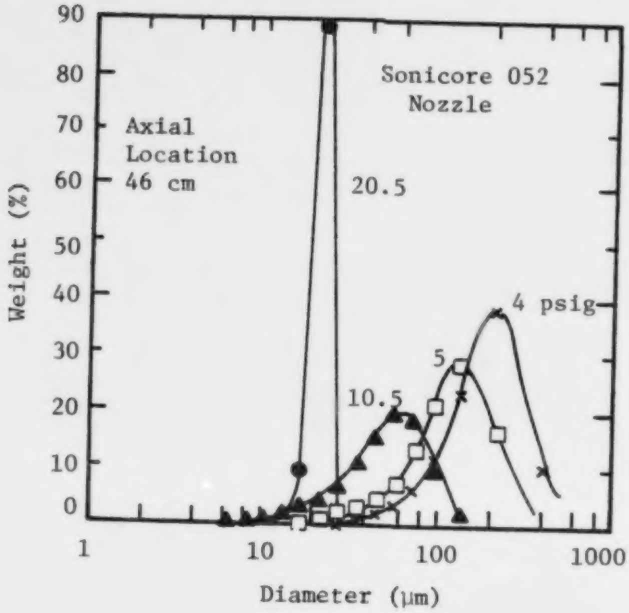

(b) Axial Variation[3]

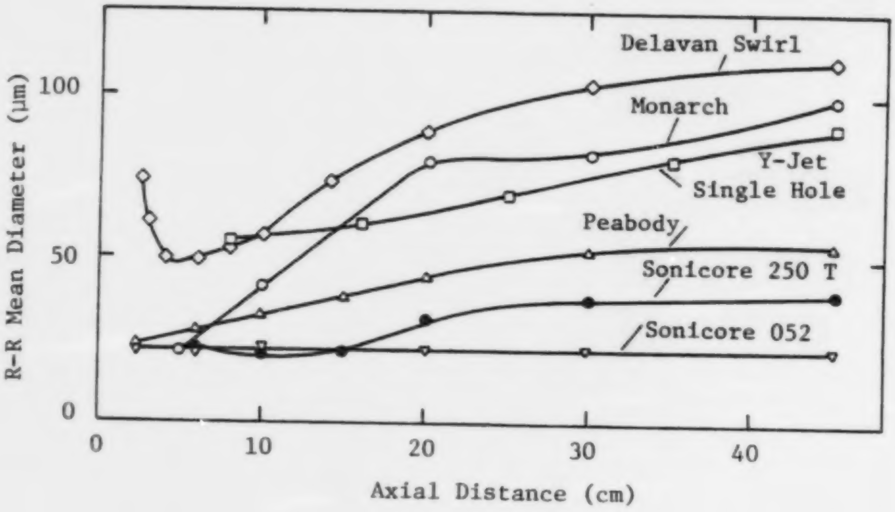

Figure 4. Droplet Size Results--Laser Diffraction.

In Figure 4b, the variation of Rosin-Rammler mean diameter with axial distance is shown. The effect of nozzle type on this variation is also demonstrated. Note that the nozzle employed in the tunnel furnace studies (Sonicore 052) exhibits no variation of mean diameter with axial distance.

The information provided by Figure 4a can be applied to the NO_x emission data from the tunnel furnace to provide some insight into the cause-effect relationship between nozzle and emission. From Figure 5, it is apparent that under the fuel-lean combustion conditions of the tunnel furnace larger droplets and/or broader size distribution contribute to lower NO_x emission. However, these data, though instructive, are not sufficient to fully assess the relationship of NO_x emission to nozzle performance. The additional information required includes spatial (axial and radial) resolution of droplet size and velocity of individual droplets. The immediate objectives of the present experiment are directed to evaluating the methods available for providing this additional information.

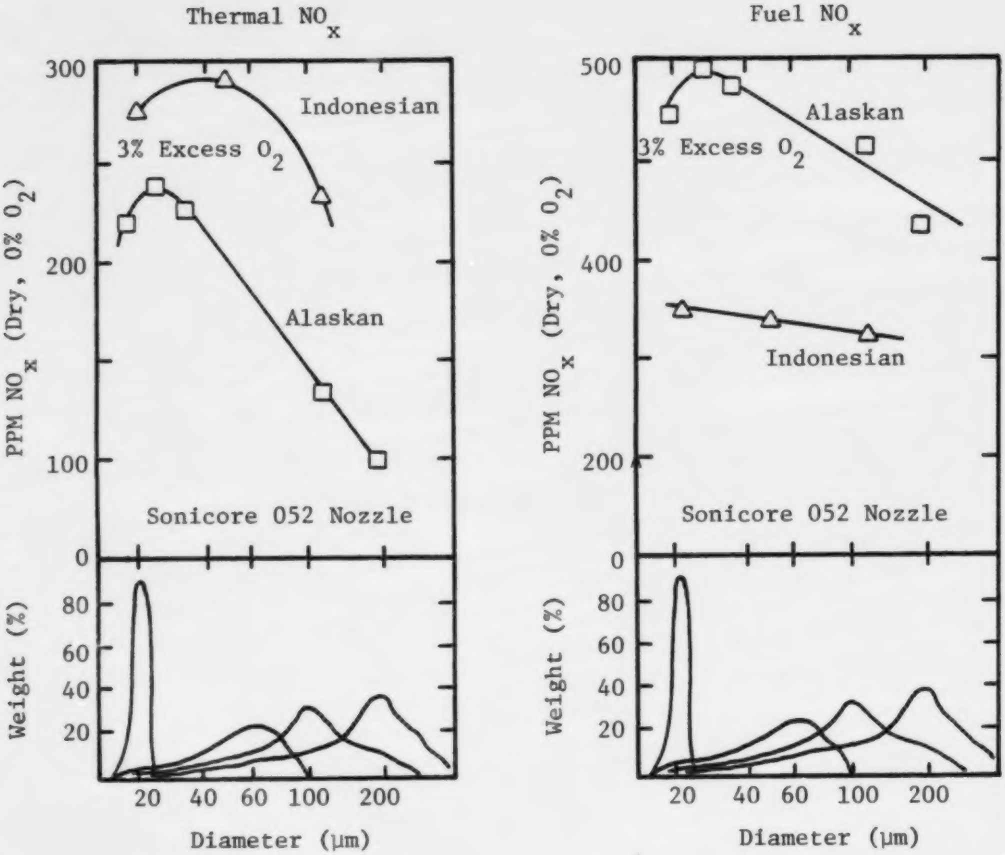

Figure 5. NO$_x$ Emission from a Tunnel Furnace--
Relationship to Drop Size and Distribution.

SECTION III

PRESENT EXPERIMENT

Facility

A schematic of the present experiment is shown in Figure 6. The cold chamber is shown in Figure 6. The cold chamber is patterned after the firetube combustor with respect to the diameter and the ability to accommodate a variety of inlet geometries and swirl. For the present inlet configuration, emphasis is placed on nozzle performance in the absence of both complex entry geometry and swirl. Screen air is introduced at a low velocity through a perforated disk to suppress recirculation of vapor mist, and primary air is introduced as an annular jet with outside and inside diameters of 12.7 cm and 2 cm respectively.

Particle Sizing Diagnostics

The following three nonintrusive laser techniques are being assessed and used to characterize spray performance:

- visibility
- holography
- diffraction

Visiblity is a point measurement technique and was selected because of the potential to (1) measure simultaneously droplet size and velocity, and (2) resolve spatially droplet size and velocity distributions. Holography provides an instantaneous, three-dimensional "picture" of the droplet field and was selected to check the visiblity and diffraction techniques. Diffraction was selected because, although velocity and spatial resoltuion are not provided, the technique has been extensively tested (e.g., Reference 6), is used by many investigators, and is relatively fast in providing processed data.

The responsibility for providing and operating the visibility and holography techniques is assumed by Spectron Development Laboratories under subcontract. A description of the two systems may be found in the following paper (Reference 7).

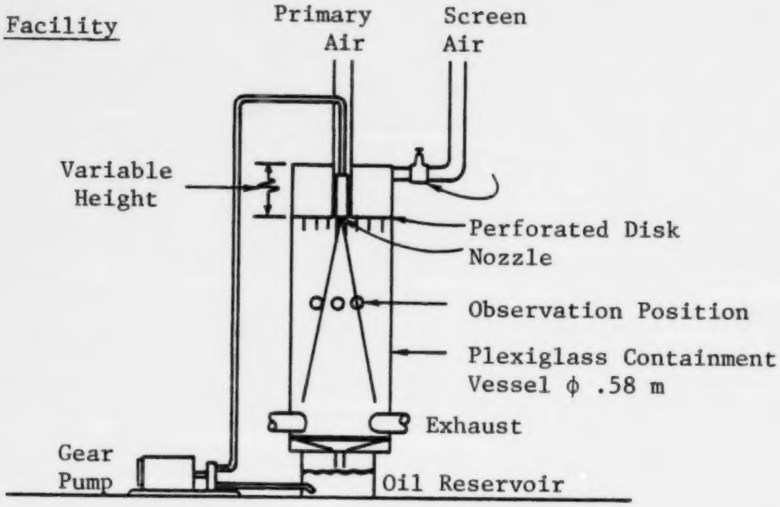

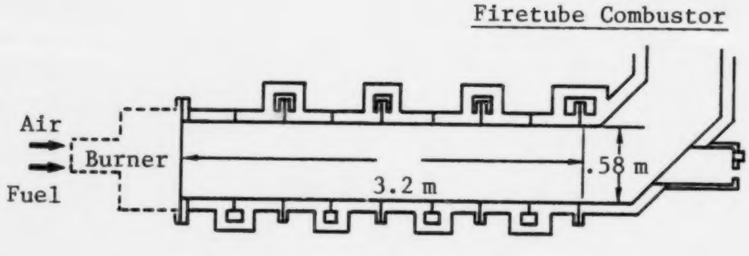

Figure 6. Present Experiment.

Test Matrix

The test matrix used to apply and assess the applicability of visibility and holography is presented in Figure 7 along with a cross section of the nozzle employed. The nozzle is a Sonicore 052 twin-fluid atojizer. Air is conveyed through the central core of the nozzle. The fuel oil is introduced downstream of the throat of a converging-diverging section. According to the manufacturer, "...as the gas expands through a converge-diverge section and into a reasonator cap at supersonic velocity, the reflected shockwaves focus the sonic energy between the resonator cap and the body of the nozzle. Fuel pumped into the stock wave is literally exploded into a fine, highly combustible mist."[8]

(a) Operating Conditions

- Nozzle: Sonicore 052
- Fuel: Diesel #2
- Fuel Rate (Gal/Hr): 0.5*, 1.0
- Atomizing Air Pressure (psig): 5, 10, 15, 20
- Primary Air (M/S): 0, 2.2, 5, 10, 18
- Screen Air (M/S): 0.4 M/S
- Axial Location: 2, 5, 10, 15, 20, 30, 40 CM
- Radial Location (Visibility): CL, ±½, ±1, ±1½-inch

* underline designates base condition

(b) Sonicore Nozzle

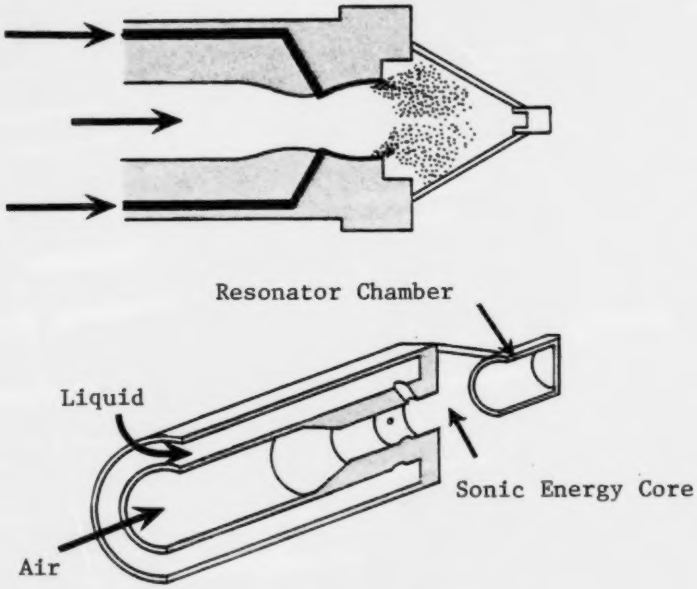

Figure 7. Test Matrix

SECTION IV

RESULTS

Visibility/Holography Assessment

The visibility and holography results and comparisons are provided in the following paper (Reference 7). The results have only recently been submitted,[9] and are presently under study. Selected data are presented below to (a) illustrate the value that spatially resolved size and velocity data can provide in the interpretation of sprays, and (b) identify the differences outstanding between the visibility and IFRF laser diffraction results.

Spray Performance

In addition to providing a comparative test for the visibility and holography measurement techniques, the test matrix was designed to provide a cursory examination of the spray performance of a select nozzle, in this case the Sonicore. Both radially and axially resolved droplet distribution data, and droplet velocity data were obtained.

Spatially Resolved Droplet Size Distributions. An example of spatially resolved size distributions is presented in Figure 8. In Figure 8a, distributions are presented at three axial locations (5, 10 and 20 cm), and three radial locations (0, 1.27 and 2.54 cm from the centerline). In Figure 8b, the volume mean diameter is plotted for these spatially located points. The results indicate that the mean diameter increases and the distribution broadens as radial distance increases from the centerline, and the mean diameter decreases and the distribution narrows as the axial distance from the nozzle increases.

Spatially Resolved Droplet Velocity. An example of spatially resolved droplet velocity data is presented in Figure 9 for two separate screen air velocities and one select droplet size (52.7 μm). The results indicate that droplets along the centerline relax to the terminal velocity at a rate substantially below the rate of those droplets radially displaced from the

(a) Spatial Variation of Size Distribution (5 psig)

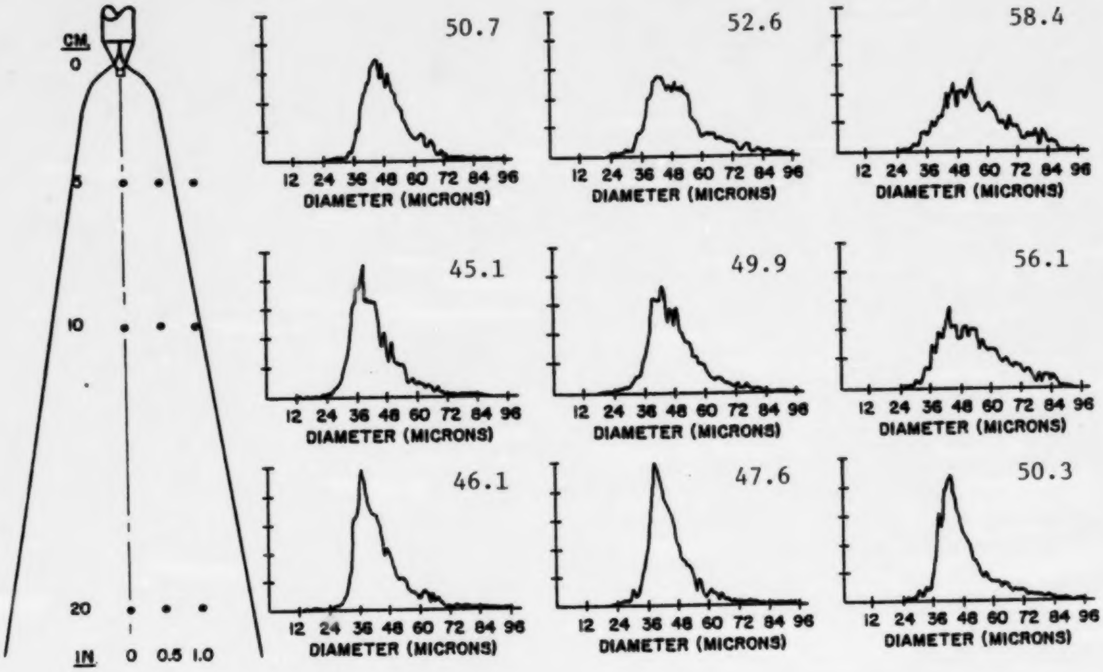

(b) Spatial Variation of Mean Diameter (5 psig)

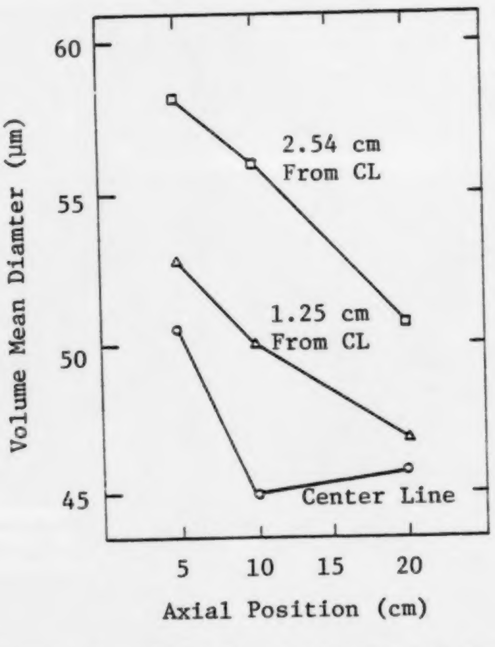

Figure 8. Visibility Results--Spatially Resolved Size Distribution.

(a) Screen Air Velocity, 2.2 m/sec (5 psig)

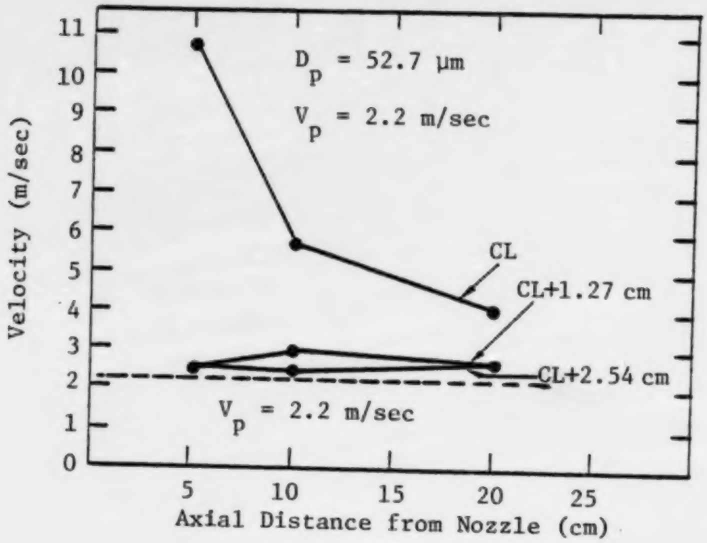

(b) Screen Air Velocity, 10 m/sec (5 psig)

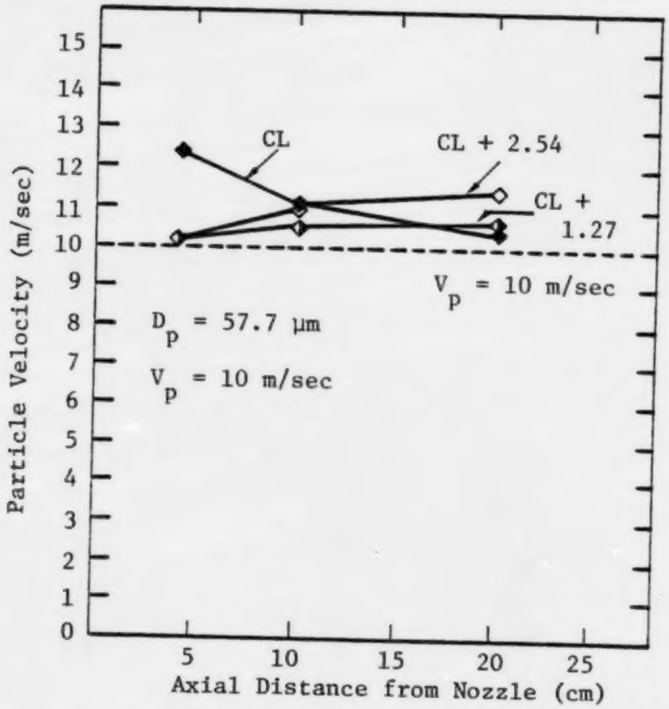

Figure 9. Visibility Results--Spatially Resolved Droplet Velocity.

centerline. These data are necessary to analyze and explain axial and radial variations in size distribution. Such an analysis for the present study awaits the resolution of inconsistencies between the visibility and IFRF diffraction data.

Comparison of IFRF and Visibility Data

A comparison of the IFRF and visibility data for the Sonicore nozzle is presented in Figure 10. It is apparent from this plot that the visibility technique measures a narrower distribution and a lower mean diameter than the diffraction technique. The possible reasons for these differences include (1) differences in the conduct of the two experiments, and (2) fundamental problems associated with the techniques, application of the techniques, and/or the analysis and interpretation of the measured data.

Differences in the Two Experiments. The differences in the two experiments that could potentially explain the differences in the results (Figure 10) include:

- Different Facilities — The IFRF chamber is 5 feet in diameter whereas the EER chamber is 2 feet in diameter.
- Different Nozzles — Although the same nozzle type was used in the two experiments, the identical nozzle was not employed in each experiment.
- Different Oil Type — The viscosities of the oils used for the IFRF diffraction and visibility experiments were 1.3 and 9.2 CST respectively.
- Differences in Data Plotted — The IFRF diffraction data plotted in Figure 10 represent the mean size distribution as viewed across the entire spray, whereas the visibility data plotted in Figure 10 represent the mean size distribution at the centerline of the spray. The data of Figure 8 indicate that the visibility data change little with radial distance. However, a few large droplets (dp > 100 μm) at radial distances greater than that included in the visibility data set (2.54 cm from the centerline) could significantly broaden the visibility-derived size distribution.

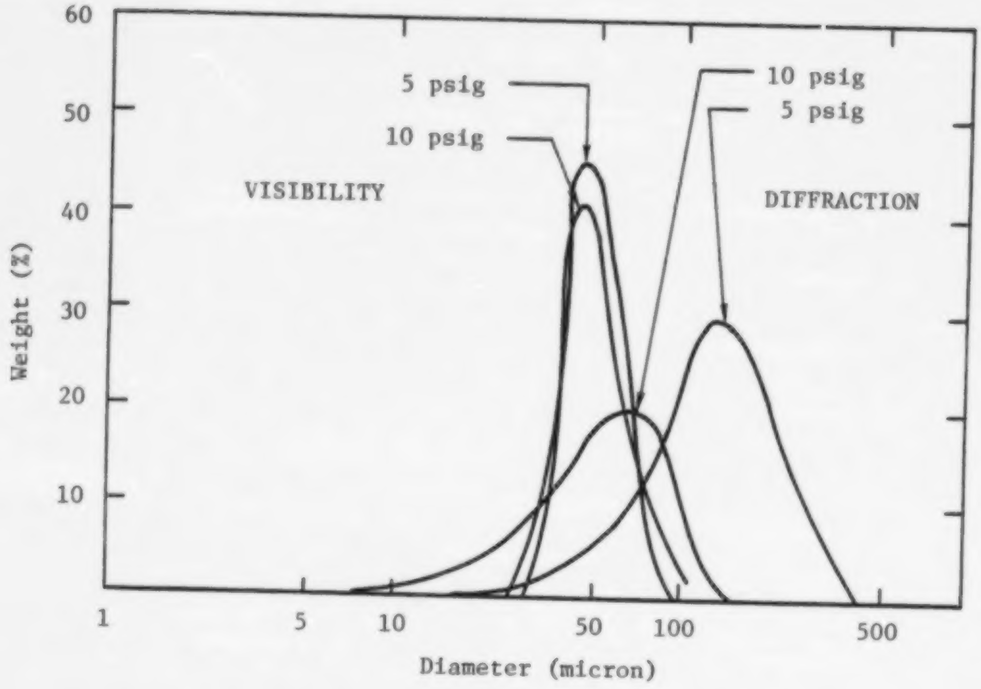

Figure 10. IFRF Diffraction and Visibility Results--Size Distribution.

Fundamental Problems with the Techniques. The fundamental problems associated with the techniques, application of the techniques, and/or the analysis and interpretation of the measured data that could potentially explain the differences in the results (Figure 10) include:

Laser Diffraction

- Assumed Size Distribution — The Rosin-Rammler size distribution may not be applicable to the spray used.
- Software — The software may have a deficiency (e.g., iteration method for optimization of size distribution fit). This is doubtful considering the extensive use and testing of the method.

Laser Visibility

- Signal Optimization — The steps employed in the present program to optimize the data rate may have preferentially filtered the larger size droplets.
- Dynamic Range — The dynamic size range of the visiblity system employed may be too restrictive to obtain the full size distribution. Problems were encountered with saturated signals on the large end of the distribution and with signals just below the sensitivity level on the small end.

Next Step

The next step is to resolve the differences between the visiblity and IFRF diffraction measurements of the Sonicore nozzle. The approach adopted is to use the laser diffraction technique in the EER cold chamber for the identical operating conditions, identical nozzle, and identical oil employed for the visibility tests. In addition, the holograms will be systematically surveyed to assess the presence and number density of large droplets (dp > 100 μm), especially at radial distances exceeding 2.54 cm. (This illustrates a benefit of laser holography. In this case, the holography provides a three-dimensional "photograph" of the spray field used for the visiblity tests. As a result, questions such as those raised, can be addressed with the benefit of a permanent record of the spray field.)

Upon resolution of the discrepancy, the nozzles evaluated in the firetube simulator studies will be characterized in the presence and absence of the conical inlet and swirl shown in Figure 1a. The cold flow studies will be followed by hot flow studies in a reactor with optical access and features similar to the cold spray chamber, namely the flexibility to introduce complex aerodynamics (i.e., recirculation and swirl) stepwise.

SECTION V

SUMMARY

A program has been established to explain the dependency of NO_x emission in fuel-oil combustion to atomizing nozzle type, and nozzle operating conditions. Toward this end, a cold chamber spray rig, patterned after the firetube simulator at EER, has been built for the purpose of characterizing nozzle spray behavior. As the initial step in the program, nonintrusive optical techniques are being applied and evaluated for (1) consistency of data measured, and (2) applicability to studying the spray behavior most likely important to NO_x emission. The optical techniques include diffraction, visibility, and holography.

At this juncture in the program, the visibility measurements have been concluded. Significant differences exist between these data and data acquired in an independent program conducted at the IFRF. The resolution of these differences is now in progress.

Once these differences are resolved, the nozzles earlier employed in the firetube combustor will be characterized in the cold chamber first without and then with the conical inlet and swirl vanes employed in the firetube combustor studies (Figure 1a). The program will then address the relation of nozzle performance to NO_x emission in a reactor equipped to introduce stepwise recirculation and swirl from a baseline operation in the absence of complex aerodynamics.

REFERENCES

1. England, G. C., M. P. Heap, R. T. Horton, D. W. Pershing, and G. Flament, "The Control of Pollutant Formation in Fuel Oil Flames -- The Influence of Oil Properties and Spray Characteristics," Proceedings of the Third Stationary Source Combustion Symposium; Volume II. Advanced Processes and Special Topics, EPA-600/7-79-050b, February 1979, p. 41.

2. Heap, M. P., D. W. Pershing, G. C. England, J. W. Lee, and S. L. Chen, "The Influence of Fuel Characteristics on Nitrogen Oxide Formation -- Bench-Scale Studies," Proceedings of the Third Stationary Source Combustion Symposium; Volume II. Advanced Processes and Special Topics, EPA-600/7-79-050b, February 1979, p. 3.

3. Flament, G., and R. Payne, "Effects of Fuel Properties and Atomization Parameters on NO_x Control for Heavy Liquid Fuel-Fired Package Boilers," Final Report, Subcontract EER-8317-1 (Energy and Environmental Research Corporation), IFRF Do. No. 3130110, August 1979.

4. Swithenbank, J., J. M. Beér, D. S. Taylor, D. Abbot, and G. C. McCreath, "A Laser Diagnostic Technique for the Measurement of Droplet and Particle Size Distribution," University of Sheffield, Department of Chemical Engineering and Fuel Technology Report HIC 245, 1976.

5. Flament, G., and R. Payne, "Sonicore Atomizers -- Measurements of Droplet Size Distribution," Progress Report Number 1, Subcontract EER-8317-1 (Energy and Environmental Research Corporation), IFRF Doc. No. 3131/1, June 1978.

6. Negus, C., and B. J. Azzopardi, "The Malvern Particle Size Distribution Analyzer: Its Accuracy and Limitations," Harwell Report AERE-R 9075, December 1978.

7. Hess, C. F., and W. D. Bachalo, "The Application of Droplet Sizing Interferometry and Holography to the Measurement of Spray Droplet Size and Velocity," in this volume, 1980.

8. Bulletin S-300, Sonic Combustion Systems, Pennsauken, New Jersey.

9. Hess, C. F., and W. D. Bachalo, "Characterization of a Sonicore Nozzle," Final Report, Subcontract EER-8318-9 (Energy and Environmental Research Corporation), Spectron Development Laboratories Report No. 80-6531.

THE APPLICATION OF DROPLET SIZING INTERFEROMETRY AND HOLOGRAPHY TO THE MEASUREMENT OF SPRAY DROPLET SIZE AND VELOCITY

C. F. Hess and W. D. Bachalo
Spectron Development Laboratories
Costa Mesa, California 92626

and

R. Seeker and G. S. Samuelsen
Energy and Environmental Research Corporation
Irvine, California 92714

Fifth EPA Fundamental Combustion Research Workshop
Newport Beach, California
January 23-25, 1980

ABSTRACT

Droplet sizing interferometry and laser holography are used in a fuel spray study. The size and velocity distributions of the fuel droplets produced by a sonicore nozzle in a cylindrical rig are obtained. The two techniques are evaluated and compared. The power and flexibility of the interferometer in the study of the fuel droplet size and velocity are demonstrated. The data obtained by the two techniques are compared and shown to agree very well.

SECTION I
INTRODUCTION

This paper discusses the application of two optical techniques used to characterize the droplet field produced by a sonicore nozzle under laboratory conditions. They are droplet sizing interferometry (DSI) and holography.

These techniques were used to obtain the size and velocity of fuel droplets in the presence of a surrounding air stream. The experiments were performed under cold conditions (no combustion) with an interest in droplet size and velocity correlations, size stratification and droplet evaporation. These parameters play an important role in the pollution formation and combustion efficiency of real combustion systems.

Because of the complex nature of the flow (two phases, small droplets, high number densities, recirculation, etc.) non-intrusive measuring methods must be used to avoid disturbing the flow. The methods must also have very high resolution since the droplets can be very small and move at high speeds. The techniques must be flexible enough to access the measuring volume from any direction since physical obstacles will be present in most combustion applications. Droplet sizing interferometry proved to be a very strong technique to study these fuel sprays, since it meets the criteria listed above. Holography was also used, since it provided a quick profile of the shape of the plume and its resolution was adequate to confirm the results obtained with the DSI.

The discussion of the nozzle behavior can be found in Reference 1 and the total collection of results is presented in Reference 2.

SECTION II

DESCRIPTION OF THE DROPLET SIZING INTERFEROMETER

Technique

In the DSI system, two laser beams are crossed at the position where the measurements are to be taken. This is called the probe volume. An interference pattern of dark and bright fringes (Figure 1) is formed at the probe volume. When droplets move across this interference pattern they project it to the plane of a collecting lens. This projection is a function of the droplet size. Figure 2 illustrates the interference pattern projected by a suspended droplet.

The light collected by the lens is concentrated into a photomultiplier tube that puts out an electric signal with the same time and amplitude variation as the scattered light. Two parameters of this signal provide the size and velocity information. They are the amount of modulation and the time that the droplet takes to travel between two bright fringes. Figure 3 illustrates how the signal produced by a small particle (compared to the fringe spacing) has a small amplitude but a large percent of modulation. The large particles on the other hand produce a large amplitude with little modulation.

This leads to the definition of visibility (V), which is a measurement of the amount of modulation:

$$V = 2\left|\frac{\int_{A_{lens}} \left|E_{s_1}\right| \left|E_{s_2}\right| \cos\sigma \, dA}{\int_{A_{lens}} \left\{\left|E_{s_1}\right|^2 + \left|E_{s_2}\right|^2\right\} dA}\right| , \qquad (1)$$

where E_{s_1} and E_{s_2} are the scattered field of the two laser beams, and σ is the phase angle between the two fields. Notice that these fields are integrated over the area of the lens, which is an indication of the importance of the F/# of the collecting lens in the definition of visibility. Since the scattered fields are functions of the droplet size [3], equation (1) provides a direct relationship between the droplet size and visibility.

The time between two bright fringes (inverse of Doppler frequency) is directly related to the velocity of the droplet. This relationship can be

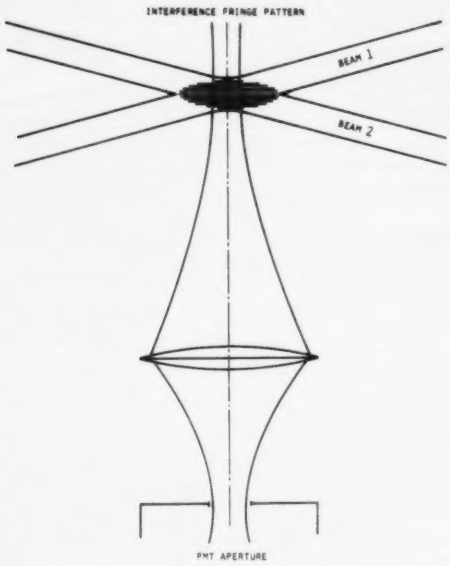

Figure 1. Probe Volume Formed by Crossing Two Laser Beams.

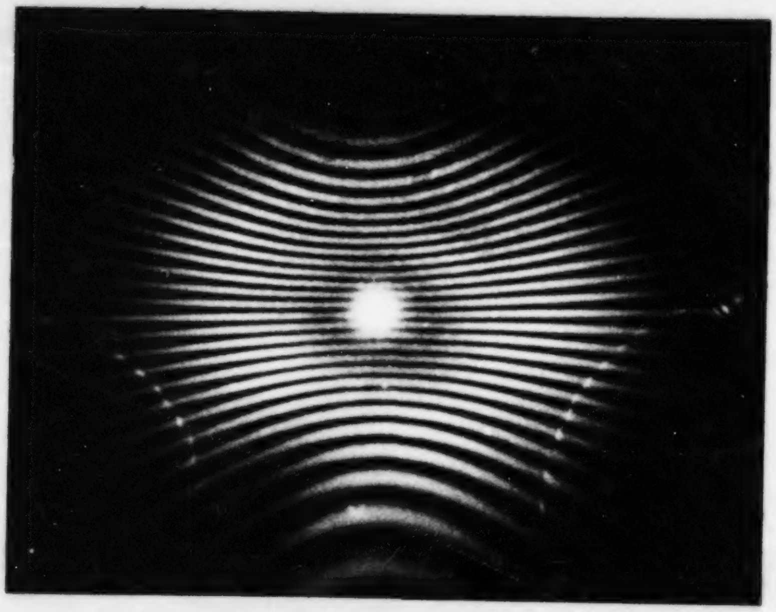

Figure 2. Fringe Pattern Projected in the Forward Direction by a Droplet.

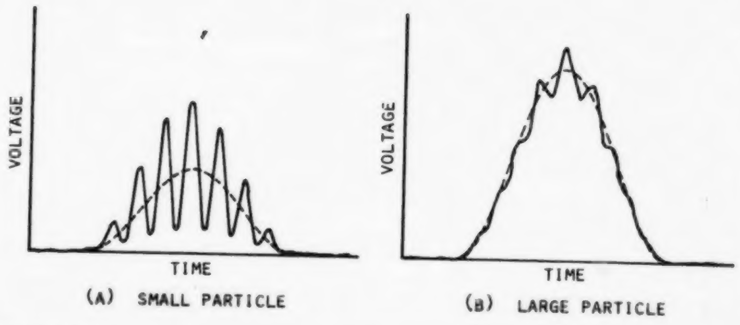

(A) SMALL PARTICLE (B) LARGE PARTICLE

Figure 3. The Effect of Particle Size on the Signal Visibility and Amplitude.

expressed by:

$$U = \frac{\delta}{t_D} \quad , \qquad (2)$$

where U is the velocity normal to the fringes, δ is the fringe spacing and t_D is the time between fringes. A complete description of the technique can be found in Reference [4].

Apparatus

The apparatus of the droplet sizing interferometer consisted of three separate items. The optical system, the VP-1000 signal processor and the DMS computerized system.

The optical system was constructed on a breadboard. It consisted of a HeNe laser, transmitting lenses, a diffraction grating, transmitting mirrors and collecting lenses. The laser beam is focused by L_1 on the diffraction grating (Figure 4). There, it is split into several beams according to the diffraction modes. Only the ± 1 modes are allowed through and the others are masked out. Since the lens L_2 is one focal distance from the diffraction grating, the beams coming out of L_2 are parallel and collimated. The ratio of L_2 to L_1 determines the beam diameter before it is focused by L_3. The separation of the beams is controlled by f_2. This provides an independent means of selecting the fringe spacing and the probe volume size. The laser beams are then focused by L_3 on the probe volume. This is the region in space where measurements are obtained. Figure 5 illustrates this probe volume in the presence of a fuel spray.

The light scattered by the particles crossing the probe volume is collected by L_4 and then focused by L_5 on the photomultiplier tube. Both the transmitting and the receiving optics are mounted on traverse mechanisms which allow them to scan throughout the plume at any one axial position. To change axial positions the nozzle was moved up and down.

The signal coming out of the photomultiplier is then processed in the VP-1000 signal processor. The Doppler frequency and the visibility is thus obtained. These parameters are then input to the data management system (DMS)

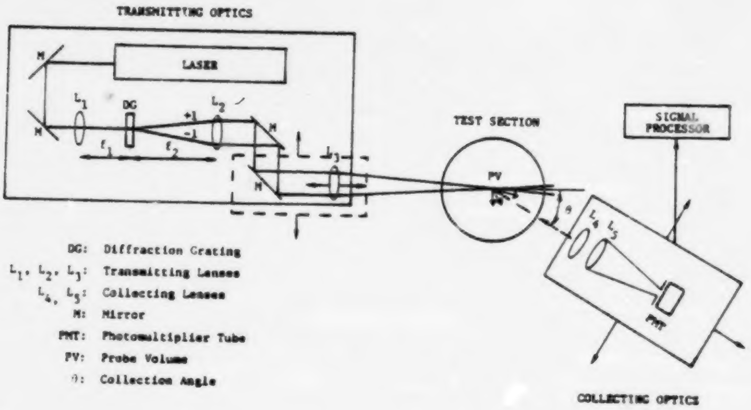

Figure 4. Schematic of Optical Apparatus for Droplet Size and Velocity.

Reproduced from
best available copy.

Figure 5. Photograph of Spray Nozzle with Crossing Beams.

which displays histograms of size and velocity and stores in diskettes the visibility and period of each droplet.

Photographs of the system are shown in Figures 6 and 7. Figure 6 shows the transmitting optics used in the experiments. The diffraction grating is mounted on an a.c. syncronous motor to provide frequency shift, if necessary. This feature was not used since the measured velocities were within the processor's range. The lenses and photomultiplier are mounted on a traversing platform.

The lenses in both the transmitting and collecting optics are achromats in order to minimize aberration. The transmitting mirrors are flat to one quarter wavelength.

The entire system including the test rig is shown in Figure 7. Notice that the incident laser beams and the scattered light travel through quartz windows located on the side of the plexiglass test rig. These windows were placed at a collection angle of 30° in order to obtain a small probe volume and a large scattered light intensity.

Figure 6. Photograph of Breadboard Model.

Figure 7. Interferometric System with Rig.

SECTION III

DESCRIPTION OF HOLOGRAPHY SYSTEM

Holography is a recording technique which stores for later reconstruction, all the coherent optical information that has passed through or reflected from a volume and subsequently fell upon a holographic plate. This information is mixed with a reference wave to produce a three-dimensional field. The technique is described in Reference [5].

Figure 8 shows a schematic of the transmitter and Figure 9 one of the receiver. The information or object beam goes through two glass windows into the test volume.

The system consists of a HeNe laser for alignment and a ruby laser to take the hologram. The laser beam is split into an information beam and a reference beam. Either beam is expanded, spatially filtered and collimated. The information beam goes through the fuel spray while the reference beam bypasses the test section. The two beams are then mixed on a holoplate in the plate holder.

The shutter in front of the plate holder only allows light to enter while the recording is taking place. This minimizes the influence of extraneous light sources. The room was kept dark as a precaution.

Figure 10 shows a photograph of the holocamera in the presence of the nozzle test rig. Ths transmitter and receiver are aligned in a forward scattering mode around the rig. Optical grade quarz windows of 7 cm diameter were placed on either side of the rig to transmit the information beam.

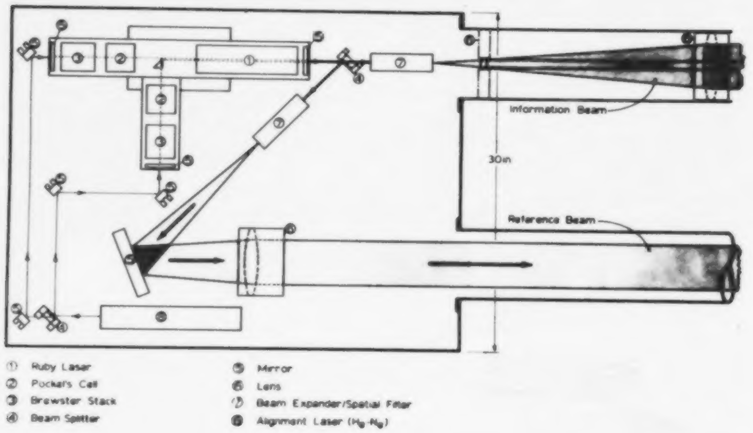

Figure 8. Holocamera System Transmitter Module.

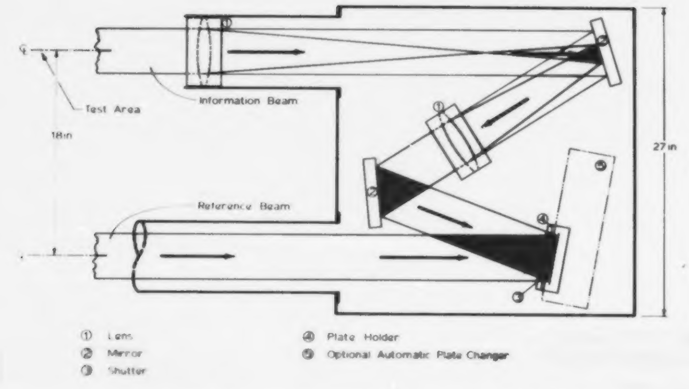

Figure 9. Holocamera System Receiver Module.

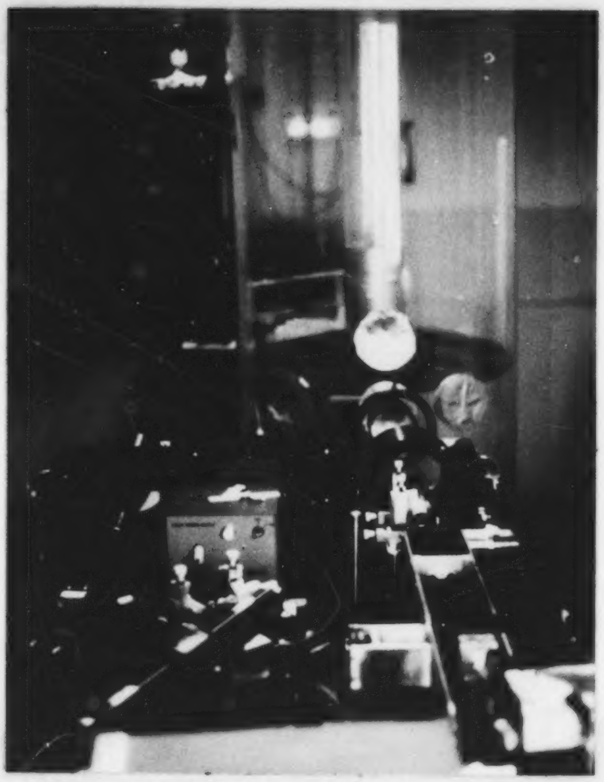

Figure 10. Photograph of Holographic Transmitter
with Nozzle Rig.

SECTION IV
RESULTS

Droplet Sizing Interferometer

The parameters used in the various experiments were selected to optimize the present size range, velocity range and number density. Figure 11 is the visibility versus size curve used in all the experiments.

This curve corresponds to a collection angle of 30°, a collection F/# of 5.3, a laser wavelength of 0.6328 µm and an index of refraction of 1.4, as indicated. The error due to index of refraction will be less than 6% (Reference [6]). Note that the average value of d/δ is 4.5. To optimize a given size range this value should correspond to the average diameter. Hence the value of δ is thus obtained. For example, if the average diameter is 45 µm, then $\delta = 10$ µm will be the best choice.

Notice that once the fringe spacing (δ) is selected, the velocity of any droplet can be obtained from equation (2), since the processor measures t_D. Typical values of δ used in these tests were 10 and 16 µm.

In the presence of very high number density flows (near nozzle exit), the probe volume was chosen very small (80 to 120 µm in diameter). This will reduce the probability of multiple particles being detected at the same time.

The data acquisition process was performed in the following way. The output of the photomultiplier tube which contained the signal scattered by individual droplets was processed in the VP-1000 signal processor. There, the visibility and Doppler period was extracted from these signals. These pairs of parameters were then digitized and sent to the data management system (DMS) after some validation checks were performed. The DMS displayed histograms of size and velocity or period and visibility, depending on the computer program used. These histograms, which are formed in a few seconds, provide a direct indication of the results. The data were then stored in diskettes to allow further analysis.

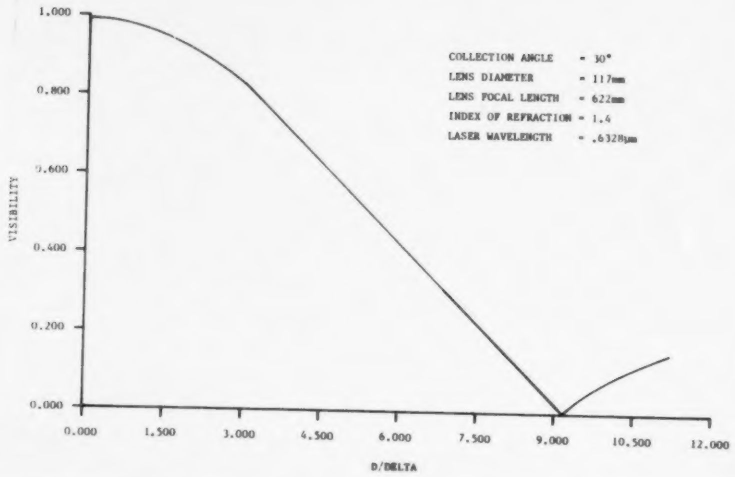

Figure 11. Relationship between Visibility and Droplet Size for Specified Parameters.

```
MAXIMUM FREQUENCY=0.1

N=3062
D10=50.6
D20=51.3
D30=52.1
D32=53.7
S=8.46
KURTOSIS=1.38
```

```
EERC/EPA DATA
SDL TASK11 RUN 8R
```

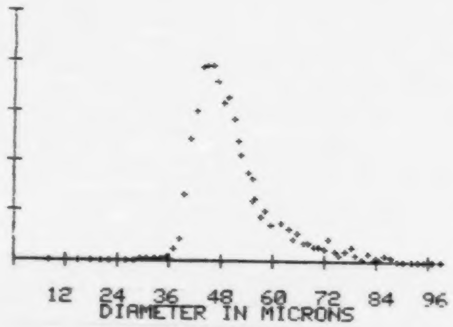

```
SIZE     COUNT
 98.9      0
 97.1      0
 95.4      0
 93.8      0
 92.2      0
 90.7      0
 89.2      0
 87.7      3
 86.3      5
 84.9      1
 83.5      2
 82.2      9
 80.9      2
 79.6      6
 78.3     16
 77.1     10
 75.8      6
 74.6     12
 73.4     25
 72.1     14
 70.9     17
 69.8     16
 68.6     21
 67.4     20
 66.2     32
 65.1     36
 63.9    39
 62.3     45
 59.6     44
 58.4     59
 57.2     53
 56.1     74
 55.5     72
 55.2    100
 54.6    106
 52.7    130
 52.2    147
 51.1    172
 49.9    199
 48.7    192
 47.4    218
 46.2    239
   45    239
 43.7    236
 42.4    183
 41.1    147
 39.8     79
 38.4     25
 37.1     13
 35.6      4
 34.2      2
 32.7      1
 31.2      1
 29.6      0
 27.9      0
 26.2      0
 24.3      0
 22.3      0
 20.2      0
 17.9      0
 15.3      0
 12.3      0
  8.2      0
```

Figure 12. Typical Droplet Size Histogram.

A typical size distribution is shown in Figure 12. The histogram and the table below show the number of droplets with a given size. The parameters under the histogram are various mean diameters (linear, surface, volumetric and sauter), the size standard deviation and the kurtosis. Figure 13 is an example of a size-velocity correlation. It indicates the velocity of different size particles. These measurements were made at various positions throughout the plume in an effort to study the relative shear of the different droplets and their trajectory. Typical average droplet size measured varied between 40 and 60 μm. The axial droplet velocities ranged from 2 to 12 m/s. These values depend on the conditions run and the position in the plume. A complete set of data can be found in Reference [2].

Holography

Holograms (single and double pulse), interferometric holograms and flash photographs were made to characterize the nozzle.

These measurements were made with the standard SDL holography system. A ruby laser provided a very short pulse (20 ns) capable of recording very fast moving objects. The images were premagnified up to three times to increase the resolution. The diameter of the holograms was 7 cm.

Measurements were made both at the plume and the exit of the nozzle. To vary the axial position, the nozzle was moved up and down. The radial variation is contained in the three dimensional recording of the droplet field.

Due to the high number density and dirt on the windows, the smallest resolvable droplet was about 15 μm. Data were recorded in the form of glass plates that were later reconstructed and analyzed. Photographs of some reconstructed holograms were made to simplify the data reduction. However to obtain the size of the droplets it was preferred to use the actual hologram since it provided higher resolution and the 3-D effect could be used to distinguish small droplets from speckle.

Figures 14 and 15 are photographs of reconstructed holograms of the fuel spray. Figure 14 shows the flow field near the exit of the nozzle for a pressure of 10 psi. There, ligaments are breaking into droplets. Figure 15

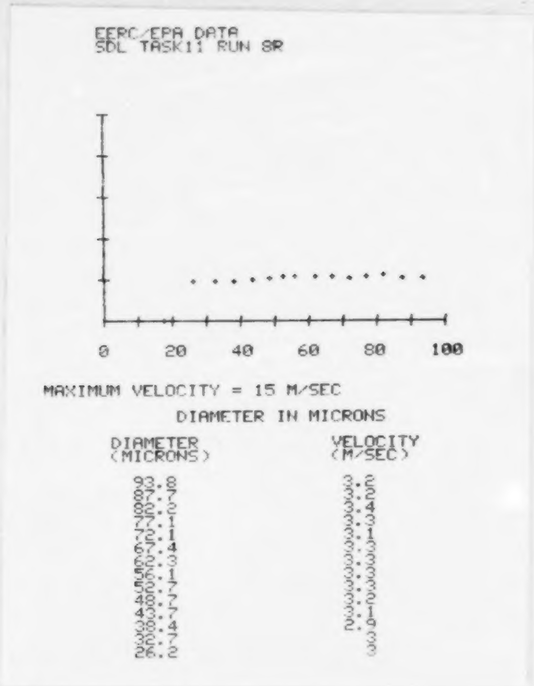

```
EERC/EPA DATA
SDL TASK11 RUN 8R

MAXIMUM VELOCITY = 15 M/SEC
          DIAMETER IN MICRONS

   DIAMETER             VELOCITY
   (MICRONS)            (M/SEC)

     93.8                 3.2
     87.7                 3.2
     82.2                 3.4
     77.1                 3.3
     72.1                 3.1
     67.4                 3.3
     62.3                 3.3
     56.1                 3.3
     52.7                 3.3
     48.7                 3.2
     43.7                 3.1
     38.4                 2.9
     32.7                   3
     26.2                   3
```

Figure 13. Typical Droplet Velocity-Size Correlation.

Figure 14. Photograph of Hologram near Nozzle Exit Pressure of 10 psi, Primary Velocity of 2.2 ms.

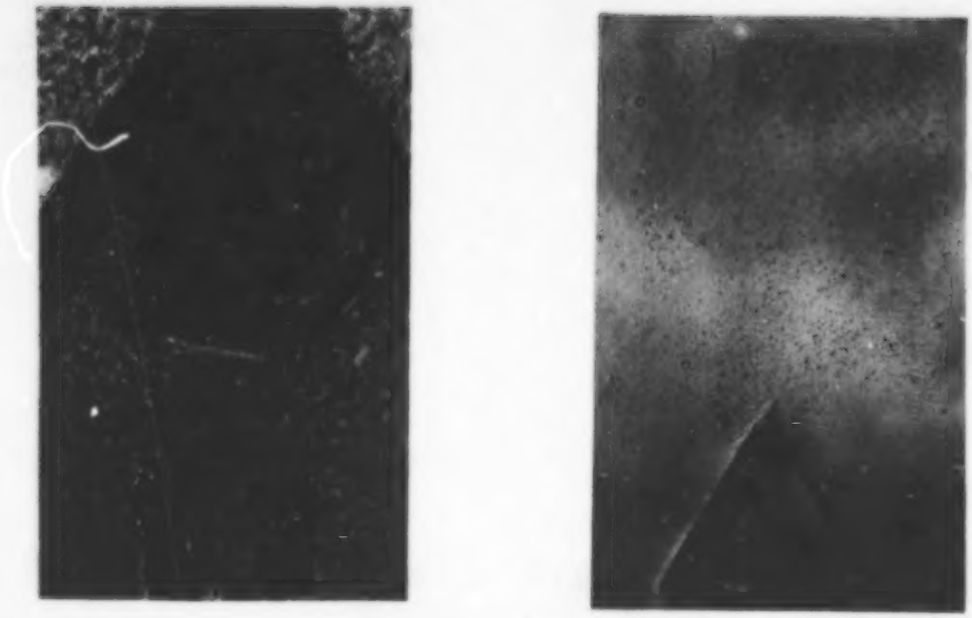

Figure 15. General View and Closeup of Spraying Nozzle Pressure of 5 psi, Primary Velocity of 10 ms.

shows the same nozzle, but the pressure is 5 psi. Notice that most of the ligaments in this case are still unbroken when they hit the resonator cup. The entire droplet field can be seen on Figure 15b.

Interferometric holograms were made near the resonator cup in an effort to define the shock wave produced there. This shock was not observed which leads us to believe that the holograms did not have enough resolution due to the large distance traveled.

Comparison Between Holography and DSI Data

The size of the droplets was estimated from several holograms corresponding to the conditions run with the DSI. A microscope objective with a graduated reticle was used to measure and count the droplets. Bins, 30 μm wide, were thus obtained. This number is an indication of the error (± 15 μm) associated with the holographic data. Both the DSI and holography data were normalized to the maximum number of counts. The results are plotted in Figure 16.

The curves agree well. The mode in both cases is identical and the shape of the curves is very similar. There is a natural tendency, during the analysis of a hologram, to search for the larger particles since they are immediately caught by the eye. This causes the shift to the larger sizes in the holography data.

Although both methods can provide the droplet size distribution, DSI is a more powerful technique to study fuel sprays. It can measure both the size and the velocity of the droplets at very high data rates. Since the signals are electronically processed, considerable data analysis can be performed with a minimum of human interaction. Holography will be very attractive in the study of irregularly shaped objects and multi-phase flows.

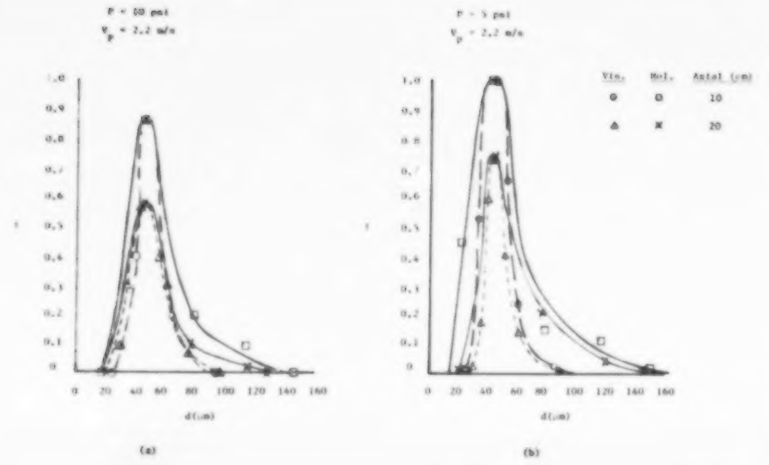

Figure 16. Holography and Visibility Data of Fuel Spray Nozzle Within 0.5 Inch of Centerline and Various Axial Positions.

SECTION V

CONCLUSIONS

1. The DSI instrument proved to be very powerful to study fuel sprays.
    - It measures the size and velocity of individual droplets.
    - It is a point measurement.
    - Distinguishes air velocity from droplet velocity.
    - Provides immediate data display.
    - System is adaptable to various spray rig configurations.
2. Holography is adequate for sizing droplets but the analysis of holograms is very time consuming.
3. The results obtained using holography and DSI compared very well.
4. All the above factors combined to produce a successful program at EERC.

REFERENCES

1. Seeker, W. R. and Samuelsen, G. S., "Spray Characterization", in this volume, 1980.

2. Hess, C. F. and Bachalo, W. D., "Characterization of a Sonicore Nozzle," Final Report to EERC, SDL No. 80-6531, 1979.

3. van de Hulst, H., "Light Scattering by Small Particles," John Wiley & Sons, Inc., New York, 1957.

4. Bachalo, W. D., "A Method for Measuring the Size and Velocity of Spheres by Dual Beam Scatter Interferometry," submitted to Applied Optics, 1979.

5. Trolinger, J. D., "Particle Field Holography," Applied Optics, Vol. 14, No. 5, 1975.

6. Bachalo, W. D., Hess, C. F. and Hartwell, C. A., "An Instrument for Spray Droplet Size and Velocity Measurements," presented at ASME Winter Meeting at New York, December 1979.

CHARACTERIZATION OF LONG TURBULENT PULVERIZED COAL DIFFUSION FLAMES

R. Payne
International Flame Research Foundation
IJmuiden, Holland

Fifth EPA Fundamental Combustion Research Workshop
Newport Beach, California
January 23-25, 1980

No manuscript for this presentation was received at the time of the meeting. A final report on the subject subcontract is included in the FCR Program Final Report Series.

SESSION V

MODEL DEVELOPMENT

T. J. TYSON
SESSION CHAIRMAN

DEVELOPMENT OF A COHERENT FLAME MODEL FOR TURBULENT CHEMICALLY REACTING FLOWS

F. E. Marble
California Institute of Technology
Pasadena, California 91109

and

J. E. Broadwell
Engineering Sciences Lab
TRW, Inc.
Redondo Beach, California 90278

Fifth EPA Fundamental Combustion Research Workshop
Newport Beach, California
January 23-25, 1980

ABSTRACT

The coherent flame model is applied to the methane-air turbulent diffusion flame with the objective of describing the production of nitric oxide. The example of a circular jet of methane discharging into a stationary air atmosphere is used to illustrate application of the model. In the model, the chemical reactions take place in laminar flame elements which are lengthened by the turbulent fluid motion and shortened when adjacent flame segments consume intervening reactant. The rates with which methane and air are consumed and nitric oxide generated in the strained laminar flame are computed numerically in an independent calculation.

The model predicts nitric oxide levels of approximately 80 parts per million at the end of the flame generated by a 30.5 cm (1 foot) diameter jet of methane issuing at 3.05×10^3 cm/sec (100 ft/sec). The model also predicts that this level varies directly with the fuel jet diameter and inversely with the jet velocity.

A possibly important nitric oxide production mechanism, neglected in the present analysis, can be treated in a proposed extension to the model.

ACKNOWLEDGEMENT

The authors wish to acknowledge an essential contribution of the technical staff of the Energy and Environmental Research Corporation to this work.

I. CONCLUSIONS

A theoretical model of a turbulent diffusion flame has been developed and applied to a methane jet burning in air. The model predicts nitric oxide levels of approximately 80 parts per million at the end of the flame generated by a 30.5 cm (1 foot) diameter jet of methane issuing at 3.05×10^3 cm/sec (100 ft/sec). In the model this level varies directly with the fuel jet diameter and inversely with the jet velocity. A possibly important nitric oxide production mechanism, neglected in the present analysis, can be treated in a proposed extension to the model.

II. RECOMMENDATIONS

Additional experimental data describing nitric oxide production in turbulent methane-air flames of different dimensions is needed to assist in the establishment of the scaling laws. Such data would also allow a critical assessment of the present state of the coherent flame model and guide its further development. It is recommended that such experiments and the proposed extension of the model be carried out.

III. INTRODUCTION

The coherent flame front model (Ref. 1) is a description of fast chemical reactions in turbulent flow in which the reactions are assumed confined to thin flame surfaces. The turbulent flame structure then consists of a distribution of these surface elements. The model describes the manner in which the flame elements are stretched and dispersed by the turbulent motion, as well as the mechanism by which neighboring flame surfaces consume the intervening reactant and annihilate each other. These processes are shown schematically in Figure 1. A considerable advantage of the coherent flame model is that it effectively separates the detailed structure of the laminar flames from the fluid mechanics so that systems with complex chemical reactions may be treated nearly as easily as simple ones.

The work to be described here treats the methane-air flame and the attendant production of nitric oxide. The individual flame surfaces have internal distributions of temperature and reactants that favor the production of nitric oxide. The nitric oxide so produced diffuses back out of the heat zone into the cooler portions of the flame surface structure. The production then appears as that stored in the flame surface as well as that deposited in the products resulting from flame annihilation.

Now it is clear that the mechanism described above neglects the nitric oxide produced "in the bulk" which, in the present picture, consists of the products resulting from flame annihilation, slowly mixing with unconsumed reactants. The additional production is of two parts: 1) that generated in the products and 2) that generated in flames supported by reactants contaminated by combustion products. In the following work, an effort has been made to account for the second of these, that due to "re-processing" the reaction products. The first requires a major effort to account properly for this mechanism and, while an outline of the proposed technique is given, no implementation of calculations have been performed.

IV. THE FLAME STRUCTURE MODEL

For purposes of this analysis, the turbulent flame is assumed to consist of a distribution of laminar diffusion flame elements. The fuel and oxidizer, which exist on one or the other side of the flame element, are either the pure gases--the injected fuel and the ambient oxidizer--or fuel and oxidizer that has been diluted by thorough mixing with combustion products.

To make this picture quantitative, we define the flame surface density Σ to be the flame surface area per unit volume. Both in this concept and in the assumptions of the flame elements, the dimensions of the flame surface are very large in comparison with its thickness, so that the characterization of the structure by the flame surface area is reasonable. The local flame surface density is altered by three processes: 1) flame surface production resulting from fluid straining motions in the plane of the flame, 2) turbulent transport by which flame elements are carried from one region of the fluid to another by large scale turbulent fluctuations, and 3) flame annihilation, in which flame surfaces consume the intervening fuel or oxidizer with the result that these flame surfaces vanish.

The flame surface elements that are involved in this representation are not the usual laminar diffusion flame structures, but are dominated by the straining motions of the reactants in the plane of the flame. In this circumstance, the structure of the flame is no longer time-dependent, but is fixed by the local straining rate of the fluid. Then $\varepsilon \sim 1/\text{time}$ is the straining rate, and $D \sim (\text{length})^2/\text{time}$ is the molecular diffusion coefficient, then the flame assumes a local thickness $\sim \sqrt{D/\varepsilon}$ and consumes reactants at a volumetric rate $\sim \sqrt{D\varepsilon}$ per unit flame surface area. If the strain rate ε varies from point to point in the turbulent region, or varies with time as one follows the fluid mass, then the flame will be assumed to vary its structure in a quasi-steady manner. This theory of time-dependent diffusion flames in a straining gas motion is given in Appendix A.

When the flame surface density Σ and the strain rate ε are known locally, the reactant consumption rates within this region are known also because they are fixed by the flame structure. The actual flame structure may be calculated to any degree of approximation between the simplest, where the chemical reaction rates are very rapid so that the reactant consumption is controlled by molecular diffusion, to the detailed structure involving the complete chemistry with appropriate rates. The flame structure with finite rates requires numerical calculation, but, because it is a steady one-dimensional problem, the actual calculations may be accomplished with relative ease.

The appropriate form of the equation describing the flame surface density may be deduced from first principles by considering the distortion and migration of surface elements, fixed to the fluid, in a turbulent medium (Ref. 2). Here, it will be sufficient to motivate the form by physical reasoning and then to suggest the manner in which the various terms scale with features of the flowfield and the chemistry of the flame structure. Now in a fluid with mean velocity components U_i, the expression

$$\frac{D\Sigma}{Dt} \equiv \frac{\partial\Sigma}{\partial t} + U_j \frac{\partial\Sigma}{\partial x_j}$$

gives the change in flame density following a mean fluid element. According to our model described earlier, this change may be written in the following form

$\frac{D\Sigma}{Dt}$ = turbulent diffusion of flame surface into the region

+ increase of individual surface element area by turbulent straining motions

− reduction in flame surface resulting from local consumption of one of the reactants.

In these calculations, the turbulent diffusion of flame surface will be described using a turbulent diffusivity and the assumption that the turbulent fluctuation velocities are large in comparison with molecular diffusion velocities, familiar from usual turbulent treatments of heat and mass transport. Thus, if we denote $\mathcal{D}$ the turbulent diffusion coefficient that arises in the description of momentum exchange, the turbulent diffusion term applicable to the treatment of the turbulent circular jet, which we treat as our example, is

$$\frac{1}{r}\frac{\partial}{\partial r}\left(r\,\mathcal{D}\,\frac{\partial\Sigma}{\partial r}\right)$$

where the appropriate boundary layer approximation has been made. The rate of increase of an element of flame surface area is proportional to the strain rate in the turbulent fluctuations. Under the assumption that this strain rate is proportional to the rate of strain in the mean motions, the rate of increase in flame surface density is thus proportional to the product of the strain rate of mean motion and the local flame density. Then, calling α the unknown constant of proportionality, we take the second term on the right equal to

$$\varepsilon \Sigma \equiv \alpha \left|\frac{\partial W}{\partial r}\right| \Sigma$$

where, again, we have written the term in the form appropriate to the circular jet, W being the velocity component of the mean motion in the direction of the symmetry axis.

The general nature of the process by which flame surface is removed from the field is best pictured by considering two neighboring laminar diffusion flame fronts parallel to each other and containing one constituent, say, fuel, between them. As the motion progresses, the intervening fuel is consumed and both elements of flame surface are extinguished. A similar process takes place if the intervening constituent is the oxidizer. To make the mechanism quantitative consider a volume containing many flame elements. The fraction of local volume occupied by fuel is proportional, under our assumption of constant density, to the mass fraction κ_1 of fuel. Moreover, the rates of reactant consumption by an element of laminar flame are presumed known from detailed calculations of that flame structure. If we call v_1 the volume rate of consumption of fuel per unit flame area, the rate at which volume occupied by fuel is being consumed in a unit volume of space is $v_1 \Sigma$. But that unit volume of space contains only a fraction κ_1 of fuel so that the rate of fuel consumption in a unit volume of space divided by the amount of fuel contained in that volume is $v_1 \Sigma/\kappa_1$. Thus, if the flame surface area is nearly uniformly distributed over the region, this expression gives also the fractional rate of flame surface annihilation so that the flame surface area reduction rate due to fuel consumption is

$$(v_1 \Sigma/\kappa_1) \Sigma = \frac{v_1}{\kappa_1} \Sigma^2$$

In a completely similar manner, we may reason that the flame surface area reduction due to consumption of oxidizer is proportional to

$$\frac{v_2}{\kappa_2} \Sigma^2$$

and because in a given region, individual surface elements are being removed by either the exhaustion of fuel or of oxidizer, the two expressions will be considered independent and additive.

If now we collect the various terms that have been discussed, it is possible to write in detail the conservation equations for flame surface density

$$U \frac{\partial \Sigma}{\partial r} + W \frac{\partial \Sigma}{\partial z} = \frac{1}{r} \frac{\partial}{\partial r} \left(r \, D \frac{\partial \Sigma}{\partial r} \right) + \varepsilon \, \Sigma - \lambda \frac{v_1}{\kappa_1} \Sigma^2 - \lambda \frac{v_2}{\kappa_2} \Sigma^2 \qquad (1)$$

The form of equation has been chosen to be that appropriate for the analysis of the circular jet.

The conservation equations for the individual species are conventional except for the terms describing the reactant consumption by chemical reaction. These will be given in terms of the flame surface density and the reactant consumption for a unit flame surface supplied by one-dimensional flame calculations. For the fast chemical reaction, we need consider only three constituents, the fuel κ_1, the oxidizer κ_2, and the product κ_3, related by the fact that the sum of mass fractions is unity

$$\kappa_1 + \kappa_2 + \kappa_3 = 1 \qquad (2)$$

so that only two of these, κ_1 and κ_2, need be treated in detail. The actual chemistry, in contrast to the overall reaction between fuel and oxidizer, is contained within the one-dimensional flame structure.

The consumption rate of fule per unit volume is simply the product of the effective influx velocity v_1, the flame surface density Σ, and the mass fraction κ_1^* of fuel in the fuel-containing constituent of the turbulent structure. The conservation equation for fuel may be written down directly as

$$U \frac{\partial \kappa_1}{\partial r} + W \frac{\partial \kappa_1}{\partial z} = \frac{1}{r} \frac{\partial}{\partial r} \left(r \, D \frac{\partial \kappa_1}{\partial r} \right) - \kappa_1^* \, v_1 \, \Sigma \qquad (3)$$

Similarly, the conservation equation for the oxidizer component is

$$U \frac{\partial \kappa_2}{\partial r} + W \frac{\partial \kappa_2}{\partial z} = \frac{1}{r} \frac{\partial}{\partial r} \left(r \, D \frac{\partial \kappa_2}{\partial r} \right) - \kappa_2^* \, v_2 \, \Sigma \qquad (4)$$

It remains to define the consumption rates v_1 and v_2 for the fuel and oxidizer components. Regardless of whether these quantities are defined through use of infinitely fast reaction rates or by detailed calculation of the one-dimensional flame structure, they depend upon the reactant concentrations on each side of the flame, κ_1 and κ_2, and the local strain rate ε of the mean flow. It is this latter item which couples the local diffusion flame structure to the gasdynamic structure.

V. THE TURBULENT CIRCULAR FUEL JET

The detailed solution for a turbulent flame structure described in the manner outlined in the previous section requires a turbulence model for the mean flow and, because there is a choice of turbulence model to be used, it is preferable to go directly to the example of interest rather than describe the procedure in general. For the problem of the circular fuel jet, we shall choose the elementary model utilizing a scalar turbulent diffusivity. Furthermore, we shall, in the interests of simplicity, neglect the change of mean gas density associated with the chemical reactions. This restriction in no way implies that the density change is a negligible factor. Rather the use of a turbulence model for flows of non-uniform density introduces a degree of uncertainty of its own which makes it additionally difficult to judge the merits of the flame model.

Under these restrictions, the gasdynamic field is described by the equations

$$\frac{1}{r}\frac{\partial}{\partial r}(rU) + \frac{\partial W}{\partial z} = 0 \tag{5}$$

$$U\frac{\partial W}{\partial r} + W\frac{\partial W}{\partial z} = \frac{1}{r}\frac{\partial}{\partial r}\left(r\,\frac{\tau_{rz}}{\rho}\right) \tag{6}$$

where the pressure of the far field has been assumed constant. Using the eddy-diffusivity model for the turbulent shear stress τ_{rz}, we write

$$\frac{\tau_{rz}}{\rho} = \mathbf{D}\frac{\partial W}{\partial r} \tag{7}$$

where $\mathbf{D}$ is the turbulent analogue to the kinematic viscosity. The customary difficulty arises here in the choice, rather than the determination, of the eddy diffusivity. For the circular jet, however, the choice is made simpler by the fact that the jet momentum, which is conserved along the direction of flow, has the dimension of $(\text{velocity})^2 \times (\text{length})^2$. And because $\mathbf{D}$ has the dimension of (length) x (velocity), there being no other characteristic dimensions in the problem, it is evident that the turbulent diffusivity is proportional to the square root of the jet momentum, and hence is a constant.

It is possible to find a similarity solution for the turbulent jet, or more properly for a point momentum source. To carry this out, it proves convenient to introduct a modified radial dimension

$$\eta = \sqrt{\frac{3}{8}}\,\frac{\sqrt{\mu}}{D}\,\frac{r}{z} \tag{8}$$

where μ is the constant jet momentum flux

$$\mu = \int_0^\infty W^2\, r dr \tag{9}$$

The stream function ψ, with the usual properties that $U = -\frac{1}{r}\frac{\partial\psi}{\partial z}$, $W = \frac{1}{r}\frac{\partial\psi}{\partial r}$, may then be written in the form

$$\psi = D z\, F(\eta) \tag{10}$$

Substitution into the momentum equation, Equation 6, yields the ordinary differential equation for $F(\eta)$

$$-\left\{\frac{1}{\eta} FF'' + \frac{1}{\eta} F'F' - \frac{1}{\eta^2} FF'\right\} = \frac{d}{d\eta}\left(F'' - \frac{1}{\eta} F'\right)$$

which may be integrated once to give

$$-\frac{1}{\eta} FF' = F'' - \frac{1}{\eta} F' \tag{11}$$

the constant of integration being zero because $\frac{1}{\eta} F'$ and F'' vanish for large η. Fortunately, the solution for Equation 11 may be written simply as

$$F(\eta) = \frac{\eta^2}{1 + \frac{1}{4}\eta^2} \tag{12}$$

which satisfies the requirement that the stream function vanish on the symmetry axis, $\eta = 0$, and satisfies identically the momentum conservation relation $\mu = \int_0^\infty W^2\, rdr$, as

$$\frac{3}{8}\int_0^\infty \left(\frac{F'}{\eta}\right)^2 \eta\, d\eta = 1 \tag{13}$$

The velocity components of the mean flowfield are then

$$W = \frac{3}{8}\frac{\mu}{D}\frac{1}{z}\left(\frac{F'}{\eta}\right)$$

$$= \frac{3}{4}\frac{\mu}{D}\frac{1}{z(1 + \frac{1}{4}\eta^2)^2} \qquad (14)$$

and

$$U = -\sqrt{\frac{3}{8}}\,\mu\,\frac{1}{z}\left(\frac{F}{\eta} - F'\right)$$

$$= \sqrt{\frac{3}{8}}\,\mu\,\frac{1}{z}\;\frac{\eta(1 - \frac{1}{4}\eta^2)}{(1 + \frac{1}{4}\eta^2)^2} \qquad (15)$$

Now explicit solution of the flame density and reactant conservation relations require a quantitative form for the reactant consumption rates. If the chemistry were actually of infinitely fast rate and if the mutual reactants were uncontaminated by products of combustion, the values of $\kappa_1{}^*v_1$ and $\kappa_2{}^*v_2{}^*$ appearing in Equations 3 and 4 could be written

$$\kappa_1{}^*v_1 = \beta_1\sqrt{D\varepsilon} \quad ; \quad \kappa_2{}^*v_2 = \beta_2\sqrt{D\varepsilon} \qquad (16)$$

where D is the coefficient of molecular diffusion, $\varepsilon \equiv \alpha\left|\frac{\partial W}{\partial r}\right|$ is proportional to the turbulent strain rate, and β_1, β_2 are constants for a given chemical combination, depending upon the reaction stoichiometry. Numerical calculations of strained laminar diffusion flames, which will be discussed later, suggest that for a wide range of flame straining rates and reactant dilutions, the values of κ_1v_1 and κ_2v_2 may be written

$$\kappa_1{}^*v_1 = \beta_1\,G_1(\kappa_1,\kappa_2)\sqrt{D\varepsilon} \quad ; \quad \kappa_2{}^*v_2 = \beta_2\,G_2(\kappa_1,\kappa_2)\sqrt{D\varepsilon} \qquad (17)$$

where $G_1(\kappa_1,\kappa_2)$, $G_2(\kappa_1,\kappa_2)$ depend only upon the local average reactant mass fractions and $G_1 = G_2 = 1$ for fast chemistry. The equations for reactant consumption and flame density may then be written

$$U\frac{\partial\kappa_1}{\partial r} + W\frac{\partial\kappa_1}{\partial z} = \frac{1}{r}\frac{\partial}{\partial r}\left(r\,D\,\frac{\partial\kappa_1}{\partial r}\right) - \beta_1\,G_1(\kappa_1,\kappa_2)\sqrt{\varepsilon D}\,\Sigma \qquad (18)$$

$$U\frac{\partial\kappa_2}{\partial r} + W\frac{\partial\kappa_2}{\partial z} = \frac{1}{r}\frac{\partial}{\partial r}\left(r\,D\,\frac{\partial\kappa_2}{\partial r}\right) - \beta_2\,G_2(\kappa_1,\kappa_2)\sqrt{\varepsilon D}\,\Sigma \qquad (19)$$

$$U \frac{\partial \Sigma}{\partial r} + W \frac{\partial \Sigma}{\partial z} = \frac{1}{r} \frac{\partial}{\partial r}\left(r\,D \frac{\partial \Sigma}{\partial r}\right) + \varepsilon\,\Sigma - \lambda\,\beta_1\,G_1 \frac{\sqrt{D\varepsilon}}{\kappa_1}\Sigma^2 - \lambda\,\beta_2\,G_2 \frac{\sqrt{D\varepsilon}}{\kappa_2}\Sigma^2 \tag{20}$$

$$\kappa_1 + \kappa_2 + \kappa_3 = 1 \tag{21}$$

When the chemistry is fast, so that $G_1 = G_2 = 1$, it is convenient to use a linear combination of κ_1 and κ_3 that satisfies a homogeneous diffusion equation. Such a combination is $\kappa_1 + \frac{1}{1 + \beta_2/\beta_1}\kappa_3 \equiv J$, and because a diffusion flame with fast chemistry utilizes fuel and oxidizer in the stoichiometric ratio ϕ, the quantity $\beta_2/\beta_1 = \phi$ and

$$J = \kappa_1 + \frac{1}{1+\phi}\kappa_3 \tag{22}$$

Thus J(r,z) satisfies

$$U \frac{\partial J}{\partial r} + W \frac{\partial J}{\partial z} = \frac{1}{r} \frac{\partial}{\partial r}\left(r\,D \frac{\partial J}{\partial r}\right) \tag{23}$$

with the conditions $J(\infty,z) = 0$ and hence, comparing Equations 23, 6, and 7, it is clear that $J(r,z) \sim W(r,z)$. The constant of proportionality between J and W is easily found by noting that if the actual flow of fuel injected into the stream is γ, then the flow of the product formed is $(1 + \phi)\gamma$ for large values of z where the reaction is complete and $\kappa_1 = 0$. Then the integrated flux of the product is, as $z \to \infty$

$$\int_0^\infty \kappa_3\, W\, r dr = \gamma(1 + \phi) \tag{24}$$

and because integration of Equation 23 shows that $\int_0^\infty J\, W\, r dr$ is conserved along the z direction, it follows that

$$\int_0^\infty J\, W\, r dr = \gamma \tag{25}$$

Because J is proportional to W, the integral is the same as that evaluated to ensure conservation of momentum with z and hence it follows, comparing Equations 9 and 25, that

$$J = \frac{\gamma}{\mu} W = \frac{3}{8} \frac{\gamma}{D} \frac{1}{z} \left(\frac{F'}{\eta}\right) \qquad (26)$$

We have then the algebraic relation

$$\kappa_1 + \frac{1}{1+\phi} \kappa_3 = \frac{3}{8} \frac{\gamma}{D} \frac{1}{z} \left(\frac{F'}{\eta}\right) \qquad (27)$$

in addition to the relation Equation 21 and, as a consequence, we need only work with a single species conservation Equation 19.

In order to make this identification between J(r,z) and W(r,z), it has been necessary to introduct the volume flow rate γ as well as the momentum μ of the jet. These two quantities may be used to characterize the jet velocity

$$\text{velocity} \sim \mu/\gamma \qquad (28)$$

and the characteristic dimension of the jet,

$$\text{length} \sim \gamma/\sqrt{\mu} \qquad (29)$$

when, in fact, the length $\gamma/\sqrt{\mu} = \sqrt{\pi}\ R$, where R is the initial radius of a jet with uniform velocity.

VI. FUEL JET WITH FAST CHEMISTRY

When the chemical reaction rates are fast, the relevant equations, Equations 18, 27, and 20 are simplified principally by the fact that the functions G_1, G_2 are both unity and, in general, $\beta_2 = \phi\, \beta_1$. Now if there were no reactions and if the flame straining were negligible ($\varepsilon = 0$), then the problem would possess similarity solutions of the form $\kappa_1 \sim \frac{1}{z}\, k_1(\eta)$ and $\Sigma \sim \frac{1}{z}\, \sigma(\eta)$. There is a certain advantage in writing these quantities in that form, as

$$\kappa_1 = \frac{3}{8}\frac{\gamma}{D}\frac{1}{z}\, k_1(\eta, z) \tag{30}$$

and

$$\Sigma = \frac{3}{8}\left(\frac{\sqrt{\mu}}{\alpha D}\right)^{1/2} \frac{1}{\beta_1 z}\, \sigma(\eta, z) \tag{31}$$

Now because we shall use an integral technique to obtain our final result, it is convenient to rewrite Equations 18 and 20 in similarity variables and integrate them over the flame cross section. Introducing the similarity coordinates, η and z, we have

$$\begin{aligned} &\frac{\sqrt{\frac{3}{8}\mu}}{D}\,\frac{1}{z}\frac{\partial}{\partial \eta}(r\, U\, \kappa_1) + \frac{\partial}{\partial z}(r\, W\, \kappa_1) - \frac{1}{z}\frac{\partial}{\partial \eta}(\eta\, r\, W\, \kappa_1) + \frac{r}{z}\, W\, \kappa_1 \\ &\quad = \frac{\sqrt{\frac{3}{8}\mu}}{D}\,\frac{1}{z}\frac{\partial}{\partial \eta}\left(r\, D\frac{\partial \kappa_1}{\partial r}\right) - \beta_1 \sqrt{\alpha D \left|\frac{\partial W}{\partial r}\right|}\; r\, \Sigma \end{aligned} \tag{32}$$

and

$$\begin{aligned} &\frac{\sqrt{\frac{3}{8}\mu}}{D}\,\frac{1}{z}\frac{\partial}{\partial \eta}(r\, u\, \Sigma) + \frac{\partial}{\partial z}(r\, W\, \Sigma) - \frac{1}{z}\frac{\partial}{\partial \eta}(\eta\, r\, W\, \Sigma) + \frac{1}{z}(r\, W\, \Sigma) \\ &\quad = \frac{\sqrt{\frac{3}{8}\mu}}{D}\,\frac{1}{z}\frac{\partial}{\partial \eta}\left(r\, D\frac{\partial \Sigma}{\partial r}\right) + \alpha\left|\frac{\partial W}{\partial r}\right| r\, \Sigma - \lambda \sqrt{\alpha D \left|\frac{\partial W}{\partial r}\right|}\; \beta_1\, r\, \Sigma\, \frac{\Sigma}{\kappa_1 \kappa_2} \end{aligned} \tag{33}$$

Integrate these from $\eta = 0$ to $\eta = \infty$ and take account of the behavior of κ_1 and Σ for large radii. We then have from Equation 32

$$\frac{d}{d\xi}\int_0^\infty \left(\frac{F'}{\eta}\right) k_1 \, (\eta,\xi) \, \eta \, d\eta = -\left(\frac{3}{8}\right)^{3/4} \int_0^\infty \sqrt{\frac{d}{d\eta}\left(-\frac{F'}{\eta}\right)} \, \sigma(\eta,\xi) \, \eta \, d\eta \tag{34}$$

where we have introduced a new variable for distance along the axis,

$$\xi = \frac{8}{3}\frac{\mathbf{D}}{\gamma} z \tag{35}$$

Treating the flame density relation in the same manner

$$\frac{d}{d\xi}\int_0^\infty \left(\frac{F'}{\eta}\right) \sigma \, \eta(\xi,\eta) \, d\eta = \left(\frac{3}{8}\right)^{1/2} \frac{\alpha\sqrt{\mu}}{\mathbf{D}} \int_0^\infty \frac{d}{d\eta}\left(-\frac{F'}{\eta}\right) \sigma(\eta,\xi)\eta \, d\eta$$

$$- \lambda \left(\frac{3}{8}\right)^{3/4} \int_0^\infty \sqrt{\frac{d}{d\eta}\left(-\frac{F'}{\eta}\right)} \frac{\sigma^2(\eta,\xi)}{k_1 \, \kappa_2} \, \eta \, d\eta \tag{36}$$

where in this notation

$$\kappa_2 = 1 - \frac{1}{\xi}\left((1+\phi)\frac{F'}{\eta} - \phi \, k_1\right) \tag{37}$$

To complete the solution using the integral technique, it is required to select profile shapes for the mass fraction distribution and for the flame surface density. These are chosen specifically in the following form

$$k_1(\eta,\xi) = \left(\frac{F'}{\eta}\right)\left(1 - f(\xi)\right) \tag{38}$$

$$\kappa_2(\eta,\xi) = 1 - \left(\frac{F'}{\eta}\right)\frac{1}{\xi}\left(1 + \phi \, f(\xi)\right) \tag{39}$$

$$\sigma(\eta,\xi) = \left(\frac{F'}{\eta}\right) h(\xi) \left(1 - f(\xi)\right)\left[1 - \left(\frac{F'}{\eta}\right)\frac{1}{\xi}\left(1 + \phi \, f(\xi)\right)\right] \tag{40}$$

where $f(\xi)$ and $h(\xi)$ are unknown functions of distance along the axis and will be determined through the integral relations, Equations 34 and 36. Without justifying this choice in detail, several properties are important:

a) They are exact when there is no chemical reaction.

b) They satisfy exactly the conditions given by Equation 27 among species mass fractions.

c) They satisfy the appropriate boundary condtions at the symmetry axis and at distances remote from the axis.

d) The flame surface density vanishes, as it must physically, where either the fuel or oxidizer reactants vanish.

Now the value of $F(\eta) = \eta^2/(1 + \frac{1}{4}\eta^2)$, Equation 12, is the exact solution for the stream function in the jet problem utilizing the turbulent diffusivity formulation. Utilizing this and the representations for $k_1(\eta,\xi)$, $\kappa_2(\eta,\xi)$, $\sigma(\eta,\xi)$ given in Equations 38, 39, and 40, the integrations indicated in the integral relations, Equations 34 and 26, may be carried out. The integrals are of three classes: (i) those which may be carried out in an elementary manner, (ii) those which may be reduced to an integral of $(1 + \frac{1}{4}\,^2)^{-n}$ and have the value

$$\int_0^\infty \frac{d\eta}{\left(1 + \frac{1}{4}\eta^2\right)^n} = \pi \prod_{j=1}^{n-1} \left(\frac{2(n-j) - 1}{2(n-j)}\right) \tag{41}$$

and (iii) those of the form

$$I_n = \int_0^\infty \left(\frac{F'}{\eta}\right)^n F' \sqrt{\frac{2\eta}{\left(1 + \frac{1}{4}\eta^2\right)^3}}\, d\eta \tag{42}$$

These may, after a transformation, be written as

$$I_n = (2)^{n+3}\, B\left(2n + 2 + \frac{1}{4}\;;\; 5/4\right) \tag{43}$$

$$= (2)^{n+3}\, \frac{\Gamma\left(2n + 2 + \frac{1}{4}\right)\Gamma(5/4)}{\Gamma\left(2n + 3 + \frac{1}{2}\right)} \tag{44}$$

where both the Beta function and Gamma function representations are tabulated.

If we carry out this somewhat lengthy task on Equations 34 and 36, a pair of non-linear ordinary differential equations results

$$\frac{d}{d\xi}(1-f) = -\left\{0.44424 - 0.41251\left(\frac{1 + \phi f}{\xi}\right)\right\}(1-f)h \tag{45}$$

$$\frac{d}{d\xi}\left\{\left[1 - \frac{6}{5}\left(\frac{1 + \phi f}{\xi}\right)\right] (1-f)h\right\} = \frac{\alpha\sqrt{\mu}}{\mathbf{D}}\left[0.45090 - 0.47344\left(\frac{1 + \phi f}{\xi}\right)\right]\frac{(1-f)h}{\xi}$$

$$- \lambda\,(1-f)h^2\,(0.25386)\left[1 - \frac{13}{14}\left(\frac{1 + \phi f}{\xi}\right)\right] \tag{46}$$

These are to be integrated from $\xi_o \cong 2$, the virtual origin of the jet being at $\xi = 0$, to an arbitrary value of ξ; the initial values of $f(\xi_o) = 0$ and $h(\xi_o) \equiv h_o$, where h_o gives a measure of the amount of flame surface that is present at the start of calculation. Physically, the initial value of $h(\xi_o)$ is related to an ignition process which the turbulent flame model does not, of course, describe. It is to be expected that varying the initial value h_o will have a significant effect upon the local structure of the flame, but a much smaller effect upon the development far from the origin. The values of ϕ and $\frac{\sqrt{\mu}}{\mathbf{D}}$ are fixed by the reactants and by the turbulence model, respectively. The values of α and λ, on the other hand, are numerical constants which are universal in the sense that they do not depend upon stoichiometry, momentum flux, or geometrical size of the problem.

VII. THE STRAINED LAMINAR FLAME

This section describes the strained laminar flame calculations which provide the reactant consumption and nitric oxide produciton rates used in the model. When the chemical rates are taken to be infinitely fast, an analytical solution yields the fuel and oxidizer rates written in Equation 16 and spplied in Section IV:

$$\kappa_1^* v_1 = \beta_1 \sqrt{D\varepsilon} \quad ; \quad \kappa_2^* v_2 = \beta_2 \sqrt{D\varepsilon} \qquad (47)$$

In the more general case in which fluid properties are variable, heats of reaction and kinetic rates are finite, and many chemical reactions are treated, a numerical calculation is required. The results presented in this section come from such a calculation and are the work of T. J. Tyson and his associates at the Energy and Environmental Research Corporation. The authors acknowledge with thanks their cooperation in making the results available and thank especially C. J. Kau who made, under difficult circumstances, the many computer runs we requested. The set of kinetic equations describing the methane-air reactions in the computer program were developed by the Energy and Environmental Research Corporation staff under Environmental Protection Agency Contract Number 68-02-2631 and were reported in their Monthly Progress Report No. 14, June 1978.

For the reasons given in Section III, solutions are needed for a range of strain rates and for various dilutions of the fuel and oxidizer by combustion products. The thermodynamic states of the diluted reactants are those reached when products in the form of CO_2, H_2O, and N_2 are added adiabatically to the reactants and no chemical reaction is allowed.

The combination of strain rates and dilution ratios for which calculations were made and the results are given in Table 1. (Several cases were omitted initially due to the lack of time, but were determined to be not needed when the results were examined.)

In Section III, Equation 17, the fuel and oxidizer consumption rates were written in the form:

$$\kappa_1^* v_1 = \beta_1 G_1(\kappa_1,\kappa_2) \sqrt{D\varepsilon} \quad ; \quad \kappa_2^* v_2 = \beta_2 G_2(\kappa_1,\kappa_2) \sqrt{D\varepsilon} \qquad (48)$$

Table 1. STRAINED FLAME METHANE-AIR REACTION RATES

CASE	% AIR	% FUEL	STRAIN RATE, SEC^{-1}	REACTION RATE, MOLES/CM^2-SEC			β_1 G_1	$\frac{1}{2}$ β_2 G_2
				CH_4	O_2	NO		
1	1.0	1.0	50	$2.9 \cdot 10^{-5}$	$4.75 \cdot 10^{-5}$	$3.5 \cdot 10^{-9}$	0.142	0.232
			250	6.68	10.4	1.04	0.146	0.228
			500	9.22	13.6	0.42	0.143	0.210
2	1.0	0.75	50	2.32	3.89	4.19	0.114	0.19
			200	4.60	7.56	1.56	0.113	0.185
3	1.0	0.50	50	1.96	3.3	5.99	0.096	0.161
			200	3.98	6.45	2.47	0.097	0.158
			400	6.0	9.07	1.28	0.104	0.157
			600	7.43	10.9	0.94	0.105	0.154
4	1.0	0.25	50	1.57	2.65	9.3	0.077	0.130
			200	3.24	5.23	3.98	0.079	0.128
			400	4.74	7.32	2.63	0.082	0.127
			600	5.89	8.90	1.91	0.083	0.126
6	0.75	0.75	50	2.02	3.27	5.57	0.099	0.160
			200	4.78	6.44	2.41	0.105	0.158
			400	6.22	8.96	1.25	0.108	0.155
			600	7.69	10.8	0.77	0.109	0.153
7	0.75	0.50	50	1.71	2.80	7.34	0.084	0.137
			200	3.60	5.51	3.45	0.088	0.135
			400	5.26	7.75	2.01	0.091	0.134
			600	6.53	9.33	1.35	0.092	0.132
8	0.75	0.25	50	1.38	2.26	10.5	0.068	0.111
			200	2.87	4.46	5.17	0.070	0.109
			400	4.18	6.25	3.21	0.072	0.108
			600	5.20	7.58	2.40	0.073	0.107
10	0.50	0.75	50	1.59	2.44	7.14	0.078	0.119
			200	3.39	4.79	3.66	0.083	0.117
			600	6.13	8.0	1.68	0.087	0.113
11	0.50	0.50	50	1.35	2.09	8.69	0.066	0.102
			200	2.86	4.13	4.69	0.070	0.101
			400	4.20	5.78	3.10	0.073	0.100
			600	5.22	6.46	2.31	0.074	0.098
12	0.50	0.25	50	7.11	1.72	11.1	0.054	0.084
			200	2.31	3.41	6.24	0.057	0.083
			400	3.38	4.77	4.31	0.058	0.083
			600	4.21	5.76	3.33	0.059	0.081
14	0.25	0.75	50	1.02	1.4	8.46	0.050	0.069
			200	2.21	2.72	5.19	0.054	0.067
			400	3.25	3.77	3.77	0.056	0.065
			600	3.99	4.45	2.94	0.056	0.063
15	0.25	0.50	50	0.88	1.21	9.52	0.043	0.059
			200	1.88	2.37	5.95	0.046	0.058
			400	2.77	3.30	4.43	0.048	0.057
			600	3.44	3.94	3.58	0.049	0.054
16	0.25	0.25	50	0.75	1.02	11.2	0.037	0.050
			200	1.55	2.01	6.93	0.038	0.049
			400	2.27	2.80	5.25	0.039	0.048
			600	2.83	2.35	4.35	0.040	0.047

The functions $\beta_1 G_1$ and $\beta_2 G_2$ are also given in Table 1 and, for each composition, are indeed almost independent of the strain as they are, exactly, when the reaction rates are infinite. The average values of these functions for each dilution ratio are collected in Table 2. Only the function for the fuel is needed and is represented with acceptable accuracy by the expressions:

$$\beta_1 = 0.142 \tag{49}$$

$$G_1 = \frac{3}{7}\kappa_1 + \frac{4}{7}\kappa_2 \tag{50}$$

The treatment of the nitric oxide production rate is somewhat more empirical. It was noted that this rate decreased approximately with $\varepsilon^{\frac{1}{2}}$. We introduce, therefore, the variable H/τ defined by

$$\frac{H}{\tau} = \frac{\dot{\omega}_{NO}\ \varepsilon^{1/2}}{\rho\sqrt{D}} \tag{51}$$

where $\dot{\omega}_{NO}$ is NO production in mass per unit flame area per unit time, and observe that the dependence of the NO production on strain is represented within about a factor of two in this way. The values of H/τ for cases 3 and 12, shown in Table 3, are representative examples. Average values for all compositions are given in Table 4 and were found to depend, approximately, linearly upon the variable $(\kappa_1 + \kappa_2)$, as Figure 1 shows. The fit to this data used in the analysis in Section VI is

$$\frac{1}{\tau} = 4 \times 10^{-3}\ \mathrm{sec}^{-1} \tag{52}$$

$$H = \{2 - (\kappa_1 + \kappa_2)\} \tag{53}$$

It is significant that the chemical kinetics code from which these calculations were made, gives the result, shown in Figure 2, that NO production rate actually increases as the reactants are diluted with hot combustion products. This result might not have been expected, but because examination of this code was not the aim of the present work, this interesting result was not examined in detail. One may speculate that the increase of flame temperature accompanying reactant dilution and the "re-processing" of combustion product in the hot flame contribute to this trend.

The computations which yield the above discussed rates also determine the

Table 2. FUEL AND OXIDIZER CONSUMPTION FUNCTIONS

β_1 G_1				
κ_1 / κ_2	1	0.75	0.50	0.25
1.00	0.142	0.113	0.100	0.080
0.75	0.123	0.105	0.088	0.070
0.50	0.098	0.084	0.046	0.038
0.25	0.060	0.053	0.046	0.038

β_2 G_2				
κ_1 / κ_2	1	0.75	0.50	0.25
1.00	0.44	0.38	0.31	0.256
0.75	0.376	0.314	0.268	0.218
0.50	0.246	0.232	0.20	0.166
0.25	0.150	0.132	0.114	0.096

Table 3. NITRIC OXIDE PRODUCTION FUNCTION; DEPENDENCE ON STRAIN RATE

Case	ϵ	$H/\tau \times 10^3$
3	50	27.5
	200	22.7
	400	16.6
	600	14.9
12	50	50.9
	200	57.3
	400	55.9
	600	52.9

Table 4. NITRIC OXIDE PRODUCTION FUNCTION

Case	$H/\tau \times 10^3$	Case	$H/\tau \times 10^3$
1	1.0	10	3.0
2	1.4	11	4.2
3	2.0	12	5.6
4	3.5	14	4.8
6	2.0	15	5.6
7	2.9	16	6.6
8	4.5		

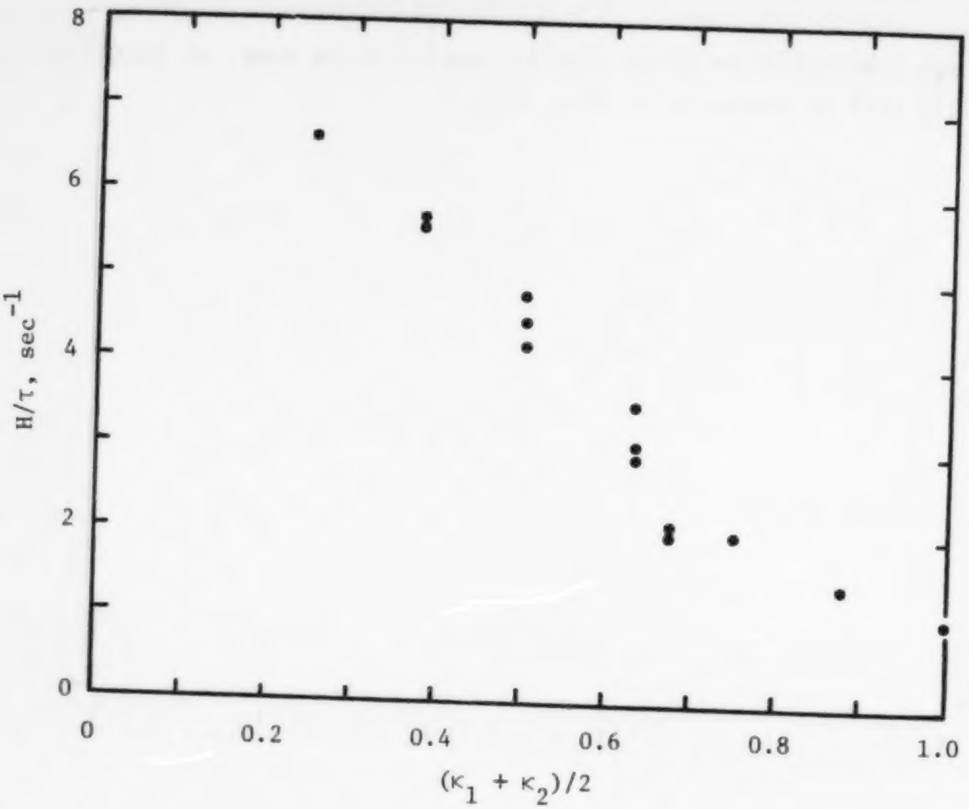

Figure 2. Dependence of Nitric Oxide Production on Reactant Dilution.

detailed structure of the laminar flame. A complete set of concentration profiles and the temperature distribution for case 6 are shown in Figures B-1 through B-8 in Appendix B. Figures B-9 through B-11 contain a few results for the same reactant compositions, but a lower strain rate. Since a thorough examination of these results remains to be done, no further analysis will be presented at this time.

VIII. NITRIC OXIDE PRODUCTION IN FUEL JET

If we denote by κ_N the mass fraction of nitric oxide, we may write the nitric oxide conservation (or production) relation as

$$U \frac{\partial \kappa_N}{\partial r} + W \frac{\partial \kappa_N}{\partial z} = \frac{1}{r} \frac{\partial}{\partial r} \left(r \, \mathbf{D} \frac{\partial \kappa_N}{\partial r} \right) + \frac{1}{\tau} H(\kappa_1, \kappa_2) \sqrt{\frac{D}{\varepsilon}} \, \Sigma \tag{54}$$

where the rate relation for the production of nitric oxide, developed in the preceding section, has been employed. In this expression, $1/\tau$ is an absolute rate constant, and $H(\kappa_1, \kappa_2)$ is the function that accounts for the effects of free stream reactant dilution upon nitric oxide production within the flame. If Equation 54 is rewritten in the form

$$\frac{\partial}{\partial r} \left(r \, U \, \kappa_N \right) + \frac{\partial}{\partial z} \left(r \, W \, \kappa_N \right) = \frac{\partial}{\partial r} \left(r \, \mathbf{D} \frac{\partial \kappa_N}{\partial r} \right) + \frac{1}{\tau} H(\kappa_1, \kappa_2) \sqrt{\frac{D}{\varepsilon}} \, r \, \Sigma \tag{55}$$

use of the similarity variables and the stream function leads to the result

$$\begin{aligned} &- \frac{\partial}{\partial \eta} \left\{ \frac{\eta}{z} \left(\frac{F}{\eta} - F' \right) \kappa_N \right\} + \frac{\partial}{\partial z} \left\{ \eta \left(\frac{F'}{\eta} \right) \kappa_N \right\} - \frac{1}{z} \frac{\partial}{\partial \eta} \left\{ \eta^2 \left(\frac{F'}{\eta} \right) \kappa_N \right\} \\ &\quad + \frac{1}{z} \left(\eta \left(\frac{F'}{\eta} \right) \kappa_N \right) = \frac{\partial}{\partial \eta} \left\{ \eta \, \frac{\partial \kappa_N}{\eta} \right\} \\ &\quad + \frac{8}{3} \frac{z\mathbf{D}}{\mu} \ell \, H(\kappa_1, \kappa_2) \, \eta \sqrt{\frac{D \, \mathbf{D}^2 \, z^2}{\left(\frac{3}{8} \mu \right)^{3/2}} \Big/ \frac{d}{d\eta} \left(- \frac{F'}{\eta} \right)} \, \Sigma \end{aligned} \tag{56}$$

where we define $\ell = 1/\tau\sqrt{\alpha}$.

Now we wish to calculate the ratio of nitric oxide flux $\int_0^\infty \rho \, W \, \kappa_N (2\pi r) dr$ to the total product flux $\int_0^\infty \rho \, W \, (2\pi r) dr$ and this ratio becomes

$$\int_0^\infty \rho \, W \, \kappa_N \, (2\pi r) \, dr \Big/ \int_0^\infty \rho \, W \, (2\pi r) \, dr = \int_0^\infty \kappa_N \left(\frac{F'}{\eta} \right) \eta \, d\eta \Big/ \int_0^\infty \left(\frac{F'}{\eta} \right) \eta \, d\eta$$

But the integral in the denominator is equal to 4/3 and, hence,

$$\Phi_N = \frac{3}{4} \int_0^\infty \kappa_N \left(\frac{F'}{\eta} \right) \eta \, d\eta \tag{57}$$

Thus if, returning to Equation 56, we integrate this over the jet cross section and take account of behavior of the stream function at large radii

$$\left\{\frac{d}{dz} + \frac{1}{z}\right\} \int_0^\infty \kappa_N \left(\frac{F'}{\eta}\right) \eta \, d\eta$$

$$= \left(\frac{8}{3}\right)^{3/2} \frac{\ell \, z^2 D^2}{\mu \sqrt{\frac{3}{8}^{1/2} \mu}} \sqrt{\frac{D}{\mu^{1/2}}} \int_0^\infty \left[\frac{d}{d\eta}\left(- \frac{F'}{\eta}\right)\right]^{-1/2} H \, \Sigma \, \eta \, d\eta$$

or

$$\left\{\frac{d}{dz} + \frac{1}{z}\right\} \Phi_N = 2 \left(\frac{8}{3}\right)^{3/4} \frac{\ell D^2}{\mu^{3/2}} \sqrt{\frac{D}{\mu^{1/2}}} \, z^2 \int_0^\infty \left[\frac{d}{d\eta}\left(- \frac{F'}{\eta}\right)\right]^{-1/2} H \, \Sigma \, \eta \, d\eta \tag{58}$$

Now this expression may be put in a more suitable form for integration by introducing the dimensionless distance along the axis, ξ, Equation 35, and the representation of the flame surface area, Σ, given by Equation 31. The resulting relation

$$\left(\frac{d}{d\xi} + \frac{1}{\xi}\right) \Phi_N = 2 \left(\frac{3}{8}\right)^{9/4} \frac{\ell}{\beta_1} \left(\frac{\gamma^2}{\mu^{3/2}}\right) \xi \int_0^\infty H \, \sigma \left\{\frac{d}{d\eta}\left(- \frac{F'}{\eta}\right)\right\}^{-1/2} \eta \, d\eta \tag{59}$$

contains a dimensionless group (ℓ/β_1) $(\gamma^2/\mu^{3/2})$ which will be of considerable physical significance in developing the scaling laws for the production of nitric oxide in flame structures. The volume flow, γ, and momentum flow, μ, may be represented in the forms

$$\mu = W_0^2 \left(\frac{R^2}{2}\right)$$

$$\gamma = W_0 \left(\frac{R^2}{2}\right)$$

where W_0 is the effective average velocity from a jet of radius R. Substitution of these expressions into Equation 59 yields the equation for the nitric oxide concentration

$$\left(\frac{d}{d\xi} + \frac{1}{\xi}\right) \Phi_N = \frac{\ell \, d}{\beta_1 W_0} \left(2^{-1/2}\right) \left(\frac{3}{8}\right)^{9/4} \int_0^\infty \xi \left\{\frac{d}{d\eta}\left(- \frac{F'}{\eta}\right)\right\}^{-1/2} H \, \sigma \, \eta \, d\eta \tag{60}$$

where d = 2R is the initial jet diameter.

The representation of $\sigma(\eta,\xi)$, appropriate to the integral solution, is given by Equation 40, and the function $H(\kappa_1,\kappa_2)$, developed in the preceding section, will be written

$$\begin{aligned} H(\kappa_1,\kappa_2) &= 2 - (\kappa_1 + \kappa_2) \\ &= 1 + \kappa_3 \\ &= 1 + (1 + \phi)\,\frac{f}{\xi}\left(\frac{F'}{\eta}\right) \end{aligned} \tag{61}$$

These relations for $\sigma(\eta,\xi)$ and $H(\kappa_1,\kappa_2)$ allow the integration to be carried out in the following manner. Writing the integral in detail

$$\begin{aligned} \int_0^\infty \xi \left\{\frac{d}{d\eta}\left(-\frac{F'}{\eta}\right)\right\}^{-1/2} H\,\sigma\,\eta\,d\eta &= \xi(1-f)h \int_0^\infty \left\{\frac{d}{d\eta}\left(-\frac{F'}{\eta}\right)\right\}^{-1/2} \left(\frac{F'}{\eta}\right)^2 \eta\,d\eta \\ &+ (1-f)h\,\phi(1-f) \int_0^\infty \left\{\frac{d}{d\eta}\left(-\frac{F'}{\eta}\right)\right\}^{-1/2} \left(\frac{F'}{\eta}\right)^3 \eta\,d\eta \\ &- (1-f)h\,(1+\phi f)(1+\phi)\,\frac{f}{\xi} \int_0^\infty \left\{\frac{d}{d\eta}\left(-\frac{F'}{\eta}\right)\right\}^{-1/2} \left(\frac{F'}{\eta}\right)^4 \eta\,d\eta \end{aligned} \tag{62}$$

In a manner similar to the procedure used in evaluating certain of the integrals in the flame surface density earlier, each of these integrals is of the form

$$\int_0^\infty \left\{\frac{d}{d\eta}\left(-\frac{F'}{\eta}\right)\right\}^{-1/2} \left(\frac{F'}{\eta}\right)^n \eta\,d\eta \equiv J_n \tag{63}$$

where we know $F(\eta)$ so that

$$\frac{F'}{\eta} = 2\left(1 + \frac{1}{4}\eta^2\right)^{-2}$$

With some variable transformation and rearrangement, we may find that

$$\begin{aligned} J_n &= 2^n \mathbf{B}\left\{2(n-1) - \frac{1}{4}\ ;\ \frac{3}{4}\right\} \\ &= 2^n \frac{\Gamma\left\{2(n-1) - \frac{1}{4}\right\} \Gamma\left\{\frac{3}{4}\right\}}{\Gamma\left(2n - \frac{3}{2}\right)} \end{aligned} \tag{64}$$

and, thus, the integrals may be evaluated numerically with the aid of tabulated values of the real gamma function.

If these numerical evaluations are carried out and we define a variable P_N, proportional to the nitric oxide formation,

$$\Phi_N = \left(\frac{1}{\beta_1}\right)\left(\frac{k\ d}{W_0}\right) P_N \tag{65}$$

The differential equation for P_N is then

$$\frac{d\ P_N}{d\xi} = -\frac{1}{\xi} P_N + \left\{0.058308\ \xi + 0.063842\ \phi\ (1 - f) - 0.091893\ (1 + \phi)\ \frac{f(1 + \phi\ f)}{\xi}\right\} (1 - f)h \tag{66}$$

which is to be solved in conjunction with Equations 45 and 46 for the reacting jet structure.

IX. FUEL JET WITH FINITE RATE CHEMISTRY

The calculations for the detailed structure of methane flames, discussed in Section V, permit a somewhat more realistic description of the turbulent flame structure than that afforded by the fast chemistry employed in Section IV. In addition, because these calculations were carried out with various degrees of reactant dilution with combustion products, it is possible to account for the dilution of the unburned reactants which takes place as one proceeds along the jet. It will be recalled that the model described in Section IV, the combustion rate was entirely diffusion controlled and the reactant concentration far from the flame structure is assumed to be that of the uncontaminated reactants supplied to the jet and the oxidizer field. This is certainly a limit, in one sense, because the consumption per unit area of the flame is a maximum and, hence, the total flame surface area required to consume the fuel in the jet, is a minimum. It is reasonably evident, then, that the nitric oxide produced within the flame itself is well below the actual physical value, if not a minimum.

Another sort of limit that may now be considered follows from the assumption that the combustion products, which are produced in burned out portions of flame, are immediately mixed with the reactants. In this limit, the values of κ_1, κ_2 with which to evaluate the laminar flame structure are the local mean values which we employ in our flame model.

The fact that extensive numerical calculations of Section V show that the reactant consumption rate per unit area is proportional to $\sqrt{D\varepsilon}$ permits the representation for fast chemistry to be carried over not only for finite reaction rates but also for contaminated reactants. Referring again to Equation 17, we select

$$\beta_1 = 0.142 \tag{67}$$

$$G_1(\kappa_1,\kappa_2) = \frac{3}{7}\kappa_1 + \frac{4}{7}\kappa_2 \tag{68}$$

on the basis of the calculations described in Section V. Thus, omitting the details of a calculation which parallels quite closely that of Section IV, the integrated fuel consumption and flame surface density equations are

$$\frac{d}{d\xi}\int_0^\infty \left(\frac{F'}{\eta}\right) k_1(\eta)\eta \, d\eta$$

$$= - \left(\frac{3}{8}\right)^{3/4} \int_0^\infty \left\{\frac{d}{d\eta}\left(- \frac{F'}{\eta}\right)\right\}^{1/2} \left(\frac{3}{7}\kappa_1 + \frac{4}{7}\kappa_2\right) \sigma(\eta,\xi)\eta \, d\eta \tag{69}$$

and

$$\frac{d}{d\xi}\int_0^\infty \left(\frac{F'}{\eta}\right) \sigma(\eta,\xi)\eta \, d\eta = \left(\frac{3}{8}\right)^{1/2} \left(\frac{\alpha \sqrt{\mu}}{D}\right)\int_0^\infty \frac{d}{d\eta}\left(- \frac{F'}{\eta}\right) \sigma(\eta,\xi)\eta \, d\eta$$

$$- \lambda \left(\frac{3}{8}\right)^{3/4} \int_0^\infty \left\{\frac{d}{d\eta}\left(- \frac{F'}{\eta}\right)\right\}^{1/2} \frac{\sigma^2(\eta,\xi)}{k_1 \kappa_2} \left(\frac{3}{7}\kappa_1 + \frac{4}{7}\kappa_2\right) \eta \, d\eta \tag{70}$$

which are the counterparts of Equations 34 and 36 that were valid for undiluted reactants. The forms of k_1, κ_2, σ, given by Equations 38, 39, and 40, and the known function $F(\eta)$ allow the explicit evaluation of the integrals that occur utilizing again the results given by Equations 42 through 44 which were useful in developing the equations for the fuel jet and fast chemistry. These relations are then, in detail, required for numerical computation

$$\frac{d}{d\xi}(1-f) = - A g \tag{71}$$

$$C \frac{dg}{d\xi} = \frac{\alpha \sqrt{\mu}}{D} B \frac{g}{\xi} - \lambda A \frac{(g)^2}{1 - f} \tag{72}$$

where a new variable

$$g(\xi) \equiv \left[1 - \frac{6}{5}\left(\frac{1 + \phi - f}{\xi}\right)\right](1-f)h \tag{73}$$

has been introduced. The variable coefficients are

$$A = 0.25386 \frac{1 - \frac{13}{14}\frac{1 + \phi f}{\xi}}{1 - \frac{6}{5}\frac{1 + \phi f}{\xi}} + 0.17679 \left(\frac{1-f}{\xi} - \frac{4}{3}\frac{1 + \phi f}{\xi}\right)\frac{1 + \frac{5}{4}\frac{1 + \phi f}{\xi}}{1 - \frac{6}{5}\frac{1 + \phi f}{\xi}} \tag{74}$$

$$B = 0.45090 \left(1 - \frac{21}{20} \frac{1 + \phi f}{\xi}\right) \qquad (75)$$

$$C = 1 - \frac{6}{5} \frac{1 + \phi f}{\xi} \qquad (76)$$

It will be found, upon detailed inspection, that Equations 71 and 72 reduce to Equations 45 and 46, respectively, when the second term in A, Equation 74, is deleted.

X. RESULTS OF SPECIFIC JET CALCULATIONS

The model of turbulent chemical reactions in fuel jets, which has been presented, rests upon three empirical constants which, if the physics of the model were accurate, would be universal constants. While this universality is not likely, it is to be hoped that the results will be general for turbulent fuel jets and for flows that are reasonably similar to fuel jets. The first of these, which in our representaton appears as $\sqrt{\mu}/\mathbf{D}$, is well known and valid for all turbulent jets and, as a matter of fact, does not enter explicitly in our calculations. The second empirical constant is $\alpha \sqrt{\mu}/\mathbf{D}$ which enters in connection with the turbulent straining of the flame surface area. It is well known that the turbulent straining rate in a field of inhomogeneous turbulence is related to the mean flow in a manner that depends upon the type of field (i.e., turbulent jet, mixing region, boundary layer, etc.) but is the same for similar flow fields. Thus, when we assume the turbulent straining of the flame surface to be directly proportional to the straining rate of the mean flowfield, we acknowledge an unknown constant of proportionality, but one that will be of the same value for all turbulent fuel jets. This proportionality appears in the form of $\alpha \sqrt{\mu}/\mathbf{D}$.

The flame shortening process is probably the most controversial of the features in the turbulent combustion model which we have presented. If the physical picture, based upon the consumption of regions of fuel or oxidizer, is substantially correct, then there is a constant of proportionality which, for a specific type of turbulent flowfield, connects the actual annihilation of flame surface to the related dimensionless quantities which result from our model. This constant appears as λ in our calculations.

Now even a cursory appraisal of the equation describing the development of the flame surface area suggests that the values of $\alpha \sqrt{\mu}/\mathbf{D}$ and λ are intimately related to the beginning and end of the jet, respectively. When the flame is first ignited, for low values of ξ, the value of $\alpha \sqrt{\mu}/\mathbf{D}$ determines both the rate of growth of flame surface area and the reactant consumption per unit area. But as the flame density grows and regions within the flame develop where one of the reactant concentration values is low, the terms describing the annihilation of flame surface become important and balance, to some extent, the flame surface growth resulting from turbulent straining. A sort of balance is reached between the straining and annihilation terms, respectively, proportional to $\alpha\sqrt{\mu}/\mathbf{D}$ and to λ, which sets the rate at which reactants are consumed in the jet. Together they determine the length of the flame required to consume the fuel. The two quantities also determine the growth of combustion intensity at the beginning of the flame and the point along the flame length at which the combustion intensity reaches its peak.

Because these quantities are readily observable from experiments with gaseous fuel jets, the suitable values for the parameter have been determined in previous work to be approximately

$$\lambda = 5.0$$

$$\frac{\alpha\sqrt{\mu}}{\mathbf{D}} = 2.0$$

These values are based largely upon the extensive experiments of Hawthorne, et al (Ref. 3). These same data have allowed a satisfactory check of the variations of flame length with fuel stoichiometry.

Using the model described, together with values of the two constants thus determined, calculations have been made for the production of nitric oxide in fuel jets burning methane in air at atmospheric pressure and temperature. The first of these calculations used Equations 45 and 46, describing the fuel jet with fast chemistry and undiluted reactants, together with the differential equation, Equation 66, describing the production of nitric oxide within the flame structure. The interesting result of this computation is shown in Figure 3 where quantities proportional to the centerline fuel concentration and the integrated average nitric oxide concentration are shown as functions of the distance from the virtual origin of the jet measured in terms of the initial jet diameter. The quantity 1-f, referring to Equations 30 and 38, measures the centerline fuel concentration as a fraction of the value that would be observed if there were no chemical consumption of fuel, but only that dilution which would result from mixing with the ambient gas. This, if 1-f remained at the value unity, no chemical reaction would be taking place. Conversely, when 1-f approaches zero, it signifies that the fuel has been consumed, not simply mixed with a non-reacting diluent, until it is scarcely detectable. The nitric oxide concentration P_N, defined by Equation 65, increases very rapidly at the start of flame, levels off, and then drops

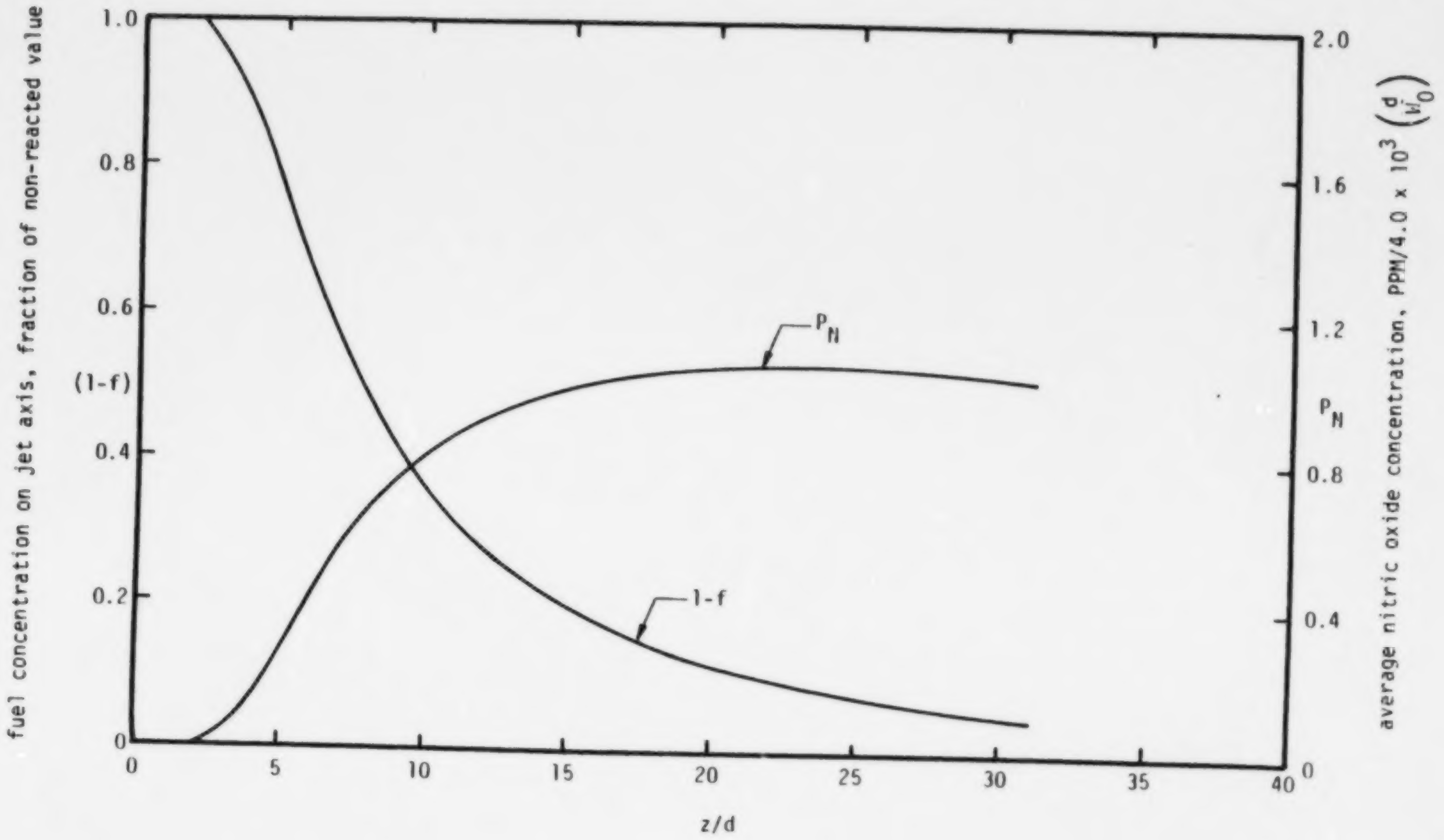

Figure 3. Fuel concentration on jet axis and integrated nitric oxide concentration. Methane-air flame; fast kinetics and no reactant dilution.

slightly as the flame end is approached. To interpret this behavior physically, one must recall that the nitric oxide concentration is averaged over the entire jet including all entrained but unburned oxidizer. The initial rise parallels that of the flame surface density because, until the flame annihilation mechanism begins to be important, the nitric oxide is retained within the flame structure. The subsequent tendency to level off results from the gradual decrease of flame surface density as the fuel is consumed, as well as the continued entrainment of air into the jet structure. The final decrease in nitric oxide concentration results from the mixing of the existing nitric oxide and additional, non-reacting oxidizer.

The maximum value of P_N attained is about unity, and the physical value of concentration may be estimated using Equation 65. Recalling the calculated values $k = 5.66 \times 10^{-4}$ $\sec^{-1}$ and $\beta_1 = 0.142$, we find that the actual concentration is

$$\phi_N \cong 4.0 \times 10^{-3} \left(\frac{d}{W_0}\right) P_N \qquad (77)$$

so that for a one foot diameter burner with an efflux velocity of 100 feet/second, $\phi_N \cong 4.0 \times 10^{-5}$ or 40 parts per million.

The results of a corresponding calculation are shown in Figure 4 for the model in which the laminar diffusion flame calculations are based upon the local mean reactant concentrations rather than upon the uncontaminated values. The results consequently account for the lower reactant consumption rate per unit flame area, the greater flame surface density which develops as a consequence and the greater production of nitric oxide. This system is defined by the differential equations, Equations 71 and 72, and the more complicated coefficients given by Equations 74, 75, and 76. Again, the production of nitric oxide is described by the differential equation, Equation 66.

The fuel concentration, as appears by comparison of the two figures, is not strongly affected by the inclusion of reactant vitiation so far as either the length of the flame or the concentration distribution is concerned. This result illustrates very well the manner in which fuel consumption rate by a flame element and the total flame surface area within the jet envelope, compensate so that this product is essentially constant. The nitric oxide production, however, responds nearly proportionally to the flame surface density and, as a

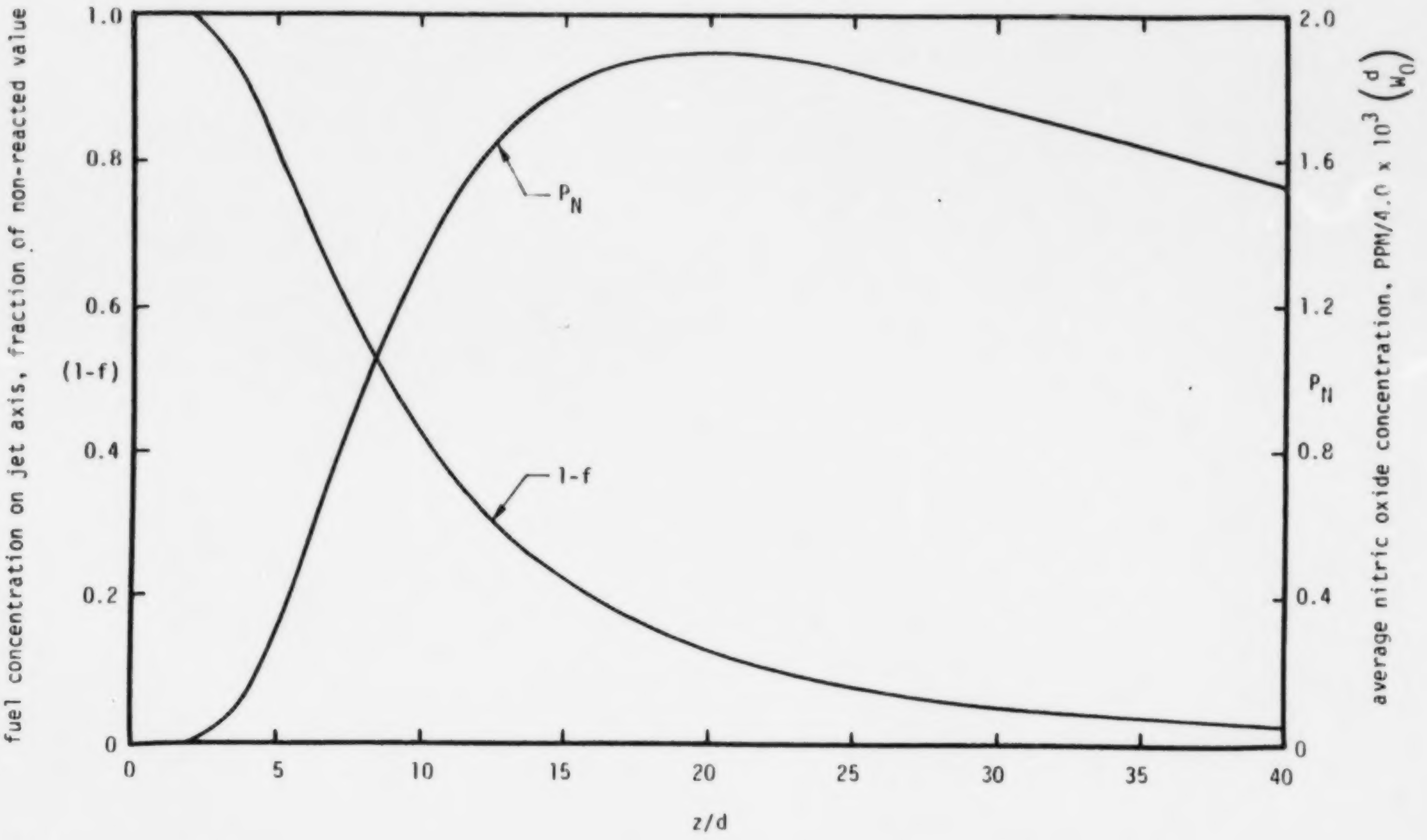

Figure 4. Fuel concentration on jet axis and integrated nitric oxide concentration. Methane-air flame; detailed reaction kinetics and reaction dilution with reaction products.

consequence, is higher for the flame structure that accounts for vitiation. In this case, the nitric oxide production is nearly doubled from jet calculations utilizing uncontaminated reactants.

The scaling law for nitric oxide production is contained in Equation 65:

$$\Phi_N = \frac{1}{\beta_1} \frac{\ell\ d}{W_0} P_N \tag{78}$$

in which β_1 and ℓ are constants and P_N is independent of the fuel jet diameter and velocity. The prediction, then, is that the nitric oxide concentration at the end of the flame varies linearly with diameter and inversely with the jet velocity.

Sufficient experimental data is not yet available for critical comparison with the predicted nitric oxide concentration values or with the scaling law. The observed levels, however, are considerably higher than those given by Equation 78 and appear to have a weaker dependence on jet diameter than this equation predicts. The difference in concentration level may come from the reactions, neglected in the analysis, which take place in the burned-off portions of the flame. The extension of the model described in the next section is intended to account for these additional reactions.

XI. AN EXTENSION OF THE COHERENT FLAME MODEL

The coherent flame model, as originally formulated and as applied in the preceding sections, assumes that chemical reaction rates are fast relative to mixing rates. This section outlines an extension of the model which allows both fast and slow reactions to be treated. The motivation for such an extension is the need for a description of the nitric oxide production which occurs in the methane-air flame after the more rapid energy producing reactions are complete.

In the model, as applied in Sections VI and VII, all reactions take place in the strained laminar flame. When these are all fast, the species consumption and production rates are equal to the rate per unit flame area multiplied by the flame area per unit volume. That is, there are no further reactions in the products generated when portions of the flame sheet burn off in the flame shortening process. Reactions that are slow, however, such as those which lead to nitric oxide, may continue in such regions. It is the purpose of the model extension to account for these additional reactions.

It is clear that for a kinetic system of any complexity, such as that for methane-air, the reactions taking place in the product gases must be treated numerically as they are presently in the strained flame. Such a requirement necessitates a simplification in some aspect of the model if the computational effort is to remain reasonable. A somewhat different view of the turbulent mixing process, about which there is some disagreement (even between the present authors), appears to provide sufficient simplification. The approach is suggested by the many experiments on mixing layers, for example, those of Brown and Roshko (Ref. 4) and Konrad (Ref. 5), and, more recently, on turbulent jets (Ref. 6) which may be interpreted to imply that it is in the breakdown of large-scale structures that molecular mixing and the subsequent chemical reactions occur, i.e., that the reactants are entrained into the layer and jet by large inviscid motions and subsequently mix as the large structure breaks down. If this interpretation is correct, it suggests the approximation that mean quantities be taken as independent of the transverse, y, or radial, r, direction and that attention be concentrated on the axial (or, in a sense, temporal) variations. We assume then that, in both the mixing layer and the axisymmetric jet, the mean quantities, velocity, concentration, flame surface density, and so forth, depend only on the axial dimension, x.

With the above simplifications in mind, the model extension may be described as follows. Within the mixing layer or jet, the reactants are divided by the flame sheet into two streams: one containing fuel and the other oxidizer. The reaction between fuel and oxidizer, being fast, occurs only within the flame sheet. The slow reactions, those resulting in NO for instance, take place both within the flame sheet and in the two fluid streams. The chemical constitution of the two bulk fluids is determined by four processes: (1) the volume reactions, (2) the continuous addition to them of the products of the flame sheet reactions that occurs during flame shortening, (3) the addition of newly-entrained fuel and oxidizer, and (4) the removal of reactants entering the flame sheet. (In the fuel jet, only the oxidizer fluid is continuously replenished by new reservoir gas.) The mass rate with which flame sheet products are added to the bulk gas is to be put equal to the flame shortening rate multiplied by the flame mass per unit area. This latter quantity, as well as the composition, is given by the strained flame structure calculation. The division of these products between fuel and oxidizer streams is a required input to the model. The calculations of Sections VI and VII and experimental data will serve as guides in choosing this parameter. If the reaction rates can be divided into two groups, one fast and the other slow relative to mixing rates, then to a good approximation, the bulk fluids are homogenous and the reactions can be described by standard kinetic codes modified to allow for the above described addition and removal of reactants.

With the fuel and oxidizer gas composition known and the strain rate determined by the local fluid mechanics, the strained flame computation can be made as before. What is needed, therefore, are simultaneous, coupled computations of the reactions within the bulk fluid, the strained flame reactions, and the flame shortening rate.

The equation governing the flame surface area is the same as that in the original model. For the mixing layer of width, y, the expression is

$$U \frac{d}{dx} (y \Sigma) = \alpha \varepsilon \Sigma y - \lambda \left[v_1 \Sigma^2/\kappa_1 + v_2 \Sigma^2/\kappa_2 \right] y$$

This equation, the stream tube, and the strained flame equations are to be solved simultaneously for the variation of the chemical properties with x.

With regard to the strained flame calculation, the strain rate and stream compositions vary slowly compared to the flow times within the flame. The calculation, therefore, may be viewed as a quasi-steady one with the properties within the flame changing instantaneously with change in the bulk fluid state. It may not be necessary to make this computation at each axial station. The results described in Section V suggest the possibility of interpolation between a few such stations.

As the above described calculation proceeds step by step in the axial direction, the change in flux of each chemical species in the mixing layer, for example, is given by the equation

$$U \frac{d(\mathrm{flux})_i}{dx} = \alpha_1 U_1 \kappa_i(\infty) + \alpha_2 U_2 \kappa_i(-\infty) + v_i \Sigma y + \dot{\Omega}_{i,f} + \dot{\Omega}_{i,0}$$

in which $(\mathrm{flux})_i$ is the total flux of species i, (∞) and $(-\infty)$ refer to the fuel and oxidizer streams, and the $\dot{\Omega}$'s are the total production rates in the bulk streams. The other symbols are defined in Figure 5 or have the meanings given in the earlier sections.

It is recognized that this brief sketch leaves many details unclear. Some have been omitted to simplify the discussion, but others remain to be worked out. It is hoped, however, that the physical picture on which the model is to be constructed has been adequately described.

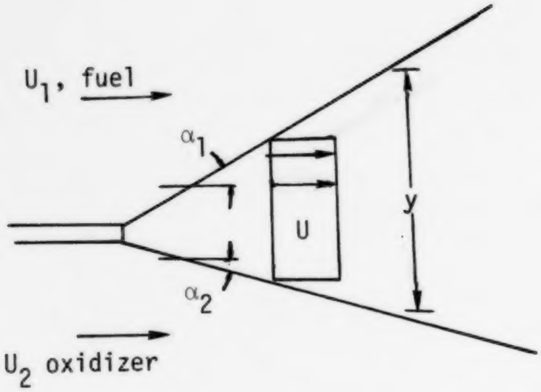

Figure 5. The two-dimensional mixing layer.

XII. CONCLUDING REMARKS

As was implied by the remarks at the end of Section VII, more experimental data is needed on the production of nitric oxide in methane-air flames, particularly of different scale, before a critical assessment can be made of the present analysis. The theoretical results already obtained, however, suggest the usefulness of a further application and development of the model.

XIII. REFERENCES

1. Marble, F. E., and Broadwell, J. E., "The Coherent Flame Model for Turbulent Chemical Reactions," Project SQUID Technical Report No. TRW-9-PU, January 1977.

2. Batchelor, G. K., "The Effect of Homogeneous Turbulence on Material Lines and Surfaces," Proc. Roy. Soc. A213, p. 349.

3. Hawthorne, W. R., Weddell, D. S., and Hottel, H. C., "Mixing and Combustion in Turbulent Gas Jets," Proceedings Third Symposium on Combustion, Flame, and Explosion Phenomena, p. 266, Williams and Wilkens Co., Baltimore, Md., 1948.

4. Brown, G., and Roshko, A., "On Density Effects and Large Structure in Turbulent Mixing Layers," J. Fluid Mech., 64, pp. 775-816.

5. Konrad, J. H., "An Experimental Investigation of Mixing in Two-Dimensional Turbulent Shear Flows with Applications to Diffusion-Limited Chemical Reactions." Project SQUID, Purdue University, Indiana, Technical Report CIT-8-PU.

6. Dimotakis, P., private communication.

XIV. APPENDIX A

LAMINAR DIFFUSION FLAMES WITH FAST CHEMICAL KINETICS

The reactant consumption rates enter into the problem in the form v_1 and v_2, the volumes of fuel and oxidizer consumed per unit flame area, respectively, and play roles both in the species conservation relations and in the equations describing the flame surface density. These quantities are assumed to be determined locally by the flame structure and to depend only upon local quantities; in particular, for the diffusion flame, they are determined by fuel and oxidizer concentrations and a local fluid mechanical property. As shall be illustrated, they may be determined analytically when the kinetics are fast. The important point to keep in mind is that the entire flame structure and chemical kinetics are coupled with the field analysis rather weakly, so that the consideration of complex kinetics complicates only the local flame structure and not the formulation of the flowfield and the flame distribution.

As the first example, consider the diffusion flame with rapid kinetics; in this approximation the reaction takes place at a surface of infinitesimal thickness. Utilizing the coordinates x and y to signify distances parallel to and normal to the flame surface, supposed to lie along $y = 0$, the fuel and oxidizer concentrations satisfy the equations

$$\frac{\partial\kappa_1}{\partial t} + u\,\frac{\partial\kappa_1}{\partial x} + v\,\frac{\partial\kappa_1}{\partial y} = \frac{1}{\rho}\,\frac{\partial}{\partial y}\left(\rho D\,\frac{\partial\kappa_1}{\partial y}\right) \tag{A1}$$

$$\frac{\partial\kappa_2}{\partial t} + u\,\frac{\partial\kappa_2}{\partial x} + v\,\frac{\partial\kappa_2}{\partial y} = \frac{1}{\rho}\,\frac{\partial}{\partial y}\left(\rho D\,\frac{\partial\kappa_2}{\partial y}\right) \tag{A2}$$

where

$$\frac{\partial u}{\partial x} + \frac{\partial v}{\partial y} = 0 \tag{A3}$$

when the heat of reaction is negligible and the gas density ρ is a constant. For the classical diffusion flame, the field is independent of x, but the solution is time dependent. Then, since $\frac{\partial u}{\partial x} = 0$, $v = v(t)$ which, as will appear, is not generally zero. Then introducing the variable

$$\zeta = \frac{y}{\sqrt{Dt}} \tag{A4}$$

and taking

$$v(t) = \Lambda\sqrt{\frac{D}{t}} \tag{A5}$$

the species conservation equations are reduced to a similarity form and become

$$\frac{d^2\kappa_i}{d\zeta^2} + \left(\frac{\zeta}{2} - \Lambda\right)\frac{d\kappa_i}{d\zeta} = 0 \tag{A6}$$

where i = 1, 2 for fuel or oxidizer, respectively. This pair of differential equations is required to satisfy the conditions that the fuel and oxidizer mass fractions take on the values $\kappa_1(\infty)$ and $\kappa_2(-\infty)$ at $y = +\infty$ and $y = -\infty$, respectively and that the mass flux to the diffusion flame, y = 0, supplies fuel and oxidizer in the stoichiometric ratio. This latter condition is explicitly

$$\frac{\rho D \dfrac{\partial\kappa_1}{\partial y}(0,t)}{-\rho D \dfrac{\partial\kappa_2}{\partial y}(0,t)} = f \tag{A7}$$

where f is the known, constant stoichiometric fuel-oxidizer ratio. It is not difficult to show that the appropriate solution is

$$\kappa_1 = \kappa_1(\infty)\,\frac{\mathrm{erf}\left(\frac{\zeta}{2} - \Lambda\right) + \mathrm{erf}\,(\Lambda)}{1 + \mathrm{erf}\,(\Lambda)} \tag{A8}$$

and

$$\kappa_2 = \kappa_2(-\infty)\,\frac{\mathrm{erf}\left(-\frac{\zeta}{2} + \Lambda\right) - \mathrm{erf}\,(\Lambda)}{1 - \mathrm{erf}\,(\Lambda)} \tag{A9}$$

satisfying the differential Equation (A6) and the boundary conditions at $y = \pm\infty$. The stoichiometry condition (Equation A7) then determines the characteristic value Λ, and it is a matter of calculation to show that this gives the result

$$\frac{\kappa_1(\infty)\,[1 - \mathrm{erf}\,(\Lambda)]}{\kappa_2(-\infty)[1 + \mathrm{erf}\,(\Lambda)]} = f \tag{A10}$$

Now $\kappa_1(\infty)/\kappa_2(-\infty)$ is the imposed fuel-oxidizer ratio of the problem, and the quotient of this with the stoichiometric fuel-oxidizer ratio

$$\frac{\kappa_1(\infty)/\kappa_2(-\infty)}{f} \equiv \Phi \tag{A11}$$

is frequently called the equivalence ratio. Thus, the value of Λ becomes

$$\Lambda = \operatorname{erf}^{-1}\left(\frac{\phi - 1}{\phi + 1}\right) \tag{A12}$$

This quantity defines the value of the transverse gas velocity

$$v(t) = \sqrt{\frac{D}{t}}\ \operatorname{erf}^{-1}\left(\frac{\phi - 1}{\phi + 1}\right) \tag{A13}$$

which is required to keep the flame stationary at the x-axis. With this solution, the values of the reactant volume consumption rates may be calculated as

$$v_1 = \kappa_1(\infty)\ \sqrt{\frac{D}{\pi t}}\ \left(\frac{\phi + 1}{2\phi}\right)\ e^{-\Lambda^2} \tag{A14}$$

and

$$v_2 = \kappa_2(-\infty)\ \sqrt{\frac{D}{\pi t}}\ \left(\frac{\phi + 1}{2}\right)\ e^{-\Lambda^2} \tag{A15}$$

This result exhibits the intuitively clear result that the consumption rates decrease with increasing time, because the diffusion layers that supply the reactants grow thicker with time. The equivalence ratio, which determines the value of Λ, is known because $\kappa_1(\infty)$ and $\kappa_2(-\infty)$ are equal to the values remote from the turbulent flame since the diffusion zone thickness is assumed small in comparison with flame front spacing. At any point within the turbulent flame, therefore, the reactant consumption rates are known in terms of the time t elapsed since the formation of the flame.

In discussing the turbulent flame structure it was emphasized that the turbulent motions tend to extend the flame surface and that the significant part of this extension consists of strain rate in the plane of the flame. Now, if the flame is aligned with the x-axis and the remaining axes chosen so that straining rate is along the x-axis, the resulting strained diffusion flame is also directly soluble. In the particular instance when the straining rate in the fluid is large, i.e., where

$$\varepsilon \equiv \frac{\partial u}{\partial x} \tag{A16}$$

is large and constant, Equations (A1) through (A3) take the form

$$\frac{\partial \kappa_i}{\partial t} + v \frac{\partial \kappa_i}{\partial y} = \frac{\partial}{\partial y}\left(D \frac{\partial \kappa_i}{\partial y}\right) \tag{A17}$$

and

$$\varepsilon + \frac{\partial v}{\partial y} = 0 \tag{A18}$$

If we solve the problem as previously posed, the solution has a brief transient followed by a steady solution which we may obtain by neglecting $\partial\kappa_i/\partial t$ and taking v and κ_i to be functions of y only. Then introducing the variable

$$\zeta \equiv \frac{y}{\sqrt{D/2}} \tag{A19}$$

$$v = -\varepsilon y + \sqrt{2\varepsilon D}\,\Lambda \tag{A20}$$

with Λ unknown, the differential equation (A17) becomes

$$\frac{d^2\kappa_i}{d\kappa^2} + \left(\frac{\zeta}{2} - \Lambda\right)\frac{d\kappa_i}{d\zeta} = 0 \tag{A21}$$

formally identical with Equation (A6). The conditions for $y \pm \infty$, as well as stoichiometry condition at the flame front, are also identical with those of the time-dependent flame, and, hence, the solution for the strained flame is likewise given by Equations (A8) and (A9) together with Λ evaluated by Equation (A12), but with ζ as defined in Equation (A19). The corresponding volume consumption rates of reactants are easily calculated

$$v_1 = \kappa_1(\infty)\sqrt{\frac{D\varepsilon}{2\pi}}\left(\frac{\phi + 1}{\phi}\right)e^{-\Lambda^2} \tag{A22}$$

and

$$v_2 = \kappa_2(-\infty)\sqrt{\frac{D\varepsilon}{2\pi}}\left(\phi + 1\right)e^{-\Lambda^2} \tag{A23}$$

Thus, so far as the local flame structure is concerned, the features relevant to the turbulent flame calculation are determined by the local strain rate.

X. APPENDIX B

TEMPERATURE AND CONCENTRATION PROFILES FOR STRAINED LAMINAR METHANE-AIR FLAMES

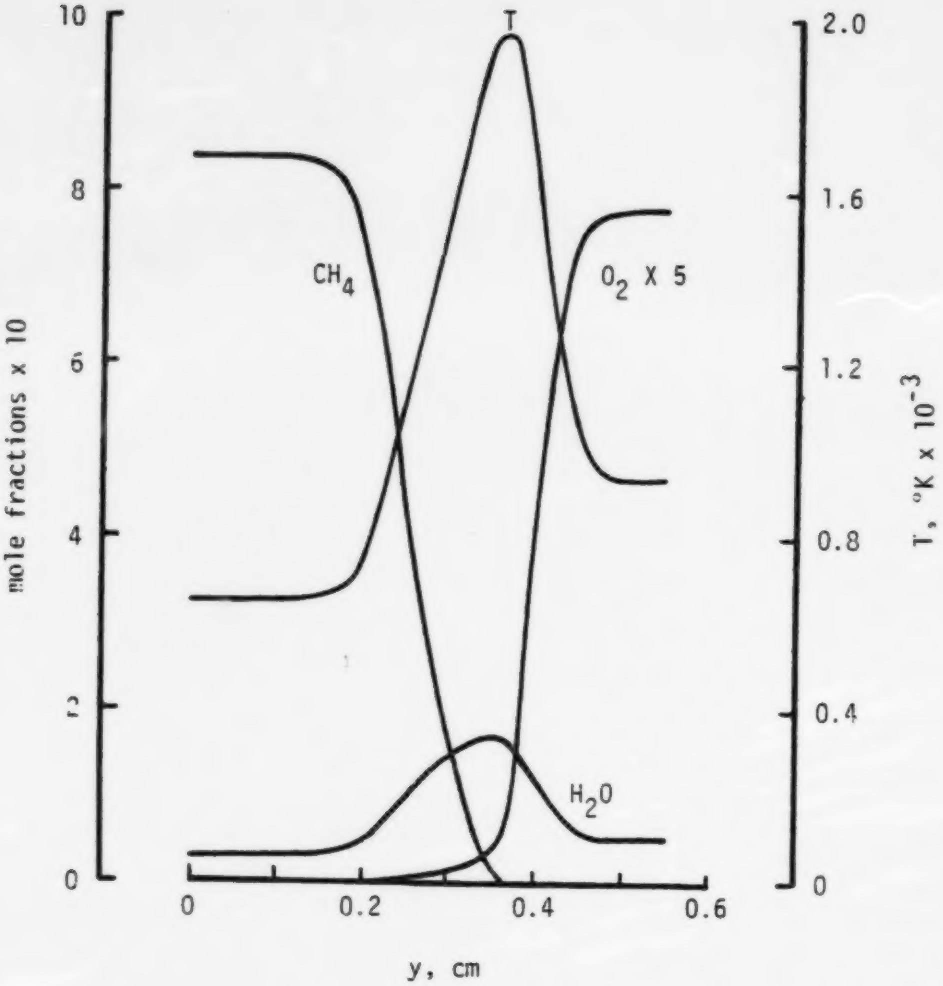

Figure B-1. Temperature, CH_4, O_2, and H_2O distributions in strained laminar methane-air flame; $\varepsilon = 600\ \text{sec}^{-1}$, $\kappa_1 = \kappa_2 = 0.75$.

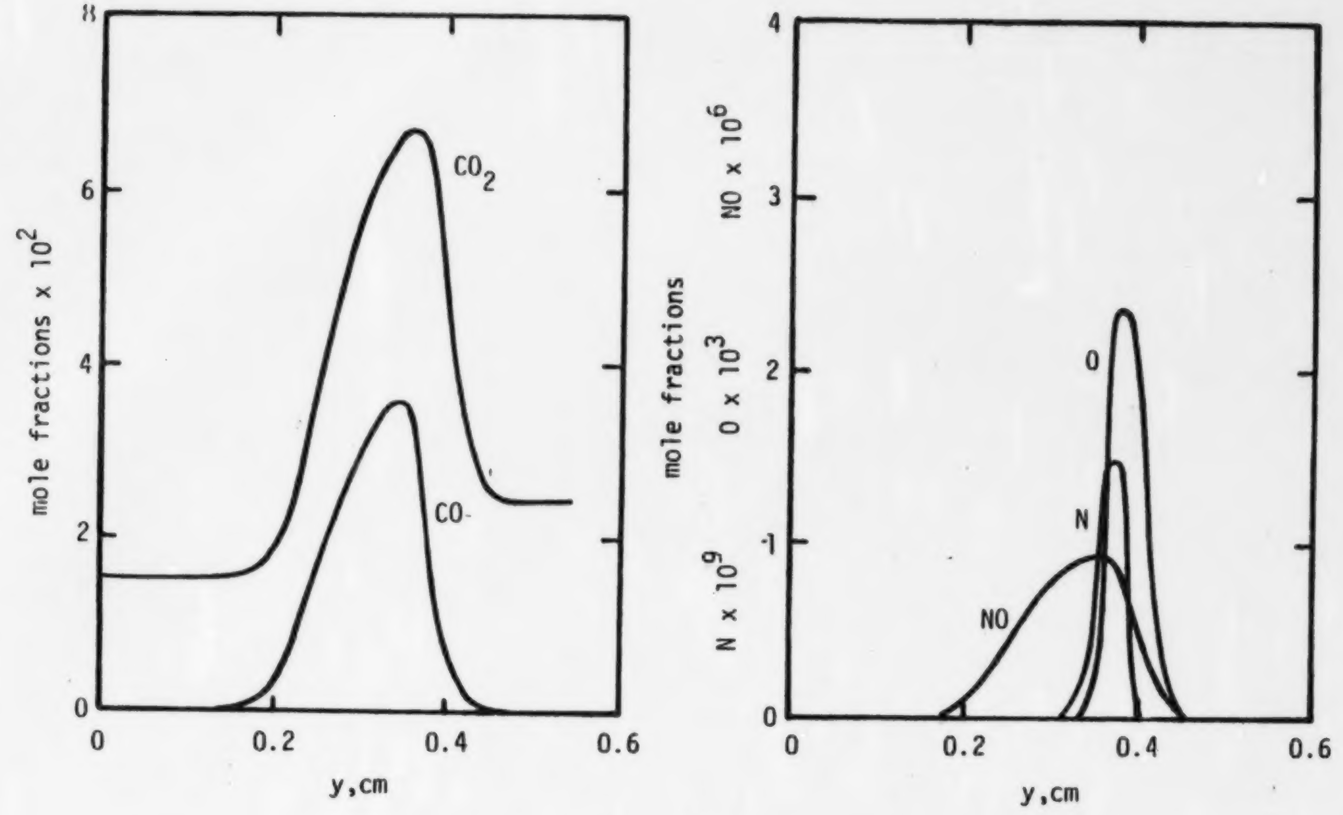

Figure B-2. CO_2, CO, O, N, and NO distributions in strained laminar methane-air flame; $\varepsilon = 600\ sec^{-1}$, $\kappa_1 = \kappa_2 = 0.75$.

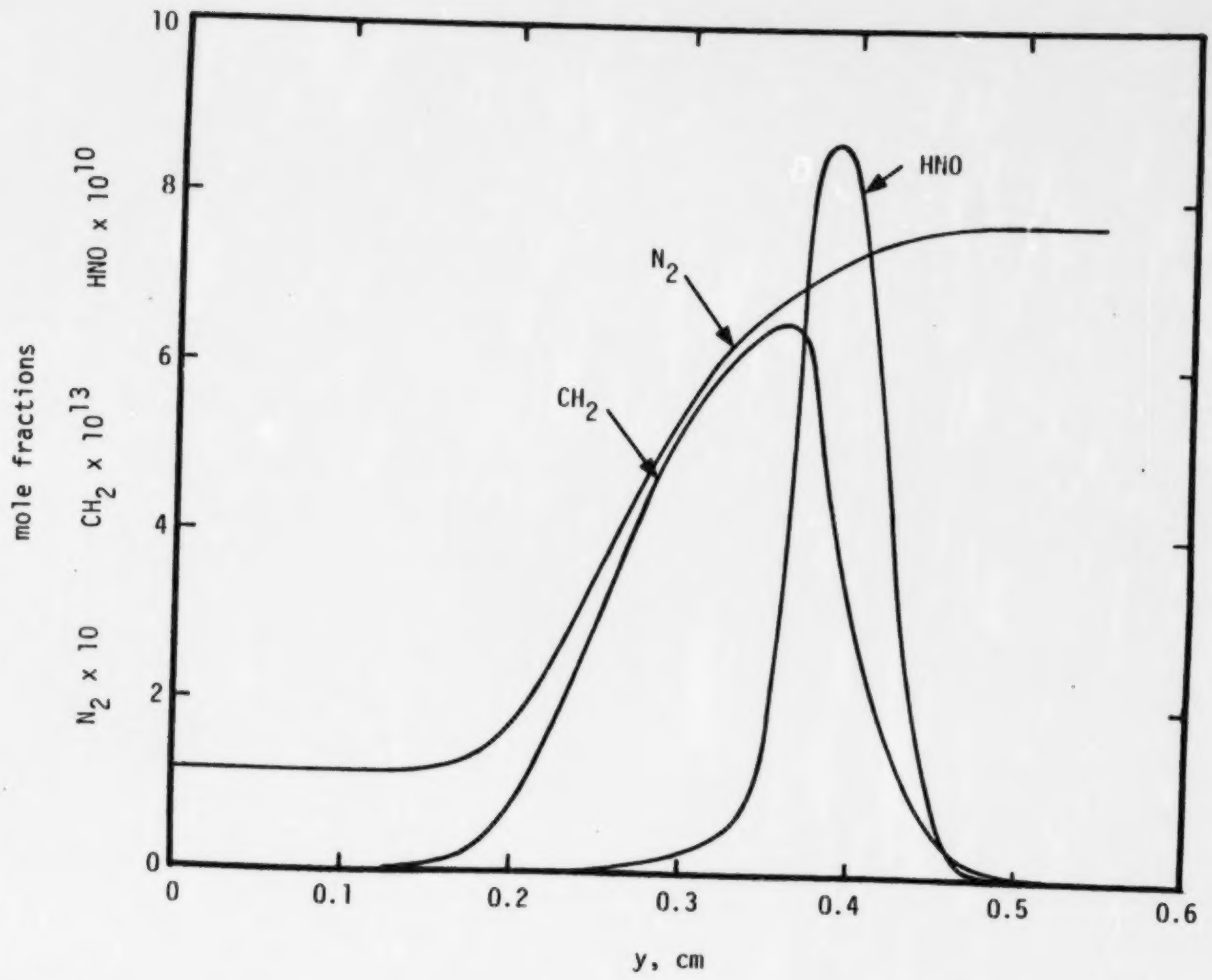

Figure B-3. CH_2, N_2, and HNO distributions in strained laminar methane-air flame; $\varepsilon = 600\ \mathrm{sec}^{-1}$, $\kappa_1 = \kappa_2 = 0.75$.

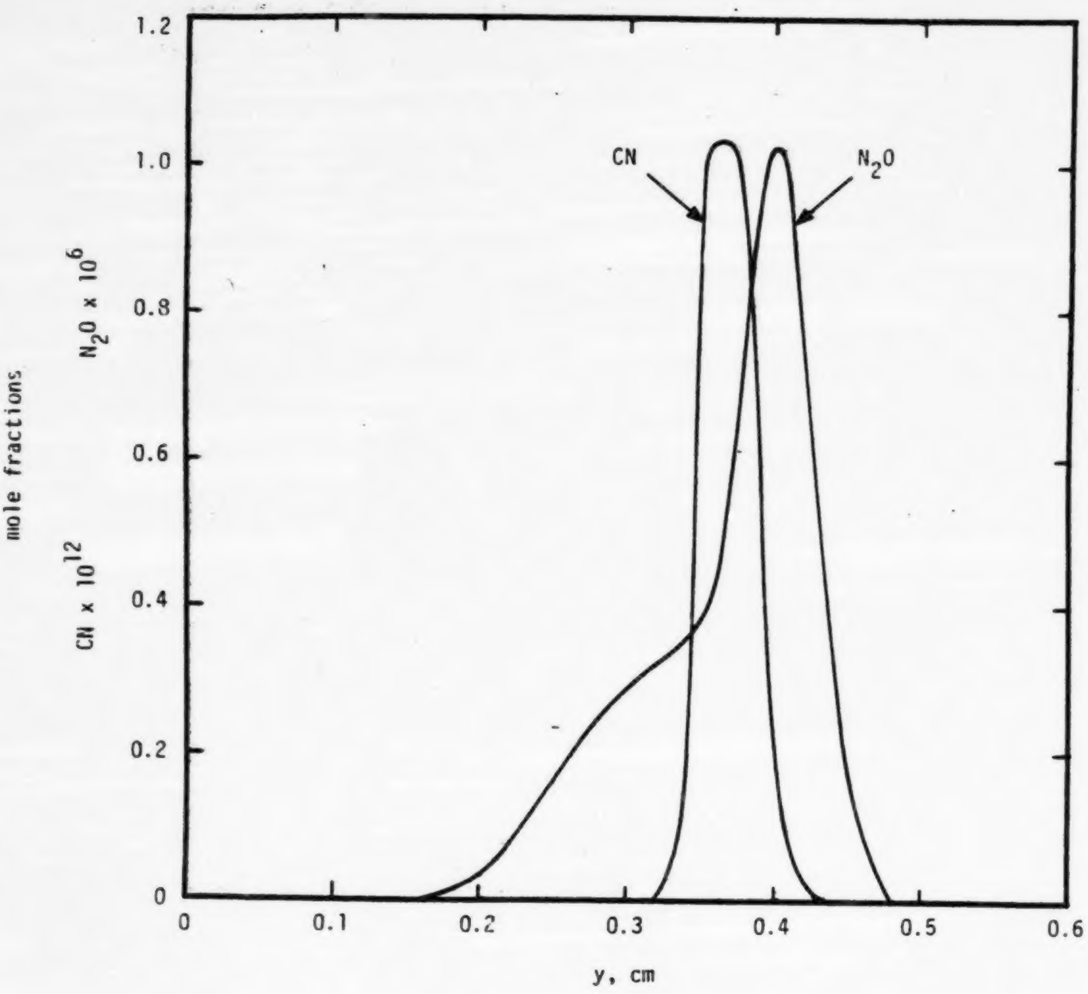

Figure B-4. CN and N_2O distributions in strained laminar methane-air flame; $\varepsilon = 600\ \text{sec}^{-1}$, $\kappa_1 = \kappa_2 = 0.75$.

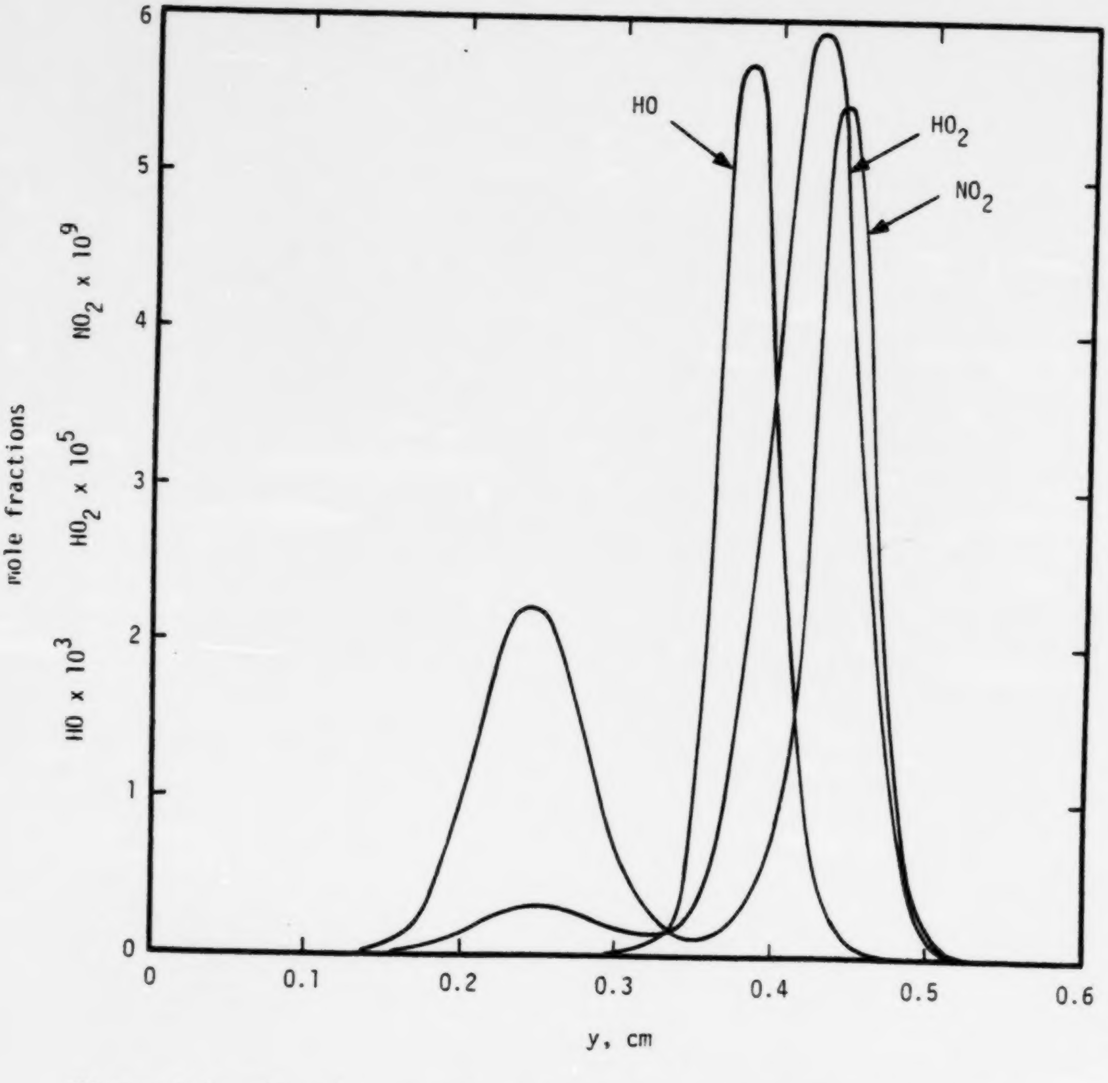

Figure B-5. HO, HO_2, and NO_2 distributions in strained laminar methane-air flame; $\varepsilon = 600\ \text{sec}^{-1}$, $\kappa_1 = \kappa_2 = 0.75$.

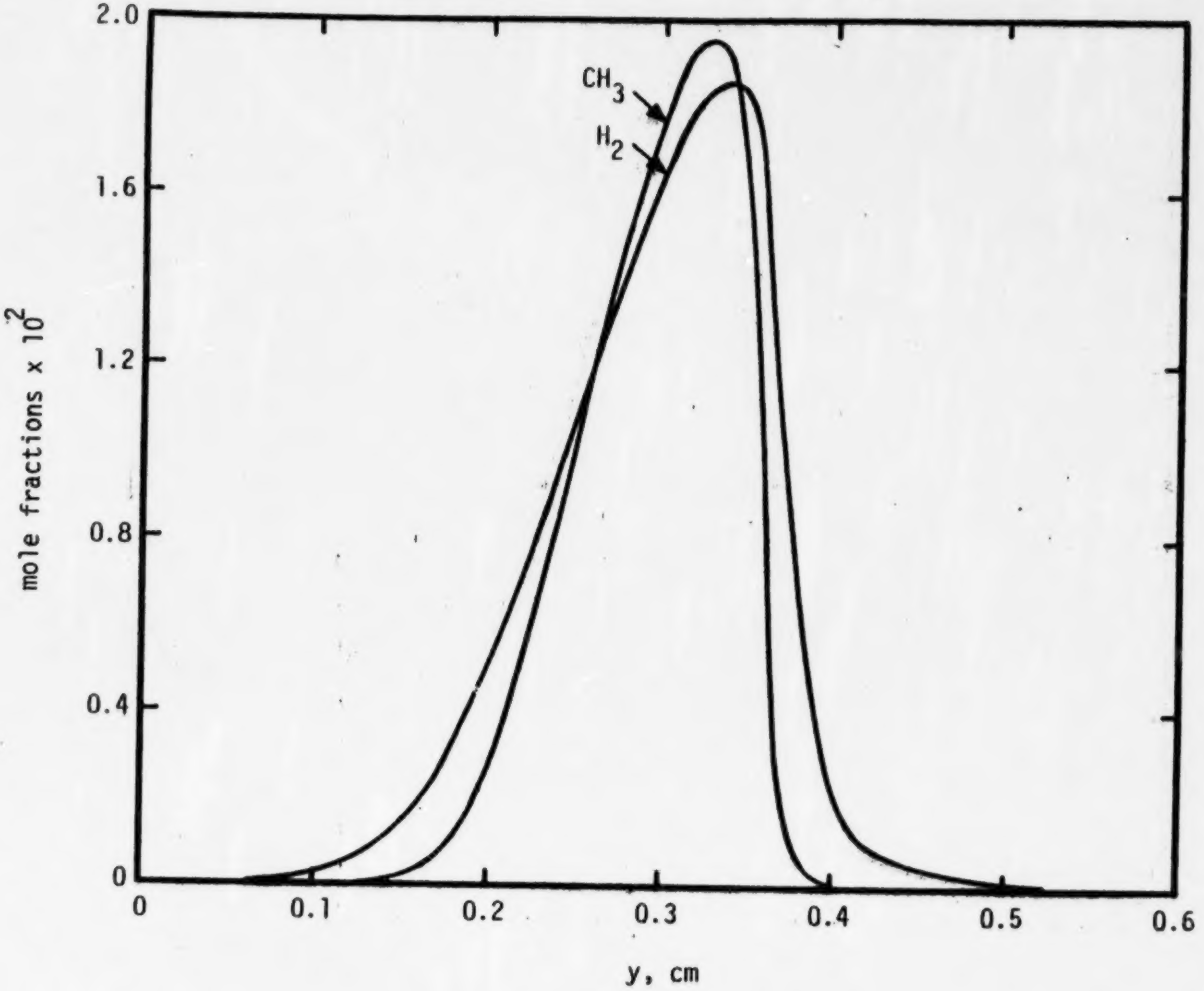

Figure B-6. CH_3 and H_2 distributions in strained laminar methane-air flame, $\varepsilon = 600\ \text{sec}^{-1}$, $\kappa_1 = \kappa_2 = 0.75$.

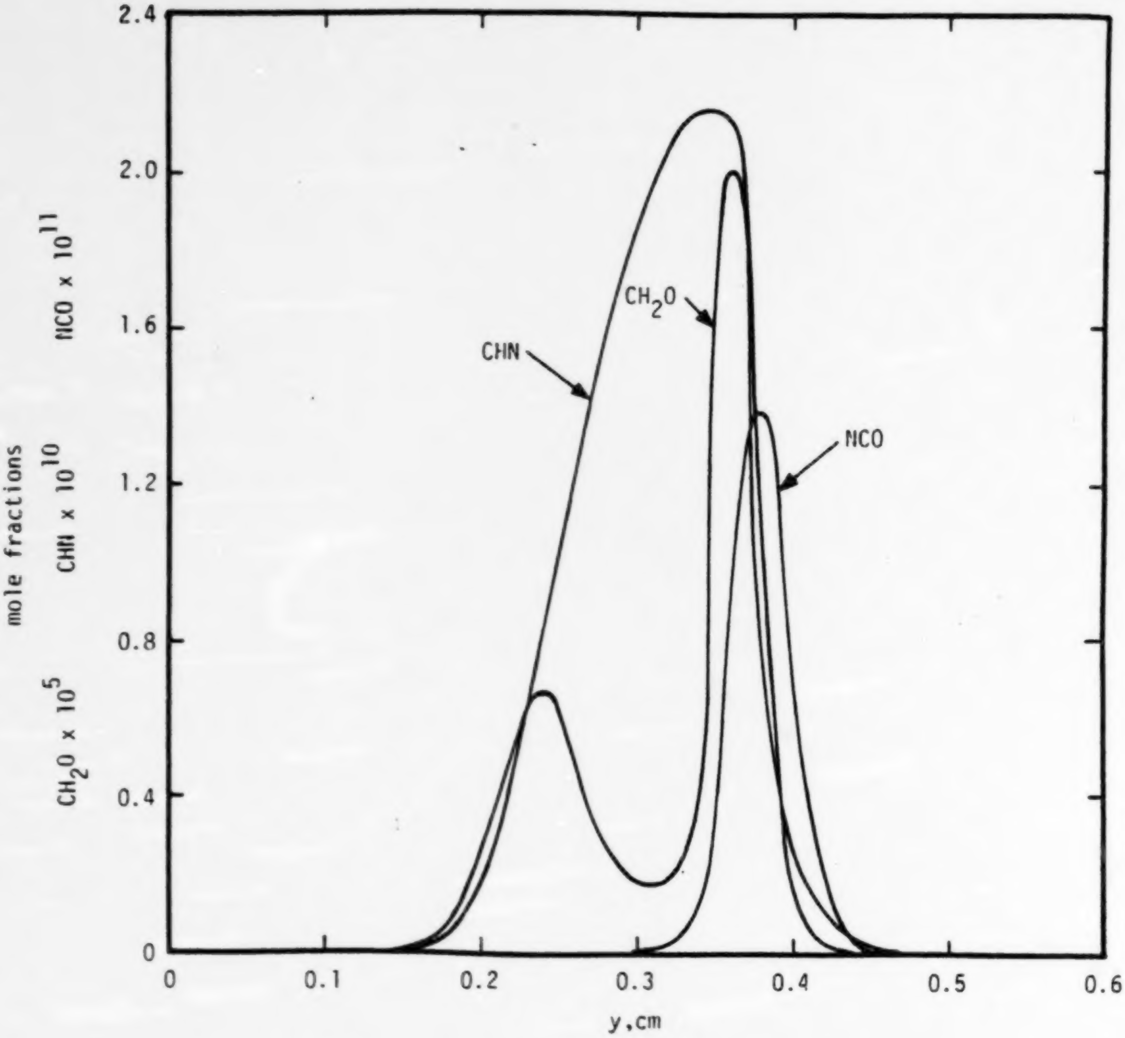

Figure B-7. CHN, CH_2O, and NCO distributions in strained laminar methane-air flame; $\varepsilon = 600\ sec^{-1}$, $\kappa_1 = \kappa_2 = 0.75$.

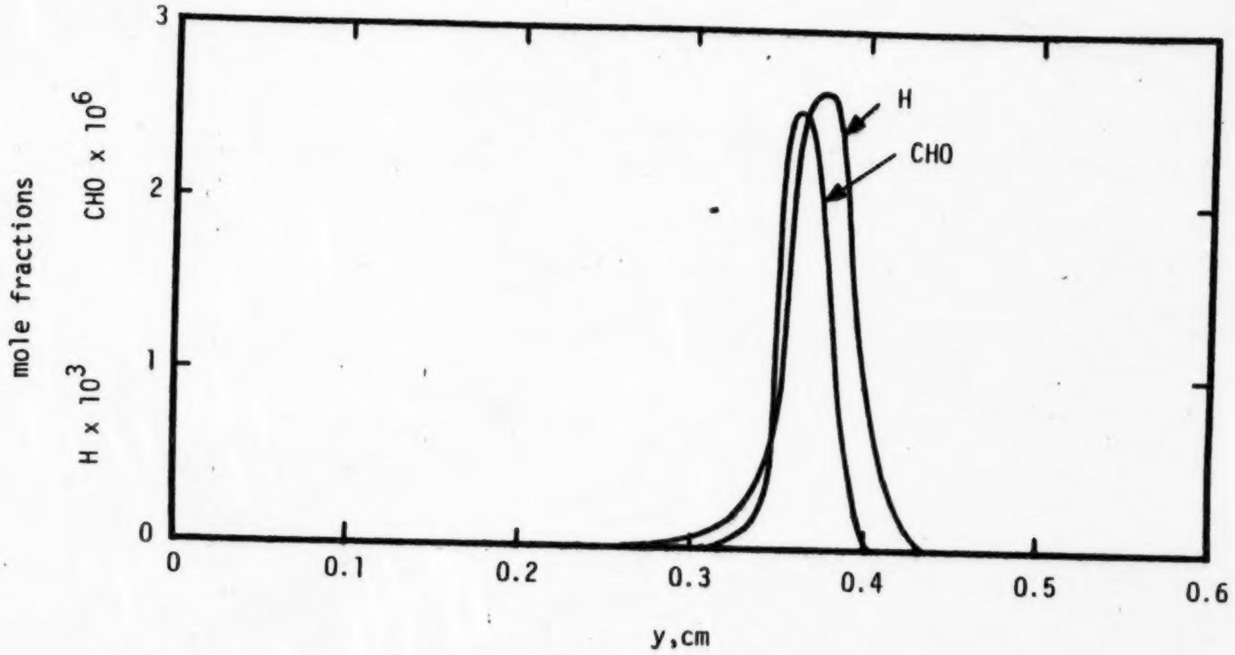

Figure B-8. H and CHO distributions in strained laminar methane-air flame; ε = 600 sec^{-1}, $\kappa_1 = \kappa_2 = 0.75$.

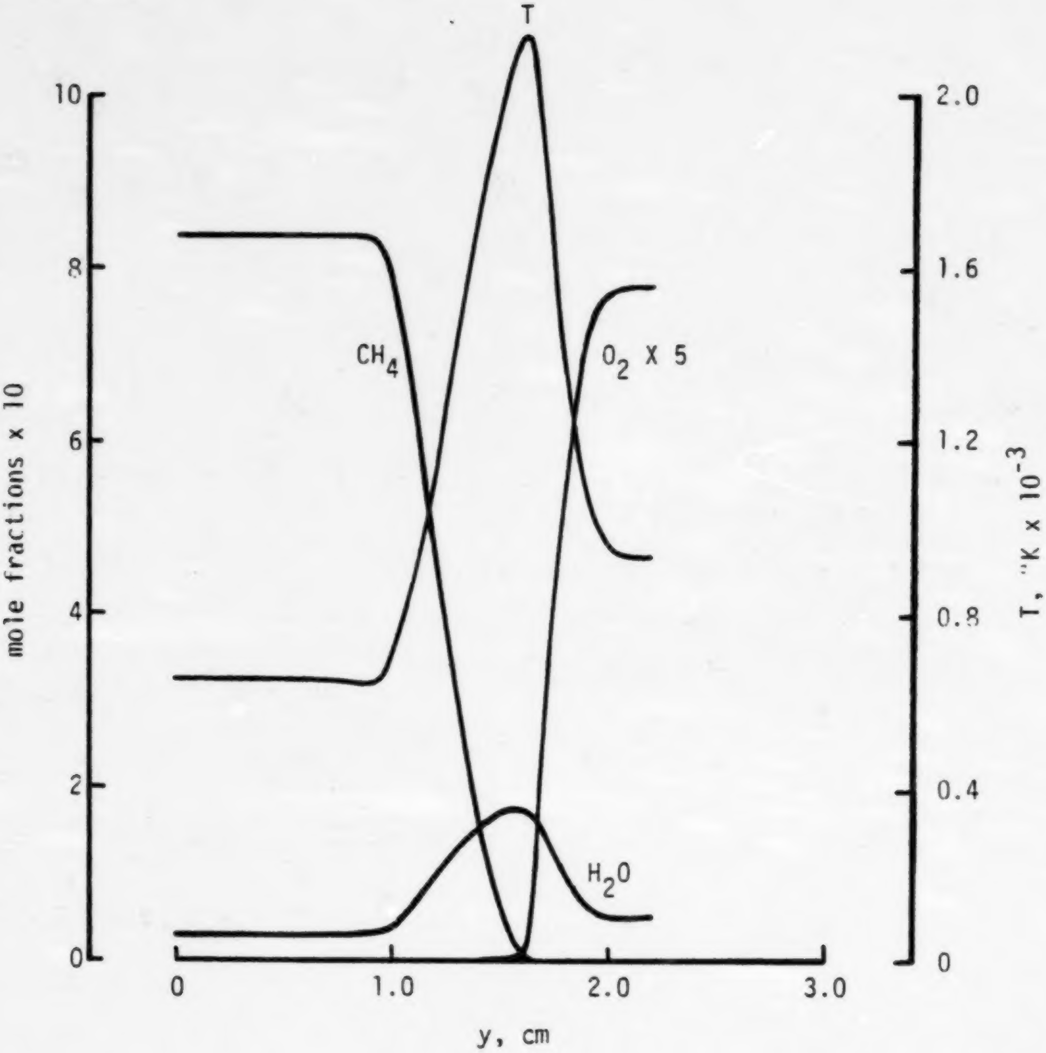

Figure B-9. Temperature, CH_4, O_2, and H_2O distributions in strained laminar methane-air flame; $\varepsilon = 50\ \text{sec}^{-1}$, $\kappa_1 = \kappa_2 = 0.75$.

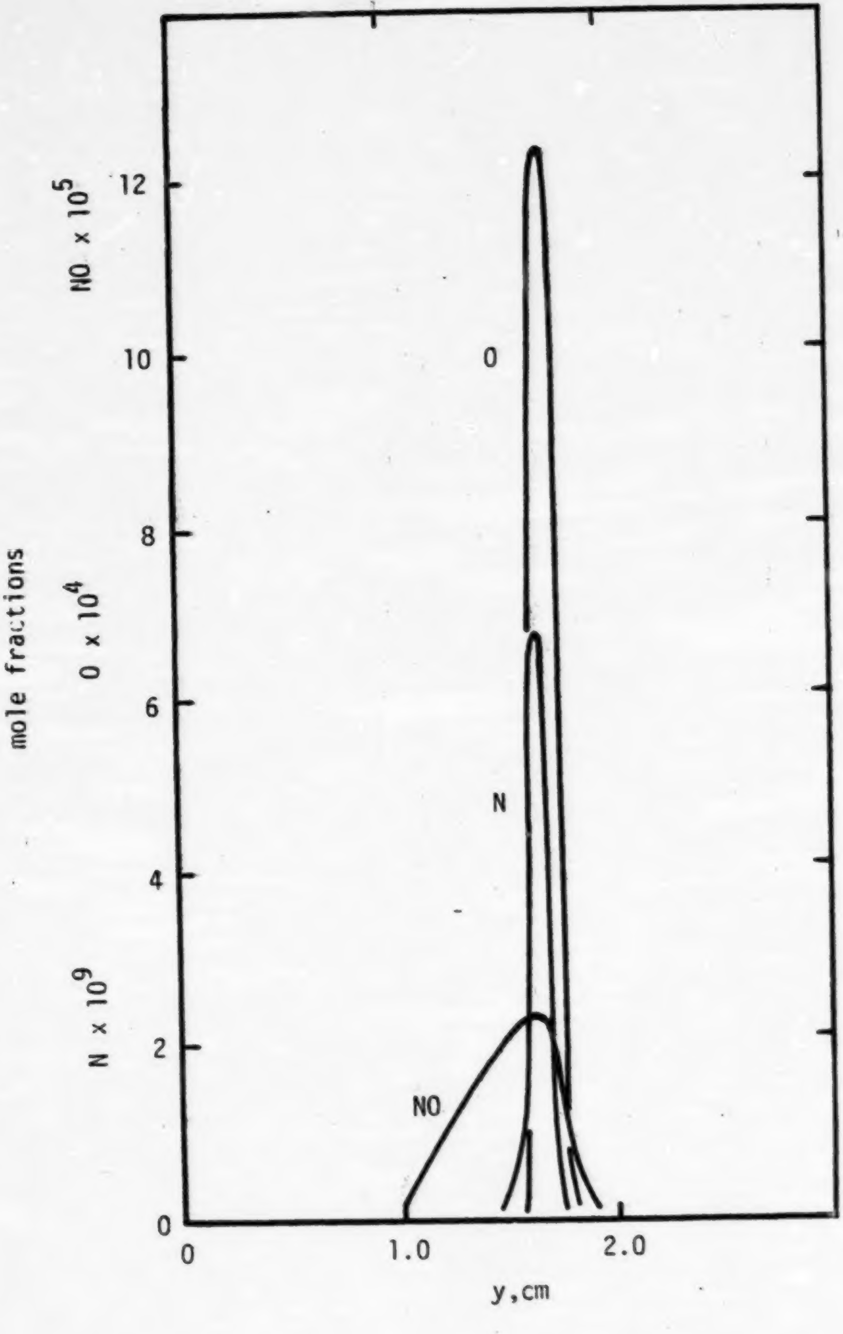

Figure B-10. O, N, and NO distributions in strained laminar methane-air flame; $\varepsilon = 50\ \text{sec}^{-1}$, $\kappa_1 = \kappa_2 = 0.75$.

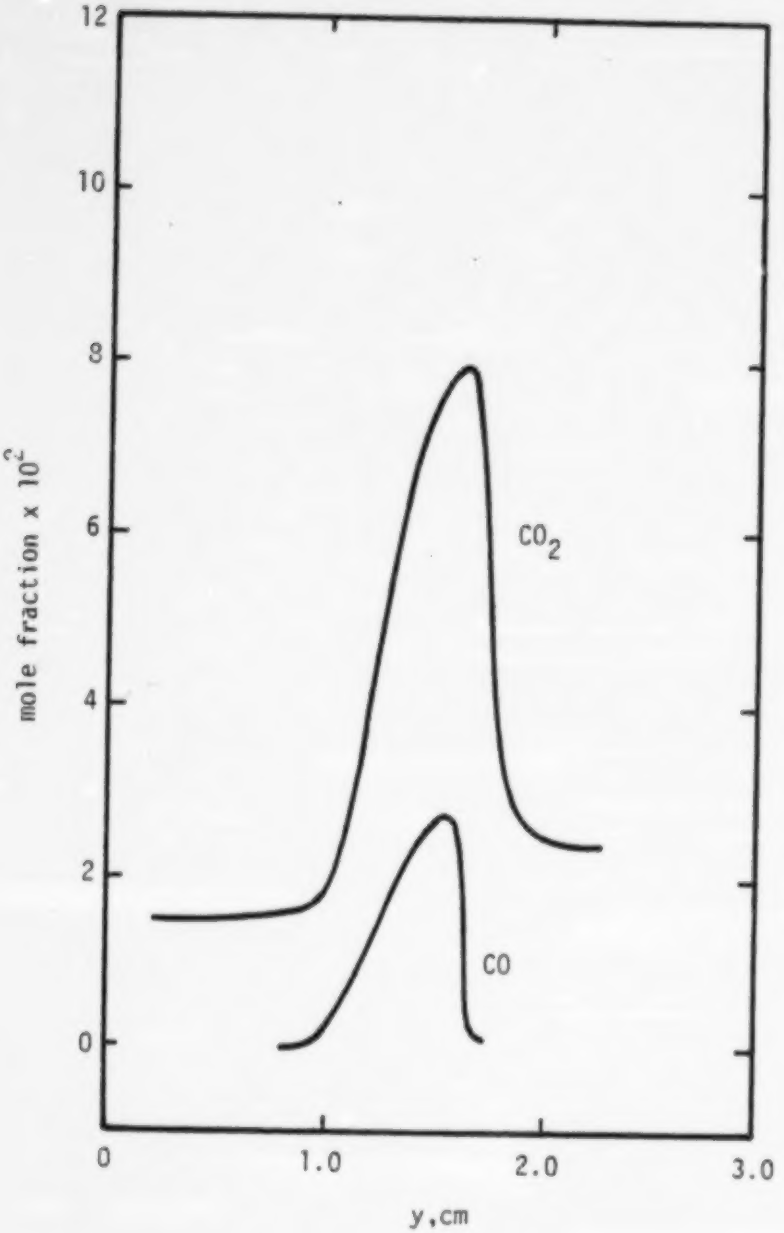

Figure B-11. CO_2 and CO distributions in strained laminar methane-air flame; ε = 50 sec^{-1}, $\kappa_1 = \kappa_2 = 0.75$.

GENERAL KINETIC ANALYSIS CODES

C. J. Kau and T. J. Tyson
Energy and Environmental Research Corporation
Irvine, California 92714

Fifth EPA Fundamental Combustion Research Workshop
Newport Beach, California
January 23-25, 1980

SECTION I

INTRODUCTION

The Fundamental Combustion Research Program (FCR) includes several program areas, one of these is concerned with the development and application of engineering analysis tools. It is intended that these tools will play a strong role in the following wide ranging areas:

- Data analysis
- Limit-case studies
- Modular modelling of complex systems
- Simple modelling of complex fluid mechanical behavior

A strong data analysis capability is required to extract the maximum amount of mechanistic information from the results of the experimental programs. In limit-case studies certain phenomena are assumed to dominate the process while other phenomena are suppressed in order to examine the implications of specific phenomenological behavior. Modular modelling implies the modelling of a complex system using a collection of limit-case elements linked together by means of empirical knowledge of the exchange of heat and mass between these elements. The motivation for semi-empirical modelling results from an inability to describe and couple all the phenomena present in a complex system in a single, unified, mathematical model. This is due to the limitation of numerical techniques and the poor understanding of turbulent transport. These simple models are under development to describe in a gross manner the fluid mechanical behavior of two phase turbulent flames.

This paper describes the development and capabilities of one analysis tool - a general kinetic analysis code. This code is capable of analyzing various types of premixed and diffusion flames. The generality of the code allows the computation of flame systems of various configurations (e.g. one-dimensional time dependent planar or spherical, steady two-dimensional planar, and steady axisymmetric non-recirculating reacting flow systems). Several phenomenological turbulent eddy viscosity models which are based upon mixing length theory have been incorporated into the code. The "chemistry package" is capable of treating up to 200 reaction steps involving up to 52 species.

SECTION II

CODE DESCRIPTION

The general kinetic analysis code is capable of describing two dimensional (or axisymmetric) laminar (or time averaged turbulent) boundary layer type flow with chemical reaction. The governing equations are developed from the complete Navier-Stokes equations by incorporating boundary layer assumptions as follows:

1. Momentum transfer in the main-stream direction is negligible when compared to the momentum transfer in cross-stream direction.
2. The momentum equation in the cross-stream direction is negligible when compared to that of main-stream direction.
3. Energy and mass diffusion in main-stream direction are negligible when compared to diffusion in the cross-stream direction.

The governing equations written in physical coordinates are:

Continuity Equation

$$\frac{\partial}{\partial x} (\rho u r^{\alpha}) + \frac{\partial}{\partial r} (\rho v r^{\alpha}) = 0 \tag{1}$$

Momentum Equation

$$\rho u \frac{\partial u}{\partial x} + \rho v \frac{\partial u}{\partial r} = - \frac{dp}{dx} + \frac{1}{r^{\alpha}} \frac{\partial}{\partial r} (\mu r^{\alpha} \frac{\partial u}{\partial r}) + \rho g_x \tag{2}$$

Species Equation

$$\rho u \frac{\partial \alpha_i}{\partial x} + \rho v \frac{\partial \alpha_i}{\partial r} = \frac{1}{r^{\alpha}} \frac{\partial}{\partial r} (\rho D_i r^{\alpha} \frac{\partial \alpha_i}{\partial r}) + \dot{w}_i \tag{3}$$

Energy Equation

$$\begin{aligned} \rho c_p \left(u\frac{\partial T}{\partial x} + v\frac{\partial T}{\partial r}\right) &= u \frac{\partial P}{\partial x} + \mu\left(\frac{\partial u}{\partial r}\right)^2 + \dot{q}_r + \frac{1}{r^{\alpha}} \frac{\partial}{\partial r} (\lambda r^{\alpha} \frac{\partial T}{\partial r}) \\ &+ \frac{\partial T}{\partial r} \sum \rho D_i \, C_{pi} \frac{\partial \alpha_i}{\partial r} - \sum_{i=1}^{k} h_i \dot{\omega}_i \end{aligned} \tag{4}$$

Equation of State

$$\rho = \frac{P}{82.06\ T \sum_i \alpha_i} \tag{5}$$

In equations 1 through 4, α is a geometric index. By setting α = 0, 1, or 2, the equations can be obtained in terms of two-dimensional cartesian, polar cylindrical, or spherical coordinates, respectively. By setting u = 1 and ignoring the momentum equation (Eq. 2), the equations become time-dependent one-dimensional and the x coordinate represents transient time.

The species equation (3) must satisfy the following conservation law

$$\sum_i M_i \alpha_i = 1.0 \tag{6}$$

which defines that the "sum of mass fractions equals to one," and for consistency, one of the species equations (Eq. 3) is replaced by Eq. 6. Another conservation law which must be satisfied is that "chemical reactions neither create nor destroy matter." Thus:

$$\sum_i M_i \dot{w}_i = 0 \tag{7}$$

Summing up Eq. (3) over all species and noting Eq. (6) and Eq. (7) we obtain the condition:

$$\sum M_i \rho D_i \frac{\partial \alpha_i}{\partial r} = 0 \tag{8}$$

This implies that not all the diffusion coefficients are independent; therefore, in actual calculation the diffusivity of the dominant species is not specified and the Eq. (6) is used to replace the species equation of the dominant species. The fifth right-hand term of the energy equation, Eq. (4), can be rewritten as:

$$\frac{\partial T}{\partial r} \sum_i \left[\left(C_{pi} - \frac{M_i}{M_R} C_{P_R} \right) \rho D_i \frac{\partial \alpha_i}{\partial r} \right] \tag{9}$$

which is the consequence of Eq. (8) and the subscript "R" refers to the dominant species.

The simplest and most common types of boundary conditions incorporated in the code are:

1. Zero order boundary condition: The known value of the dependent variable is specified at the boundary.
2. First order boundary condition: The first derivative (with respect to y-coordinates) of the dependent variable is specified.
3. Second-order boundary conditions: The second-order derivative (with respect to y-coordinate) of the dependent variable is specified.

For multicomponent laminar flow the viscosity and conductivity of the mixture are evaluated from component properties using the empirical formulations of Wilke and Wassilyewa (see Ref. 1). The code allows the estimation of multicomponent diffusivity from the binary diffusion coefficient of unlike molecules which requires extensive computational time. Diffusivities can also be estimated by the bifurcation approximation(2) which is less time consuming, but also less accurate. For turbulent flow system, the code includes two phenomenological eddy viscosity models; those of Ferri(3) and Schetz(4).

The code employs a linearized implicit finite difference network. Thus, all the dependent variables, except cross-stream velocity, of all the grid points at the same coordinate line (or at the same integration step) are solved simultaneously in coupled fashion. Thus, the inversion of a block tri-diagonal matrix is required at each integration step. This numerical scheme is so efficient that the computation required for a typical run is only about one tenth to one fifth of alternatives such as an implicit/explicit method(5) or an operator splitting method(6).

SECTION III

APPLICATIONS

Free Jet Diffusion Flame

The first example of the application of the general kinetic analysis code is a hydrogen-jet with maximum nozzle exit velocity of 1000 cm/sec which is issuing into still air. This same case was examined by Kee and Miller(6). The distributions of the initial velocity and the temperature profiled are shown in Figure 1. The ignition source is arbitrary and represents a small fraction of the input energy. The calculation was done in a physical coordinate system with uniform grid spacing in r-direction (initially with 25 grid points including two free-stream points).

The flame expands rapidly in the radial direction near the exit plane of the nozzle. Thus, the code allows the addition of grid points (at free-stream condition) whenever the "next-to-the-last" radial grid point value of temperature, velocity or species differ from the corresponding free-stream value by more than a specified percentage of free-stream value. The number of grid points is not allowed to grow unbounded, the number of points is halved (eliminate every other point) where maximum number of points (50) is reached. The reaction mechanism used in these calculations was a H_2-subset of the basic EER kinetic set(7) which involves 9 species (H_2, O_2, N_2, O, H, OH, H_2O_2, HO_2) and 18 reactions.

The numerical results of this calculation are shown in Figures 2 through 5. Figure 2 shows the flame isotherms. The flame length, which is defined by the peak temperature at the center line, is 5.8 cm. Figure 3 shows the distribution of downstream velocity and cross-stream velocity at a distance of 5 nozzle radii from exit plane. The distributions of major stable species and temperature (at $X/R = 5.0$) are plotted in Figure 4. It should be noted that the peak temperature is on the rich side of the flame and is very close to the calculated adiabatic flame temperature since flame radiation was not included. Distribution of radical species at the same axial location are plotted in Figure 5.

The entire calculation which extends 13 cm from the exit plane, takes 930 noniterative integration steps in the X-direction. The computer time is approxi-

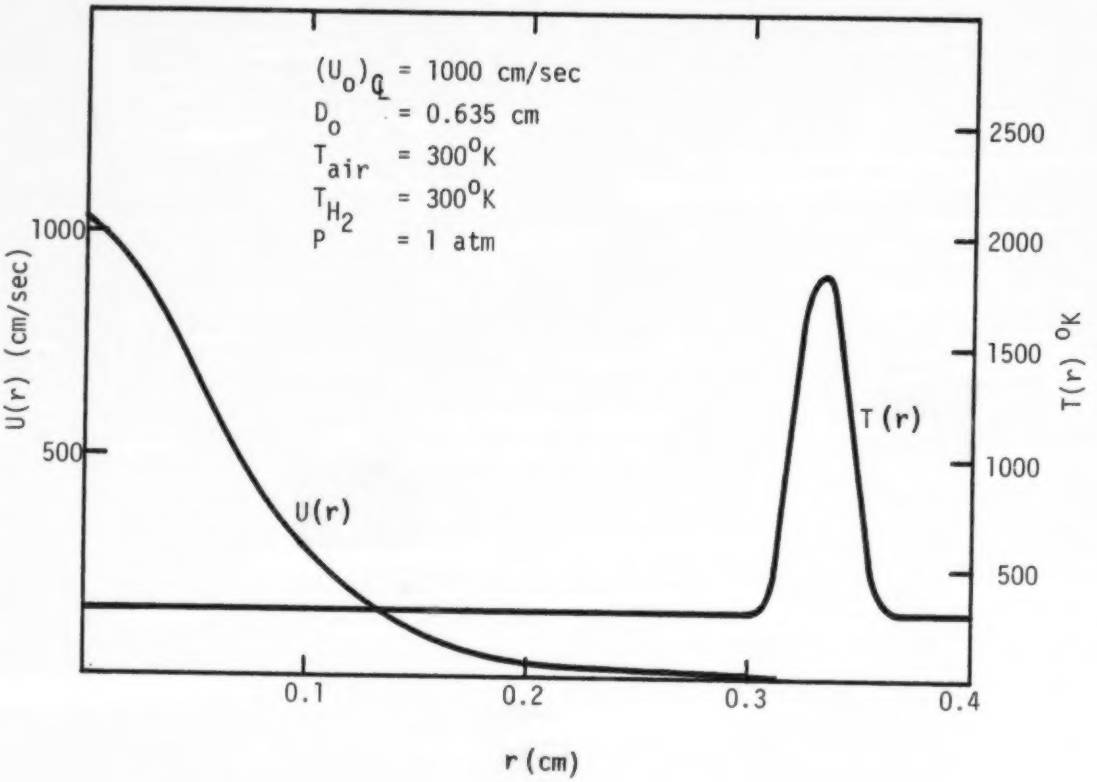

Figure 1. Initial Velocity and Initial Temperature Distribution.

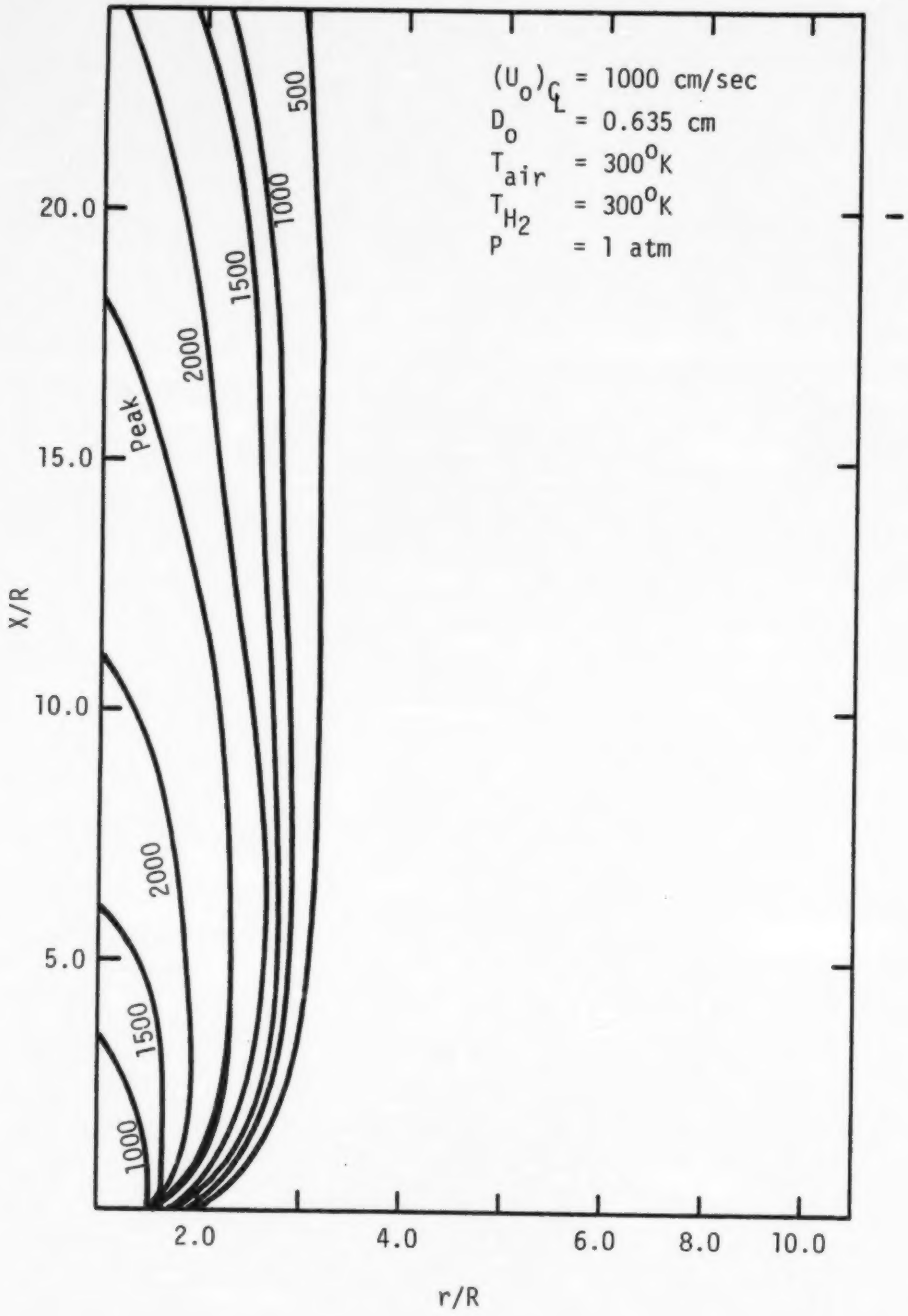

Figure 2. Isothermal Contours for Laminar H_2/Air Diffusion Flame.

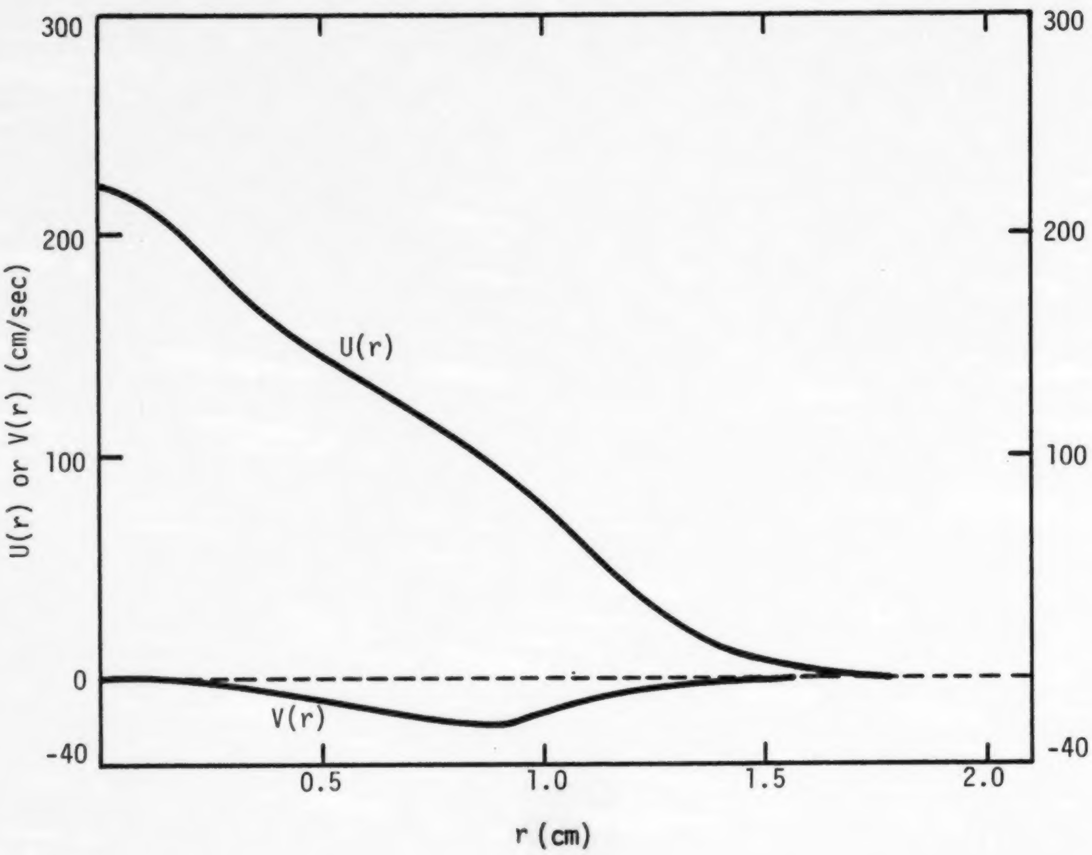

Figure 3. Velocity Components U(r) and V(r) at X/R = 5.0.

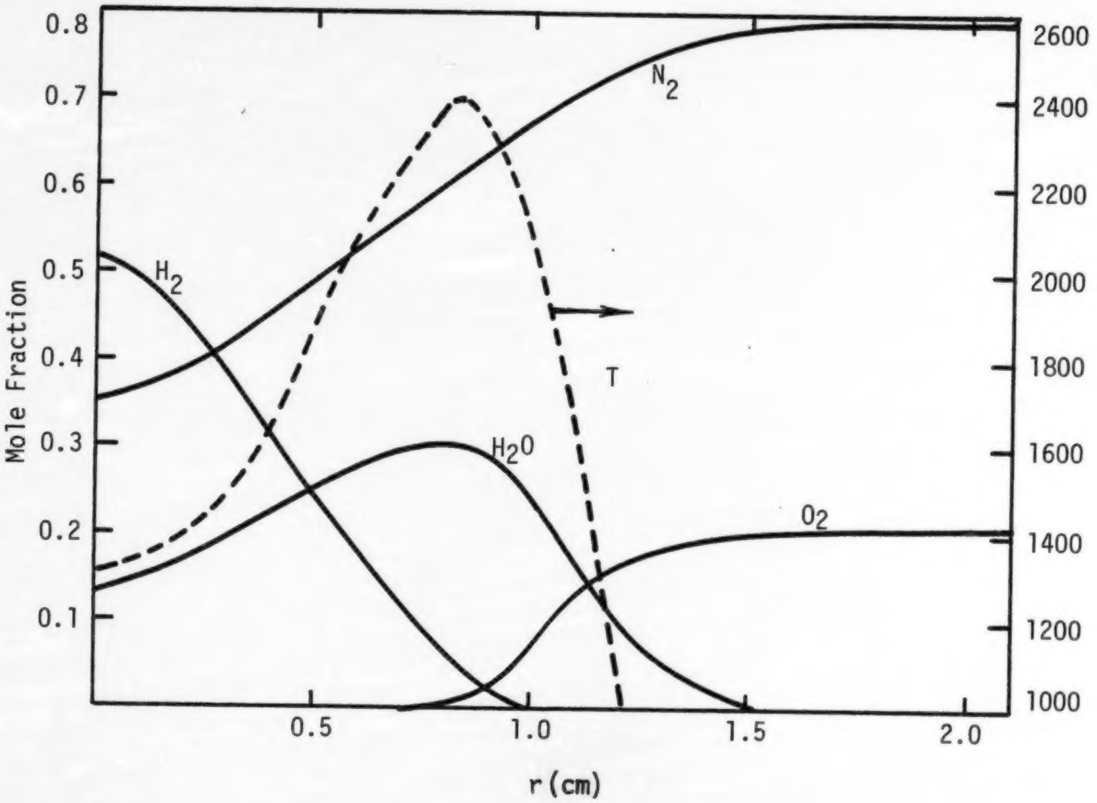

Figure 4. Distribution of Stable Species and Temperature at X/R = 5.0.

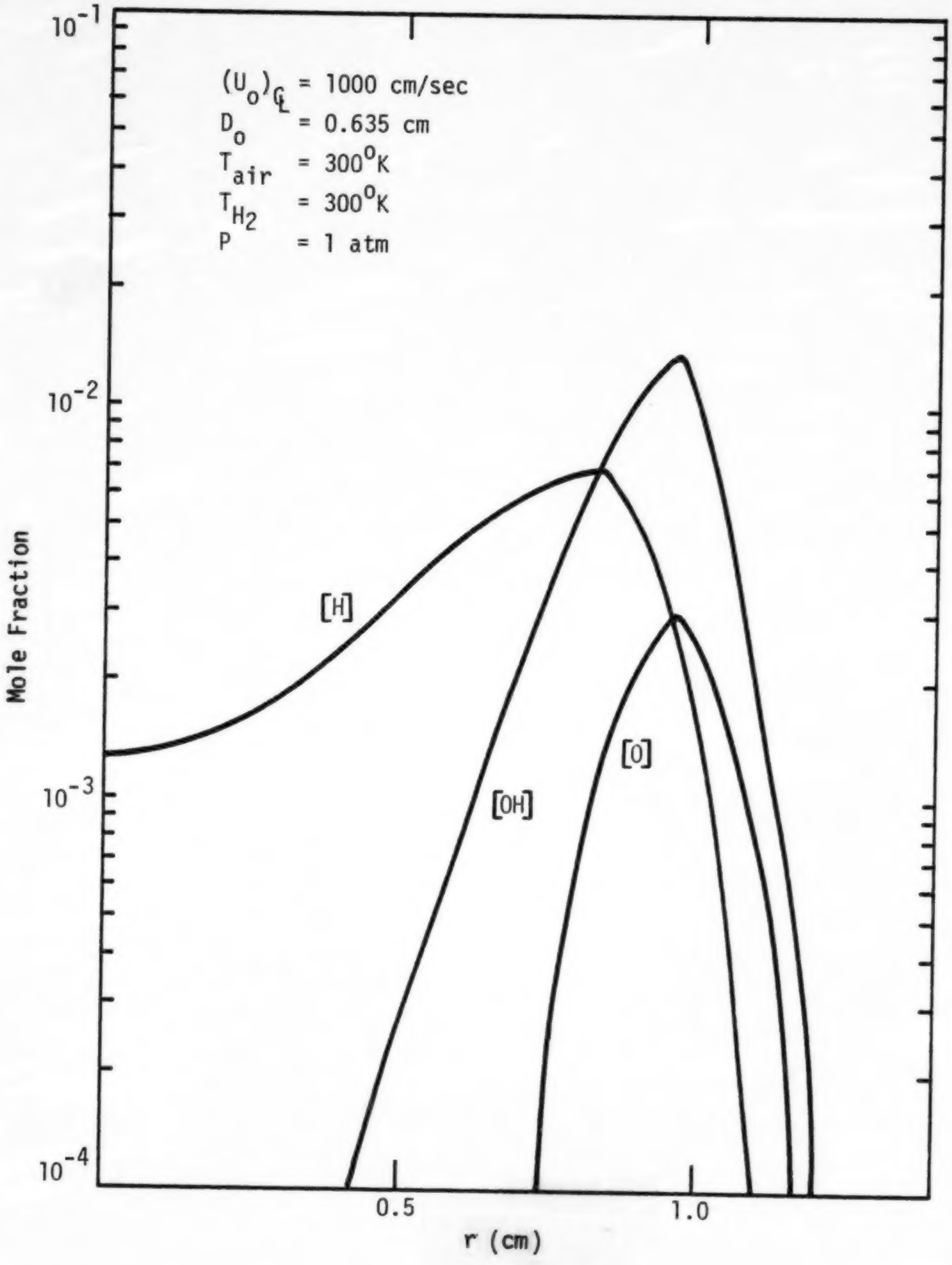

Figure 5. Distributions of Radical Species in an H_2/Air Diffusion Flame at X/R = 5.0.

mately 200 sec cpu time (CDC 7600 computer) which is equivalent to about one twentieth of the computational time used by Kee and Miller$^{(6)}$ for the same calculation using a split-operator method. The numerical results of the present calculation are expected to differ from those of Kee and Miller, since the formulation of diffusion coefficients and the reaction mechanism are different.

Fuel Nitrogen Conversion in Confined, Co-flowing Diffusion Flames

Under EPA Contract 68-02-2196 Clark et al$^{(8)}$ investigated fuel nitrogen conversion in simple diffusion flames of simulated low BTU gas (LBG). The parameters of interest were the methane content of the (LBG) and the form of the fuel nitrogen species, either NO or NH_3. The simulated LBG was a mixture of $CO/H_2/N_2$ doped with 3059 ppm of NO or NH_3. Table 1 lists the basic flame parameters of the examples investigated and Figure 6 presents a sketch of the experimental arrangement.

The predicted and measured exhaust level are compared in Figure 7 and 8 for NH_3 and NO doping, respectively. It can be seen that the kinetic mechanism$^{(7)}$ predicted exhaust values which are close to the measured level. The exhaust NO levels without dopant, i.e. thermal NO, also shown in Figures 7 and 8, do not agree perfectly with the experimental data. The discrepancy is due to the sensitivity of thermal NO level to the flame sheet temperature. The predicted flame temperature for the flame sheet of the flame with 10 percent CH_4 (in fuel) ranges from 1960^oK to 1720^oK and is sensitive to the accuracy of the heat transfer model.

Calculations were made for the NO doping case with 10 percent methane to establish the effect of flame temperature on fuel nitrogen conversion. Figure 9 shows the peak flame sheet temperature, total NO, and NO with the thermal contribution subtracted, as a function of increasing heat transfer, i.e., decreasing flame sheet temperature. Heat transfer increases linearly with the radiation index shown in Figure 9. The index has a value of zero for the adiabatic case and a value of one for the heat transfer associated with a simple radiation model. Although the peak flame sheet temperature varies by over 200^oK, the total NO level remains approximately constant. This is due to the increase of thermal NO production as the flame sheet temperature increases. If this thermal NO is taken into account the calculations indicate that fuel nitrogen conversion decreases significantly as the flame sheet temperature increases.

Table 1. Basic Flame Parameters

Case No.	1	2	3
Percent CH_4 in Fuel	0	5	10
Fuel Mean Velocity (cm/sec)	685	685	685
Air Mean Velocity (cm/sec)	13.15	17.53	21.92
Air Temperature (^oK)	367	367	367
Fuel Temperature (^oK)	367	367	367
Visual Flame Length (cm)	35.5	40.6	50.8

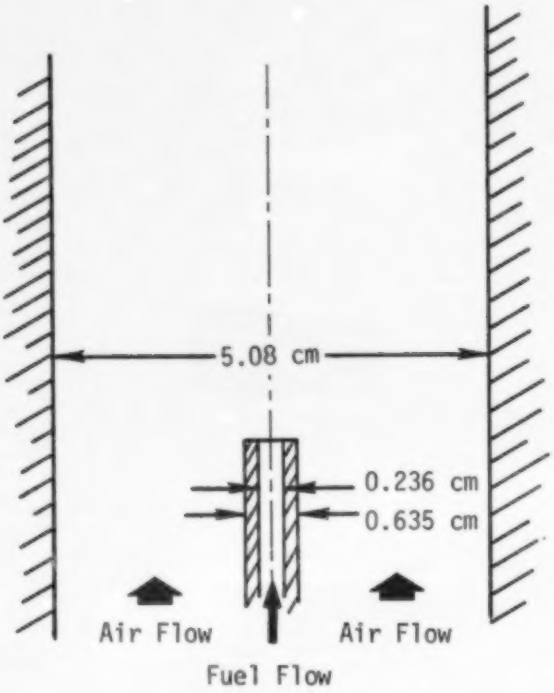

Figure 6. Diffusion Flame Burner.

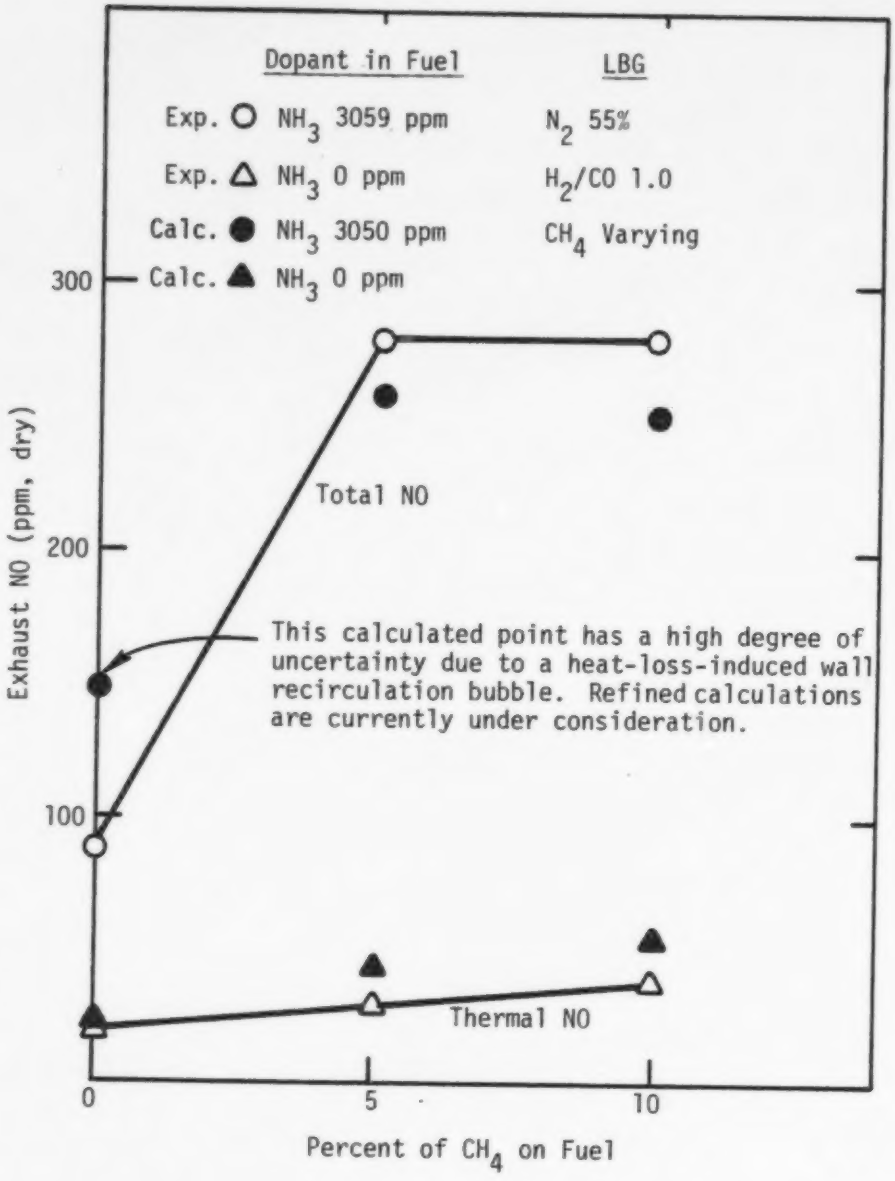

Figure 7. Influence of CH_4 Content on NH_3 Conversion in LBG Diffusion Flames.

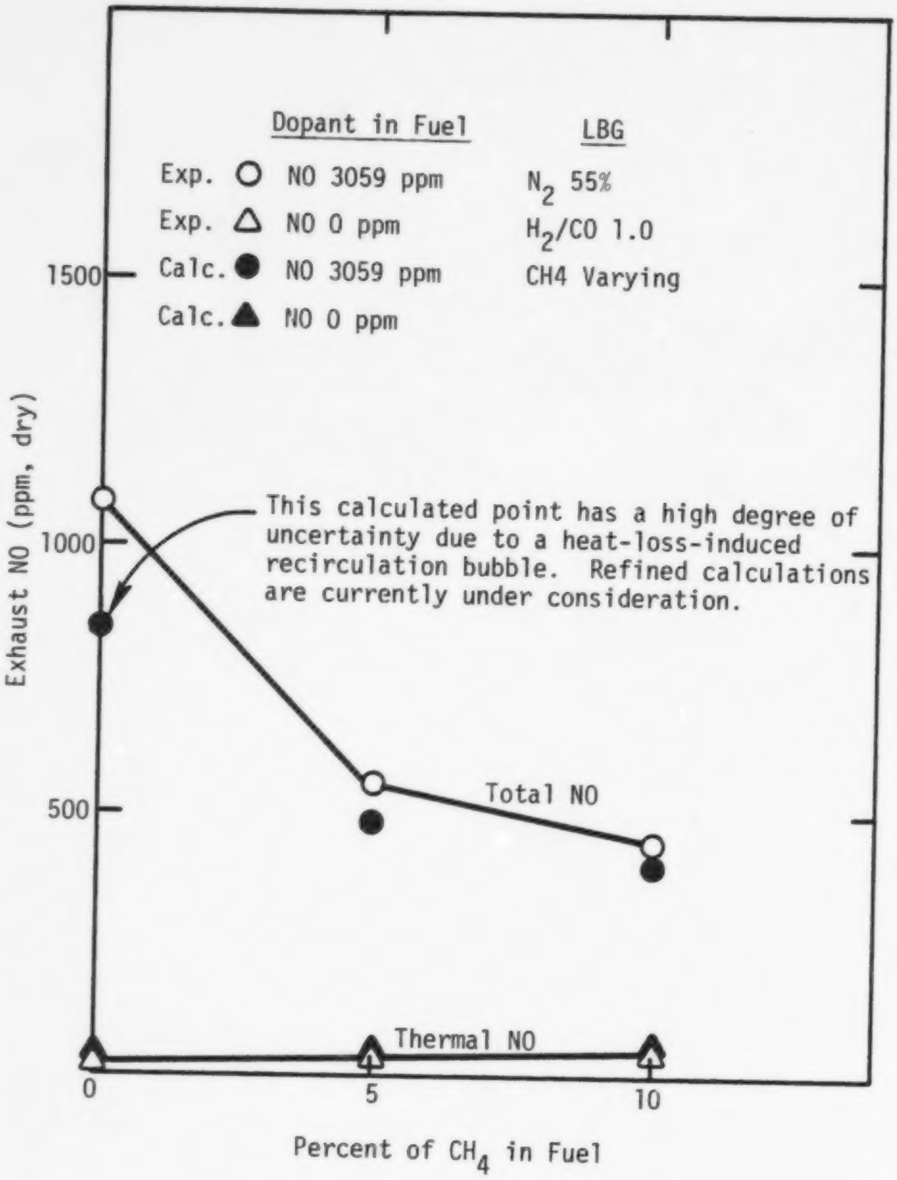

Figure 8. Influence of CH_4 Content on NO Conversion in LBG Diffusion Flames.

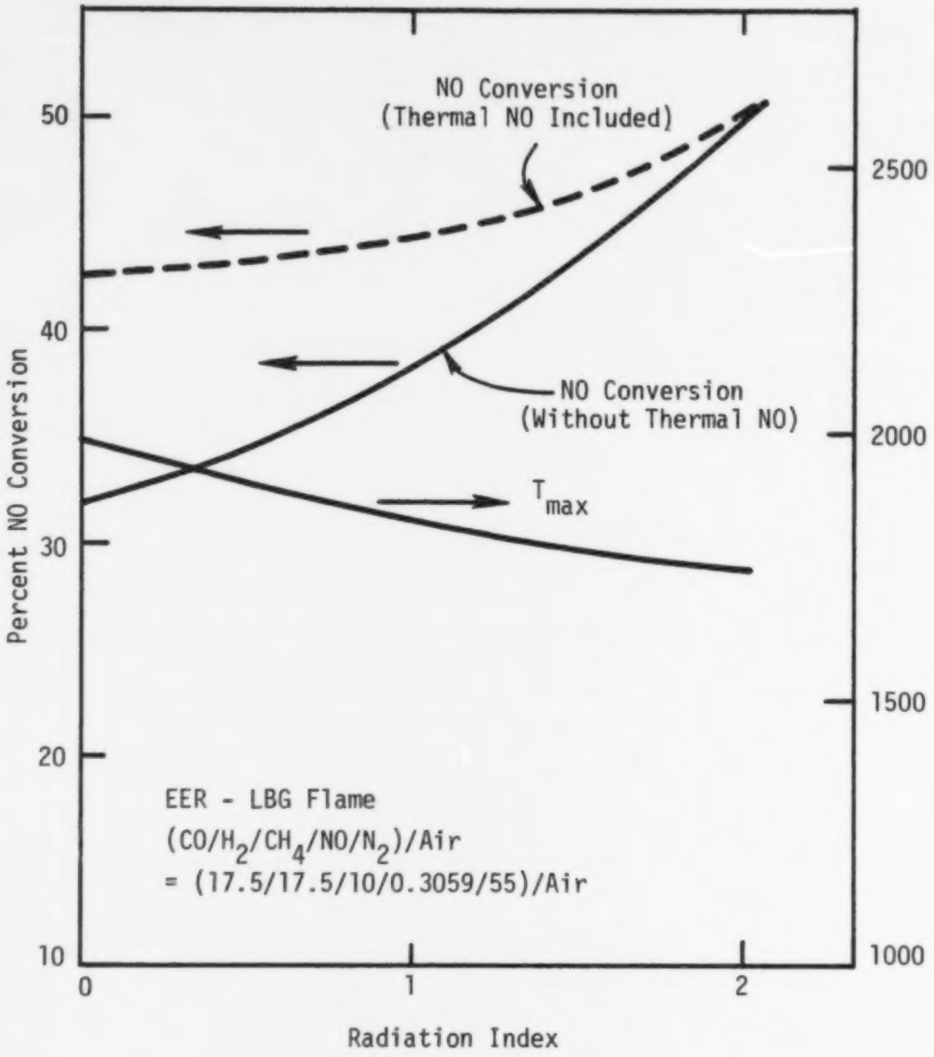

Figure 9 . Influence of Temperature on NO Conversion in Diffusion Flames--10 Percent CH_4.

Constant Strain-Rate Laminar Diffusion Flame

The constant strain-rate laminar diffusion flame refers to a planar non-premixed diffusion flame with external fuel and oxidizer flow undergoing uniform accelerations (e.g. $u = ax$) such that the strain rate, $\frac{du}{dx}$, is independent of position along the flame. This situation exists, for example, near the stagnation point in opposed-jet combustion. More importantly, it characterizes the flamelet behavior of the fuel/oxidizer "eddy" interface in a non-premixed turbulent flame. In those regions, the strain rate is slowly varying. It can be shown that the solution to the Navier-Stokes equation describing the behavior of a constant strain-rate, laminar diffusion flame is self-similar in the streamwise (x) direction and can be represented by the boundary layer equations under uniformly accelerating flow.

The general kinetic analysis code inherently contains the proper formulation for this class of problem. The computation can start with an arbitrary distribution and marches forward in the streamwise direction until a steady solution is achieved. The pressure gradient in the momentum equation is obtained from the Bernoulli equation in differential form, i.e.

$$\rho u \frac{du}{dx} = - \frac{dp}{dx} \tag{10}$$

by noting that the fuel side acceleration $u = ax$, and thus:

$$\frac{dp}{dx} = - \rho a^2 x \tag{11}$$

The sample calculation presented below is for a CH_4/air opposed jet diffusion flame (see Figure 10). The fuel side strain rate is set to be 250 $(\frac{1}{sec})$ and both fuel and air streams are at 300^oK and at atmospheric pressure. The velocity (v) profile for the steady solution is plotted in Figure 11. The displacement δ is the distance between the imaginary (nonreacting and invicid solution) stagnation points of the fuel and air jets. For this case δ is 0.15 cm. The CH_4, O_2 and temperature profiles are shown in Figure 12. The peak flame temperature is about 1950^oK. This peak temperature decreases with increasing strain rate since the higher the strain rate the thinner the flame zone and the shorter the effective residence time of the reactants in reaction zone. Figure 13 shows the flame temperature as a function of strain rate. A critical value of strain rate is shown to be 650 $(\frac{1}{sec})$ beyond which a flame cannot exist

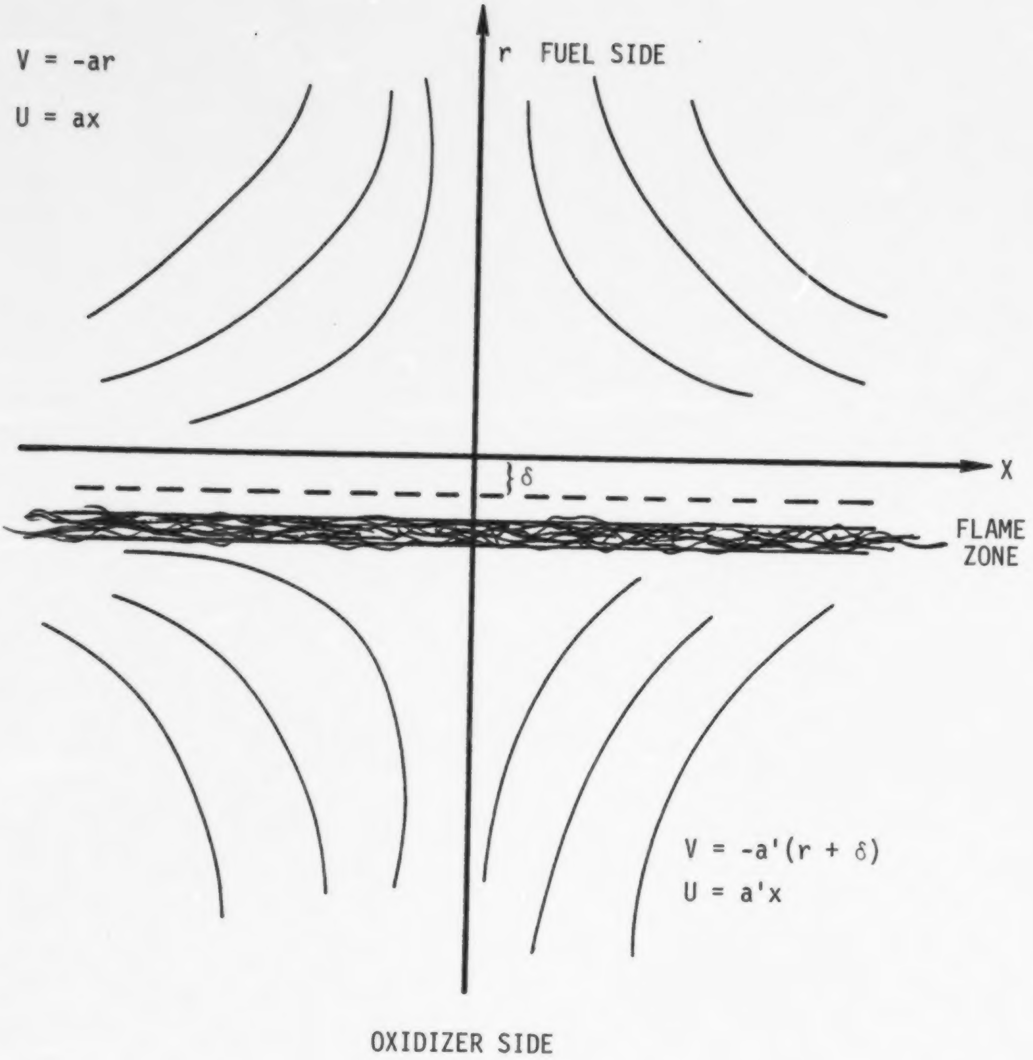

Figure 10. Schematic of Opposed-Jet Diffusion Flame.

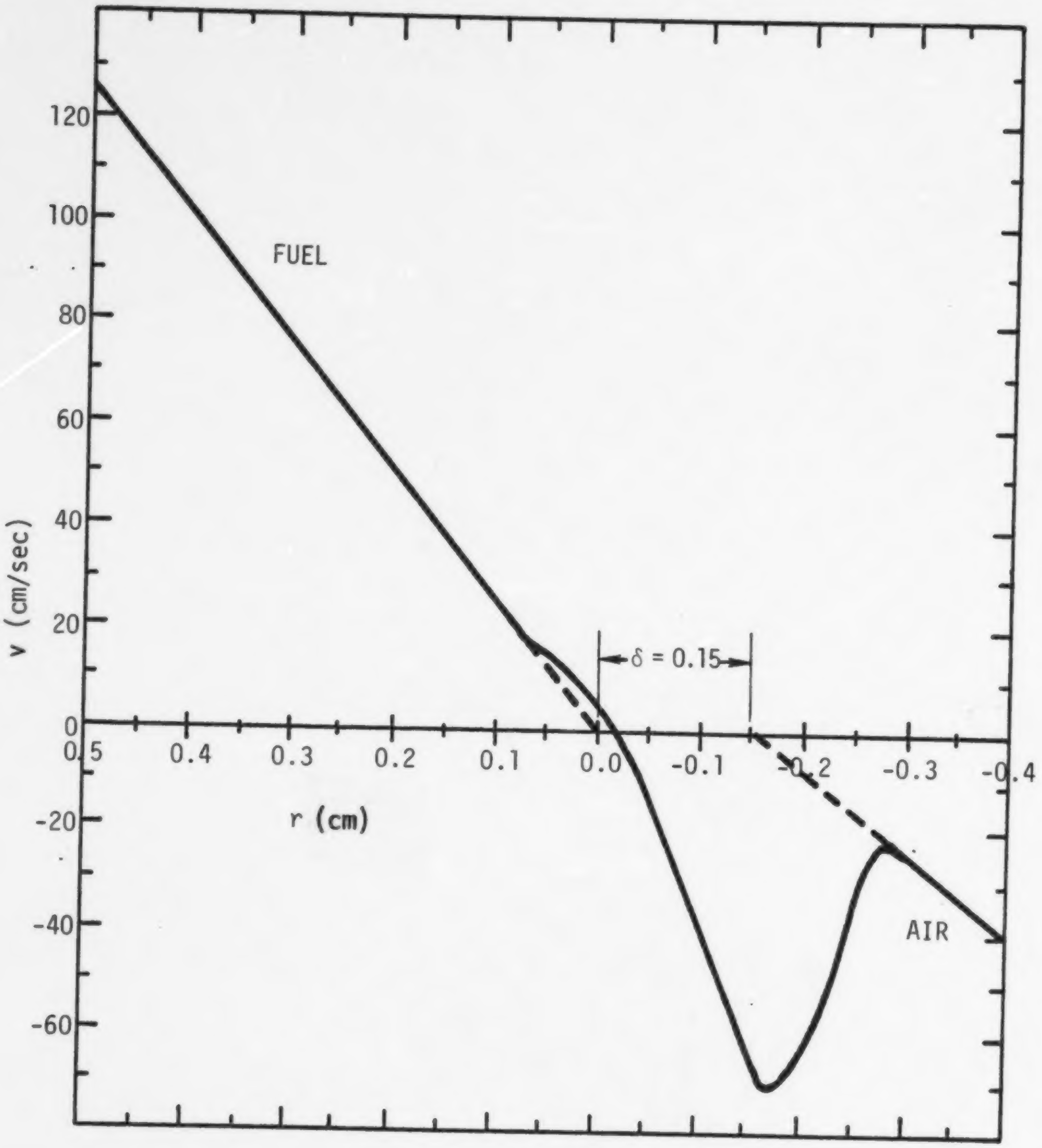

Figure 11. Velocity Profile of CH_4/Air Opposed-Jet Diffusion Flame (a=250 1/sec).

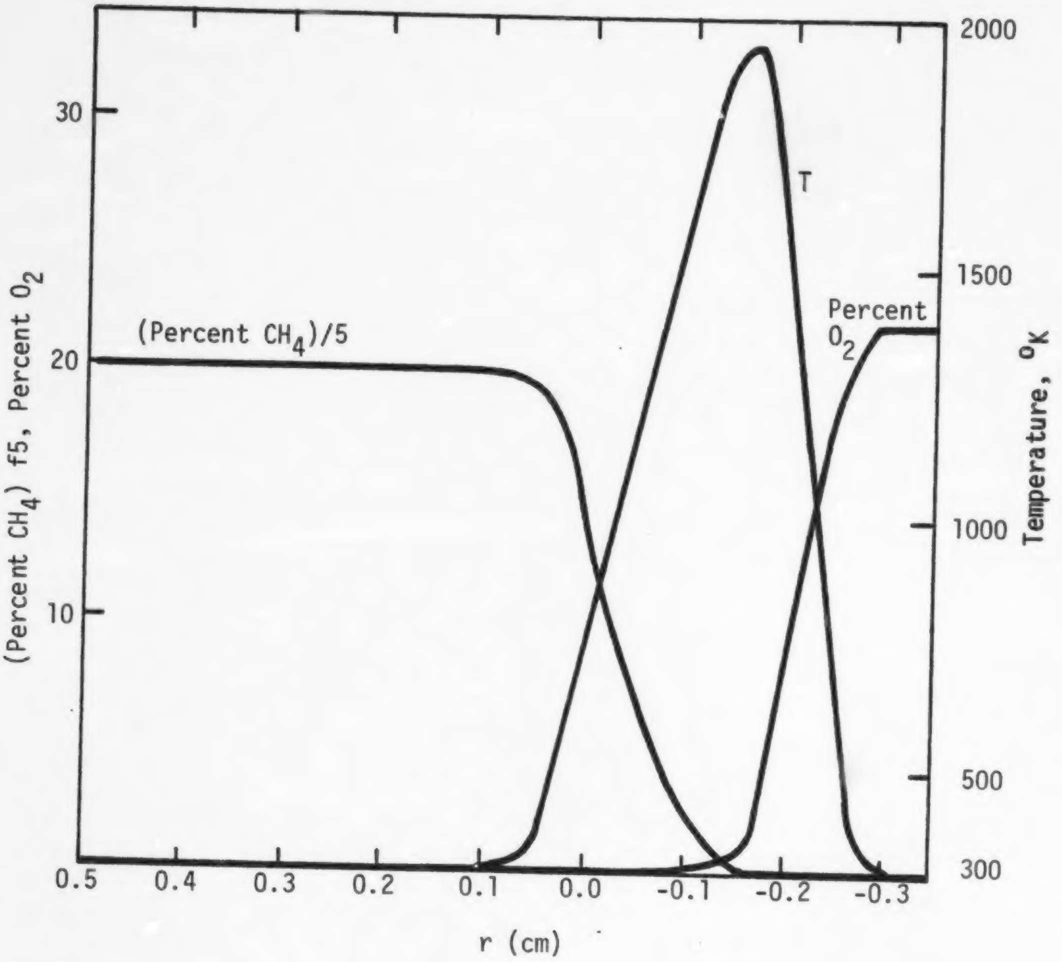

Figure 12. CH_4 and O_2 Profiles of CH_4/Air Opposed-Jet Diffusion Flame (a=250 1/sec).

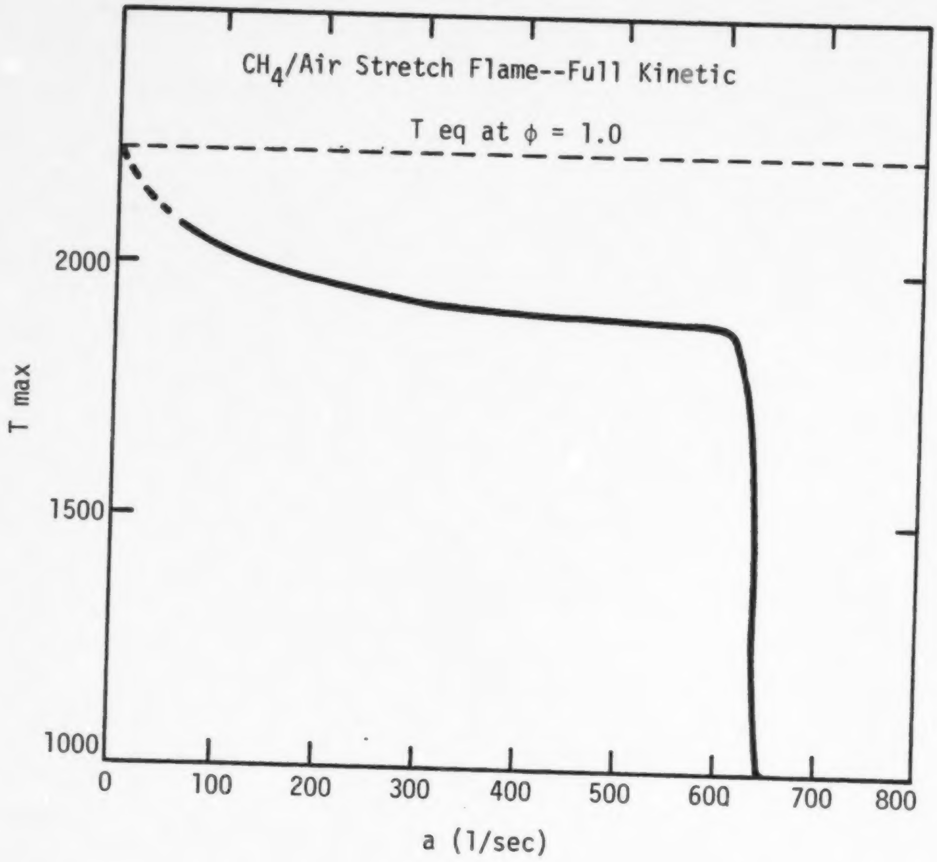

Figure 13. Flame Temperature vs. Strain Rate for CH_4/Air Opposed Jet Diffusion Flame.

(i.e. the extinction limit). This critical value is a function of reaction chemistry only and is independent of molecular transport coefficient (i.e. independent of Reynolds number). This is due to the fact that the molecular transport coefficient (e.g. viscosity) influences the solution only through an affine transformation of the r coordinate, i.e. $\eta = r \sqrt{\frac{a}{\nu}}$. The self-similar solution of temperature and species concentration are functions of η only. Viscosity affects flame thickness and therefore the total burning rate.

The computations are carried out by using a subset of the basic EER kinetic mechanism(7) including 71 reaction and 28 species. The computational time per case is approximately 4 minutes CPU time on a CDC 7600. Further results obtained with this model have been reported in the previous paper in this symposium volume.

SECTION IV

CONCLUSION

A computer code which is capable of analyzing various types of premixed and diffusion flames has been developed. The generality of the code allows the computation of various flame system configurations such as one dimensional time dependent spherical or plane systems or steady axisymmetric non-recirculating reacting flows. Physical phenomena such as laminar unequal species diffusivities, radiation heat loss and flame holder recombination effects are included. The code contains two turbulent eddy viscosity models based upon mixing length theory. The kinetic package can treat up to 200 reactions involving 52 species. The code employs a linearized implicit finite difference network which enables the use of an extremely efficient numerical scheme. The code has been exercised against several test cases including flat flames, opposed jet diffusion flames and simple co-flowing diffusion flames.

REFERENCES

1. Reid, R. C., Prensnitz, J. M., and Sherwood, T. K., "The Properties of Gases and Liquids," 3rd Edition, 1977.
2. Bartlett, E. P., Kendall, R. M., and Rindal, R. A., "A Unified Approximation for Mixture Transport Properties for Multicomponent Boundary Layer Applications," NASA CR-1063, 1967.
3. Ferri, A. J., "Review of Problems in Application of Supersonic Combustion," J. Roy. Aeron. Soc. 68 p. 575, 1964.
4. Schetz, J. A., "Turbulent Mixing of a Jet in Co-Flowing Stream," AIAA, Vol. 6, No. 10, 1968.
5. Kau, C. J., Pergament, H. S., and Mikatarian, R. R., "A New Computational Technique for Chemically Reacting Free-Shear Layer Flows," Symposium on Application of Computers to Fluid Dynamic Analysis and Design," Polytechnic Institute of Brooklyn, N.Y., Paper 4A(4), 1973.
6. Kee, R. J., and Miller, J. A., "A Split-Operator, Finite Difference Solution for Axisymmetric Laminar Jet Diffusion Flames," Sandia Laboratories, Livermore, CA, Report No. SAND 77-8502, 1977.
7. Corley, T. L., "Development of a Kinetic Mechanism to Describe the Fate of Fuel Nitrogen in Gaseous Systems," this volume.
8. Clark, W. D., et al, "Combustor Concepts for Advanced Power Generating Systems Firing Low Btu Gas," EPA Contract No. 68-02-2196.

LIST OF NOMENCLATURE

C_{pi} : specific heat of species i

D_i : diffusion coefficients $(\frac{cm^2}{sec})$

M_i : molecular weight of species i

P : pressure

P_i : partial pressure of species i

$\dot{q}_r$: radiative heat transfer rate $(\frac{cal}{cm^3\text{-}sec})$

r : cross-stream coordinate (cm)

T : temperature (^oK)

u : downstream velocity (cm/sec)

v : cross-stream velocity (cm/sec)

$\dot{W}_i$: chemical production rate $(\frac{mole}{cm^3\text{-}sec})$

x : downstream coordinate (cm)

y : cross-stream coordinate

Superscripts

i : equation index

Subscripts

i : species index

R, r : reference species

Greek Symbols

α : geometric index

α_i : ith species concentration ($\frac{\text{mole}}{\text{gm}}$)

ρ : density ($\frac{\text{gm}}{\text{cm}^3}$)

λ : heat conductivity (cal/cm-sec-$^{\circ}$K)

μ : molecular/turbulent viscosity